The Role of Displacement Damage in Irradiation Affected Corrosion of 316L Stainless Steel

By

Rigel D. Hanbury

A dissertation submitted in partial fulfillment
of requirements for the degree of
Doctor of Philosophy
(Nuclear Engineering and Radiological Sciences)
in The University of Michigan
2022

Doctoral Committee:

Professor Gary S. Was, Chair
Professor Fei Gao
Dr. Jonas Heuer, Naval Nuclear Laboratory
Professor Katsuyo S. Thornton
Dr. Peng Wang

Rigel Hanbury

rigelh@umich.edu

ORCID iD: 0000-0003-1839-3503

Acknowledgements

I thank my advisor, Dr. Gary Was, for many hours spent reading my writing and discussing my research. His knowledge of the field, keen intuition, and clarity have greatly benefitted me and my research. I also thank the members of my committee: Dr. Fei Gao, Dr. Katsuyo Thornton, Dr. Peng Wang, and Dr. Jonas Heuer.

I am greatly appreciative of the many members of the Was research group for their support, contributions, and friendship: Dr. Kale Stephenson, Dr. Shyam Dwaraknath, Dr. Stephen Raiman, Dr. Elizabeth Getto, Dr. Anthony Monterrosa, Dr. Justin Hesterberg, Dr. Stephen Taller, Dr. Gerrit VanCoevering, Dr. Drew Johnson, Dr. David Woodley, Dr. Peng Wang, Dr. Miao Song, Dr. Mi Wang, Dr. Wenjun Kwang, Dr. Kiran Mandapaka, Dr. Calvin Lear, Dr. Donghai Du, Dr. Kai Chen, Dr. Lijin Dong, Dr. Srinivasan Swaminathan, Rajan Bhambroo, Samara Levine, Robert Whalen, Katey Thomas, Valentin Pauly, Logan Clowers, and Abdullah Alsinglawi.

I also thank the Michigan Ion Beam Laboratory staff, Dr. Ovidiu Toader, Dr. George Jiao, Dr. Fabian Naab, Dr. Ethen Uberseder, Dr. Kai Sun, Thomas Kubley, Robert Hensley, Prashanta Niraula, who made my experiments possible and provided support in the late hours of the night. Thanks to the Nuclear Engineering and Radiological Sciences department staff Peggy Gramer, Garnette Roberts, and Jennifer Melms. Thanks to the staff at the Michigan Center for

Materials Characterization, Dr. Haiping Sun, Dr. Allen Hunter, Dr. Tao Ma, and Dr. Bobby Kerns. Thanks to Dr. Adam Matzger for the use of the Raman Spectrometers.

Thanks to my parents, Patricia and Jonathan Hanbury, for their unconditional love and support. Thanks to my brother, Orion Hanbury, for being a true friend I can always talk with.

A special thanks to Stephen Taller without whom this dissertation would not have been possible. Your passion and drive have always been inspiring to me.

I also thank the financial support of the University of Michigan College of Engineering and NSF grant #DMR-0320740 and EDF Contract No. 8610-5920005571. This research was performed under appointment to the Rickover Fellowship Program in Nuclear Engineering sponsored by Naval Reactors Division of the National Nuclear Security Administration.

Table of Contents

List of Tables

List of Figures

List of Appendices

Abstract

The objective of this research is to determine the effects of radiation-induced displacement damage on the corrosion of 316L stainless steel in high temperature water. The benchmark experimental approach was to transmit 5.4 MeV protons through 316L stainless steel and into an autoclave containing 320 °C water. The displacement damage rate is set to a nominal 7×10^{-7} dpa/s, and the resulting radiolysis-inducing dose rate is 650–700 kGy/s. To separate the effects of water radiolysis from displacement damage, a specialized sample geometry and steam environment were employed. 316L stainless steel bars were placed in the autoclave with a face parallel to the proton beam to receive exposure to similar levels of water radiolysis with negligible displacement damage. Steam at 480 °C with a low partial pressure of water yields a low water radiolysis with less than 1 kGy/s while keeping the 7×10^{-7} dpa/s damage rate. Irradiation-corrosion exposures of 316L were performed in both steam and water for 24 h and 72 h, and the different irradiated conditions were compared to oxide films from non-irradiated regions of the same sample. Oxide films were characterized by Raman spectroscopy, scanning electron microscopy, scanning transmission electron microscopy, and energy dispersive X-ray spectroscopy.

The thermodynamics of the corrosion system in both water and steam was modelled to compare with experimental results and provide a basis for corrosion kinetics models. A new concept of excess volume was devised to explain the stability of inner oxide porosity in different environments. Porosity measured experimentally and excess volume were found to correlate well

with corrosion rates observed; however, solid state diffusion through the oxide layer predicts a reverse trend between corrosion rate and oxygen activity from non-irradiated observations. The rate-limiting step for most corrosion in this work was found to be oxygen transport to the metal/oxide interface via pores.

Radiolysis had the effect of increasing the system oxygen activity, reducing the corrosion rate, and causing inner oxide dissolution. The increased oxygen activity reduces excess volume which results in lower corrosion rates from decreased porosity despite the active dissolution of the protective oxide layer. In steam, radiolysis was found to have no effect on the corrosion rate because the quantity was reduced as designed.

Displacement damage effects were found to be dependent on the environment. In radiolyzed water, displacement damage had no significant effect on the corrosion rate because stable pore growth was limited by the reduced excess volume. Because solid state diffusion was not rate-limiting, radiation enhanced diffusion had no measurable effect. In steam, however, displacement damage caused a large increase in the corrosion rate and a corresponding increase in inner oxide porosity. Therefore, the role of displacement damage is to increase the size of pores in the inner oxide layer, but only where pore formation is thermodynamically favored. Porous inner oxides are more permeable to oxygen which increases the corrosion rate through elevated oxygen penetration to the metal.

Chapter 1

Introduction

Nuclear power must play a critical role in mitigating climate change by reducing carbon emission in electricity production. Nuclear power plants have the best features of both fossil fuel plants and renewable energy sources: reliable baseload electricity production with zero primary carbon emissions. As energy storage and renewable energy technologies are developed, nuclear power can serve as a bridge to a clean energy future. To this end, research efforts must support the maintenance and operation of current reactors in addition to the design and construction of new reactors.

Safe and reliable operation of nuclear power plants depends on mitigating deleterious effects of corrosion and radiation on materials. Commercial nuclear reactors in the United States are a fleet of aging light water reactors (LWRs), and many are seeking life extensions from the Nuclear Regulatory Commission (NRC). Life extensions require assurances of an additional 20 years of safe operation which depend on prediction and prevention of component failure. Beyond LWRs, many advanced reactor designs use more corrosive coolants and higher temperatures, such as molten salt, which will require tighter corrosion controls for NRC licensing. Excessive corrosion problems can result in a temporary reactor shutdown or, if severe, decommissioning. Therefore, managing corrosion is foundational for the nuclear power industry.

In reactors, a major corrosion failure mechanism is stress corrosion cracking (SCC) of core components. The radiation environment of a nuclear reactor core accelerates material failure

by irradiation assisted stress corrosion cracking (IASCC). IASCC is a complex phenomenon consisting of many interdependent variables and has defied full understanding despite decades of research. Corrosion is a key component of SCC, and mechanistic understanding of radiation effects on corrosion provide foundational knowledge for IASCC. Furthermore, knowledge of radiation effects on corrosion has applications beyond IASCC, such as nuclear waste storage, and will benefit the nuclear community in the design, construction, and maintenance of new and old reactors alike. This work will focus on radiation effects on aqueous corrosion because water is the coolant for most operating reactors.

Improved understanding of radiation effects on corrosion will enable better material and water chemistry choices for the design and operation of LWRs. One example of how this research may impact the industry is by reducing the release of ^{60}Co from the core into the primary loop. Release of ^{60}Co is directly related to the total corrosion rate of Ni-containing core materials and the solubility of ^{60}Co in primary water [1]. Because radiation impacts both water and materials in the core, ^{60}Co release is affected by the interaction between radiation and corrosion. Therefore, materials can be selected with better radiation corrosion properties, and water additives can be adjusted to reduce the dissolution of ^{60}Co to reduce the dose rate for workers. More generally, corrosion-driven phenomena can be mitigated through design and operational choices that are informed by the radiation effects on corrosion for both existing and new LWRs.

Radiation effects on corrosion in a LWR environment can be divided into two categories: radiolysis of water and radiation damage in the solid. Water radiolysis can change the oxidation potential of the water thereby influencing the thermodynamics of corrosion. Radiation damage is atomic rearrangement caused by energetic particle collisions which generate point defects inside

the material, enhancing diffusion. Larger defects are generated through the cumulative motion of point defects, and they affect macroscopic properties like mechanical behavior and corrosion rate. Radiation damage may further affect corrosion by generating defects and enhancing diffusion in a passive oxide scale. Without simultaneous irradiation during corrosion, the synergistic effects of radiation and corrosion will not manifest.

Radiation effects on corrosion are difficult to study due to experimental limitations in combining radiation and corrosion environments. Residual radioactivity of material harvested from nuclear reactors makes characterization difficult and expensive. Compared with laboratory settings, reactor environments are not strongly controlled and poorly measured, leading to high variability and uncertainty in exposure conditions. For these reasons, ion accelerator laboratory experiments may be preferred for speed, accuracy, cost, and safety of sample handling. By separating the water and accelerator with a foil of sample material, in situ proton irradiation corrosion experiments can simulate both reactor radiation and water environments. Proton transmission through the sample material produces radiation damage inside the foil in addition to water radiolysis at the corrosion surface.

Proton irradiation is used to emulate reactor radiation for several reasons. Protons have similar mass to neutrons, so momentum transfers in ballistic collisions are comparable to a reactor. Fast neutrons also have a high collision cross-section with hydrogen, so a spectrum of energetic protons is present in LWR cores. Protons, being the lightest ion, have the longest range in any material, and this allows them to most easily transmit entirely through a thin foil sample.

The objective of this work is to provide a better understanding of how radiation affects the corrosion of stainless steel in high temperature water using in-situ proton irradiation.

Chapter 2

Background

Irradiation assisted corrosion (IAC) is a complex phenomenon caused by the intersection of a material, water chemistry, and radiation. Understanding the constituent processes of corrosion, displacement damage, and water radiolysis is necessary to gain understanding of their combination. Each of these topics are discussed in this chapter using Figure 2.1 as a roadmap. Each section attempts to compare this work with reactor conditions to keep the research grounded in practical applications.

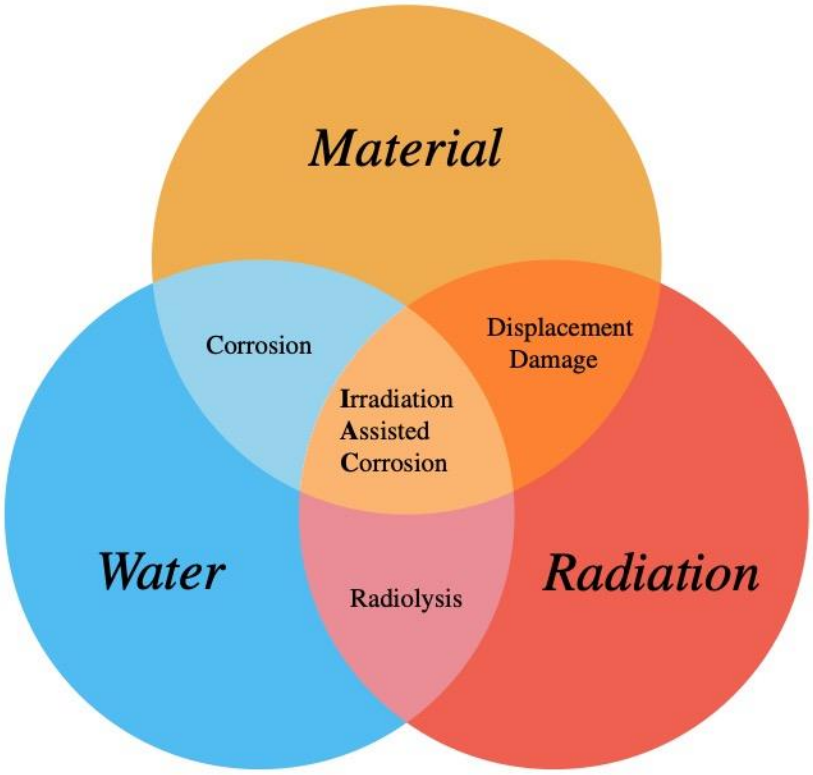

Figure 2.1. Venn diagram of irradiation assisted corrosion.

2.1. Stainless Steel

A brief examination of the properties of stainless steel, specifically 316L, is necessary to understand its behavior in both a corrosive environment and under irradiation. Alloys are primarily described by elemental composition and secondarily by the fabrication and processing steps that yield the microstructure. Both aspects are important for corrosion and radiation response, so each will be discussed in the following subsections.

2.1.1. Composition and Structure

The alloy used in this work, and commonly used in nuclear applications, is 316L stainless steel, so focus will be placed on this alloy. 316L and many other grades of stainless steels are defined by the American Iron and Steel Institute (AISI) and the American Society for Testing and Materials (ASTM) [2]. Stainless steel gains its "stainless" moniker from its corrosion resistance [3]. The 300 series stainless steels are iron alloys with chromium and nickel as major (> 5 wt.%) alloying elements. The phase of 300 series stainless steels is entirely austenite by design. More specifically, 316L stainless steel also includes manganese and molybdenum as minor (< 5 wt.%) alloying elements. Finally, there are maximum limitations on a few other elements: carbon, phosphorus, sulfur, silicon, and nitrogen. Specific alloy requirements as defined by ASTM are collected in Table 2.1 for 316L.

Table 2.1. Maximum (and minimum where applicable) content in wt.% of elements in 316L stainless steel as defined by ASTM A240 [2].

	C	N	Si	P	S	Cr	Mn	Fe	Ni	Mo
316L	0.030	0.10	0.75	0.045	0.030	16.0–18.0	2.00	Bal.	10.0–14.0	2.00–3.00

Each added element serves a purpose, and each limit for impurities avoids specific deleterious effects. Iron, as the main component, is inexpensive and offers decent strength and ductility in the austenite phase. Chromium provides the corrosion resistance for the alloy [4]; more detail will be provided in later sections. Nickel is added to stabilize the austenite phase at

ambient temperatures, offsetting the ferritic base metal nature of iron and chromium [4]. Molybdenum is added to improve corrosion resistance to pitting and acidic conditions [4]. Manganese scavenges sulfur from the bulk by forming MnS_2 inclusions, thereby decreasing the ductile to brittle transition temperature [3]. Phosphorus forms various precipitates at high temperatures that embrittle the material [4]. Sulfur and phosphorus can both segregate to grain boundaries and enable intergranular corrosion [5]. Carbon is added to steels for strength and to stabilize austenite; however, in austenitic stainless steels, carbon precipitates with chromium in grain boundaries at elevated temperatures (>500 °C) [4]. Chromium carbide precipitation is called sensitization, and it reduces the chromium content around grain boundaries, enabling intergranular attack [3–5]. The limit for carbon is only 0.03 wt.% in 316L compared with the 0.08 wt.% maximum for 316 to reduce sensitization [2,4,5]. Nitrogen, like carbon, may be added to increase strength and stabilize austenite [4], but unlike carbon, nitrogen does not cause, and even delays, sensitization [5]. Finally, silicon tends to segregate at grain boundaries and slightly reduces intergranular corrosion resistance [3].

Even within alloy impurity limits, precipitates can form under some conditions that may affect corrosion behavior. 300 series stainless steels maintain high corrosion resistance by uniformly distributing chromium throughout the austenite phase, so precipitates often reduce corrosion resistance by removing chromium from solution [5]. Other defects in the microstructure can change corrosion behavior by serving as fast diffusion paths or preferential oxide nucleation sites. Conditions that result in precipitation and sensitization are important insofar as they can be avoided. The time-temperature-transformation plot for 316L stainless steel is in Figure 2.2 which shows the conditions under which carbides and other precipitates can

form. Carbides are the first precipitate to form in 316L (at grain boundaries) if held at 600 °C for ~1 h or at 550 °C for ~10h.

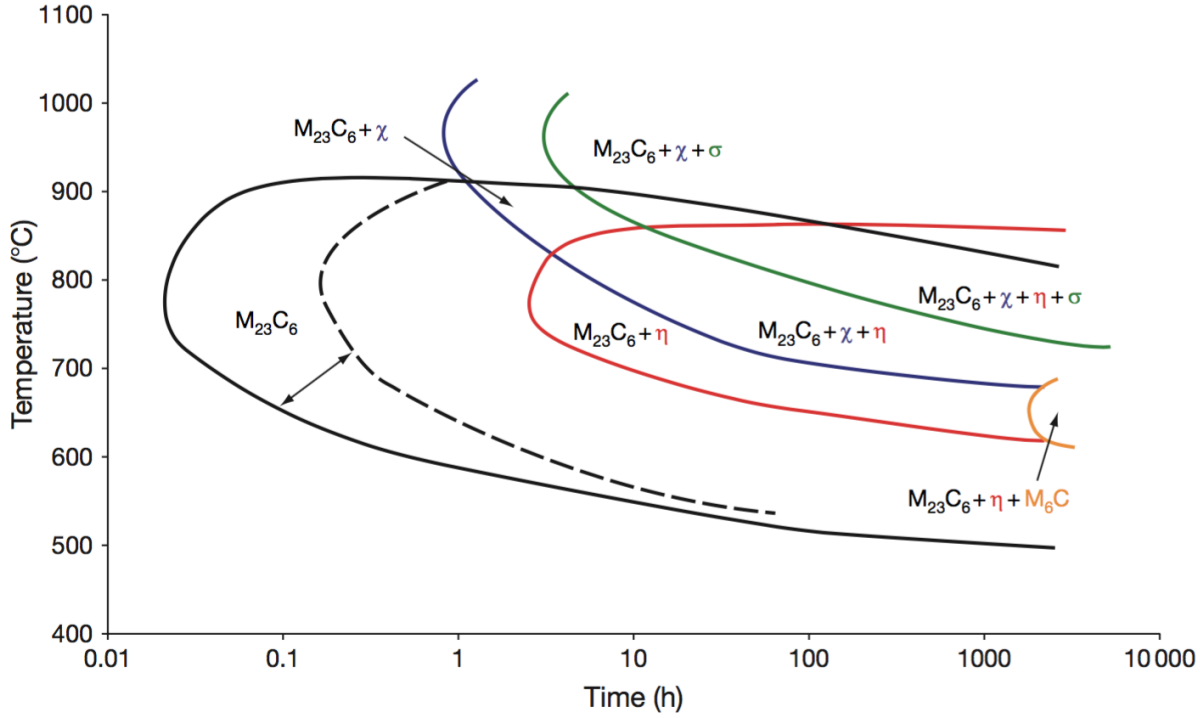

Figure 2.2. Time-temperature-transformation plot for a typical 316L stainless steel. Solid lines represent 1260 °C solution anneal temperature and dashed line 1090 °C, reproduced from [4].

Processing treatments after fabrication are usually simple for 300 series stainless steel. Often the material is rolled and then solution annealed to achieve the desired grain size and to dissolve any residual precipitates such as delta ferrites or chromium carbides [4]. Finally, additional cold work may be applied to harden the material for its application. As such, the microstructure in austenitic stainless steels consists of network dislocations and grain boundaries. Without applied cold work, the network dislocations are minimal, so grain boundaries are the only significant feature in solution annealed austenitic stainless steels. Furthermore, many of the grain boundaries formed by cold work are twins which have better corrosion resistance than random high angle grain boundaries [6].

In the applications relevant to this work, only the major elements—iron, chromium, and nickel—contribute significantly to the corrosion process. Other elements are only important in anomalous conditions where precipitation or sensitization has occurred. Therefore, the behavior of these three major elements will be the focus.

2.1.2. Surface condition

Surface preparation has a significant effect on corrosion behavior [7–12]. Various methods of cutting, grinding, polishing, and cleaning affect the surface of the material.

There are three features of a surface that depend on the preparation procedure: damage layer, roughness, and contamination. Cutting and grinding both impart a subsurface damage layer with heavy cold work features regardless of the bulk condition. Cutting and grinding also leave the surface with roughness. Lastly, foreign material, such as machining oil, may adhere to the surface and interfere with corrosion behavior.

Each surface feature may alter corrosion behavior, so it is common practice to minimize the damage layer, roughness, and contamination where the surface condition is not of particular interest. Non-abrasive cutting methods, like electrodischarge machining (EDM), impart a minimal damage layer, but also introduce some contamination. Grinding is best done in stages of decreasing abrasive particle size, followed by solution polishing in decreasing particle size. Skipping stages can fail to remove the full damage layer despite removing the surface roughness. Electropolishing is a common finishing step for polishing that reduces roughness and does not add any damage layer to the surface. Cleaning is also very important and depends on the surface finishing step. Cleaning should be done just before exposure; pre-exposure characterization work (like electron backscatter diffraction) can contaminate the surface [13].

2.2. Water chemistry

Light water, as the primary coolant for light water reactors (LWRs), is the corrosion medium used in this work. Both pressurized water reactors (PWRs) and boiling water reactors (BWRs) are commonly in use for commercial power generation. It is worth discussing the primary water chemistry of both reactor types as they are frequently simulated in literature.

Reactor temperatures vary throughout the core in both space and time, whereas laboratory autoclaves can and should be well-controlled for repeatability. Temperatures selected for autoclaves are typically at the upper end of the expected temperature for reactor core components. Typical temperatures used in literature are 288°C for BWRs and 320°C for PWRs.

Impurities and additives in reactor water chemistry affect material degradation in LWRs. Impurities are unintentional solutes in the coolant, such as chloride or ferrous ions, whereas additives are introduced in a controlled manner. The goal of additives in a LWR primary loop is to mitigate IASCC, lower the shutdown dose rates, and improve fuel performance [14,15]. Unfortunately, additives sometimes improve one factor at the cost of another: for instance, hydrogen addition reduces SCC susceptibility at the cost of increased reactor shutdown dose rates from ^{60}Co transport in BWRs [15]. Ultimately, the goal of all water chemistry control in a commercial LWR is to reduce maintenance, operation, and refueling costs.

The earliest reactors had many material degradation issues caused by impurities—mostly sulfides and chlorides—in the water [15]. Once water purity was well controlled in LWRs, further changes to the water chemistry were developed to improve performance. Water chemistry now differs greatly between PWR and BWR primary loops to accommodate differences in design and need. BWRs have very pure water with mostly gas additions, whereas PWRs have

significant additions. Despite the differences, irradiation-assisted stress corrosion cracking remains an issue in both reactor types.

A timeline of major changes in PWR water chemistry since the 1970s for US plants is presented in Figure 2.3. Hydrogen overpressure (around 30 to 45 mL/kg) has long been utilized in PWRs to reduce corrosion product transport, redeposition, and radiolysis [15]. Many BWRs have changed from oxygenated normal water chemistry (NWC) to hydrogen water chemistry (HWC) to reduce cracking.

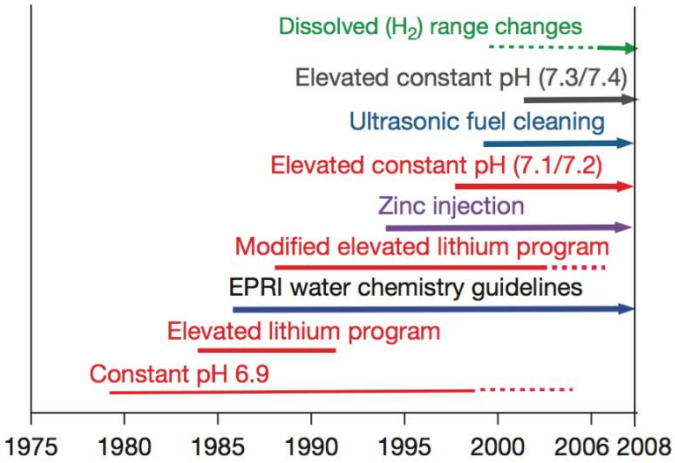

Figure 2.3. Changes in PWR water chemistry over time reproduced from [16].

Boric acid is added to PWR primary water as a "burnable poison" to reduce excess nuclear reactivity [16]. The initial boric acid concentration is on the order of 2000 ppm at start-up and is gradually consumed over the course of the operation. Acidity from boric acid is counteracted by addition of LiOH to a maximum concentration of 2.2 ppm. Lithium hydroxide reduces corrosion product transport by maintaining a specific pH (offsetting the boric acid) thereby reducing radiation fields after shutdown. Originally, a pH of 6.9 was selected to minimize the solubility of Fe_3O_4; however, 7.4 pH minimizes the solubility of $NiFe_2O_4$, which has been identified as the primary component of crud on fuel cladding [15]. Many plants still do not operate at 7.4 pH for fear of fuel cladding corrosion acceleration [15]. Studies by Andresen et

al. have concluded that boron, lithium, and pH have minimal effect on SCC initiation or growth, so these parameters can be adjusted for other operating concerns without a strong effect on material degradation [15,17,18].

While boric acid does not strongly affect SCC, it can be important for other corrosion phenomena and degradation. Leakage of borated water onto the pressure vessel head occurred at the Davis-Besse Nuclear Power Station in 2002 resulting in significant corrosion of the low alloy steel and penetrated to the stainless steel cladding [19]. The Davis-Besse incident has proven that boric acid is not negligible for corrosion concerns.

Two minor additions to LWR primary water chemistry have been adopted to mitigate some corrosion-related issues. Depleted zinc nitrate is an additive developed for BWRs to displace radioactive cobalt isotopes from the spinel oxide lattice and reduce shutdown dose rates. The success of zinc injection for reducing radiation fields in BWRs has led to similar implementation in PWRs. Research has shown that zinc injection also inhibits SCC significantly in PWR primary water [15], and zinc has been shown to greatly decrease the corrosion rate in hydrogenated conditions [20]. Noble metal addition is also practiced in both BWRs and PWRs to further reduce cracking susceptibility [15]. By catalyzing hydrogen decomposition on surfaces, the effective electrochemical corrosion potential (ECP) is reduced substantially thereby decreasing cracking. Noble metal additions are rarely practiced in the literature autoclave tests, so it is important to note these differences when comparing reactor data to laboratory experiments.

2.3. Corrosion

For metals, corrosion is an electrochemical reaction wherein the metal atoms are oxidized. For the purposes of this work, “corrosion” will be used interchangeably with

“oxidation”. There are mechanical means by which material can be removed from surfaces, such as fretting and erosion, but these will not be considered here.

The fate of oxidized metal atoms is important in the corrosion process. Oxidized metal atoms (cations) either dissolve into the corrosion medium or form a corrosion product film on the surface. Thermodynamics dictates which corrosion products may form in the metal/oxidant system. The primary thermodynamic measure for aqueous corrosion is the ECP, which is a subset of the more general oxidation potential. For stainless steels in high temperature water at moderate ECP, the corrosion products are oxides, and the oxide film is a transport barrier for further oxidation reactions. Small quantities of iron and nickel are soluble in water at high temperatures [9,21], and at high oxidation potential, chromium solubility becomes non-negligible [22].

There are many common observations of oxide films formed on stainless steel at high temperatures (150–600 °C):

- Stainless steel forms a two layered oxide structure [5,9,31–38,23–30].
- The inner oxide layer, closest to the metal, is a Cr-rich spinel oxide [5,9,31–38,10,21,25–30].
- The inner oxide can be porous [9,34,36,38,39].
- The outer oxide consists of Fe-rich (and Ni-containing) particulate oxides [5,9,32–38,21,25–31].
- At the metal/oxide interface, nickel enriches in the metal [28,32–36,38–40].
- The original metal surface is preserved as the interface between the inner and outer oxides [33,38,39,41,42].
- Dissolved hydrogen increases [20,29,31,33] or decreases [26] the corrosion rate.

- The inner oxide is [35,36,38], or is not [25,26] epitaxial with the metal substrate.

Based on these observations, the research community has proposed various theories on the mechanisms of stainless steel corrosion in high temperature water. There is general agreement on the formation of the inner oxide layer via solid state mechanisms [9,24]. Many studies attributed the outer oxide formation to a dissolution-recrystallization mechanism [21,24,43,44], but there is also strong evidence for a solid-state growth mechanism for the outer oxide [9,23,39]. Robertson [9,23] proposed the two layered structure forms by oxygen ingress to the metal surface via pores to form the inner oxide and cation diffusion to the outer layer. These mechanisms are necessary for understanding the corrosion kinetics.

Corrosion mechanisms inform the corrosion rate via kinetics. There are four general kinetic regimes of corrosion presented in Figure 2.4; listed in ascending order of oxidation potential:

1. Immunity to corrosion occurs below the corrosion potential (E_{corr}) of the metals in the alloy.
2. Active corrosion is the free corrosion of the alloy without producing a protective oxide film, generally resulting in high corrosion rates between the corrosion potential (E_{corr}) and the passivation potential (E_{pass}).
3. Passive corrosion is a relatively low corrosion rate caused by passive oxide film formation slowing the corrosion rate between the passivation potential (E_{pass}) and the dissolution potential (E_{diss}).
4. Trans-passive corrosion is a break-down and dissolution of the passive oxide resulting in a second active corrosion regime of increasing corrosion rate with oxidation potential above the dissolution potential (E_{diss}).

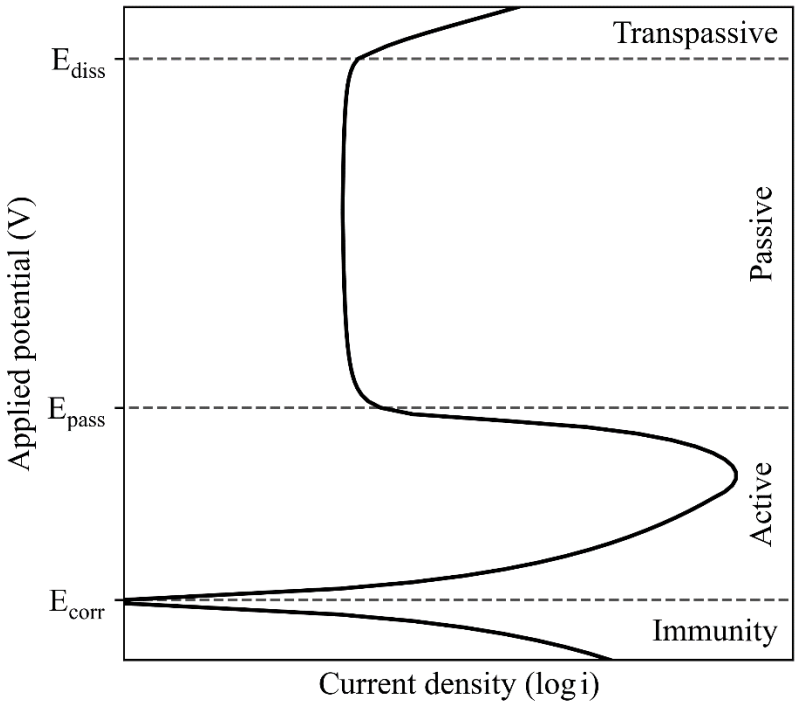

Figure 2.4. Schematic anodic polarization curve of a passivating material.

Only some materials exhibit passive corrosion behavior, such as stainless steel. Even so, passive corrosion behavior is dependent on the combination of environment and material. The following sections will discuss the thermodynamics that determine the oxide film structure, the properties of those oxides, and the kinetics of corrosion.

2.3.1. Thermodynamics

There are many possible corrosion products for stainless steel, and thermodynamics dictates which products will form. Oxide speciation and composition is important for passive oxidation kinetics which will be discussed in the next subsection. Here, the thermodynamics will be used to determine the stable corrosion products in LWR conditions.

For any electrochemical reaction, the Nernst equation relates environmental variables to the ECP, which is the thermodynamic driving force for corrosion [3].

$$E = E^0 - \frac{RT}{zF} ln\, Q_r \qquad \text{Eq. 2.1}$$

Here, E is the ECP, E^0 is the standard cell potential, R is the universal gas constant, T is temperature, z is the number of electrons exchanged in the redox reaction, F is Faraday's constant, and Q_r is the reaction quotient. It should be noted that ECP is typically referenced to the standard hydrogen electrode (SHE). The activity of each species involved in the reaction is included in the reaction quotient, and solids are taken as unity.

The oxidation half reactions of major elements in austenitic stainless steel—iron, nickel, and chromium—are useful for determining the corrosion products; the cell potentials are listed in Table 2.2. The valence of these cations ranges only from 2–3, so only a limited number of oxide structures may form.

Table 2.2. Standard corrosion cell potentials for iron, nickel, and chromium [45].

Oxidation half reaction	Standard cell potential (V_{SHE})
$\mathrm{Cr} \rightarrow \mathrm{Cr}^{3+} + 3e^-$	–0.74
$\mathrm{Fe} \rightarrow \mathrm{Fe}^{2+} + 2e^-$	–0.44
$\mathrm{Ni} \rightarrow \mathrm{Ni}^{2+} + 2e^-$	–0.25
$\mathrm{Fe} \rightarrow \mathrm{Fe}^{3+} + 3e^-$	–0.04
$\mathrm{Cr}^{3+} + 4\mathrm{H_2O} \rightarrow \mathrm{HCrO_4^-} + 7H^+ + 3e^-$	+1.350

For aqueous corrosion conditions, the Nernst equation is often used to make a map of dominant corrosion products over ECP and pH. The activity of oxygen and the pH are often included in the reaction quotient, allowing the ECP to be plotted as a function of pH for any reaction. After considering the various corrosion reactions, stable regions for all species can be determined resulting in a Pourbaix diagram. Examples of the iron-water system at 300 °C are presented in Figure 2.5.

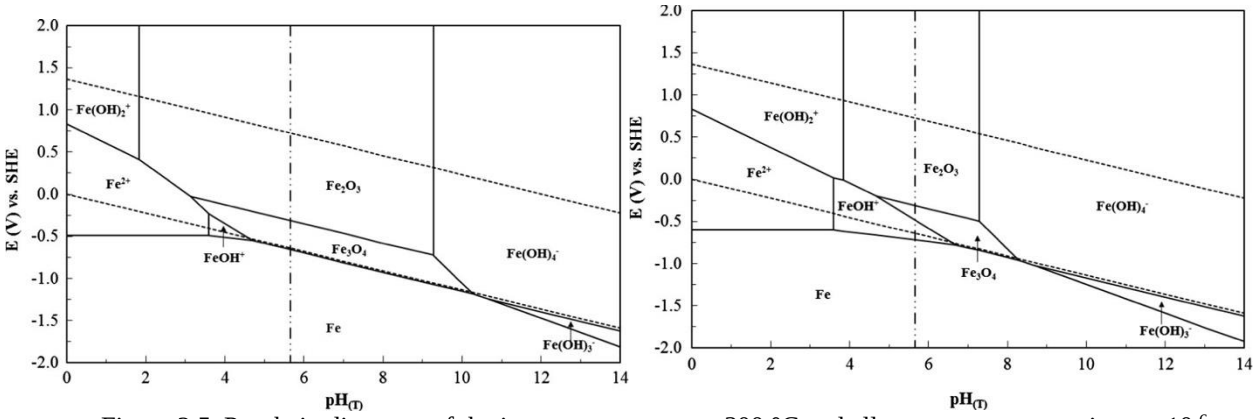

Figure 2.5. Pourbaix diagrams of the iron-water system at 300 °C and all aqueous concentrations at 10^{-6} mol/kg (left) and 10^{-8} mol/kg (right) [46].

Three common structures are dominant in potential-pH diagrams for iron, chromium, and nickel: halite, spinel, and corundum. Halite oxides form with iron and nickel: FeO and NiO. Spinel oxides accommodate all three elements in four endpoint compositions: Fe_3O_4, $FeCr_2O_4$, $NiFe_2O_4$, and $NiCr_2O_4$. Corundum oxides include iron and chromium: Fe_3O_4 and Cr_3O_4. For stainless steels, halite is rare because Cr^{3+} is the most readily oxidized cation and is not accommodated in that structure. Using the pH and ECP ranges for different LWR conditions, Pourbaix diagrams can yield expected oxide structures collected in Table 2.3. Pourbaix diagrams only show these endpoint compositions, but solid solutions within each structure are often observed [44]. Furthermore, more detailed thermodynamics suggest that more than one oxide structure can be stable under a single set of conditions [47].

Table 2.3. Dominant oxide structures for LWR conditions for different metal/water systems with the target element in bold using 300 °C Pourbaix diagrams.

	NWC	HWC	PWR	Ref.
ECP (mV)	+110	–510	–600	[15,22]
pH	~5.6	~5.6	~7.0	[15]
Fe	Fe_2O_3	Fe_3O_4	Fe_3O_4	[48]
Cr	Cr_2O_3	Cr_2O_3	Cr_2O_3	[49]
Ni	NiO	NiO	NiO	[50]
Fe-Cr-Ni	$NiFe_2O_4$	$NiFe_2O_4$	$NiFe_2O_4$	[51]
Fe-**Cr**-Ni	$NiCr_2O_4$	$FeCr_2O_4$	$FeCr_2O_4$	[51]
Fe-Cr-**Ni**	$NiFe_2O_4$	NiO	NiO	[51]

As described earlier, the inner oxide is Cr-rich, and the outer oxide is Fe-rich. Since the outer oxide is not always continuous, both inner and outer oxides are exposed to the same water conditions, so both oxides must coexist within the same thermodynamic conditions. The Pourbaix diagram oxides in Table 2.3 find that the Fe-rich oxide is $NiFe_2O_4$ and the Cr-rich oxide is either $NiCr_2O_4$ or $FeCr_2O_4$ [51]. With a more detailed Gibbs free energy minimization, Kurepin et al. shows that two separate oxide phases are in equilibrium in LWR conditions [47].

Chromium is known to add corrosion resistance to steels, and the inner oxide is enriched in chromium. Therefore, some intrinsic properties of the inner oxide must affect the corrosion kinetics and reduce the corrosion rate. The inner oxide has a spinel structure in virtually all conditions, so it is necessary to understand how the composition—particularly chromium content—changes the intrinsic properties of spinel oxides.

2.3.2. Oxide properties

Spinel oxides enriched in chromium serve to decrease the kinetics of corrosion. Transport properties of oxygen and metal atoms are the relevant properties for corrosion kinetics. Some authors suggest cation diffusion is rate-limiting [33], but others suggest anion diffusion [36]. Both will be discussed, but greater emphasis will be placed on the cation diffusion coefficient because there is more literature for cation diffusion.

There are many features of the oxide chemistry and structure that affect the atomic diffusion coefficient, so a detailed explanation of spinels is warranted. Spinels have an AB_2O_4 structure wherein A is a 2+ valence cation, B is a 3+ valence cation, and O is a 2- anion. These ions are arranged among three atomic sublattices in the spinel structure. The oxygen sublattice is a standard face-centered cubic structure with octahedral and tetrahedral spaces between atoms.

Two thirds of cations are in octahedral positions, and the remaining third of cations are in tetrahedral positions [52].

There is a degree of freedom in spinels called inversion wherein lower valence cations occupy higher coordination number sites. In a normal spinel, the 3+ cations occupy the octahedral positions, and 2+ cations occupy tetrahedral positions. However, inverted spinels have tetrahedral positions occupied by 3+ cations and octahedral positions filled with half 3+ and half 2+ cations. The fraction of tetrahedral sites occupied by 3+ cations is the inversion parameter.

Table 2.4. Crystal field preference energies (CFPE) (kJ/mol) for ions in octahedral positions within a spinel oxide from [33,53].

Ion	Fe^{3+}	Fe^{2+}	Ni^{2+}	Cr^{3+}
CFPE	0	17	86	158

Cation site preference for octahedral sites is an important component of the free energy for different spinel compositions and is listed in Table 2.4. The higher the preference energy, the more likely that particular cation occupies the octahedral position, so Cr^{3+} is most likely found in octahedral positions. For stainless steel corrosion, virtually all cations in the spinel oxide are Fe^{2+}, Fe^{3+}, Cr^{3+}, and Ni^{2+}. Interactions between these cations and their configuration determine the energy of mixing which is minimized at equilibrium. More relevant to corrosion, gradients in the energy of mixing in non-equilibrium compositions provide a driving force for atomic motion.

The phase space for Fe-Cr-Ni spinels does not allow any solid solution; there is a large miscibility gap between Fe^{3+} and Cr^{3+} spinels [44,47]. The phase map in Figure 2.6 demonstrates various equilibria between Fe-rich and Cr-rich spinel oxides, matching general experimental observations of inner and outer oxides. This miscibility gap between the inner and outer oxides may provide a driving force for Fe and Ni to transport to the outer oxide. However, it is still necessary to determine the diffusion behavior that limits Fe and Ni transport with Cr content.

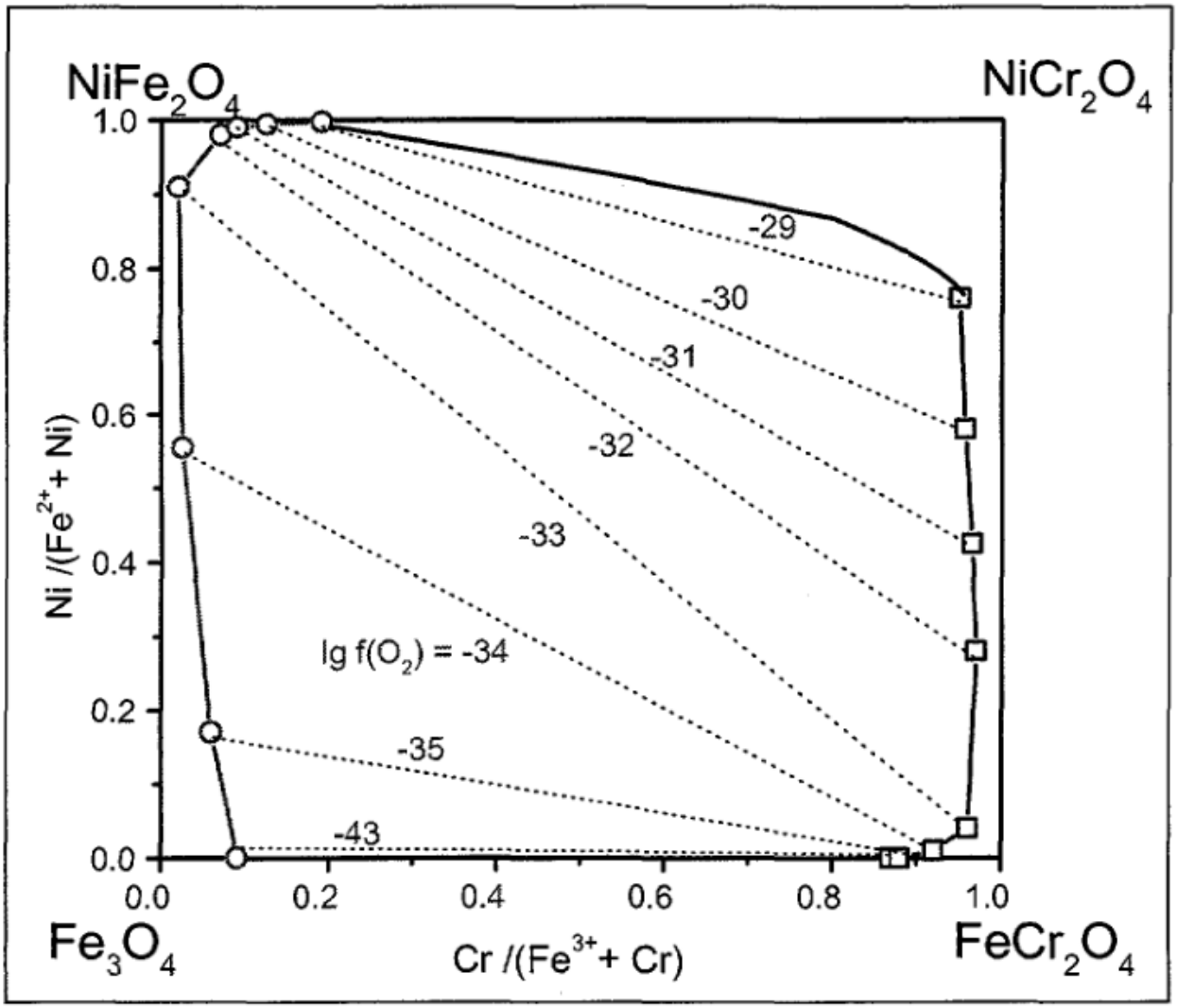

Figure 2.6. Miscibility gap in the Fe-Cr-Ni spinel system with tie lines at different $\log_{10}$ oxygen activities from [47].

It is important to note that there are several different types of diffusion coefficients. Both cation and anion diffusion coefficients are atomic diffusion coefficients (D^*) which describe the mobility of atoms. Atomic motion in solids is enabled by interstitials and vacancies (point defects) as carrier species. Atomic diffusion coefficients are derived from the concentrations of point defects and their respective diffusion coefficients.

$$D_A^* = D_{A,v}^* + D_{A,i}^* = D_{A,v}^0 C_v + D_{A,i}^0 C_i$$

The atomic (sometimes tracer or self) diffusion coefficient D^* of atom A is transported by either vacancies v or interstitials i and their corresponding diffusion coefficients D^0 and concentrations C. Atomic diffusion coefficients can be applied in Fick's first and second laws where atomic concentration gradients are present. Ion mobility can be derived from these atomic diffusion coefficients using the Einstein relation. To calculate the atomic diffusion coefficient, the point defect concentrations and diffusion coefficients are required.

Magnetite (Fe_3O_4) is the most studied of the four endmembers of the Fe-Cr-Ni spinel system, so it will be used as a case study for all spinels in the system. Thermal point defect concentrations in magnetite are a function of both temperature and oxygen activity. The temperature dependence follows an Arrhenius relation with the formation energy. The oxygen activity dependence in Eq. 2.2 is derived from the equilibrium constants for the defect formation reactions, and the experimental data follow this relation very well [54].

$$C_v \propto a_{O_2}^{2/3}$$
$$C_i \propto a_{O_2}^{-2/3} \qquad \text{Eq. 2.2}$$

Point defect diffusion coefficients are affected by both the temperature and the diffusing tracer element in otherwise pure magnetite. The temperature dependence is a typical Arrhenius relationship with a migration energy. At trace concentrations, iron and nickel have similar diffusion coefficients, but chromium has approximately two orders of magnitude lower interstitial and vacancy diffusion coefficients, see Figure 2.7 [55,56].

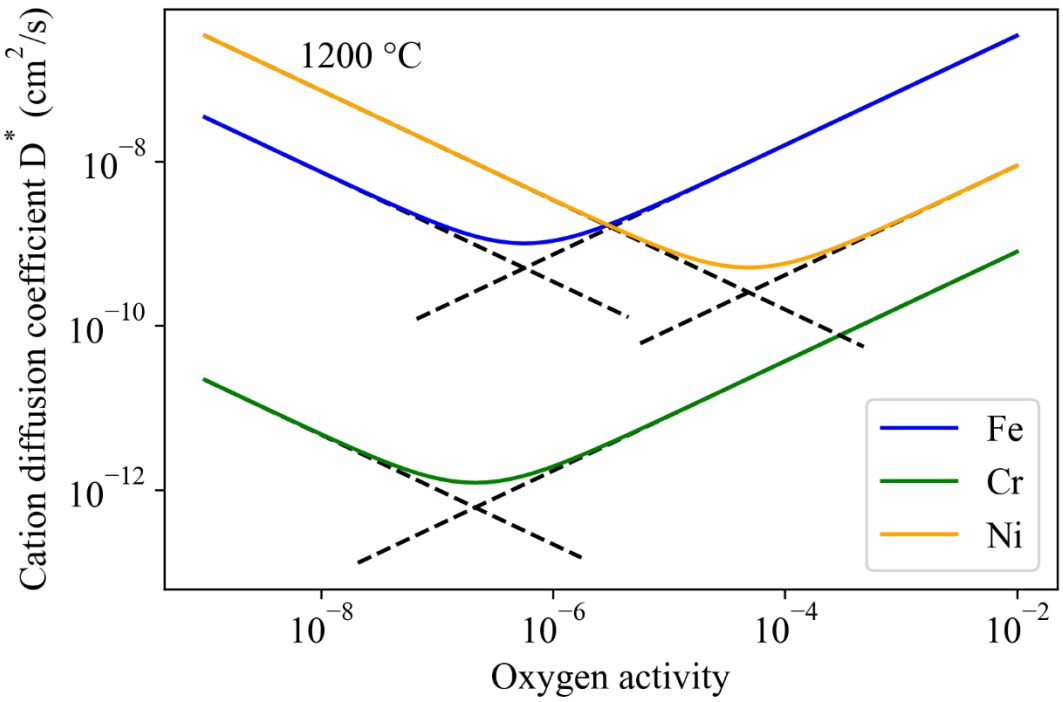

Figure 2.7. Cation tracer diffusion coefficients in magnetite at 1200 °C replotted from [55].

Moving beyond magnetite, the atomic diffusion coefficient is a function of composition of the spinel oxide. Both thermal vacancy and interstitial concentrations decrease with increasing chromium content in the spinel [56]. From Fe_3O_4 to $Fe_{1.5}Cr_{1.5}O_4$, the point defect equilibrium constant decreases by two orders of magnitude. The result is a decrease in the atomic diffusion coefficient for all cations in the spinel structure.

Chromium content further suppresses the diffusion of other elements by modifying diffusion correlation. Modeling Fe and Cr in the spinel structure as a binary random alloy, composition dependence of correlation factors can be determined using the ratio of diffusion coefficients [57,58]. A percolation threshold exists when a slow-moving species, such as chromium in spinels, is abundant enough to block most point defect motion. The correlation factor approaches zero for the fast diffusor below the threshold and rapidly increases above the threshold. This percolation behavior likely explains the threshold Cr content needed to generate a highly protective oxide on stainless steels.

Anion diffusion is governed by the same equations and principles as cations. However, literature on anion diffusion is sparse and does not include data on composition. Analogous to cations, anion vacancy concentration varies with the oxygen activity to either a –1/2 or +1/6 power depending on the oxygen activity regime, and empirically follows a –0.135 power [59]. At low oxygen activities, oxygen vacancies pair with cation interstitials to maintain charge balance resulting in a –1/2 power dependence, and at high oxygen activities, oxygen vacancies pair with cation vacancies to maintain stoichiometry resulting in a +1/6 power dependence [60]. The oxygen atomic diffusion coefficient is significantly smaller than any cation diffusion coefficient [9,23,59,61]. Solid state oxygen diffusion is much slower than measured corrosion rates would require [9,59], so the lattice diffusion of oxygen is irrelevant for corrosion. Presumably, the grain boundary diffusion coefficient of oxygen in spinels would be higher, but there is no literature regarding this value. The lattice diffusion coefficient is low enough that even a factor of 1000 would not result in a significant change in the ultimate flux of oxygen through spinels.

Another important property of the spinel oxide is the metal atom density relative to that of the metal phase. A useful concept relating the oxide film thickness to the depth of corroded metal is called the Pilling-Bedworth Ratio (PBR) [62]. The PBR is defined as the ratio between the number density of metal atoms in the metal to the number density of metal atoms in the oxide, assuming no dissolution. Alternatively, the PBR can be defined as the ratio of the volume of the oxide film to the volume of the metal oxidized to yield that oxide film. The most common case is when PBR > 1, which is true for stainless steel, where the oxide film is thicker than depth of metal oxidized. PBR will be used later in this work to interpret the oxide film morphology of stainless steels.

2.3.3. Kinetics

The goal of corrosion kinetics is to be able to predict the extent of corrosion with time. Most corrosion rate data are empirical and macroscopic for practical applications of determining the service life of components. These empirical fits are very important for engineering applications but provide little scientific insight into the corrosion process. Mechanistic understanding of corrosion can improve the predictive capacity for other scientific and engineering purposes.

A corrosion mechanism defines each step of the corrosion process. The slowest step determines the speed of the overall corrosion reaction. There are two categories of steps in corrosion: interfacial reactions and transport phenomena. Interfacial reactions include the oxidation of metal at the metal surface and reduction of oxygen at the solution interface. Transport phenomena include convection of oxygen from the bulk water; diffusion of metal to the surface; and transport of cations, anions, and electric charge across the corrosion product scale.

Identification of the rate limiting step is key for understanding the kinetics. Steps in a mechanism are sequential events, so corrosion proceeds at the rate of the slowest step. As noted earlier, corrosion rate decreases with increasing thickness of the protective oxide film. The only steps in any mechanism that depend on oxide thickness are the transport steps within the oxide. One of the following: cation transport, anion transport, or charge transport through the passive oxide must be the rate limiting step. A comparison of diffusion coefficients with literature data shows that the solid-state oxygen lattice diffusion coefficient [61,63] is very low compared with corrosion rate data, so it cannot be a part of the mechanism. Therefore, oxygen transport through the inner oxide has a short circuit path which is confirmed by ^{18}O tracer profiles [9,23,43,64,65].

Two short circuit paths are proposed by various authors: grain boundary diffusion [43], and a network of pores [9,23,39,66]. Iron-containing spinels have a very high electrical conductivity above the Verwey transition at 113 K [67], so charge transport is rarely rate-limiting. Therefore, cation transport is the rate limiting step in most cases.

Cation transport depends on two features of the oxide: the transport path length and the cation diffusion coefficient. Generally, the path length is taken to be the oxide film thickness on the assumption that the transport properties are anisotropic and that corrosion proceeds one-dimensionally. The cation diffusion coefficient was discussed earlier to be a function of temperature, oxygen activity, and composition. Specifically, the chromium content of spinel oxides greatly reduces cation diffusion coefficients.

Only the thickness of the inner oxide layer, not the outer oxide, contributes significantly to the rate of cation transport [21,44]. The outer oxide has virtually no chromium content under most high temperature water conditions except in very oxidizing conditions [26]. Therefore, cation diffusion coefficients are much larger in the outer oxide compared with the inner oxide. Some literature has demonstrated this by removing a large portion of outer oxide between exposures, showing no change in the corrosion kinetic [68].

A simple model for passive corrosion kinetics is the parabolic law which can be derived from Fick's first law [65,69]. The instantaneous corrosion rate is

$$\frac{\mathrm{d}x}{\mathrm{d}t} = \frac{k}{x} \qquad \text{Eq. 2.3}$$

where x is the inner oxide thickness, t is time, and k is the parabolic rate constant. The parabolic rate constant is directly proportional to the atomic diffusion coefficient and shares the same units. Omitting any initial oxide thickness, the analytical solution to this differential equation yields the time dependence of corrosion for comparison with empirical data here:

$$x(t) = \sqrt{2kt} \quad \text{Eq. 2.4}$$

This parabolic law does not capture the full physics, so empirical corrosion data are often fit to a modified parabolic rate law:

$$x(t) = (2kt)^{1/n} \quad \text{Eq. 2.5}$$

where n is an additional fitting parameter that returns the original parabolic rate law when $n = 2$ [70]. Note that the units of k no longer match that of an atomic diffusion coefficient in this empirical fitting function, so this formulation does not have a theory underpinning it.

Reported oxidation rates vary widely among the literature, see Figure 2.8. Data within each study is much more consistent than across the literature, indicating large changes between heats of material, methodology, or equipment. In general, the parabolic rate constant has a positive correlation with temperature and a negative correlation with Cr content in the alloy. There are many complicating factors including, but not limited to: dissolved gas content, autoclave material, surface condition, pH, cold work, pressure, and static vs. flowing autoclave.

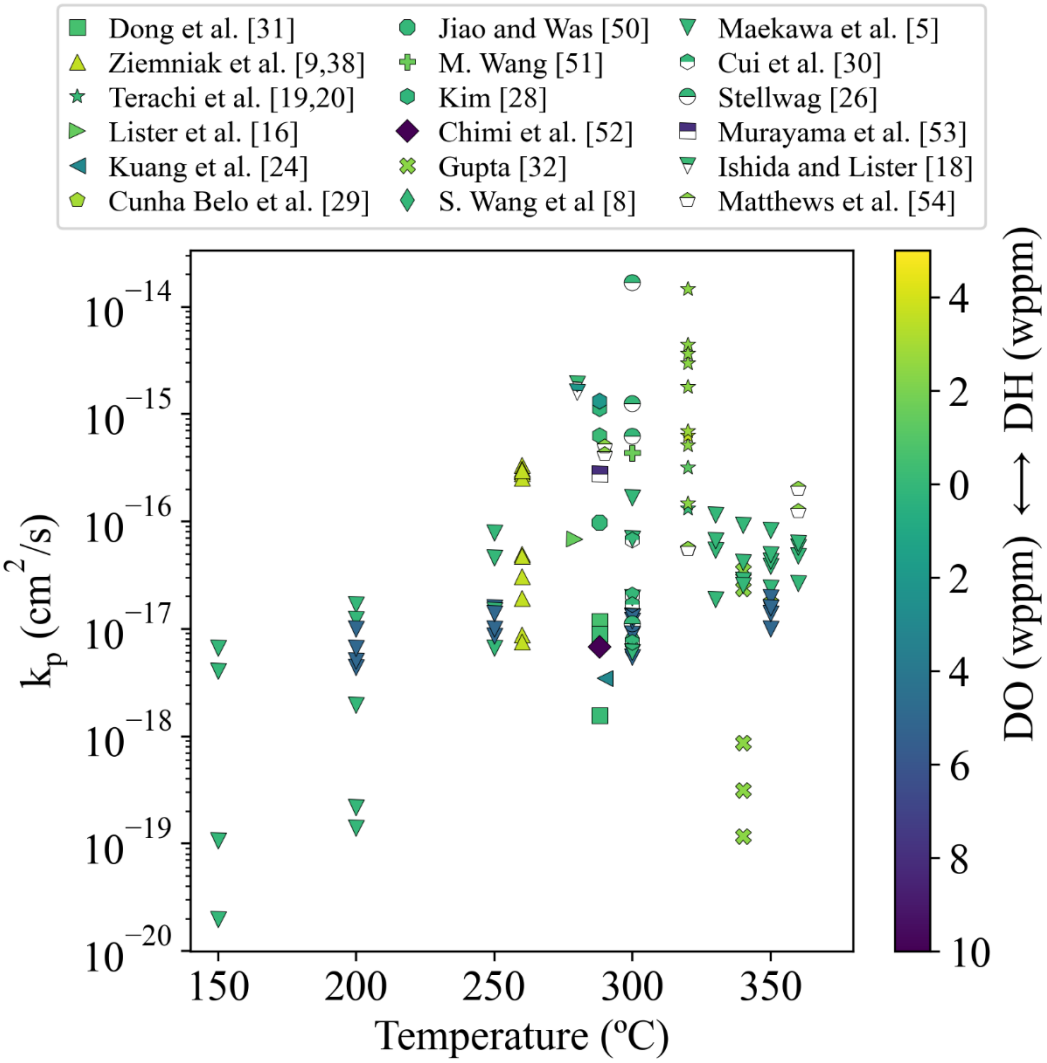

Figure 2.8. Literature data of 304/316 stainless steel water oxidation compiled as parabolic rate constant k_p versus temperature and the marker color corresponds to the dissolved gas content on stainless steels in water or steam conditions [6,8,30–33,37,44,71–74,11,12,21,24,26–29].

Several authors note that the ratio between the inner and outer oxide layer thicknesses is approximately 1:1 regardless of corrosion time [33,39,42]. In these cases, transport of oxygen inward and metal atoms outward are tied to the same mechanism, otherwise the thickness ratio would not be consistent. Fe-Cr corundum oxides have very similar density to Fe-Cr-Ni spinels, so the oxide film thickness is not expected to change with structure. An “available space” model proposed by Rouillard et al. provides a mechanistic explanation for this phenomenon [39,66]. As cation vacancies arrive at the metal oxide interface they condense as pores, exposing the metal to

the pore network, and thus oxygen. Then oxides form quickly on the exposed metal, refilling the pore and halting oxidation until cation vacancies unblock the pore again. In this way, the oxygen ingress is limited to the cation diffusion rate.

Corrosion kinetics of stainless steels in high temperature water are very complex and dependent on many parameters. Simplistic 1D models decently describe the behavior with time; however, the various parameters that alter the kinetics are inadequately described within the parabolic rate constant. The core concepts of parabolic rate corrosion appear to be correct, but the literature leaves a lot to be desired in mechanistic understanding of the corrosion process. Further complexity is added when considering the effects of radiation on corrosion.

2.4. Radiation

Radiation is the emission of an energetic particle. There are many sources for radiation, namely nuclear reactors, particle accelerators, and radioisotopes. The relevant particles for this work consist of charged particles—ions, electrons, and positrons—and neutral particles—photons and neutrons.

There are many ways in which radiation interacts with matter, but only the two processes relevant to corrosion will be considered: radiolysis of water and radiation-induced displacement damage. Water radiolysis is breaking chemical bonds in water by energy deposition from radiation. Radiation-induced displacement damage is atomic displacement in a crystal lattice by ballistic collisions knocking atoms out of lattice sites. The energy needed for water radiolysis (10.12 eV [75]) is a lower threshold than displacements in a steel (40 eV [76]).

Charged particles interact via the Coulombic force causing radiolysis and/or displacements within the target material. At higher energies, ions impart target atoms—called “knock-on” atoms—with enough energy to cause their own secondary collisions. Secondary

knock-on atoms may themselves cause tertiary knock-on atoms and so on. A highly energetic collision may cause a cascade of branching collisions. Electrons and positrons at achievable energies do not possess enough momentum to cause a cascade; they are only capable of individual displacement or ionization.

Photons can only induce radiolysis by imparting energy to electrons and are rarely able to cause displacements. Only three matter interactions are available to photons: photoelectric effect, Compton scattering, and pair production. Both photoelectric effect and Compton scattering impart energy upon electrons in the medium, and pair production simply creates one electron and one positron. Photon-scattered electron energy may be above the ionization threshold for water but is virtually never above the displacement threshold.

Neutrons can cause both radiolysis and displacements via direct and indirect means. Fast (energetic) neutrons may collide with atomic nuclei and cause individual displacements or cascades. Any neutron, depending on the energy and target nucleus, may induce a nuclear reaction thereby releasing energetic ions or photons which may cause displacements or radiolysis accordingly. Fast neutrons are the primary cause of radiation damage in nuclear reactor cores. Fast neutrons are often defined as either >0.5 MeV or >1 MeV; however, there is a continuous spectrum of neutron energies that varies throughout a reactor core. Example neutron spectra for two core positions in a PWR is presented in Figure 2.9.

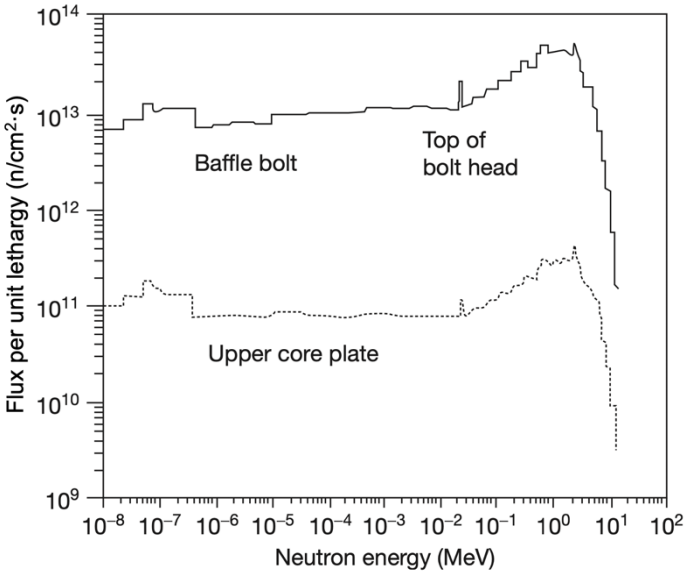

Figure 2.9. Neutron flux spectra for PWR reactor internal components from [77].

For irradiation there are three main parameters that define the radiolysis and displacement response of materials. First, particle type affects the propensity of inducing radiolysis or displacements due to momentum transfer as outlined above. Second, particle energy determines the probability of different interactions and the quantity of radiolysis and displacement events. Last, particle flux determines the overall rate of radiolysis or displacement damage occurring in the target medium. Specifics of displacement damage and water radiolysis will be discussed in the following sections.

2.4.1. Radiation-Induced Displacement Damage

Displacements are a fundamental unit of radiation damage in a crystalline solid. Other radiation effects in solids, such as transmutation, will not be discussed in this work. A displacement is defined as the ejection of an atom from its lattice site and the subsequent injection of the displaced atom elsewhere in the crystal. Two point defects—called a Frenkel pair—are created by this displacement process: a vacancy in the lattice and an interstitial atom between lattice sites. The production of displacements by irradiation will be discussed first,

followed by rate laws governing point defects, and finally point defect effects on material properties.

Calculation of displacements depends on both the irradiating particle and the target material. Differences in particle type and energy E_i can be flattened into a probability distribution of primary knock-on atoms (PKA) of energy T in the target material. For any given PKA energy T, the number of displacements can be calculated using the Kinchin-Pease model [78]. Integration over all PKA energies T yields the average number of displacements generated by the irradiating particle of energy E_i. Integrating once more over irradiating particle energies E_i and the particle flux ϕ_i yields the displacement rate in the target material. Both impinging particle energy E_i and the particle flux ϕ_i are affected by many possible stochastic interactions, so they cannot be calculated analytically. To avoid the analytical calculation, displacement damage rates are often calculated using Monte Carlo codes. The result is the ability to relate incident particle energy and flux to the damage rate at a specified location within a target.

Another feature of radiation damage events to note is the displacement cascade. Cascade size is known to affect the resulting radiation damage; large defect clusters may be directly produced by a single cascade [79]. Different combinations of particle type, energy, and flux may yield the same number of displacements but yield varying results due to cascade size effects.

The differences between irradiating particles for displacement damage is best illustrated through their respective matter interactions. Neutral particles (neutrons and photons) have probabilistic interactions with matter following an exponential mean free path expression [80]. Charged particles have deterministic interactions with matter that are split into two kinds: nuclear and electronic stopping power. Stopping power is the unit energy lost per unit length traveled by an energetic particle. For charged particles, the lower energy regime is dominated by

nuclear stopping which induces displacements. Higher energies are dominated by electronic stopping which does not cause displacements. The highest number of displacements caused by a charged particle is observed near the end of the track where nuclear stopping is highest—this is called the Bragg peak.

Displacement damage is often given the unit of displacements per atom (dpa), which is the average number of times each atom in a crystal lattice has been displaced. The point defect generation rate K_0 is in units of dpa/s and is equal for both vacancies and interstitials. Point defects annihilate on recombination, so there is a recombination rate constant K_{iv} which is taken to be an elementary reaction dependent on the concentration of vacancies C_v and interstitials C_i. Point defects may also annihilate at sinks (features of the microstructure or a free surface) having a concentration C_s of sink s and elementary rate constants K_{vs} and K_{is} for vacancies and interstitials, respectively. A pair of differential equations describing the point defect concentration in the bulk material can be written [78].

$$\frac{\mathrm{d}C_v}{\mathrm{d}t} = K_0 - K_{iv}C_iC_v - \sum_s K_{vs}\,C_vC_s$$
$$\frac{\mathrm{d}C_i}{\mathrm{d}t} = K_0 - K_{iv}C_iC_v - \sum_s K_{is}\,C_iC_s \qquad \text{Eq. 2.6}$$

One consequence of elevated point defect concentration is radiation enhanced diffusion (RED). Point defect concentrations directly impact the atomic diffusion coefficient via Eq. 2.6. Radiation always elevates point defects above their thermal concentrations. However, at high temperature it is possible for radiation to produce a negligible change in the concentrations and thus in the atomic diffusion coefficient. RED is the most important feature for corrosion because corrosion is a transport limited process, and changes to the diffusion coefficient should change the rate constant for corrosion.

Radiation induced segregation (RIS) is an unusual feature of irradiation where chemical segregation is observed at sinks. For instance, in austenitic stainless steels, nickel and silicon are observed enriched at grain boundaries while chromium is depleted [81]. The inverse Kirkendall model generally explains this phenomenon by noting elemental affinity for vacancies or interstitials. A mismatch between vacancy and interstitial diffusion coefficients will result in a net elemental flux for equal point defect fluxes. RIS is a gradual process which reaches a steady state at <10 dpa for neutrons and protons [82].

Several microstructural features can be produced by irradiation [83]. Generally, point defects can cluster together and form a persistent feature which usually impacts bulk behavior, e.g., hardness. Dislocation loops are very common features formed under irradiation. Cavities may be formed by clustering vacancies with or without a trapped gas (usually helium as a transmutation product). Precipitation may be induced by irradiation and depends on the chemistry of the material, but precipitates are rarely formed by irradiation of austenitic stainless steel.

2.4.2. Radiolysis of Water

Water radiolysis causes chemical changes within the water which can impact corrosion behavior. Energy deposition by energetic particles breaks bonds and ionizes water to form radiolysis products. Initial radiolysis products tend to be short-lived, such as ions, radicals, or aqueous electrons. Short-lived products will quickly react with one another to form long-lived or stable compounds, only four of which exist: H_2, O_2, H_2O, and H_2O_2.

The direct impact of short-lived radiolysis products on corrosion is uncertain. Concentrations of short-lived products are unmeasurable, but kinetic modeling gives the expected yields [84]. Even with calculated concentrations, interactions with the corrosion

reaction or ECP are not known. Due to the short-lived nature of these species, only radiolysis directly at the surface could cause any effect.

Long-lived radiolysis products can cause significant changes in the ECP because they can have a cumulative effect. Unlike their short-lived counterparts, long-lived products will alter bulk water chemistry. Reforming water will not result in any water chemistry change, but the other three compounds will. Both H_2 and O_2 are often added to control the ECP, so they have well-documented effects mentioned earlier. Hydrogen peroxide is a stronger oxidizer than O_2, causing a rapid increase of ECP with concentration as shown in Figure 2.10 [26]. Unlike H_2 and O_2, which are formed by thermal decomposition of water, H_2O_2 is not present in the feedwater of LWRs. Depending on the nature of the radiation, radiolysis product yields increase linearly with dose or saturate at some concentration [84].

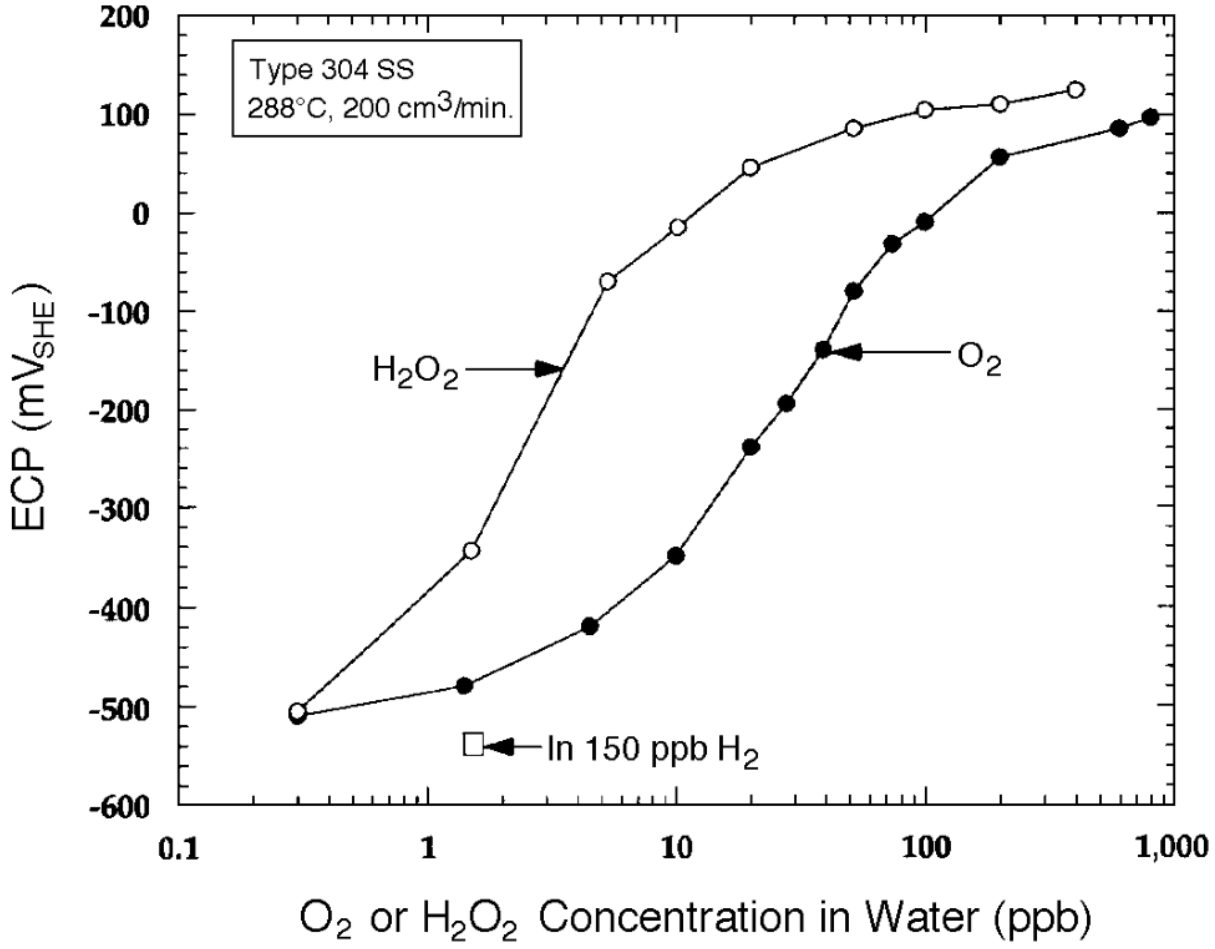

Figure 2.10. Effect of oxygen and hydrogen peroxide on the electrochemical corrosion potential [26].

Like displacement damage, the particle type, energy, and flux impact the radiolysis of water. In the case of radiolysis, the stopping power is called linear energy transfer (LET) which largely flattens the differences in particle type and energy. Somewhat analogously to displacement damage cascades, photons and electrons only produce a small amount of hydrogen peroxide which saturates after a small dose, whereas ions and neutrons can produce large concentrations of hydrogen peroxide linearly with dose. This difference can be attributed to the lower LET of photons and electrons when compared to ions and neutrons.

High LET particles increase the overall yield of hydrogen peroxide, and high particle flux cannot compensate for the LET difference. When comparing irradiation of water by different

particles to the same dose, higher LET particles (He^+) produce more hydrogen peroxide than lower LET particles (H^+) [85]. Furthermore, low LET irradiation accelerates the decomposition of hydrogen peroxide toward the saturation concentration appropriate to the LET when the hydrogen peroxide is stable sans irradiation.

Neutron LET is complicated by the possibility of nuclear reactions in addition to direct energy deposition by scattering interactions with nuclei. The LET of neutrons is increased by the addition of boron to the water as is the case in PWRs. The nuclear reaction $^{10}\mathrm{B} + n \rightarrow {}^{7}\mathrm{Li} + \alpha$ produces two energetic light ions which significantly increases the effective LET of neutrons [86]. Naturally, the neutron LET will be a function of the neutron energy spectrum in terms of direct energy deposition.

The effective LET of the radiation fields in LWRs is more comparable to ion irradiation than photon or electron irradiation. In addition to the ions generated by nuclear reactions with boron, fast neutrons can collide with oxygen and hydrogen creating high energy PKAs. There is known to be a spectrum of proton energies in a LWR core [87]. The gamma radiation in a LWR core will contribute negligible radiolysis where neutron irradiation is present; however, outside of the core gamma irradiation may substantially affect corrosion.

Water chemistry influences the radiolysis product yield. Dissolved oxygen and dissolved hydrogen shift the equilibrium constants of many radical reactions. Notably, dissolved hydrogen decreases the production of hydrogen peroxide except at very high LET [84]. Hydrogen also promotes the decomposition of hydrogen peroxide under low LET irradiation [84]. The use of hydrogen in LWR feedwater is often cited as reducing the deleterious effects of radiolysis [15]. Both lithium hydroxide (typical in PWRs) and dissolved iron ions (from steel corrosion) promote hydrogen peroxide production by water radiolysis [86].

Temperature also plays a large role in radiolysis yields since many of the rate constants follow typical Arrhenius behavior. At higher temperature, the kinetics of various decay processes are enhanced. Therefore, higher temperatures will result in progressively lower ECP response from radiolysis.

2.5. Irradiation Assisted Corrosion

A synopsis of the experimental work done on the effects of radiation on corrosion is needed to gain a picture of the current scientific understanding. For studies of IAC there is virtually no consistency between experimental and characterization methods. Therefore, each relevant work will be discussed in some detail to extract the useful information and its limitations. First, exposures of irradiated material to autoclave environments will be discussed for the effects of cumulative radiation damage on corrosion. Then, in situ irradiation corrosion experiments will be discussed in order of radiation source: reactor, isotope gamma, and ion irradiations.

2.5.1. Sequential Irradiation and Corrosion

As mentioned above, radiation damage accumulates into defects that alter the microstructure of the bulk material. The effects of radiation defects on corrosion behavior must be understood to separate the effects of irradiation on the corrosion process itself. Therefore, studies of ex situ irradiation and corrosion of stainless steel will be discussed here.

The effect of proton irradiated 316 stainless steel microstructure on corrosion in simulated BWR NWC conditions has been studied by Jiao and Was [71]. Tensile bars were irradiated to 5 dpa in a limited area then subjected to a constant extension rate tensile (CERT) test in simulated BWR NWC. Inner oxide film thickness depended greatly on the surface grain orientation in both irradiated and non-irradiated regions and is presented in Table 2.5. No

statistical significance of irradiation effects on corrosion could be determined due to the magnitude of difference by grain orientation. Therefore, 5 dpa of proton irradiation has, at most, a minor effect on corrosion behavior in NWC conditions.

Table 2.5. Inner oxide thickness measured on proton-irradiated 316 stainless steel tensile sample exposed to BWR NWC conditions at 288 °C for 70 h [71].

	Inner oxide thickness (nm)	
	Grain 1	Grain 2
Non-irradiated	70 ± 12 nm	< 10 nm
Irradiated (5 dpa)	63 ± 16 nm	~5 nm

Similar work on proton irradiated 304NG stainless steel in simulated PWR primary water was performed by Deng et al. [88]. Bulk oxide thickness measured by X-ray photoelectron spectroscopy (XPS) was not significantly different between 0 dpa and 0.5 dpa; however, oxide thickness began to increase for 1.5, 3, and 5 dpa as presented in Figure 2.11. Intergranular oxidation increased starting at 0.5 dpa which correlated well with Cr depletion at the boundary from RIS as presented in Figure 2.12. This study shows that proton irradiation defects do increase corrosion rates in PWR conditions; however, the bulk radiation defects are less important than the Cr depletion that occurs at grain boundaries.

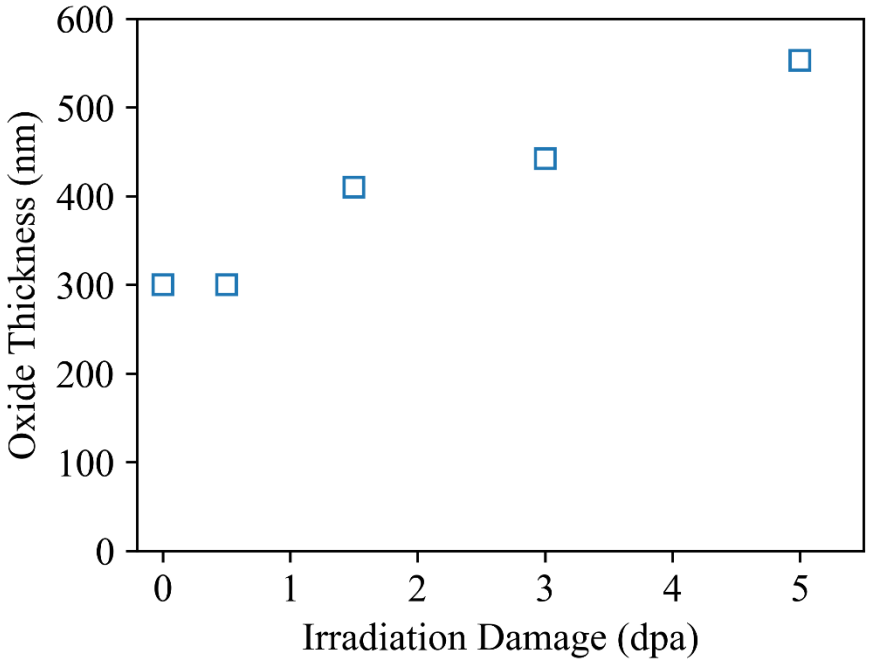

Figure 2.11. Total oxide thickness measured by XPS sputtering of proton irradiated 304NG stainless steel exposed to simulated PWR primary water at 320 °C for 500 h, replotted from [88].

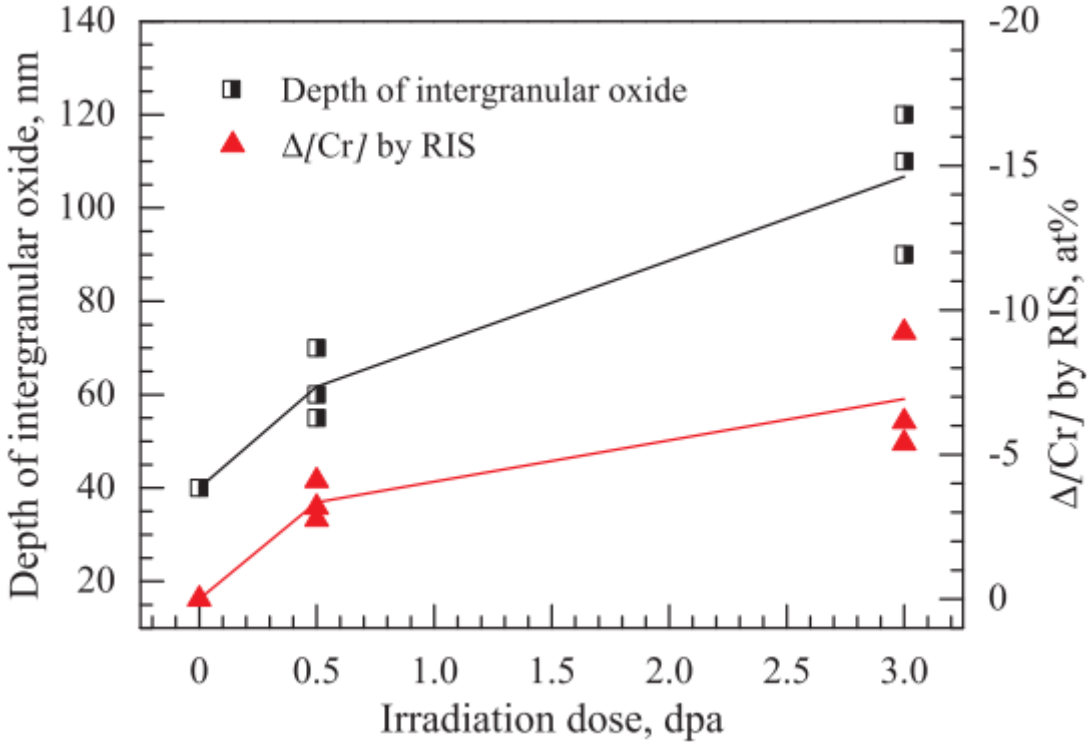

Figure 2.12. Intergranular oxidation depth and total Cr RIS observed on proton irradiated 304NG stainless steel exposed to simulated PWR primary water at 320 °C for 500 h from [88].

Fukumura et al. performed SCC testing in simulated PWR primary water of cold worked (CW) 316 stainless steel from flux thimble tubes from an operating PWR at doses of 3, 19, and 73 dpa [89]. Observed inner oxide thickness and intergranular corrosion changed dramatically from 3 dpa to 19 dpa and very little change from 19 dpa to 73 dpa indicating saturation with respect to corrosion behavior as presented in Figure 2.13. Furthermore, scanning electron microscopy (SEM) surface imaging revealed little difference between 0 dpa and 3 dpa. This work indicates that there is a minimum threshold before radiation causes significant effects on the bulk corrosion (consistent with Deng et al. [88]), but also radiation effects begin to saturate at moderate damage (~19 dpa).

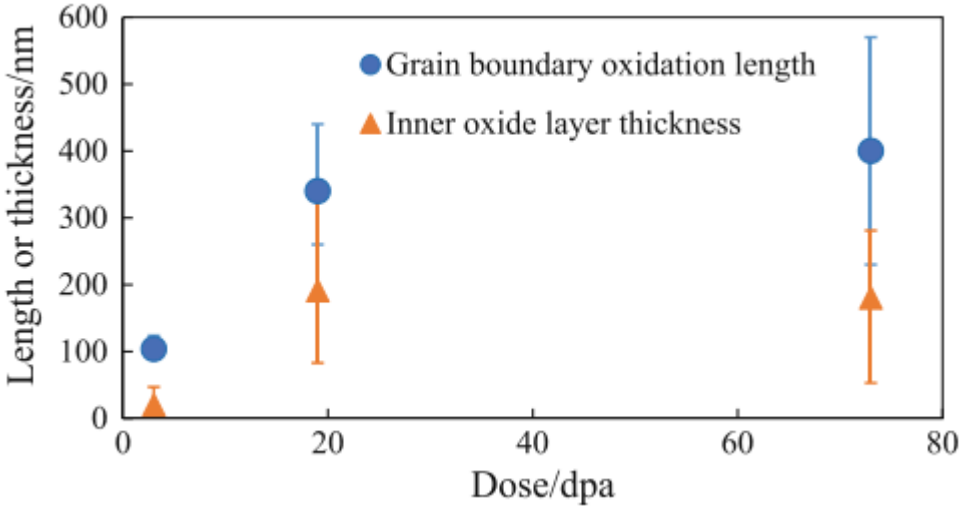

Figure 2.13. Both inner oxide thickness and intergranular oxidation measurements on reactor irradiated CW 316 stainless steel exposed to simulated PWR primary water at 320 °C for 1149 h from [89].

Perrin et al. performed a set of oxidation experiments on proton-irradiated 316L stainless steel in simulated PWR primary water at 320 °C [43]. The exposure was completed in two parts: the first exposure lasted 620 h, and the second exposure was 25% ^{18}O enriched water for either 17 h or 404 h. After the combined 1024 h of exposure, the inner oxide thickness of the irradiated condition was 60 nm, which was slightly thinner than the non-irradiated case of 90 nm. The difference was attributed to possible grain orientation differences which would be consistent with

Jiao and Was [71]. Secondary ion mass spectroscopy from the oxide after the longer second exposure is presented in Figure 2.14, showing a bimodal profile of ^{18}O in the oxide. A schematic of tracer profiles in oxides is given in Figure 2.15, showing a clear match with the short-circuited oxygen diffusion behavior predicted by Atkinson [65]. This work shows an unusual result of decreased corrosion kinetics on proton-irradiated material, but also clear evidence of oxygen short-circuit behavior in simulated PWR primary water conditions.

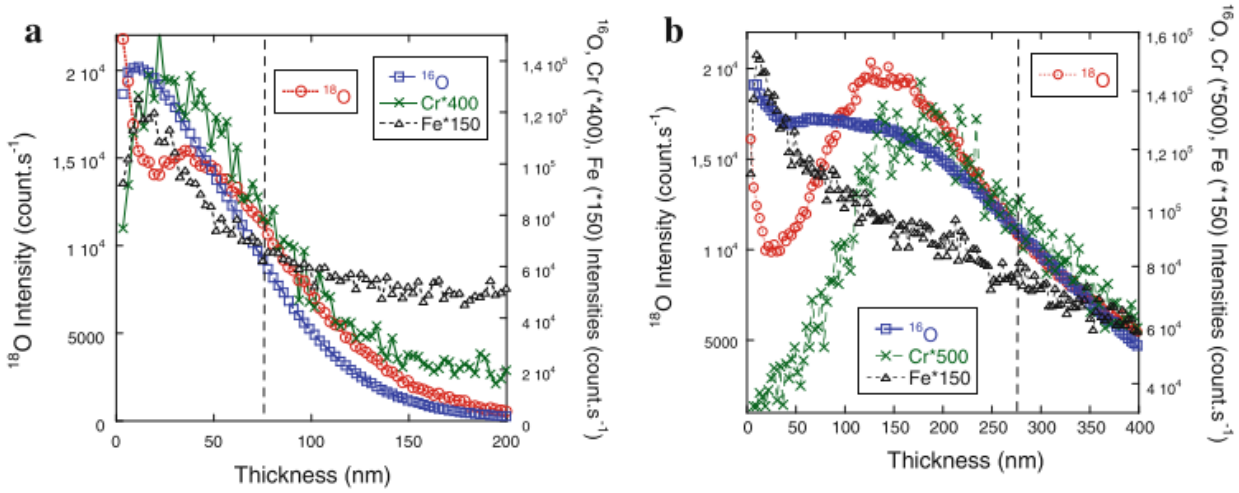

Figure 2.14. Secondary ion mass spectroscopy profiles from proton-irradiated (a) and non-irradiated (b) 316L stainless steel exposed to simulated PWR primary water for 620 h followed by 404 h of ^{18}O enriched water from [43].

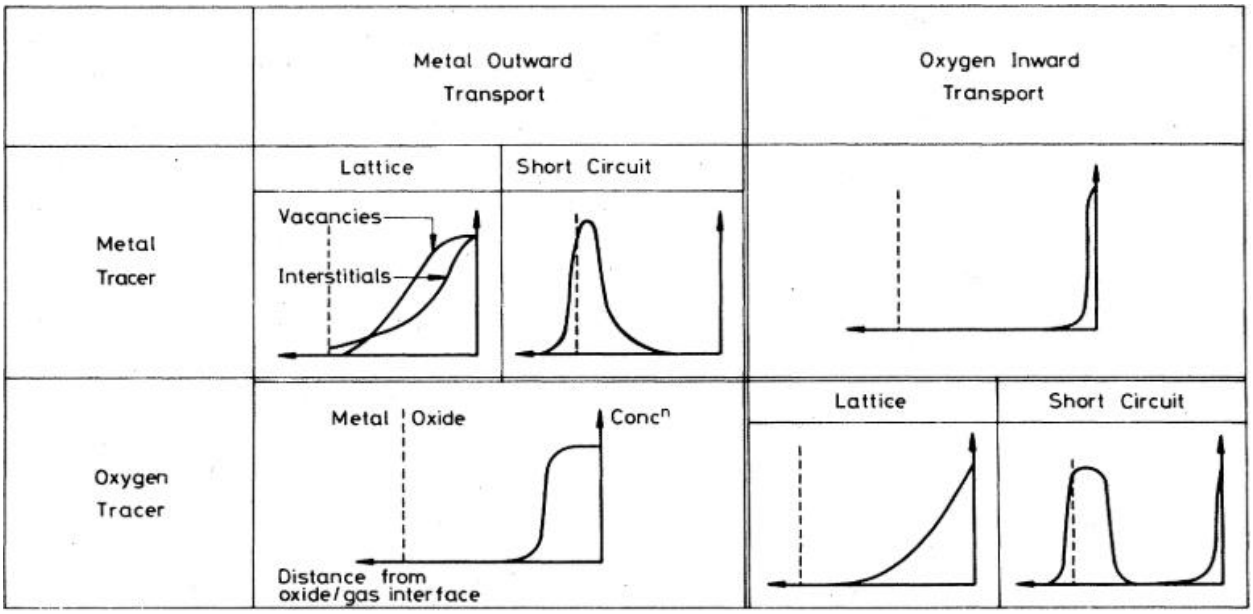

Figure 2.15. Schematic tracer diffusion profiles for different oxidation mechanisms from [65].

Gupta performed tensile tests in simulated PWR primary water on iron ion irradiated 304L and dual irradiated 304L with iron and helium ions to 5 dpa for 360 h [30]. The oxide thicknesses are presented in Table 2.6, showing that self-ion irradiation significantly increases the inner oxide thickness. Another experiment by Gupta compared the effect of static autoclave size on the oxide thickness for the dual irradiated conditions, wherein the inner oxide thickness increased from 8–10 nm in the small autoclave to 90–100 nm in the large autoclave. This work demonstrates the importance of flowing autoclaves and static autoclave size on corrosion behavior as well as a qualitative increase of corrosion rate with self-ion irradiation.

Table 2.6. Oxide thickness comparison of 304L stainless steel tensile bars irradiated with Fe and He ions to 5 dpa and exposed to simulated PWR primary water for 360 h from [30].

Sample	Thickness	
	Outer oxide (nm)	Inner oxide (nm)
Unirradiated	20 – 100	5 – 6
5 dpa – Fe	1 – 3	10 – 20
5 dpa – FeHe	10 – 20	8 – 10

Boisson et al. compared oxidation behavior on 1 dpa proton-irradiated 316L stainless steel exposed to 325 °C simulated PWR primary water for 24 hours [36]. Inner oxide thickness from similar grain orientations in the non-irradiated case was 10 ± 2 nm and in the irradiated case was 53 ± 6 nm. This increase was very large compared with other literature; this change may be attributable to the short corrosion time accentuating the difference in thickness.

Lin et al. performed corrosion tests of proton irradiated 308L weld metal in simulated PWR conditions [34]. This 308L material had both δ-ferrite and austenite phases characterized for their respective corrosion behaviors in non-irradiated, 0.5 dpa, 1.5 dpa, and 3 dpa. Both austenite and δ-ferrite phases showed increased corrosion with radiation damage levels, see

Figure 2.16. Lin et al. found sensitivity to radiation damage as low as 0.5 dpa on bulk corrosion which shows a greater sensitivity to total irradiation damage than Deng et al. [88] or Fukumura et al. [89], but is comparable to Boisson et al. [36].

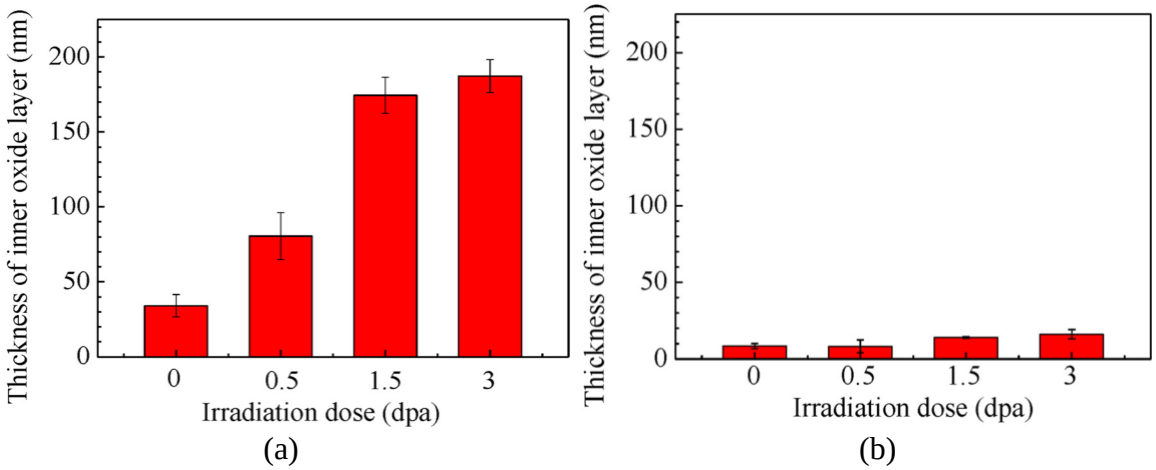

Figure 2.16. Inner oxide thickness measured on the austenite (a) and δ-ferrite (b) phases of 308L stainless steel weld metal proton irradiated to different damages and exposed to simulated PWR primary water conditions from [34].

2.5.2. Nuclear Reactor Irradiation-Assisted Corrosion

Corrosion that occurs within an operating reactor is the motivating topic of this dissertation, so it is important to discuss the effects of reactor irradiation on corrosion. Unfortunately, very little published data on reactor corrosion of stainless steels in LWRs exists. However, more data is available for zirconium alloy corrosion under irradiation, so some of this data will be discussed here to provide additional evidence of reactor irradiation affecting corrosion.

Asher et al. performed in-pile experiments on three zirconium alloys using three different environments to compare corrosion behavior: atmospheric 250–450 °C steam/CO_2, 340 °C hydrogenated (20 mL/kg) water, and 340 °C oxygenated (200 ppb) water [90]. The radiation fields for these in-pile experiments were a fast neutron flux of 4×10^{13} n/cm^2.s, a thermal neutron flux of 4×10^{14} n/cm^2.s, and a γ intensity of 10^9 R/h. The weight gain measurements for these

experiments in descending order were oxygenated water, steam/CO_2, hydrogenated water, and non-irradiated as presented in Figure 2.17. This work demonstrated that radiation accelerates zircaloy corrosion in all cases, and that dissolved hydrogen reduces, but does not eliminate, radiation effects.

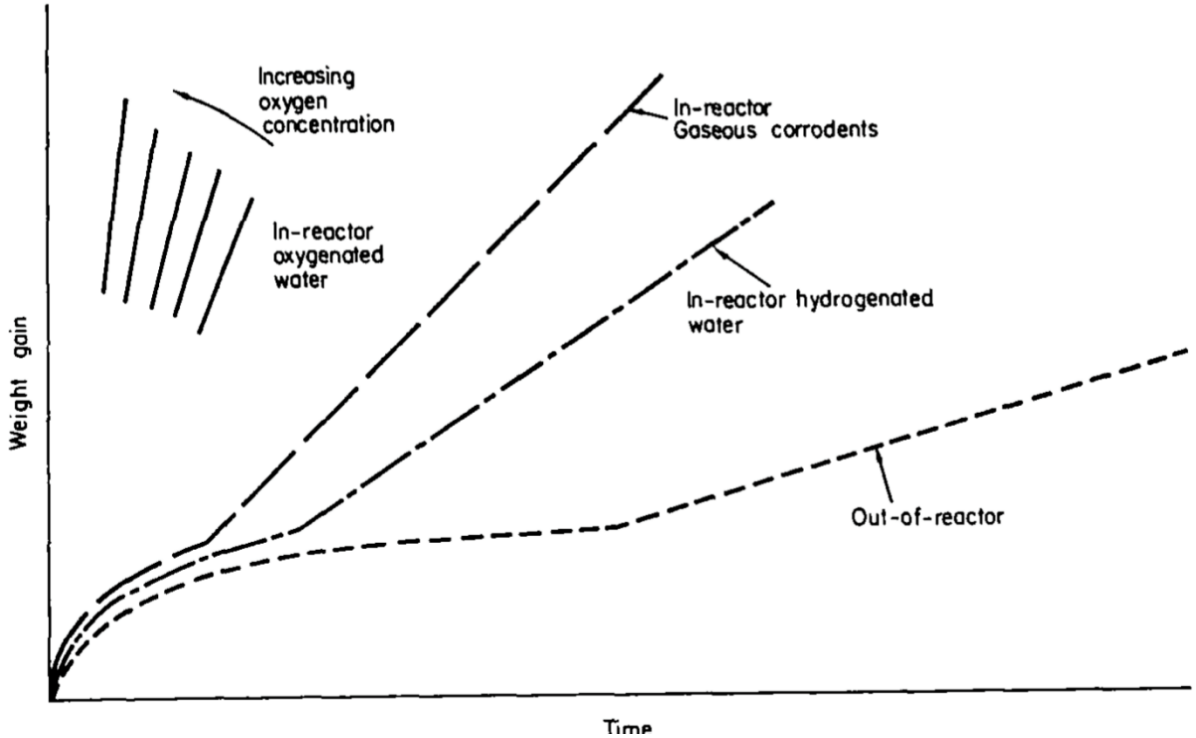

Figure 2.17. Schematic comparison of zircaloy oxidation in different water chemistry in-pile compared with out-of-pile conditions from [90].

Another similar set of experiments by Asher et al. compared four different heats of zirconium alloys exposed to moist CO_2 at 300 °C in reactor and 300–340 °C out of reactor [91]. Some heat treatments of Zr-2.5Nb showed no effect of irradiation on corrosion, whereas one heat treatment of Zr-2.5Nb and Zircaloy-2 showed irradiation corrosion at 300 °C is comparable to 340 °C in the non-irradiated case as presented in Figure 2.18. This work indicates that irradiation can accelerate the corrosion kinetics substantially in zirconium.

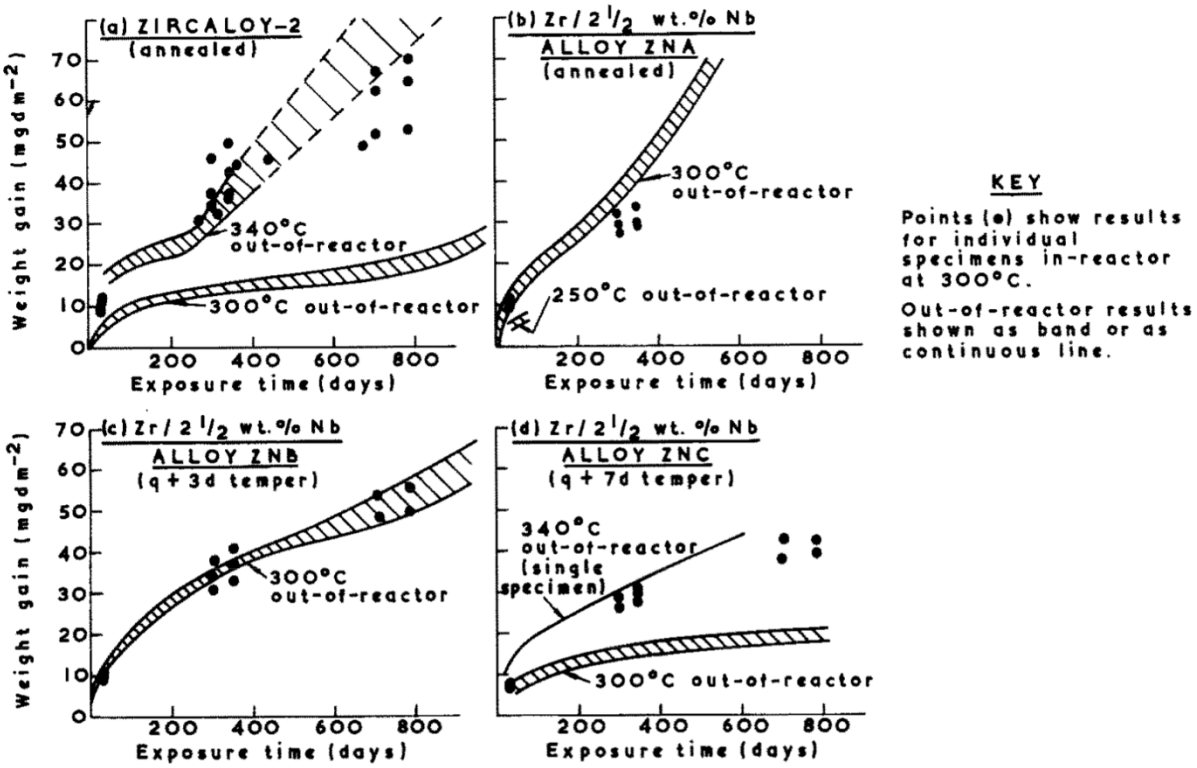

Figure 2.18. Comparison of different zirconium alloy heats oxidation in-pile to various temperatures out-of-pile from [91].

Vankeerberghen et al. performed in-pile electrochemical measurements of two steels (316 and EUROFER 97, a ferritic-martensitic 9-Cr steel) in a near room temperature water environment [92]. With increasing thermal neutron flux, the electrochemical potential increased and the polarization resistance decreased for both materials. This result demonstrated some direct evidence of radiolysis affecting the ECP for stainless steels and some change in the electrical properties of the oxide film.

Additional work by Bosch et al. performed in-pile electrochemical measurements in simulated PWR conditions on 304 and 306 stainless steels at 300 °C [93]. In this work, the corrosion potential and polarization resistance did not change significantly between in-pile and out-of-pile measurements. Electrochemical impedance spectroscopy results indicated a thicker oxide layer formed on the in-pile samples compared with the out-of-pile samples. The reduced potential response from the flux when compared to the low-temperature in-pile measurements of

Vankeerberghen et al. [92] was consistent with faster recombination kinetics of radiolysis products at higher temperature. Still, the change in spectroscopic measurements of the oxide indicates some effect of reactor irradiation on increasing the corrosion rate of stainless steels.

2.5.3. Gamma-Irradiation-Assisted Corrosion

Gamma irradiation is a more accessible form of irradiation which impacts a larger number of practical applications such as waste storage in addition to nuclear reactors. As mentioned earlier, gamma irradiation only causes water radiolysis, not displacement damage, so it effectively separates the effects of water radiolysis from displacement damage on corrosion.

Daub et al. have shown that ^{60}Co gamma irradiation (6.8 kGy/h) effects on room temperature alkaline ECP of carbon steel can be simulated by using an equivalent concentration of H_2O_2 in solution [94]. Electrical measurements of the oxide showed very similar properties between gamma exposed and hydrogen peroxide exposed samples, see Figure 2.19. The main difference was the extended amount of time needed under gamma irradiation to saturate the ECP of the system compared to non-irradiated exposure to an initial H_2O_2 concentration. Without initial H_2O_2, irradiation must take time to produce the H_2O_2 before affecting the ECP. This work shows that the hydrogen peroxide production of water radiolysis directly changes the ECP, and short-lived products do not immediately increase the ECP.

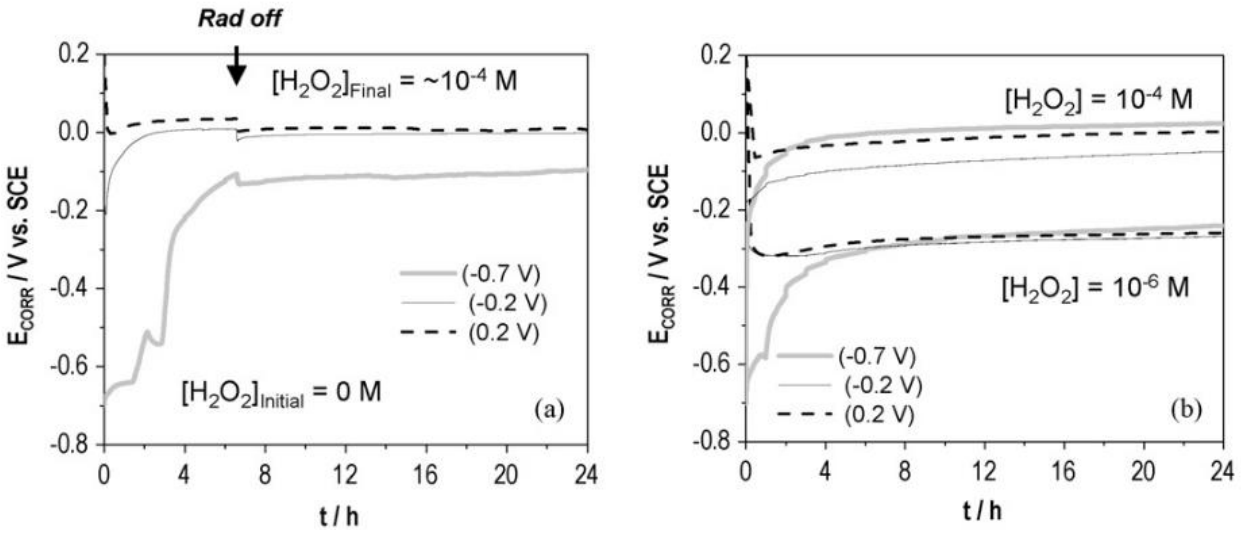

Figure 2.19. Effects of pre-grown oxide film potential, initial H_2O_2 concentration, and gamma irradiation on the evolution of corrosion potential of carbon steel with time from [94].

Another work by Daub et al. explored the effect of ^{60}Co gamma irradiation on alkaline and neutral corrosion of carbon steel at 150 °C [95]. Here, the gamma irradiation in alkaline conditions induced the formation of hematite. Furthermore, irradiation decreased the corrosion rate by altering the oxide speciation and forming a more passive oxide. This work shows that the ECP increase of gamma radiolysis can still occur at higher temperatures, that the oxidation rate can be affected by radiolysis, and oxide structure changes are induced by radiolysis.

Similar experiments were performed using ^{60}Co gamma irradiation (0.5 kGy/h) and 250 °C of 304 stainless steel by Kawaguchi et al. and Ishigure et al. [96,97]. The oxide film was not directly measured, but solid iron oxide particulate and aqueous iron ion release was periodically measured from the autoclave outlet. The insoluble crud increased dramatically with irradiation, but the soluble ions did not change significantly as presented in Figure 2.20. This indicates that the solubility limit of iron was reached in the outlet regardless of irradiation. Still, more iron was released under irradiation as a solid precipitate in the outlet, so the local solubility was increased under irradiation. Additionally, increased flow rate through the autoclave yielded an increase in solid iron collected in the irradiated case. This correlation further indicates an increase in iron ion

solubility under gamma irradiation. This work does not indicate any changes in the corrosion behavior directly, but the radiolysis induced changes in the water chemistry increase the iron ion solubility which may impact the dissolution component of corrosion.

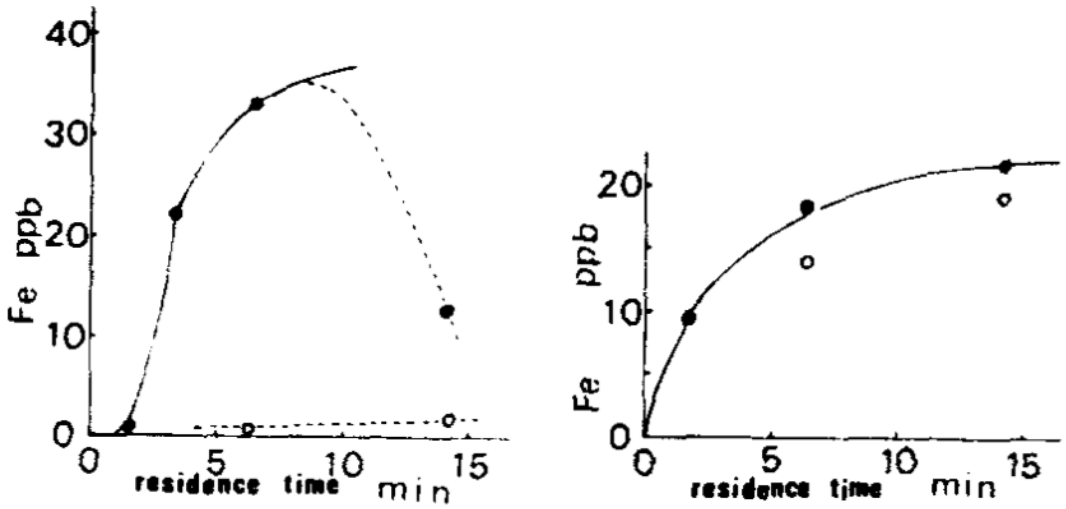

Figure 2.20. Comparison of iron particulate (left) and iron ion (right) release with (filled circles) and without (open circles) gamma irradiation from 304 stainless steel exposed to 250 °C water containing 20 ppb O_2 from [97].

To summarize, radiolysis in isolation appears to only impact the water chemistry in two ways: elevating the ECP via hydrogen peroxide production and increasing the solubility of ions.

2.5.4. Ion Irradiation Assisted Corrosion

Ion irradiation is a more accurate simulation of reactor irradiation because, unlike gamma irradiation, ions can induce both displacement damage and water radiolysis. The experiment method for using ion irradiation to study irradiation effects on corrosion was pioneered by Lewis and Hunn [98]. A vessel containing the corrosion medium was separated from the ion beam source by a thin foil of sample material. In this configuration, the ion beam was accelerated with enough energy to transmit through the sample foil (causing displacements) and into the corrosion medium (causing radiolysis).

The relevant experiment performed by Lewis and Hunn used a 2.0 MeV proton beam through a 12 μm austenitic 18Cr-10Ni-3Mo stainless steel foil (990 keV at the metal/water interface) for a duration of 4 hours. The proton current density was 1–2 $\mu A/cm^2$, and the temperature at the foil surface increased to 80 °C from beam heating. Two control experiments were performed at room temperature and at 90 °C (to account for the beam heating) for 4 hours each. Oxide thickness was measured by elastic recoil detection for all three cases: 5 atomic layers were measured for the room temperature sample; 20 layers for the 90 °C sample; and 100 layers for the irradiated sample. This shows a factor of 5 increase in the total corrosion rate under irradiation.

More recent work by Lapuerta et al. examined the effect of proton irradiation on the corrosion of pure iron for nuclear waste storage [99,100]. Two configurations were used: transmission through iron foil into water and irradiation through humid air first then transmitted through an iron foil into argon. Unfortunately, neither work compared the oxygen uptake (i.e., corrosion) between irradiated and non-irradiated samples. An increase in the corrosion rate was noted in aerated water compared with deaerated water under irradiation. This indicates that water radiolysis does not flatten the differences in initial water chemistry.

Muzeau et al. examined the open circuit potential response of 316L stainless steel to proton irradiation in simulated PWR primary water [87]. The autoclave was static and was filled with the feedwater mixture before attaching to a cyclotron for 34 MeV proton irradiation. Samples were exposed to multiple short irradiations at different fluxes and temperatures while continuously measuring the potential difference between a Pt electrode in the cell with the sample material. Shifts in the potential were observed during irradiation, and the magnitude of the shift increased with increasing proton flux. Repeated irradiations decreased the potential shift

until no response was observed. Below 250 °C, the magnitude of the irradiation-induced potential shift increased with decreasing temperature. These results indicate: water radiolysis induced ECP changes depend on the irradiation flux, protective oxides and radiolysis product saturation cumulatively builds resistance to further irradiation, and lower temperature water is more sensitive to radiolysis.

Wang et al. performed additional proton irradiation assisted corrosion experiments using the same equipment as Muzeau et al. [87,101]. Here, 23 MeV protons were transmitted through a 900 μm thick 316L disc and into a static corrosion cell filled with up to 300 °C water at 90–100 bar. The proton flux ranged from 6.6×10^{7} to 6.6×10^{11} H^{+} $m^{-2}s^{-1}$ or an equivalent current density range of 1.1×10^{-6} to 1.1×10^{-7} nA cm^{-2}. Even at these extremely low fluxes, a noticeable increase in the ECP was observed on the order of tens of mV. Much like the work of Muzeau et al., repeated irradiation reduced the potential shift observed under irradiation. Again, this cumulative effect was most likely caused by the static cell water chemistry changing over time and the development of a passive film. One new finding of this work was that higher hydrogen content suppresses the potential response, demonstrating the efficacy of dissolved hydrogen in suppressing radiolysis effects on corrosion.

The thesis work of Wang also includes electron IAC of 316L in similar conditions to the proton work [72]. No measurements of oxide thickness were conducted, however the oxide structure was examined and compared with non-irradiated controls. Many of the oxide features are consistent with literature of non-irradiated corrosion: a double layer with spinel inner oxide that is porous and partially epitaxial with the substrate in a fine-grained polycrystalline layer. Two major differences are observed after irradiation: the formation of hematite in the outer oxide and chromium dissolution. Hematite in the outer oxide was consistent with the positive oxidation

potential shift observed and expected with elevated ECP [48]. Chromium dissolution was observed alongside pitting on the surface, both observations are consistent with elevated potential to a greater degree than hematite formation. This work demonstrated some direct effects of irradiation changing the structure of the oxide film formed in addition to altering the water chemistry.

Proton IAC of 316L was also done by Raiman et al. using a flowing water loop and 320 °C water with 3 wppm H_2 [22,102–104]. IAC experiments lasted 4–72 h and had a proton flux such that the damage rate at the corroding surface of the metal was either 7×10^{-7} or 7×10^{-6} dpa/s and the radiolysis was 400–4000 kGy/s. Three distinct regions were observed and characterized: the irradiated region in the beam path, the non-irradiated region away from the beam path, and the radiolysis flow region where radiolysis products were transported by convection. Inner oxide thickness was measured in each region under each condition and is presented in Figure 2.21. A notable decrease in oxide thickness was observed under irradiation and in the radiolysis flow region compared with non-irradiated conditions. Furthermore, elemental analysis in Figure 2.22 shows that chromium was depleted in the inner oxide for both irradiated and flow regions relative to non-irradiated inner oxides. Raman spectroscopy was used to confirm the Cr depletion in the inner oxide and observed the presence of hematite both in irradiated and radiolysis flow regions. The inner oxide showed some signs of dissolution in irradiated and radiolysis flow cases, and no evidence of dissolution was present in the non-irradiated region. This set of work primarily demonstrated the effects of radiolysis increasing potential, causing hematite formation, and depleting chromium in the inner oxide. Because there were no substantial differences between irradiated and flow regions, the changes in oxidation behavior were caused by water radiolysis and not displacement damage. Raiman et al. speculated that displacement damage may

have accelerated the oxidation rate in the irradiated region over the flow region and the non-irradiated region despite the oxide thickness measurements. It is possible that radiolysis shifts the dominant mode of corrosion to dissolution, hence the decrease in oxide thickness under irradiation and radiolysis flow. However, there is no quantitative measure of the dissolution in this work, so no effect of displacement damage is observed.

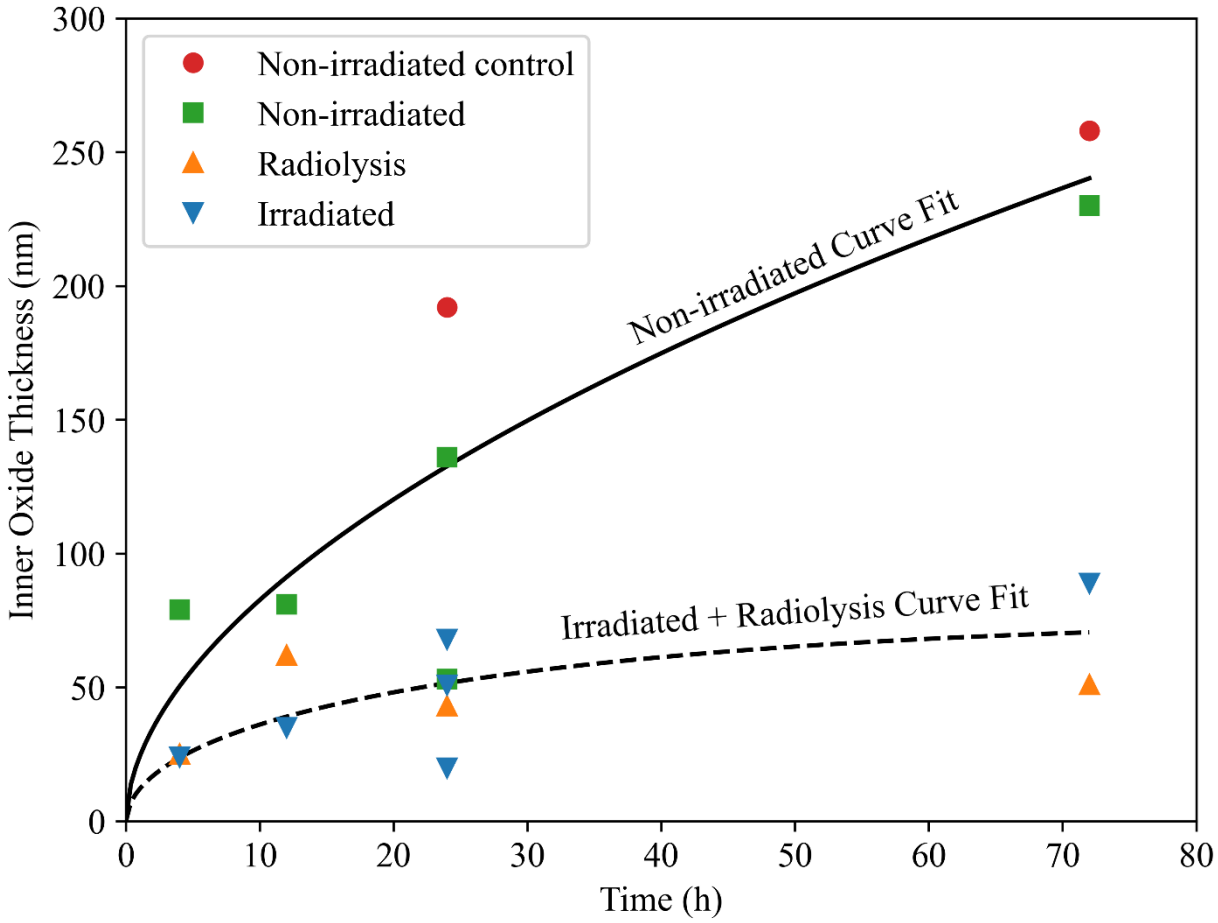

Figure 2.21. Inner oxide thickness measured on proton irradiation assisted corrosion of 316L stainless steel in 320 °C water containing 3 wppm H_2 adapted from [104].

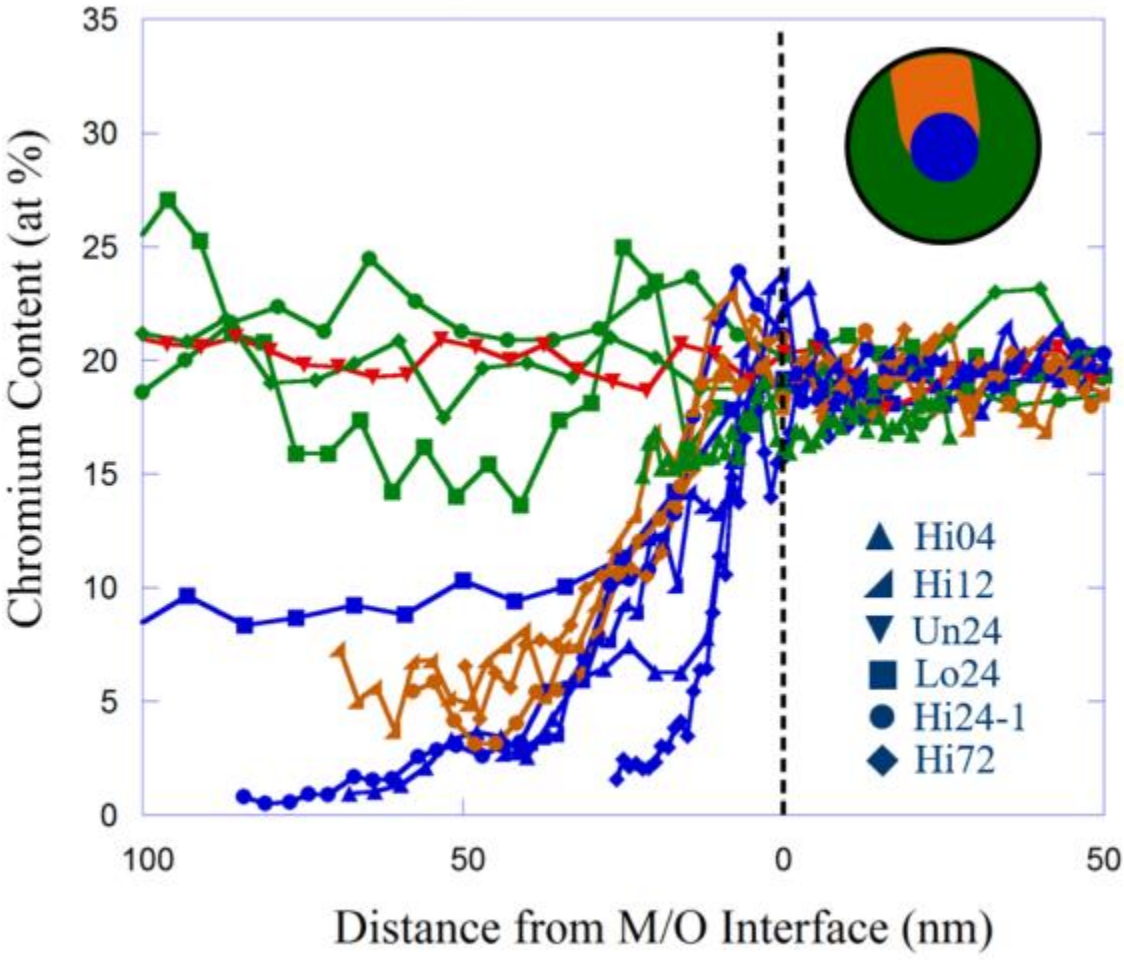

Figure 2.22. Chromium content measured by energy-dispersive X-ray spectroscopy of inner oxides in irradiated, radiolysis flow, and non-irradiated regions of 316L stainless steel exposed to proton irradiation assisted corrosion in 320 °C water containing 3 wppm H_2 from [103]. The legend identifiers refer to the damage rate and exposure duration in hours: "Hi" for 7×10^{-6} dpa/s, "Lo" for 7×10^{-7} dpa/s, and "Un" for a non-irradiated control.

From all irradiation assisted corrosion literature, there are only a few radiation effects on corrosion that have been observed:

- Cumulative radiation damage results in faster corrosion kinetics [71,88,89].
- Water radiolysis changes the electrochemical corrosion potential [22,72,87,95,101,103].
- Water radiolysis causes increased dissolution of metal ions and oxides [22,72,96,97,103].

- Oxide thickness increases under irradiation in some cases [98] and decreases in others [95,103,104].

Literature reported radiation effects on corrosion are mostly limited to preexisting irradiated microstructures and water radiolysis effects. Changes in oxidation kinetics from radiation are mixed, and the mechanisms causing the changes are unclear between water radiolysis and displacement damage. The effect of radiation-induced displacement damage on oxidation kinetics represents a clear gap in the scientific understanding of radiation effects on corrosion.

Chapter 3

Objective

The objective of this work is to determine the role of displacement damage in simultaneous irradiation-corrosion of stainless steel in high temperature water. A hypothesis regarding the role of displacement damage in stainless steel corrosion follows:

Displacement damage in the inner oxide produces excess point defects that increase the cation diffusion coefficient, and thus increase the corrosion rate when cation transport is rate-limiting. However, radiolysis increases the thermal concentration of cation vacancies in the inner oxide by changing the oxygen activity in the water thereby dominating the cation diffusion coefficient and relegating displacement damage to a negligible contribution. Radiolysis may also change the corrosion mechanism to be rate-limited by oxygen transport, which would decouple displacement damage from the corrosion rate. Because the radiolysis effects on the oxide are thermodynamic and the displacement damage effects are kinetic, radiolysis effects supersede those of displacement damage. Consequently, radiolysis can either dominate or suppress displacement effects on corrosion rate.

To test this hypothesis, a combination of aqueous exposure with and without simultaneous ion irradiation, careful characterization of the microstructure, and thermodynamic and kinetic modeling were utilized. To achieve the main objective, four sub-objectives were established.

The first sub-objective is to determine the mechanisms of oxide growth and dissolution of stainless steel in high temperature water without irradiation. Understanding the effects of radiation on corrosion requires a robust understanding of the underlying corrosion processes. Oxide film characterization and development of a dissolution measurement technique are used in tandem with thermodynamic and kinetic models to infer the corrosion mechanisms.

The second sub-objective is to determine the separable effects of radiolysis on corrosion. Some amount of radiolysis is inevitable with displacement damage, so understanding its effect is necessary to deconvolute the effects of radiolysis from displacement damage. A new sample geometry was deployed to expose a bar sample to water radiolysis with negligible displacement damage during irradiation-corrosion of a disc sample. Subsequent characterization of the oxide film composition, structure, and thickness of the bar sample achieves this sub-objective.

The third sub-objective is to determine the separable effects of displacement damage on corrosion. A new experimental setup was designed using a low-pressure steam environment to minimize the radiolysis relative to displacement damage. While steam is not a perfect replacement of an aqueous environment, the fundamental effects of displacement damage can be observed with minimal radiolytic interference in steam. Again, subsequent characterization of the oxide film composition, structure, and thickness achieves this sub-objective.

The fourth sub-objective is to determine the effects of displacement damage in combination with water radiolysis. Experiments in high temperature water with simultaneous displacement damage and radiolysis at the corrosion surface are performed. Characterization and comparison to the isolated effects of radiolysis and displacement damage will yield their covariance.

Completion of these four sub-objectives yields the effects of displacement damage on corrosion with and without radiolysis. Finally, these findings were extrapolated to reactor conditions to gain some insight into the corrosion component of IASCC.

Chapter 4

Experiments and Methods

This chapter describes the equipment, facilities, and procedures used to conduct irradiation corrosion experiments and the subsequent characterization of the oxide film formed on the sample material. The last section describes the Thermo-Calc modeling parameters used to evaluate oxide composition and properties.

4.1. Design

Irradiation corrosion experiments require both a system to maintain the corrosion environment and a radiation source. To combine the radiation and corrosive environment, a specialized vessel is needed to ensure a known amount of radiation reaches the desired corrosion surface. The facility for performing these irradiation corrosion experiments was first described by Raiman et al. [105] and expanded as part of this dissertation to include a preheater for steam capability. For the work presented here, energetic H^+ ions are transmitted through sample material and into the corrosion environment consisting of either 320 °C water or 480 °C steam. The target for radiation is to cause a damage rate of 7×10^{-7} dpa/s at the corrosion surface to match the lower damage rate of Raiman et al. [104]. First, the flowing water autoclave system design is presented. Second, the accelerator and beamline facility for irradiation corrosion experiments is presented. Finally, the sample design is presented.

4.1.1. Autoclave System

The autoclave system is designed to deliver simulated light water reactor (LWR) conditions in a flowing water system as shown in Figure 4.1. Modifications to the system were made to accommodate a steam environment using a carrier gas shown in Figure 4.2.

For both operation modes, a filtration loop with a deionization filter is run continuously on the main column to ensure high water purity. Dissolved gas content is controlled by bubbling gas (hydrogen or air) through the main column and maintaining overhead pressure via a back-pressure regulator. Dissolved oxygen content and conductivity were continuously monitored on the filtration loop where they were recorded as inlet values. Dissolved oxygen content and conductivity were also monitored continuously in the return leg where they were recorded as outlet values.

Water gas content was calculated using Henry's Law and controlled using the column overhead pressure [106]:

$$C_{\mathrm{gas}} = M_{\mathrm{gas}} P_{\mathrm{col}} k_H^{\circ} \, exp\left(\frac{\mathrm{d}\ln \mathrm{k_H}}{\mathrm{d}(1/\mathrm{T})}\left[\frac{1}{T} - \frac{1}{298.15\ \mathrm{K}}\right]\right) \qquad \text{Eq. 4.1}$$

where the gas mass fraction in water C was calculated from the gas molecular weight M, the absolute partial pressure of the gas in the column overhead P_{col}, Henry's constant k_H°, and the derivative term which is the temperature dependence of Henry's constant. For molecular hydrogen, Henry's constant is 0.00078 mol/(kg·bar), and the derivative is 500. K [106]. For molecular oxygen, Henry's constant is 0.0013 mol/(kg·bar), and the derivative is 1500. K [106]. The ambient pressure was assumed to be 0.95 bar and the column temperature 293 K.

When the autoclave was not in use, the autoclave portion of the loop was circulated continuously while bypassing the autoclave itself. Continuous flow through the supply and return legs keeps the piping and instrumentation clean and functional.

When emulating PWR conditions, the target pressure was 13.1 MPa, and the target temperature was 320 °C in the autoclave. The pressure was supplied by two parallel dual piston preparative pumps in the supply leg and maintained by a back pressure regulator rated to 41 MPa in the return leg. Heat was supplied by a heating band on the autoclave body, and a regenerative heat exchanger was used to reduce the required heat load. The temperature was controlled by a Watlow thermocontroller using a type K thermocouple inside the autoclave. Outlet water was cooled and depressurized through the return leg and recovered in the primary column.

In steam mode, the target pressure was 1.4 MPa, and the target temperature was 480 °C in the autoclave. The gas regulator controlled the carrier gas pressure from the cylinder. Two preparative pumps supplied water pressure in the supply leg. A Grafoil needle valve controlled the autoclave pressure at the autoclave outlet. Heat was supplied by a heating band on the autoclave body and heating tape on the preheater/boiler. Temperature in the preheater and the autoclave were controlled by two Watlow thermocontrollers by using one in-line type K thermocouple between the preheater and autoclave and one thermocouple inside the autoclave. The outlet steam and carrier gas were expanded through the needle valve and discharged into an open sparge tank partially filled with water.

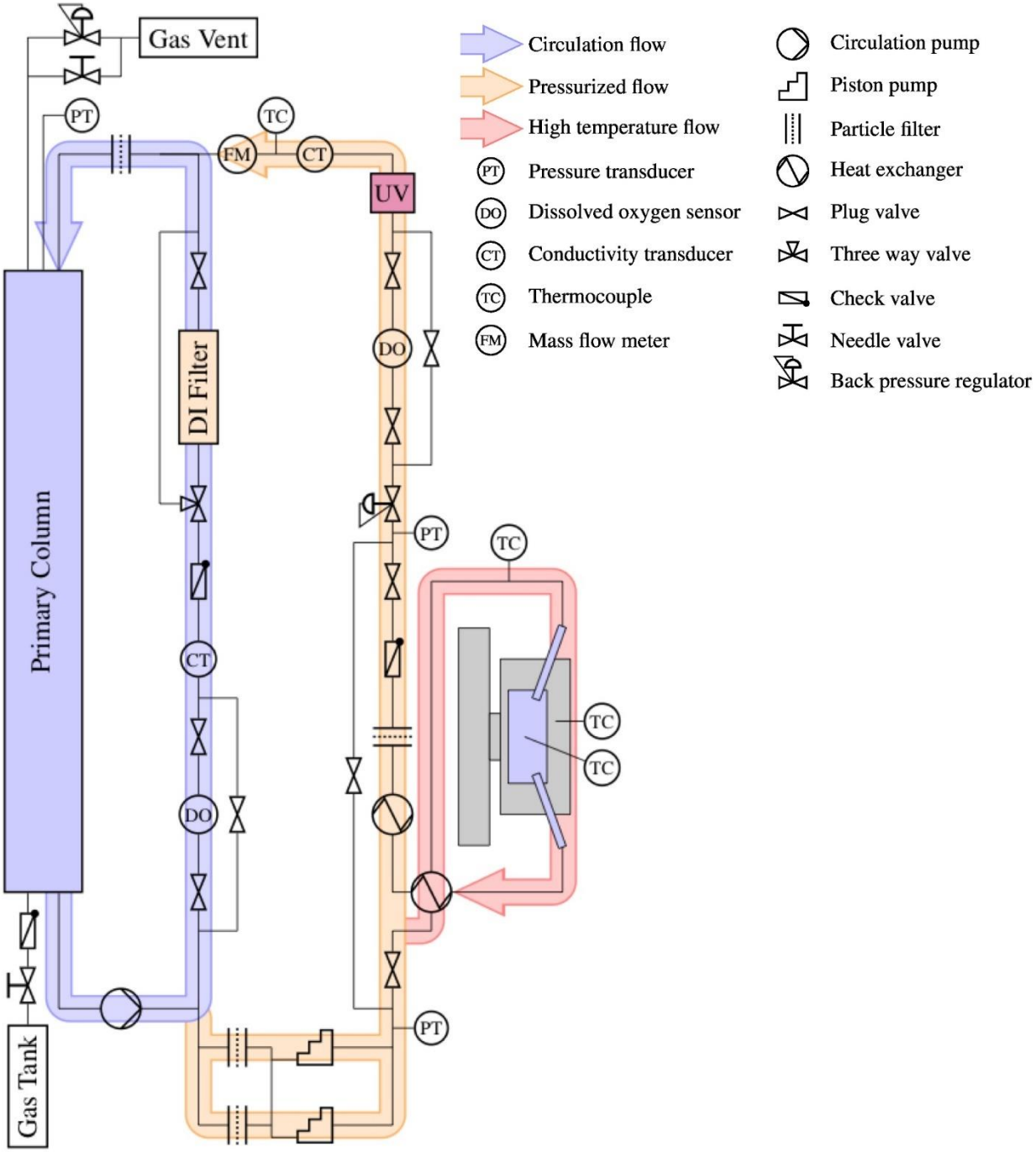

Figure 4.1. Process flow diagram for the irradiation assisted corrosion cell operating in aqueous loop mode.

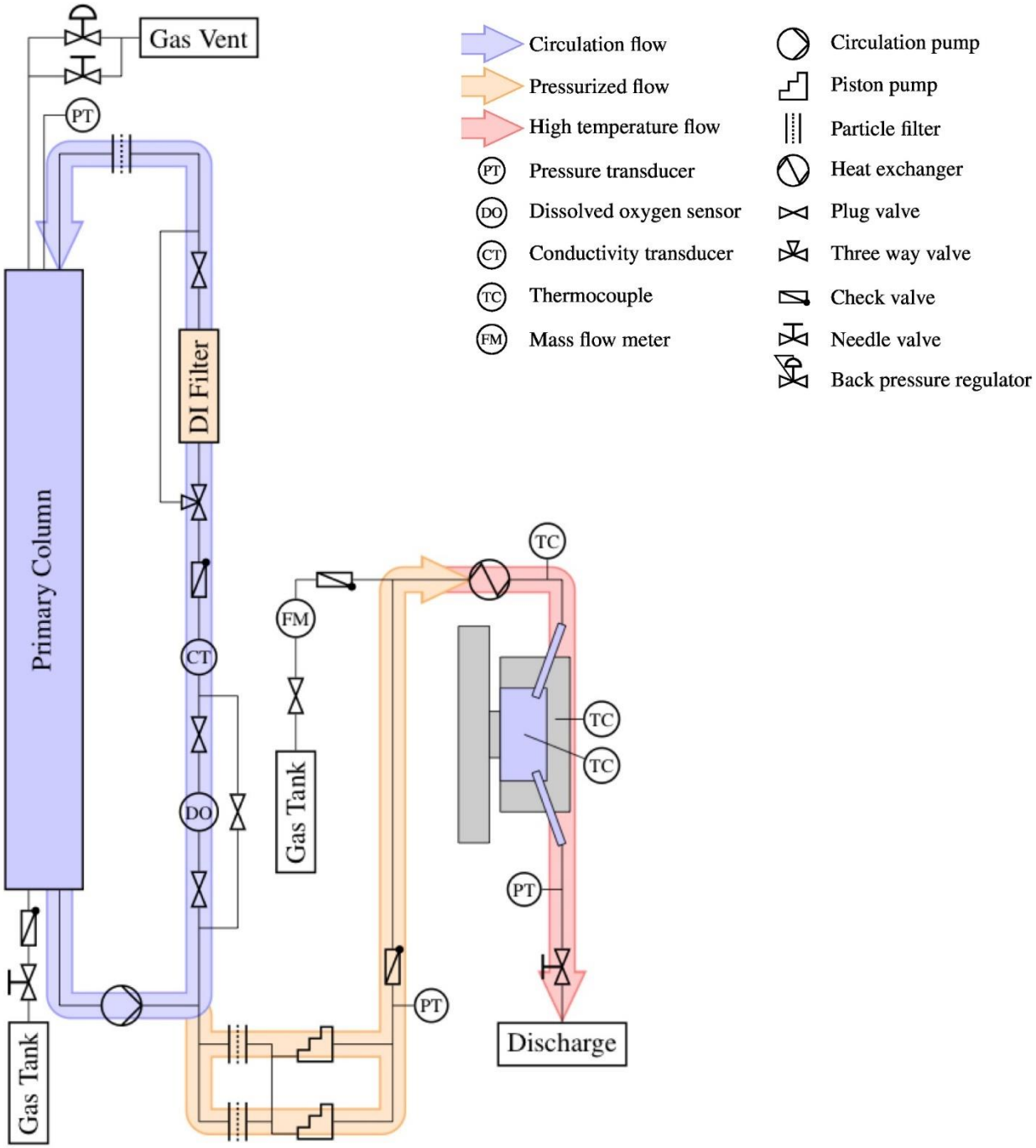

Figure 4.2. Process flow diagram for the irradiation assisted corrosion cell operating in steam once-through mode.

4.1.2. Accelerator and Beamline

The H^+ beam for irradiation corrosion experiments was produced at the Michigan Ion Beam Laboratory (MIBL) shown in Figure 4.3. The beam production can be summarized in five

parts: ion source, low energy leg, accelerator, high energy leg, and beamline. The source was a NEC Toroidal Volume Ion Source (TORVIS) which output 30 keV H^- ions. In the low energy leg, a magnet filtered and steered ions from the source to the accelerator. The NEC 3 MV Tandem Pelletron accelerated the H^- ions to 5.4 MeV H^+ ions. The high energy leg filtered the accelerated beam using another magnet and steered it into the irradiation corrosion beamline. The final beam focusing, shaping, and dosimetry was completed in the beamline where it was delivered to the target shown in Figure 4.4. The target for IAC experiments is discussed in Section 4.1.3.

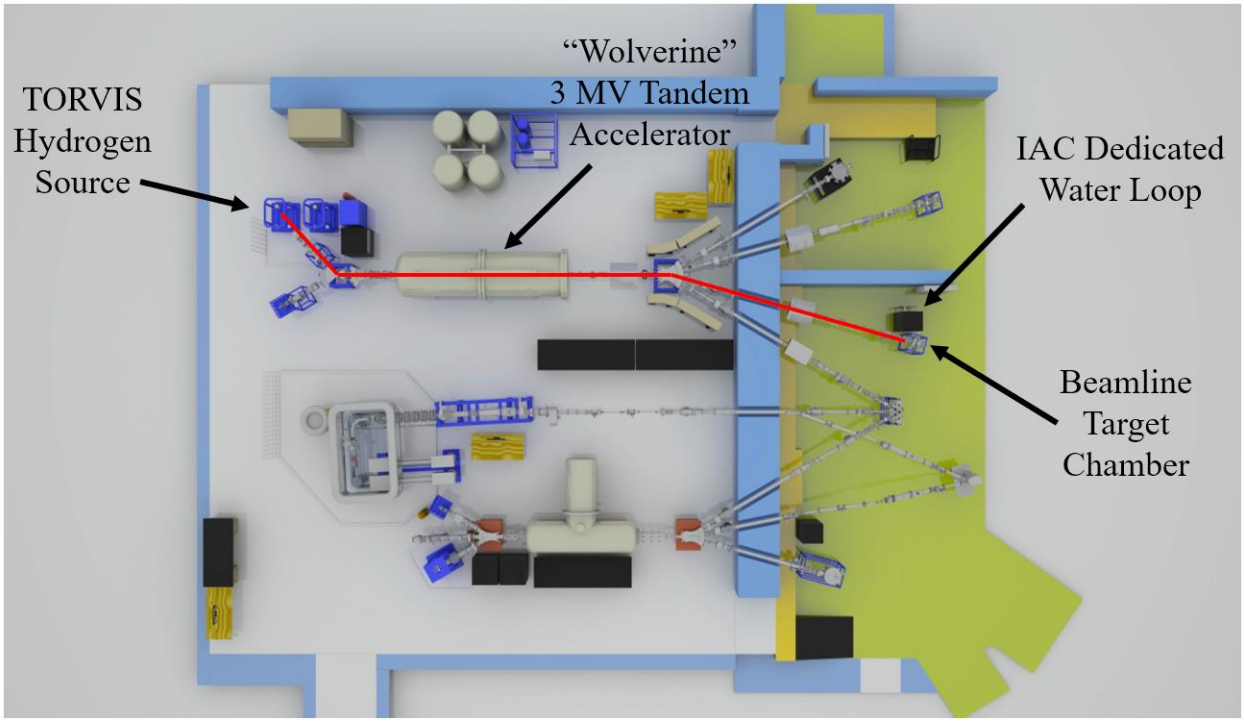

Figure 4.3. Schematic of the Michigan Ion Beam Laboratory locating the source, accelerator, and irradiation assisted corrosion beamline.

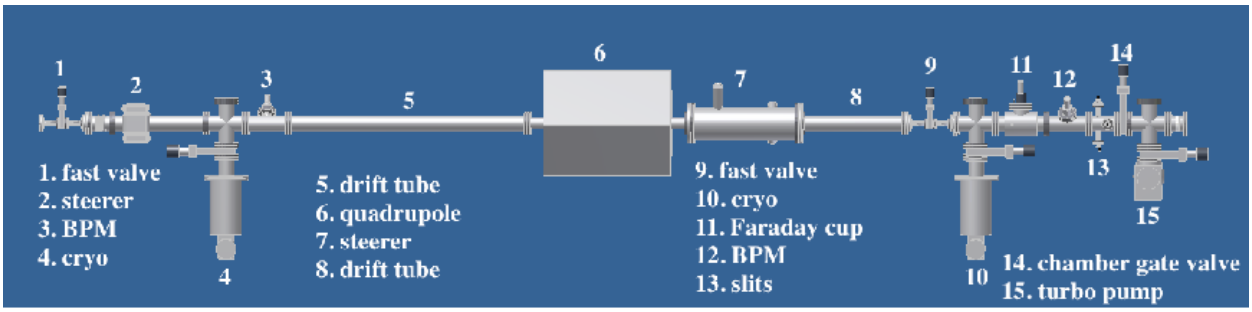

Figure 4.4. Schematic of the irradiation assisted corrosion beamline at the Michigan Ion Beam Laboratory.

4.1.2.1. Beam Focusing and Shaping

The low energy beam was focused into the accelerator using Einzel lenses and magnetic steerers. The high energy beam was focused by a quadrupole, and a beam profile monitor in the beamline was used to determine the beam shape. The beam was focused to yield a ~2 mm FWHM beam diameter. In the beamline, the beam was raster-scanned 255 Hz horizontally and 2061 Hz vertically to generate a consistent time-averaged current density on-target. The edges of the beam were cut off by a slit aperture system to define a rectangular beam shape of a known area.

4.1.2.2. Beam Current

Total beam current was measured by retractable Faraday cups positioned at various locations between the source and target. The slit apertures continuously collected and recorded current from the edges of the raster-scanned beam, providing on-line monitoring of beam current. A final Faraday cup between the slits and target is used to measure the current reaching the stage.

4.1.2.3. Pressure Monitoring

Several ion gauges are located at the low energy leg, high energy leg, and beamline. Four ion gauges are present on the irradiation chamber, two of which were used for recording pressure, the other two support the safety system for the irradiation corrosion beamline.

4.1.2.4. Equipment Safety

In the event of a sample breach, two fast-closing gate valves can isolate the beamline from the high energy leg and the accelerator. Both fast-closing gate valves close automatically if one or both ion gauges in the chamber rise above a selected threshold. If the sample ruptures between the autoclave and the beamline, these valves will protect most equipment from a damaging inrush.

4.1.2.5. Radiation Safety

During irradiation of stainless steel with high energy protons, prompt neutrons and gamma rays are produced in significant quantity. The autoclave was directly shielded with borated polyethylene clad in lead sheet on a cart. Various interlocks are employed to prevent exposure of personnel to radiation hazards.

4.1.3. Sample Design

Sample design is critical to irradiation corrosion experiments because the sample must transmit radiation into the water and serve as a barrier between pressurized water and a high vacuum system. The primary goal is the transmission of the radiation through the sample material. One mitigating factor of the sample design was minimization of cold work induced by hydrostatic stress. Another factor for consideration is that high energy protons induce both prompt and delayed radioactivity in the sample material by nuclear reaction. To achieve transmission of the proton beam without deforming the sample material, there are three main considerations: ion stopping, hydrostatic stress, and radioisotope production. Increasing the sample thickness reduces deformation from hydrostatic stress but is limited by the range of the proton beam. Increasing the proton energy allows transmission through thicker sample material

but induces more residual radioactivity in the sample. So, sample thickness and proton energy are the two parameters used to optimize the sample design.

An improvement on earlier sample designs was employed in this work. A precipitation hardened stainless steel (17-4 PH) was used in place of some sample thickness, creating a two-disc geometry. Both discs were sandwiched between a washer and a 1 mm diameter beam aperture as presented schematically in Figure 4.5. The presence of a stronger "backing" material decreases the deflection, and thereby deformation, of the sample material. Another benefit was that the backing material degraded the proton energy before reaching the sample material which reduces residual radioactivity in the sample disc. The sample disc can be completely separated from the backing disc after exposure, so the activity of the backing disc does not have to fall within the activity constraints of the characterization laboratories.

Radioisotope production cross-sections increase monotonically with proton energy between the relevant energy scale of 0 MeV to 6 MeV. Some nuclear reactions have non-zero energy thresholds which can create sharp changes in the expected radioactivation. Therefore, it was prudent to select an energy below the threshold for a major contributor to limit residual radioactivity. Because this work was on stainless steel (>50% ^{56}Fe), the ^{56}Fe(p,n)^{56}Co nuclear reaction was selected as the limiting reaction which has an energy threshold of 5.45 MeV [107]. The selected beam energy was 5.43 MeV to avoid this reaction and inform the sample thickness determination.

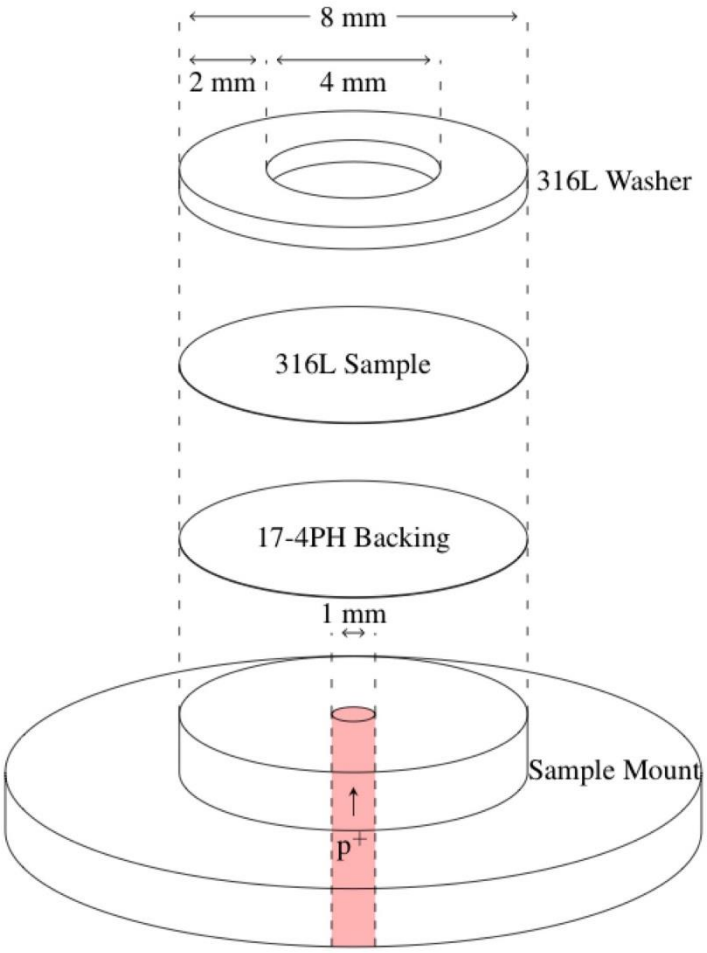

Figure 4.5. Schematic two-disc sample geometry for irradiation assisted corrosion.

With the ion energy selected, the ion stopping and damage rate was calculated with depth in the sample material to determine the maximum sample thickness. The Stopping and Range of Ions in Matter (SRIM-2013) [108] Monte Carlo software was used to perform this calculation. As an example, the damage rate caused by a 5.43 MeV H^+ beam is plotted sequentially through 17-4PH with a thickness of 38 μm and 316L with a thickness of 70 μm in Figure 4.6. Near the damage peak at ~93 μm, small changes in thickness or beam energy result in large changes of damage rate. To design an experiment with a well-controlled damage rate, a maximum total thickness of ~80 μm was selected to avoid the damage peak region and allow proton transmission into the water for radiolysis. With a 42 μm 316L sample thickness and water at 320

°C, the dose rate at the sample surface was calculated relative to the target 7×10^{-7} dpa/s using SRIM-2013 as illustrated in Figure 4.7. A cubic fit of the displacement damage in the metal and another cubic fit of the radiolysis dose rate in the water were evaluated at the water-facing surface of the 316L sample material.

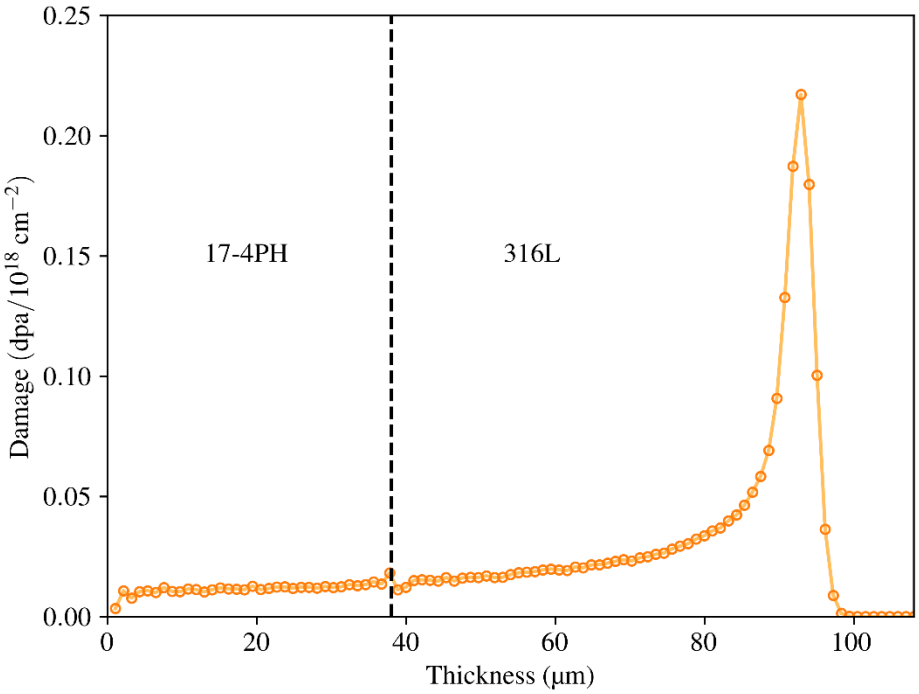

Figure 4.6. SRIM-2013 damage calculation through 38 μm 17-4 PH and 70 μm 316L per 10^{18} cm^{-2} fluence of 5.43 MeV protons.

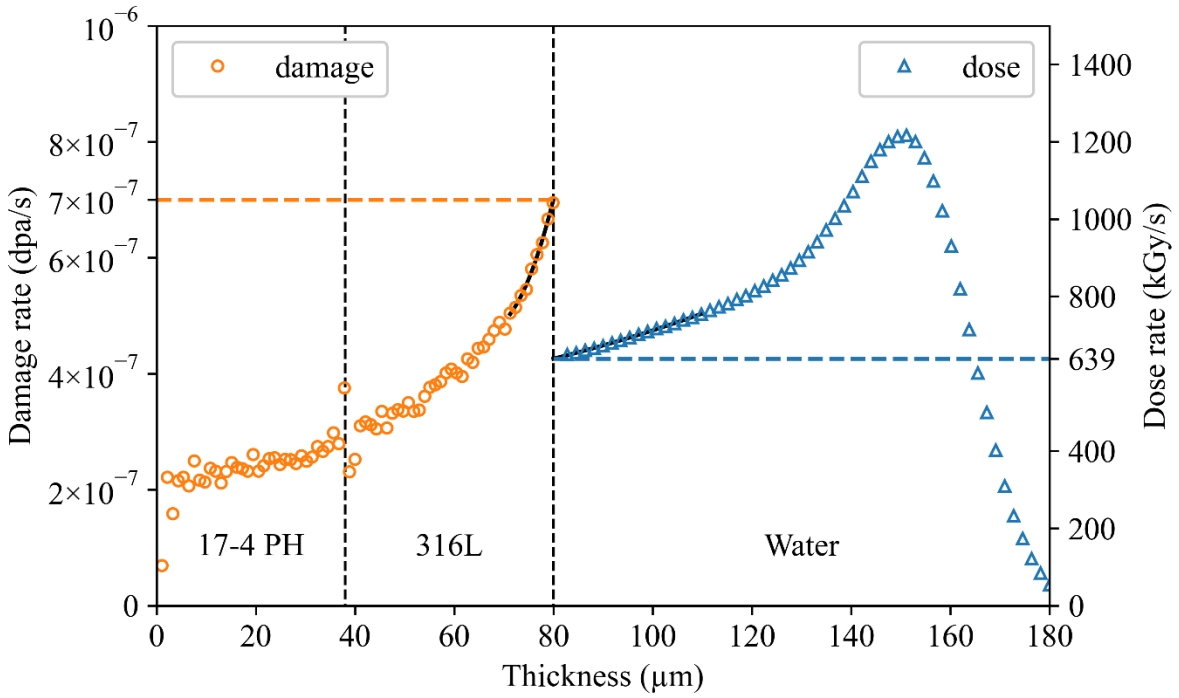

Figure 4.7. SRIM-2013 damage and dose rate calculations through 38 μm 17-4 PH and 42 μm 316L into 100 μm water at 320 °C at a current density of 3.31 μA/cm^2 to achieve 7×10^{-7} dpa/s at the corrosion surface.

Given the 80 μm maximum total thickness, deformation of sample material caused by hydrostatic stress determined both the minimum thickness of backing and sample material. The Young's modulus for 316L is ~190 GPa [109] and for 17-4PH it is ~200 GPa [110]. The 0.2% yield strength at ~320 °C for both are ~214 MPa [109] and 1103~1275 MPa [110], respectively. The sample geometry (see Figure 4.5) is a case between two standard statics problems: a simply supported circular plate and a clamped circular plate. At the center of the aperture the maximum deflection w_{max} can be calculated as follows [111]:

$$w^s_{max} = \frac{(5+\nu)Pr^4}{64(1+\nu)D} \quad w^c_{max} = \frac{Pr^4}{64D} \qquad \text{Eq. 4.2}$$

$$D = \frac{Et^3}{12(1-\nu^2)}$$

where c is the clamped case, s is the simply supported case, ν is Poisson's ratio, P is the hydrostatic pressure, r is the beam aperture radius, D is the flexural rigidity, E is Young's

modulus, and t is the thickness. The maximum stress σ_{max} also occurs in the center of the aperture [111]:

$$\sigma_{max}^{s} = \frac{3(3+\nu)Pr^2}{8t^2} \quad \sigma_{max}^{c} = \frac{3(1+\nu)Pr^2}{8t^2} \qquad \text{Eq. 4.3}$$

As previously mentioned, one constraint is to minimize the cold work on the sample material, so only the maximum strain was considered. Because the yield strengths differ vastly between the two materials, they were treated separately. The thin 316L sample will yield to the pressure and transmit the stress to the backing 17-4 PH, but the plastic deformation of the sample is limited by the deflection of the backing. Using this constraint, the expected strain on the sample material was calculated for both bounding cases against the relative thickness of sample and backing material in Figure 4.8. Based on this analysis, the minimum thickness of backing material to ensure the sample material is below its yield stress is ~60 μm. However, thinning the sample material to 20 μm cannot be done reliably, so a few percent strain was considered acceptable so the target backing material thickness was 35~40 μm.

To summarize, the selected ion beam was 5.43 MeV H^+ that transmits through a 40~50 μm 17-4 PH backing material, 30~40 μm 316L sample material, and into the corrosion medium.

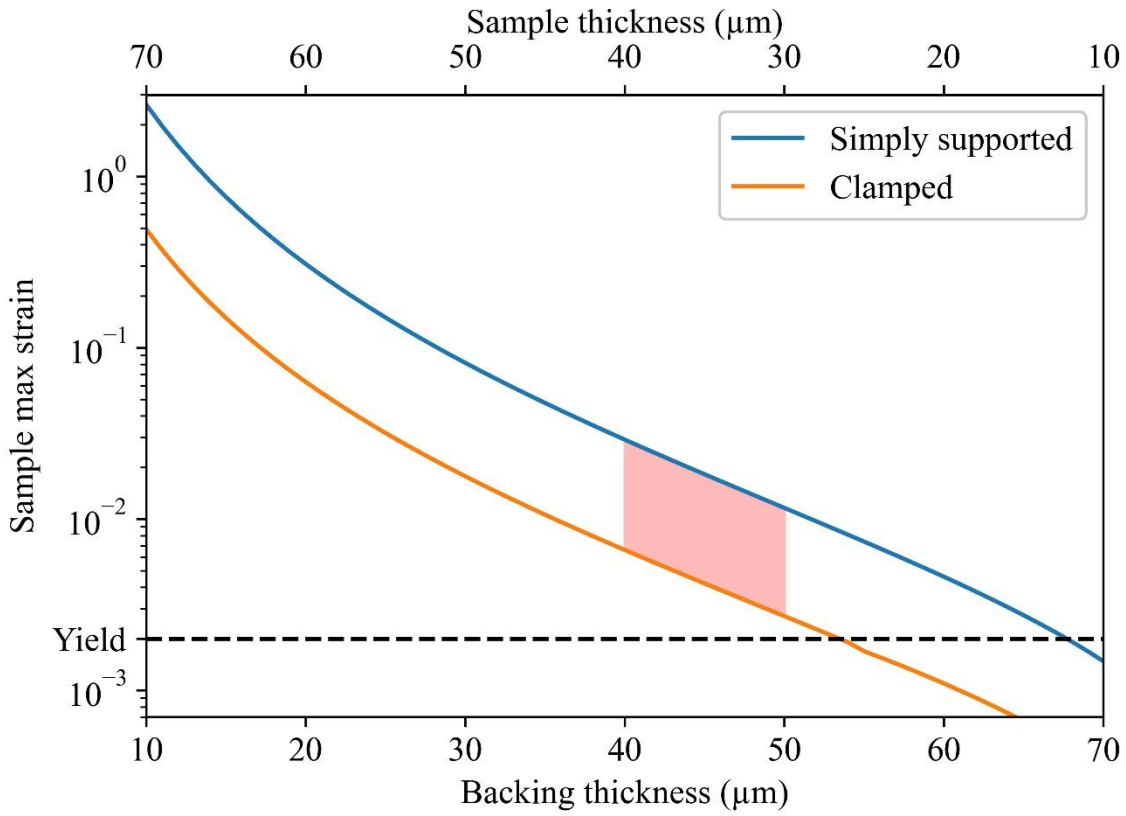

Figure 4.8. Relation between the sample strain in the center of the beam aperture with 17-4 PH backing thickness given that the total thickness is 80 μm. The shaded region indicates the expected strain for the target sample/backing thicknesses.

4.1.3.1. Dissolution Measurement

As part of the first sub-objective, measurement of dissolution is needed to fully characterize the corrosion rate. Direct measurement of dissolution is possible for a whole sample by measuring the metal content in the autoclave outlet. However, the irradiated area on the sample is small relative to the total sample size and other steel components of the autoclave system. These additional surface areas will add significant noise to any direct signal of dissolution via water analysis. Therefore, rather than direct measurement of dissolution, the total oxidation was measured, and the dissolution was inferred from the following relation:

$$\text{metal corroded} = \text{metal in oxide} + \text{metal dissolved} \qquad \text{Eq. 4.4}$$

Total oxidation was measured using a marker layer implanted beneath the surface of the sample material before any corrosion experiment. The marker serves as a reference to the original metal surface even after corrosion occurs. Depth of total metal oxidation can be measured by comparing the retracted metal surface to the original metal surface reconstructed from the marker layer.

Helium was chosen as the marker layer material for several reasons. Helium is chemically inert, so it does not influence the electrochemical reactions that compose corrosion. Helium is a very light element, so implantation of helium will induce minimal radiation damage in the sample material. Bubbles are easily formed in austenitic stainless steels with helium. Bubbles are also easy to image alongside the oxide film in cross-sectional electron microscopy.

For visibility, high amounts of swelling were desired for these bubbles, and the highest swelling is achieved through hot helium implantation at 600 °C in austenitic stainless steel [112]. However, there is a competing issue of sensitization which occurs at 600 °C in under 1 h (Figure 2.2). A temperature of 550 °C was chosen instead to mitigate the possibility of sensitization while still producing a high visibility marker layer. The helium fluence was empirically chosen to be 10^{16} cm^{-2} with a few test implantations at 550 °C.

Marker layer depth is dependent on the beam energy, and the energy was chosen to exceed the depth of corrosion. Based on the results of Raiman et al., the corrosion of 316L stainless steel was only 200~300 nm after 72 h. An implantation depth twice the corrosion depth was needed to avoid bubble interference with corrosion. The He^+ beam energy was chosen to be 400 keV because implantation was calculated to be minimal in the first 400 nm of the surface, and the implantation peak was at ~830 nm. Radiation damage and implanted concentration of helium are presented in Figure 4.9 and compared to 24 h of proton irradiation at 7×10^{-7} dpa/s.

The damage caused by the helium beam near the corrosion surface is ~0.01 dpa compared with the minimum damage used for proton irradiation of ~0.06 dpa.

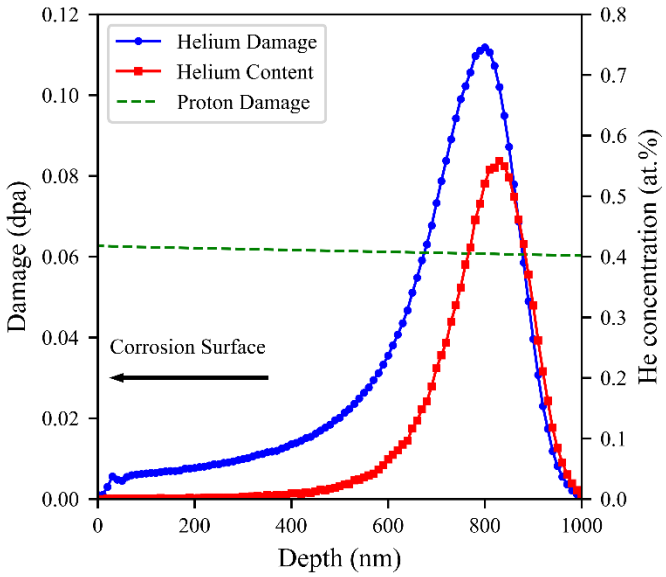

Figure 4.9. SRIM-2013 damage and range calculation for 400 keV He^+ implantation to 10^{16} cm^{-2} compared with proton irradiation for 24 h reproduced from [113].

4.1.3.2. Radiolysis Isolation

Ion transmission through the sample yields both radiation damage in the solid and radiolysis of water localized in the area defined by the beam aperture. While it is desirable to combine all radiation corrosion effects at once, separation of radiolysis from displacement damage is part of the second sub-objective. Introducing a sample bar on top of the existing sample and partially eclipsing the aperture, as presented schematically in Figure 4.10, yields a surface where direct radiolysis is generated but radiation damage is negligible. This geometry creates a surface where a known dose rate of radiolysis is actively generated during corrosion without the beam passing through the material. Dose rates along the bar were the same as those plotted in the water region of Figure 4.7.

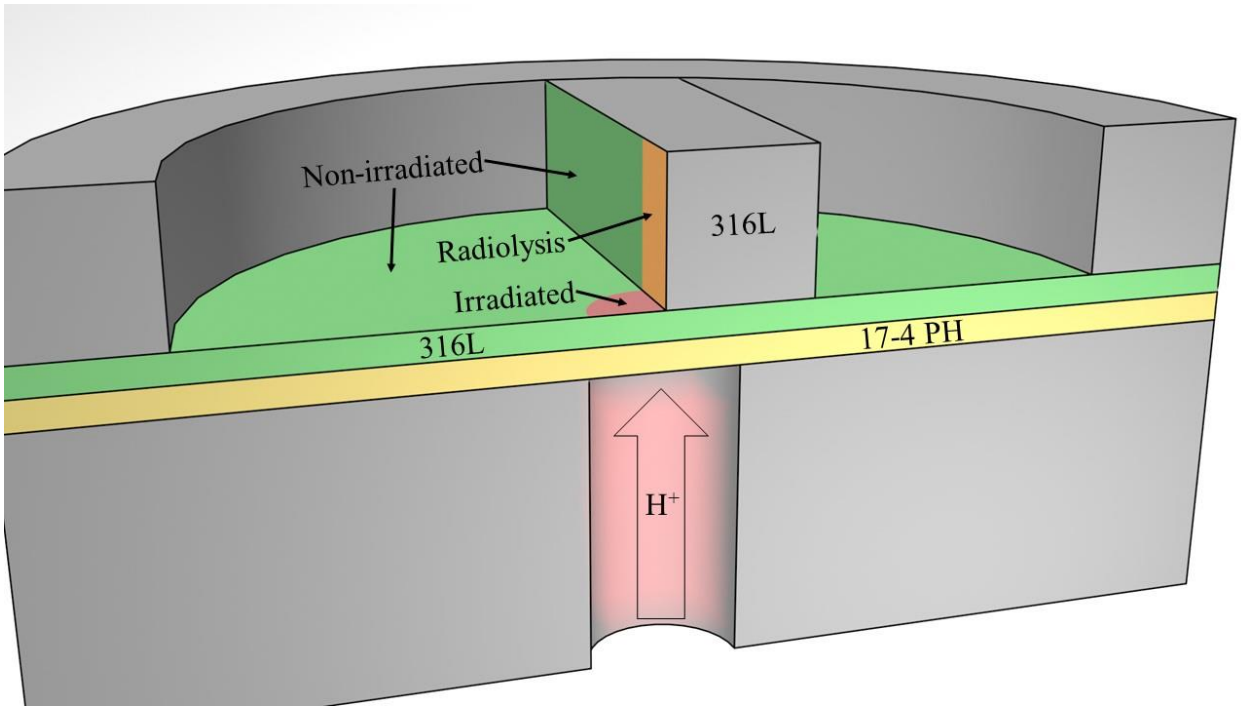

Figure 4.10. Schematic of radiolysis isolation bar geometry with all three regions labelled: irradiated, non-irradiated, and radiolysis.

4.1.3.3. Displacement Damage Isolation

For the third sub-objective, displacement damage must be separated from radiolysis. A low-pressure steam environment was chosen to replace the PWR water environment to maintain the same displacement damage while mitigating radiolysis. To approximate the PWR thermodynamics, Ar-3%H_2 was used as a carrier gas in a controlled ratio with water. Acceleration of oxidation kinetics was desired to ensure statistically significant differences of irradiation effects, so the chosen temperature was 480 °C.

Previous studies have used 480 °C hydrogenated steam to accelerate SCC kinetics in alloy 600 [114,115]. Instead of using the Ni/NiO transition as the thermodynamic reference point, the Fe_3O_4/Fe_2O_3 transition was used. More specifically, hematite does not form in the outer oxide at nominal PWR conditions, so the steam exposures were designed to be well below the hematite formation potential but still yield a duplex oxide structure. The expected oxygen activity for this transition was calculated using Thermo-Calc 2020b [116]. Oxygen partial

pressure in the gas mixture was calculated using partition functions of decomposition equilibrium constants [117]. Resulting oxygen partial pressures for a fixed water flow rate of 0.2 mL/min and total pressure of 1.5 MPa are plotted in Figure 4.11. For Ar-3%H_2 flow rates up to 5 L/min, the oxygen partial pressure is several orders of magnitude below the transition to hematite. Therefore, a moderate flowrate of ~1 L/min was chosen for the steam experiments.

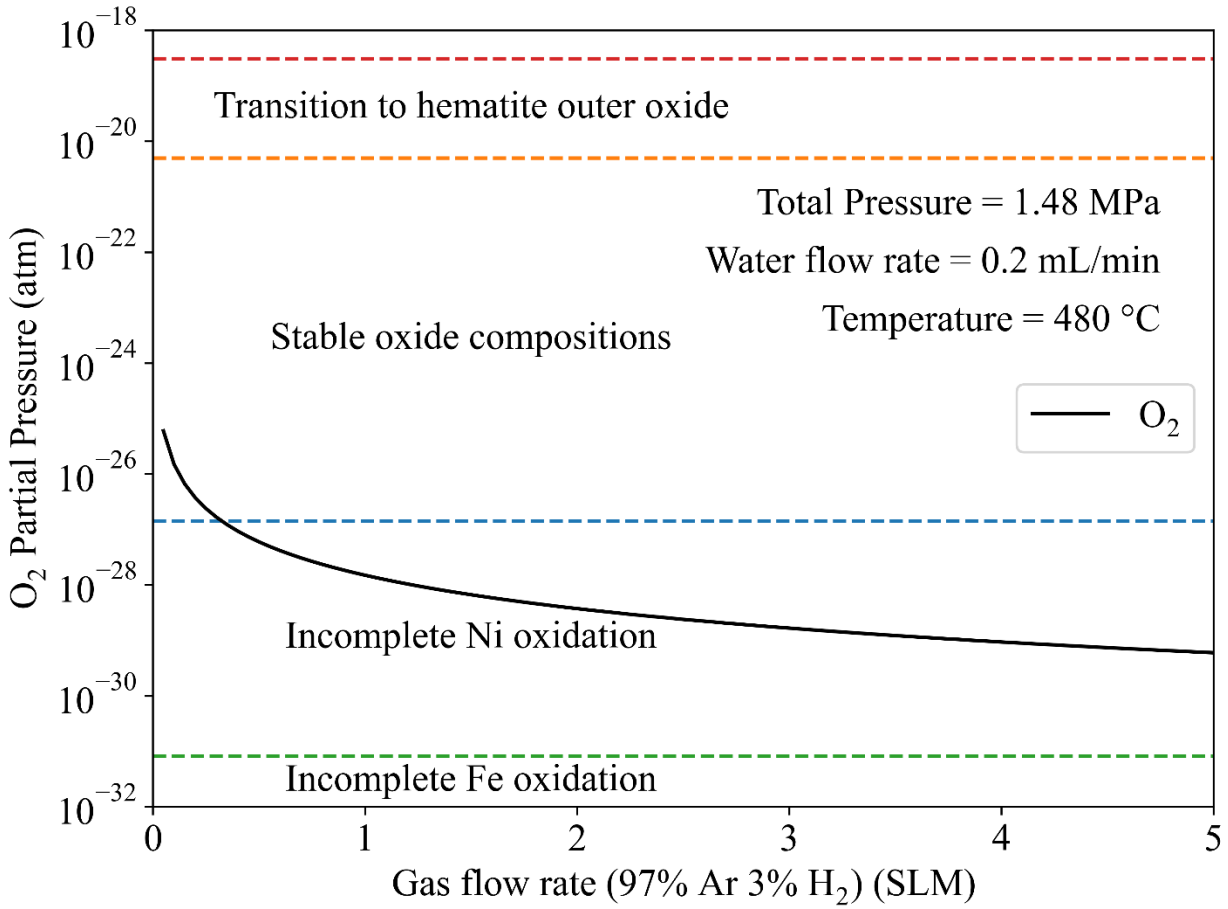

Figure 4.11. Expected oxygen partial pressure of Ar-3%H_2 steam gas mixture at 480 °C using a fixed water flow rate and variable gas flow rate and compared to various oxide regimes identified using Thermo-Calc by dashed lines.

Using the gas mixture in SRIM-2013, the damage and dose rates were re-calculated in Figure 4.12. It is important to note that the dose rate of 8.26 kGy/s includes the Ar content of the gas mixture. Assuming dose is partitioned by atomic number, the combined dose rate experienced by water and hydrogen was 0.196 kGy/s. This value is a factor of 3000 less than

liquid phase radiolysis from Figure 4.7, so radiolysis of water in the gas mixture was relatively small. Furthermore, the residence time in the autoclave was much lower with steam, so radiolysis products have less opportunity to accumulate.

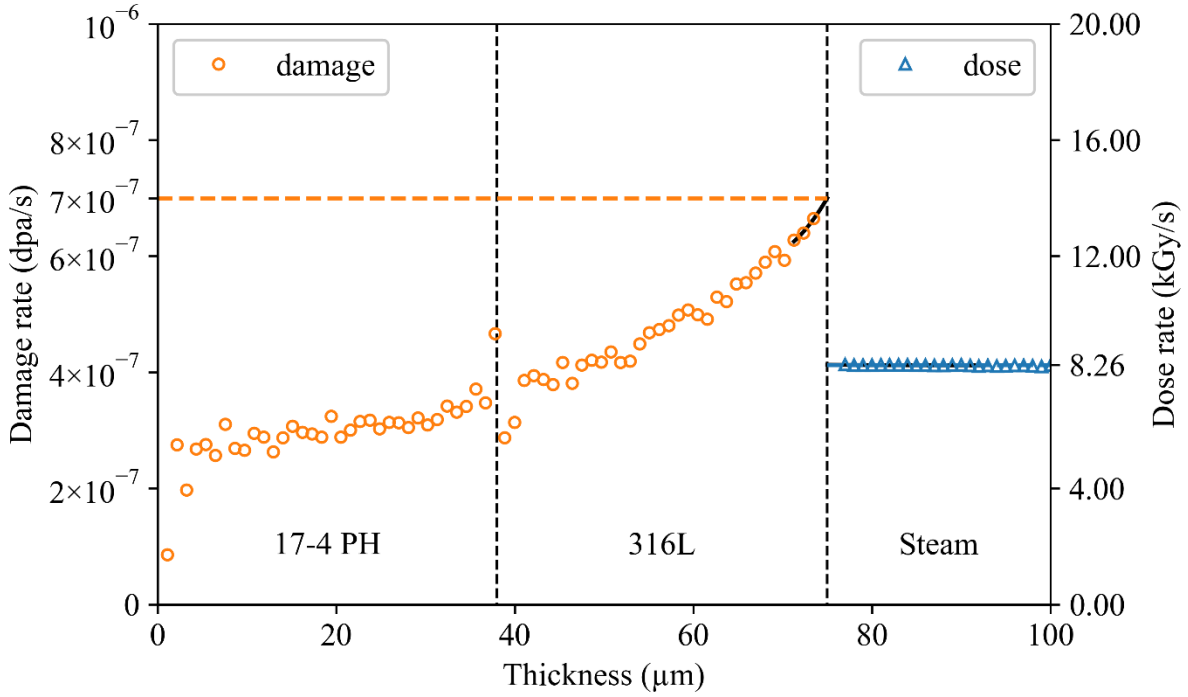

Figure 4.12. SRIM-2013 damage and dose rate calculations through 38 μm 17-4 PH and 37 μm 316L into 20 μm Ar-H_2-steam at 480 °C at a current density of 4.12 μA/cm^2 to achieve 7×10^{-7} dpa/s at the corrosion surface.

4.2. Procedure

This section details experimental procedures used for this research using the designs described in the previous section. Sample and backing material compositions are described below along with preparation procedures used for each kind of experiment. Finally, procedures for autoclave exposures with and without irradiation will be described. Calculations of damage and dose rates using SRIM 2013 as well as the recorded experimental conditions of the autoclave and beamline for each experiment are presented in Appendix A.

4.2.1. Sample Preparation

To achieve the sample designs presented in Section 4.1.3, three separate pieces were needed: 316L sample disc, 316L sample bar, and 17-4 PH backing disc.

The sample material used in this research was 316L heat 626032 with its composition listed in Table 4.1 with a grain size of 23 μm. This 316L material was solution annealed at 1050 °C for 30 minutes, cold worked to 5%, and finally heat treated at 1100 °C for 10 minutes [113]. The 316L stock material is a 5.08 cm diameter rod. Radial slices 400 μm thick were cut by electric discharge machining (EDM) from which several 8 mm diameter discs were punched out. Similarly, 1 mm × 1 mm cross-section bars were cut from a 1 mm thick radial slice of the 316L stock material using EDM. These longer bars were cut into 4 mm × 1 mm × 1 mm bars using a low-speed diamond wafering saw.

Table 4.1. Elemental composition of 316L heat 626032 with the received composition, the composition measured by X-ray fluorescence (XRF) using a wavelength-dispersive X-ray spectroscopy (WDS) detector, and the combination of the two previous compositions was used as the alloy composition throughout this work.

wt. %	C	N	O	Al	Si	P	S	Ti	V	Cr	Mn	Fe	Ni	Cu	Mo
Received	0.028	0.08	0.003		0.59	0.01	0.01			17.6	1.78	**65.5**	12.0		2.39
WDS				<0.01	0.6	0.021	<0.02	<0.009	0.032	17.4	1.77	64	11.8	0.07	2.38
Combined	0.028	0.08	0.003		0.6	0.016	0.01		0.032	17.5	1.775	**65.6**	11.9	0.07	2.385

The backing material was 17-4 PH with a nominal composition of 17 wt.% Cr and 4 wt.% Ni. The 17-4 PH stock material is an 8 mm diameter rod from which ~500 μm slices were taken using a diamond wafering saw.

4.2.1.1. Polishing

Several 316L discs with 8 mm diameter were attached to a stainless steel puck using Pelco Crystalbond 509 Clear and ground on a polishing wheel with 240 grit SiC paper until the EDM contamination layer was removed from both sides. Afterwards, grinding on one face continued with SiC paper in stages: 240 grit, 320 grit, 400 grit, 600 grit, 800 grit, and 1200 grit. Following the grinding step, diamond solution polishing was completed in stages: 3 μm, 1 μm,

and 0.25 µm. Finally, to minimize the damage layer and surface roughness, sample discs were vibratory polished with 0.02 µm colloidal silica for ~20 hours.

Similarly, 316L bars were polished using the same procedure as the discs after removing the EDM layer from all six faces.

A subset of both polished 316L bars and 316L discs were implanted with helium as a marker layer following the procedure in Section 4.2.1.2. He implanted and non-implanted 316L discs were thinned following the procedure in Section 4.2.1.3.

4.2.1.2. Helium Implantation

Implantation with helium was completed using the 400 keV Implanter in MIBL. This accelerator delivers a raster-scanned 400 keV He^+ beam to the stage. Ion charge implanted into the stage was collected and integrated to stop at the desired fluence. The implantation stage has a copper head with an internal heating element and two thermocouples: one on the atmosphere side and one fixed to the beam-facing side with a screw. Three implantations were performed for material in this work: two sets of 316L discs and one set of 316L bars. For each implantation, operating conditions were recorded and are presented in Figure 4.13, Figure 4.14, and Figure 4.15, respectively.

The target temperature for the implantations was 550 °C, but the measured temperatures ranged from 460 °C to 550 °C. The difference between front and back thermocouples varied greatly between the three implantations indicating inconsistent contact for both thermocouples. The heater power was kept as high as possible without exceeding 800 °C on the back thermocouple which prevented reaching 550 °C at the front thermocouple for two of the implantations. The temperature does not affect the implantation depth; only the size of bubbles is

decreased by lower implantation temperature. Therefore, these implanted specimens were used regardless of the achieved implantation temperature.

Sample material was mounted on the copper implantation stage using silver paste and cured with a heat gun. The stage was loaded into the chamber, the chamber was evacuated, and the stage was heated in vacuum. Samples were implanted with helium to a fluence of 10^{16} ions/cm^2 within 4 hours. After implantation was complete and the stage was allowed to cool, the samples were removed and cleaned in methanol to remove the bulk of the silver paste. Sample bars had excess silver paste removed from each unpolished side with 1200 grit SiC paper before use. Sample discs were thinned in the next section by grinding the unpolished face thereby removing any residual silver paste.

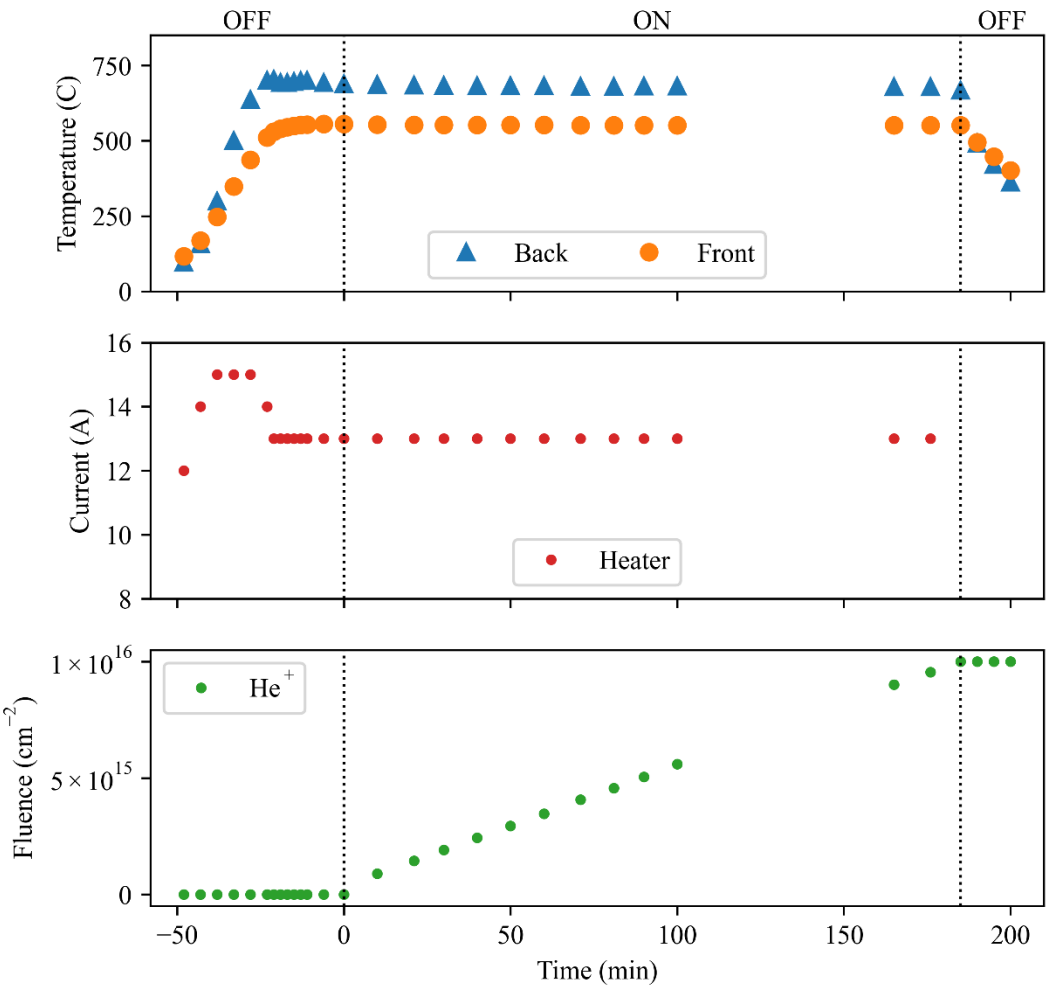

Figure 4.13. Implantation of set #1 of 316L discs to a 400 keV He^+ fluence of 10^{18} cm^{-2} at a temperature of 552.2 °C ± 1.5 °C.

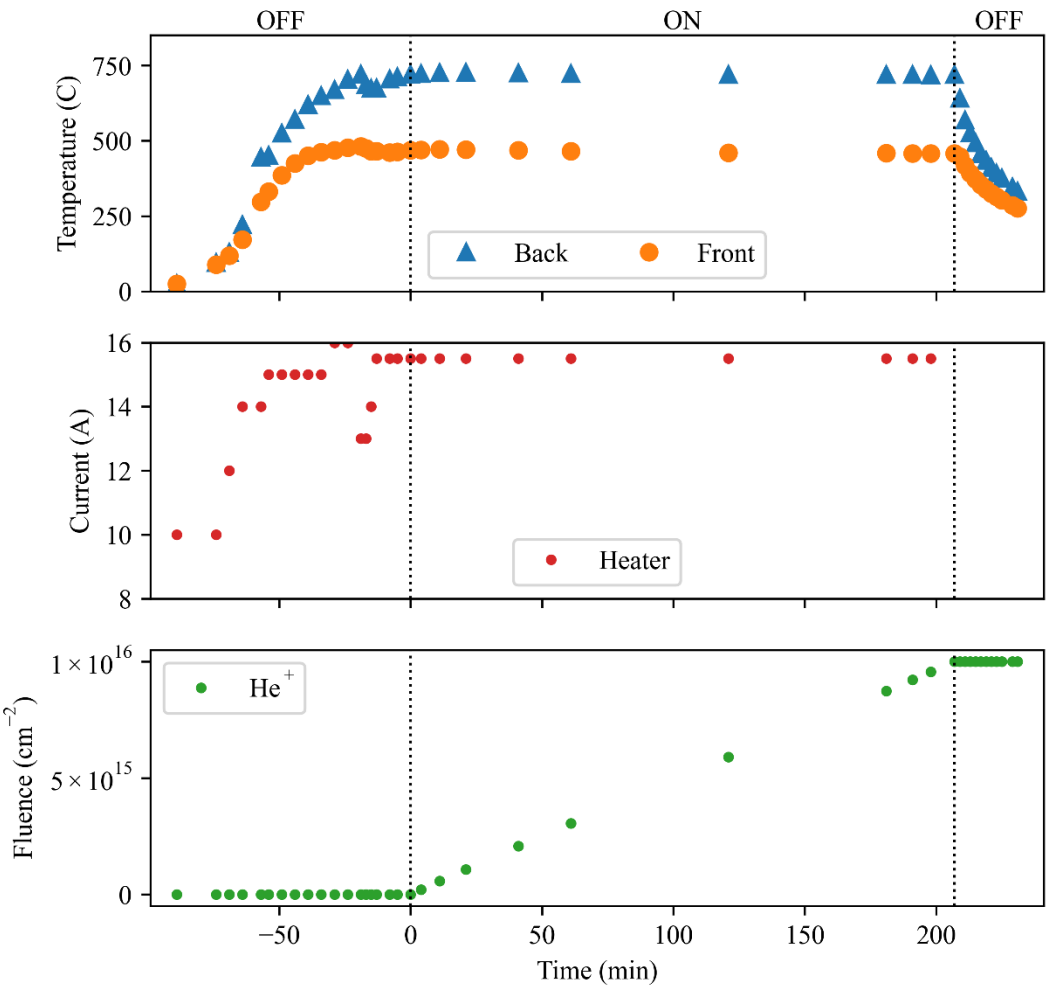

Figure 4.14. Implantation of set #2 of 316L discs to a 400 keV He^+ fluence of 10^{18} cm^{-2} at a temperature of 464.9 °C ± 5.4 °C.

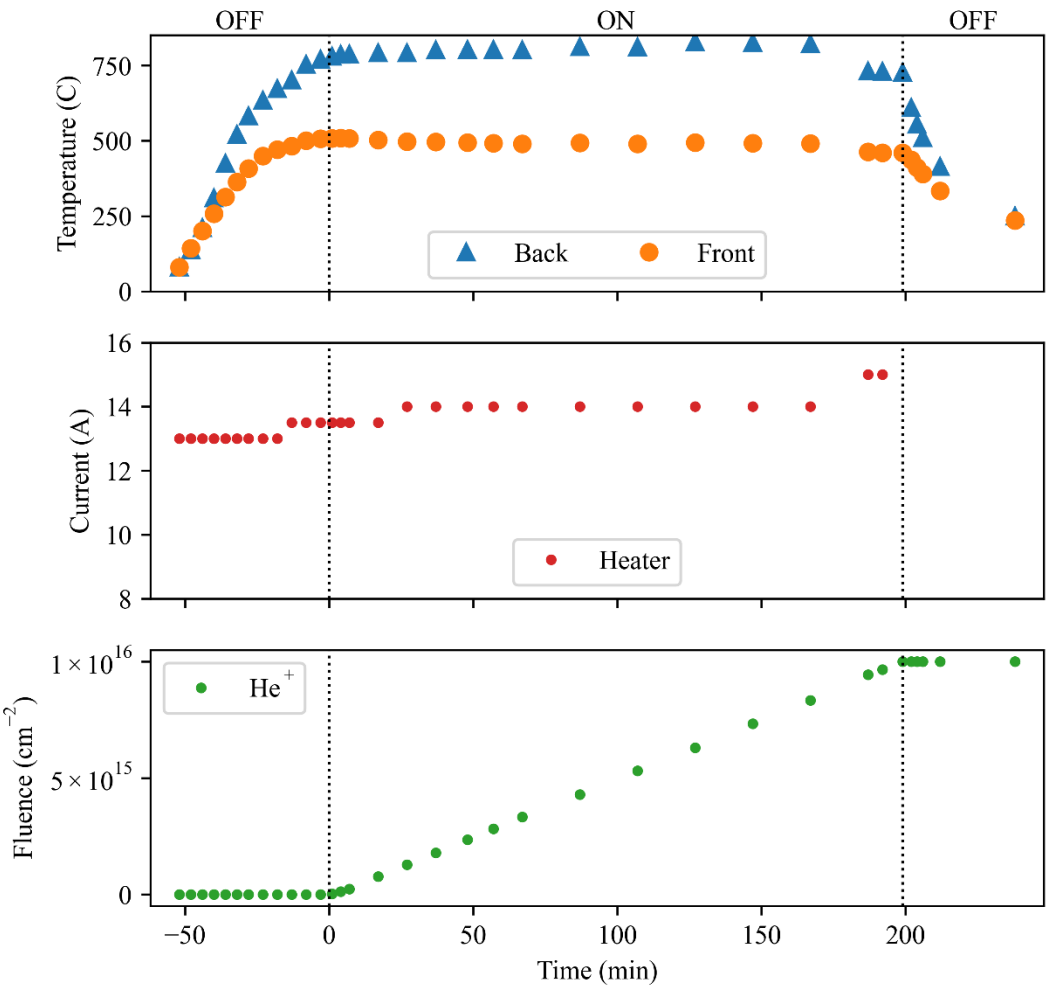

Figure 4.15. Implantation of 316L bars to a 400 keV He^+ fluence of 10^{18} cm^{-2} at a temperature of 493 °C ± 13 °C.

4.2.1.3. Thinning

To achieve the desired thickness (~35 µm), polished 316L sample discs were thinned using the reverse face. Similarly, 17-4 PH backing discs were also thinned using the same procedure. The polished face was attached to a Gatan Disc Grinder using Crystalbond, and thinning was completed using SiC paper, again in stages: 240 grit, and 600 grit. Once the desired thickness was reached, the disc was removed from the grinder stub, thoroughly cleaned with acetone to remove the Crystalbond, and thickness verified with a depth gauge.

4.2.1.4. Mounting

Both backing and sample discs were welded circumferentially together between a sample mount and a washer as shown in Figure 4.5. Sample mounts had an 8 mm diameter face for this purpose with a concentric 1 mm diameter beam aperture that restricts the irradiation to a circular region of the sample. Sample mounts and washers were polished with 600 grit SiC paper before welding. Sample and backing discs were sandwiched between a washer and sample mount concentrically and held in place with a simple jig. Sample mount assemblies were welded with an Orion 150s Pulse Arc Welder using a tungsten electrode and argon shielding gas around the circumference of the discs using 15 ms weld time with 8~10 J pulses without agitation.

The weld between the mount and sample/backing functioned as a seal between vacuum at the beam aperture and the pressurized autoclave environment. Sample mounts also had sealing surfaces for the water/air interface and the vacuum/air interface. Control specimens were welded to a blank sample mount which did not have a beam aperture.

For radiolysis isolation experiments, a 316L bar was placed on the sample surface inside the washer. The bar was held in place with tweezers, and a single welding pulse was used to attach the bar to the washer.

After welding was completed, each sample mount was loaded into a dead leg test cell and pressurized to 13.8 MPa for 15 minutes to test the seal integrity. If any water leaked through the weld to the beam side of the mount, the weld was repeated until it passed this test.

4.2.1.5. Cleaning

Completed sample mounts were cleaned by ultrasound for 10 minutes each in acetone, methanol, and ethanol. After each mount was air dried, it was loaded into a small vacuum chamber and plasma cleaned with a forward power of 20 W for 15 min with an Evactron EP

Series Plasma De-Contaminator. Afterwards, the mount was loaded into the IAC cell for the appropriate experiment.

4.2.2. Control Exposures

Three exposures were completed without any irradiation to serve as control specimens for irradiated samples. The conditions of the control exposures are listed in Table 4.2. Two control experiments were conducted for 24 h and 72 h in high temperature hydrogenated water, and one additional experiment was conducted for 24 h in high temperature aerated water. See Figure A.1, Figure A.2, and Figure A.3, respectively.

High water purity was maintained in the water loop by continuously running the circulation loop both during experiments and idle times. For hydrogenated water exposures, the inlet conductivity was under 0.052 µS/cm, whereas it was 0.27 µS/cm for the aerated exposure.

The gas content in the water was achieved by bubbling gas through the main column. The overhead pressure in the column was controlled using a back pressure regulator to the gas vent, see Figure 4.1. Henry's Law is used to calculate the expected dissolved hydrogen content in the water from the overhead pressure using Eq. 4.1. Dissolved oxygen (DO) content was directly measured using inlet and outlet DO sensors and was also calculated using the column overhead pressure in the aerated case. For the two hydrogenated control experiments, the overhead pressure of pure H_2 was held at ~188 kPa to maintain a hydrogen content of 3 mg/kg. For the aerated experiment, compressed air was used as the gas, and the column pressure was kept low at ~109 kPa for an expected DO of 10.4 mg/kg.

Once the column was prepared for hydrogenated or aerated conditions, the sample mount was loaded into the autoclave with a zirconium gasket for the water/air seal. The autoclave was mounted onto the end of the IAC beamline in MIBL and attached to the water loop. Water was

run through the vessel and pressurized to the target pressure of ~13.1 MPa at a flow rate of 15 mL/min. After 15 minutes, the water seals on the vessel, inlet, and outlet were checked for leaks, and the seal was reseated until no leaks were found. Afterwards, the cell was heated to the target temperature of 320 °C, held at temperature for the appropriate duration of 24 h or 72 h, and finally cooled by disabling the heat. Once the temperature dropped below 95 °C, the cell was depressurized, and the cell was cooled to room temperature without changing the flow rate. Once cool, the cell was bypassed in the water loop, and the sample mount was unloaded from the cell and air dried. Finally, the 316L disc (and bar, if applicable) was separated from the mount using a rotary cutting disc to remove the weld.

Before going further, it is worth noting the sample nomenclature used throughout the rest of this document. Experimental conditions are abbreviated into a single capital letter followed by a number. The letter refers to the nominal water and irradiation conditions for the experiment, and the number is the experiment duration in hours e.g., X24. There are four letters used in this work: W (Water with irradiation), X (water eXcluding irradiation), A (Aerated water), and S (Steam with irradiation). Both W and X refer to 320 °C 13.1 MPa 3 mg/kg H_2 water, but W is irradiated and X is not irradiated. A is 320 °C 13.1 MPa 8 mg/kg O_2 water without irradiation. S is 480 °C 1.45 MPa, 170 g/kg H_2 argon-steam with irradiation.

Values recorded by the autoclave system are presented as a function of time for control sample X24 in Figure A.1. Similarly, the values for control sample X72 are presented in Figure A.2. For sample X72 there was a period where the autoclave control program was frozen and data was not recorded, which caused the gap in recorded data. The thermocontrollers and pumps function independently of the program, so the water flow and temperature were maintained in this gap. There was a small fluctuation in temperature when the control program restarted

because it automatically set the thermocontroller setpoint to 16 °C for a few seconds before it was manually reset to 320 °C. Finally, for control sample A24, the values are presented in Figure A.3. For A24, the inlet and outlet conductivity were very high because the system had not been exposed to such a high potential before. It is likely more Fe in solution caused this increase. All control samples' autoclave parameters were averaged over the time at temperature and these values are presented in Table 4.3.

Table 4.2. Nominal conditions of non-irradiated control exposures of 316L stainless steel in high temperature water.

ID	Duration (h)	Temperature (°C)	Gas content (mg/kg)	Pressure (MPa)	Beam	Helium (10^{16} cm^{-2})	Radiolysis Bar
A24	24	320	8 (O_2)	13.1	No	Yes	No
X24	24	320	3 (H_2)	13.1	No	Yes	No
X72	72	320	3 (H_2)	13.1	No	Yes	No

Table 4.3. Autoclave water loop conditions recorded for non-irradiated control exposures of 316L stainless steel in high temperature water.

ID	Temperature (°C)	Gas content (mg/kg)	Dissolved Oxygen (mg/kg)	Pressure (MPa)	Inlet Conductivity (µS/cm)	Outlet Conductivity (µS/cm)
A24	320.12 ± 0.88	10.373 ± 0.015	8.336 ± 0.036	13.33 ± 0.11	0.2705 ± 0.0052	4.87 ± 0.83
X24	320.04 ± 0.69	3.04920 ± 0.00042	< 0.001	13.33 ± 0.11	0.051418 ± 0.000014	0.193 ± 0.037
X72	320.0 ± 2.3	3.0460 ± 0.0014	< 0.001	13.34 ± 0.14	0.051477 ± 0.000049	0.164 ± 0.026

4.2.3. Irradiation Assisted Corrosion Experiments

4.2.3.1. PWR Primary Water Simulation

IAC experiments require simultaneous operation of the autoclave system and ion beam accelerator equipment. A primary goal in the operation of these systems was minimizing the amount of time the sample was at the target temperature without the beam. To achieve this, the beam was prepared before each sample was brought to temperature, and irradiation began as soon as the target temperature was reached. After the full duration of the experiment, the beam

was blocked, and the autoclave heat was switched off simultaneously. Otherwise, the autoclave was operated identically to the control experiments in Section 4.2.2.

The proton beam was prepared by MIBL staff using the equipment outlined in Section 4.1.2. The 5.43 MeV proton beam with < 2 mm FWHM was delivered to the IAC beamline and raster-scanned over the stage and slits. To ensure a uniform current density on the stage, beam overscan on the slits was calculated by using the FWHM as the overscan distance. For example, a 4 mm × 4 mm area defined by the slits was overscanned to 8 mm × 8 mm, so less than one quarter of the total beam current was applied to the stage. Ion current passing through the slits was measured by a final Faraday cup periodically to ensure the correct damage rate was achieved. Ion current on each slit was continuously recorded and monitored throughout the irradiation as a measure of the total current consistency. Additionally, the vacuum pressure was recorded along the IAC beamline in three locations.

Table 4.4. Nominal conditions of proton irradiated exposures of 316L stainless steel in high temperature hydrogenated water.

ID	Duration (h)	Temperature (°C)	Gas content (mg/kg)	Pressure (MPa)	Helium (10^{16} cm^{-2})	Radiolysis Bar
W24-1	24	320	3 (H_2)	13.1	No	No
W24-2	24	320	3 (H_2)	13.1	No	No
W24-3	24	320	3 (H_2)	13.1	No	No
W24-4	24	320	3 (H_2)	13.1	Yes	No
W24-5	24	320	3 (H_2)	13.1	No	Yes
W24-6	24	320	3 (H_2)	13.1	Yes	Yes
W72-1	72	320	3 (H_2)	13.1	Yes	No
W72-2	72	320	3 (H_2)	13.1	Yes	Yes

Nominal conditions and sample geometry of each proton irradiated experiment are listed in Table 4.4. Recorded autoclave conditions are listed in Table 4.5. Beam conditions are listed in Table 4.6. Damage rates in the sample and dose rates in the water were calculated using SRIM 2013 for the listed current densities in Table 4.6 and are plotted in Figure A.4 through Figure A.18. Plots of the recorded autoclave and beam conditions are presented in Figure A.5 through

Figure A.19. Sample W24-4 had a small gap in the beam data collection due to an error in the recording program, but the irradiation continued during that time. Sample W72-1 had an issue with the accelerator and was interrupted for ~10 h before restarting, so the sample was cooled during that time. Sample W72-2 had abnormally high outlet conductivity readings that were later determined to be caused by a contaminated filter on the outlet in the return leg, so the actual cell conductivity was likely low.

Table 4.5. Autoclave water loop conditions recorded for proton irradiated exposures of 316L stainless steel in Table 4.4.

ID	Temperature (°C)	Gas content (mg/kg)	Dissolved Oxygen (mg/kg)	Pressure (MPa)	Inlet Conductivity (µS/cm)	Outlet Conductivity (µS/cm)
W24-1	319.99 ± 0.38	3.1257 ± 0.0010	< 0.001	13.228 ± 0.016	0.051534 ± 0.000055	0.0657 ± 0.0018
W24-2	319.99 ± 0.35	3.1224 ± 0.0019	< 0.001	13.218 ± 0.023	0.051584 ± 0.000021	0.05919 ± 0.00082
W24-3	319.98 ± 0.57	3.1349 ± 0.0059	< 0.001	13.281 ± 0.018	0.051383 ± 0.000022	0.0662 ± 0.0026
W24-4	320.02 ± 0.72	3.1750 ± 0.0018	< 0.001	13.260 ± 0.011	0.051477 ± 0.000011	0.0665 ± 0.0021
W24-5	320.02 ± 0.42	3.1803 ± 0.0068	< 0.001	13.398 ± 0.091	0.051619 ± 0.000021	0.0975 ± 0.0042
W24-6	320.05 ± 0.70	3.0324 ± 0.0010	< 0.001	13.415 ± 0.011	0.051683 ± 0.000026	0.0625 ± 0.0016
W72-1	320.00 ± 0.57	3.1447 ± 0.0039	< 0.001	13.356 ± 0.015	0.051517 ± 0.000027	0.0596 ± 0.0017
W72-2	320.0 ± 3.2	3.0567 ± 0.0024	< 0.001	13.213 ± 0.017	0.051704 ± 0.000036	0.455 ± 0.033

Table 4.6. Beam conditions recorded for proton irradiated exposures of 316L stainless steel in Table 4.4.

ID	Backing (µm)	Sample (µm)	Current density (µA/cm2)	Damage Rate (dpa/s)	Dose Rate (kGy/s)	Slits
W24-1	36 ± 2	42 ± 2	3.44 ± 0.25	$(6.54 \pm 0.48) \times 10^{-7}$	622 ± 46	4 mm × 4 mm
W24-2	42 ± 2	38 ± 2	3.44 ± 0.22	$(7.18 \pm 0.47) \times 10^{-7}$	667 ± 44	7 mm × 4 mm
W24-3	38 ± 2	34 ± 2	4.47 ± 0.27	$(6.97 \pm 0.42) \times 10^{-7}$	694 ± 42	7 mm × 4 mm
W24-4	42 ± 2	38 ± 2	3.44 ± 0.24	$(7.18 \pm 0.50) \times 10^{-7}$	667 ± 46	7 mm × 4 mm
W24-5	24 ± 2	50 ± 2	4.27 ± 0.12	$(7.12 \pm 0.20) \times 10^{-7}$	694 ± 20	7 mm × 4 mm
W24-6	51 ± 2	27 ± 2	3.63 ± 0.13	$(6.88 \pm 0.25) \times 10^{-7}$	652 ± 24	4 mm × 4 mm
W72-1	40 ± 2	38 ± 2	3.63 ± 0.32	$(6.86 \pm 0.60) \times 10^{-7}$	656 ± 58	7 mm × 4 mm
W72-2	38 ± 2	34 ± 2	4.53 ± 0.13	$(7.06 \pm 0.20) \times 10^{-7}$	703 ± 20	4 mm × 4 mm

4.2.3.2. Steam Exposure

IAC experiments in steam were performed in a similar manner to IAC experiments in water, but with the autoclave system operated in steam mode.

The water loop was prepared identically to the earlier control and IAC hydrogenated water exposures. A different autoclave vessel was used with a built-in ring seal, so no gasket was used between the sample mount and vessel body. After plasma cleaning, a sample mount was loaded into the autoclave and mounted onto the beamline. A leak test was performed using 1.5 MPa water and repeated until no leaks were observed. Afterwards, the Ar-3%H_2 gas flow was started at a low flow rate to purge the residual water and to provide a reducing environment during heat-up. Once the temperature of the autoclave reached 400 °C, the gas flow rate was increased to 1.0 L/min, and the cell pressure was set to 1.5 MPa. Once the autoclave reached the target temperature, water flow was set to 0.2 mL/min into the inlet stream, and the beam was unblocked for the experiment duration. During the experiment, adjustments to the outlet valve were made to maintain the gas flow. At the end of the duration, the beam, heating, and water flow were stopped, but the gas flow was continued until the sample cooled.

Table 4.7. Nominal conditions of proton irradiated exposures of 316L stainless steel in high temperature hydrogenated steam.

ID	Duration (h)	Temperature (°C)	Gas Content in Water	Pressure (MPa)	Helium (10^{16} cm^{-2})	Radiolysis Bar
S24	24	480	170 g/kg H_2	1.45	Yes	Yes
S72	71.3	480	170 g/kg H_2	1.45	Yes	Yes

Table 4.8. Autoclave water loop conditions from proton irradiated exposures of 316L stainless steel in Table 4.7.

ID	Temperature (°C)	Gas content (g/kg)	Pressure (MPa)	Inlet Conductivity (µS/cm)	Gas Flow (L/min)
S24	479.96 ± 0.21	179 ± 21	1.497 ± 0.016	0.051137 ± 0.000020	1.00 ± 0.12
S72	479.96 ± 0.24	166 ± 17	1.557 ± 0.039	0.051216 ± 0.000083	0.890 ± 0.092

Nominal conditions and sample geometry of both steam IAC experiments are listed in Table 4.7. Recorded autoclave conditions are listed in Table 4.8. Beam conditions are listed in Table 4.9. Damage rates in the sample and dose rates in the water were calculated using SRIM 2013 for the listed current densities in Table 4.9 and are plotted in Figure A.20 and Figure A.22.

Plots of the recorded autoclave and beam conditions are presented in Figure A.21 and Figure A.23. Notably, the duration of S72 was only 71.3 h rather than 72 h due to a failure in the TORVIS negative hydrogen source, so the experiment was stopped early.

Table 4.9. Beam conditions from proton irradiated exposures of 316L stainless steel in Table 4.7.

ID	Backing (μm)	Sample (μm)	Current Density ($\mu A/cm^2$)	Damage Rate (dpa/s)	Dose Rate (kGy/s)	Slits
S24	46 ± 2	26 ± 2	4.52 ± 0.62	$(6.89 \pm 0.95) \times 10^{-7}$	5.43 ± 0.74	4 mm × 4 mm
S72	49 ± 2	28 ± 2	3.95 ± 0.43	$(6.98 \pm 0.77) \times 10^{-7}$	5.56 ± 0.61	4 mm × 4 mm

4.3. Characterization

After each experiment, the sample material was separated from the sample mount. Sample discs (and bars where applicable) were mounted onto conductive SEM stubs with copper tape. Sample material was kept on these stubs for all characterization work.

Virtually all characterization work was completed as postmortem examination of the sample surface. The only exception was measurement of the implanted helium bubble marker layer to calibrate the total oxidation measurement.

Characterization in this work can be divided into qualitative surface characterization and quantitative analysis by cross-section. Surface imaging included optical microscopy for general examination of the outermost surface of the oxide film, Raman spectroscopy for qualitative phase analysis of corrosion products, and scanning electron microscopy (SEM) for general oxide morphology.

As mentioned in the sample design section, there are three distinct regions on which separate characterization of the corrosion film was achieved by selective cross-sectioning. The irradiated region was defined as the region of the disc where the beam emerges into the autoclave environment, generating both displacement damage and radiolysis. The radiolysis region only existed on the bar where the beam passed over the surface of the bar. Finally, the non-irradiated

region was the area on the bar and the area on the disc far away from the beam path. Areas between the irradiated and non-irradiated regions of a sample disc are affected by diffusion and convection of radiolysis products, so these areas were avoided.

4.3.1. Surface Analysis

4.3.1.1. Optical Microscopy and Raman Spectroscopy

Both optical microscopy and Raman spectroscopy were performed with a Renishaw inVia confocal Raman microscope using either 20x or 50x objective lenses. Raman spectroscopy was done using StreamLine™ mapping to capture the spatial differences between regions. All six samples in the W24 set and W72-1 were examined with Raman mapping, and all W24 samples except W24-4 were imaged with optical microscopy.

Optical images were taken using the motorized stage to produce a montage of 20x or 50x magnification images. Raman maps were taken over an area within the montage using a 532 nm laser and evaluated for corundum and spinel content. Spatial and phase information from the maps was used to determine the location and extent of radiolysis effects.

4.3.1.2. Scanning Electron Microscopy

Samples were imaged primarily with a Thermo Scientific Nova NanoLab and occasionally with a Thermo Scientific Helios 650, Thermo Scientific Helios G4 PFIB, or a Thermo Scientific Scios 2. Specific imaging conditions varied depending on the features being examined. All images were secondary electron images acquired using accelerating voltages between 5–15 keV. Low magnification images were used to distinguish regions on the sample, and higher magnification was used to examine the oxide morphology on the surface.

4.3.2. Cross-Section Analysis

Analysis of the oxide film with depth was performed on cross-sections extracted from different regions. Cross-sections were prepared by extracting them from the sample surface using a focused ion beam (FIB). Oxide thickness and total oxidation measurements were taken from cross-sections using transmission electron microscopy (TEM), and oxide composition measurements were taken with energy dispersive X-ray spectroscopy (EDS).

4.3.2.1. Cross-Sectional Sample Preparation

Cross-sectional samples for TEM characterization were prepared across multiple SEM/FIB dual beam microscopes: Thermo Scientific Nova NanoLab, Thermo Scientific Helios 650, Thermo Scientific Helios G4 PFIB, and Thermo Scientific Scios 2. All FIB systems used a Ga liquid metal ion source except the PFIB which used a Xe gas source. To prepare for TEM analysis, cross-sections were cut from the sample, attached to PELCO lift-out TEM grids (mostly copper but some molybdenum), and thinned using the procedure below. Note that the procedure is general, and alterations to the procedure were made on a case-by-case basis for the cross-sections in this work.

First, a site for cross-sectioning was selected from the non-irradiated, irradiated, or radiolysis region. Within the region, a boundary in outer oxide morphology was selected with the aim of extracting a grain boundary and two or more surface grain orientations. The target boundary was chosen as the center of the cross-section. The length of the cross-section was perpendicular to the boundary to yield an “edge-on” grain boundary.

A ~500 nm layer of platinum was deposited on the selected site using the electron beam in a 22 µm × 2 µm rectangle. This layer serves to protect the outermost surface of the oxide from

the ion beam. Additional protective platinum and carbon layers were deposited using the ion beam to increase the total layer thickness to 2~3 μm.

Trenches were cut on either side of the protective layers to expose the cross-section. The cross-section was thinned to ~1 μm in the trenching process. The cross-section was then undercut in a "J cut" about 3~4 μm beneath the original sample surface. A probe was welded to the upper corner of the cross-section using ion beam platinum. The cross-section was detached from the sample, and it was extracted using a nano-manipulator probe. The cross section was welded into the center of the groove of an "M" post on the TEM grid using ion beam platinum before it was cut free from the probe.

Finally, the cross-section on the TEM grid was thinned as a ~20 μm "window" leaving some protective platinum/carbon on either side. The bulk of the thinning was completed using 30 keV Ga ions in a cleaning cross-section ± 2° from parallel until the cross-section was 100~200 nm thick. Additional thinning was completed with a 5 keV Ga ion beam, again in a cleaning cross-section ± 2° from parallel, to remove some FIB damage. A final cleaning step using 2 keV Ga ions was done as a beam shower on either side of the cross-section.

4.3.2.2. Oxide Thickness and Total Oxidation Measurement

The TEMs used for thickness measurements were JEOL 2010F and JEOL 2100F at the Michigan Center for Materials Characterization and a Thermo Scientific Tecnai F20 (TF20) at the Bettis Atomic Power Laboratory. For samples W24-1 and W24-2, imaging for oxide measurements was performed on the JEOL 2010F in conventional TEM mode using bright field. All other samples were imaged using either the 2100F or TF20 with scanning TEM (STEM) using a high angle annular dark field (HAADF) mode. The imaging magnification was 100000× on the 2100F and 79000× on the TF20 to capture the oxide film and the implanted bubble layer

in the same images where applicable. For both microscope/magnification pairs, the pixel size was between 0.65~0.70 nm/px, and the image resolution was 2048 × 2048. The same magnifications were used regardless of the presence of bubbles for consistency.

Each cross-section was imaged along the full length of the window in about 20 images. A montage was created for each cross-section from these images to ensure no area was double counted. Both the inner oxide and the implanted helium bubble layer are fully in the frame of the montage, so both inner oxide thickness and total oxidation measurements were performed on these montages.

For clarity it is necessary to define the terms inner oxide thickness, total oxidation, and dissolution. Inner oxide thickness is the total thickness of oxide between the metal and either the outer oxide or the surface when there is no outer oxide. Total oxidation is the thickness of metal that has been oxidized. Dissolution is the loss of inner oxide thickness to any process which is generally assumed to be dissolution; however, conversion into outer oxide or spallation would fall into this definition. Due to the inward growing nature of the inner oxide, the thickness of inner oxide is equal to the total oxidation measurement because it occupies the same volume that used to contain metal. Therefore, dissolution is a derived quantity that is the difference between the inner oxide thickness and total oxidation, see Eq. 4.4.

Each layer thickness was determined by measuring the distance between the upper and lower bounds of the layer in each column of pixels as visualized in Figure 4.16. For the inner oxide, the lower bound is the metal / oxide interface, and the upper bound is either the inner / outer oxide interface or the exposed surface of the inner oxide. For total oxidation, the lower bound is also the metal / oxide interface, but the upper bound is the original metal surface. Except for the original metal surface, each boundary was determined from the contrast difference

between the layers on either side. The original metal surface is a fixed distance from the helium bubble layer depth; the determination of which is described below and shown in Figure 4.16a. Finally, inner oxide dissolution is derived by subtracting the inner oxide thickness from total oxidation as exemplified in Figure 4.17.

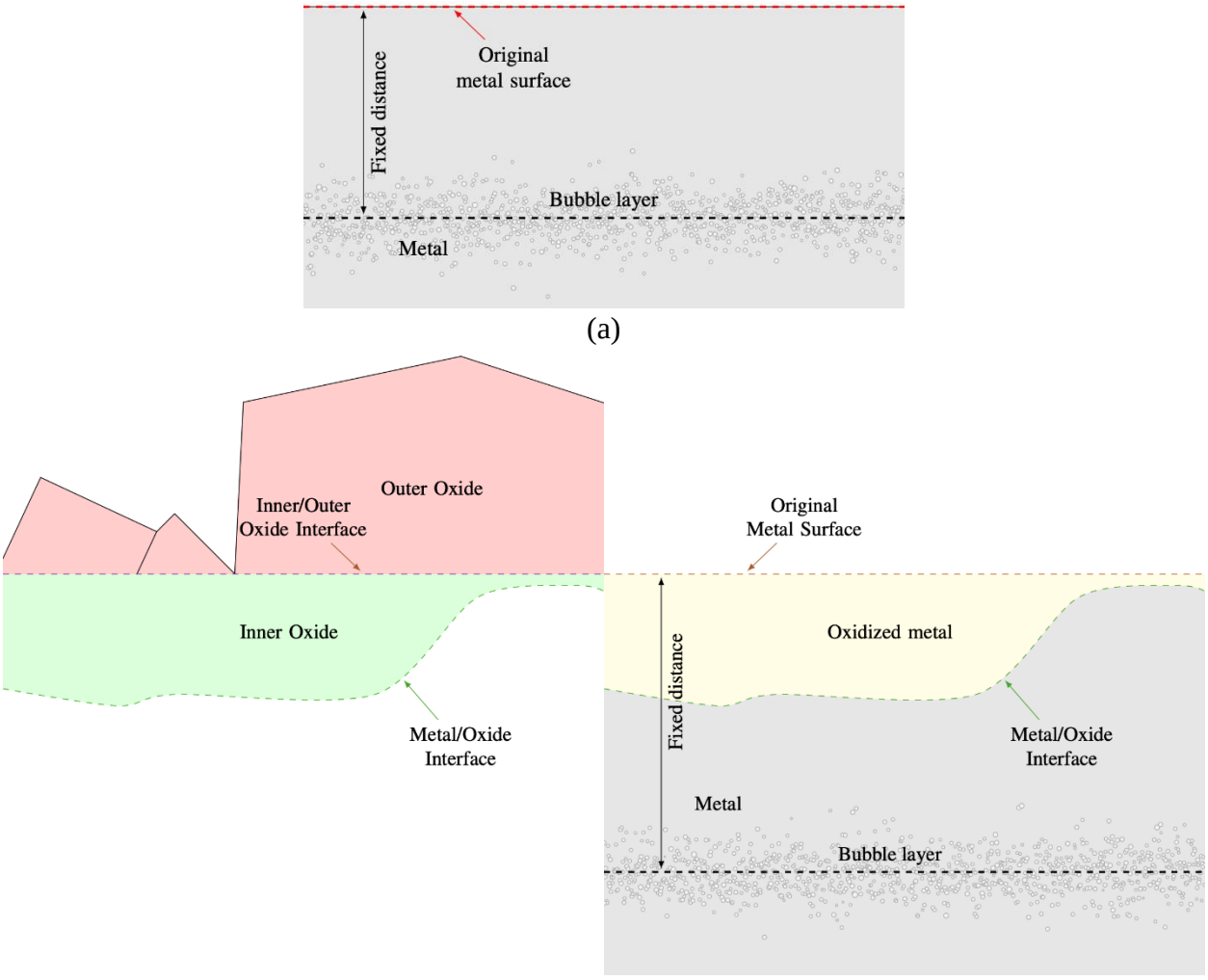

Figure 4.16. Schematic showing how the surfaces are identified to measure the inner oxide thickness and total oxidation.

Helium bubbles from hot implantation form a diffuse layer, so measuring a single value of the layer's depth is not straightforward. Identification of bubbles was performed using ImageJ by first running each image through a bandpass filter, binarizing the image, and then using the "analyze particles" function. This yields the depth and area of each bubble, and the depth

distribution is roughly a Gaussian skewed towards the surface. The mean of a Gaussian fit of this distribution was used as the depth of the layer. Bubble distribution fitting was repeated for each image, and the output is a coordinate point on each image in the montage. These points were fit to a 2nd order polynomial to generate a continuous bubble layer depth across the montage. This process was first completed on helium implanted material before exposure to calibrate this measurement of average depth of the bubble layer relative to the original metal surface. Finally, the bubble layer depth is offset by the calibration measurement to yield the original metal surface line across the entire cross-section montage.

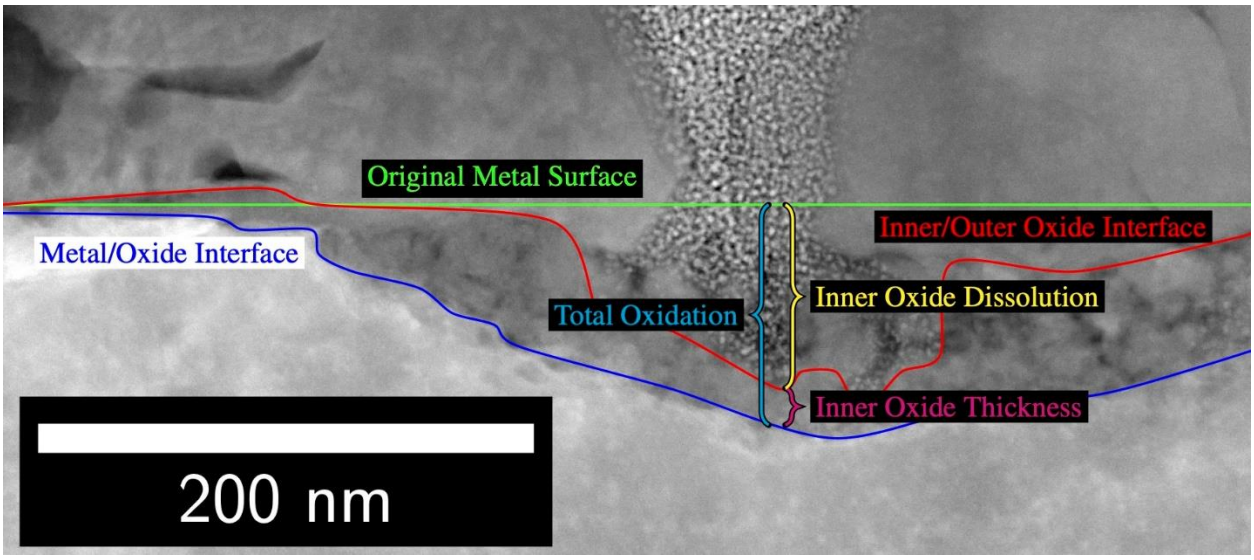

Figure 4.17. Example showing the respective measurement of inner oxide thickness, total oxidation, and inner oxide dissolution.

Using the original metal surface and boundaries defined earlier, the inner oxide thickness and total oxidation are measured in each column of pixels across the montage. Additionally, the dissolution is calculated by subtracting the two measurements in each column of pixels. From this data set, the overall mean and standard deviation are calculated for each cross-section and for each region of all samples. Furthermore, histograms of inner oxide thickness, total oxidation, and dissolution are generated for each sample region and presented.

Error measurements for inner oxide thickness, total oxidation, and dissolution are made with modified versions of the measurement techniques themselves. For both inner oxide thickness and total oxidation, the primary source of error is the degree to which the metal/oxide interface is edge-on with the finite thickness of the cross-section from which they were measured. Total oxidation also includes a calibration error that is described below. The primary error for both inner oxide thickness and total oxidation is ambiguous regions that contain both metal and oxide through the thickness of the cross-section. To quantify this error, a second "metal/oxide interface" was identified, capturing all ambiguous areas, and the measurement was repeated to gain a "maximum" measurement. The difference between the averages of these datasets yields the error value, and the same is true for subset of those datasets. The inner/outer oxide interface was not treated in the same way because the cross-sections are taken such that this interface is edge-on throughout the thickness.

Error measurement for dissolution consists of two components: calibration error and total oxidation relative error. The metal/oxide interface is not used in the calculation of dissolution, so the edge-on error is not directly applicable to this measurement. Calibration error is simply the standard deviation of the difference between the actual metal surface and the reconstructed metal surface for the calibration cross-sections; the value of this is 11.4 nm. The error of the total oxidation measurement relative to the dissolution measurement is included to capture any high percentage errors between the reconstructed original metal surface and the new metal surface. Multicomponent errors (e.g., total oxidation and dissolution) were combined using a root sum square as is standard for addition and subtraction error propagation. Examples of inner oxide thickness, total oxidation, and dissolution error calculations are provided in Appendix B.

4.3.2.3. Oxide Composition Measurement

Oxide composition was measured using STEM-EDS on a JEOL 2100F and a Thermo Scientific F200X G2 Talos at the Michigan Center for Materials Characterization and a Thermo Scientific TF20 at the Bettis Atomic Power Laboratory. Each EDS scan included some part of metal significantly below the metal / oxide interface to serve as the standard composition. Quantitative EDS data in atomic percentage was calculated using the Cliff-Lorimer method [118] with K-factors from the standard ROI of the scan assuming the composition in Table 4.1. Because oxygen is a trace impurity in the material composition and has low EDS emission, only the major metal elements (Fe, Cr, and Ni) were quantified in EDS. The oxygen signal is still presented as net counts for differentiating oxides from the metal phase. Like oxygen, the net platinum signal is presented to identify the outer edge of the oxide. EDS data are presented as either linescans or maps along with the associated STEM HAADF image of the scanned area.

Error calculations for EDS measurements were taken to be the combination of error from the calculation of the Cliff-Lorimer K-factor and the net counts for each relevant element. For net counts, the error is taken to be simply the square root of the number of counts. For the K-factor error, the ROI taken to be the standard was consolidated into an effective single point, and the relative variance of each K-factor is the sum of the relative variance for Fe and the quantified element. For each data point, the relative variance is the sum of relative variance for the Fe and the quantified element for that point itself, combined with the relative variance of the K-factor. The final error is the calculated atomic percentage multiplied by the square root of the sum of all the listed relative variances, repeated multiple times where necessary. An example of error calculations is provided in Appendix B.

4.4. Thermodynamic Modeling

Thermo-Calc was used to calculate equilibria of the stainless steel corrosion system along the continuum of oxygen activity. Both water and steam conditions were modelled to cover the environments achieved in this work. The range of oxygen activity covers hydrogenated, aerated, and radiolyzed water and steam. The water condition is 320 °C and 13.1 MPa, and the steam-argon environment is 480 °C and 1.5 MPa.

Thermo-Calc software was used with the Thermo-Calc software steel and FE-alloys (TCFE) database to calculate equilibria in a simplified system containing only Fe, Cr, Ni, and O. The original mole fractions of Fe, Cr, and Ni in the alloy were renormalized to make a pseudo-model alloy for the purposes of these calculations. The system was defined with a constant 3 moles of metal and the amount of O was stepped from 0 mol to 5 mol in 0.05 mol increments or finer. The number of moles was chosen for convenience with spinel stoichiometry (3 mol metal and 4 mol oxygen), but the amount is arbitrary because all results are intrinsic properties. Results of the modeling are presented in Chapter 5.

Thermo-Calc is software that calculates thermodynamic equilibria using the CALPHAD (CALculation of PHAse Diagrams) method. This method can be summarized as a Gibbs free energy minimization numerical solver that uses databases for interaction parameters between elements for different phases. As such, the use of CALPHAD to calculate equilibria for an alloy under different environmental conditions merely requires the contents of the alloy and the conditions as listed in Table 4.10. Many of the results from this modeling can be compared against Kurepin et al. [47] which used a similar Gibbs free energy minimization approach on the Fe-Cr-Ni-O system. While the results of Kurepin et al. show a variety of results which can be

compared to the modeling in this work, the modeling done here uses the more specific composition and environment (320 °C instead of 290 °C) relevant to this work.

Table 4.10. Parameters used for Thermo-Calc single axis equilibrium calculations.

	Water	Steam
Temperature (K)	593	753
Pressure (bar)	131	14.8
Fe (mol)	2.0508	
Cr (mol)	0.5918	
Ni (mol)	0.3574	
Initial $\ln a_{O_2}$	-80	

There are three main drawbacks to consider for the application of a CALPHAD method. First, as the CALPHAD method solves for thermodynamic equilibria, it is not easily suited to account for metastable phases without some kinetic information. While Thermo-Calc does have kinetic modeling in DICTRA, this module was not used in this work. Second, the database limits the scope to the elements, phases, and parameters contained within the database. However, the Fe-Cr-Ni ternary system and their oxides are well-characterized materials for most properties. One notable exception is the lack of data on anion vacancy concentration in Fe-Cr-Ni spinels. Third, there is no spatial information contained in the equilibrium calculations. The depth at which oxides form on the alloy surface will be determined later in this work by combining the equilibrium datasets with kinetic information and a wholistic description of the corrosion system.

Chapter 5

Results

This chapter presents the characterization results of the oxide film formed in the experiments detailed in Chapter 4. Results are collected in three sections distinguished by the corrosion and radiation environments of the experiments as detailed in Table 5.1. Section 5.1 includes only control experiments wherein the sample material was not exposed to radiation. Section 5.2 includes all proton irradiation experiments in 320 °C hydrogenated water. Section 5.3 includes all proton irradiation experiments in 480 °C hydrogenated argon-steam.

The characterization techniques used to obtain the results are described in Section 4.3. Results are divided into subsections based on the perspective of the characterization: plan-view surface analysis or cross-sectional analysis. Generally, surface characterization provides only qualitative information about the oxide film, whereas results from cross-sectional characterization are more often quantitative.

Table 5.1. List of nominal conditions of all corrosion (and irradiation) experiments performed on 316L.

ID	Duration (h)	Temperature (°C)	Gas Content in Water	Pressure (MPa)	Beam	Helium (10^{16} cm^{-2})	Radiolysis Bar
A24	24	320	8 mg/kg O_2	13.1	No	Yes	No
X24	24	320	3 mg/kg H_2	13.1	No	Yes	No
X72	72	320	3 mg/kg H_2	13.1	No	Yes	No
W24-1	24	320	3 mg/kg H_2	13.1	Yes	No	No
W24-2	24	320	3 mg/kg H_2	13.1	Yes	No	No
W24-3	24	320	3 mg/kg H_2	13.1	Yes	No	No
W24-4	24	320	3 mg/kg H_2	13.1	Yes	Yes	No
W24-5	24	320	3 mg/kg H_2	13.1	Yes	No	Yes
W24-6	24	320	3 mg/kg H_2	13.1	Yes	Yes	Yes
W72-1	72	320	3 mg/kg H_2	13.1	Yes	Yes	No
W72-2	72	320	3 mg/kg H_2	13.1	Yes	Yes	Yes
S24	24	480	170 g/kg H_2	1.45	Yes	Yes	Yes

S72	71.3	480	170 g/kg H_2	1.45	Yes	Yes	Yes

5.1. Non-irradiated corrosion experiments

Results from characterization of 316L sample material exposed to 320 °C water without irradiation are presented in this section. Because there was no irradiated region on these samples, surface analysis was not performed.

5.1.1. PWR Control exposures – X24 and X72

Control experiments X24 and X72 were helium implanted 316L discs exposed to 320 °C hydrogenated water for 24 h and 72 h, respectively.

5.1.1.1. Inner Oxide Thickness and Total Oxidation

Both inner oxide thickness and total oxidation were measured from cross-sections in HAADF-STEM imaging. Image montages of example cross-sections are presented in Figure 5.1 for X24 and Figure 5.2 for X72. Inner oxide measurement and the reconstructed original metal surface for these same cross-sections are presented in Figure 5.3 for X24 and Figure 5.4 for X72. Each pixel column of each inner oxide thickness and total oxidation measurements were taken as individual measurements and collected across all cross-sectional samples in Figure 5.5 for X24 and Figure 5.6 for X72. Both histograms for X24 show only one clear mode of corrosion, whereas X72 has two modes of corrosion: mode 1 at very shallow depths, mode 2 at a depth greater than the single mode of X24. Both modes of oxidation can be seen in Figure 5.4 where the inner oxide is mostly in the range of 200~500 nm thick or is <50 nm thick. The arithmetic mean and standard error of inner oxide thickness and total oxidation for X24 and X72 are presented in Table 5.2. The case of X72 is used as an example for the calculation of error in Appendix B. Additionally, the two modes of corrosion are separated by a simple threshold and

the same statistics are presented for X72, whereas X24 is clearly lacking mode 1 corrosion. It is important to note that the dissolution for both datasets are within error of zero.

It is useful to explain why total oxidation and dissolution measurements may be negative where inner oxide thickness measurements are always positive. Measurements of the inner oxide thickness are entirely manual, so it is impossible to find a negative measurement of thickness. Total oxidation and dissolution measurements both use the reconstructed original metal surface (derived from the helium bubble layer) which results in a static random error in both measurements. Barring any systematic error in the original metal surface reconstruction, the mean of the measurement will still be an accurate estimator of the true value because they are calibrated to the actual depth of the bubble layer before exposure. For these control experiments—X24 and X72—the dissolution mean is within error of zero meaning that the true dissolution is either very small or zero. If one were to exclude the negative measurements of dissolution, then the mean would erroneously imply a significant positive dissolution where there is little to none.

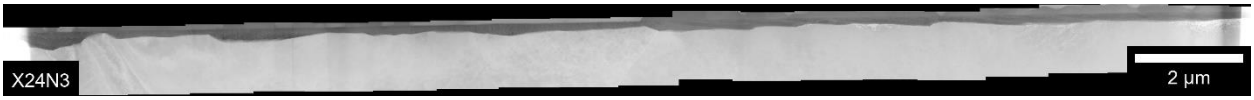

Figure 5.1. TEM micrograph collage showing a cross-section of the oxidized surface from control experiment X24.

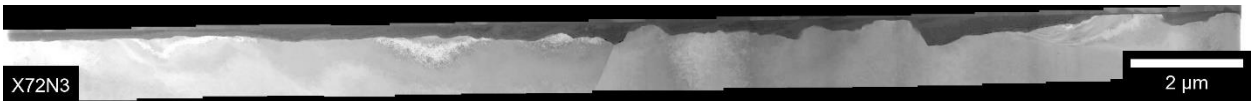

Figure 5.2. TEM micrograph collage showing a cross-section of the oxidized surface from control experiment X72.

Table 5.2. Mean values of inner oxide thickness and total oxidation measurements from non-irradiated control experiments in 320 °C hydrogenated and aerated water split into lower and upper modes of corrosion and combined.

		Total			Mode 1			Mode 2		
ID	Region	Mean Inner Oxide Thickness (nm)	Mean Total Oxidation (nm)	Mean Dissolution (nm)	Frac. (%)	Mean Inner Oxide Thickness (nm)	Mean Total Oxidation (nm)	Frac. (%)	Mean Inner Oxide Thickness (nm)	Mean Total Oxidation (nm)

X24	Non-irradiated	155 ± 15	164 ± 15	7 ± 11	0	–	–	100	155 ± 15	164 ± 15
X72	Non-irradiated	179 ± 18	183 ± 21	5 ± 11	18	20.7 ± 5.4	32 ± 13	82	213 ± 17	216 ± 20

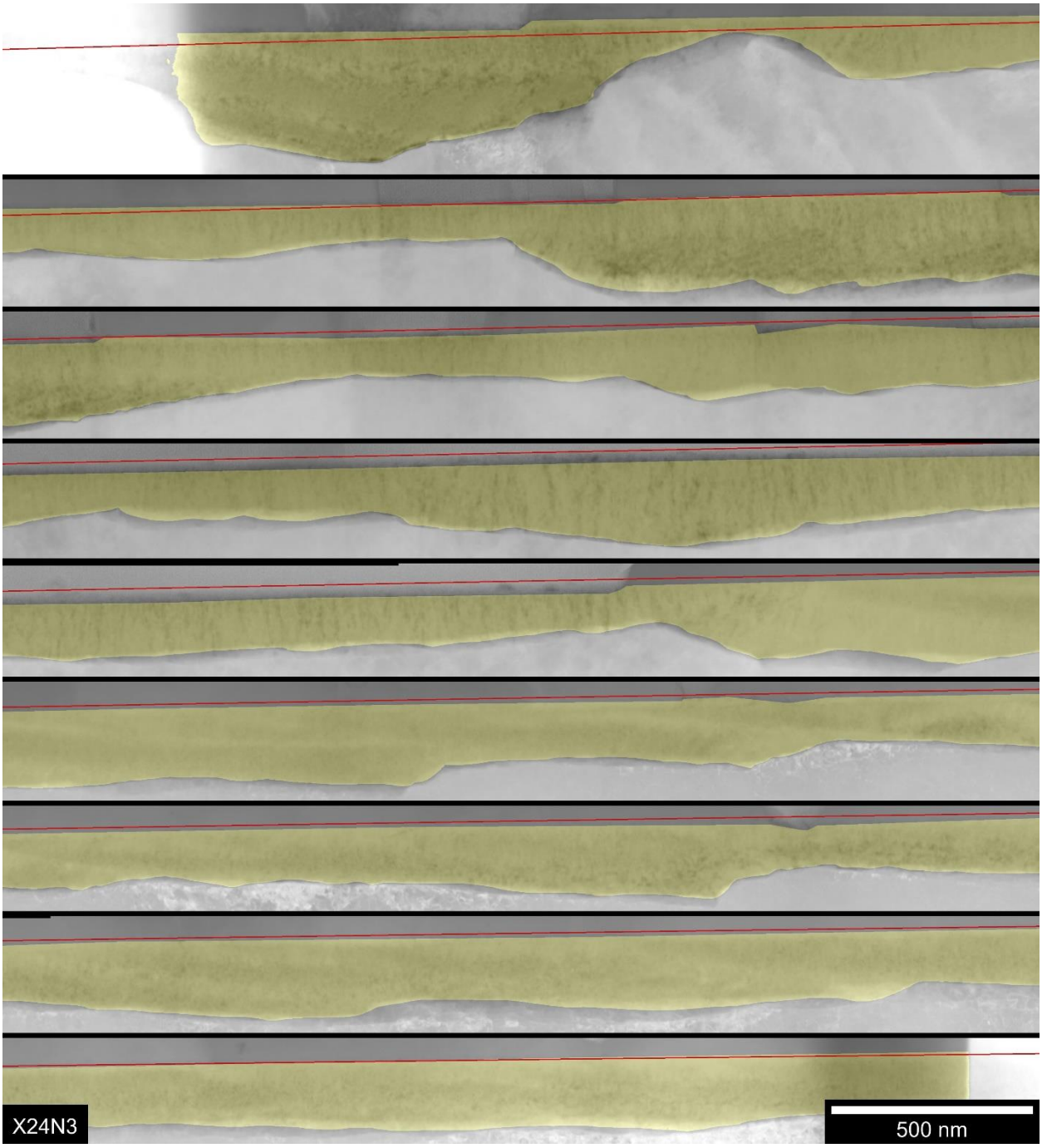

Figure 5.3. TEM micrograph collage highlighting the inner oxide area in yellow and the reconstructed original metal surface as a red line from control experiment X24.

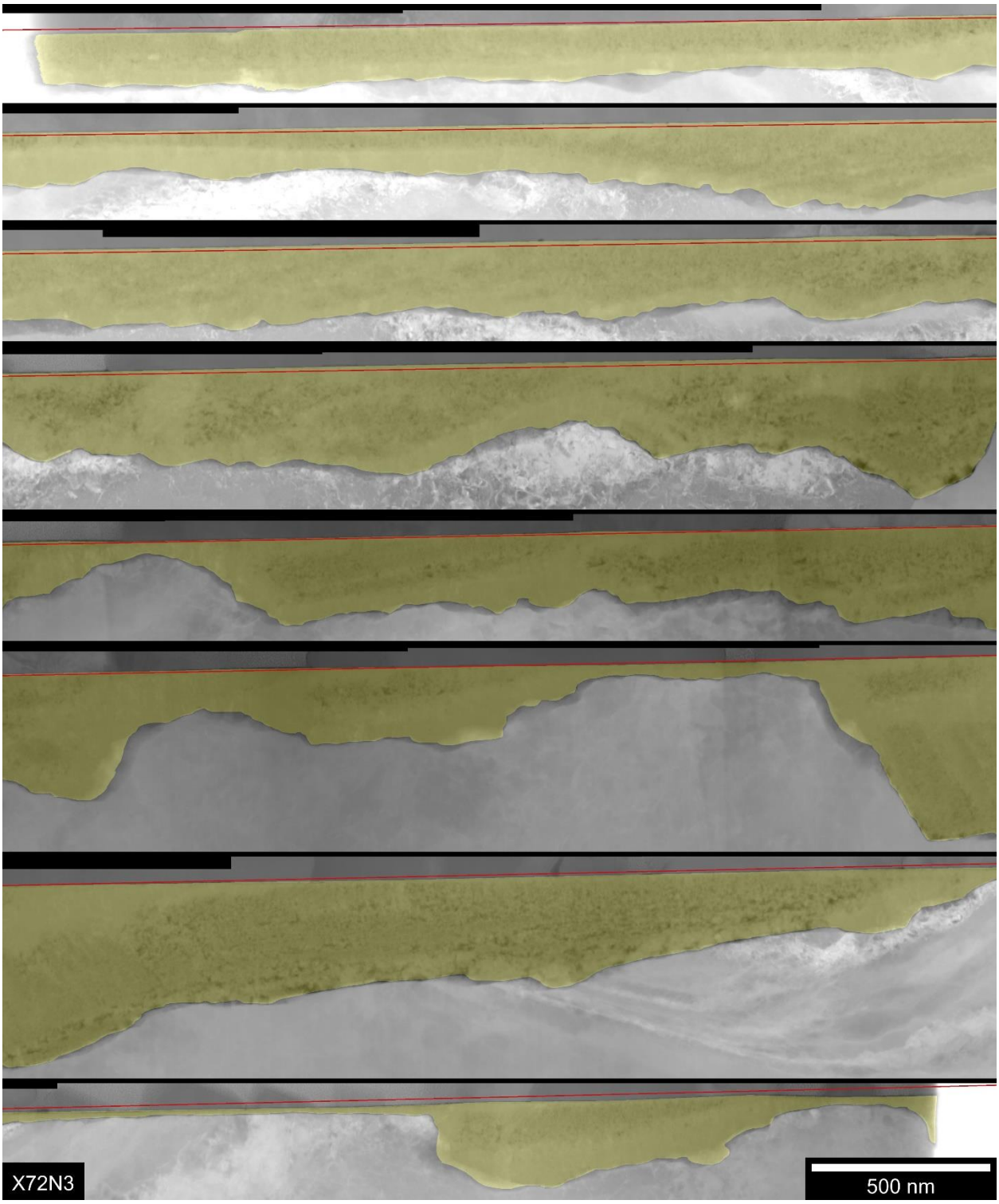

Figure 5.4. TEM micrograph collage highlighting the inner oxide area in yellow and the reconstructed original metal surface as a red line from control experiment X72.

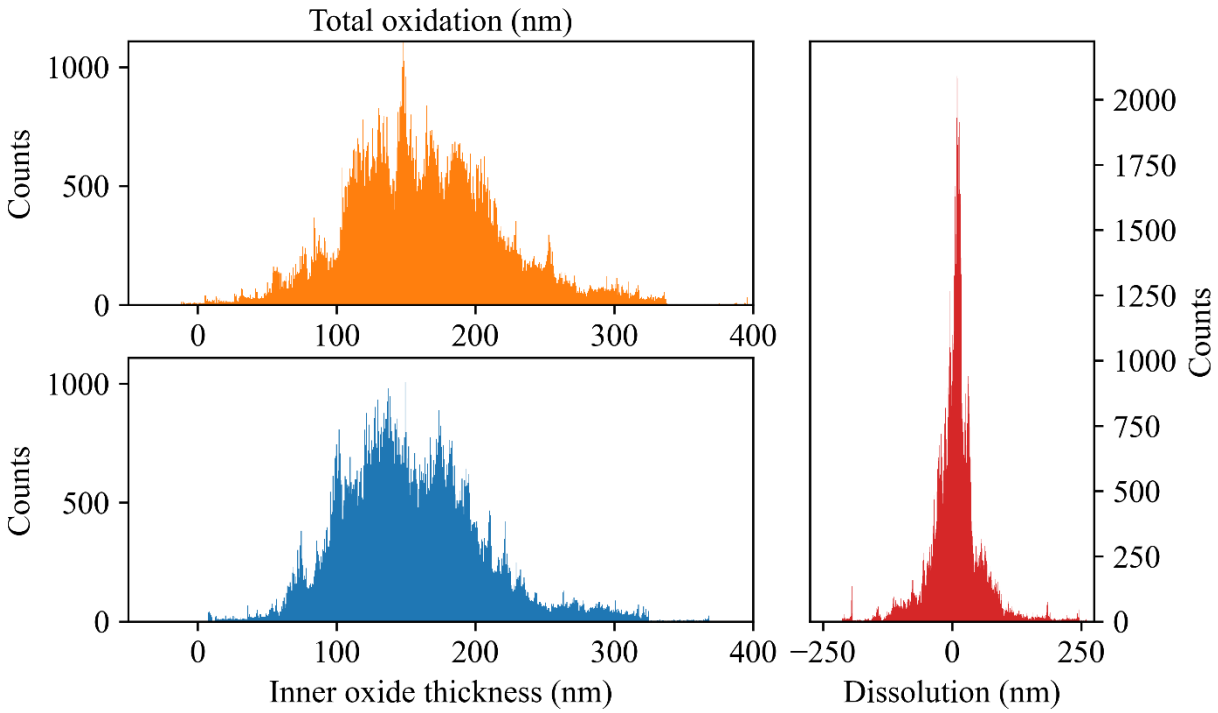

Figure 5.5. Histogram of inner oxide thickness and total oxidation measurements on specimen X24.

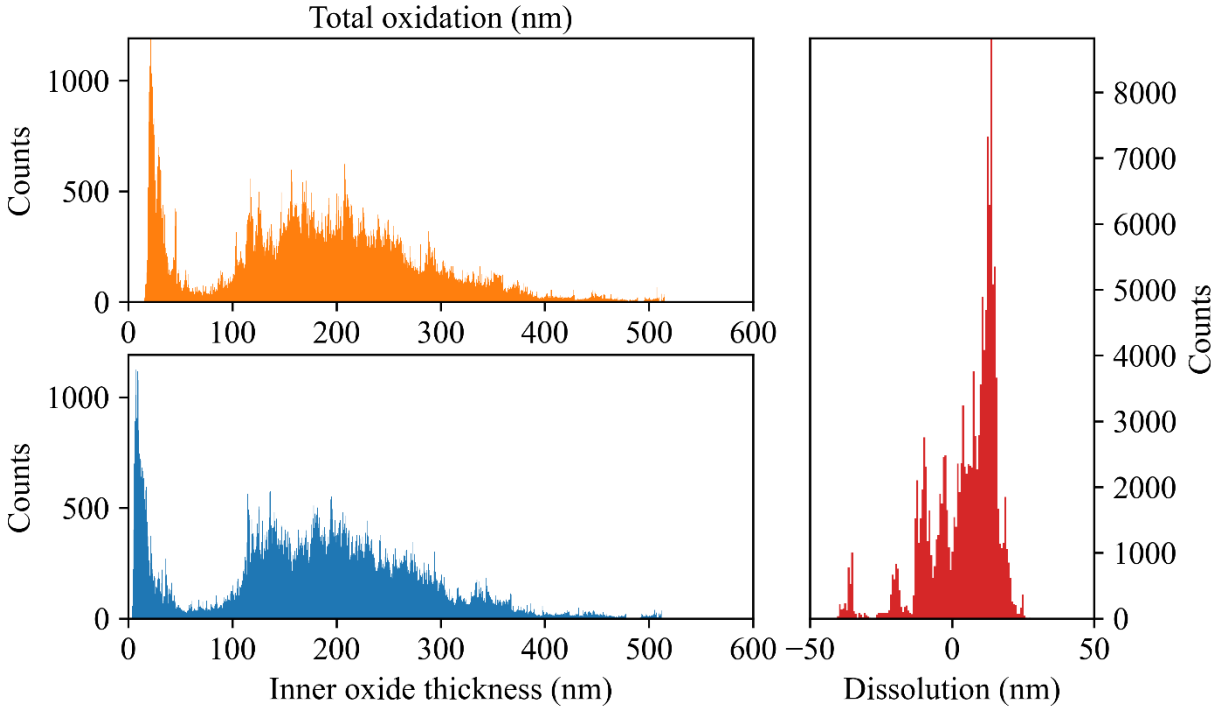

Figure 5.6. Histogram of inner oxide thickness and total oxidation measurements on specimen X72.

5.1.1.2. STEM-EDS

Composition profiles of the inner oxide are presented in Figure 5.7 from control experiment X72. One point from the EDS profile is taken as an example of error calculation in Appendix B. Both STEM-EDS scans were taken from the same cross-section and only a few hundred nanometers apart. However, the chromium profile is significantly different between the two scans. The more porous inner oxide has a Cr content of ~60 at.% of metal atoms, whereas the denser oxide has a Cr content of ~40 at.% of metal atoms.

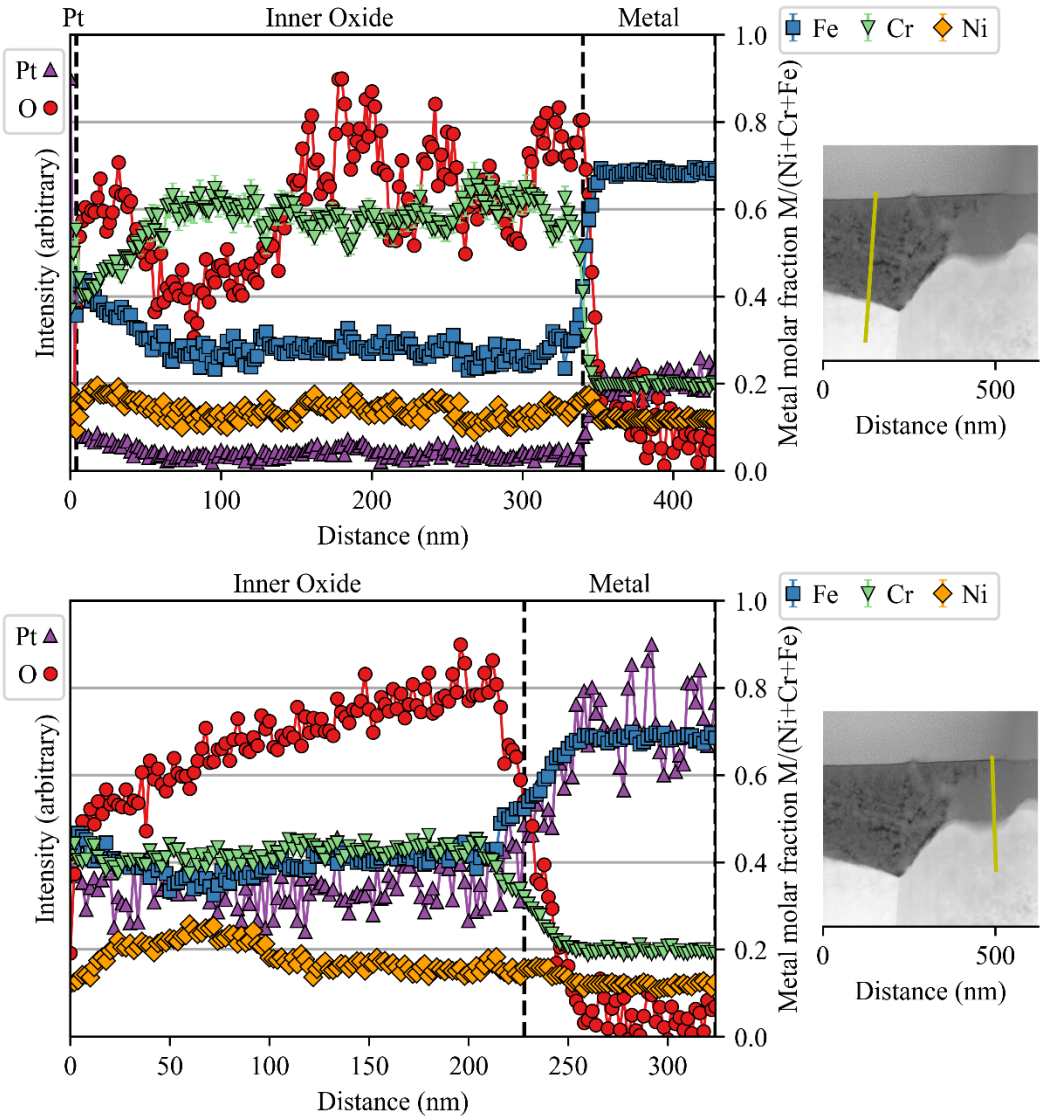

Figure 5.7. STEM-EDS linescans though the oxide and associated micrograph from the control experiment X72.

5.1.2. Aerated exposure – A24

The final control sample A24 was exposed to the same nominal conditions as X24, but the water contained 8 mg/kg O_2 instead of 3 mg/kg H_2.

5.1.2.1. SEM surface characterization

Surface micrographs from A24 are shown in Figure 5.8. The surface is covered in a uniform distribution of small outer oxide particles with sizes less than 500 nm. Two kinds of outer oxide particles are visible: polyhedral crystallites which appear darker, and the brighter equiaxed oxide particles.

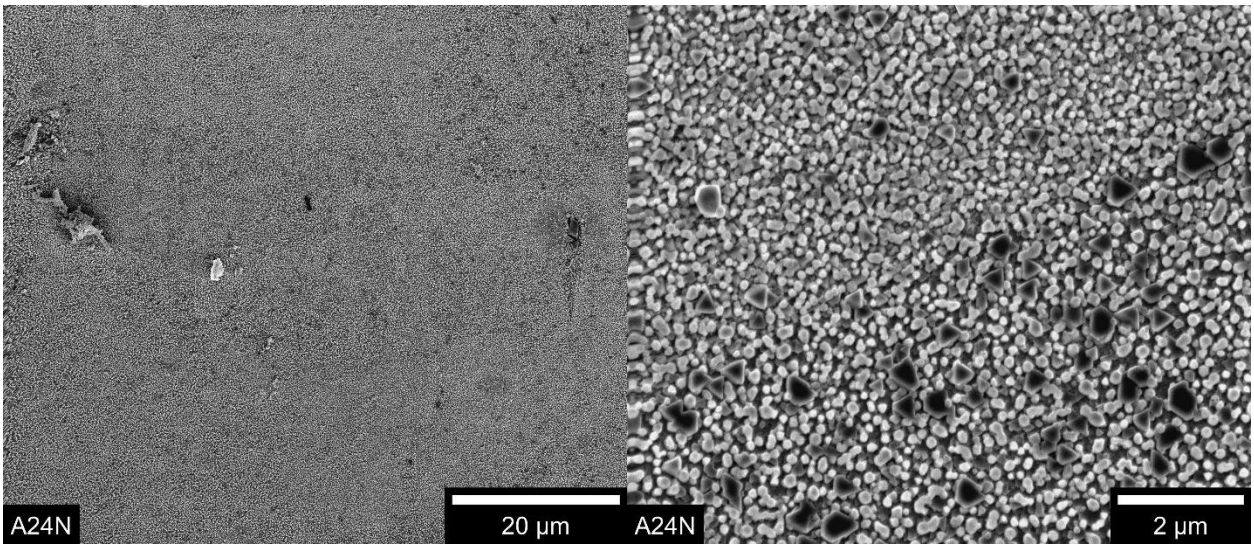

Figure 5.8. SEM micrographs from the oxidized surface of control experiment A24.

5.1.2.2. Oxide Thickness and Total Oxidation

Like the other control specimens, inner oxide thickness and total oxidation measurements for A24 were taken from collaged HAADF-STEM micrographs as exemplified in Figure 5.9 and tabulated in Table 5.3. The inner oxide is highlighted in Figure 5.10, and the reconstructed original metal surface is overlaid to demonstrate the spatial arrangement of the measurements. Histograms of both measurements are presented in Figure 5.11 showing a similar profile between both with some additional spread in the total oxidation.

Figure 5.9. TEM micrograph collage showing a cross-section of the oxidized surface from control experiment A24.

Figure 5.10. TEM micrograph collage highlighting the inner oxide area in yellow and the reconstructed original metal surface as a red line from control experiment A24.

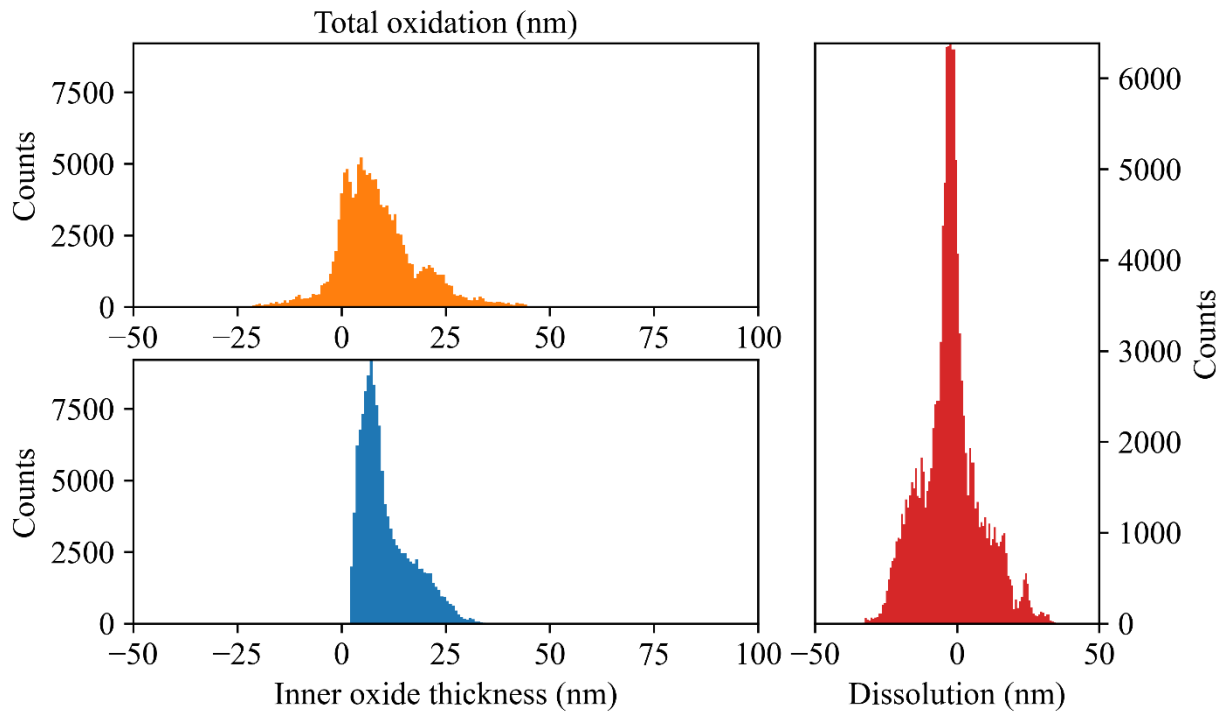

Figure 5.11. Histogram of inner oxide thickness and total oxidation measurements on specimen A24.

Table 5.3. Mean values of inner oxide thickness and total oxidation measurements from non-irradiated control experiments in 320 °C hydrogenated and aerated water split into mode 1, mode 2 corrosion, and combined.

		Total			Mode 1			Mode 2		
ID	Region	Mean Inner Oxide Thickness (nm)	Mean Total Oxidation (nm)	Mean Dissolution (nm)	Frac. (%)	Mean Inner Oxide Thickness (nm)	Mean Total Oxidation (nm)	Frac. (%)	Mean Inner Oxide Thickness (nm)	Mean Total Oxidation (nm)
X24	Non-irradiated	155 ± 15	164 ± 15	7 ± 11	0	–	–	100	155±15	164±15
X72	Non-irradiated	179 ± 18	183 ± 21	5 ± 11	18	20.7±5.4	32 ± 13	82	213±17	216±20
A24	Non-irradiated	11.0 ± 4.0	9 ± 12	-2 ± 11	–	–	–	–	–	–

5.1.2.3. STEM-EDS

One composition profile of the oxide is presented in Figure 5.12 from control experiment A24. Within the very thin inner oxide region there is a peak in the Cr content.

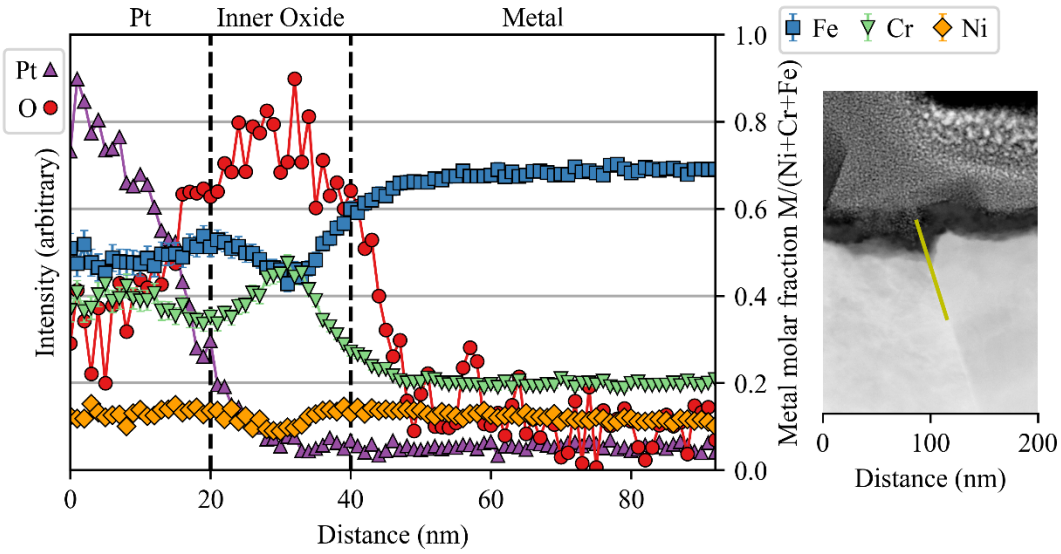

Figure 5.12. STEM-EDS linescans though the oxide and associated micrograph from the control experiment A24.

5.2. Water irradiation corrosion

The results presented in this section are from corrosion experiments on 316L simultaneously irradiated with a proton beam. For all irradiation corrosion experiments, the nominal damage rate at the corrosion surface was 7×10^{-7} dpa/s, and the durations were either 24 h or 72 h. The results from experiments in a 320 °C hydrogenated water environment will be presented in this section. The results from experiments in a 480 °C hydrogenated argon-steam environment will be presented in Section 5.3.

Two sets of experiments in a water environment are presented in this section: W24 consists of six experiments with a 24 h duration, and W72 consists of two experiments with a 72 h duration, see Table 5.1. Only W24-4 and W24-6 were helium implanted within the W24 set, so only inner oxide thickness measurements were taken from the other four experiments. Furthermore, only W24-5, W24-6, and W72-2 had a bar for radiolysis isolation, so all radiolysis region measurements in this section are from these three experiments.

5.2.1. Optical, Raman, SEM surface characterization

Because there are distinct regions on irradiated sample surfaces, surface analysis was used to gather qualitative information about the oxides formed within each region. Optical microscopy provides an indication of outer oxide coverage and some information about changing oxide thickness from thin film interference visible as color changes. Raman spectra included signals for spinel oxides in all areas of all analyzed samples, so only the Raman signal for hematite was extracted and mapped for each experiment.

For experiment W24-1, the optical micrograph and the Raman hematite map from the same area is presented in Figure 5.13. Significant coloration is observed in the circular area of the irradiated region with thin film interference patterns to the left, indicating the direction of radiolysis product flow. The bright areas in the Raman map show the partial presence of hematite in the oxide within the irradiated region in addition to some spurious signal well into the non-irradiated region on the right side of the map. Partially spalled oxides were present in the non-irradiated region of W24-1, and so the laser from the Raman microscope burned away the oxides and partially oxidized pre-existing magnetite into hematite. Therefore, hematite was only observed in the native oxide within the irradiated region.

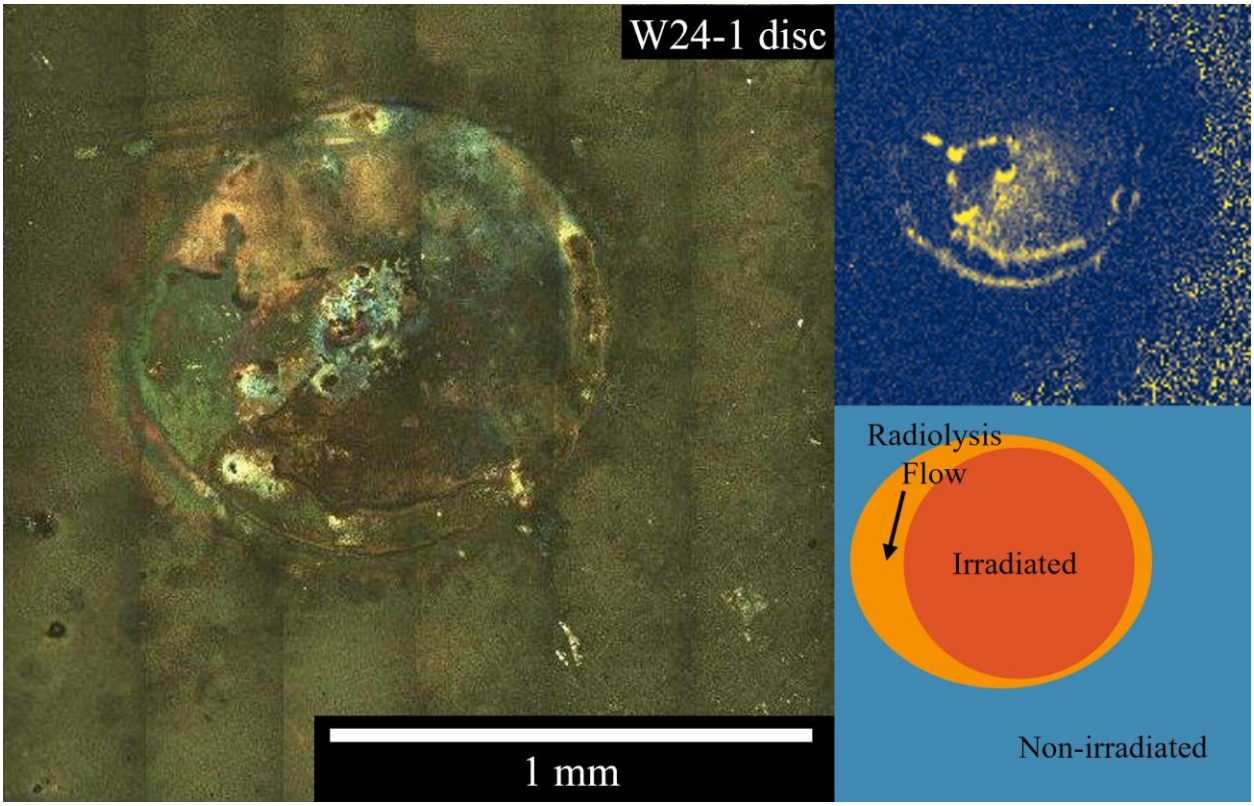

Figure 5.13. Optical micrograph (left), Raman hematite map (upper right), and region schematic (lower right) of the oxidized surface from experiment W24-1.

For experiment W24-2, the optical micrograph and the Raman hematite map from the same area are presented in Figure 5.14. The irradiated region is captured in the lower righthand portion of the image and is partially cut off on the bottom. Most of the image consists of the radiolysis flow region with a small region at the top righthand corner as non-irradiated. Most of the irradiated and non-irradiated regions are blackened from the outer oxide particles, but some reddish coloration can be seen throughout the irradiated region and in the center of the radiolysis flow region. Some grain contrast is visible in the very top righthand corner, which is the non-irradiated region. The hematite map shows these regions even more distinctly. Both the irradiated region and the radiolysis region show a relatively uniform hematite signal throughout; however, at the fringes of these combined regions, a stronger hematite signal is present. Comparing the optical and Raman images, radiolysis effects extend beyond the hematite signal

which appears as a greyish color between the edge of the hematite containing area and the area with visible grain contrast.

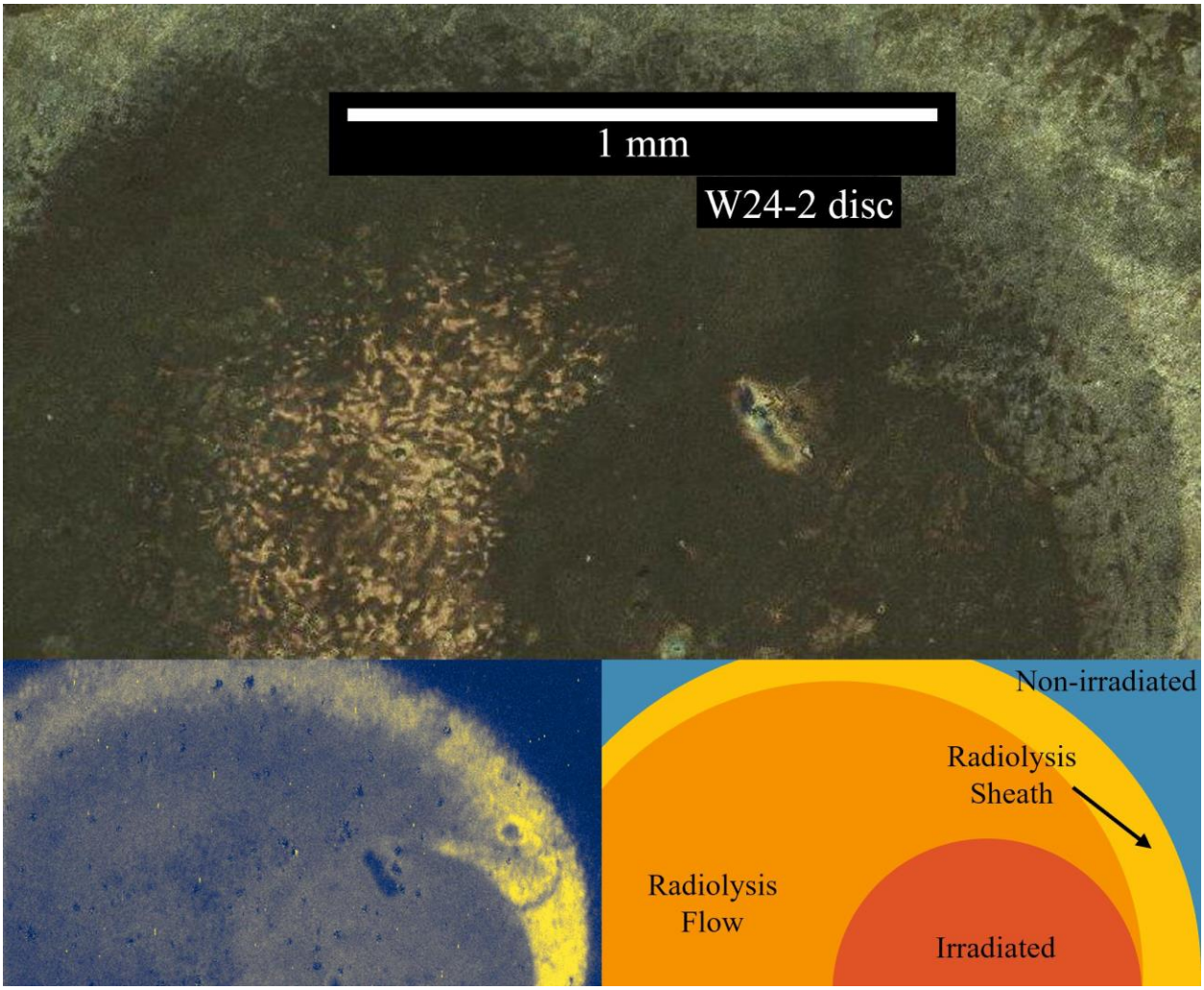

Figure 5.14. Optical micrograph (above), Raman hematite map (lower left), and region schematic (lower right) of the oxidized surface from experiment W24-2.

For experiment W24-3, the optical micrograph and the Raman hematite map from the same area are presented in Figure 5.15. Here, the optical image captures most of the exposed area including the circular irradiated region in the center, the radiolysis flow region in the top half, and the crescent-shaped non-irradiated region. Thin film interference is very clearly visible here in the irradiated and radiolysis flow regions as the blue, yellow, and red coloration. Grain contrast is clearly visible in the irradiated and non-irradiated regions, but it is almost entirely

invisible in the radiolysis flow region. Like W24-2, the sheath surrounding the combined irradiated and radiolysis flow regions shifts from a darker color near the irradiated region to a greyish color before dissipating into the grain contrast of the non-irradiated region. The Raman map of hematite for this sample has a low signal to noise ratio, so only the sheath of the irradiated and radiolysis flow regions is visible.

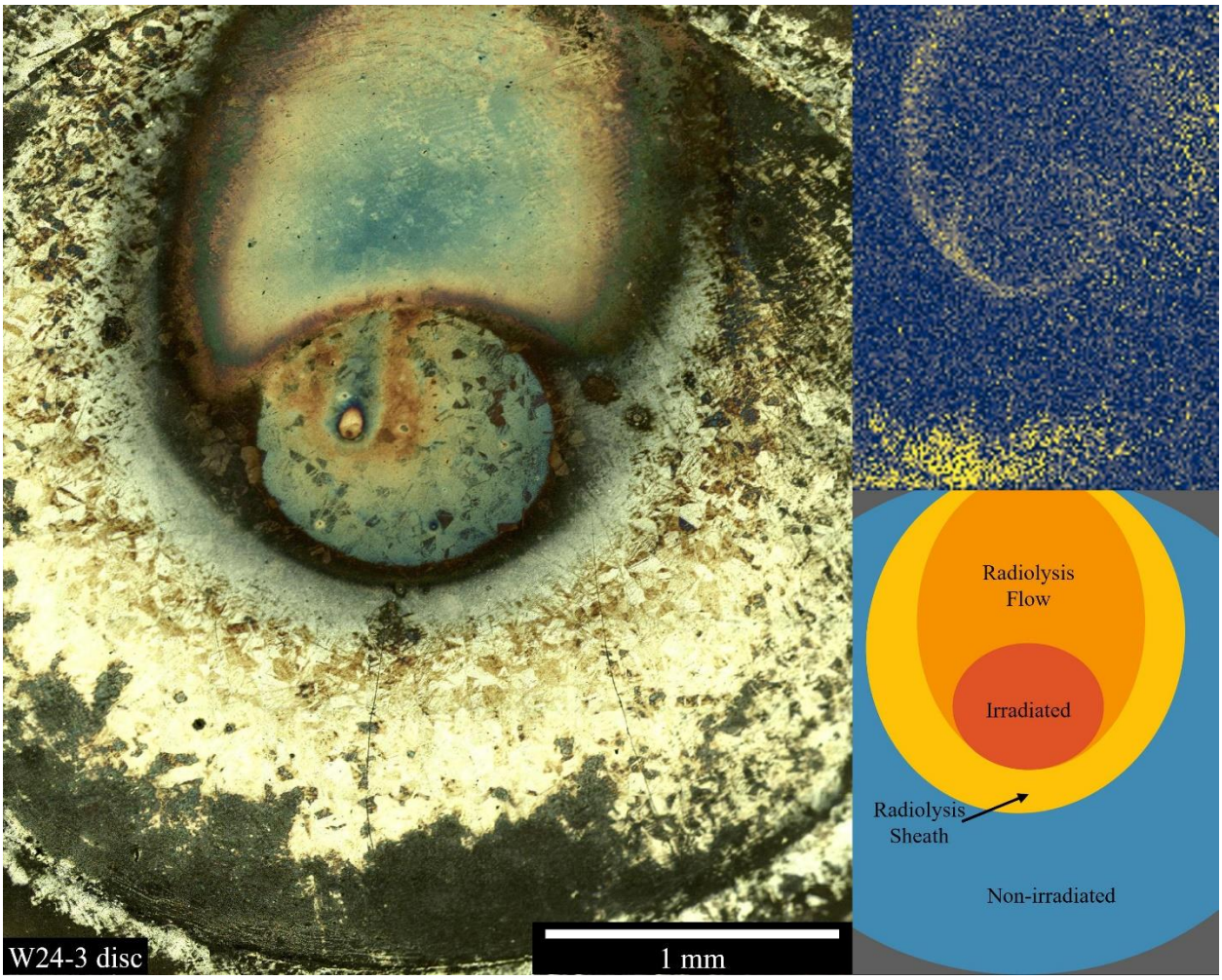

Figure 5.15. Optical micrograph (left), Raman hematite map (upper right), and region schematic (lower right) of the oxidized surface from experiment W24-3.

For experiment W24-4, the optical micrograph and the Raman hematite map from the same area are presented in Figure 5.16. The optical image is largely out of focus because of sample curling, so there is a line of focus extending from the top left to the center bottom of the image. General observations are comparable to W24-3. Thin film interference coloration is

visible in the irradiated and radiolysis flow regions. Grain contrast is present in all regions except for the sheath which appears thinner than in W24-3. The Raman hematite map has a clear artifact of the focusing wherein the hematite signal is much stronger in-focus. Ignoring this artifact, the hematite signal appears uniform within the irradiated and radiolysis regions, whereas the sheath is relatively higher intensity despite the contrast being washed out from the focusing artifact. This hematite signal closely resembles the results from W24-2.

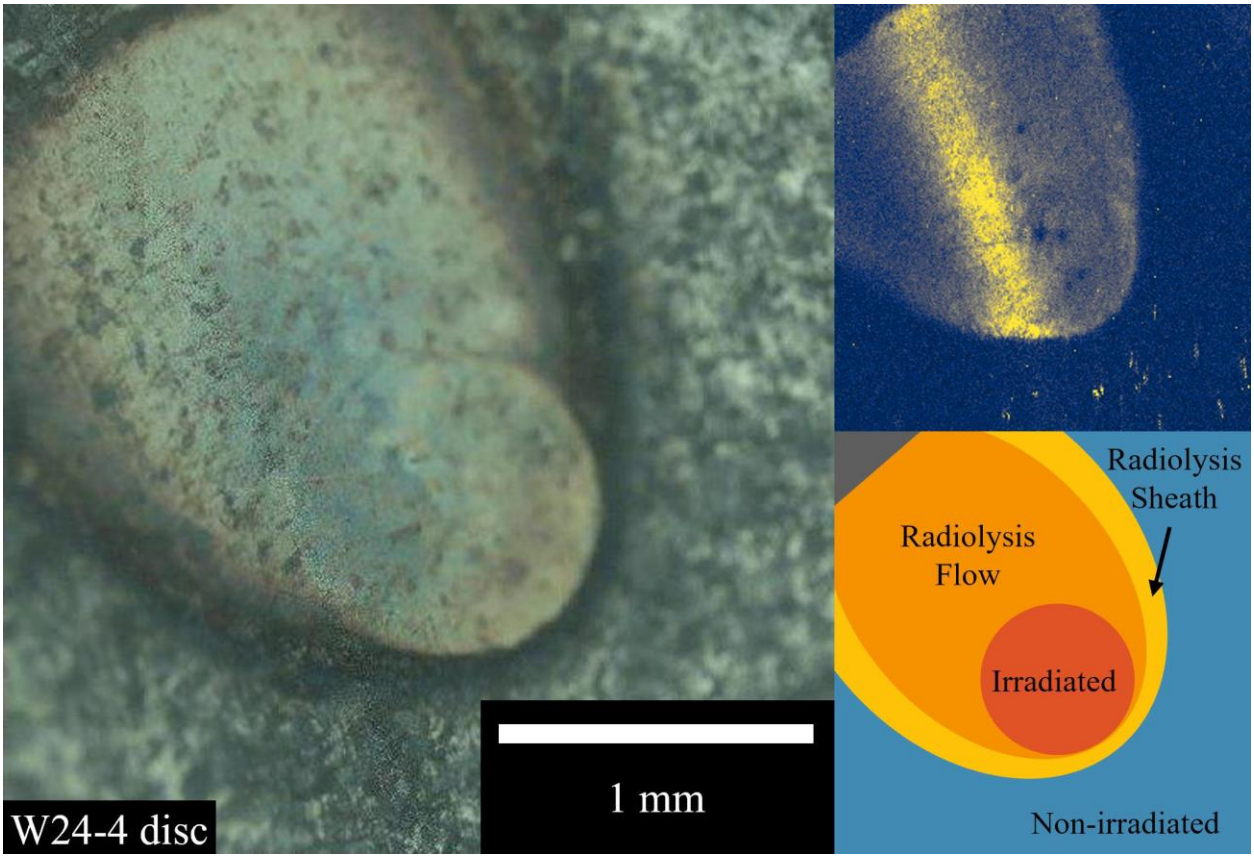

Figure 5.16. Optical micrograph (left), Raman hematite map (upper right), and region schematic (lower right) of the oxidized surface from experiment W24-4.

For experiment W24-5, the disc optical micrograph and the Raman hematite map from the same area are presented in Figure 5.17, and the bar micrograph and Raman map are presented in Figure 5.18. The optical image of the disc clearly shows some response of the oxide film from the bar that eclipsed the beam aperture in W24-5. Underneath the bar, the oxide appears a lighter grey than the surrounding darker oxide within the non-irradiated region, and the circular

irradiated region has distinct oxide coloration under the bar (lower left) and not under the bar (upper right). The radiolysis flow region is less apparent in this sample than the previous three but can be identified by the reddish color of thin film interference above the irradiated region. The flow was likely impacted by the presence of the bar, so the size of the flow region is diminished beyond being cut in half by the bar. The optical image of the bar shows a clear radiolysis region with vibrant thin film interference colors, the width of which is ~1 mm corresponding to the beam aperture diameter. However, there is a burr on the bottom of the bar that partially blocked the radiolysis region on the center left side creating a curved thin film interference pattern that was anomalous. The flow region on the bar appears dark with suppressed grain contrast and extends to the right while gradually growing taller. The non-irradiated region of the bar displayed clear grain contrast that was largely suppressed in the radiolysis region. The Raman hematite map on the disc showed a strong hematite signal within the irradiated region, and a weaker signal from the flow region. Within both, underneath the bar the signal was slightly suppressed leaving a clear outline of the prior location of the bar. The sheath was not clearly present on this disc, but the hematite signal was still very strong at the edge of the irradiated region opposite the flow region. The Raman hematite map for the bar shows a clear hematite signal like W24-2. The burr suppressed the hematite signal in the local area, but the rightmost portion of the radiolysis region shows some hematite signal, and a slightly stronger signal is visible throughout the flow region. A sheath surrounding the combined radiolysis and flow regions has the strongest hematite signal.

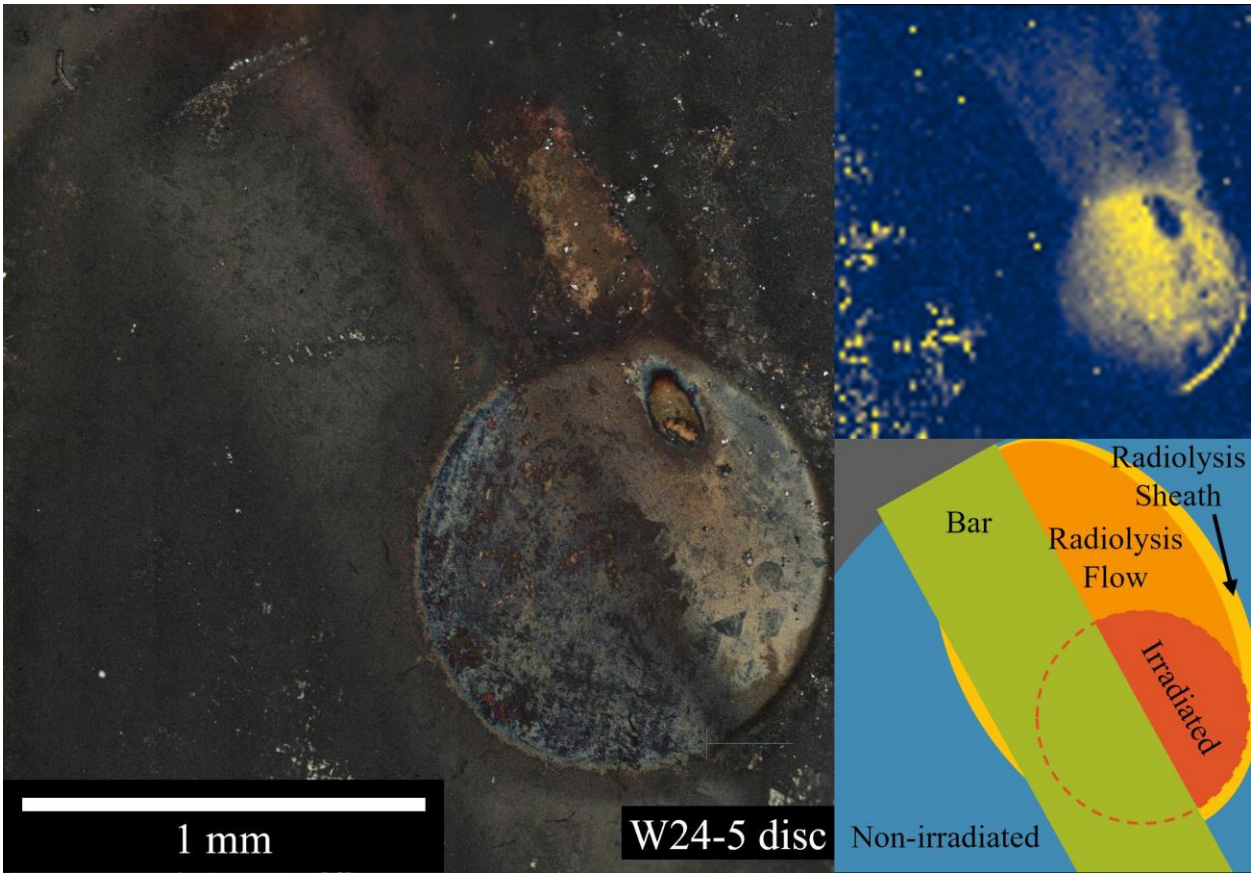

Figure 5.17. Optical micrograph (left), Raman hematite map (upper right), and region schematic (lower right) of the oxidized disc surface from experiment W24-5.

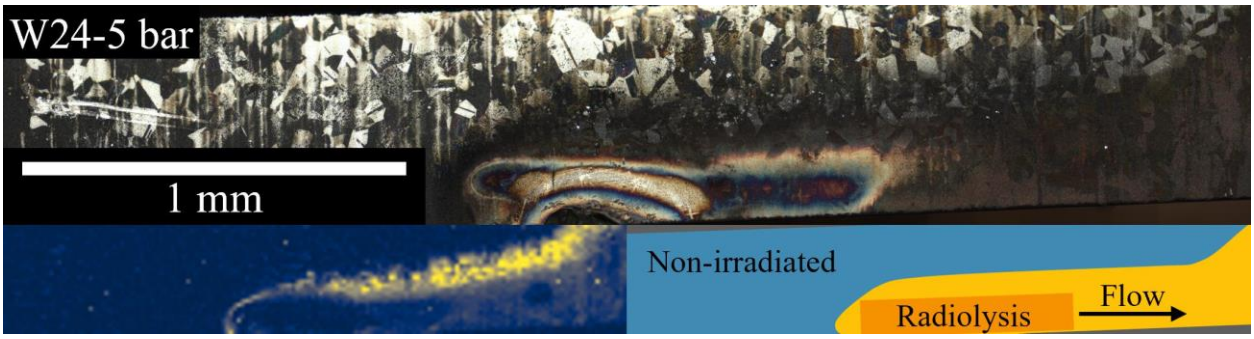

Figure 5.18. Optical micrograph (left), Raman hematite map (upper right), and region schematic (lower right) of the oxidized bar surface from experiment W24-5.

For experiment W24-6, the optical micrograph of the disc and the Raman hematite map from the same area are presented in Figure 5.19, and the micrograph of the bar along with the Raman map are presented in Figure 5.20. The optical image of the disc shows a clear outline of the bar, like W24-5, where one edge of the bar draws a sharp line tangential to the circular irradiated region, and the other edge is a diffuse line approximately through the center of the

irradiated region. Grain contrast is visible in all areas except the irradiated region underneath the bar where thin film interference coloring is strongly reddish. The flow region is not clearly visible except underneath the bar on the left side of the image as a stronger bluish color. The Raman map of hematite for the disc shows very little due to a poor signal to noise ratio. The optical image of the bar shows a very clear radiolysis region and a flow region to the right, like W24-5, with thin film interference coloring within and near the radiolysis region. Grain contrast is visible in the non-irradiated region, and significant spalling can be observed in the non-irradiated region. The Raman map of hematite for the bar shows a barely visible outline of the radiolysis region and spurious signals in the non-irradiated region from spalling oxides as observed in W24-1.

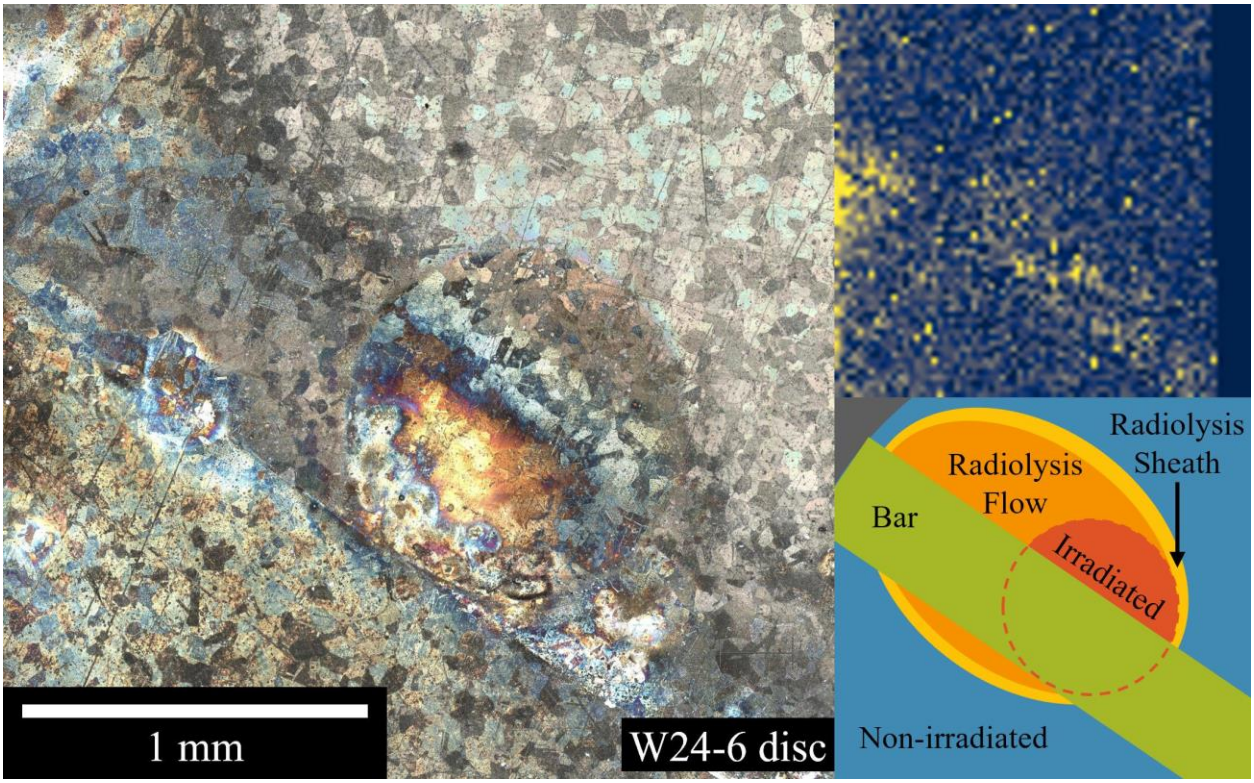

Figure 5.19. Optical micrograph (left), Raman hematite map (upper right), and region schematic (lower right) of the oxidized disc surface from experiment W24-6.

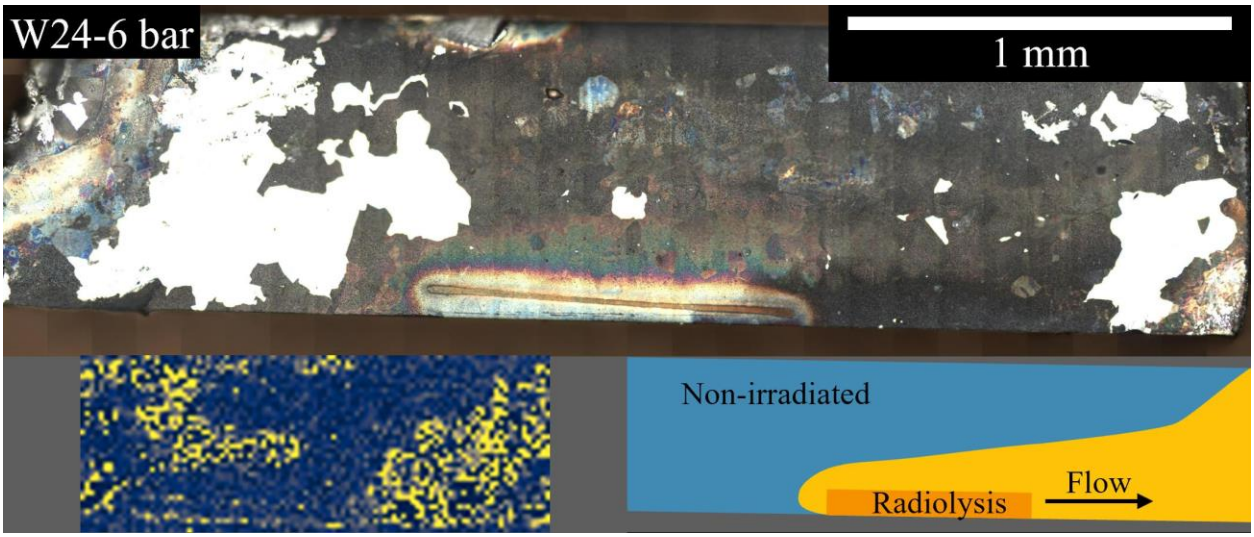

Figure 5.20. Optical micrograph (left), Raman hematite map (upper right), and region schematic (lower right) of the oxidized bar surface from experiment W24-6.

SEM micrographs comparing the different regions from the W24 experiments are presented in Figure 5.21. The non-irradiated region has exclusively polyhedral crystallites, some of which have agglomerated into continuous coverage. Elsewhere, the inner oxide is exposed, and some contrast can be observed wherein the lighter oxide is thinner than the darker oxide. The distribution of outer oxides is consistent over a single grain, and grain contrast can be observed by comparing the areal density of outer oxide coverage and the orientation of the crystallites. The irradiated region shows two types of outer oxide with complete coverage of the inner oxide. The oxides are either darker polyhedral crystallites or equiaxed lighter particles, much like A24 in Figure 5.8. The outer oxide distribution tends to change very little, if at all, between grains, however the orientation of the polyhedral crystallites is still dependent on the underlying grain. The radiolysis region shows a uniform outer oxide distribution along the horizontal direction, but continuously changing in size in the vertical direction corresponding to the direction of the proton beam. A band of a higher volume of outer oxide particles irregular in shape can be observed in both SEM and the optical image of W24-6 (Figure 5.20).

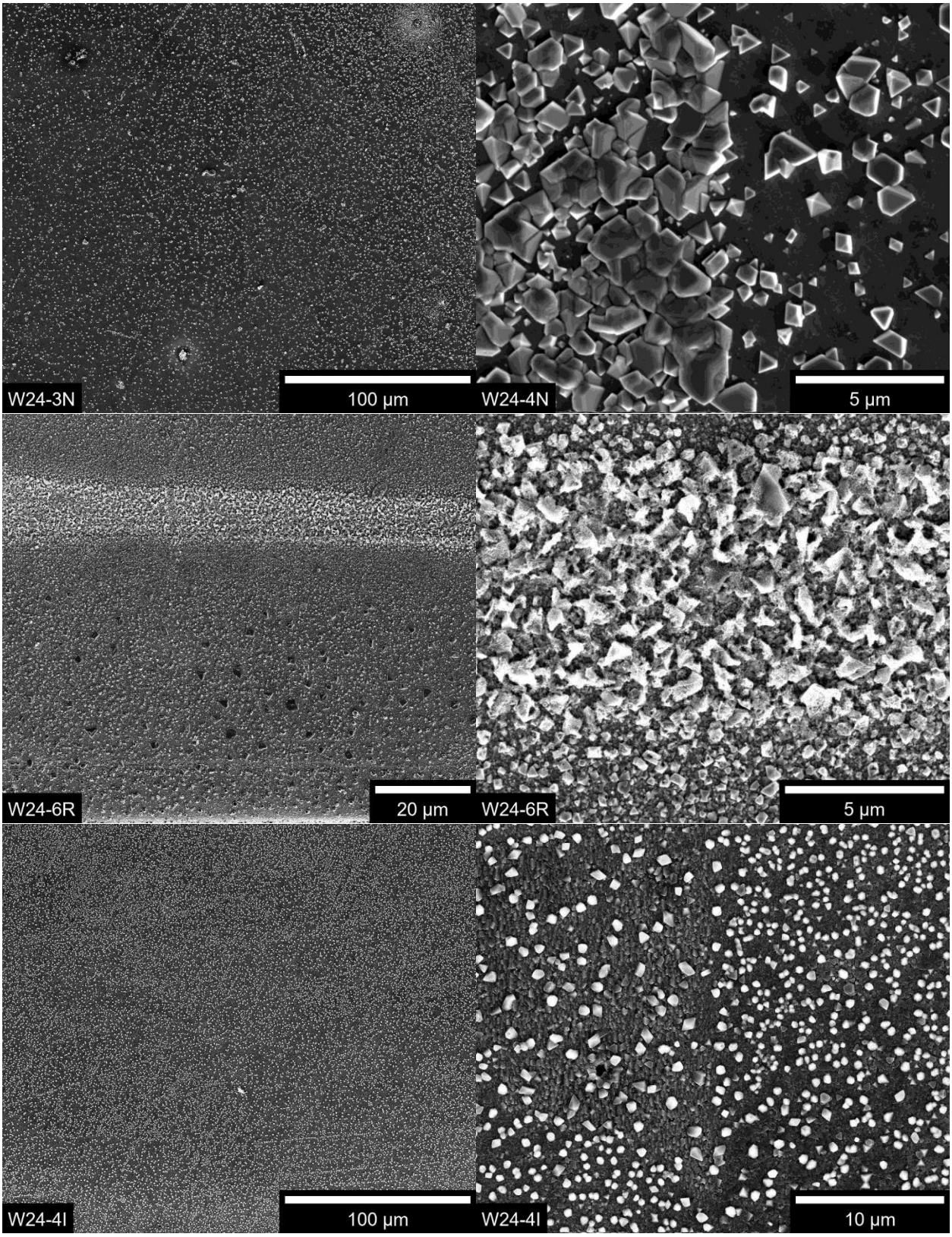

Figure 5.21. SEM micrographs showing the oxidized surface from the W24 experiment set. The upper pair is from the non-irradiated region of W24-3 and W24-4; the middle pair is from the radiolysis region of W24-6; and the lower pair is from the irradiated region of W24-4.

A Raman map of the hematite signal for W72-1 is presented in Figure 5.22. Unfortunately, an optical image could not be saved due to a file size issue with the software. The hematite signal is largely uniform within the irradiated region, and there is a small visible flow region directly below the irradiated region. The rim of the irradiated region shows a stronger signal, much like the sheath in W24-2, while the general size of the regions is comparable to W24-1. Optical microscopy and Raman mapping were not performed on W72-2.

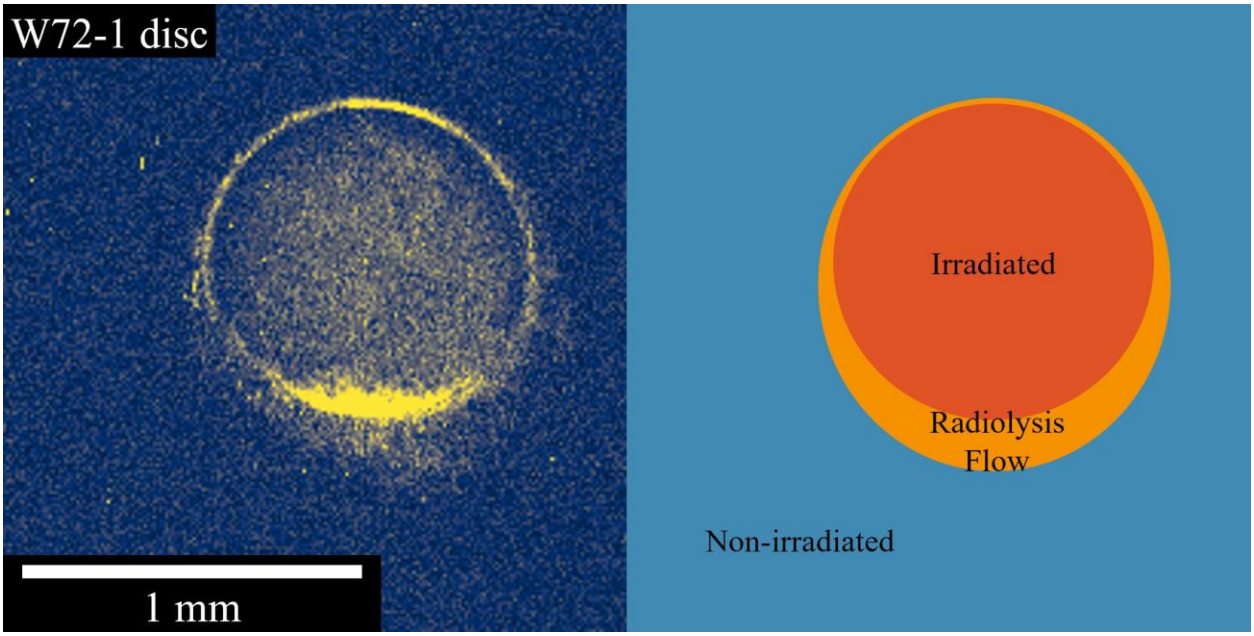

Figure 5.22. Raman hematite map (left) and region schematic (right) of the oxidized surface from experiment W72-1.

SEM imaging on W72-2 is presented in Figure 5.23 for all three regions. Grain contrast is clearer in the W72 experiments than in the W24 experiments for the non-irradiated region. Some of the polyhedral crystallites have become more irregular, but still faceted, and the agglomerated particles are more continuously fused than in W24 experiments. The irradiated region shows some grain contrast from the orientation of the crystallites. The coverage is virtually total, and the shape of the crystallites are all irregular but mostly still faceted. The radiolysis region here has the proton beam direction horizontal with the edge of the bar on the left side of the image. The oxides appear more uniform in both directions except directly adjacent to the edge of the

bar. The outer oxides are a mix of irregular faceted crystallites, much like the irradiated region, in addition to brighter rod or plate shaped outer oxide particles. Furthermore, the gaps between the larger particles are filled with a very fine coverage of small particles with indistinct shape.

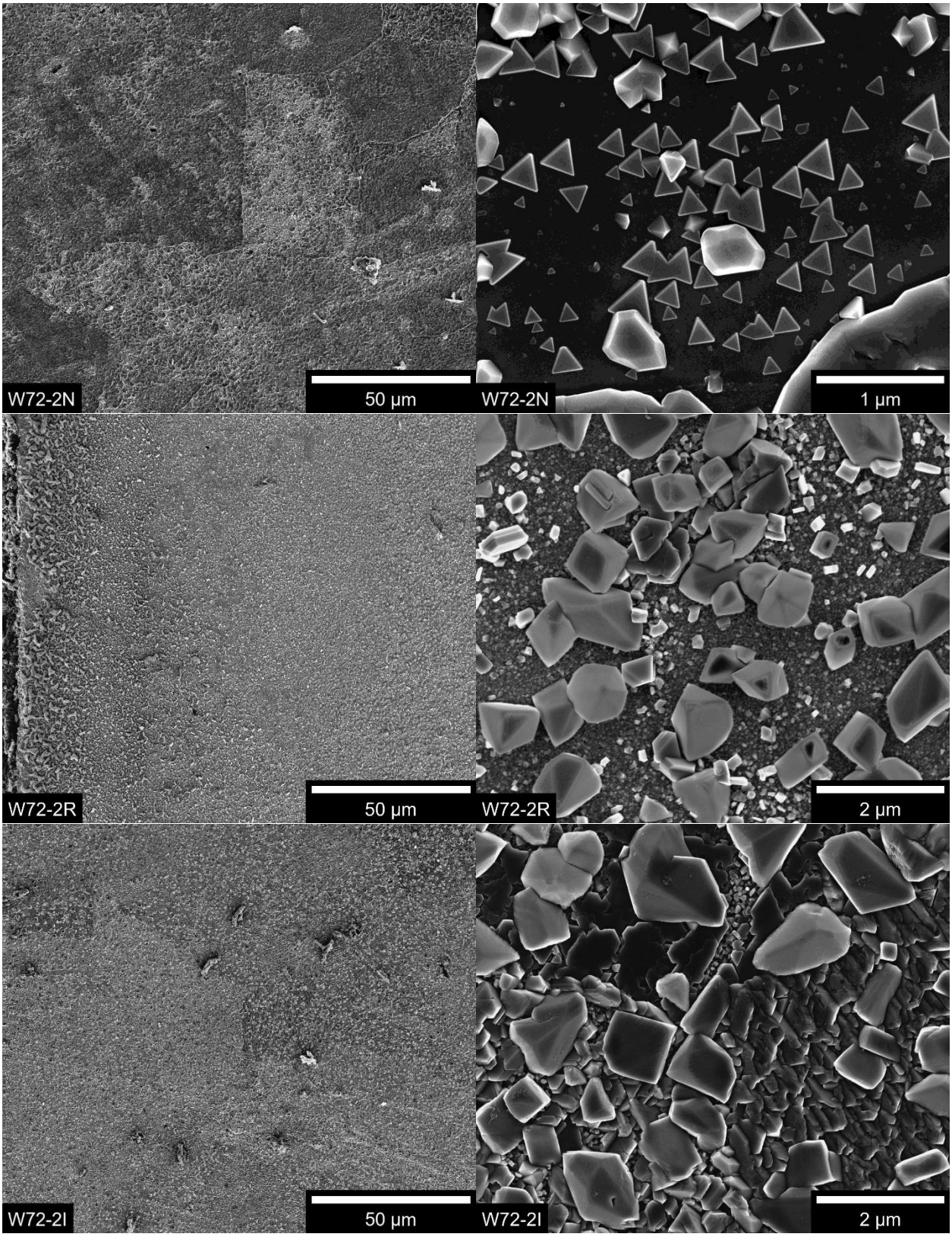

Figure 5.23. SEM micrographs showing the oxidized surface from W72-2. The upper pair is from the non-irradiated region; the middle pair is from the radiolysis region; and the lower pair is from the irradiated region.

5.2.2. Oxide thickness, total oxidation, and STEM-EDS

Following the same procedure as the control experiments, both inner oxide thickness and total oxidation were measured from cross-sections in HAADF-STEM imaging. Image montages of example cross-sections from all three regions are presented in Figure 5.24 for W24 experiments and in Figure 5.25 for W72 experiments. The characterization of these experiments is divided into subsections for each region characterized.

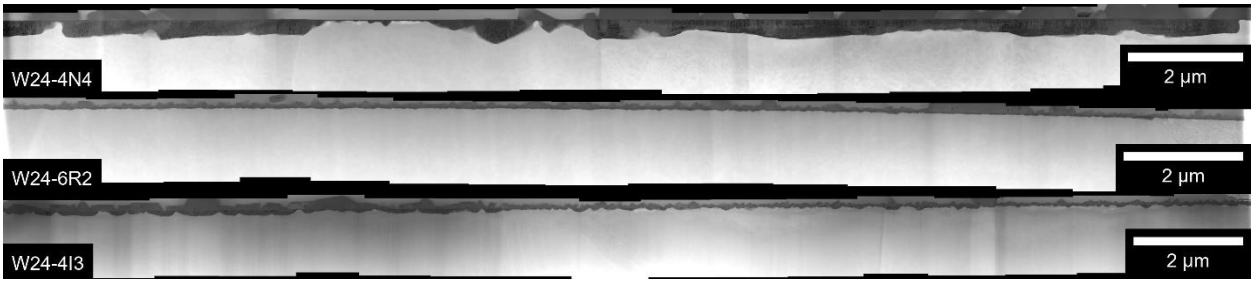

Figure 5.24. TEM micrograph collages showing cross-sections of the oxidized surface from the W24 experiment set. The upper collage is from the non-irradiated region of W24-4; the middle collage is from the radiolysis region of W24-6; and the lower collage is from the irradiated region of W24-4.

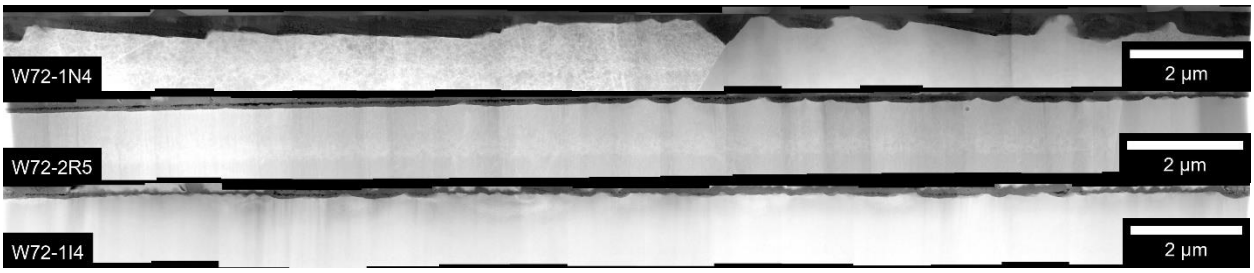

Figure 5.25. TEM micrograph collages showing cross-sections of the oxidized surface from the W72 experiment set. The upper collage is from the non-irradiated region of W72-1; the middle collage is from the radiolysis region of W72-2; and the lower collage is from the irradiated region of W72-1.

5.2.2.1. Non-irradiated region

Representations of the inner oxide measurements and the reconstructed original metal surfaces from cross-sections of the non-irradiated regions of W24-4 and W72-1 are presented in Figure 5.26 and Figure 5.27 respectively. Measurements of inner oxide thickness on specimens without helium-implantation (W24-2 and W24-3) are plotted as a histogram in Figure 5.28. The measurements were collected across all cross-sectional samples from the non-irradiated regions. They are plotted as a histogram in Figure 5.29 for helium-implanted W24-4 and W24-6, and in

Figure 5.30 for the two W72 samples (both helium-implanted). The strong mode 1 peak in W24-2 and W24-3 in Figure 5.28 is in contrast with both the W24-4 and W24-6 histogram in Figure 5.29 and the histogram from X24 in Figure 5.5 wherein the low corrosion rate mode is very weak, but the higher mode represents most of the data. The match in the total oxidation between the non-irradiated region and the control is very good. Results from X72 in Figure 5.6 and W72 match more closely, although the lower mode is slightly weaker in W72 than in X72. The arithmetic mean and standard error of these measurements are presented in Table 5.4 along with the separation of the two modes. Comparing inner oxide thickness and total oxidation for the non-irradiated regions of W24-4 and W24-6, there is general agreement. Comparing inner oxide thickness between the helium implanted tests (W24-4 and W24-6) and not implanted tests (W24-2 and W24-3), the mode 1 peak is much weaker in the helium implanted experiments, but the location of each mode is similar. When all the W24 experiments are aggregated together, the total mean inner oxide thickness is significantly reduced from the overrepresentation of mode 1 in W24-2 and W24-3. The difference in the total averages is an artifact of the differing datasets rather than a measure of significant dissolution of the inner oxide. Instances of negative dissolution are not truly “negative dissolution” or some sort of precipitation; rather, negative values for dissolution are the result of intrinsic measurement error. The negative dissolution is important to keep in place because when the true value of dissolution is near zero, the negative values in the normal distribution contribute to the accuracy of the mean estimator. Without including the negative dissolution values, the overall average dissolution would have significant bias toward positive values and lead to erroneous conclusions. The aggregated W72 data is slightly higher than W24, as expected for a longer duration, and the inner oxide compared with total oxidation shows no significant difference.

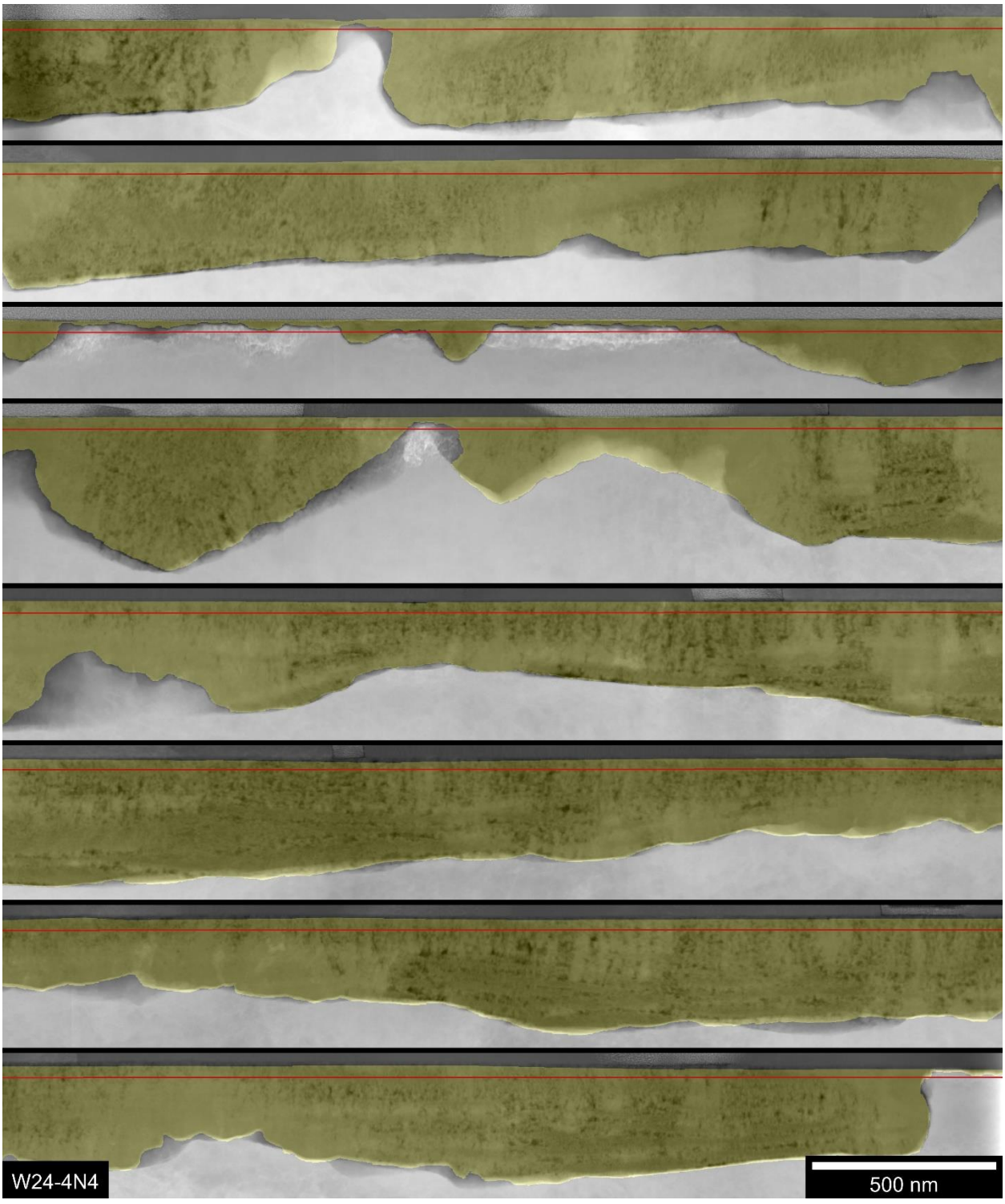

Figure 5.26. TEM micrograph collage highlighting the inner oxide area in yellow and the reconstructed original metal surface as a red line from the non-irradiated region of experiment W24-4.

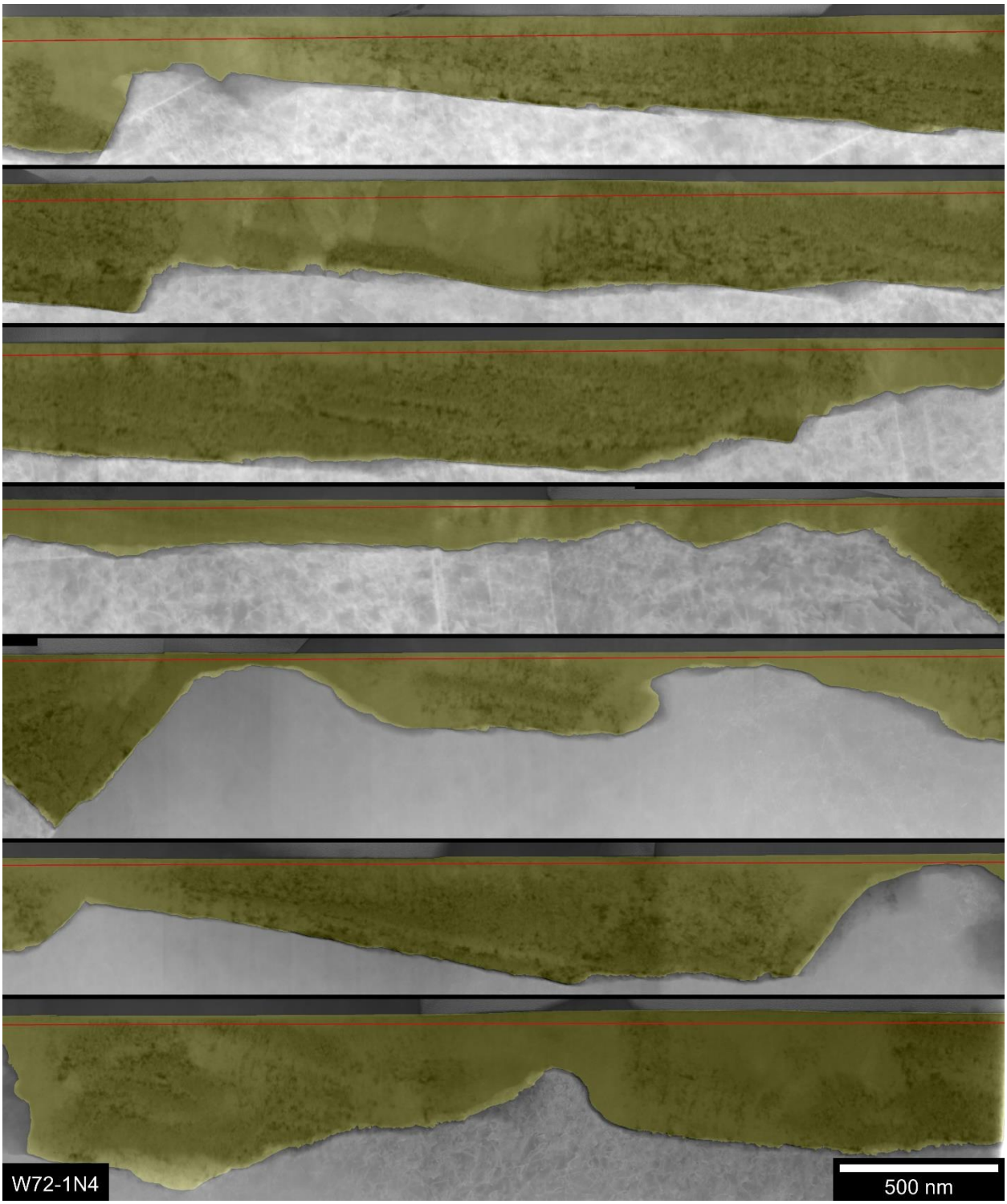

Figure 5.27. TEM micrograph collage highlighting the inner oxide area in yellow and the reconstructed original metal surface as a red line from the non-irradiated region of experiment W72-1.

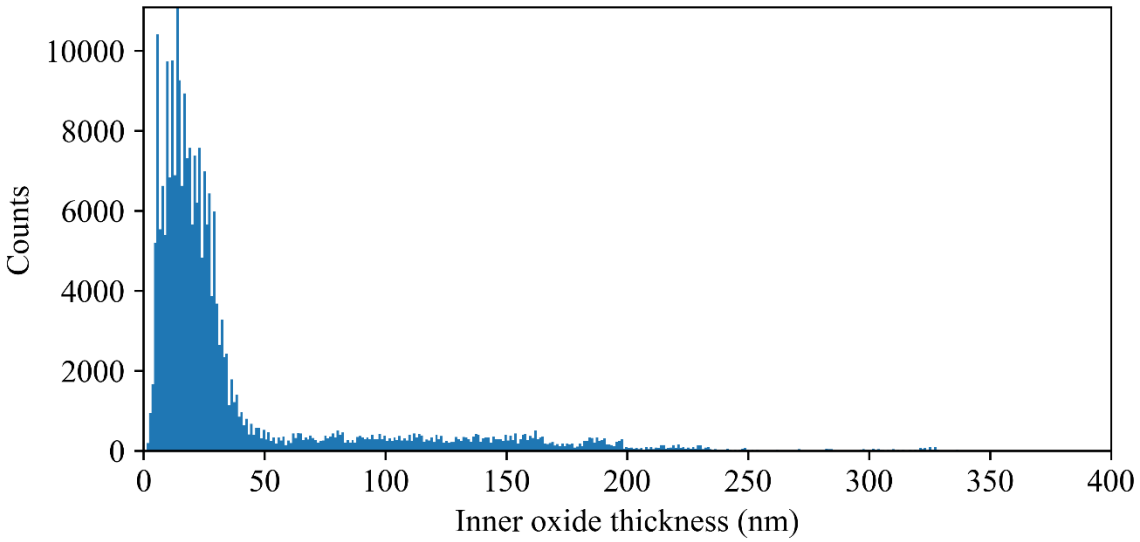

Figure 5.28. Histogram of inner oxide thickness measurements from the non-irradiated regions of the W24-2 and W24-3 experiments.

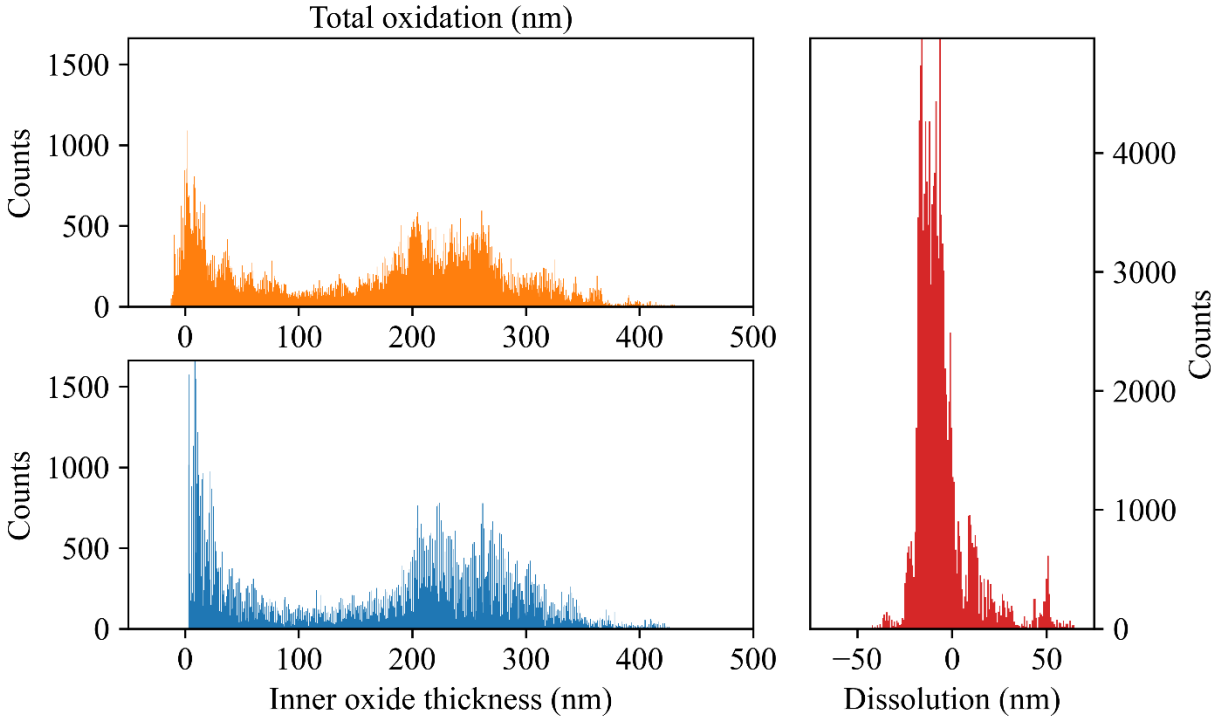

Figure 5.29. Histogram of inner oxide thickness and total oxidation measurements from the non-irradiated regions of the W24-4 and W24-6 experiments taken together.

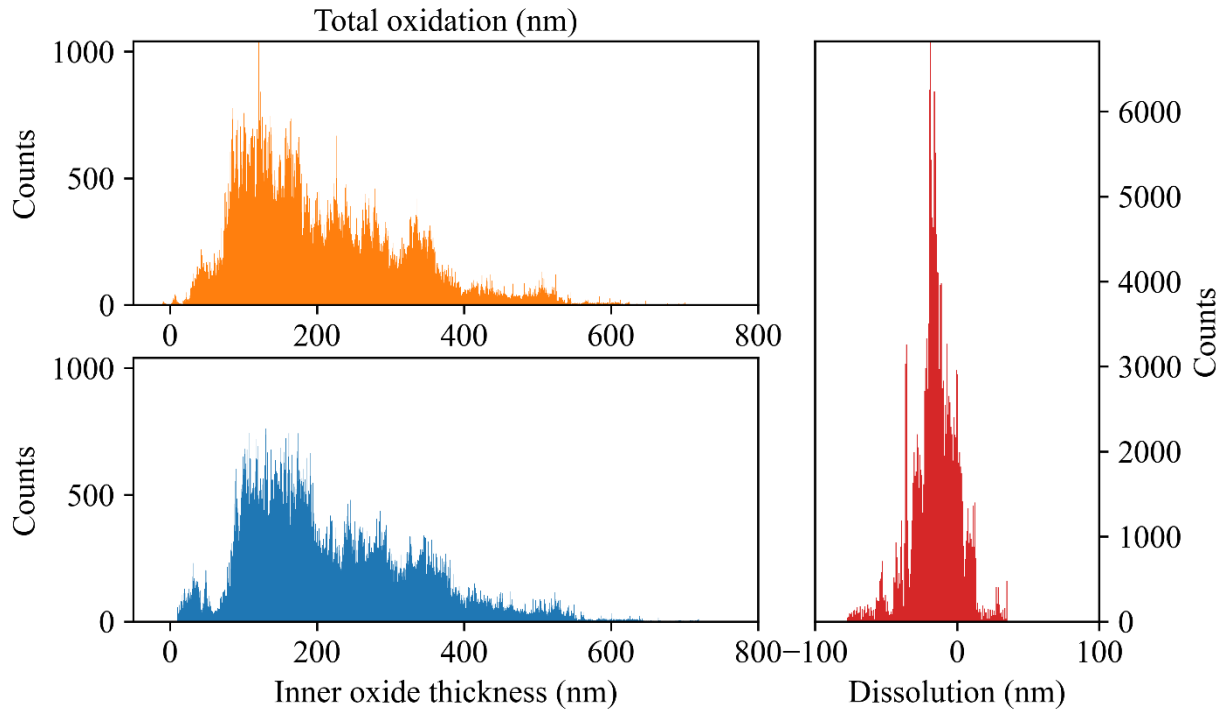

Figure 5.30. Histogram of inner oxide thickness and total oxidation measurements from the non-irradiated regions of the W72-1 and W72-2 experiments taken together.

Table 5.4. Mean values of inner oxide thickness and total oxidation measurements from the non-irradiated regions of 24 h and 72 h experiments in 320 °C water split into mode 1 corrosion, mode 2 corrosion, and combined.

		Total			Mode 1			Mode 2		
ID	Region	Mean Inner Oxide Thickness (nm)	Mean Total Oxidation (nm)	Mean Dissolution (nm)	Frac. (%)	Mean Inner Oxide Thickness (nm)	Mean Total Oxidation (nm)	Frac. (%)	Mean Inner Oxide Thickness (nm)	Mean Total Oxidation (nm)
W24	Non-irradiated	83 ± 12	174 ± 19	-5 ± 11	67	21.4 ± 6.3	26 ± 12	33	206.2 ± 8.5	227 ± 17
W72	Non-irradiated	223 ± 17	208 ± 20	-15 ± 11	4	41.1 ± 4.2	52 ± 12	96	231 ± 15	217 ± 18

5.2.2.2. Radiolysis region

TEM micrographs showing the inner oxide measurement and the reconstructed original metal surface in cross-sections of the radiolysis region are presented in Figure 5.31 for W24-6 and in Figure 5.32 for W72-2. No evidence of inner oxide dissolution can be seen in the W24-6 example, but dissolution is clearly visible in W72. A histogram of inner oxide thickness in the radiolysis region of the bar specimen without helium implantation (W24-5) is in Figure 5.33. The measurements were collected across all cross-sectional samples from the radiolysis region and

plotted as a histogram in Figure 5.34 for W24-6 and in Figure 5.35 for W72-2. W24-5 has a sharp peak for mode 1 corrosion in the inner oxide thickness and a broader mode 2, whereas W24-6 shows only a strong mode 2 peak in both inner oxide thickness and total oxidation. The corrosion modality is indistinct for W72 in either histogram, there is only one broad peak that is skewed towards lower inner oxide thickness, but there are two separate modes in the total oxidation. The divergence between the inner oxide thickness and total oxidation histogram shapes is due to the significant positive dissolution measurement which collapses the inner oxide thickness measurements into a single peak; therefore, the measurements were not separated by modes. The range in the total oxidation of W24 and the higher thickness peak relative to the inner oxide thickness implies dissolution. The statistics for the radiolysis region are also presented in Table 5.4. The inner oxide thickness and total oxidation are not different within error for W24, and the dissolution is within error of zero. For W72 the inner oxide dissolution is significant. The radiolysis region has much lower values for both inner oxide thickness and total oxidation than the non-irradiated region in the overall average and the second mode average.

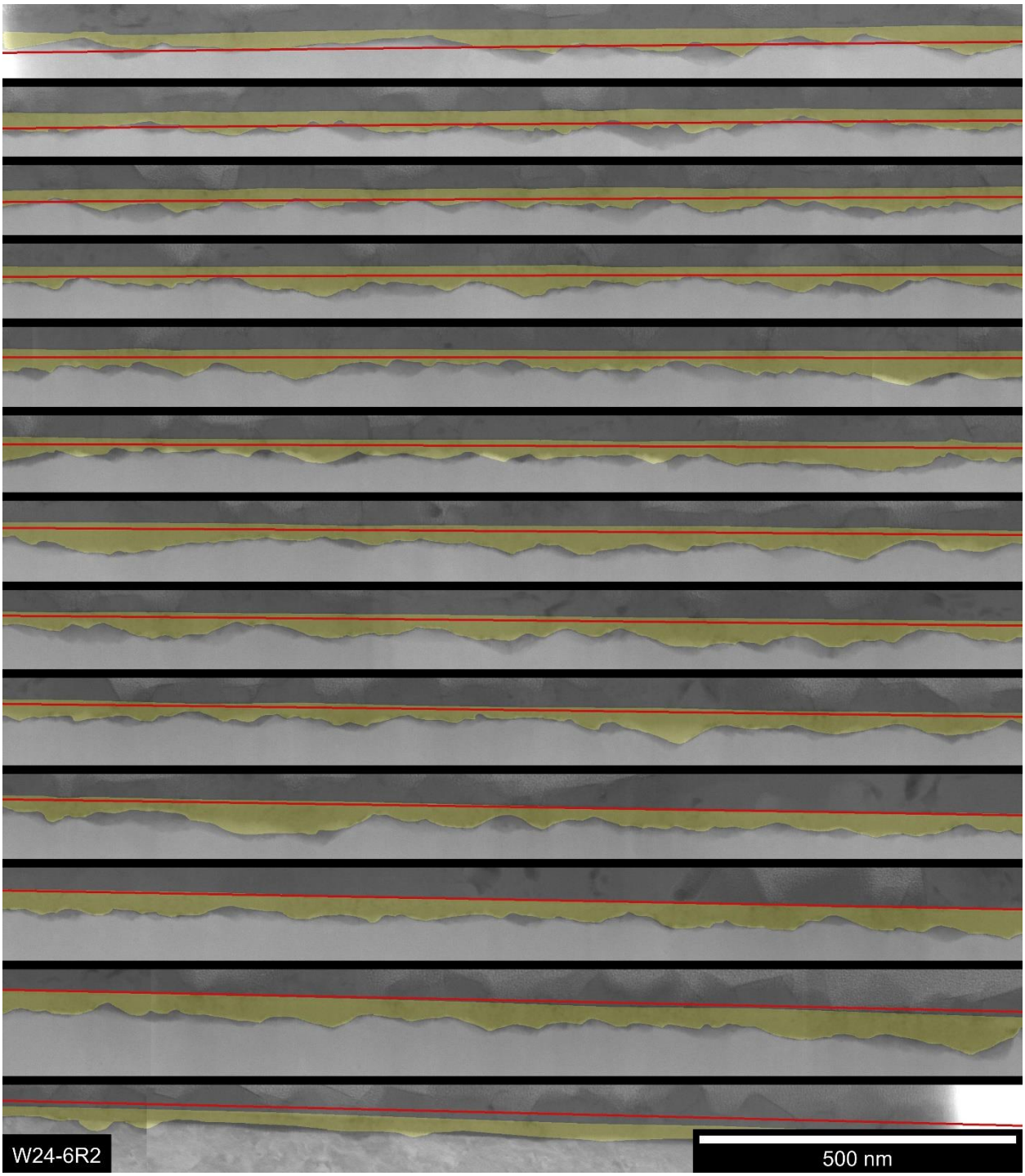

Figure 5.31. TEM micrograph collage highlighting the inner oxide area in yellow and the reconstructed original metal surface as a red line from the radiolysis region of experiment W24-6.

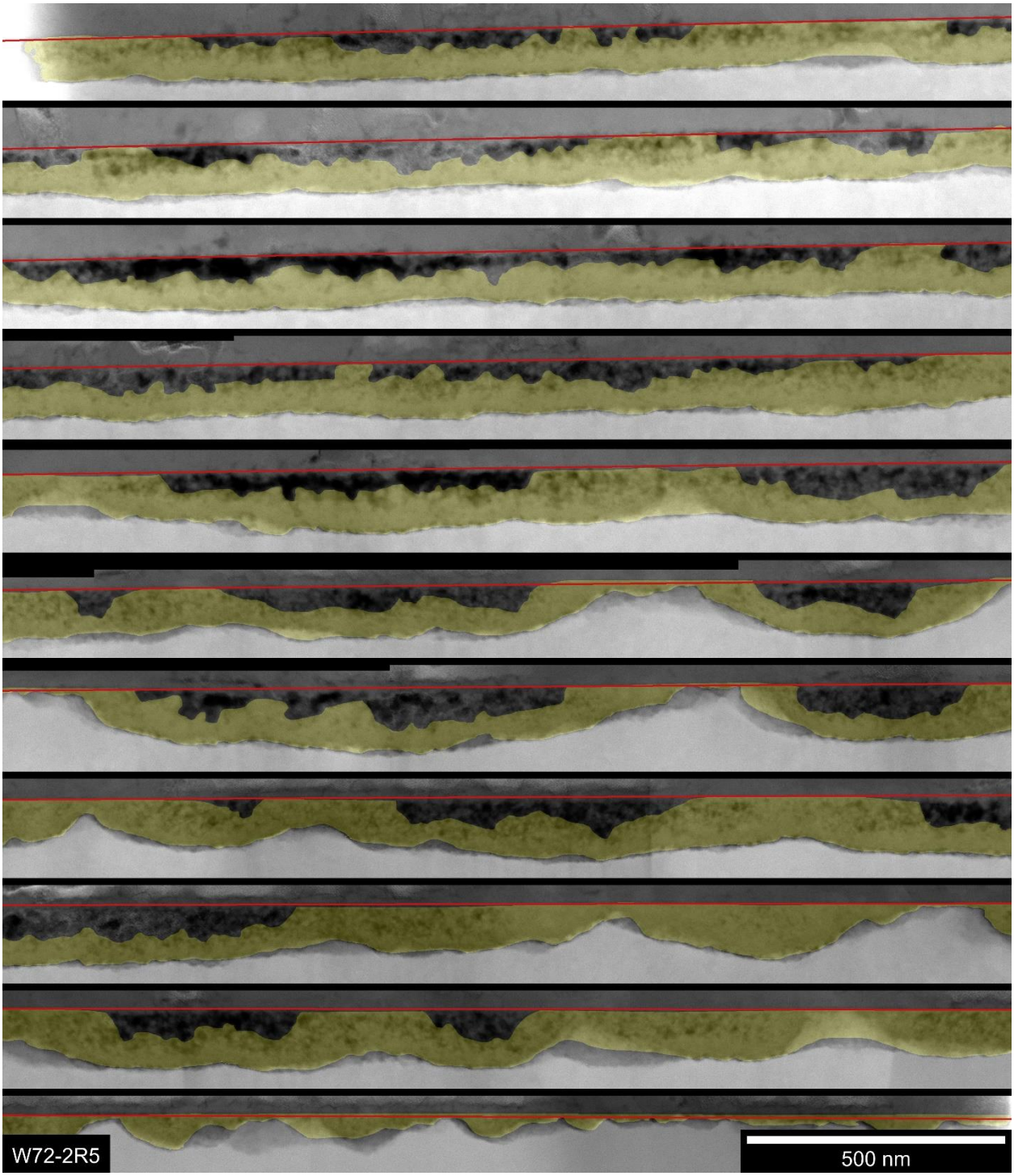

Figure 5.32. TEM micrograph collage highlighting the inner oxide area in yellow and the reconstructed original metal surface as a red line from the radiolysis region of experiment W72-2.

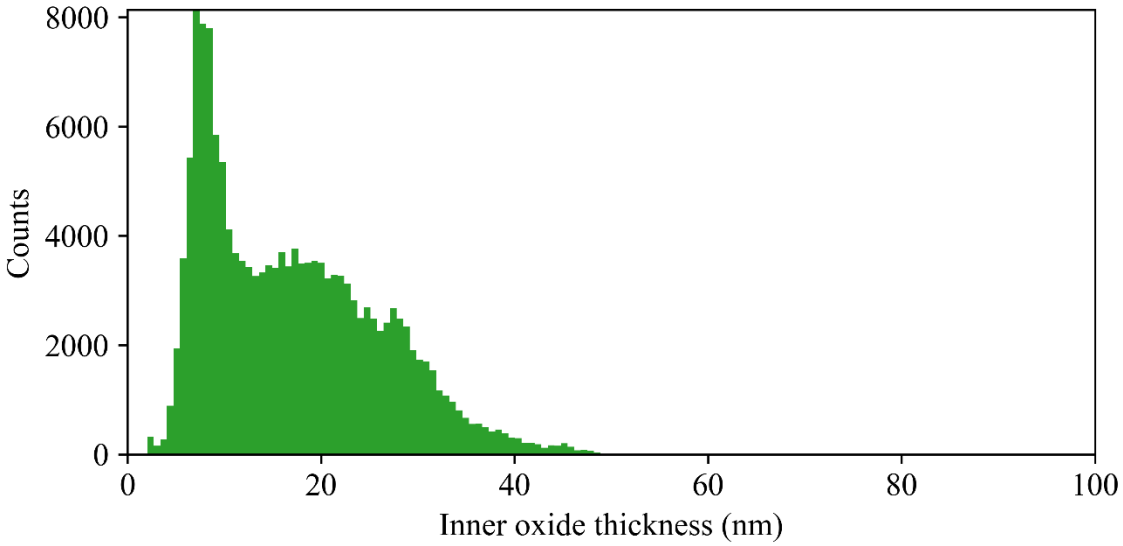

Figure 5.33. Histogram of inner oxide thickness measurements from the radiolysis region of the W24-5 experiment.

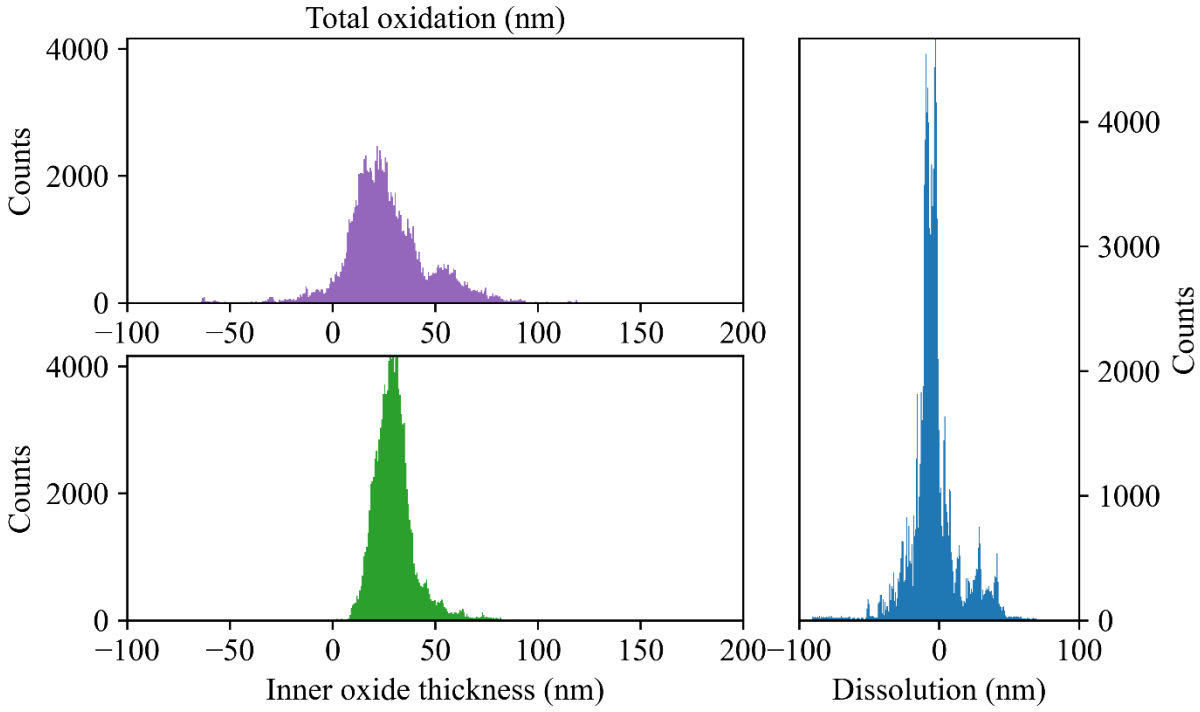

Figure 5.34. Histogram of inner oxide thickness and total oxidation measurements from the radiolysis region of the W24-6 experiment.

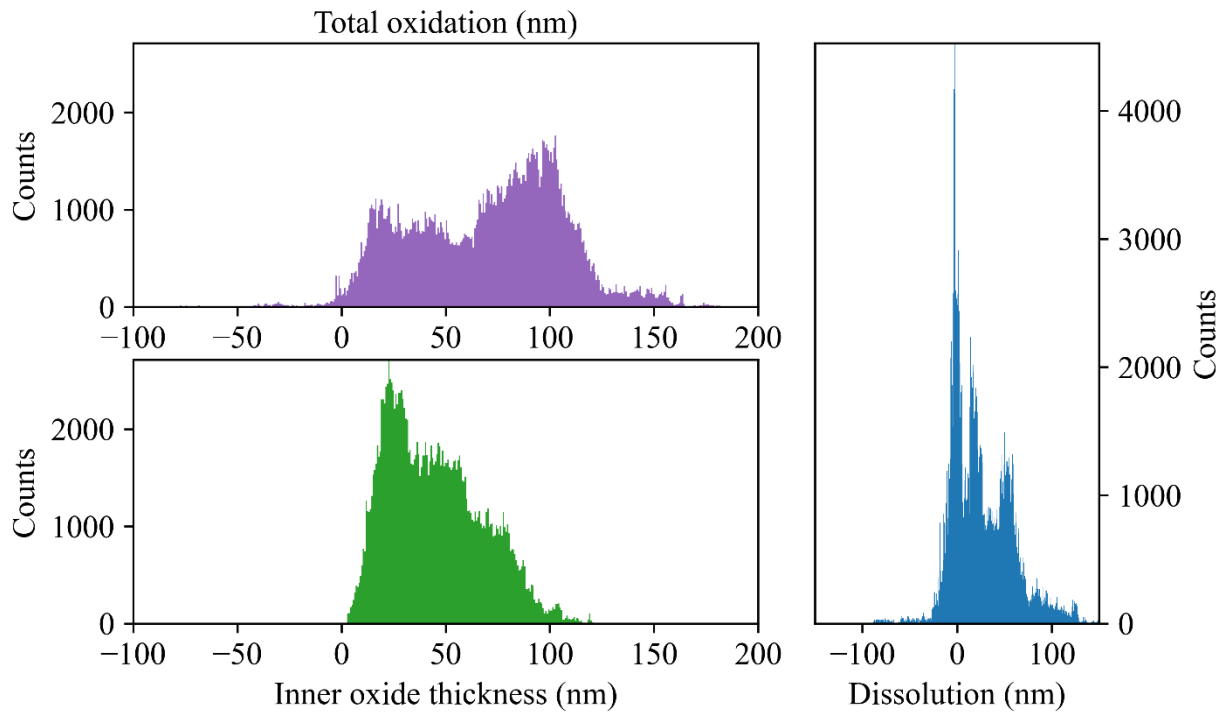

Figure 5.35. Histogram of inner oxide thickness and total oxidation measurements from the radiolysis region of the W72-2 experiment.

Table 5.5. Mean values of inner oxide thickness and total oxidation measurements from both non-irradiated and radiolysis regions of 24 h and 72 h experiments in 320 °C water split into mode 1 corrosion, mode 2 corrosion, and combined.

		Total			Mode 1			Mode 2		
ID	Region	Mean Inner Oxide Thickness (nm)	Mean Total Oxidation (nm)	Mean Dissolution (nm)	Frac. (%)	Mean Inner Oxide Thickness (nm)	Mean Total Oxidation (nm)	Frac. (%)	Mean Inner Oxide Thickness (nm)	Mean Total Oxidation (nm)
W24	Non-irradiated	83 ± 12	174 ± 19	-5 ± 11	67	21.4 ± 6.3	26 ± 12	33	206.2 ± 8.5	227 ± 17
	Radiolysis	23.0 ± 8.9	29 ± 16	-3 ± 12	28	9.8 ± 1.8	10 ± 12	72	28.2 ± 8.3	34 ± 14
W72	Non-irradiated	223 ± 17	208 ± 20	-15 ± 11	4	41.1 ± 4.2	52 ± 12	96	231 ± 15	217 ± 18
	Radiolysis	45 ± 13	70 ± 17	25 ± 12	–	–	–	–	–	–

5.2.2.3. Irradiated region

TEM micrographs showing the inner oxide measurement and the reconstructed original metal surface in cross-sections of the irradiated region are presented in Figure 5.36 for W24 and in Figure 5.37 for W72. Clear signs of dissolution can be seen in both examples where the top layer of the inner oxide dips well below the reconstructed original metal surface line. Inner oxide thickness measurements from W24-2 and W24-3 are collected into a histogram in Figure 5.38.

The measurements were collected across all cross-sectional samples from the irradiated region and plotted as a histogram in Figure 5.39 for W24-4 and W24-6. The same measurements are plotted in Figure 5.40 for W72-1 and W72-2. The modality of the inner oxide thickness in all three histograms for both W24 and W72 irradiated regions is exhibited as the skewed tail to larger values of thickness, but there is no clear separation between the two modes. Despite the clear evidence in the micrographs of inner oxide dissolution, the histogram for W24 is spread among negative and positive values resulting in an erroneously low total oxidation measurement. Two particular cross-sections had exceptionally low reconstructed original metal surfaces that frequently intersected the remaining metal in the sample; these cross-sections are the source of error for the low total oxidation measurement, but the source of this error is unknown. The W72 histogram of total oxidation shows a definite increase relative to the inner oxide thickness. The statistics for the irradiated and radiolysis regions are also presented in Table 5.6 showing an inner oxide thickness comparable to the radiolysis region in W24, but total oxidation and dissolution are within error of zero. For W72, the total oxidation was significantly greater than the inner oxide thickness, yielding significant dissolution in the irradiated region as in the radiolysis region. All other regions have a dissolution measurement that is within error of zero. Compared to the non-irradiated region, the irradiated region has significantly lower inner oxide thickness and total oxidation.

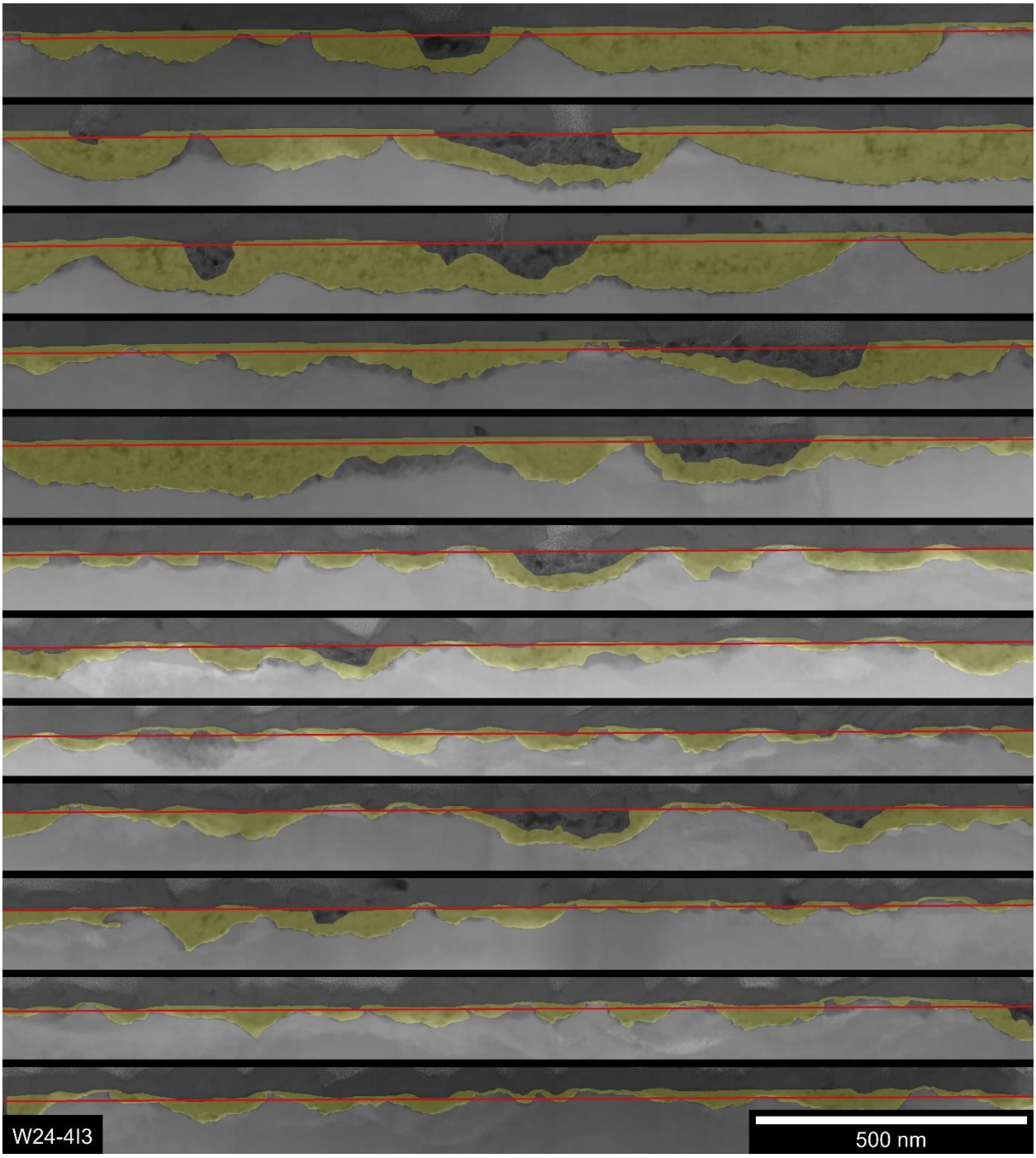

Figure 5.36. TEM micrograph collage highlighting the inner oxide area in yellow and the reconstructed original metal surface as a red line from the irradiated region of experiment W24-4.

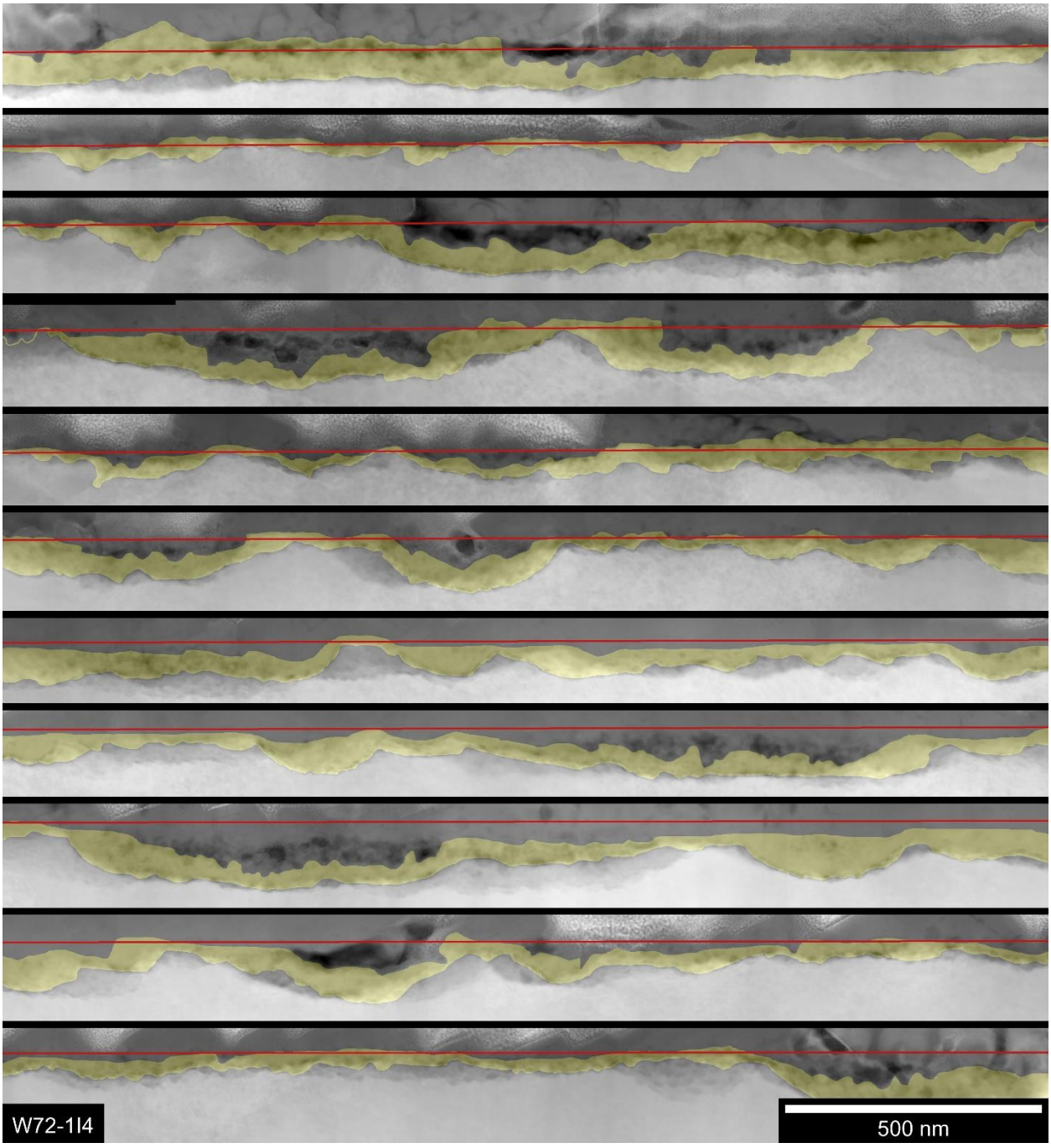

Figure 5.37. TEM micrograph collage highlighting the inner oxide area in yellow and the reconstructed original metal surface as a red line from the irradiated region of experiment W72-1.

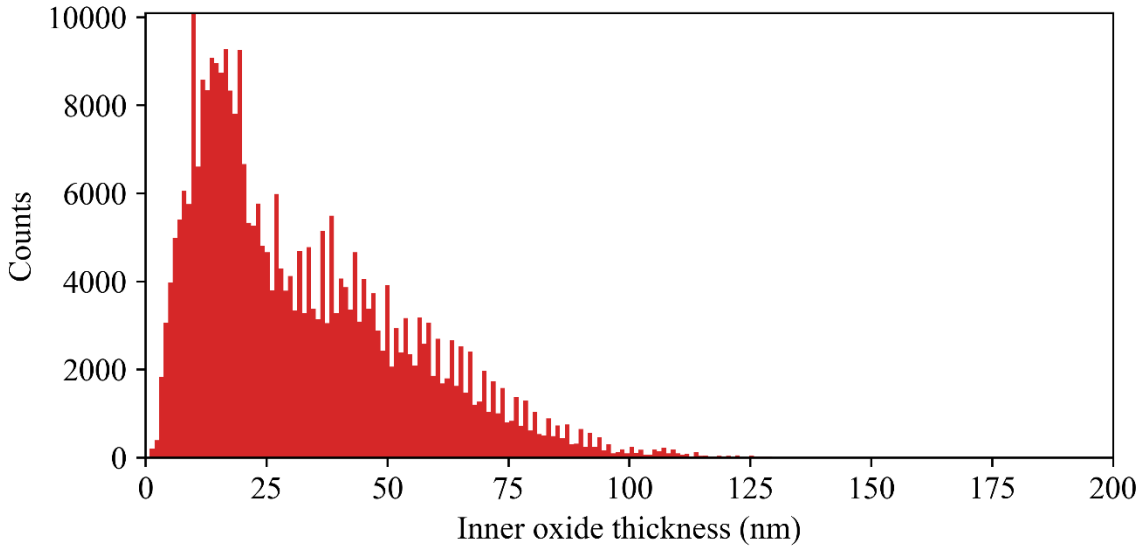

Figure 5.38. Histogram of inner oxide thickness measurements from the irradiated regions of the W24-2 and W24-3 experiments.

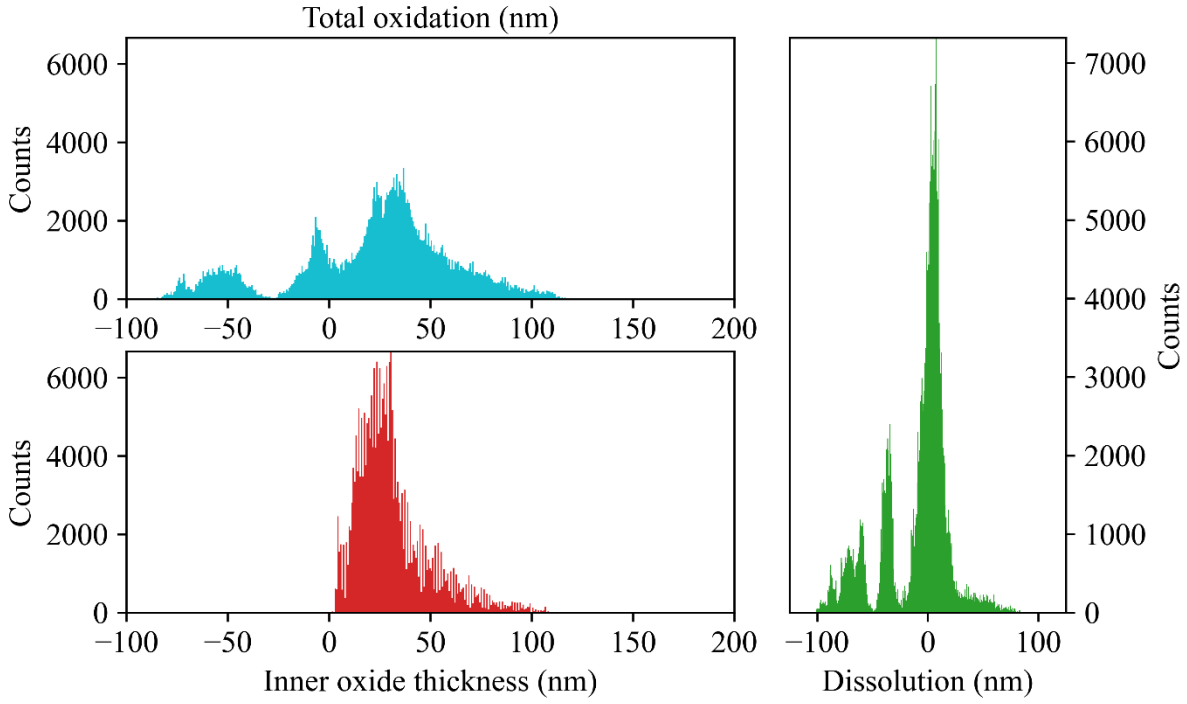

Figure 5.39. Histogram of inner oxide thickness and total oxidation measurements from the irradiated regions of the W24-4 and W24-6 experiments.

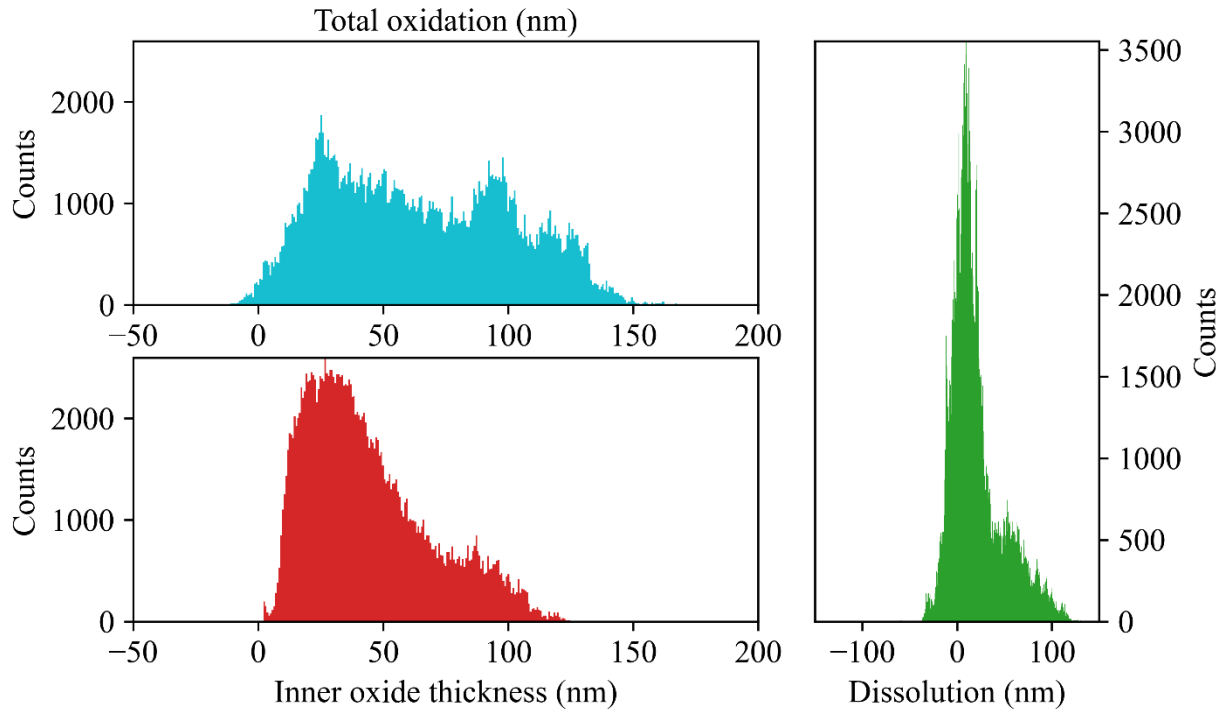

Figure 5.40. Histogram of inner oxide thickness and total oxidation measurements from the irradiated regions of the W72-1 and W72-2 experiments.

Table 5.6. Mean values of inner oxide thickness and total oxidation measurements from control and irradiated experiments in 320 °C water split into mode 1 corrosion, mode 2 corrosion, and combined.

		Total			Mode 1			Mode 2		
ID	Region	Mean Inner Oxide Thickness (nm)	Mean Total Oxidation (nm)	Mean Dissolution (nm)	Frac. (%)	Mean Inner Oxide Thickness (nm)	Mean Total Oxidation (nm)	Frac. (%)	Mean Inner Oxide Thickness (nm)	Mean Total Oxidation (nm)
X24	Non-irradiated	155 ± 15	164 ± 15	7 ± 11	0	–	–	100	155±15	164±15
X72	Non-irradiated	179 ± 18	183 ± 21	5 ± 11	18	20.7±5.4	32 ± 13	82	213±17	216±20
A24	Non-irradiated	11.0 ± 4.0	9 ± 12	-2 ± 11	–	–	–	–	–	–
	Non-irradiated	83 ± 12	174 ± 19	-5 ± 11	67	21.4±6.3	26 ± 12	33	206.2±8.5	227±17
W24	Radiolysis	23.0 ± 8.9	29 ± 16	-3 ± 12	28	9.8±1.8	10 ± 12	72	28.2±8.3	34±14
	Irradiated	32.3 ± 8.9	40 ± 12	-9 ± 11	–	–	–	–	–	–
	Non-irradiated	223 ± 17	208 ± 20	-15 ± 11	4	41.1±4.2	52 ± 12	96	231±15	217±18
W72	Radiolysis	45 ± 13	70 ± 17	25 ± 12	–	–	–	–	–	–
	Irradiated	44 ± 13	65 ± 17	20 ± 12	–	–	–	–	–	–

5.2.3. STEM-EDS

Example composition profiles collected using STEM-EDS through the oxide and into the metal are presented in Figure 5.41 for the non-irradiated region, in Figure 5.42 for the radiolysis

region, and in Figure 5.43 for the irradiated region. The non-irradiated region shows a mostly continuous elemental profile through the inner oxide except for some small dips in Cr content that are largely compensated with increases in Fe content. Outer oxide metal content is 80–95% Fe with the remaining metal as Ni and no measurable Cr. The irradiated region has a very non-uniform profile in Cr where the Cr content peaks highest directly adjacent the metal/oxide interface, and a lower second peak exists just below the inn/outer oxide interface. The remainder of the inner oxide is largely depleted in Cr, down to ~ 5% at the nadir. The outer oxide contains more Ni than the non-irradiated region, and there is 1~2% Cr in the outer oxide. Additionally, there is a peak in the Ni profile in the metal just below the metal/oxide interface. The radiolysis region shows a Cr profile that has a weak peak near the metal/oxide interface, and a slow depletion in Cr moving toward the outer oxide. The outer oxide shows a similar composition to that of the irradiated area with ~80% Fe, ~18% Ni, and ~2% Cr. Finally, there is a small Ni peak in the metal just below the metal/oxide interface.

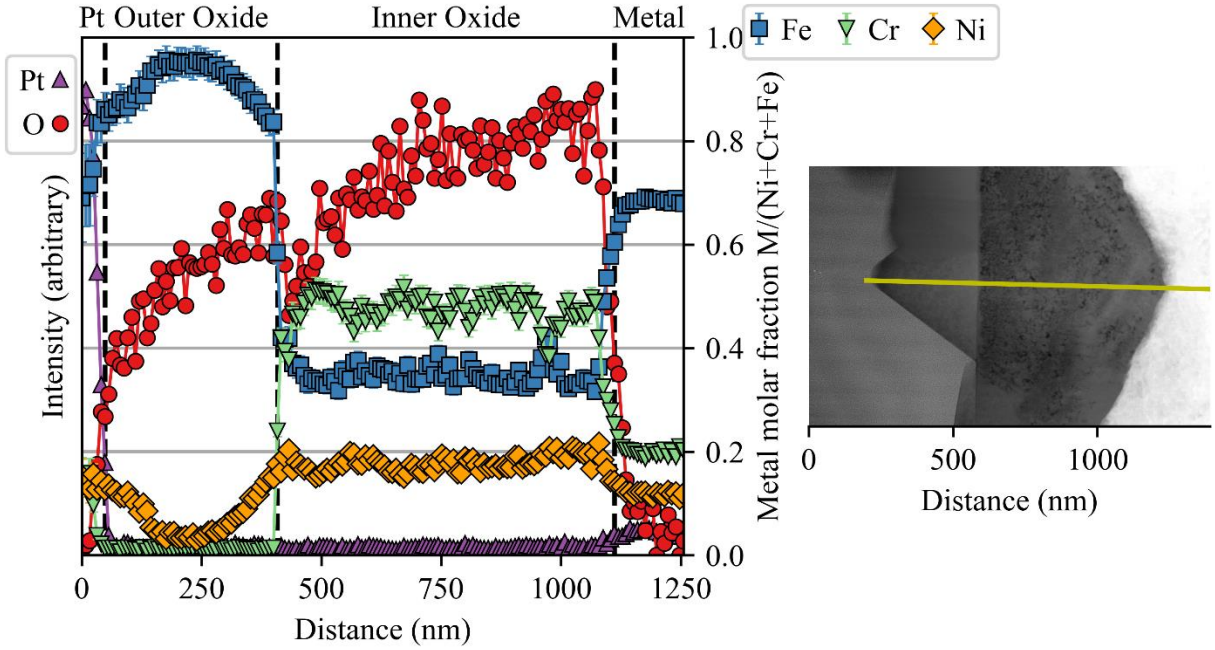

Figure 5.41. STEM-EDS linescan though the oxide and associated micrograph from the non-irradiated region of W72-1.

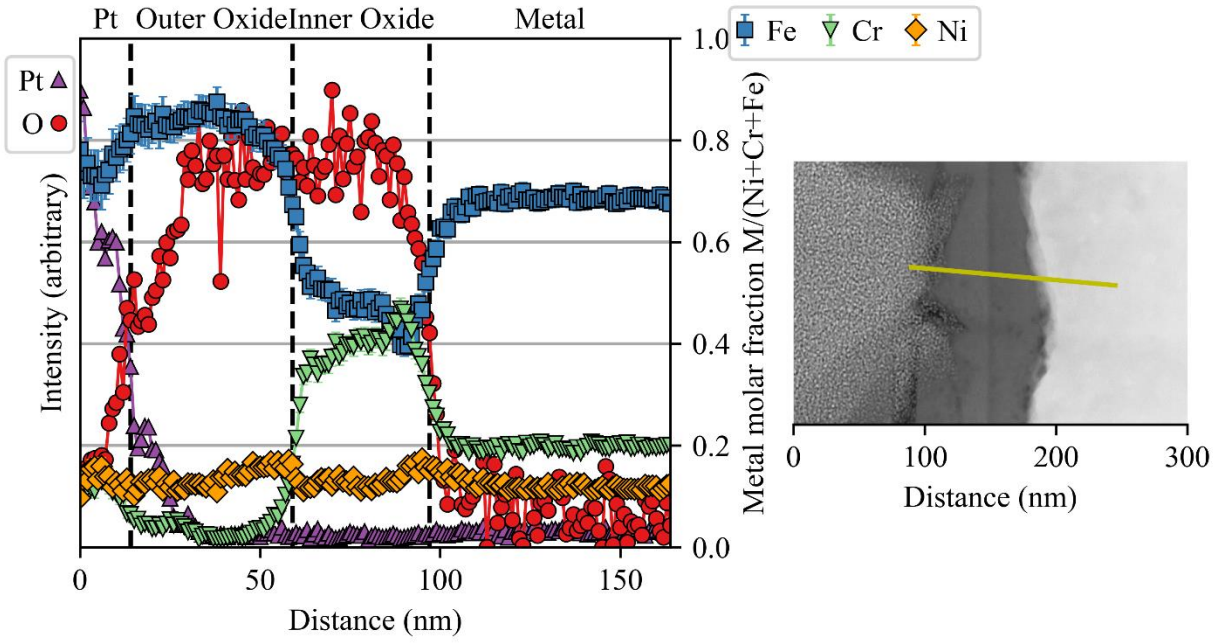

Figure 5.42. STEM-EDS linescan though the oxide and associated micrograph from the radiolysis region of W24-6.

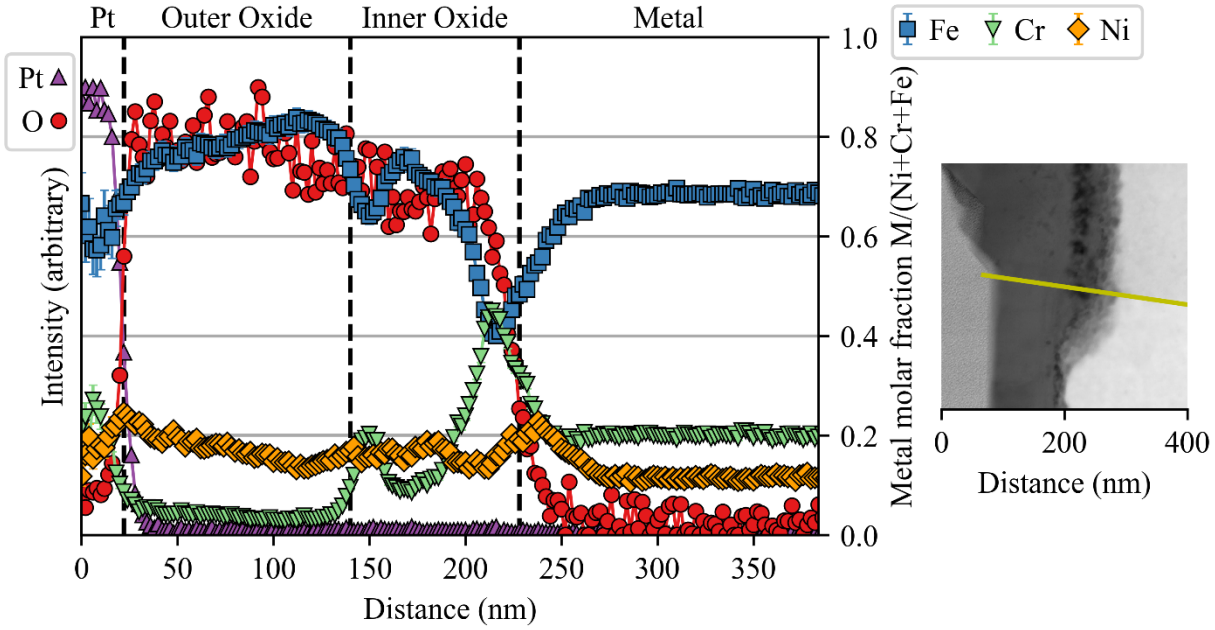

Figure 5.43. STEM-EDS linescan though the oxide and associated micrograph from the irradiated region of W72-1.

Many more linescans were collected from each region in W24 and W72 than these three figures, so elemental profiles were plotted together across the metal/oxide interface in each region for Cr in Figure 5.44, Fe in Figure 5.45, and Ni in Figure 5.46. First, the Cr profile shows

a gradual increase from the metal into the inner oxide to a constant value of ~40% in the inner oxide in the non-irradiated region. In the radiolysis region, the behavior is somewhat similar, but the increase is more rapid, and the peak concentration varies between 40~60% with a slight decrease in content with distance from the metal. Finally, the irradiated region has a very sharp peak (up to 60%) immediately into the inner oxide which quickly drops off to a final value <20%. The Fe profile for all three regions mirrors the Cr profile almost exactly with valleys instead of peaks and opposite slopes. The Ni profile shows a very small peak near the metal/oxide interface just beneath the Cr peak mostly in the radiolysis and irradiated regions. The Ni content is slightly higher in the non-irradiated region at ~20%, whereas the radiolysis and irradiated region return close to the average in the metal, ~12%.

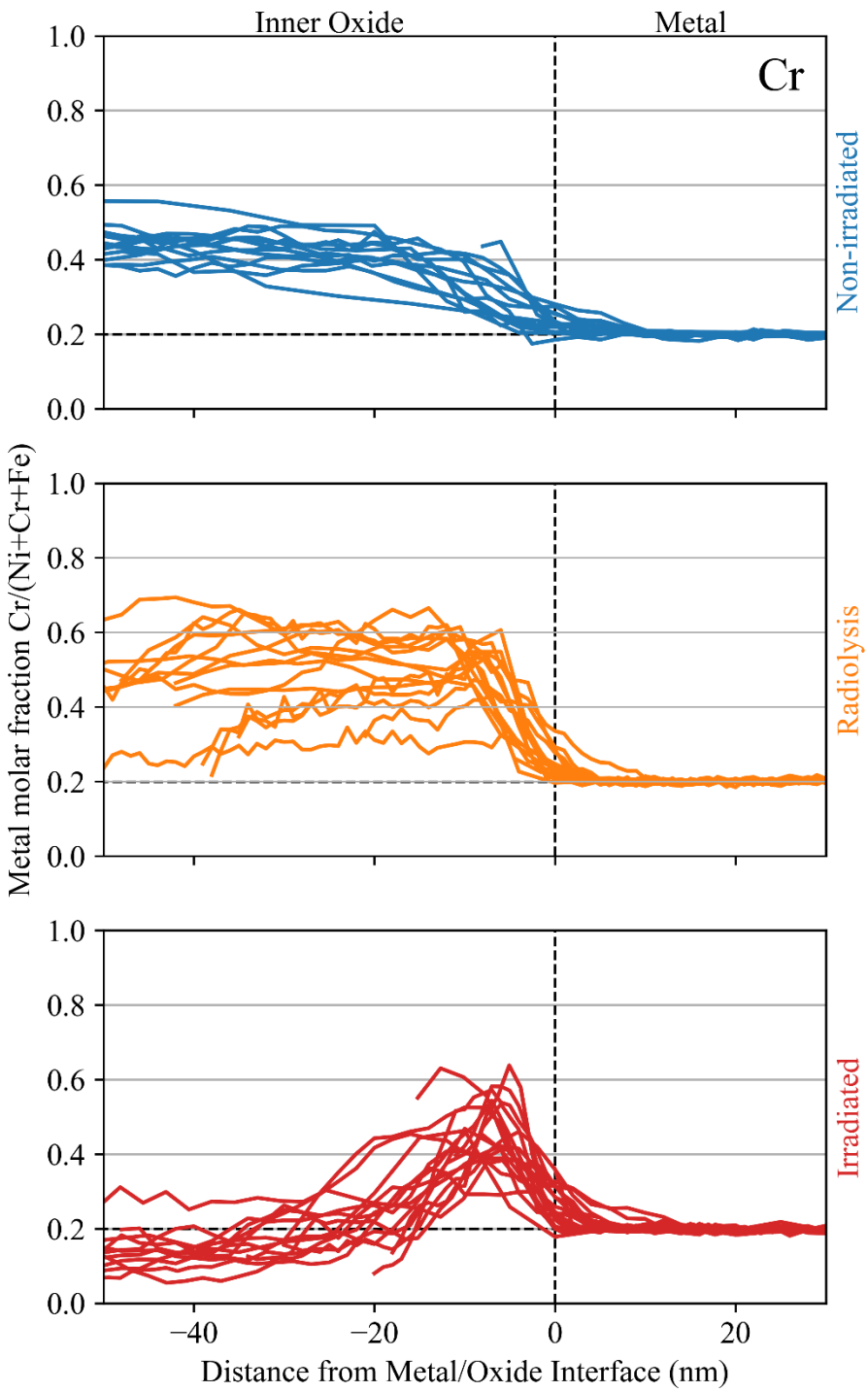

Figure 5.44. STEM-EDS linescans showing the Cr profile through the metal/oxide interface for each region of W24 and W72.

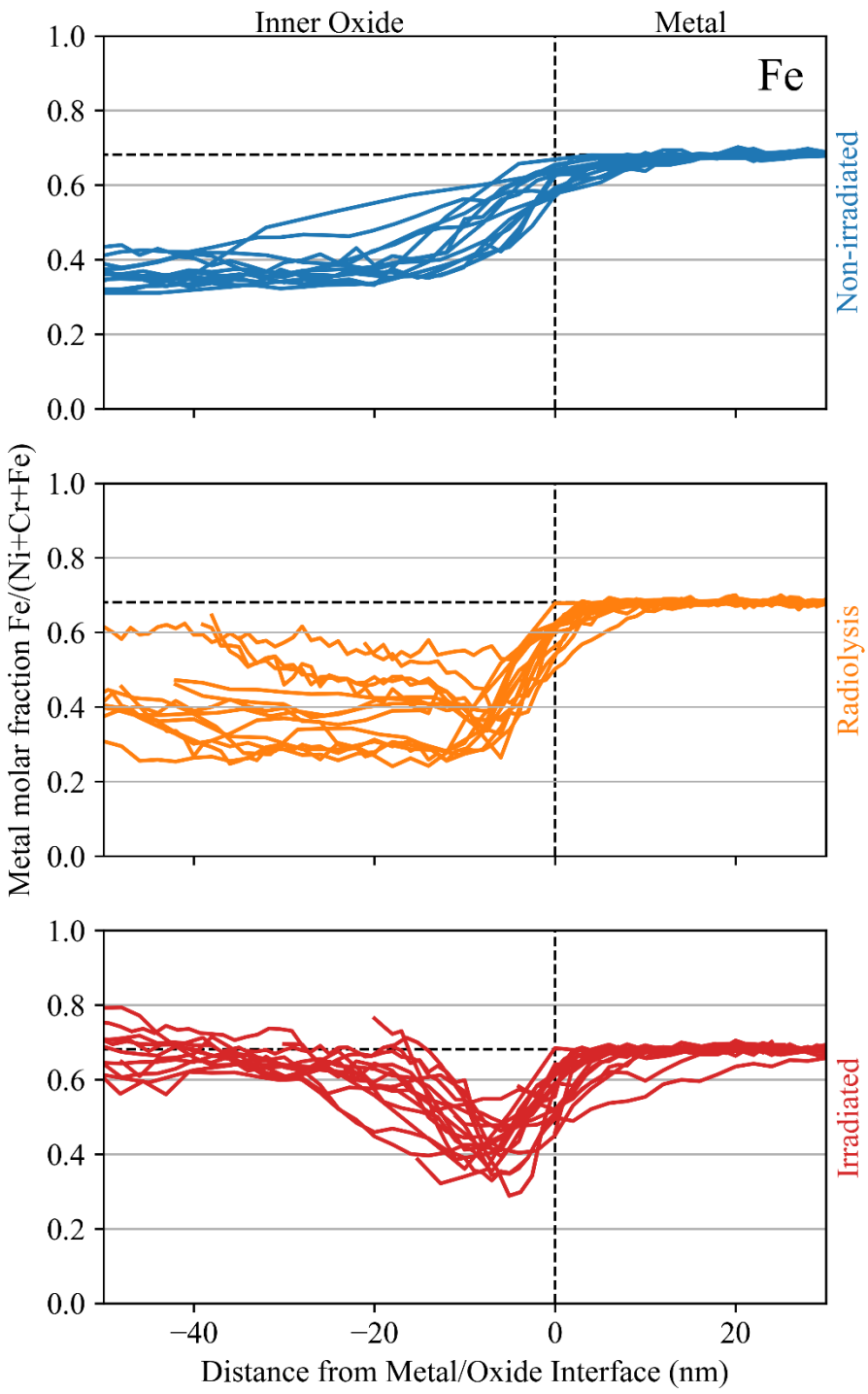

Figure 5.45. STEM-EDS linescans showing the Fe profile through the metal/oxide interface for each region of W24 and W72.

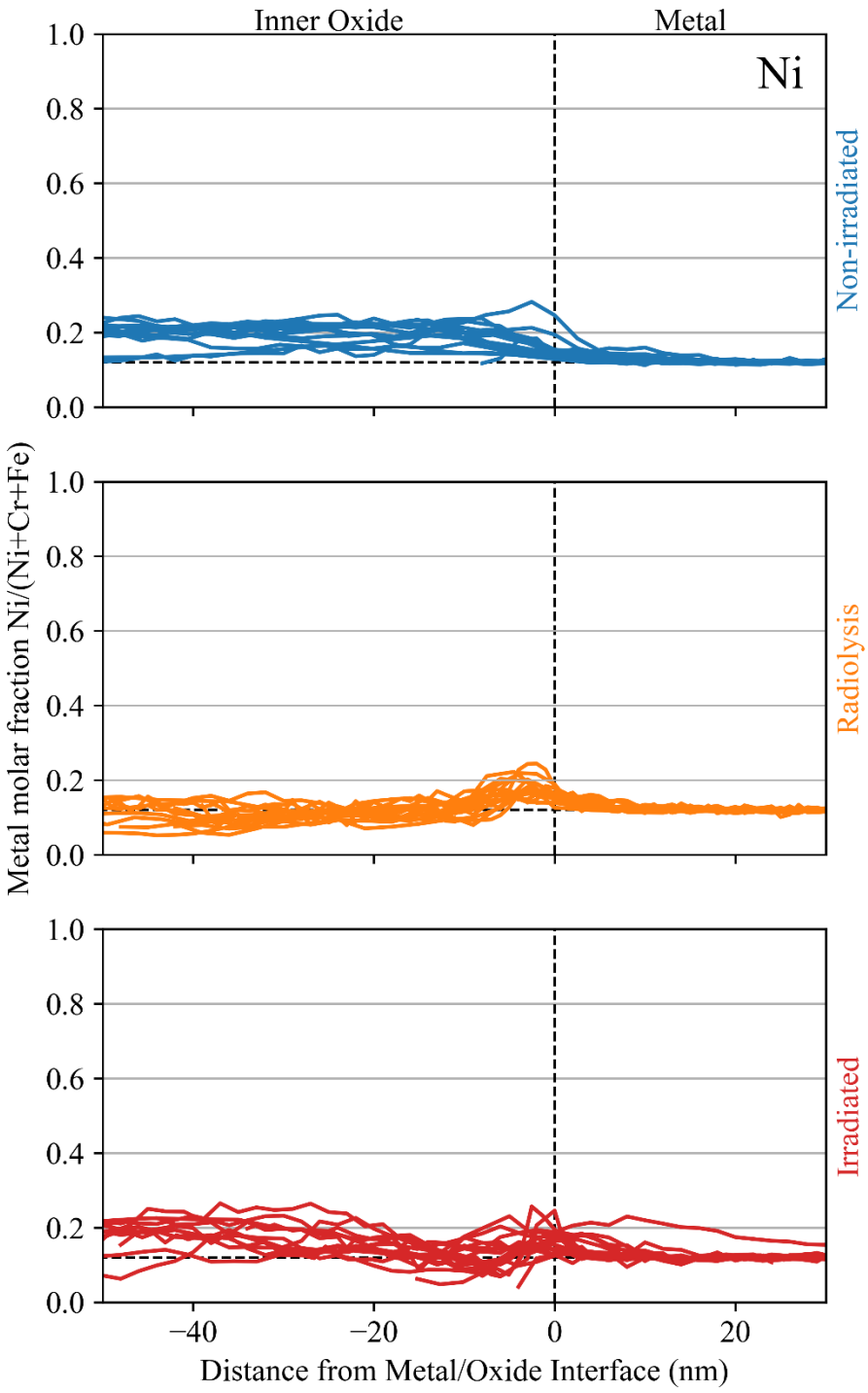

Figure 5.46. STEM-EDS linescans showing the Ni profile through the metal/oxide interface for each region of W24 and W72.

In addition to linescans, some STEM-EDS maps were collected to yield more spatial qualitative information of the oxide compositions. The non-irradiated region map is in Figure

5.47, the radiolysis region map is in Figure 5.48, and the irradiated region map is in Figure 5.49. Both net count maps and quantified metal content maps are provided to show the oxygen and platinum maps in addition to some useful comparisons between phases.

The non-irradiated region map in Figure 5.47 shows the oxide above a grain boundary centered in the image. No difference is observed between the grain boundary and the matrix in the metal for either the net counts or the metal content maps. The inner oxide just above the grain boundary appears denser in the HAADF image which corresponds to a higher Ni content visible in both net and fraction Ni maps. The outer oxide also shows some contrast in the Ni maps which may be due to a second outer oxide particle that was either consumed into a larger particle or is out-of-plane in the TEM foil. One interesting feature of the Cr net count map is the consistency in the signal between the inner oxide and the metal. Except for some small redistribution of Cr within the inner oxide structure, most of the Cr has not moved from its initial position in the metal after oxidation. Finally, there are some Fe-rich oxide stringers that can be observed in the inner oxide in the metal fraction map of Fe. These appear similar in contrast to the outer oxide, including very low counts in the Cr fraction map and a brighter signal (i.e., denser oxide) in the HAADF image.

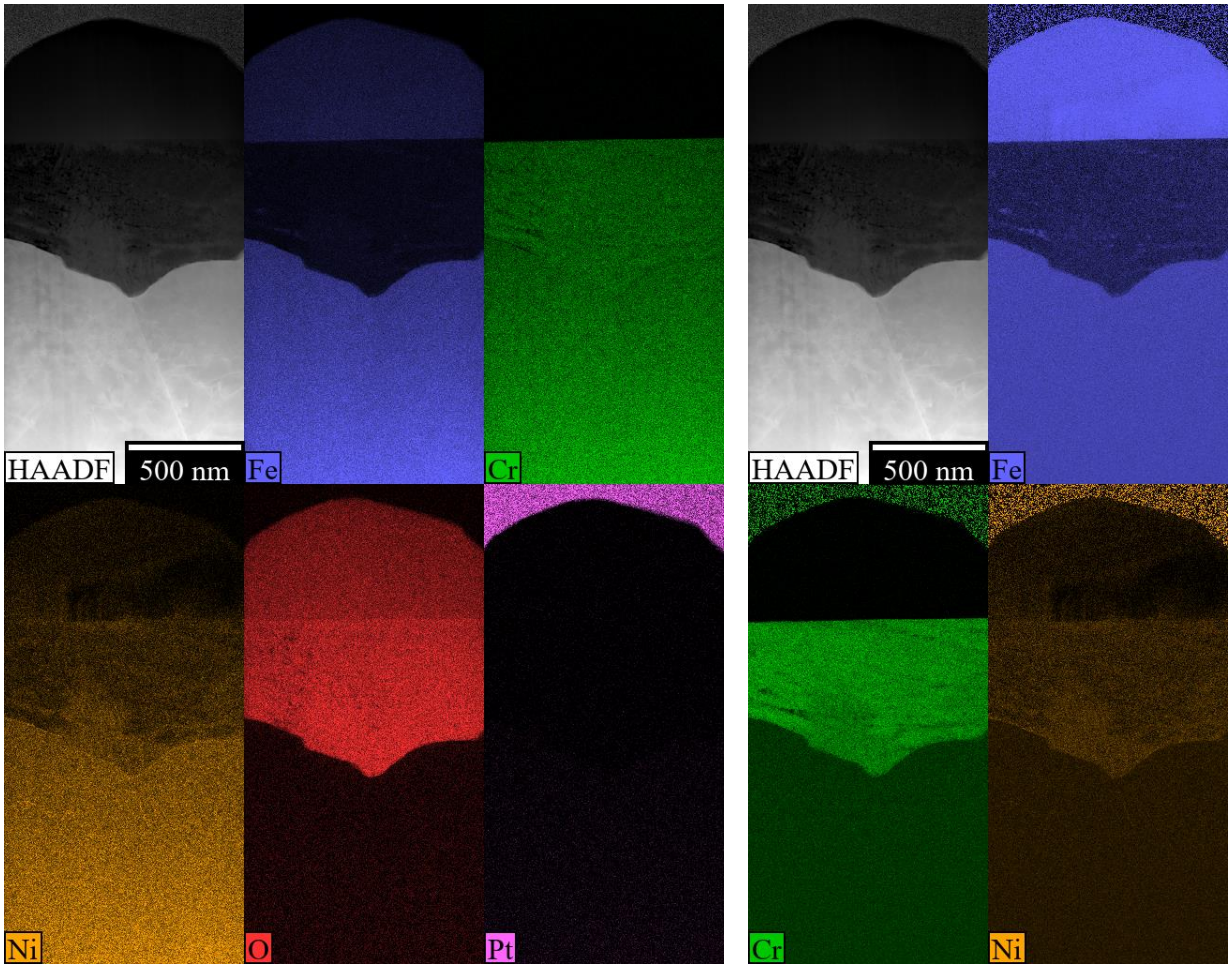

Figure 5.47. STEM-EDS map of both oxide layers above a grain boundary in net counts (left) and atomic fraction of metal (right) from the non-irradiated region of W72-1.

The radiolysis region map is in Figure 5.48, but there is no grain boundary in this map. There are two bright ovals elongated in the vertical direction most visible in the HAADF image which are artifacts of carbon deposition from STEM-EDS linescans performed prior to this map being collected. In the HAADF, porosity can be observed above and in the pit-like structures within the inner oxide layer. Unlike the non-irradiated region, the Cr net map shows a notable decrease in signal above and within these pit-like structures. In the net map and more clearly in the fraction map for Cr, enrichment of Cr is visible right at the metal/oxide interface wherever the interface is edge-on. Similarly, in the Ni fraction map a peak is also observed at the metal/oxide interface. The Fe fraction map shows a mirror of the Cr fraction map, compensating

for the lack of Cr in any given region. Within this map, the Cr depleted (and porous) inner oxide is correlated with the thicker inner oxide.

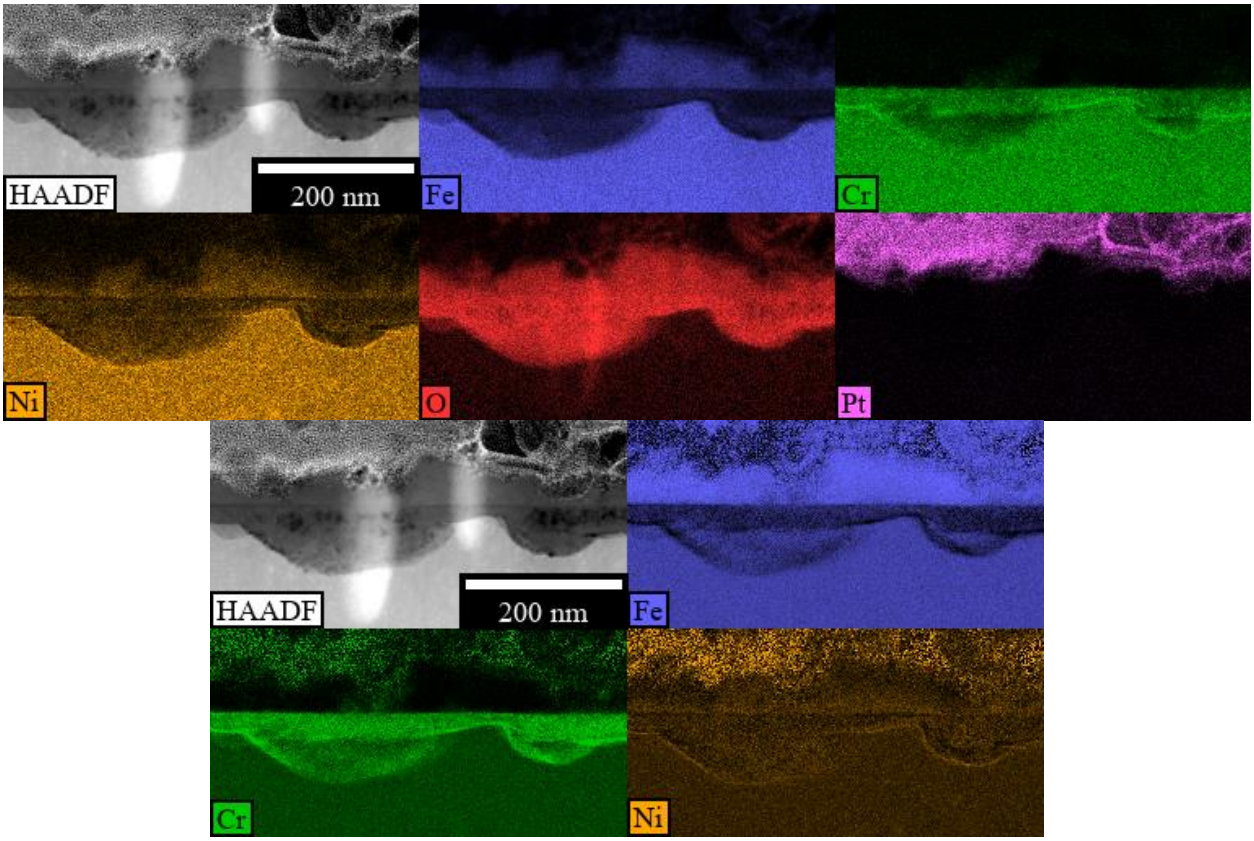

Figure 5.48. STEM-EDS map of both oxide layers above a grain boundary in net counts (above) and atomic fraction of metal (below) from the radiolysis region of W72-1.

The irradiated region map is in Figure 5.49 which has a grain boundary in the center of the map. Again, there is some extra brightness in the HAADF image extending along the line of the grain boundary and across the oxides from a previous STEM-EDS linescan in this same area. Porosity can be observed in the inner oxide in the HAADF image and faintly in the oxygen net map. In both sets of maps the grain boundary shows clear evidence of elemental segregation where the Ni is enriched and both Fe and Cr are depleted. In both the net and fraction maps, the depletion of Cr from the inner oxide on the righthand side of the maps can be clearly seen. Much like the radiolysis region map, the Cr fraction map shows a strong peak in concentration along the metal/oxide interface along with an associated increase in Ni fraction. Finally, the Cr net and

fraction maps both show a small signal from the outer oxide, consistent with the linescan from this same region.

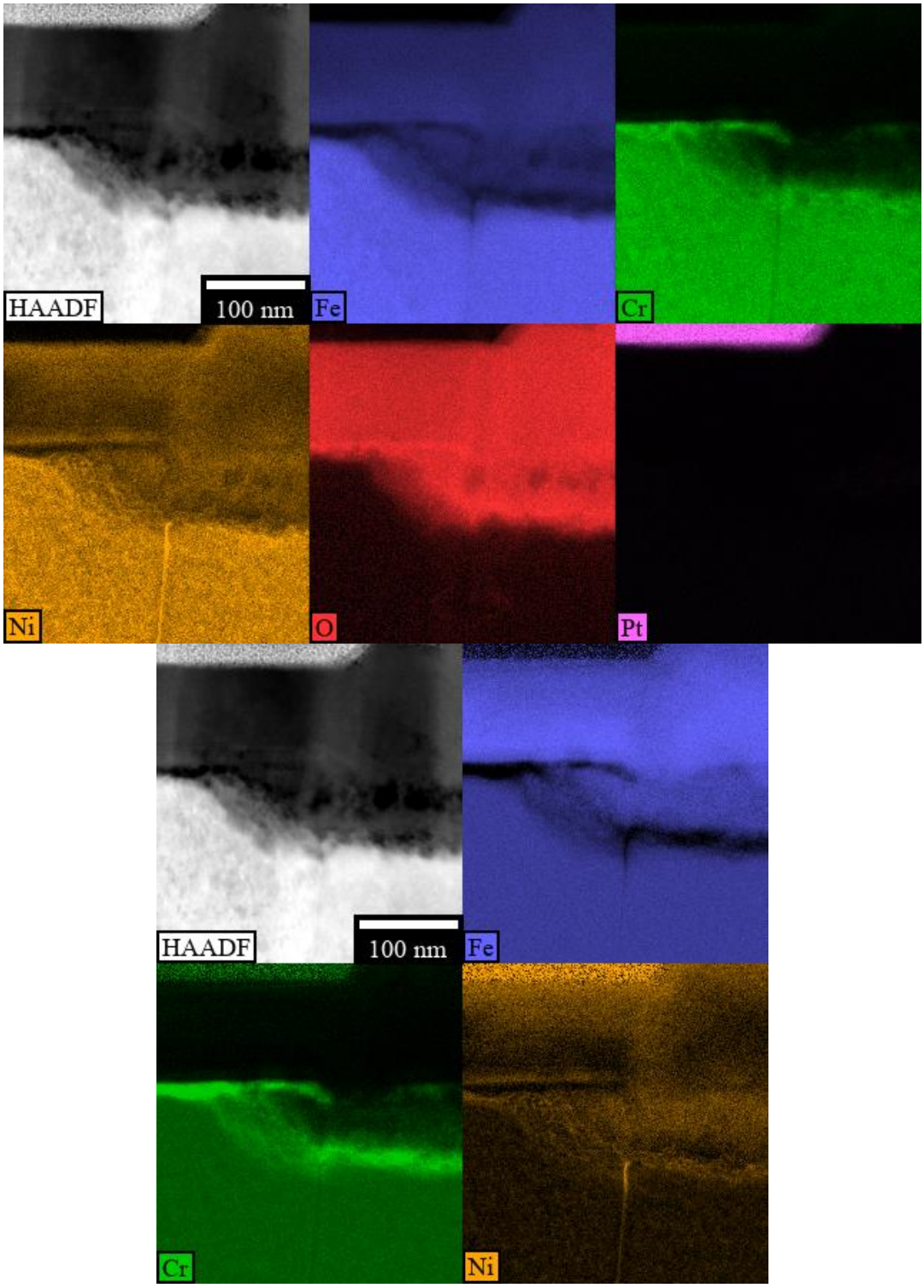

Figure 5.49. STEM-EDS map of both oxide layers above a grain boundary in net counts (above) and atomic fraction of metal (below) from the irradiated region of W72-1.

5.3. Steam irradiation corrosion – S24 and S72

Two experiments in an argon-steam environment are presented in this section: S24 with a 24 h duration, and S72 with a 71 h duration. Both experiments had a radiolysis isolation bar and were helium implanted, so both inner oxide thickness and total oxidation measurements were taken from all three regions across both samples.

5.3.1. SEM surface characterization

SEM microscopy was performed on the surface in all three regions on S24 in Figure 5.50. Both irradiated and non-irradiated regions show a very strong grain contrast at lower magnification. The radiolysis region has grain boundaries dotted with extra outer oxide particles so the grains can be easily distinguished, but the oxides on the grains themselves are very similar. In higher magnification, the non-irradiated region has relatively consistently sized polyhedral outer oxide particles with near total coverage of the surface. The irradiated region has very agglomerated outer oxide particles that sometimes form rafts; they have jagged, but still faceted, edges that appear to be dependent on the grain orientation of the underlying metal. The radiolysis region has particles that are faceted but are significantly smaller than the other two regions.

SEM microscopy was also performed on the surface of all three regions on S72 in Figure 5.51. Like S24, grain contrast is present in the irradiated and non-irradiated regions, but the contrast is lacking except for grain boundaries in the radiolysis region. Also, like S24, the outer oxide particles are mostly faceted individual particles in the non-irradiated region, agglomerated and jagged in the irradiated region, and very small in the radiolysis region.

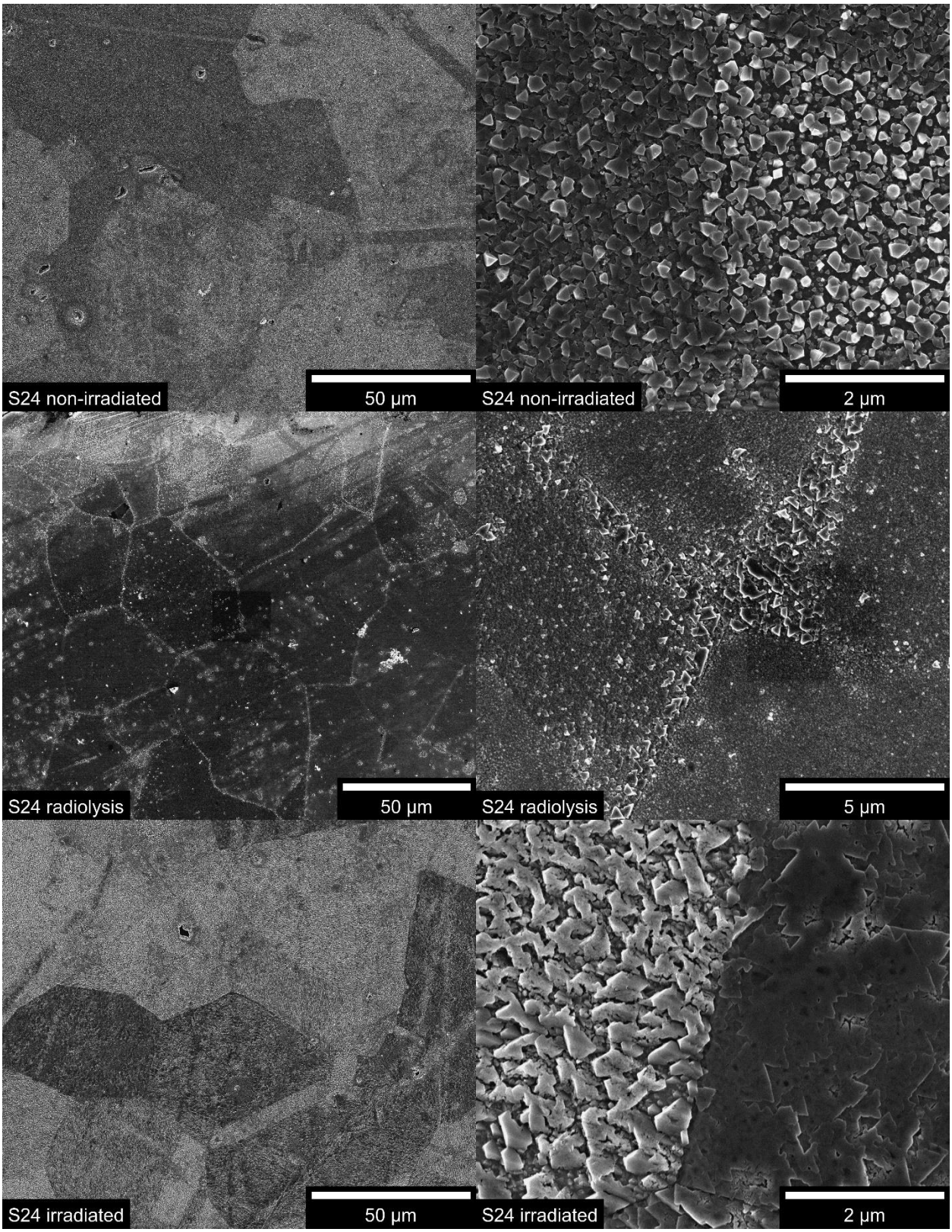

Figure 5.50. SEM micrographs showing the oxidized surface from S24. The upper pair is from the non-irradiated region; the middle pair is from the radiolysis region; and the lower pair is from the irradiated region.

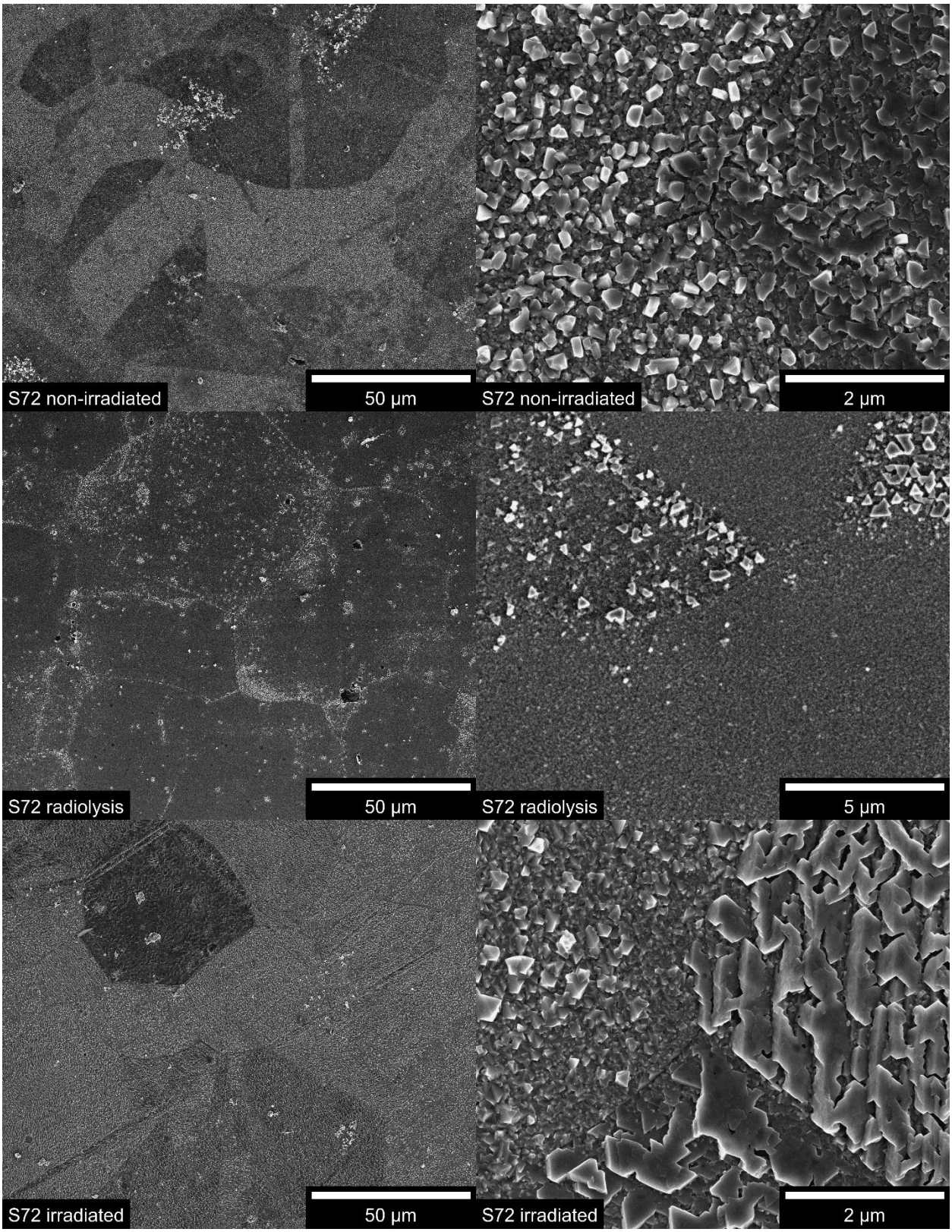

Figure 5.51. SEM micrographs showing the oxidized surface from S72. The upper pair is from the non-irradiated region; the middle pair is from the radiolysis region; and the lower pair is from the irradiated region.

5.3.2. Oxide thickness and total oxidation

Following the same procedure as the control and water experiments, both inner oxide thickness and total oxidation were measured from cross-sections in HAADF-STEM imaging. Image montages of example cross-sections from all three regions are presented in Figure 5.52 for S24 and in Figure 5.53 for S72. The characterization of these experiments is divided into subsections for each region characterized.

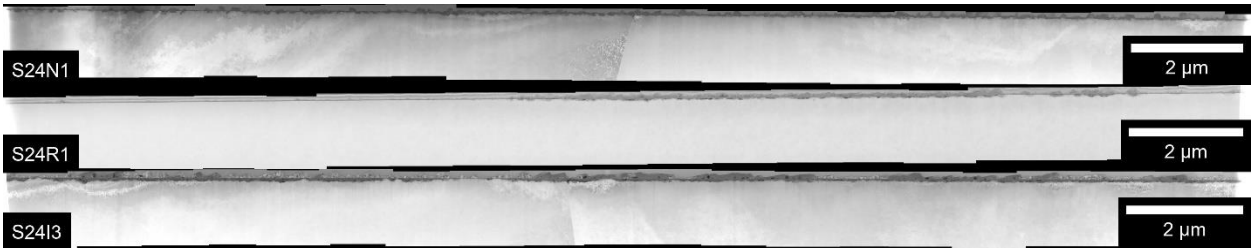

Figure 5.52. TEM micrograph collages showing cross-sections of the oxidized surface from the S24 experiment set. The upper collage is from the non-irradiated region; the middle collage is from the radiolysis region; and the lower collage is from the irradiated region.

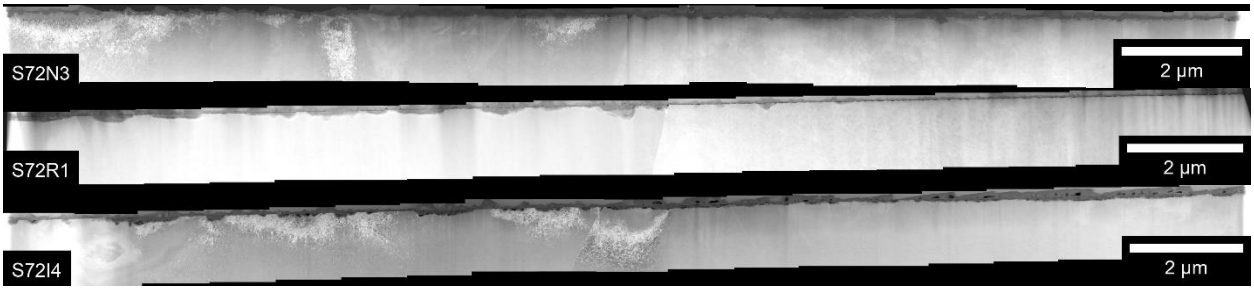

Figure 5.53. TEM micrograph collages showing cross-sections of the oxidized surface from the S72 experiment set. The upper collage is from the non-irradiated region; the middle collage is from the radiolysis region; and the lower collage is from the irradiated region.

5.3.2.1. Non-irradiated region

An example of the inner oxide measurement and the reconstructed original metal surface on a cross-section of the non-irradiated region is presented in Figure 5.54 for S24 and in Figure 5.55 for S72. Both experiments show a layer of internal oxidation below that of the inner oxide layer that was not measured. This internal oxidation takes the form of strings of small spherical oxides that have some metal between them and the inner oxide layer. A few larger pores are found in the inner oxide of both S24 and S72. Measurements collected across all cross-sections

from the non-irradiated region are plotted as histograms in Figure 5.56 for S24 and in Figure 5.57 for S72. The histograms show a clear delineation between the two corrosion modes unlike most of the water experiments. The histograms change very little between 24 h and 71 h other than a slight increase in the thickness of both modes. The arithmetic mean and standard error of these measurements are presented in Table 5.7 along with the separation of the two modes. All measurements increased slightly from 24 h to 71 h except the lower corrosion mode which did not significantly change.

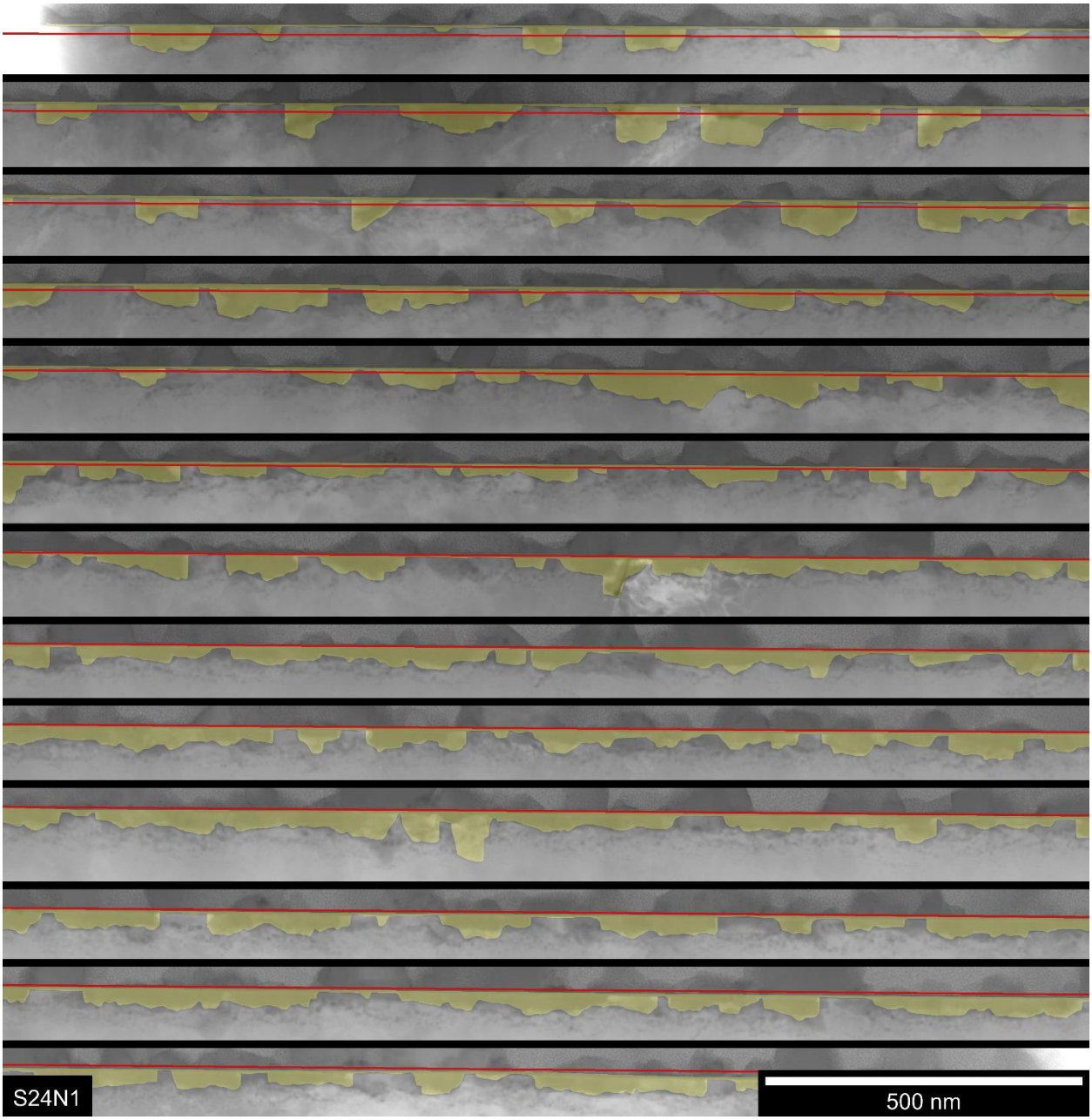

Figure 5.54. TEM micrograph collage highlighting the inner oxide area in yellow and the reconstructed original metal surface as a red line from the non-irradiated region of experiment S24.

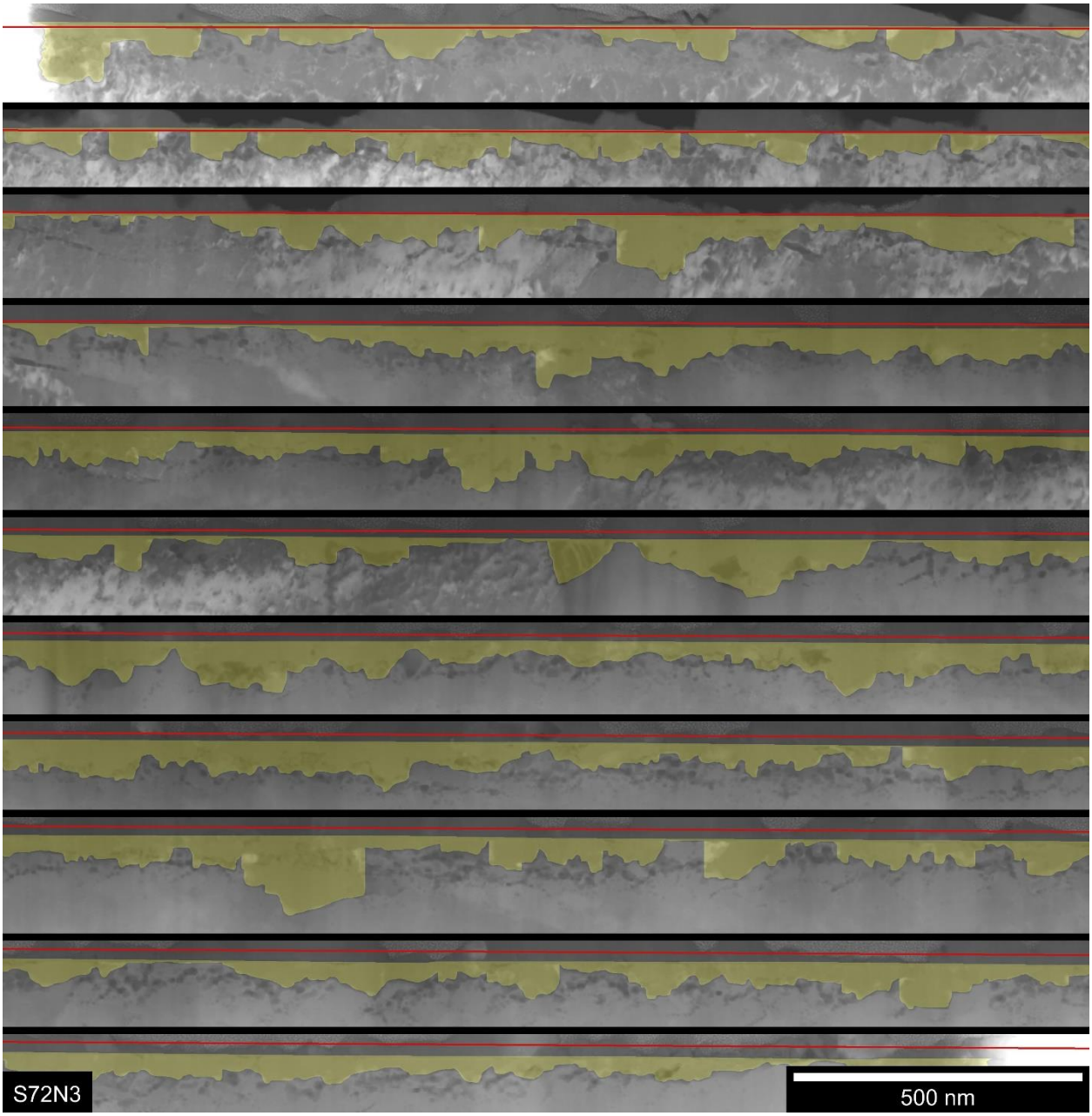

Figure 5.55. TEM micrograph collage highlighting the inner oxide area in yellow and the reconstructed original metal surface as a red line from the non-irradiated region of experiment S72.

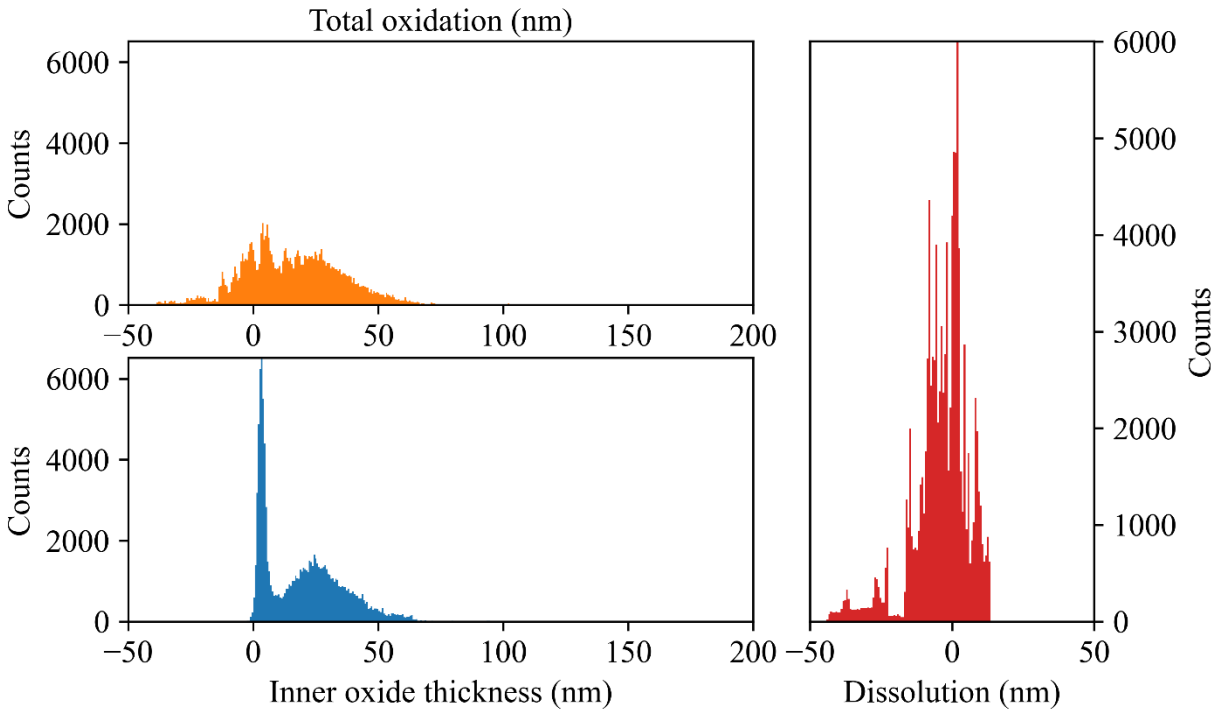

Figure 5.56. Histogram of inner oxide thickness and total oxidation measurements from the non-irradiated region of the S24 experiment series.

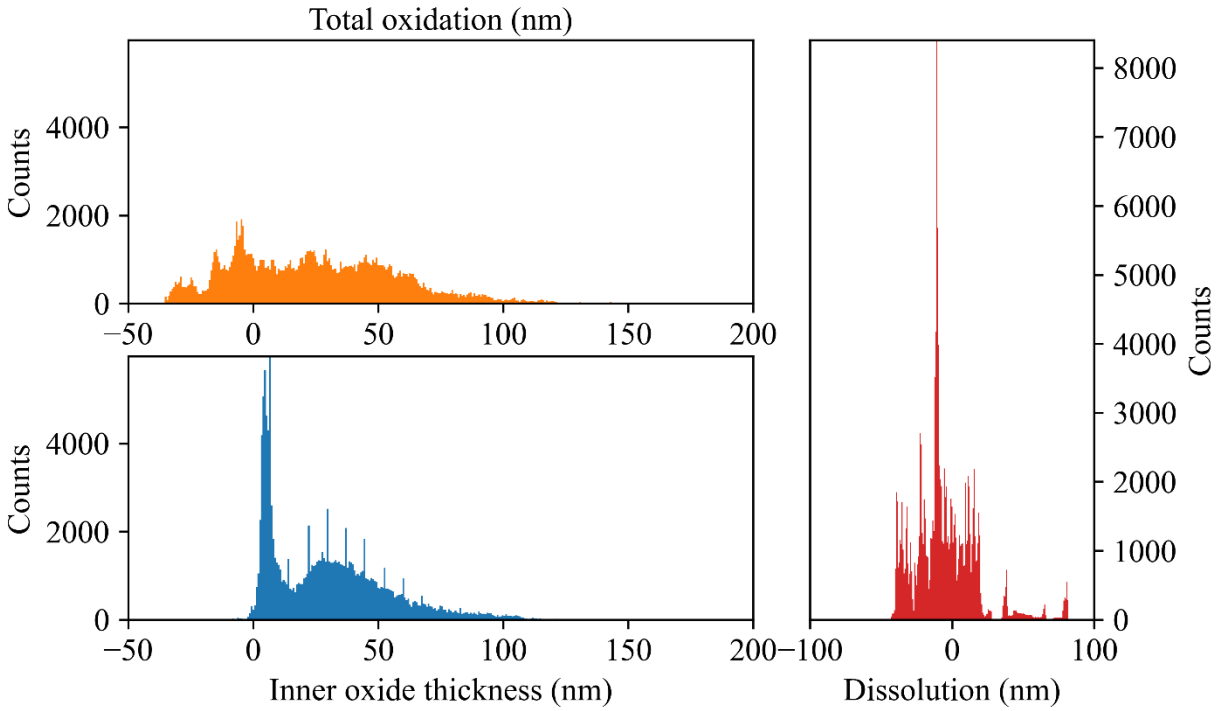

Figure 5.57. Histogram of inner oxide thickness and total oxidation measurements from the non-irradiated region of the S72 experiment series.

Table 5.7. Mean values of inner oxide thickness and total oxidation measurements from non-irradiated regions of 24 h and 72 h exposures in 480 °C argon-steam split into mode 1 corrosion, mode 2 corrosion, and combined.

		Total			Mode 1			Mode 2		
ID	Region	Mean Inner Oxide Thickness (nm)	Mean Total Oxidation (nm)	Mean Dissolution (nm)	Frac. (%)	Mean Inner Oxide Thickness (nm)	Mean Total Oxidation (nm)	Frac. (%)	Mean Inner Oxide Thickness (nm)	Mean Total Oxidation (nm)
S24	Non-irradiated	20. ± 13	16 ± 15	-3 ± 12	45	5.2 ± 2.5	7 ± 11	55	32 ± 11	32 ± 15
S72	Non-irradiated	30 ± 17	25 ± 14	-5 ± 12	36	6.7 ± 2.6	7 ± 11	64	44 ± 10	47 ± 13

5.3.2.2. Radiolysis region

An example of inner oxide measurement and the reconstructed original metal surface on a cross-section of the radiolysis region is presented in Figure 5.58 for S24 and in Figure 5.59 for S72. As with the other two regions, internal oxidation was present below the metal/oxide interface. There are larger areas with thinner inner oxide layers than the other two regions, and some of the thickest inner oxides are observed between the three regions. Measurements collected across all cross-sections from the non-irradiated region are plotted as histograms in Figure 5.60 for S24 and in Figure 5.61 for S72. Histograms show a stronger first corrosion mode than the other regions, but otherwise a similar profile. The arithmetic mean and standard error of these measurements are presented in Table 5.8 along with the separation of the two modes. Both corrosion modes show a good match between the radiolysis and non-irradiated regions; however, the total average measurements are slightly lower in the radiolysis region than the non-irradiated region. This is due to the stronger presence of the first mode which skews the total average measurements.

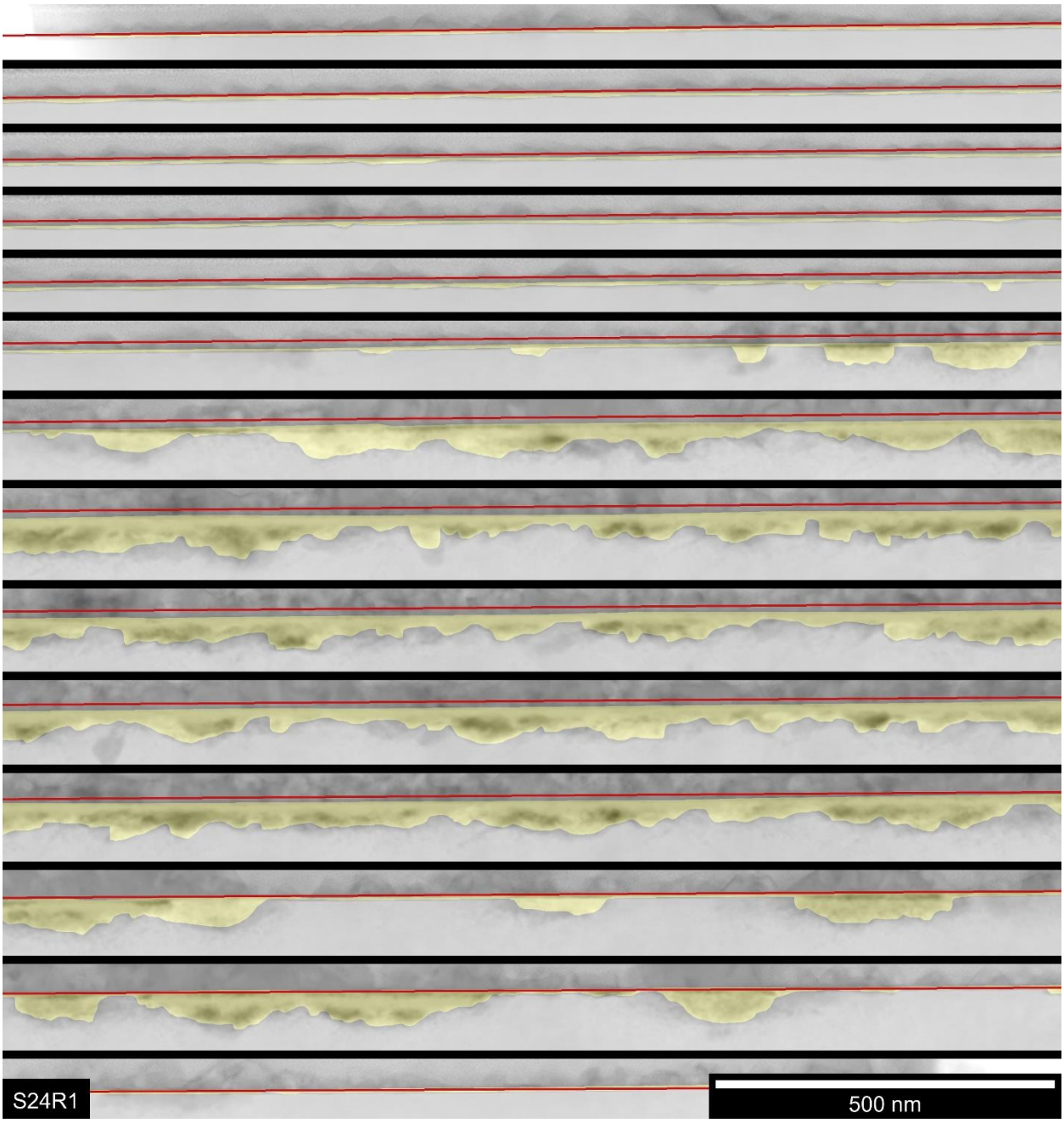

Figure 5.58. TEM micrograph collage highlighting the inner oxide area in yellow and the reconstructed original metal surface as a red line from the radiolysis region of experiment S24.

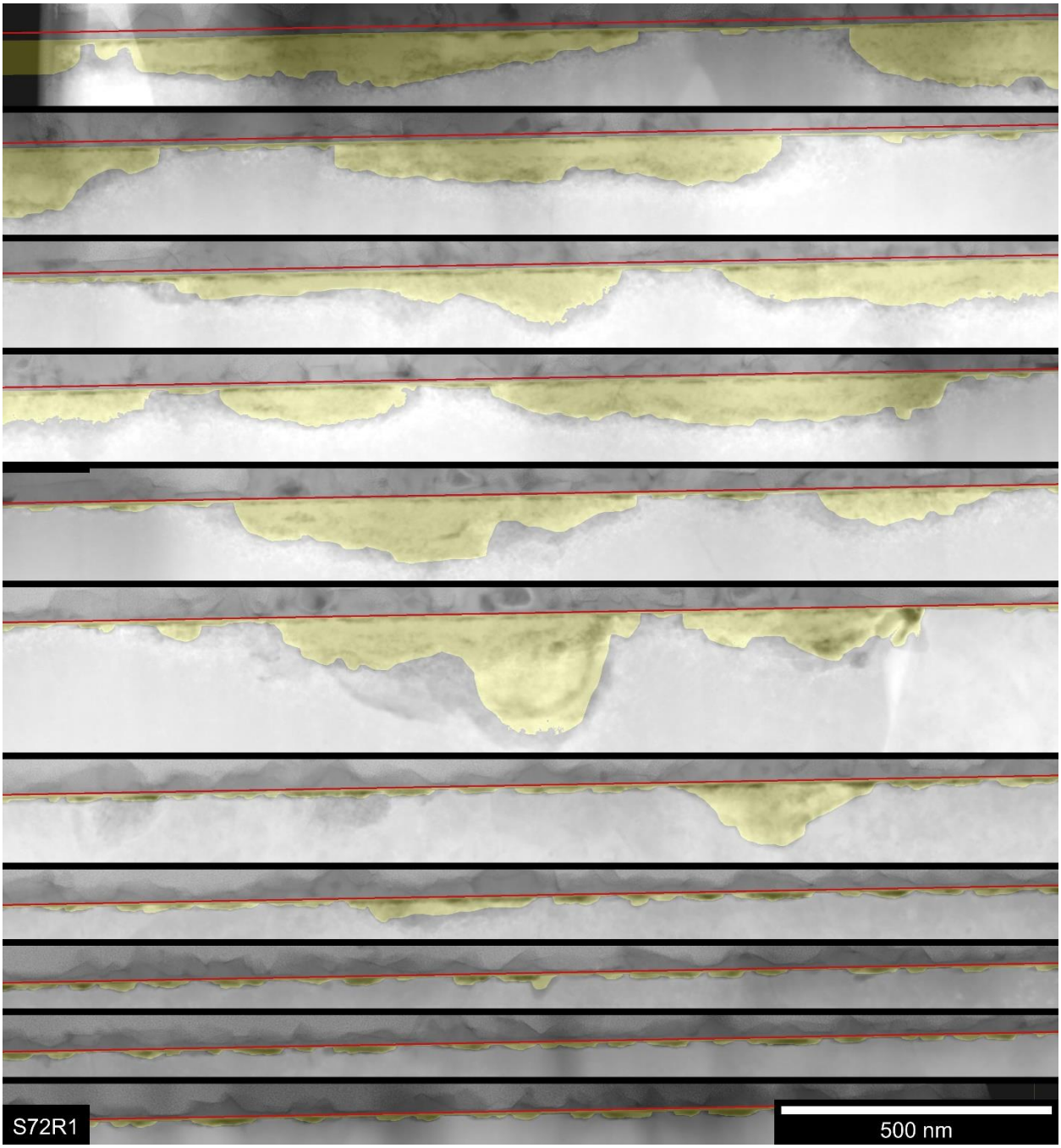

Figure 5.59. TEM micrograph collage highlighting the inner oxide area in yellow and the reconstructed original metal surface as a red line from the radiolysis region of experiment S72.

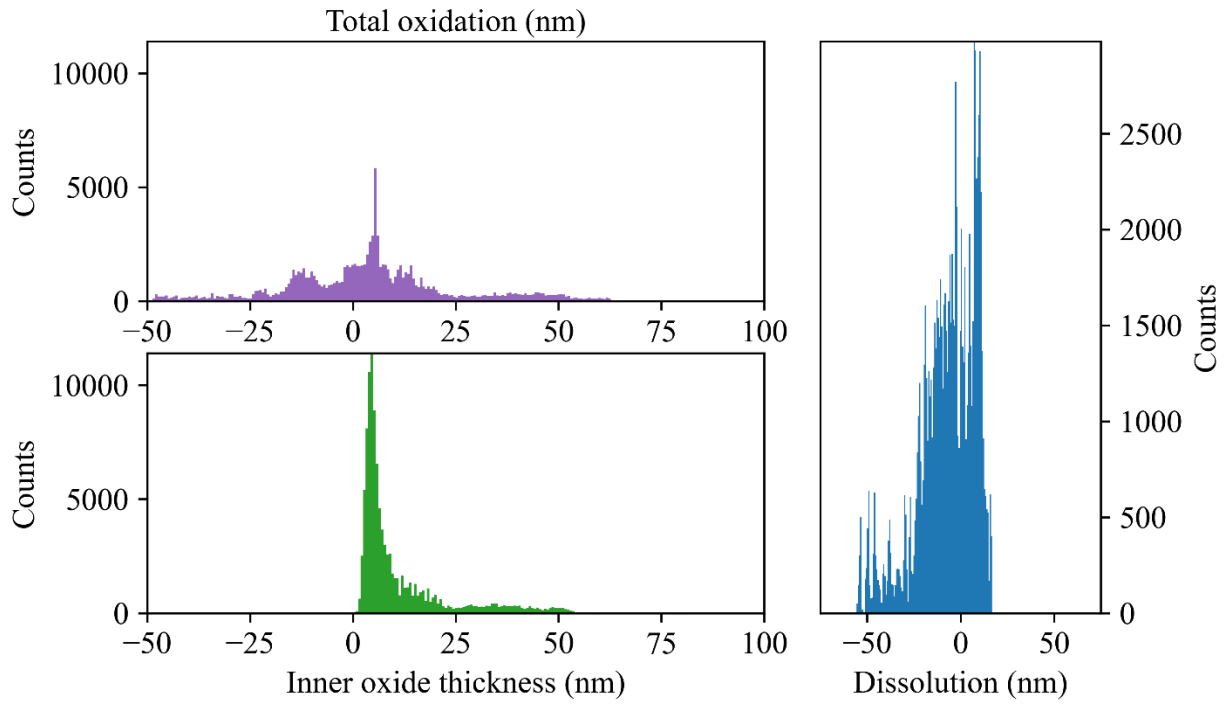

Figure 5.60. Histogram of inner oxide thickness and total oxidation measurements from the radiolysis region of the S24 experiment.

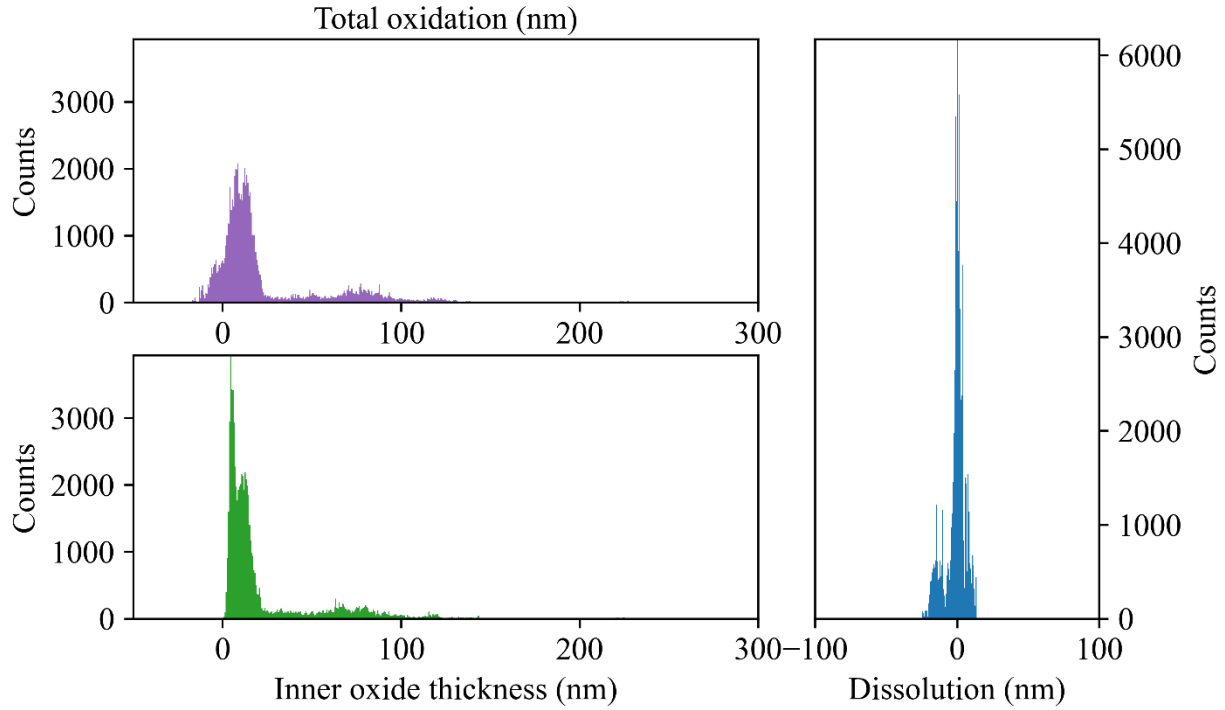

Figure 5.61. Histogram of inner oxide thickness and total oxidation measurements from the radiolysis region of the S72 experiment.

Table 5.8. Mean values of inner oxide thickness and total oxidation measurements from both non-irradiated and radiolysis regions of 24 h and 72 h exposures in 480 °C argon-steam split into mode 1 corrosion, mode 2 corrosion, and combined.

		Total			Mode 1			Mode 2		
ID	Region	Mean Inner Oxide Thickness (nm)	Mean Total Oxidation (nm)	Mean Dissolution (nm)	Frac. (%)	Mean Inner Oxide Thickness (nm)	Mean Total Oxidation (nm)	Frac. (%)	Mean Inner Oxide Thickness (nm)	Mean Total Oxidation (nm)
S24	Non-irradiated	20. ± 13	16 ± 15	-3 ± 12	45	5.2 ± 2.5	7 ± 11	55	32 ± 11	32 ± 15
	Radiolysis	11.5 ± 1.6	5 ± 13	-7 ± 14	78	6.3 ± 3.1	7 ± 11	22	30.5 ± 6.5	34 ± 16
S72	Non-irradiated	30 ± 17	25 ± 14	-5 ± 12	36	6.7 ± 2.6	7 ± 11	64	44 ± 10	47 ± 13
	Radiolysis	24 ± 17	24 ± 17	0 ± 11	66	8.6 ± 2.2	9 ± 11	34	53.1 ± 2.4	52 ± 13

5.3.2.3. Irradiated region

An example of the inner oxide measurement and the reconstructed original metal surface on a cross-section of the irradiated region is presented in Figure 5.62 for S24 and in Figure 5.63 for S72. Again, internal oxidation can be seen below the metal/oxide interface like the non-irradiated region. Significantly more porosity was observed in the inner oxides in the irradiated region than in the non-irradiated region. Measurements collected across all cross-sections from the irradiated region are plotted as histograms in Figure 5.64 for S24 and in Figure 5.65 for S72. The S24 inner oxide thickness histogram from the irradiated region shows a weak mode 1 peak (9 % of measurements), while S72 has a stronger mode 1 peak (23 % of measurements) both of which are lower than their non-irradiated or radiolysis counterparts. The arithmetic mean and standard error of these measurements are presented in Table 5.9 along with the separation of the two modes. The total average and second mode inner oxide thickness and total oxidation are significantly higher than the non-irradiated region counterparts. The first mode is not substantially different between durations or regions in the thickness value, despite difference in the fraction. The total oxidation of the irradiated region in S72 is lower than the inner oxide thickness due to some spurious negative values, yielding a significant negative dissolution

measurement, but the negative total oxidation measurements are erroneous, so the dissolution is likely close to zero.

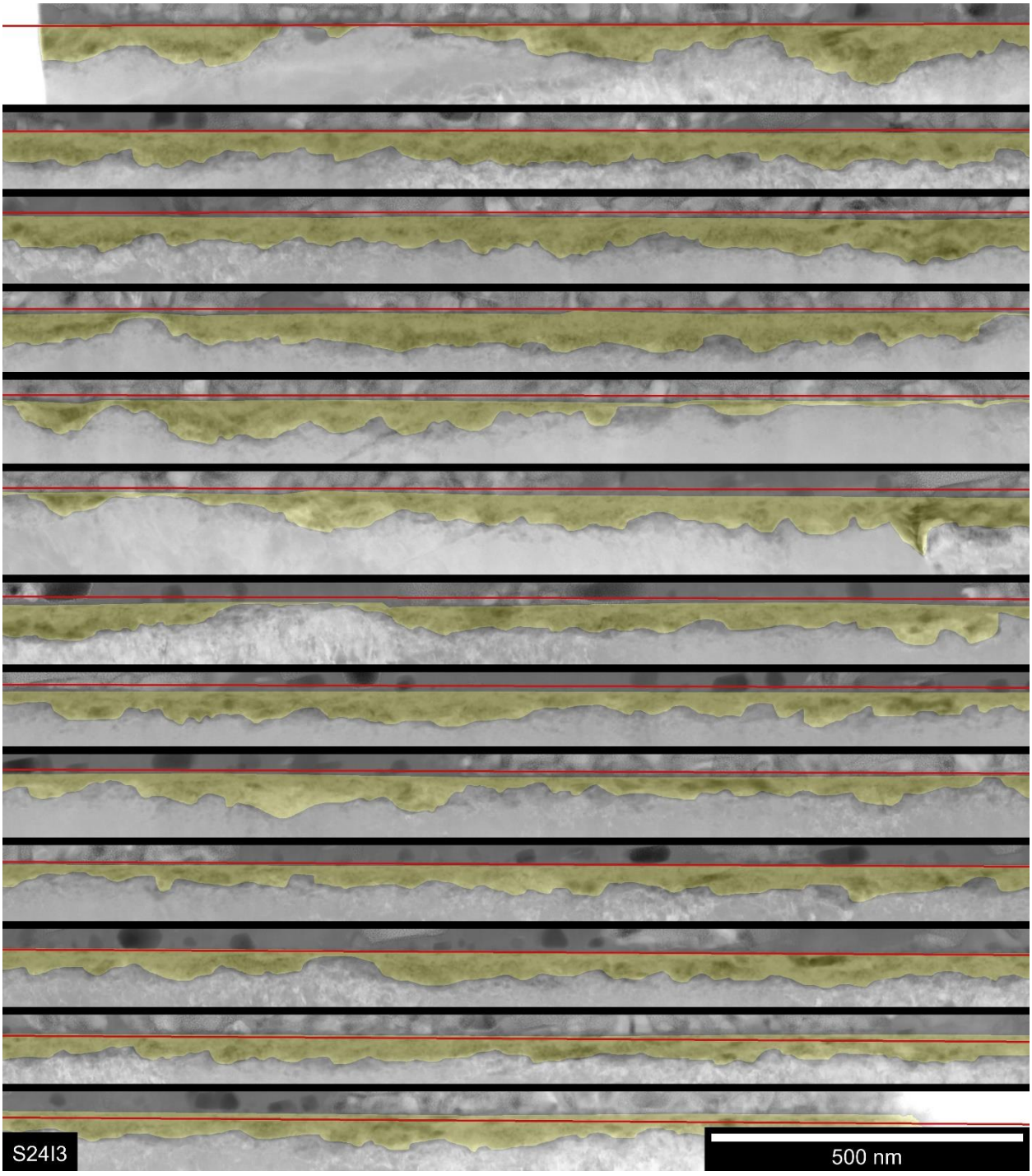

Figure 5.62. TEM micrograph collage highlighting the inner oxide area in yellow and the reconstructed original metal surface as a red line from the irradiated region of experiment S24.

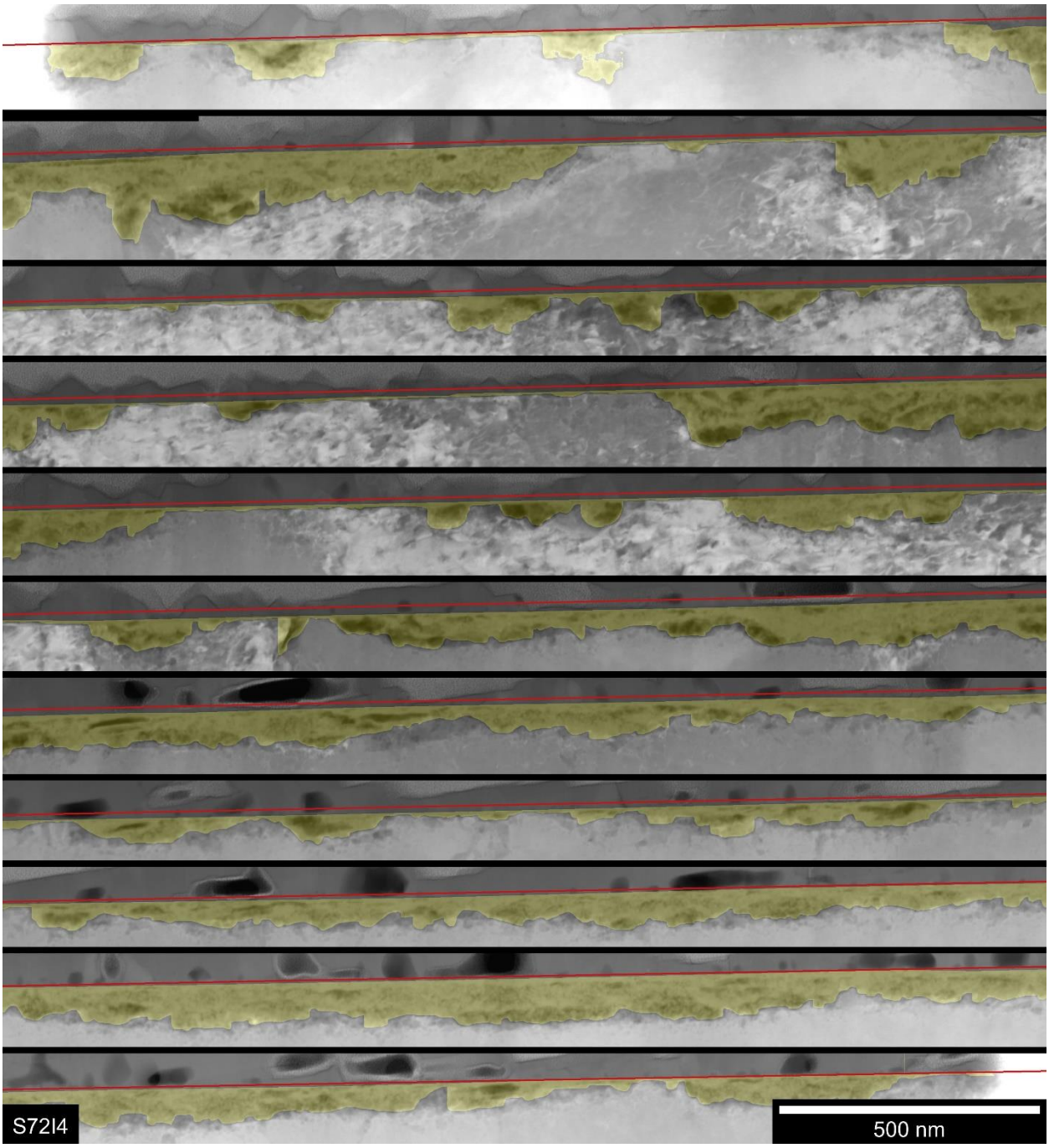

Figure 5.63. TEM micrograph collage highlighting the inner oxide area in yellow and the reconstructed original metal surface as a red line from the irradiated region of experiment S72.

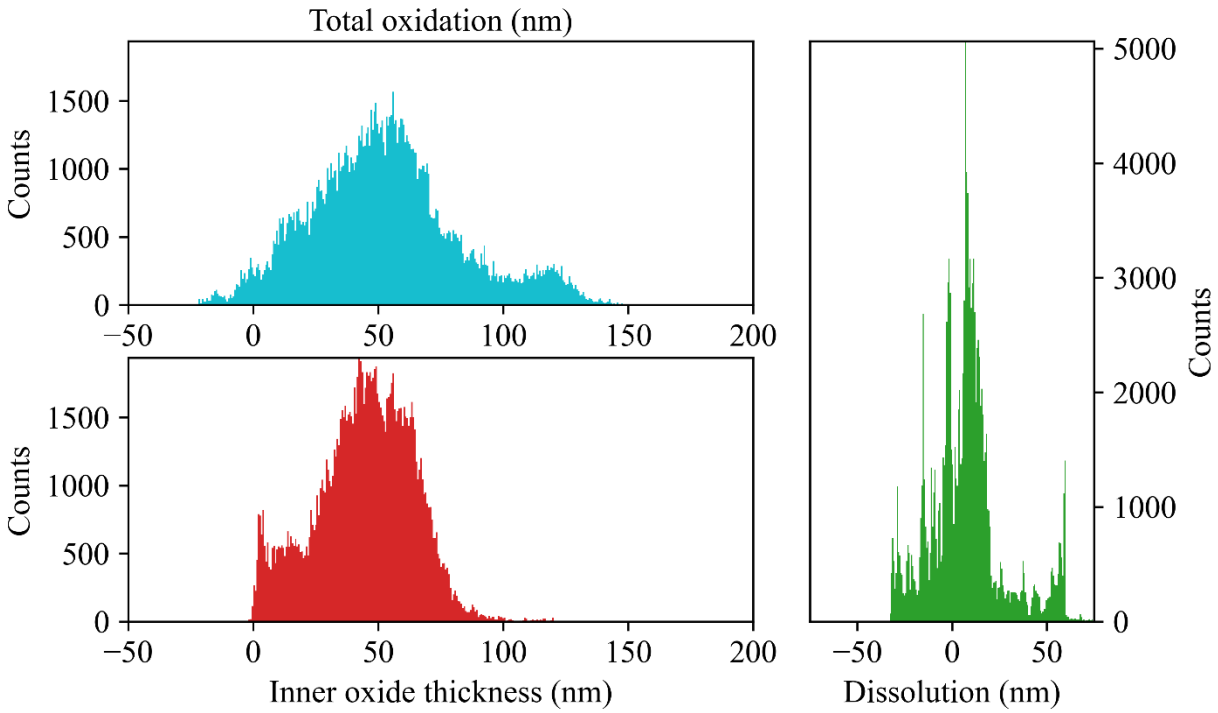

Figure 5.64. Histogram of inner oxide thickness and total oxidation measurements from the irradiated region of the S24 experiment.

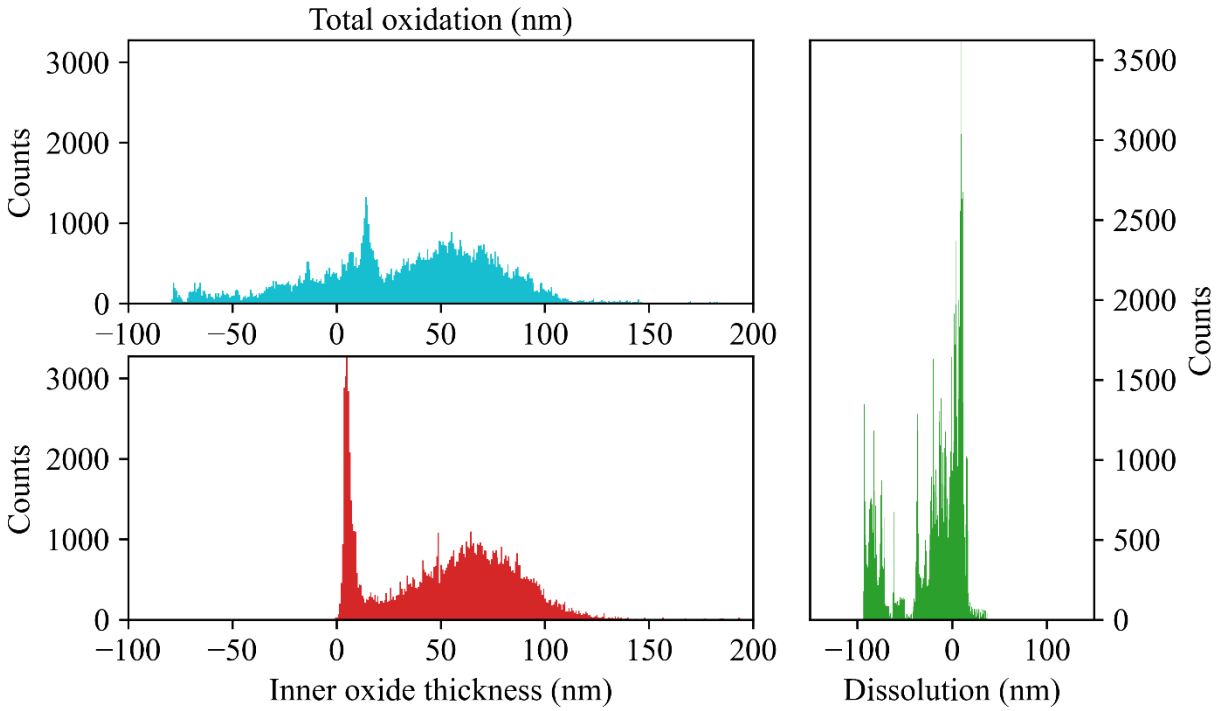

Figure 5.65. Histogram of inner oxide thickness and total oxidation measurements from the irradiated region of the S72 experiment.

Table 5.9. Mean values of inner oxide thickness and total oxidation measurements from all experiments in 320 °C water and 480 °C argon-steam split into mode 1 corrosion, mode 2 corrosion, and combined.

		Total			Mode 1			Mode 2		
ID	Region	Mean Inner Oxide Thickness (nm)	Mean Total Oxidation (nm)	Mean Dissolution (nm)	Frac. (%)	Mean Inner Oxide Thickness (nm)	Mean Total Oxidation (nm)	Frac. (%)	Mean Inner Oxide Thickness (nm)	Mean Total Oxidation (nm)
X24	Non-irradiated	155 ± 15	164 ± 15	7 ± 11	0	–	–	100	155±15	164 ± 15
X72	Non-irradiated	179 ± 18	183 ± 21	5 ± 11	18	20.7 ± 5.4	32 ± 13	82	213±17	216 ± 20
A24	Non-irradiated	11.0 ± 4.0	9 ± 12	-2 ± 11	–	–	–	–	–	–
W24	Non-irradiated	83 ± 12	174 ± 19	-5 ± 11	67	21.4 ± 6.3	26 ± 12	33	206.2 ± 8.5	227 ± 17
	Radiolysis	23.0 ± 8.9	29 ± 16	-3 ± 12	28	9.8 ± 1.8	10 ± 12	72	28.2 ± 8.3	34 ± 14
	Irradiated	32.3 ± 8.9	40 ± 12	-9 ± 11	–	–	–	–	–	–
W72	Non-irradiated	223 ± 17	208 ± 20	-15 ± 11	4	41.1 ± 4.2	52 ± 12	96	231 ± 15	217 ± 18
	Radiolysis	45 ± 13	70 ± 17	25 ± 12	–	–	–	–	–	–
	Irradiated	44 ± 13	65 ± 17	20 ± 12	–	–	–	–	–	–
S24	Non-irradiated	20. ± 13	16 ± 15	-3 ± 12	45	5.2 ± 2.5	7 ± 11	55	32 ± 11	32 ± 15
	Radiolysis	11.5 ± 1.6	5 ± 13	-7 ± 14	78	6.3 ± 3.1	7 ± 11	22	30.5 ± 6.5	34 ± 16
	Irradiated	45 ± 13	53 ± 20	8 ± 12	9	7.9 ± 1.4	9 ± 11	91	49 ± 12	58 ± 18
S72	Non-irradiated	30 ± 17	25 ± 14	-5 ± 12	36	6.7 ± 2.6	7 ± 11	64	44 ± 10	47 ± 13
	Radiolysis	24 ± 17	24 ± 17	0 ± 11	66	8.6 ± 2.2	9 ± 11	34	53.1 ± 2.4	52 ± 13
	Irradiated	53 ± 13	33 ± 16	-20 ± 13	23	6.6 ± 3.0	9 ± 12	77	66.6 ± 9.5	58 ± 15

5.3.3. STEM-EDS

Some example STEM-EDS profiles from S72 through the oxide and into the metal are presented in Figure 5.66 for the non-irradiated region, in Figure 5.67 for the radiolysis region, and in Figure 5.68 for the irradiated region. The inner oxide of the non-irradiated region shows a peak in the Cr content at ~70% of the total metal content near the metal/oxide interface and a consistent ~50% through the rest of the inner oxide, but Cr is totally absent from the outer oxide. Fe is the mirror image of the Cr profile in the inner oxide, and the outer oxide is nearly 100% Fe. Ni is enriched at the metal/oxide interface but is not present in any of the oxide film. Furthermore, some porosity can be seen in the inner oxide via the HAADF and the oxygen profile dipping in the center of the inner oxide.

In the radiolysis region, Cr starts at 40% at the metal/oxide interface and gradually increases to 75% by the inner/outer oxide interface before dropping to 0% in the outer oxide. Once again, the Fe profile mirrors the Cr profile, and the outer oxide is 100% Fe. The Ni profile peaks slightly at the metal/oxide interface and gradually decreases throughout the inner oxide to 0% about 60 nm before the outer oxide. Porosity is visible in the HAADF image and in the oxygen profile.

In the irradiated region, the Cr content at the metal/oxide interface is 60% of the metal content and gradually increases with distance from the metal/oxide interface to ~75%; it then drops more quickly to 50% near the inner/outer oxide interface before dropping sharply to 0% within the outer oxide. Again, the Fe is the mirror of the Cr profile in the inner oxide, and the outer oxide contains >95% Fe. The Ni profile shows a sharper increase at the metal/oxide interface than the non-irradiated region, and there is some (<5%) incorporation of Ni into both inner and outer oxides layers. Porosity is also visible in this linescan in the HAADF image and in the two dips in the oxygen profile in the inner oxide.

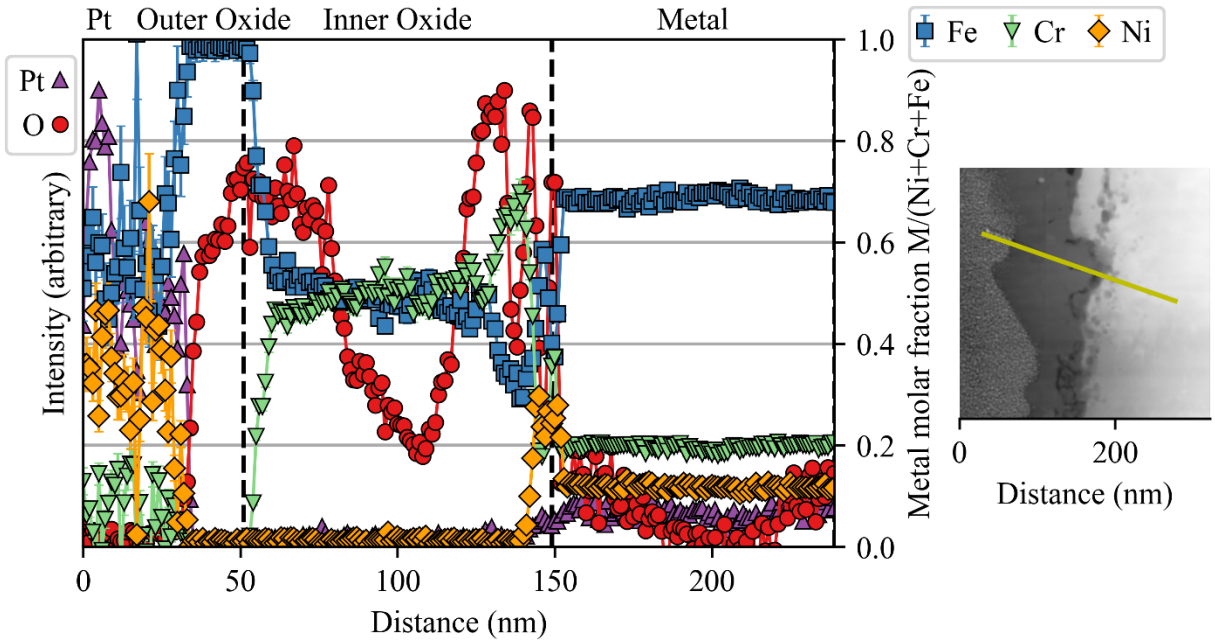

Figure 5.66. STEM-EDS linescan though the oxide and associated micrograph from the non-irradiated region of S72.

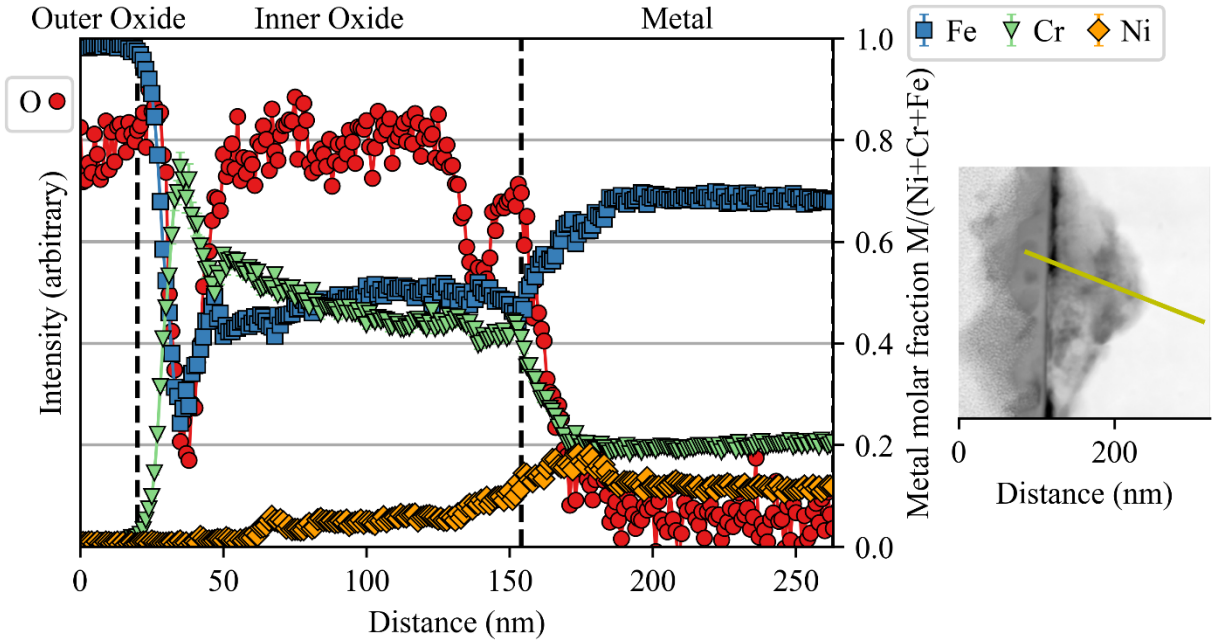

Figure 5.67. STEM-EDS linescan though the oxide and associated micrograph from the radiolysis region of S72.

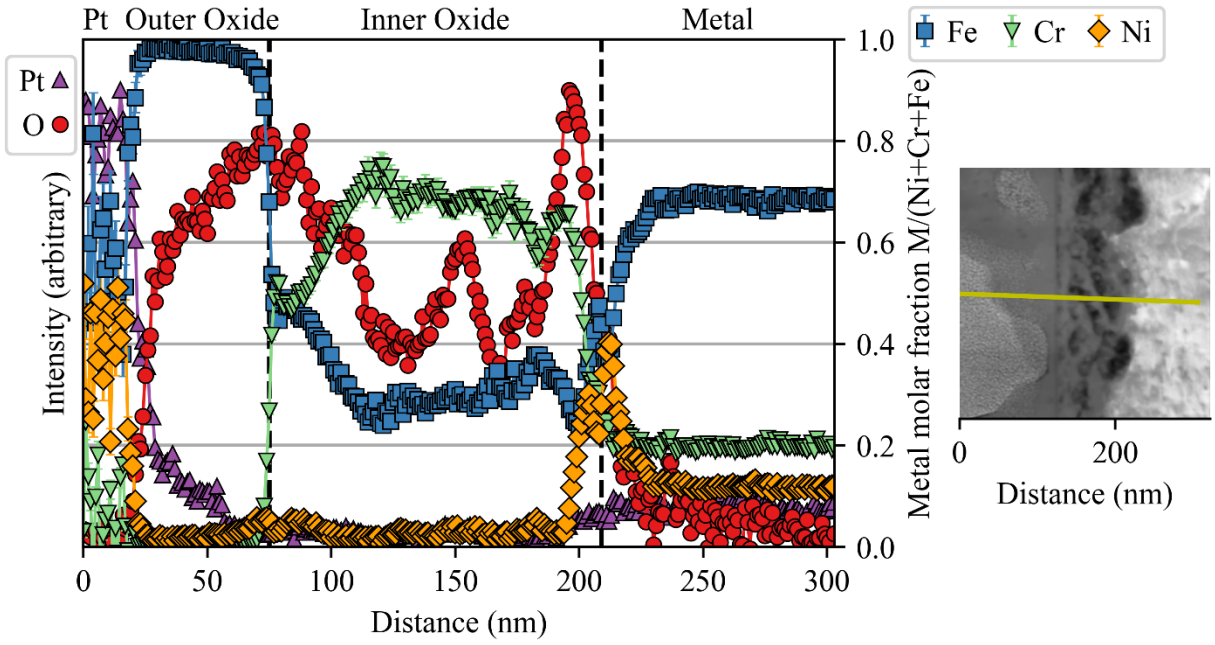

Figure 5.68. STEM-EDS linescan though the oxide and associated micrograph from the irradiated region of S72.

From the other linescans collected from S24 and S72, elemental profiles were plotted across the metal/oxide interface for Cr in Figure 5.69, Fe in Figure 5.70, and Ni in Figure 5.71. While the individual linescans showed some diversity among the different regions, collective profiles show little difference between the regions. The Cr profiles often show some peaking behavior at the metal/oxide interface followed by a relatively flat profile between 40~70%. The Cr drops off quickly upon termination of the inner oxide layer due to the low Cr content of the outer oxide in all three regions. Once again, the Fe profiles essentially mirror the Cr profiles with nadirs beside the metal/oxide interface and rapidly rising to meet the ~100% Fe content of the outer oxide. Finally, the Ni profiles always show some peaking behavior near the metal/oxide interface followed by a quick decrease to very low concentrations throughout both oxide layers.

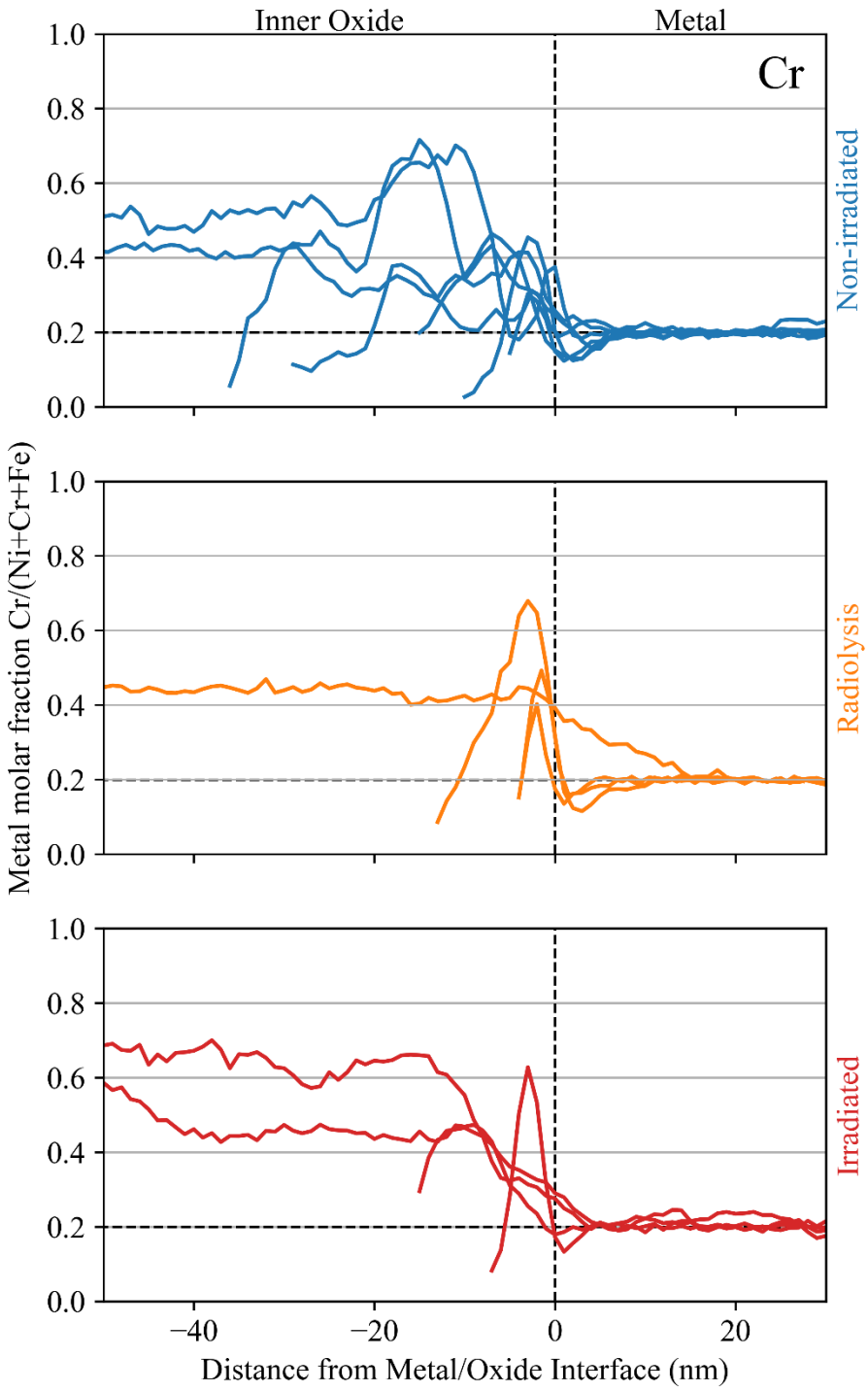

Figure 5.69. STEM-EDS linescans showing the Cr profile through the metal/oxide interface for each region of S24 and S72.

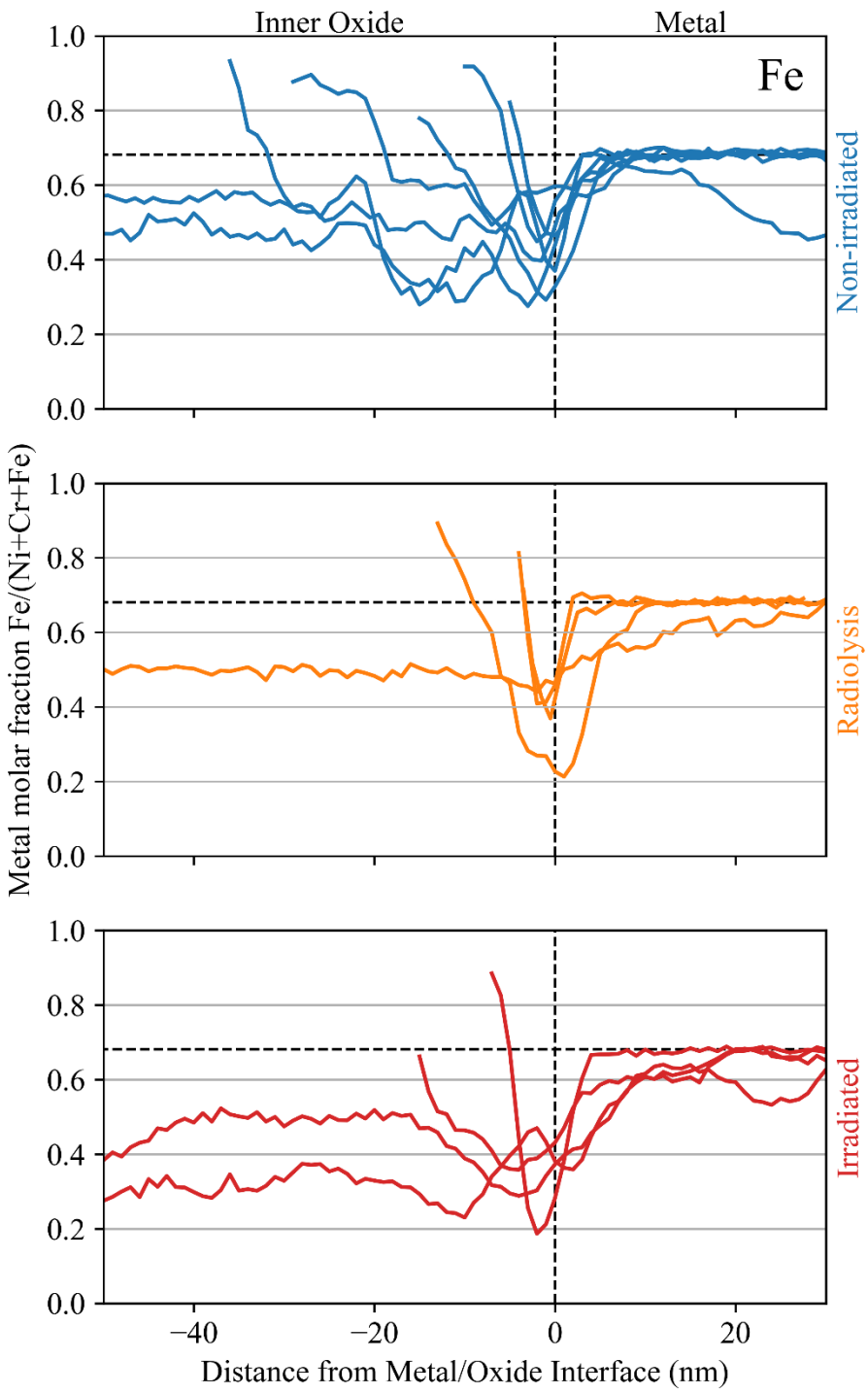

Figure 5.70. STEM-EDS linescans showing the Fe profile through the metal/oxide interface for each region of S24 and S72.

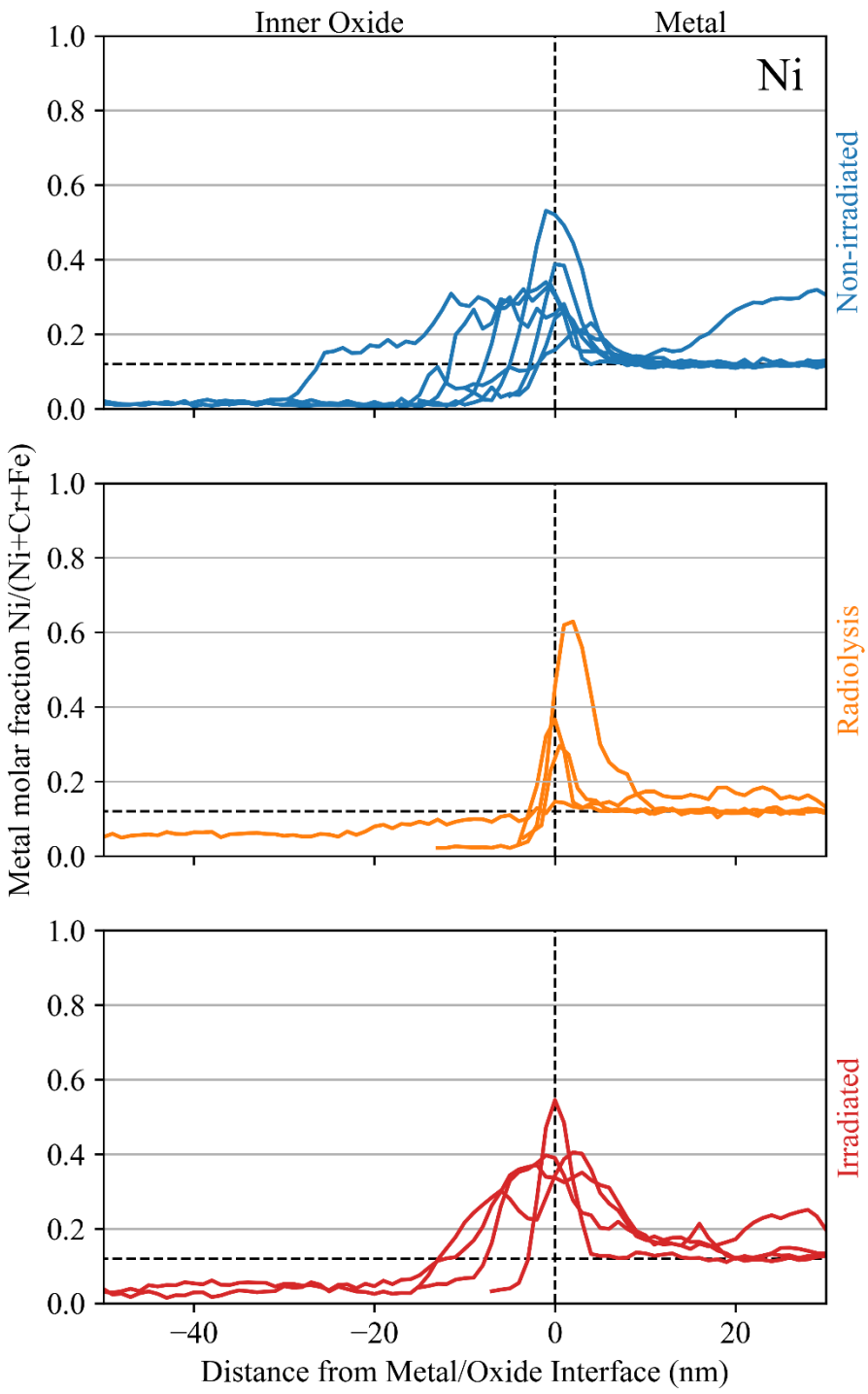

Figure 5.71. STEM-EDS linescans showing the Ni profile through the metal/oxide interface for each region of S24 and S72.

5.4. Thermodynamic Modeling

Thermo-Calc was used to calculate equilibria of the stainless steel corrosion system along the continuum of oxygen activity. First, the expected oxygen activity of the nominal conditions in this work were calculated and are indicated in the Thermo-Calc results. Oxygen activity was calculated using a statistical thermodynamics model for thermal decomposition of H_2O into HO, H, O, H_2, and O_2 [117]. The initial condition was the input water pressure, the total system pressure (including inert gas in the case of the steam experiments), and the amount of added H_2 or O_2. The oxygen activity of the nominal non-irradiated oxidation conditions in hydrogenated 320 °C water is 1.863×10^{-31} atm, and in aerated water it is 5.951×10^{-4} atm. The oxygen activity in the hydrogenated argon-steam environment at 480 °C was calculated to be 1.904×10^{-27} atm. Oxygen activity under irradiation will be calculated in the later section on radiolysis effects.

All the relevant values resulting from the Thermo-Calc modeling are given in Appendix C and are plotted in this section. In water at 320 °C and 13.1 MPa, the resulting phase composition of the system is plotted vs. oxygen activity in Figure 5.72 excluding the gas phase. The elemental composition of each phase is plotted in Figure 5.73. For the steam-argon environment at 480 °C and 1.5 MPa, the phase composition is plotted in Figure 5.74, and the elemental composition of each phase is plotted in Figure 5.75.

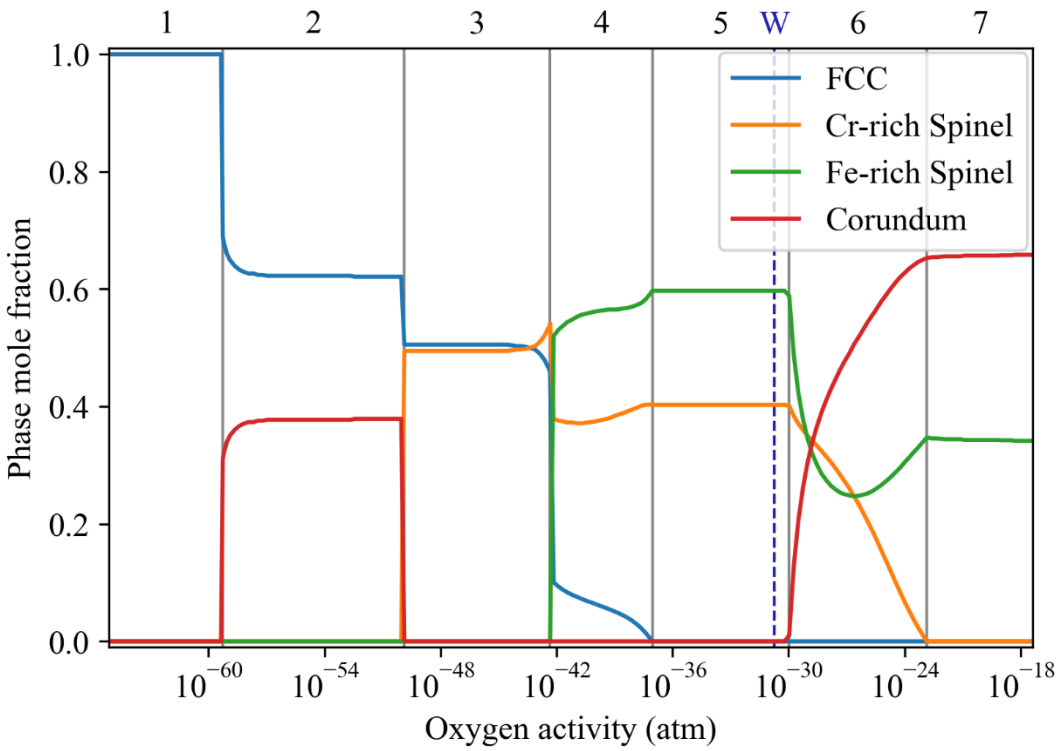

Figure 5.72. Phase composition (excluding the gas phase) of 316L with oxygen at 320 °C and 13.1 MPa as a function of oxygen activity calculated using Thermo-Calc software. “W” denotes the nominal oxygen activity with 3 mg/kg H_2 added to water.

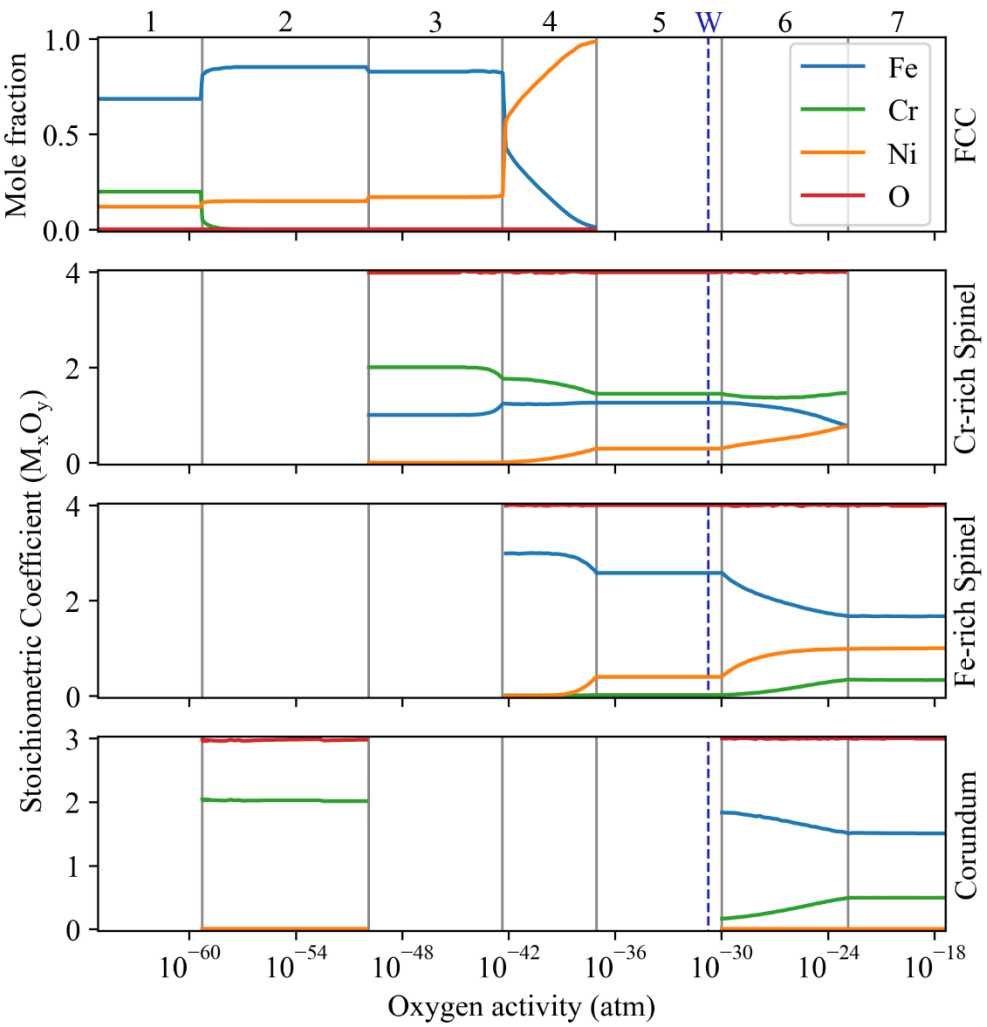

Figure 5.73. Elemental composition of each phase formed by 316L with oxygen at 320 °C and 13.1 MPa as a function of oxygen activity calculated using Thermo-Calc software. “W” denotes the nominal oxygen activity with 3 mg/kg H_2 added to water.

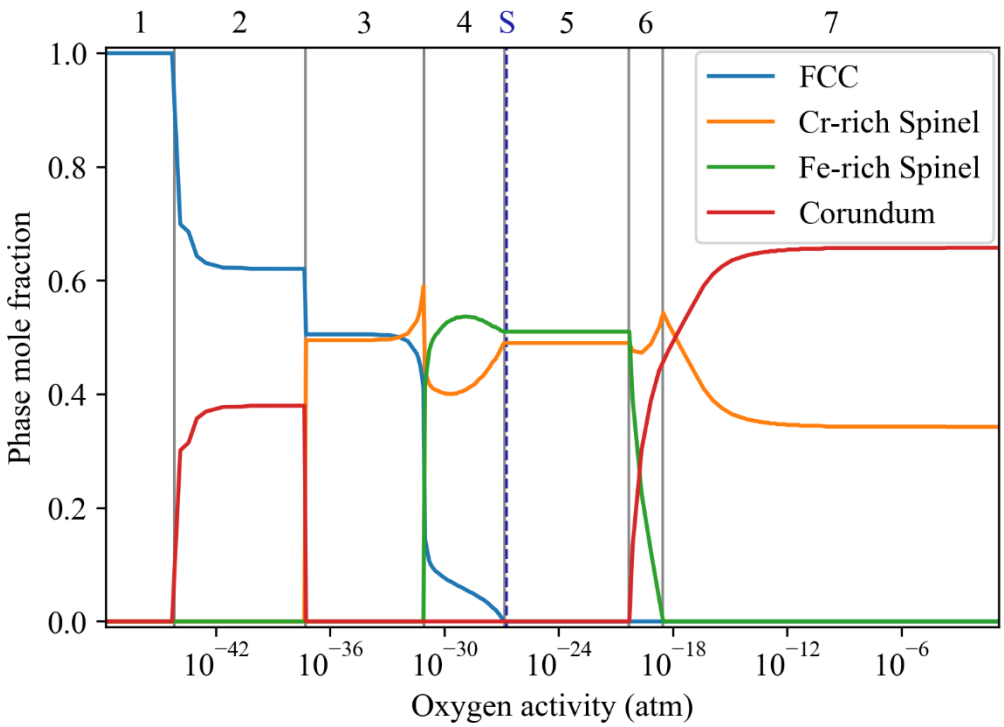

Figure 5.74. Phase composition (excluding the gas phase) of 316L with oxygen at 480 °C and 1.5 MPa as a function of oxygen activity calculated using Thermo-Calc software. “S” denotes the nominal oxygen activity with 170 g/kg H_2 added to steam.

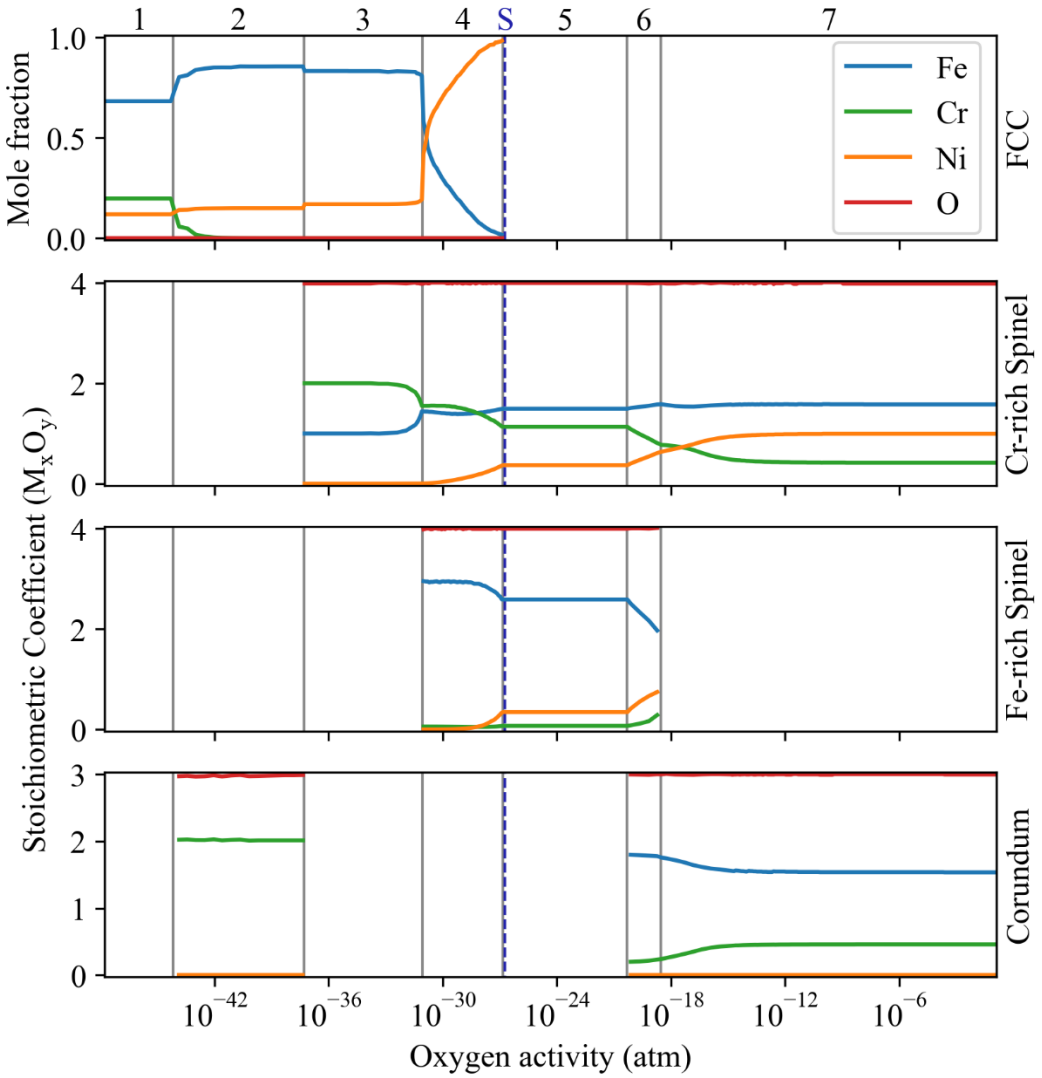

Figure 5.75. Elemental composition of each phase formed by 316L with oxygen at 480 °C and 1.5 MPa as a function of oxygen activity calculated using Thermo-Calc software. “S” denotes the nominal oxygen activity with 170 g/kg H_2 added to steam.

There are seven distinct regimes of corrosion behavior denoted in Figure 5.72 through Figure 5.75. Although the environments in this work span the regimes of 5–7, the lower regimes are also relevant because the oxide film spans the oxygen activity from the solubility limit of oxygen in the metal to that of the corrosion environment. Therefore, it is useful to examine each regime in some detail.

Regime 1 contains only metal, identified as face-centered cubic (FCC), and oxygen up to its solubility limit. Regime 1 is present in all the experiments in this work as the metal phase.

Regime 2 is where the oxygen solubility in the metal is surpassed, resulting in the precipitation of Cr_2O_3 and consuming all the Cr in the metal phase. This regime is sometimes observed as internal oxidation in the metal near the metal/oxide interface as spherical oxide precipitates [38]. This regime (and/or regime 3) is visible in all the steam conditions presented in this work on the metal side of the metal/oxide interface.

Regime 3 denotes a phase change from Cr_2O_3 to $FeCr_2O_4$ removing only the required iron from the metal to satisfy the stoichiometry. The Ni content in this spinel phase is very small, but nonzero, ranging from ~10^{-7} mole fraction to ~10^{-4} mole fraction at the upper end of oxygen activity in both water and steam conditions The internal oxidation from the steam experiments may also represent this regime near the metal/oxide interface. An interesting example of this regime in literature can be found in ref. [38] where the "inner oxide layer" consists of both a $FeCr_2O_4$ phase and a FCC phase that is enriched in Ni.

Regime 4 demarks the onset of the Fe-rich spinel phase in equilibrium with the extant Cr-rich spinel in addition to the remaining FCC phase (increasingly pure in Ni). This regime is important because it is the last regime containing a stable FCC phase, so for any environment with oxygen activities belonging to regime 4 or greater, this regime is present at the metal/oxide interface. This explains some commonly observed phenomena of Ni enrichment in the metal below the metal/oxide interface as observed in this work and in the literature [34,39,40]. In this regime, the duplex oxide structure can be partially explained by the miscibility gap between Fe-rich and Cr-rich spinel oxides which are generally reflected in the observed oxide layer compositions.

Regime 5 has the same Cr-rich and Fe-rich spinel phases as regime 4, but the metal phase is totally absent from this regime. The elemental compositions of the oxides do not change with

oxygen activity in this regime; instead, the point defect concentrations change over this regime as described later in this section. The first major difference between the 320 °C and 480 °C results are in the composition and relative quantity of the two spinel phases. At 480 °C, the Cr-rich spinel has a lower Cr content than at 320 °C; therefore, there is a greater amount of the Cr-rich phase present at 480 °C.

Regime 6 consists of a three-phase oxide equilibrium over which one spinel is oxidized into the (returning) corundum phase. Essentially, the remaining Fe^{2+} begins to be oxidized into Fe^{3+} thereby removing some spinel phase to accommodate corundum. The Cr from the Cr-rich spinel gets divided between the phases, but the majority moves to the corundum phase. Ni remains in the spinel phase because it does not oxidize to 3+, therefore resulting in an increasing Ni concentration in the spinel phases. Regime 6 is very short at 480 °C, and the Cr-rich spinel survives to regime 7, unlike the 320 °C case where the Fe-rich spinel survives although the distinction is irrelevant in practice. As the Ni concentration increases, the miscibility gap between the spinels shrinks until they merge into a single spinel phase, this occurs earlier at 480 °C because the miscibility gap is already smaller at higher temperatures. Consequently, the compositions are still approaching their final values at the beginning of regime 7 at 480 °C as the remaining Fe^{2+} continues to oxidize, whereas virtually all the Fe^{2+} is oxidized by regime 7 at 320 °C.

Regime 7 is the final identified thermodynamic state where one corundum and one spinel phase are in equilibrium. The spinel contains the entirety of the Ni from the original metal with mostly Fe and a little Cr to fill in the 3+ valence positions in the oxide. The majority of Cr and Fe are both contained in the corundum phase. Regime 7 remains stable to the point that oxygen gas in the environment is in equilibrium with the oxides at the higher end of oxygen activity. The

oxide stoichiometry is very similar between the two temperature/pressure conditions in this regime.

The elemental composition of the metal phase in both Figure 5.73 and Figure 5.75 shows the selective oxidation of Cr first followed by Fe and finally Ni. The high concentration of Ni in the remaining metal in regime 4 corresponds to the Ni enrichment observed in the metal at the metal/oxide interface. The corundum phase exists in regime 2 only as Cr_2O_3 but reappears in regime 6 as a largely Fe-rich oxide and gradually uptakes most Cr in the system by regime 7. Both the elemental composition and the oxygen activity influence the thermal point defect concentrations within the oxide species as presented in Figure 5.76 in the 320 °C water condition and Figure 5.77 in the 480 °C steam condition. One major advantage of using an energy minimization (e.g. Thermo-Calc) approach over a simplistic model of point defects with oxygen activity is the treatment of complex interactions between oxide composition and oxygen activity. The point defect concentrations will be used later in the kinetics section to calculate the diffusion coefficient of cations in the inner oxide layer.

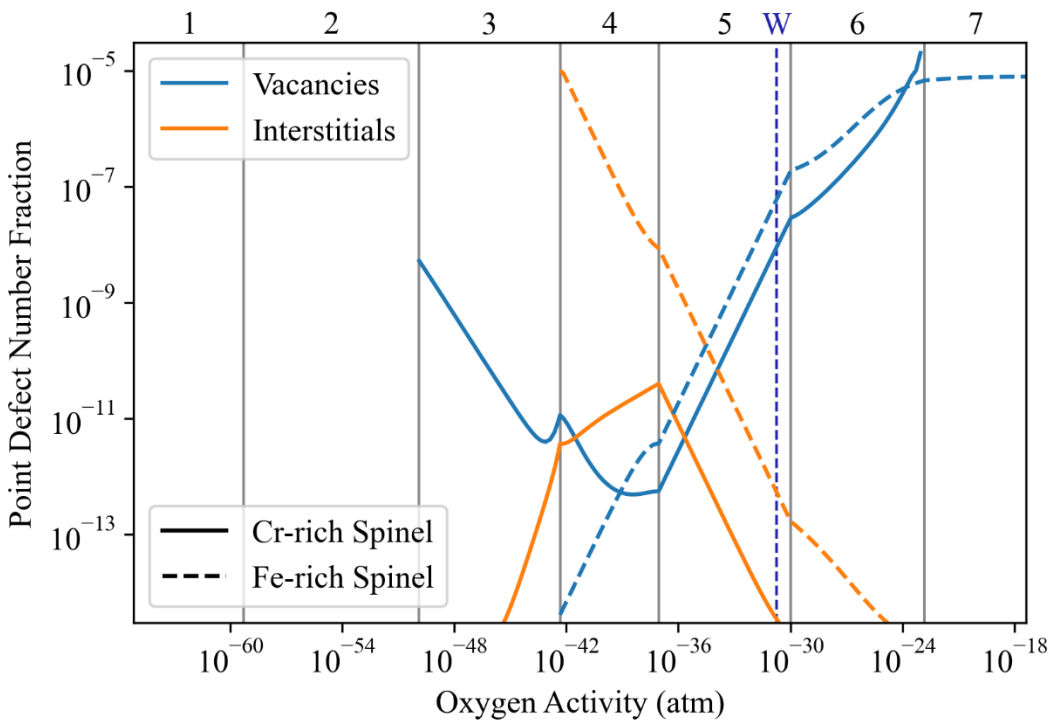

Figure 5.76. Vacancy and interstitial concentrations in both spinel phases in the 316L corrosion system at 320 °C and 13.1 MPa as a function of oxygen activity calculated using Thermo-Calc software.

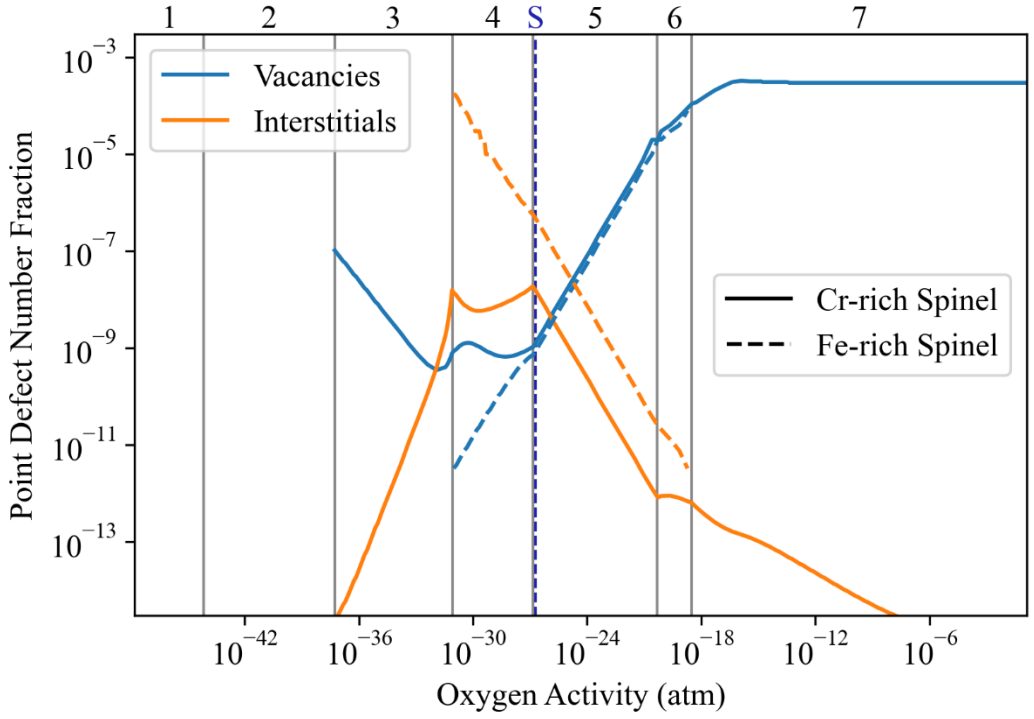

Figure 5.77. Vacancy and interstitial concentrations in both spinel phases in the 316L corrosion system at 480 °C and 1.5 MPa as a function of oxygen activity calculated using Thermo-Calc software.

Similar to results by Töpfer [56], the interstitial concentration in regime 5 is much lower in the Cr-rich spinel than the Fe-rich spinel, but the vacancy concentration is only slightly suppressed at 320 °C and is slightly enhanced at 480 °C. However, at low oxygen activities, the vacancy concentration in the Cr-rich spinel reverses its dependence on oxygen activity because the Cr content also changes with oxygen activity. The synergistic effects of oxygen activity on composition and point defects in the Cr-rich spinel are more significant compared with those of the Fe-rich spinel phase. Conversely, the Fe-rich spinel generally replicates the behavior observed by Dieckmann and Töpfer across oxygen activity for pure magnetite at 900 °C to 1200 °C where cation vacancy concentration increased and cation interstitial concentration decreased with oxygen activity to the +1/2 and –1/2 power, respectively [55,56].

Another useful result from Thermo-Calc is the chemical potential of each species as a function of oxygen activity as presented in Figure 5.78 for 320 °C and 13.1 MPa and in Figure 5.79 for 480 °C and 1.5 MPa. One feature to note is the monotonic change in chemical potential with oxygen activity for all elements except Ni. The driving force for oxygen induces motion from the environment to the metal, and the reverse for the other elements. However, in regime 4, the driving force for Ni flows from the oxide to the metal creating a hurdle for Ni incorporation into the oxide. The practical result of this feature is Ni enrichment in the metal phase in the first few nanometers directly adjacent the metal/oxide interface as observed in this work and noted in literature [34,39,40]. Furthermore, the nominal oxygen activity at 480 °C is just past the peak value for the Ni chemical potential, so there is very little driving force for Ni to be incorporated into the oxide especially in comparison with the driving force for Ni to diffuse backward into the bulk metal. Using a reference point and the system oxygen activity, the change in chemical potential can be calculated and used as the driving force for the corrosion process.

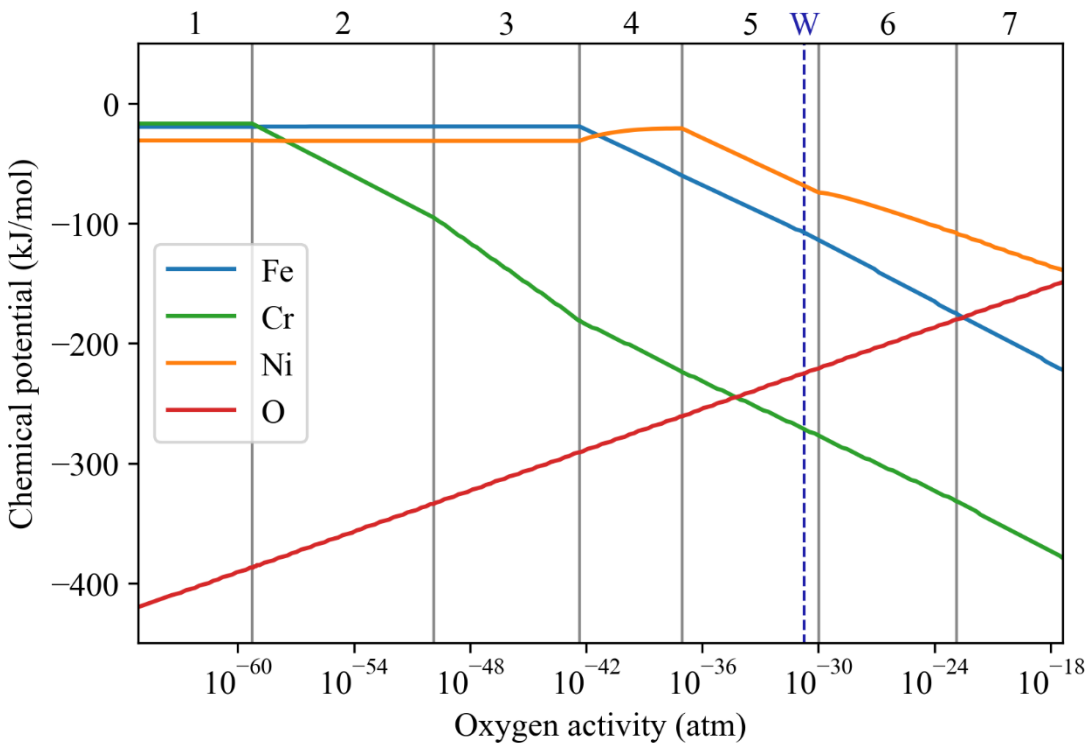

Figure 5.78. Chemical potential of each element in the 316L corrosion system at 320 °C and 13.1 MPa as a function of oxygen activity calculated using Thermo-Calc software. “W” denotes the nominal oxygen activity with 3 mg/kg H_2 added.

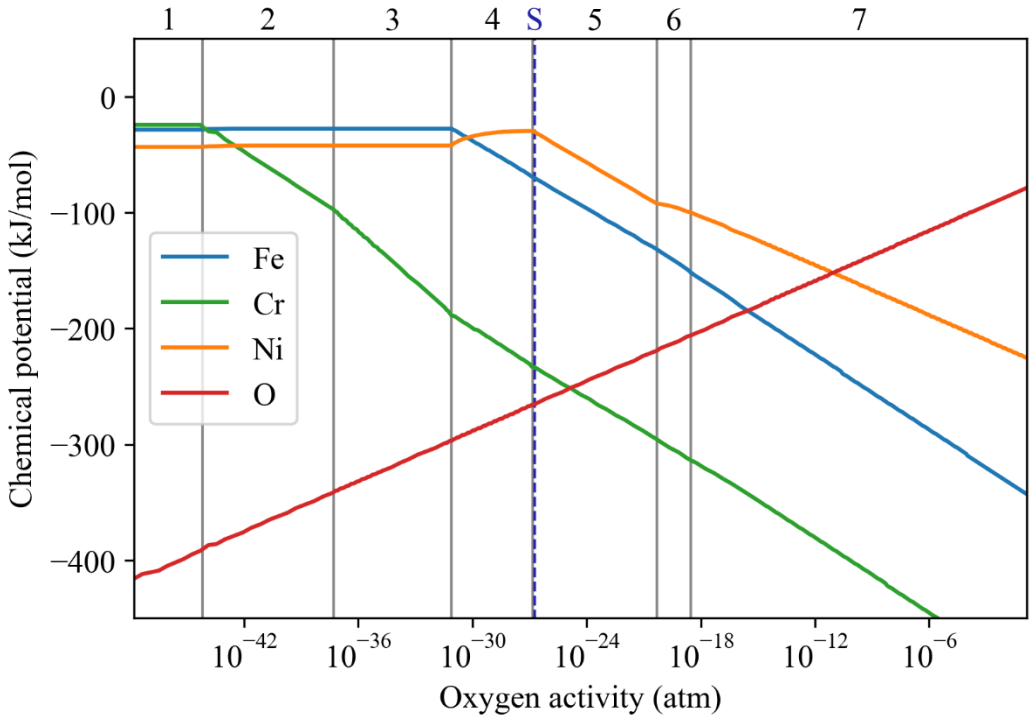

Figure 5.79. Chemical potential of each element in the 316L corrosion system at 480 °C and 1.5 MPa as a function of oxygen activity calculated using Thermo-Calc software. “S” denotes the nominal oxygen activity with 170 g/kg H_2 added.

Chapter 6
Discussion

The discussion of the results is divided by the radiation environment of the experiments. First, the results of experiments without radiation effects (including non-irradiated regions of otherwise irradiated specimens) will be discussed. Radiation effects on corrosion can only be understood by comparing to non-irradiated controls, so a detailed discussion is warranted. Second, effects of radiolysis on the water chemistry and subsequently on the corrosion behavior of radiolysis regions will be discussed. Third, the effects of radiation-induced displacement damage on corrosion in irradiated regions will be discussed. Finally, the understanding of general radiation effects on corrosion will be extrapolated to predict the effects of radiation on nominal in-core corrosion of stainless steel structural components.

6.1. Corrosion of non-irradiated 316L SS

The discussion on corrosion of the non-irradiated regions of irradiated samples and control samples is subdivided into thermodynamics and the kinetics of the corrosion mechanisms. Thermodynamics determines the driving force for processes that constitute corrosion, intrinsic material properties that affect corrosion, and phase quantity and composition. By incorporating the insights of thermodynamics along with observed oxide morphology, kinetics can be used to determine the processes that control the corrosion rate and predict how it will change with thermodynamic parameters.

6.1.1. Thermodynamics

To best interpret the corrosion observed in non-irradiated regions of otherwise irradiated samples and those of control experiments, an in-depth thermodynamic analysis was performed for the nominal conditions of these experiments. Because corrosion is a surface phenomenon and an active process, there are thermodynamic driving forces between the bulk metal and bulk environment. Experimentally, this driving force is often measured as the electrochemical corrosion potential (ECP) between a reference electrode and the specimen. The ECP is related to the oxygen activity via the Nernst equation in Eq. 2.1 ($ECP \propto ln\, a_{O_2}$). Oxygen activity is used in this work as the primary thermodynamic variable that defines the state of the system. Instead of using ECP as the driving force, chemical potential is used because it is element specific. One important feature of the oxygen activity is that it is expressed continuously throughout the oxide film thereby changing the thermodynamic state of the oxide at different depths within the oxide film. Therefore, it is necessary to examine every thermodynamic state of the corroding system between the bulk metal and the bulk environment oxygen activities.

The limitation of thermodynamic models presented is that they do not provide information on the temporal or spatial layout of the phases or compositions identified. While regimes 4, 5 and 7 all have two stable oxide phases, these phases do not necessarily segregate into different layers, yet two oxide layers are a common feature of stainless steel corrosion. Furthermore, because up to three oxides may be stable at a single oxygen activity, it is necessary that a mixture of the phases coexist within a single oxide layer. Without applying some kinetic information, it is impossible to determine the layer structure purely based on the multiple oxide phase equilibria.

6.1.2. Kinetics

To understand how radiation affects the corrosion rate, the fundamental mechanics that limit the rate of corrosion must be identified. The mechanics of corrosion can be determined by comparing the thermodynamic and kinetic predictions to the observable results. By doing so, the response of corrosion mechanisms to changes induced by radiation effects can be explored. However, the mechanisms that result in corrosion without the influence of radiation must first be established.

The mechanistic model used to describe the corrosion kinetics will be the parabolic rate law. Despite its imperfections, the parabolic rate law captures the essential relationship between oxide thickness and time for oxidation via solid state diffusion. The parabolic rate constant, as the sole parameter, contains all information about the corrosion system, but this rate constant does not have a well-defined expression. Therefore, the starting point in this work is the derivation of the parabolic rate law with the purpose of allowing for radiation effects to be later incorporated within the parabolic rate constant.

Other models for corrosion do exist, but they are not sufficiently distinct from the parabolic rate law or miss key features of the corrosion behavior of stainless steels. The Cabrera-Mott model uses the electric field as driving force for electron transport across an insulating oxide layer. Iron-containing oxides are reasonably conductive at the temperatures considered in this work, and the resulting rate law is the same form as the parabolic rate law. Other models, such as the Point Defect Model, contain parameters that are not well-defined material properties, so their use is limited to empirical fits of data rather than predictive modeling or mechanistic understanding.

6.1.2.1. Use of the Parabolic Rate Law

The derivation of the parabolic rate law for a material that grows two oxide layers is provided in Appendix D. The nomenclature for these equations is listed in Table 6.1.

In the simple case of a single oxide layer which is both the barrier and growing layer, both f_b and f_g are unity. However, if there are multiple layers, like stainless steel, barrier and growth layers must be properly identified along with the transport species A. For stainless steel corrosion in high temperature water, the barrier layer is assumed to be the inner oxide layer. The growth layer is the inner oxide if A is oxygen because it drives the inward growth of the inner oxide layer. The growth layer is the outer oxide if A is metal because metal reaching the outer oxide causes its growth.

Table 6.1. Nomenclature for the parabolic rate law calculations.

a	Oxide cation stoichiometric factor
b	Oxide anion stoichiometric factor
C_A^l	Molar concentration of element A in layer l
D_A^l	Diffusion coefficient of element A in layer l
f_l	Fraction of layer l
$\mathrm{J_A}$	Flux of element A
k_p	Parabolic rate constant
l	Oxide layer – b for barrier and g for growth
M_l	Molecular weight of layer l
N_X^l	Number density of species X in layer l
PBR	Pilling-Bedworth ratio
R	Universal molar gas constant
t	Time
T	Temperature
x	Total oxide thickness
X	Species – M for metal/cations and O for oxygen/anions
μ_A	Chemical potential of element A
μ_A^0	Standard chemical potential of element A
ρ_l	Mass density of layer l

The Pilling-Bedworth ratio (PBR) expresses the oxide thickness relative to the thickness of metal oxidized, and the PBR can conveniently determine the distribution between inner and

outer layers for expressing f_b and f_g. It has been shown in literature [33,42] and in this work that the inner oxide layer occupies the volume of metal oxidized when discounting dissolution. The ratio of metal loss to total oxide thickness is equal to the ratio of inner oxide to total oxide, PBR, because the metal loss is equal to the inner oxide thickness. Therefore, the ratio between the inner and total oxide thickness is $1/\mathrm{PBR}$ and the ratio between the outer and total oxide thickness is $(\mathrm{PBR}-1)/\mathrm{PBR}$. Substituting these values for f_b and f_g, Eq. D.13 can be expanded for both metal and oxygen transport cases below:

$$\mathrm{k_p} = -\left(\frac{\mathrm{M_g}}{\mathrm{a}\rho_\mathrm{g}}\right)\left(\frac{1-\mathrm{PBR}}{\mathrm{PBR}^2}\right)\int_{\mu_M^1}^{\mu_M^2}\frac{\mathrm{D_M^b}C_M^b}{\mathrm{RT}}\,\mathrm{d}\mu_M \qquad \text{Eq. 6.1}$$

$$\mathrm{k_p} = -\left(\frac{\mathrm{M_g}}{\mathrm{b}\rho_\mathrm{g}}\right)\left(\frac{1}{\mathrm{PBR}^2}\right)\int_{\mu_O^1}^{\mu_O^2}\frac{\mathrm{D_O^b}C_O^b}{\mathrm{RT}}\,\mathrm{d}\mu_O \qquad \text{Eq. 6.2}$$

Dissolution may be simply included into the differential equation in Eq. D.11 by including a new term j which is the dissolution rate in nm/h:

$$\frac{\mathrm{d}x}{\mathrm{d}t} = \frac{k_p}{x} - \mathrm{j} \qquad \text{Eq. 6.3}$$

Assuming the dissolution rate is not a function of time or the depth of corrosion, the differential equation in Eq. 6.3 has an analytical solution:

$$x = \frac{k}{j}\left[W\left(-\exp\left[-1-\frac{j^2}{k}t\right]\right)+1\right] \qquad \text{Eq. 6.4}$$

where W is the Lambert W function. The properties of this function are such that it starts from $x(t=0)=0$ and asymptotically approaches a steady state value of $x = k/j$ as $t \to \infty$. The total corrosion rate never approaches zero; rather, the corrosion rate slows from the rapid initial oxidation rate to asymptotically approach the dissolution rate, j, as the oxide grows at the same rate it is dissolved.

It is important to stress that x is the oxide thickness (including both inner and outer layers) and not the total oxidation, but also that j is only the dissolution rate of the barrier (inner) oxide layer. For the case without dissolution (Eq. D.12), the oxide growth rate is proportional to the oxide thickness by the Pilling-Bedworth ratio, and both the total oxidation rate and the oxide film growth rate follow a $t^{1/2}$ dependence. In the case with dissolution (Eq. 6.4), the total oxidation rate, after enough time, approaches a steady state value with a t dependence, but the initial curve resembles a $t^{1/2}$ dependence. Regardless of the parabolic rate constant, the corrosion rate with dissolution will be greater given enough time, although this time may exceed that of the component/application service time.

6.1.2.2. Additional Kinetics Considerations

With the rate laws in Eq. D.12 and Eq. 6.4 and the rate constant expressions in Eq. 6.1 and Eq. 6.2, the corrosion rate can be calculated by filling out the parameters with the thermodynamic model and by considering the corrosion mechanisms. Most of the values are directly provided by the thermodynamic analysis from Thermo-Calc results in the previous section, but there are four missing quantities: oxide densities, diffusion coefficients, the chemical potential reference state, and oxide volume fractions in the inner oxide layer. Furthermore, the discrepancy between inner oxide volume and Cr-rich oxide volume will be discussed. Finally, the calculation of parabolic rate constants from experimental data will be addressed.

Oxide density:

Oxide density was assumed to be the pure iron oxide equivalent theoretical density of 5.2 g/cm^3 for spinel (magnetite) and 5.3 g/cm^3 for corundum (hematite). The oxide density varies between 5.1 g/cm^3 for $FeCr_2O_2$ to 5.4 g/cm^3 for $NiFe_2O_4$ in the Fe-Cr-Ni spinel space [47].

Diffusion coefficients:

Diffusion coefficients for elements in spinel were extrapolated from literature values, namely Dieckmann [55] for Fe, Cr, and Ni and Millot et al. [60] for O. For cations, partial diffusion coefficients (independent of oxygen activity) were taken from Dieckmann [55] and multiplied by point defect concentrations from Thermo-Calc to yield the relevant oxygen activity dependence. There are no sublattices for oxygen vacancies and no oxygen interstitial species in the Thermo-Calc database used, so the full temperature and oxygen activity dependence was extrapolated using the expression $D_O = ap_{O_2}^{-1/2} + bp_{O_2}^{1/6}$ from Millot et al. [60]. Both a and b are partial diffusion coefficients with an Arrhenius temperature dependence. For a the pre-factor is 2.07×10^5 $cm^2 \cdot atm^{1/2}/s$, and the activation energy is 549 kJ/mol. Similarly, for b the pre-factor is 1.73 $cm^2 \cdot atm^{-1/6}/s$, and the activation energy is 276 kJ/mol. The diffusion coefficients for each element are plotted in Figure 6.1 and Figure 6.2 for water and steam cases, respectively. The cation diffusion coefficients closely mirror the vacancy concentrations from Figure 5.76 and Figure 5.77, meaning that the interstitial contribution to cation diffusion is negligible in most cases in this work. The only exception is that Ni in the Fe-rich spinel becomes dominated by interstitial diffusion in the lower oxygen activity portion of regime 4 at both 320 °C and 480 °C. The dependences of cation diffusion on oxygen activity are otherwise identical except for the magnitude: Fe and Ni both have similar diffusion coefficients, with Ni about one order of magnitude lower than Fe. The Cr diffusion coefficient is more than six orders of magnitude below both Ni and Fe, and it is slower than O diffusion below oxygen activity regime 5. Below regime 4, O diffusion approaches the Ni diffusion coefficient within one order of magnitude, but it never exceeds that of either Ni or Fe.

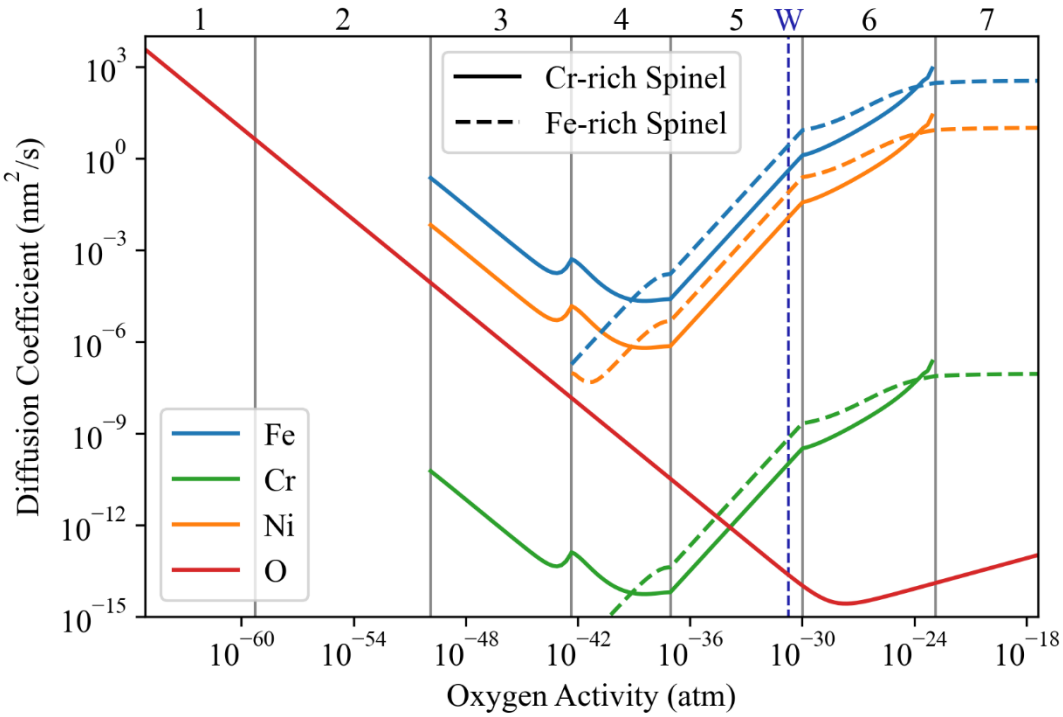

Figure 6.1. Atomic diffusion coefficients for all elements in the 316L corrosion system across oxygen activity at 320 °C and 13.1 MPa.

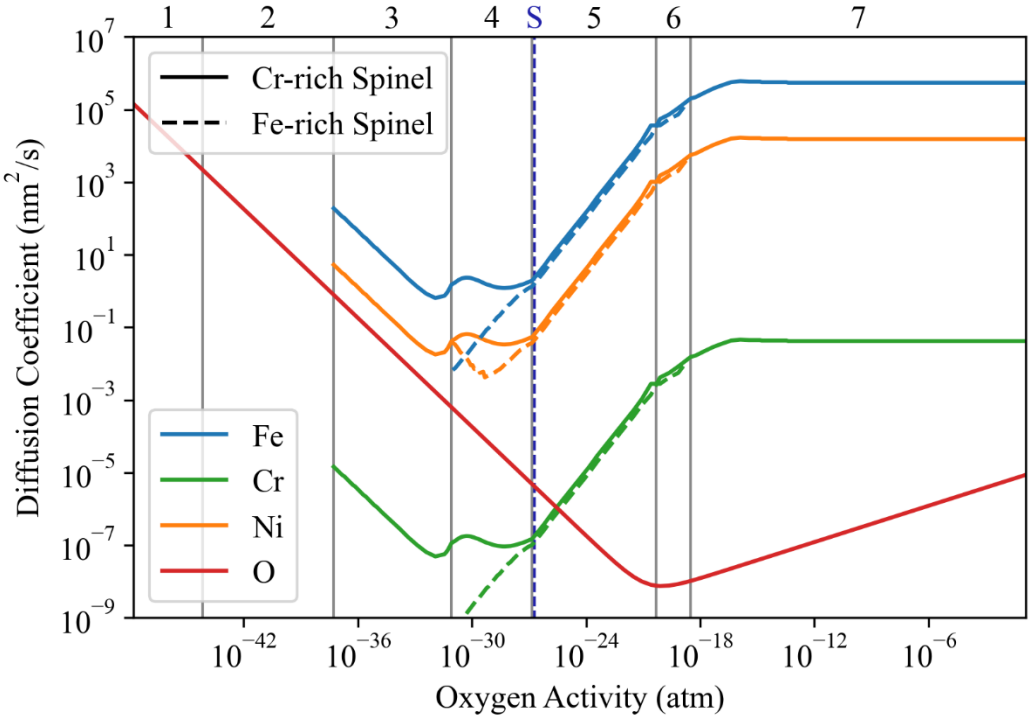

Figure 6.2. Atomic diffusion coefficients for all elements in the 316L corrosion system across oxygen activity at 480 °C and 1.5 MPa.

Chemical potential:

The reference state for integrating the chemical potential in Eq. D.13 is the next necessary component for evaluating the parabolic rate constant. Because the reference state is the lower bound of the integration of k_p through the inner oxide layer, the reference state is properly the oxygen activity at the metal/oxide interface. The reference state most strongly affects the calculation of k_p at lower activities; however, the choice of the reference state is somewhat arbitrary because it is not easily measured. Therefore, the best estimate of the oxygen activity will be chosen based on the phenomena observed at the metal/oxide interface. The transition from regime 1 to 2 would seem reasonable because the first oxide phase begins at that activity, Figure 5.74; however, the FCC phase persists through regime 4, so the transition from 4 to 5 is also reasonable as the end of the metal phase. Therefore, the reference state is bounded by regimes 2–4. The barrier layer in all observations in this work consists of spinel phase, so regime 2 can be eliminated because it contains no spinel. Regime 3 is nearly pure $FeCr_2O_4$, which is observed in EDS scans near the metal/oxide interface in some circumstances as a very thin layer. In the steam condition, Cr_2O_3 does exist as internal oxidation, but it is separate from the barrier layer and thus does not contribute to the parabolic rate constant. Furthermore, Ni enrichment in the metal phase at the metal/oxide interface is also observed in EDS scans as a minor enrichment or an extremely thin layer, so the Ni enrichment in the FCC phase spans regimes 3 and 4. Based on these phenomenological observations, the reference state selected for all conditions is the transition from regime 3 to 4 which allows for all the stated observations at the metal/oxide interface. Another justification is from the integral nature of the expression for the parabolic rate constant in Eq. D.13. If a low oxygen activity with a high diffusion coefficient was chosen as the

reference state, the resulting oxide would have a large portion of the layer with a composition consistent with that reference state, which is not observed in the experimental work.

Oxide volume fraction:

The final consideration is the volume fraction of the phases. The parabolic rate law assumes a singular, uniform oxide barrier layer, but the case of high temperature stainless steel corrosion is more complex as both Fe-rich and Cr-rich spinels may contribute to transport. Because corundum only exists in the irrelevant regimes 2, 6, and 7 (irrelevant because they do not coexist with the end of the metal phase), this phase was not treated as a potential contributor to the barrier layer. As established earlier, the inner oxide layer may contain a mixture of distinct oxide phases depending on the environment. Using a material balance and a combination of the Thermo-Calc results and the kinetic information, the relevant volume fractions in the inner oxide layer can be determined. The Pilling-Bedworth ratio for each phase was calculated separately, and the results are given in Figure 6.3 and Figure 6.4. Due to the lower diffusion coefficient for Cr, the diffusive mobility of phases in ascending order in all regimes are FCC > Cr-rich Spinel > Corundum > Fe-rich Spinel. When any two of these phases are competing to fill the inner oxide volume, the oxide phase with lower Cr content is forced to diffuse to the outer oxide where volume is effectively unlimited. Most of the inner oxide volume in regimes 4–6 is occupied by Cr-rich spinel in both cases. It is useful to note that Fe-rich spinel occupies some portion of the inner oxide in the 320 °C water condition in regimes 4 and 5. At 480 °C, the miscibility gap between Fe-rich and Cr-rich spinel has shrunk enough to yield no Fe-rich spinel in the inner oxide in regime 5. However, there is a portion of regime 4 where there is some Fe-rich spinel in the inner oxide in steam.

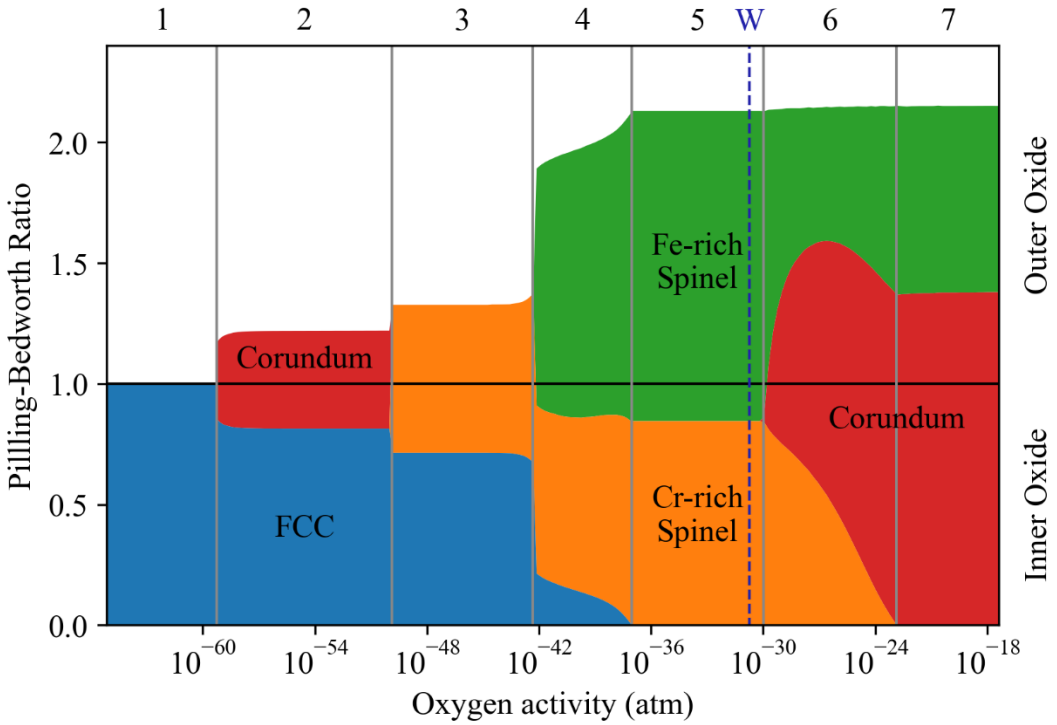

Figure 6.3. Pilling-Bedworth ratio for each phase in 320 °C 13.1 MPa Thermo-Calc modeling of 316L corrosion system separated into inner and outer oxide layers.

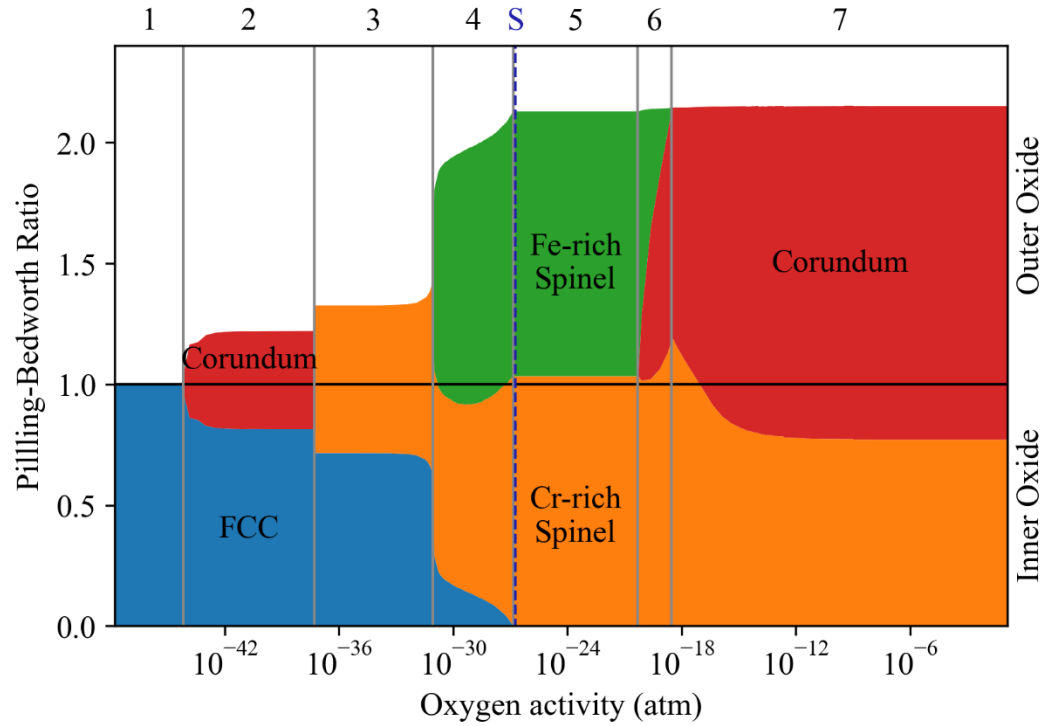

Figure 6.4. Pilling-Bedworth ratio for each phase in 480 °C 1.5 MPa Thermo-Calc modeling of 316L corrosion system separated into inner and outer oxide layers.

A brief comparison of the PBR ratio in Figure 6.3 and Figure 6.4 to the elemental analysis in Figure 5.47 and Figure 5.66 shows a good match in the distribution of oxides between the inner and outer layers. In steam (Figure 5.66), the Fe-rich spinel and Cr-rich spinels are exclusive to their respective layers. In water (Figure 5.47), the Cr-rich spinel is entirely within the inner oxide layer, and the outer oxide layer is only Fe-rich spinel. But there are some small nodes of Fe-rich spinel within the inner oxide layer which is predicted by the partial overlap of Fe-rich spinel in the inner oxide PBR in Figure 5.47.

Separation into inner and outer layers warrants further discussion. Within regimes 3–5, all Cr from the alloy is in the spinel phase where its diffusion is much slower than Fe or Ni. The slow diffusion effectively traps all Cr at the location where it first enters the spinel phase: in the inner oxide layer. The equilibrium composition of the Fe-rich spinel phase that emerges in regime 4 has very little Cr, so it can be formed with no Cr without a significant penalty to the Gibbs free energy. Because Fe and Ni are both mobile, the Fe-rich spinel may move via atomic diffusion, and the chemical potential gradient (Figure 5.78 and Figure 5.79) drives the motion of this phase toward the highest oxygen activity: the outer oxide. This explains not only how the outer oxide generally forms by the diffusion of Fe and Ni outwards, but also that all Fe-rich spinel will egress the inner oxide layer. Therefore, any Fe-rich spinel in the inner oxide layer is excess volume.

Where the Cr-rich spinel does not fully occupy the inner oxide layer (in regimes 4–7 at 320 °C), the excess volume is not necessarily occupied by another oxide phase. Despite the excess volume in the inner oxide, it is thermodynamically favorable for the Fe-rich spinel to evacuate the inner oxide and move to the outer oxide. Assuming the thermodynamic oxide compositions are realized, there are two possibilities to account for the excess volume when

kinetic limitations are considered. First, the Fe-rich spinel may remain within the inner oxide layer as implied by Figure 6.3 and Figure 6.4. Second, the Fe-rich spinel may move to the outer oxide leaving porosity in the inner oxide. Therefore, the excess volume in the inner oxide layer must consist of pores, more Fe-rich oxide phases, or a mixture of the two.

Because there is a degree of freedom in the inner oxide volume between the two spinel phases and porosity, the calculation of the parabolic rate constant will be limited by the extremes of the excess volume being entirely filled with porosity or entirely with Fe-rich spinel. Consequently, the fraction of oxide that functions as the barrier layer, f_b, is subdivided between the volume fractions of the constituent phases of the barrier layer, and an effective k_p can be calculated as follows.

$$k_p^{\text{eff}} = \sum_i v^i k_p^i \qquad \text{Eq. 6.5}$$

where v^i is the volume fraction of phase i, and k_p^i is the parabolic rate constant of phase i, and k_p^{eff} is the effective combination parabolic rate constant for the layer. The minimum k_p occurs when there is no Fe-rich spinel in the inner oxide layer and when the excess volume is only porosity, assuming cation transport does not occur through pores ($k_p^{\text{pores}} = 0$). In this case, the effective k_p will be the product of k_p in the Cr-rich spinel phase and its volume fraction. The maximum effective k_p is without porosity, and its value is the sum of the k_p in each spinel phase weighted by their respective volume fractions in the inner oxide layer.

To utilize both 24 h and 72 h experimental data, inner oxide thickness measurements were converted to parabolic rate constants to plot alongside calculations. Since oxidation rate measurements were split into two corrosion modes, only mode 2 was used. This is justified because the mode 1 corrosion has a minor contribution to the overall corrosion rate and has very

little dependence on time. Mode 1 corrosion in 480 °C steam (both inner oxide thickness and total oxidation) did not increase from 24 h to 72 h within error. Mode 1 oxide thickness in 320 °C water increased between 24 h and 72 h in the non-irradiated region.

Mode 2 oxide thickness, however, increases with time in a manner mostly consistent with the parabolic rate law for all cases. Therefore, parabolic rate constants were calculated for each experimental condition using the mode 2 oxide thickness data, where available, from Table 5.8 using Eq. D.12 and listed in Table 6.2 and plotted in Figure 6.5; otherwise, total mean values were used. In addition, exclusively for irradiated and radiolysis regions of W72, the corresponding parabolic rate constant and dissolution constant were calculated using Eq. 6.4. The diffusion coefficients for the equation are provided as a function of oxygen activity in Figure 6.1 and Figure 6.2. The concentrations of all relevant elements are plotted as a function of oxygen activity in Figure 5.73 and Figure 5.75.

Table 6.2. Parabolic rate constants and dissolution constants calculated from the experimental data in Table 5.9.

Experiment	Region	k_p (nm^2/h)	j (nm/h)
X24	Non-irradiated	528	0.30
X72	Non-irradiated	316	0.06
A24	Non-irradiated	2.50	-0.08
W24	Non-irradiated	886	-0.22
W24	Radiolysis	16.6	-0.14
W24	Irradiated	21.8	-0.37
W72	Non-irradiated	371	-0.21
W72	Radiolysis	25.5	0.35
W72	Irradiated	22.5	0.28
S24	Non-irradiated	20.8	-0.14
S24	Radiolysis	19.4	-0.28
S24	Irradiated	49.6	0.33
S72	Non-irradiated	13.3	-0.07
S72	Radiolysis	19.8	-0.01
S72	Irradiated	31.1	-0.28

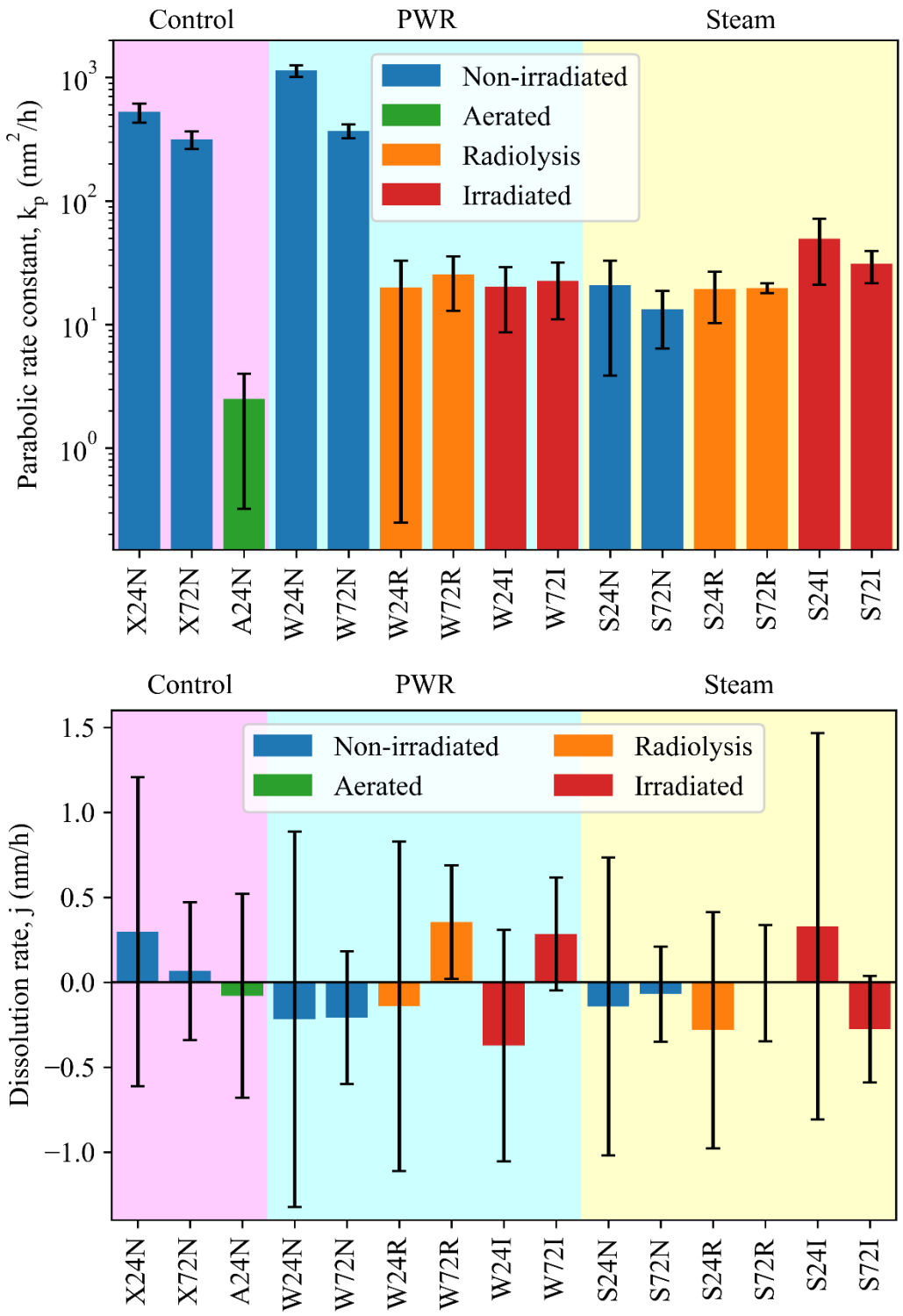

Figure 6.5. Parabolic rate constants and dissolution constants from Table 6.2.

In summary, all the missing parameters needed to calculate the parabolic rate constant were obtained. The diffusion coefficients were calculated for each element in both spinel phases

in Figure 6.1 and Figure 6.2. The oxide densities were assumed to be equal to the theoretical density of the pure iron oxide equivalents (magnetite and hematite). The chemical potential reference state was set at the transition oxygen activity between regimes 3 and 4. Volume fractions of different oxide phases within the inner oxide layer were calculated accounting for the possibilities of excess volume within the inner oxide layer. These identifications can be applied to Eq. 6.1 and Eq. 6.2 in calculating the overall parabolic rate constant, and they provide a framework for determining the distribution of oxides between the two layers. Finally, measurements of oxide thickness and total oxidation were converted into parabolic rate constants to compare with calculated values.

6.1.2.3. Application of the Parabolic Rate Law at 320 °C

For non-irradiated regions in 320 °C water, the mode 2 (thick) parabolic rate constants are plotted alongside calculations of the same using Fe and O solid state diffusion (from Figure 6.1) in Figure 6.6. Since both Fe and O transport are necessary for the growth of both oxide films, the lowest calculated rate constant should be that of the rate-limiting step. The 24 h data point is between the calculated Fe-limited k_p, and the 72 h data point is just slightly below the minimum calculated Fe-limited k_p; therefore, the agreement is good. However, solid-state oxygen diffusion clearly underestimates the measured parabolic rate constants, so the mechanism of oxygen transport cannot be solid state O^{2-} diffusion. As suggested by Robertson and others [9,34,36,39,119], oxygen transport through the inner oxide layer is facilitated by some fast path of either grain boundaries or a network of pores. Dieckmann [120] has shown that water molecules and OH^- anions may also transport through solid state diffusion in both spinel and corundum phases. Regardless of the precise mechanism, oxygen transport must be the rate-limiting step responsible for the low corrosion rate observed in the aerated case because cation

diffusion is too fast to be rate limiting. Otherwise, the corrosion rate would increase with oxygen activity which is contrary to the decrease observed between hydrogenated and aerated water. The calculation of k_p is on the assumption that cation transport is rate-limiting. Therefore, the disagreement between the calculation and the aerated corrosion rate data shows that cation transport is not rate-limiting because the corrosion rate decreases even when cation transport coefficients and chemical potential gradients both increase.

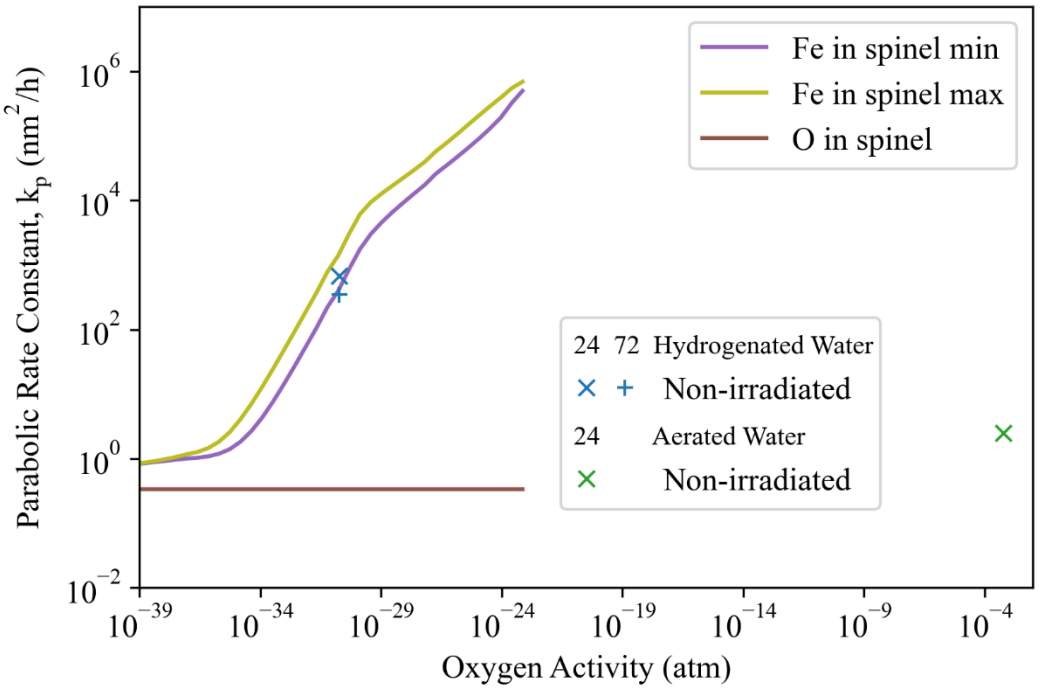

Figure 6.6. Measurements in non-irradiated regions (of W24 with X24, W72 with X72, and A24) and calculations of parabolic rate constants using Fe and O diffusion in spinel (using Eq. 6.1 and Eq. 6.2 respectively) for 316L in 320 °C 13.1 MPa water as a function of oxygen activity.

There is good agreement between the hydrogenated water condition measurements and the Fe-limited k_p calculation. However, the aerated condition measurement is entirely incompatible with Fe-based k_p. There is no slower mechanism available for cation transport outward than solid state diffusion through the inner oxide, and this mechanism would only increase the corrosion rate with increasing oxygen activity as suggested by the monotonic nature of the calculated k_p. Even for the hydrogenated case, the rate-limiting step may or may not be

cation transport, although the general agreement with the calculation makes it a feasible option. In either case, a different oxygen transport mechanism must be identified to account for the oxygen transport rate required for both hydrogenated and aerated condition corrosion rates.

Robertson [9] and Perrin et al. [43] show that oxygen reaches the metal/oxide interface by a fast transport path. Rouillard and Martinelli [39] present an "available space model" that explains the balance between the rate of oxygen transport through pores in the oxide and cation transport. Essentially, the pore network can only form by the transport of cations to the outer layer, thus limiting the rate of oxygen ingress via pores to be proportionate to cation transport. As oxygen reaches its destination at the metal/oxide interface, it creates more oxide which fills the pores (with Fe-rich spinel) thereby preventing further oxygen from reaching the interface. Countering this effect, cation (mostly Fe and Ni) transport to the outer oxide layer consumes the Fe-rich spinel in the inner oxide layer forming new pores which facilitate oxygen transport. In this scheme, the oxygen transport through pores can never exceed the rate of cation transport outward which matches experimental results in Figure 6.6 because the experimental data are all below the maximum of the cation diffusion curve. If oxygen transport exceeds cation transport, then the inner oxide would grow as a mixture of the two spinel phases, and the resulting stress would push the inner oxide layer above the metal. This would result in an oxide that does not preserve the original metal surface unlike the observations in this work and other stainless steel corrosion research [33,38,39,41,42]. However, the "available space model" preserves the original metal surface as the upper boundary of the inner oxide while explaining the role of oxygen and cation transport with porosity.

Dieckmann [120] suggests the transport of oxygen-bearing compounds through solid state diffusion in oxides may enhance oxygen transport to the metal/oxide interface. This process

would serve to increase the effective oxygen diffusion coefficient as a function of water pressure in the environment. Because this mechanism does not require fast paths for diffusion, it may apply to all the possible oxidation conditions; however, this contradicts the evidence for fast path transport. Most likely, the mode 1 oxidation could be described by solid state transport of oxygen-bearing species, whereas mode 2 corrosion appears to be accelerated by fast path (porous) transport of oxygen to the metal/oxide interface. The nucleation of pores will be somewhat stochastic, resulting in the high variance of mode 2 corrosion rates.

Grain boundaries in the oxide are unlikely to be the feature responsible for controlling the corrosion because of their relationship with Cr. Terachi et al. observed a decrease in grain size of the inner oxide layer with increasing Cr content in the alloy [33]. Furthermore, the corrosion rate on these same alloys decreased with increasing Cr content. It is likely that the inner oxide grain size is related to the volume fraction occupied by Fe-rich spinel, which should decrease with increasing Cr content of the alloy. Regardless of the reason for the grain size change, higher Cr alloys have more grain boundaries, yet the corrosion rate decreases with Cr. This leaves porosity as the key feature for facilitating oxygen transport as necessary for the corrosion reaction. Porosity and its relationship to corrosion modality will be discussed further in Section 6.1.2.5.

In summary, corrosion in the hydrogenated and aerated water conditions is rate-limited by oxygen transport through the inner oxide layer. Oxygen transport through solid-state diffusion, including grain boundaries, is responsible for mode 1 corrosion. Oxygen transport through networks of pores is identified as a mechanism consistent with mode 2 corrosion.

6.1.2.4. Application of the Parabolic Rate Law at 480 °C

As with the previous section, parabolic rate constants from the non-irradiated regions of S24 and S72 in Table 6.2 are plotted with calculated parabolic rate constants in Figure 6.7. Here,

the rate constants calculated from experimental data are significantly below the Fe-based calculation and are slightly above the O-based calculation. Because the parabolic rate constant is higher than the calculated values for oxygen diffusion, some mechanism must increase the transport rate of oxygen above its solid-state diffusion coefficient. This mechanism for oxygen transport is, therefore, the rate-limiting step.

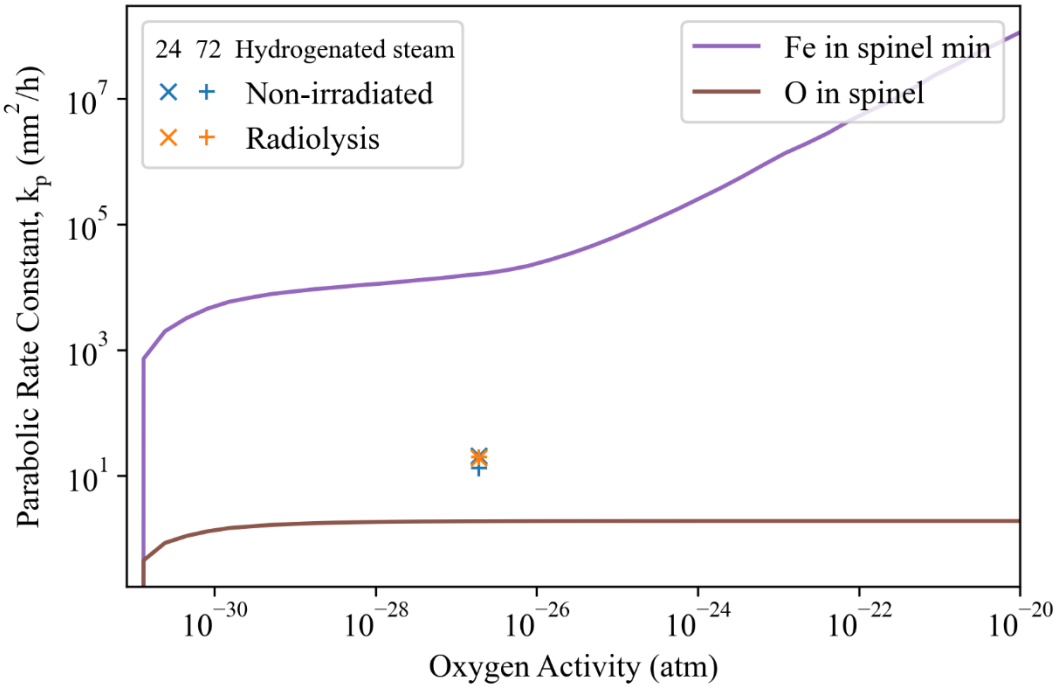

Figure 6.7. Measurements in non-irradiated regions and calculations of parabolic rate constants using Fe and O diffusion in spinel for 316L in 480 °C 1.5 MPa argon-steam as a function of oxygen activity.

As discussed in detail in the previous section, grain boundaries and porosity are both possible fast paths for the transport of oxygen to the metal/oxide interface. Another possibility is the transport of oxygen-bearing compounds though solid-state transport in the inner oxide layer. Despite the higher temperature, the parabolic rate constants are lower for the steam condition than the hydrogenated water condition. One aggravating factor for corrosion rate increase is that an elevated temperature increases the transport coefficients of all species relative to the water conditions. However, the relatively low pressure of water in the steam environment results in a decrease in driving force for transport because the oxygen activity is roughly proportional to the

water pressure. Water pressure can also more directly impact the corrosion rate if water molecules are the oxygen-bearing species that reach the metal/oxide interface [120]. Another mitigating factor is the lower excess volume, and therefore lower expected porosity, which will reduce oxygen transport. All these factors combine to position the steam parabolic rate constants one order of magnitude below the hydrogenated water condition and one above the aerated water condition shown in Figure 6.6.

One similarity between the hydrogenated steam and aerated water conditions is the magnitude of mode 1 corrosion. There are many environmental parameters that have changed between the two conditions, but mode 1 oxidation is ~7 nm for S24 and S72, and the total average oxidation in A24 is 11.0 nm. Mode 2 corrosion rates in steam are higher than those in aerated water. It is unclear if the mechanisms are the same between the two conditions for mode 2 corrosion because there are both aggravating and mitigating factors that obscure the mechanism. However, the excess volume in the inner oxide layer shares some features between the two conditions that will be discussed further in the next section.

A major difference between the water and steam conditions is the behavior of Ni. From the EDS data in steam (Figure 5.71), there is little to no incorporation of Ni into either inner or outer oxide layers, whereas Ni is incorporated into both oxide layers in water (Figure 5.47). Instead, Ni is highly enriched in the metal at the metal/oxide interface, and some metal protrusions into the inner oxide layer may be relatively stable in a manner consistent with regime 4 corrosion. This behavior is expected throughout the inner oxide layer because the environment oxygen activity is only just above the transition to regime 5, thus regime 4 behavior will dominate most of the inner oxide. Furthermore, the chemical potential of Ni in Figure 5.79

shows that there is a greater driving force for Ni to diffuse back into the bulk metal rather than incorporate into the oxide.

In summary, the rate-limiting step for corrosion in 480 °C argon-steam is consistent with solid state diffusion of oxygen through the inner oxide layer for mode 1 corrosion and oxygen transport through pores for mode 2 corrosion. Notably, these are the same rate-limiting steps identified for corrosion in 320 °C water in both aerated and hydrogenated conditions. The increased temperature yields higher transport coefficients in the inner oxide, but the low water pressure and lower inner oxide porosity decrease the transport of oxygen. This results in lower overall oxidation rates in 480 °C hydrogenated steam compared to 320 °C hydrogenated water.

6.1.2.5. Corrosion Modality and Porosity

A key factor in the proposed inner oxide growth mechanism in both 320 °C water and 480 °C steam is porosity as a transport fast path for oxygen, which controls the overall corrosion reaction rate. Fast paths facilitating higher corrosion rate provide a rationalization for the separation between mode 1 and mode 2 corrosion. Pores are not distributed uniformly throughout the oxide; where pores connect the metal to the environment the corrosion rate is high, and where the oxide is dense or has unconnected pores, the corrosion rate is low. Therefore, a more detailed analysis of inner oxide porosity in the different environments is needed to better address the differences in corrosion rate.

The “available space model” by Rouillard and Martinelli [39] fits well with the Thermo-Calc analysis performed earlier where the “available space” in the inner oxide layer is accommodated by the excess volume. Excess volume is defined by the thermodynamics of the inner oxide where there is more volume than necessary to contain the (immobile) Cr-rich spinel. The Cr-rich spinel is immobile because of the low diffusion coefficient of Cr and the free energy

of mixing which resists concentrating Cr in the spinel phase. The Fe-rich spinel phase has virtually no Cr, so the cations may transport to the outer layer and form oxides there. This makes any volume occupied by Fe-rich spinel in the inner oxide layer excess volume. The excess volume is split between pores and Fe-rich spinel, and the pores created by Fe and Ni diffusion to the outer oxide layer are the "available space" for new oxides at the metal/oxide interface.

Excess volume changes as a function of oxygen activity, and oxygen activity in the inner oxide spans the range from the metal to the environment. On the assumption that oxygen transport through the inner oxide is the rate limiting step, the logarithm of the oxygen activity will be linear through the thickness of the inner oxide. The result is a non-uniform distribution of excess volume with depth in the inner oxide layer, and the excess volume is visualized in Figure 6.8. In hydrogenated water the inner oxide has a relatively constant excess volume, and thus it is continuously porous and highly permeable for oxygen transport. In contrast, the aerated water condition has a distinct change in porosity from the metal-adjacent sublayer that is porous to an environment-adjacent sublayer that has no excess volume i.e., an impermeable layer. Finally, the steam condition has a lower overall magnitude of porosity which tapers off near both the environment and metal.

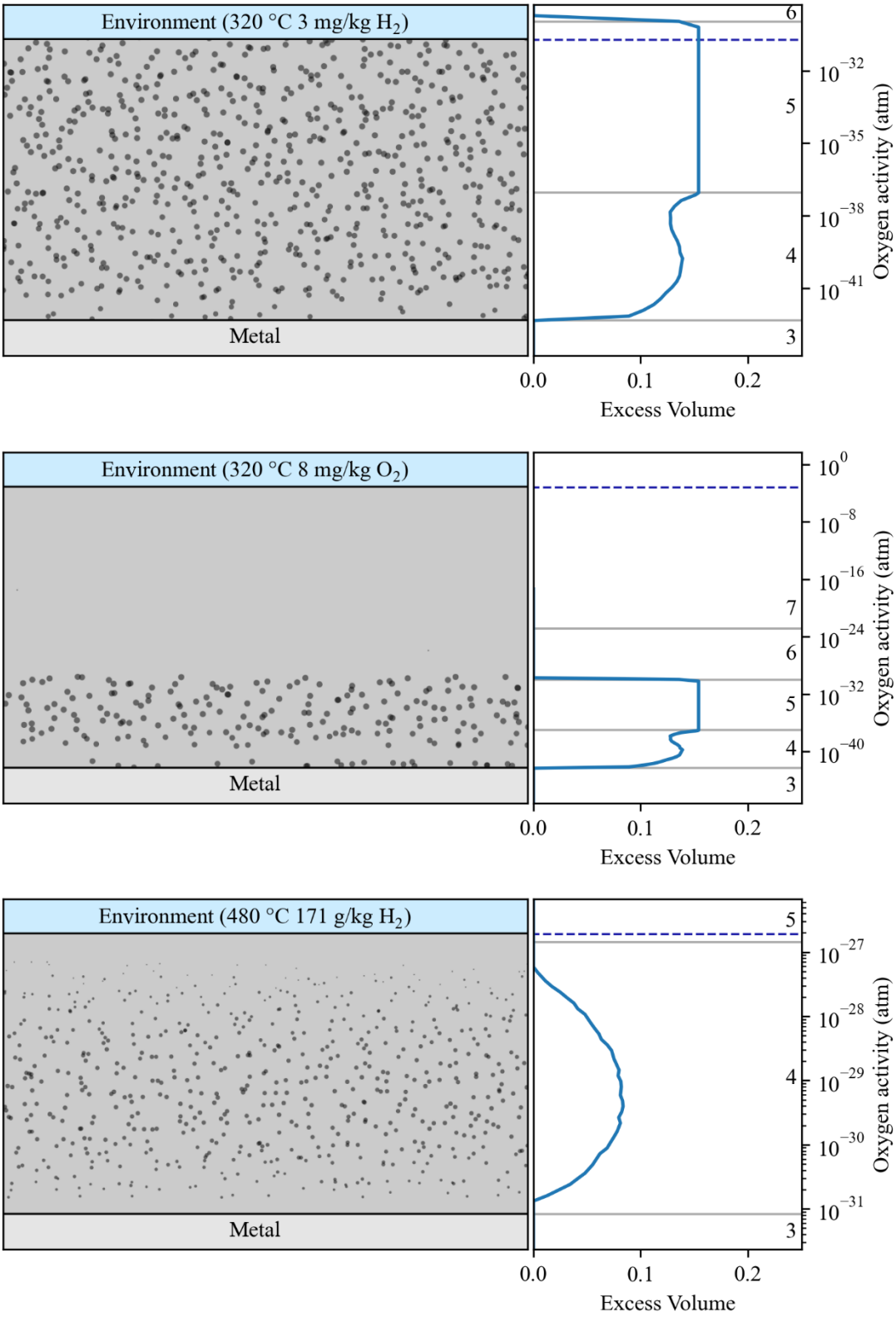

Figure 6.8. Visualization of inner oxide excess volume in the hydrogenated water condition (top), aerated water condition (middle), and hydrogenated argon-steam condition (bottom) with the nominal oxygen activity of the environment denoted by the dashed line.

For comparison with the calculated porosity distributions in Figure 6.8, some images from hydrogenated water conditions are provided in Figure 6.9 and from hydrogenated argon-steam in Figure 6.10. The radiolysis region in Figure 6.9 has a significant amount of inner oxide dissolution with little porosity except directly adjacent to the metal. The irradiated region has similar porosity localized to the metal/oxide interface. The non-irradiated region has a fine distribution throughout the layer, with higher concentrations of pores where the inner oxide is thickest. This matches the general expectation from Figure 6.8.

The images from steam in Figure 6.10 show different distributions of porosity in all three regions. The non-irradiated region is mostly dense with a few small pores. The radiolysis region has some significant porosity in the inner oxide, mostly concentrated at either interface, but some porosity is also present in the center. The irradiated region has many pores throughout the inner oxide that are largest near the metal/oxide interface. None of these regions match very well with the expectation in the steam environment from Figure 6.8. The increased porosity in the radiolysis region relative to the non-irradiated region is most likely an effect of radiolysis on the oxide. The large pores in the irradiated region are consistent with a displacement damage-driven void growth mechanism occurring in the inner oxide. Because the irradiated region shares the radiolysis condition with the radiolysis region, these smaller pores nucleate from the interaction with the environment and grow with displacement damage.

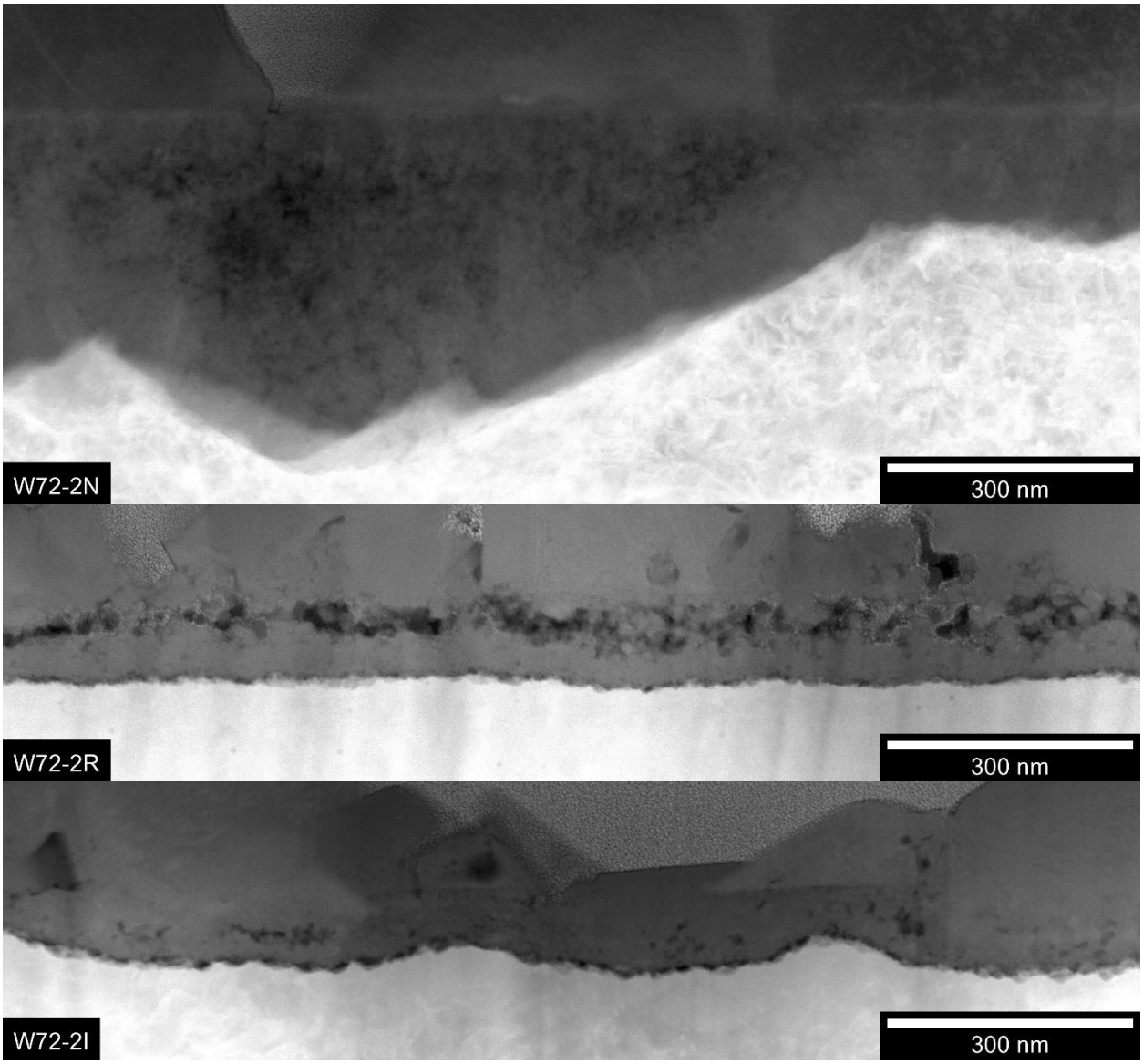

Figure 6.9. HAADF STEM micrographs of oxide layers representing porosity from the non-irradiated, radiolysis, and irradiated regions of experiment W72-2.

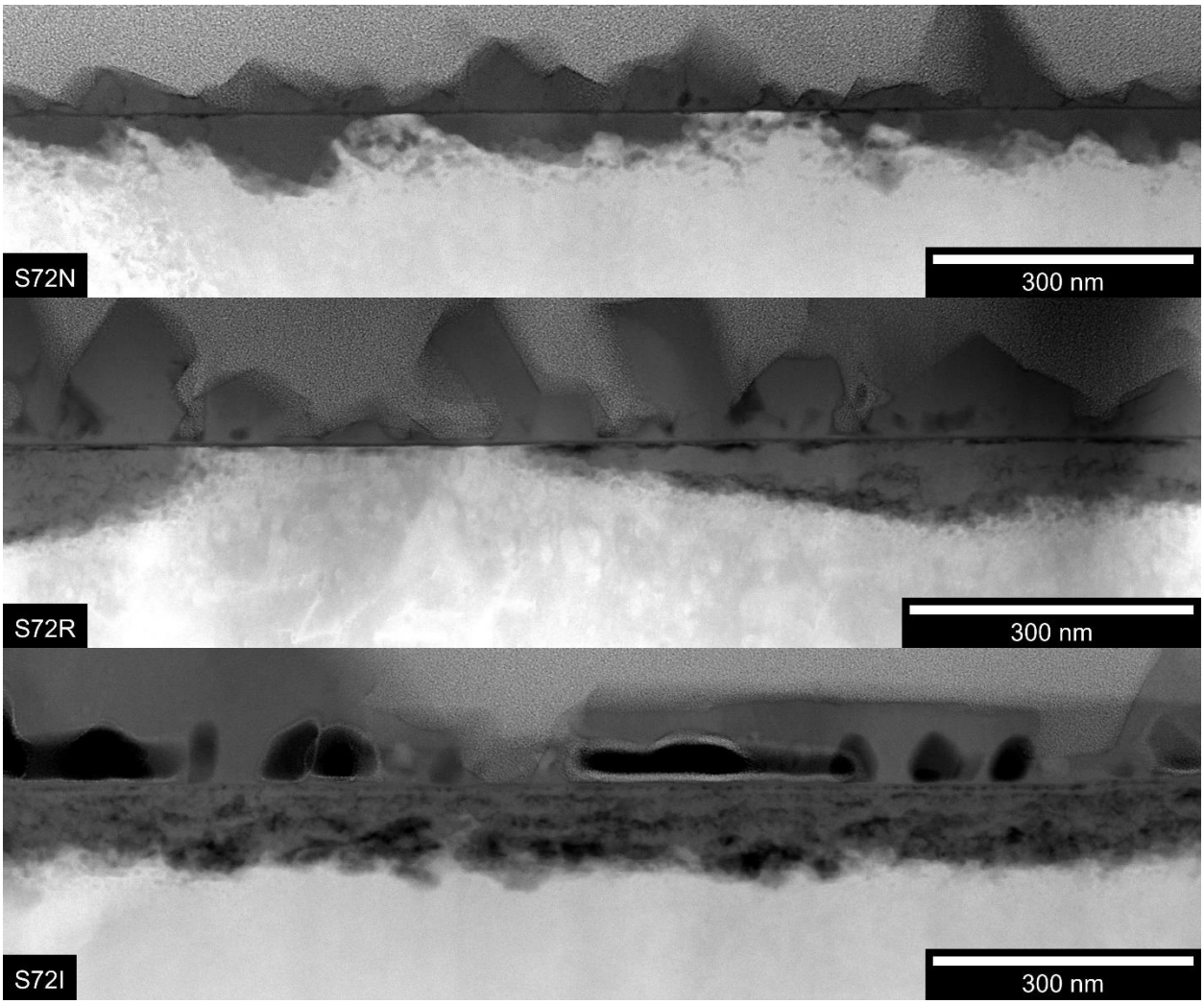

Figure 6.10. HAADF STEM micrographs of oxide layers representing porosity from the non-irradiated, radiolysis, and irradiated regions of experiment S72.

Porosity in the inner oxide facilitates the transport of oxygen by creating a fluid phase within the inner oxide layer with a higher transport coefficient. This complicates the calculation of the parabolic rate constant by introducing an additional oxygen activity dependence to the diffusion coefficient which is integrated in Eq. D.13. Allowing for the possibility that pores are somewhat interconnected, a parallel resistance model yields a maximum effective transport coefficient for the inner oxide layer.

$$D_{0,\text{eff}} = \epsilon D_{0,\text{pore}} + (1-\epsilon) D_{0,\text{ox}} \qquad \text{Eq. 6.6}$$

Here, ϵ is the volume fraction of pores in the inner oxide layer, and D_0 is the diffusion coefficient in the solid oxide, the pores, or the effective total inner oxide. However, this expression in Eq. 6.6 does not account for the changing porosity with oxygen activity throughout the inner oxide layer. This requires a series resistance model to yield an effective porosity.

$$\epsilon_{\text{eff}} = \left[\frac{1}{\mu_0^2 - \mu_0^1}\int_{\mu_0^1}^{\mu_0^2}\frac{d\mu_0}{\epsilon}\right]^{-1} \quad \text{Eq. 6.7}$$

Assuming a minimum porosity of 1%, the effective porosity is 12.7% in hydrogenated water, 1.42% in aerated water, and 2.36% in steam. To demonstrate that porosity is the controlling factor, the oxygen diffusion coefficient in the oxide ($D_{0,\text{ox}}$) is assumed to be negligible in Eq. 6.6. The diffusion coefficient for oxygen in pores ($D_{0,\text{pore}}$) is a gas diffusion coefficient which is proportional to $\sqrt{T}$, and the parabolic rate law is itself proportional to the diffusion coefficient. Therefore, excess volume can be used to calculate a parabolic rate constant for each experimental condition by fitting to the measured data as in Eq. 6.8.

$$k_p^{ev} \propto \epsilon_{\text{eff}}\sqrt{T} \quad \text{Eq. 6.8}$$

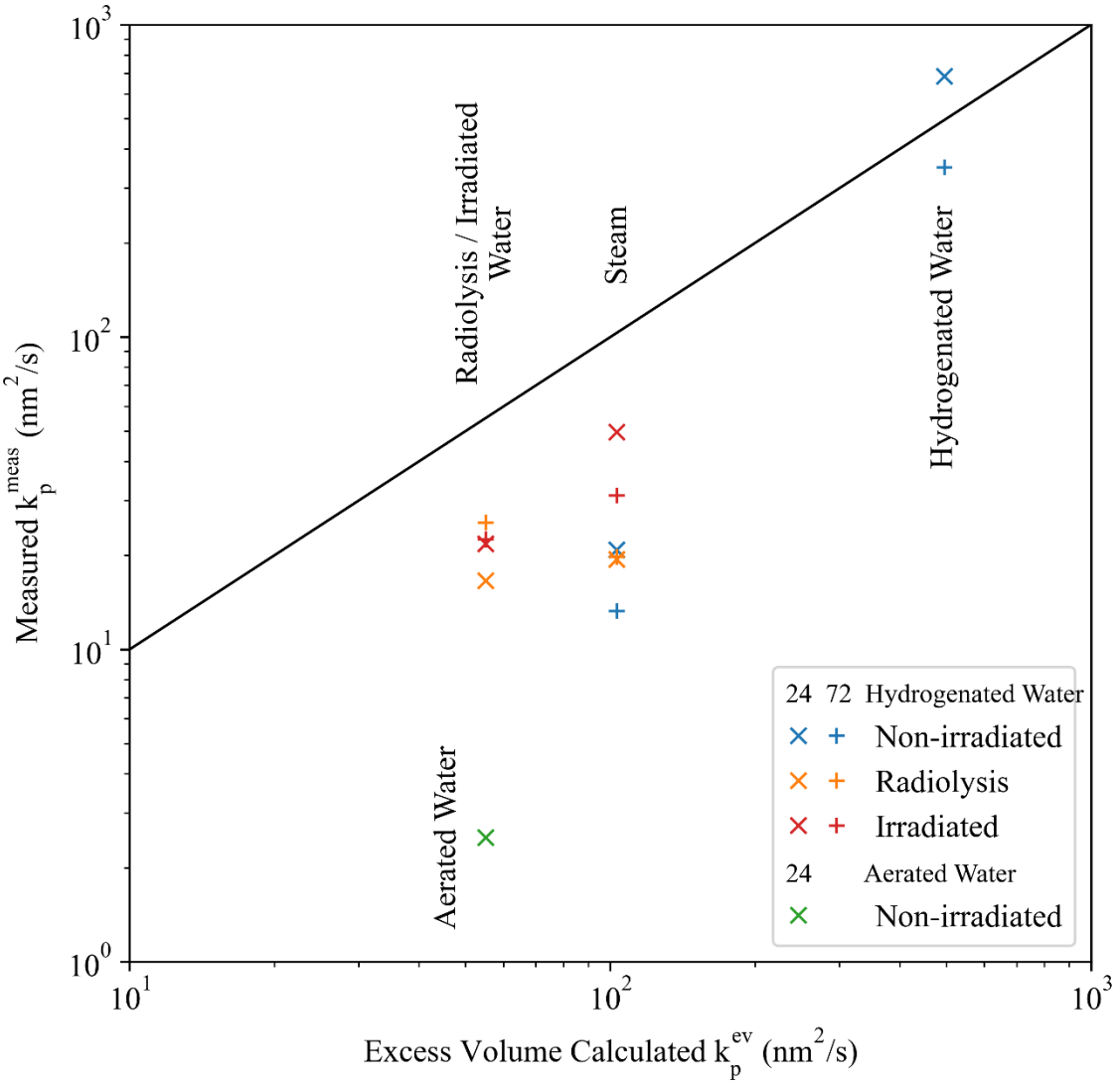

Figure 6.11. Correlation between parabolic rate constants as measured on the vertical axis and calculated using excess volume on the horizontal axis. The identity line is the solid diagonal line where the calculation and measurement are equal.

Comparing the parabolic rate constants as measured and calculated from excess volume reveals a clear correlation in Figure 6.11. The highest oxidation rate (hydrogenated water) has the most consistent excess volume; the lowest oxidation rate (aerated water) has the least excess volume or the largest non-porous sublayer. Again, steam is intermediate in both the excess volume and oxidation. It bears mentioning that the $\ln a_{O_2}$ (oxygen activity) is not necessarily linear with depth into the oxide layer, particularly if it is permeable to oxygen. However, the

chemical potential is proportional to $\ln a_{O_2}$, so it is a reasonable assumption where chemical potential is the driving force for oxygen transport.

Portions of the inner oxide without excess volume are not necessarily non-porous; however, the thermodynamics favor pore formation with excess volume because there is always a chemical potential driving force exerted on the Fe toward the outer oxide layer. If there is no excess volume or pores, the Cr-rich spinel may shed some Fe or Ni to allow some pore formation when oxygen activity decreases in the inner oxide layer as it is consumed. This kind of porosity will be much smaller than that accommodated by excess volume, but it enables the corrosion reaction to continue with rates well above those allowed by solid-state oxygen diffusion by increasing the permeability. It follows that there are areas both with and without porosity that naturally result in bimodal corrosion rates as observed. Bimodal, and generally variable, inner oxide thicknesses are consistent with a corrosion mechanism that is limited by porous transport of oxygen.

The substantial differences in localized corrosion are difficult to explain without a feature such as porosity. Take for instance W24 thickness from Table 5.9 where there is 21.4 nm thickness in mode 1 and 206.2 nm in mode 2. The parabolic rate constants calculated from these two values yield 9.54 nm^2/h in mode 1 and 886 nm^2/h in mode 2 which implies a difference by nearly a factor of 100 between the two modes. The only parameter in the parabolic rate constant that could possibly accommodate this discrepancy is the diffusion coefficient, yet there is no observed composition change which would result in such drastic changes in the material properties. Furthermore, these oxidation modes coexist within a single micron of distance across the surface, so any features that cause this modality must be nanoscale. Porosity is the most promising theory for explaining the corrosion modes observed because it fits these requirements.

The distinction between corrosion modes has been noted in literature, sometimes as localized corrosion (not to be confused with pitting), but only quantified by Sumner et al. [42]. The relative quantity of each mode is extremely important for the overall average oxidation. Comparing the non-irradiated regions of W24 and W72 with the control experiment X72 from Table 5.9 and reproduced in Figure 6.12, the inner oxide thickness and total oxidation measurements are in good agreement for both mode 1 and mode 2. One exception is mode 1 for X24 (Figure 5.5) and W72 (Figure 5.30) where the mode is completely and nearly absent, respectively. For W72, the value of mode 1 is skewed to higher values by the broad peak of mode 2 captured below the threshold, and the much lower proportion of mode 1 oxide present. Mode 2 matches within error for X72 and W72, but mode 2 for X24 is slightly lower than W24. This difference is likely just experimental variance from across the samples. X24 has double the average inner oxide thickness of W24 because the mode 1 fraction for W24 is 63% compared to the 0% for X24. Similarly, the average oxide thickness is greater for W72 than X72 due to the difference in fraction. Large scatter in corrosion rate data may be easily caused by a change in the fraction of corrosion modes rather than a change in the corrosion kinetics.

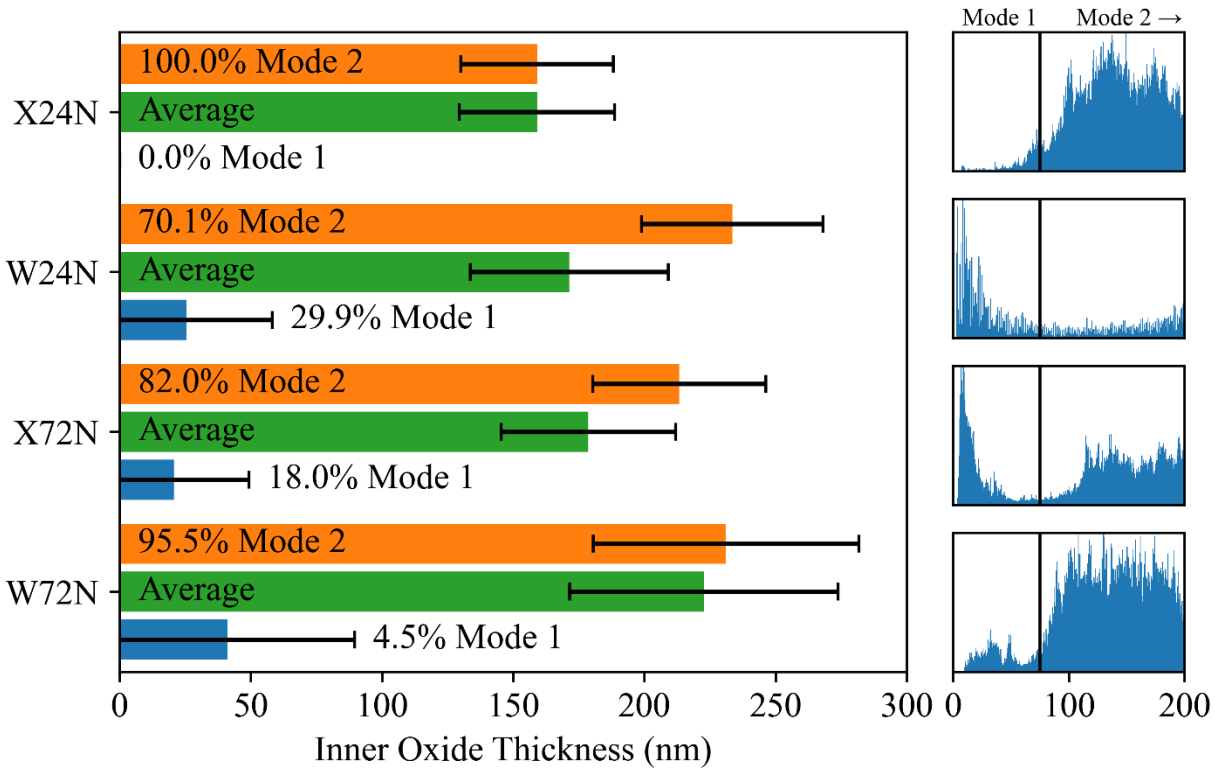

Figure 6.12. Corrosion modes and averages for control and non-irradiated experiments in hydrogenated water from Table 5.9. On the right are the inner oxide histograms to illustrate the differences between mode 1 corrosion.

One issue with this excess volume model is the presence of mode 1 corrosion in the hydrogenated water condition. If porosity in hydrogenated water extends through the inner oxide layer, then there should only be minor differences in local inner oxide thickness, but mode 1 corrosion between 20~40 nm is observed. Stainless steels grow a thin and protective oxide film in air, and this air-grown film is most likely the progenitor of mode 1 corrosion. If the entire surface is coated in a non-porous oxide film before exposure in the autoclave, there is a necessary step of breaking down, or bypassing, this initial layer. This first step in corrosion slows the initial corrosion rate in all conditions. Thus, in the hydrogenated water condition, the fraction of mode 1 corrosion is the fraction of the air-grown film remaining on the surface as a protective layer. In some cases, like the non-irradiated region of W72, this layer is nearly absent, and in others, like X24, the layer is totally absent. The difference between these samples is likely some

small difference in the surface condition before exposure such as the time between polishing and exposure in the autoclave. Another visualization including the air-grown layer is presented in Figure 6.13. A similar example from W24-4 is presented in Figure 6.14.

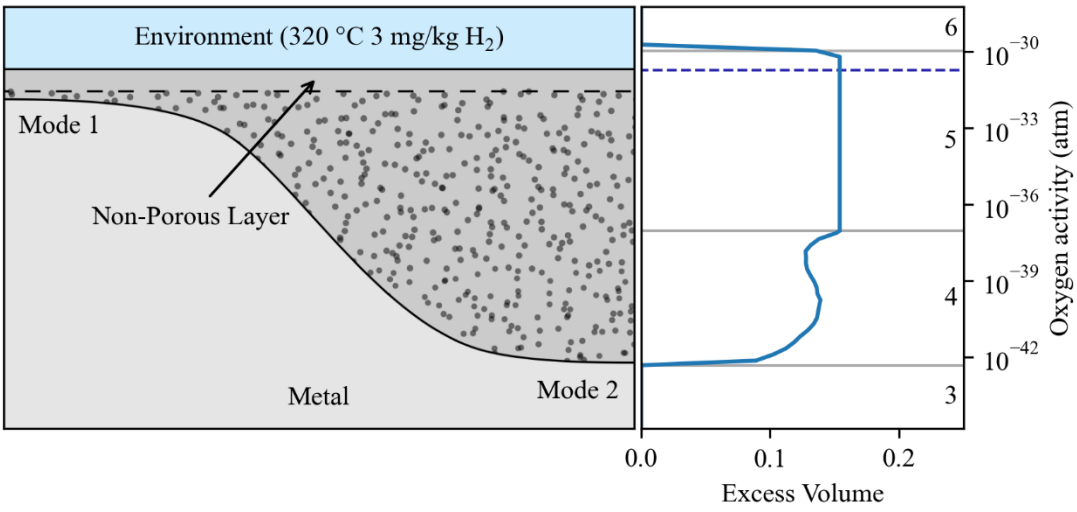

Figure 6.13. Visualization of inner oxide excess volume in mode 1 and mode 2 corrosion with a non-porous air-grown layer in the hydrogenated water condition with the nominal oxygen activity of the environment denoted by the dashed line.

The structure and thickness of the air-grown layer were not examined prior to water exposure in this work. However, the structure is likely a mixture of spinel and hematite if the oxide is not amorphous. Regardless of the exact structure, the air-grown oxide film will reduce to solely spinel in the hydrogenated water condition which is slightly less dense than corundum. The reduction in density likely opens up a path for oxygen transport resulting in mode 2 corrosion. In the aerated condition, some amount of dissolution is likely to occur which will also open a path for oxygen transport to the metal oxide interface. Based on the relative fractions of mode 2 corrosion in Table 5.9, mode 1 corrosion is minimally present after 72 hours in hydrogenated conditions, meaning that the air-grown film has a limited lifetime in this condition.

Some observations from this work can provide evidence for oxygen transport through porosity as the rate-limiting step. The thickest inner oxides observed always coincide with a very porous inner oxide layer. High amounts of porosity indicate faster oxygen transport which causes

this high corrosion rate. Another example is that outer oxide particles are sometimes protective; inner oxides beneath some outer oxide particles are very thin when exposed areas are thicker. A dense outer oxide particle will prevent oxygen from reaching the inner oxide layer, even if the inner oxide would otherwise be porous. Inner oxides are sometimes found to grow laterally, leaving some metal between the inner oxide and the surface. This phenomenon is a clear example of a certain path through the oxide facilitating transport rather than the shortest distance to the surface, as seen in Figure 6.14. The wide variation in inner oxide thickness is itself an indication of fast path diffusion because solid state diffusion would only be affected by crystallographic orientation leading to a consistent thickness for each grain.

From the example in Figure 6.14 and the pore distributions in Figure 6.8 and Figure 6.13, the relationship between corrosion modality and porosity becomes clearer. In any condition, the mode 1 corrosion will closely resemble the expected porosity in the aerated condition: a non-porous sublayer that is a significant portion of the inner oxide thickness. The aerated condition has a low corrosion rate without distinct modality because the expected mode 2 corrosion is practically identical to mode 1 corrosion in any other condition. However, in steam or hydrogenated water, once the air-grown film is bypassed by some mechanism, mode 2 corrosion begins and develops the excess volume distribution in the inner oxide layer. This justifies the previous use of mode 2 corrosion as the sole contributor to the parabolic rate constant because it is representative of corrosion in the environment. Mode 1 corrosion represents the protectiveness of the oxide grown in air, rather than that grown in the respective autoclave environment.

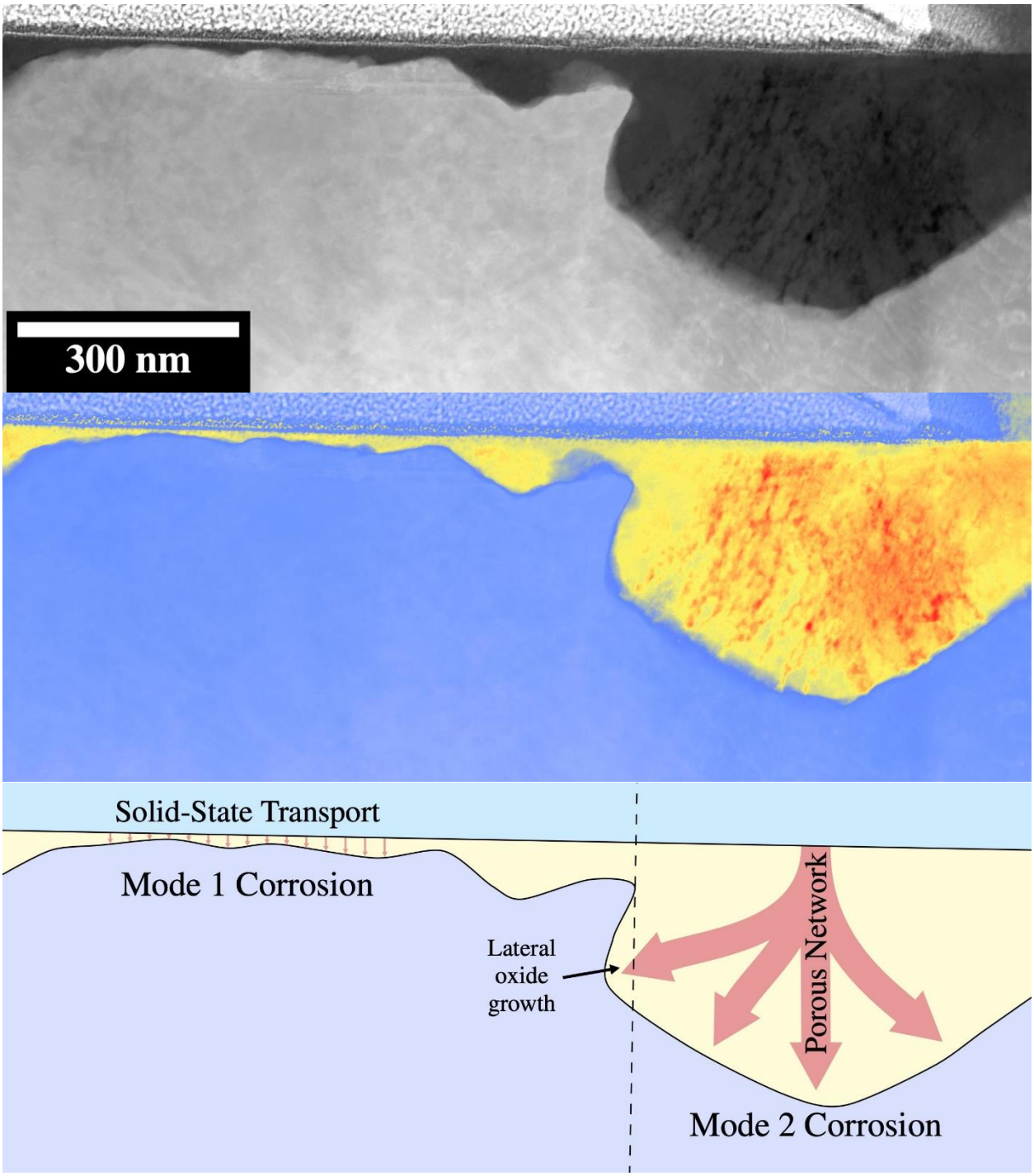

Figure 6.14. Visualization of porosity and solid-state transport driving both modes of corrosion. On top is the original HAADF STEM micrograph from W24-4 non-irradiated region, the middle is a colorized version to highlight the porosity in the inner oxide layer, and the bottom is a sketch of the same oxide showing the transport mechanisms driving their respective corrosion modes.

Additional evidence of excess volume is present in the inner oxide composition observed. The EDS data in Figure 5.47 show that Cr is clearly enriched in the inner oxide layer relative to

the metal and especially the outer oxide, but this is because Fe and Ni have been displaced from this volume. Looking at the net counts, the Cr in the inner oxide layer is nearly indistinguishable from the metal layer. The exception is some small Fe-rich oxides in the inner layer which match the excess volume and are the likely sites of pore nucleation. These Fe-rich oxides correlate with less porous oxide and likewise the higher Cr-enrichment is in the porous areas of the oxide. Ergo, the Cr remains in place in the inner oxide, but Fe and Ni may either fill in the gaps making the oxide denser, or vacate to the outer oxide leaving a porous, Cr-rich oxide layer behind.

An attempt at quantifying porosity was made by measuring the relative standard deviation of the HAADF image contrast along the oxide thickness for each region; the results are in Table 6.3. Error is calculated as the standard deviation of all porosity measurements across the given condition. Low porosity values tend to be 3~4, and high porosity values are 5 or greater. The hydrogenated water control exposures (X24 and X72) have unusually low porosity values, this may be from these oxides having finer pores that are not as easily detected. A24 has a very low porosity value as expected for the low corrosion rate. Both non-irradiated regions of W24 and W72 have high porosity values more in line with expectation than X24 and X72. The radiolysis and irradiated regions of W24 are low which is reflected in the low corrosion rate. Radiolysis and irradiated regions of W72, however, show moderately high porosity from the dissolution (or possible displacement damage) affecting the inner oxide morphology. In steam, both non-irradiated and radiolysis regions have low porosity for both S24 and S72, and the irradiated region has elevated porosity that is causally linked to the elevated corrosion rate.

Pores appear to preferentially form in the inner oxide layer along certain crystallographic directions of the metal substrate. Naturally, the angle between these directions and the surface will impact the corrosion rate, as rate-limiting oxygen transport is directed along these pores.

Porosity has a further dependence on the crystallographic orientation of the metal via the outer oxide layer. Outer oxide particles are large single crystallites with their crystallographic orientation dependent on the substrate orientation. Some grain orientations favor lateral growth of the particles along the surface, whereas others are more vertical in their growth. Greater areas of the inner oxide directly exposed to the environment increase the probability of porous networks to connect the metal/oxide interface to the environment. Therefore, the overall corrosion rate via the fraction of mode 2 corrosion may be influenced by the grain orientation of the metal.

Table 6.3. Measurement of inner oxide porosity from all experiments by region.

Experiment	Region	Porosity (arbitrary units)
X24	Non-irradiated	0.468 ± 0.075
X72	Non-irradiated	0.474 ± 0.041
A24	Non-irradiated	0.363 ± 0.030
W24	Non-irradiated	0.473 ± 0.026
	Radiolysis	0.414 ± 0.047
	Irradiated	0.449 ± 0.090
W72	Non-irradiated	0.481 ± 0.057
	Radiolysis	0.519 ± 0.057
	Irradiated	0.473 ± 0.061
S24	Non-irradiated	0.4388 ± 0.0044
	Radiolysis	0.423 ± 0.023
	Irradiated	0.523 ± 0.028
S72	Non-irradiated	0.457 ± 0.020
	Radiolysis	0.436 ± 0.060
	Irradiated	0.4821 ± 0.0099

6.1.2.6. Hydrogen and Porosity

Another factor to consider is the effect of hydrogen on the transport properties of the inner oxide. Gradual addition of hydrogen has been shown [29,33] to increase corrosion rates which is precisely opposite the trend demanded by the solid-state diffusion calculation of k_p in Eq. 6.1 and Figure 6.6. As previously established, the oxygen transport is rate-limiting and

occurs primarily through pores in the inner oxide layer. Dissolved hydrogen changes the system oxygen activity, and this influences the excess volume and pores in the inner oxide. Comparing Figure 6.8a and Figure 6.8b shows how changing the oxygen activity can stretch or squash the same excess volume profile over the inner oxide layer. Hydrogen may also play a more direct role in affecting the size, stability, and connectivity of oxide pores.

Literature shows an increase in corrosion rate with dissolved hydrogen ranging from 0 mg/kg to 4.5 mg/kg, and the transition between regime 5 and regime 6 is 1.3 mg/kg (at 320 °C). So, some of the data is within regime 6 where excess volume begins to decrease, but data from Terachi et al. [33] are mostly within regime 5 and still show a significant effect of hydrogen addition on corrosion rate. If the corrosion rate is limited by oxygen transport through pores in this literature case, the permeability of the inner oxide to oxygen or oxygen-bearing compounds appears to increase with hydrogen.

The role of hydrogen in more general stainless steel oxidation has been noted in literature, but the precise mechanism is not clear. Literature has shown that dry oxidation (air, O_2, or CO_2 without water) is slower than wet oxidation (with steam or water) for otherwise identical conditions on stainless steels [120,121]. In addition, there were high concentrations of hydrogen measured within the inner oxide layer formed during stainless steel corrosion [20,121]. It is reasonable to suspect that hydrogen plays an important role in the formation and stabilization of both individual pores and a continuous network of pores. Hydrogen adsorbs on free oxide surfaces which reduces the surface energy and insulates the fluid from the ionic solid. Water molecules may transport through the pores to the metal/oxide interface, and the liberated hydrogen from water molecule must be incorporated into the oxide or transport elsewhere (either into the metal or the environment). If hydrogen is incorporated into the oxide lattice it may alter

the transport properties by reducing the formation or migration energies of point defects. Hydrogen incorporation into the oxide film may simply be as a coating on the inner surfaces of pores. In any case, hydrogen activity in the corrosion system is inversely related to the oxygen activity, so if the pore structure is increasingly stable with hydrogen activity, the corrosion rate should decrease with increasing oxygen activity. This relationship runs counter to the k_p calculations based on solid state diffusion but matches the observation in this work between hydrogenated and aerated water and the literature on the effects of hydrogen addition to water [20,29,33].

6.1.3. Conclusion

Oxygen transport is the rate-limiting step in all circumstances for 316L corrosion in this work, although the transport mechanisms depend on the temperature and oxygen activity. The slower mode of corrosion is limited by solid state diffusion of oxygen or oxygen-bearing species through the air-grown oxide layer present before exposure, and there is no resulting increase in mode 1 oxidation from 24 h to 72 h in steam. Mode 2 corrosion is consistent with rate-limitation by oxygen transport along pore networks in the inner oxide layer and only exists where some initial defect or process creates pores which allow oxygen transport through the air-grown layer. For 320 °C hydrogenated water, the entirety of the mode 2 inner oxide has the capacity for porosity due to the excess volume. For 480 °C hydrogenated steam, the excess volume is generally lower and tapers off at either surface, so the inner oxide in this condition is moderately permeable. For 320 °C aerated water, the environment-facing sublayer of the inner oxide has no excess volume, so mode 2 corrosion is significantly slower such that it is indistinguishable from mode 1 corrosion.

6.2. Corrosion with Radiolysis

Radiolysis changes the water chemistry by increasing the activity of species without changing the amount of oxygen or hydrogen in the system. Therefore, it is assumed that the primary effect of radiolysis is to change the oxygen activity of the system, and this places radiolyzed water along the same axis as the hydrogenated and aerated conditions in this work.

The discussion of radiolysis effects will be split into two parts: radiolysis-induced water chemistry changes and their subsequent impact on the corrosion behavior.

6.2.1. Radiolysis Effect on Water Chemistry

There are two very different conditions in which radiolysis effects must be calculated: hydrogenated water and hydrogenated steam. To get an effective oxygen activity from radiolysis products, only hydrogen peroxide production will be considered. The general radiolysis reaction for the formation of hydrogen peroxide is given in Eq. 6.9.

$$2H_2O \rightarrow H_2O_2 + H_2 \qquad \text{Eq. 6.9}$$

There are short-lived radiolysis products that may increase the true oxygen activity, but the activity of these species is unknown because they are unmeasurable. Furthermore, hydrogen activity will not be strongly affected because hydrogen is already added to the system and oxide surfaces catalytically decompose molecular hydrogen, so hydrogen activity will not be strongly affected by radiolysis.

The evidence for hydrogen peroxide as the primary agent of radiolysis is in the hematite signal from Raman spectroscopy. There are expanded areas beyond the irradiated and radiolysis regions (outside the path of the beam) where hematite signals are detected at the same intensity as the irradiated region. These areas are generated by water flow from natural convection induced by beam-heating. Since there are no other radiolysis products that could survive the duration of the flow and induce a positive shift in the oxygen activity, hydrogen peroxide must

be causing this shift. Furthermore, the similar intensity of the signal indicates that there is no measurable net effect of the short-lived products, otherwise the intensity would be stronger in the irradiated/radiolysis regions.

6.2.1.1. Radiolysis in Hydrogenated Water

Because this work is not the first to explore the effects of proton-induced radiolysis on stainless steel corrosion, an interpolation of a model employed by Raiman et al. will be used to calculate the hydrogen peroxide production in this work [22]. The energy of protons emerging from the sample surface is similar between this work and that of Raiman et al. (i.e., the LET is similar), and the dose rates in this work are intermediate. The model predicts 340 µg/kg H_2O_2 for 4000 kGy/s dose rate in the water and 40 µg/kg H_2O_2 for 400 kGy/s. Using a simple polynomial fit to these values, the following expression can be used to interpolate the yield of hydrogen peroxide in µg/kg:

$$[\mathrm{H_2O_2}] = 4.167 \times 10^{-6} D^2 - 0.101 D \qquad \text{Eq. 6.10}$$

where D is the dose rate in kGy/s. The disc surface dose rate ranges from 600~700 kGy/s yielding a hydrogen peroxide concentration in the 60~69 µg/kg range. Peak dose rates on radiolysis bars (radiolysis regions) approach 1500 kGy/s or 143 µg/kg hydrogen peroxide in water.

With the range of hydrogen peroxide concentrations, the equivalent oxygen activity needs to be determined. Using the effect of oxygen and hydrogen peroxide addition on ECP by Kim [26] in Figure 2.10, an effective oxygen concentration can be determined for a given hydrogen peroxide concentration by assuming a constant ECP. From the oxygen concentration, the equilibrium oxygen activity can be calculated with the same method as the nominal conditions,

and the results are listed in Table 6.4. The oxygen activity under irradiation in this work approaches the value of oxygen activity in the aerated condition within an order of magnitude.

Table 6.4. Oxygen activity calculation from proton-induced hydrogen peroxide production compared with other nominal conditions in 320 °C water.

Added Gas	Added Gas Concentration (mg/kg)	Dose Rate (kGy/s)	Hydrogen Peroxide Concentration (μg/kg)	Equivalent Oxygen Concentration (μg/kg)	Oxygen Activity (atm)
H_2	3	0	–	–	1.863×10^{-31}
H_2	3	600	60	662	4.9×10^{-5}
H_2	3	700	69	739	5.5×10^{-5}
H_2	3	1500	143	1120	8.3×10^{-5}
O_2	8	0	–	8000	5.951×10^{-4}

Each mole of hydrogen peroxide generated from radiolysis also generates a mole of molecular hydrogen as shown in Eq. 6.9. The result is a minor increase of the hydrogen concentration; in the most extreme case of 1500 kGy/s, the resulting hydrogen concentration would be 3.016 mg/kg. This is important because it distinguishes the radiolyzed water from both aerated and hydrogenated conditions. If oxygenated water were to be radiolyzed, it would result in significant increases in the relative hydrogen activity but with minimal effect on the oxygen activity. With radiolysis, both oxygen and hydrogen activity are enhanced in a manner analogous to displacement damage with vacancy and interstitial concentrations. Therefore, the effects of oxygen activity on the oxide will resemble the aerated case, and the effects of hydrogen activity on the oxide will resemble the hydrogenated case.

The effect of the injected hydrogen atoms from the proton beam on the water chemistry is minimal. For the upper end of current density, ~4.5 μA/cm^2, and an injection depth of 100 μm, the equivalent added H_2 is 2.4 μg/kg·s. The refresh rate of the autoclave is 40 s in water (much faster in steam), so at most the accumulated concentration could be ~0.1 mg/kg. This

concentration is mitigated by convective and diffusive flow which is accelerated by the beam heating. Therefore, the effect of the injected hydrogen is considered to be negligible.

Solubility is a secondary effect on water chemistry by radiolysis that is important to this work. Fe, Ni and Cr all dissolve from the oxide to the solubility limit in the water and no further. Because the autoclave in this work is made from stainless steel, the solubility of all cations is assumed to have reached in the water above the sample for any nominal water chemistry. However, radiolysis changes oxygen activity which, in turn, changes solubility without immediately altering the concentration of any dissolved metal species. Therefore, these dissolved species will become undersaturated or supersaturated depending on the change in solubility with oxygen activity. This is only possible with radiolysis in this type of experiment where the radiolyzed water is confined to a small volume inducing local solubility changes above irradiated and radiolysis regions.

6.2.1.2. Radiolysis in Hydrogenated Steam

The environment is significantly different for the steam case in this work, especially because most of the gas is argon. The mass density of the argon-steam was calculated to be 13.2 mg/cm^3, and the dose rate in the gas was 5.43 kGy/s for S24 and 5.56 kGy/s for S72. Taking an average value of 5.5 kGy/s for both experiments, the energy deposition is still split between argon, water, and hydrogen in the gas. Normally, one would use the atomic number to distribute the energy from ion irradiation, but argon will transfer some energy back to the water due to its low heat capacity. Therefore, the mole fraction of both water and hydrogen were combined to give a conservative estimate of the effective dose rate on the water: 0.957 kGy/s. This value was applied to Eq. 6.10, and the resulting oxygen concentration and activity are listed in Table 6.5. Here, the hydrogen peroxide concentration is significantly below that plotted in Figure 2.10, and

the lowest points show that the hydrogen peroxide and oxygen concentrations return virtually equal ECP values. Therefore, it was assumed that the equivalent oxygen concentration was equal to the hydrogen peroxide concentration. Furthermore, the 150 µg/kg H_2 point (–540 mV) in Figure 2.10 is very close in ECP value to the 0.3 µg/kg O_2 and H_2O_2 points (–510 mV).

Table 6.5. Oxygen activity calculation from proton-induced hydrogen peroxide production compared with the nominal condition in 480 °C steam.

Added Gas	Added Gas Concentration (g/kg)	Dose Rate (kGy/s)	Hydrogen Peroxide Concentration (µg/kg)	Equivalent Oxygen Concentration (µg/kg)	Oxygen Activity (atm)
H_2	170	0	–	–	1.863×10^{-31}
H_2	170	0.957	0.0973	0.0973	5.951×10^{-4}

While the calculated value of oxygen activity is very high under proton radiolysis in steam, there are several mitigating factors to consider. First, the equivalent oxygen concentration is very low. According to Kim [26], 0.3 µg/kg of O_2 (and H_2O_2) (–510 mV) is nearly the same ECP as 150 µg/kg H_2 (–540 mV), so it stands to reason that a lower value would be even closer. Second, the calculation of hydrogen peroxide is an extrapolation from proton-induced radiolysis in 320 °C water where the slower reaction kinetics give more time for the necessary intermediate products to accumulate. Finally, the corrosion medium here consists mostly of argon which will interfere with the formation of hydrogen peroxide. The formation of H_2O_2 by radiolysis of water is a strong function of LET because it forms in the tracks of the energetic particle [85]. The high amounts of argon and hydrogen, in addition to the low density, will suppress the formation of hydrogen peroxide [84]. The result is that the calculated H_2O_2 concentration is an overestimate, the calculated oxygen activity can be discarded, and the oxygen activity of the nominal condition will be assumed for the radiolyzed steam condition.

6.2.2. Radiolysis Effect on Corrosion

Because both the nominal and the radiolyzed conditions are substantially different, the water and steam radiolysis effects will be discussed separately.

6.2.2.1. Radiolysis Effect on 320 °C Water Corrosion

Radiolysis regions in water show a marked decrease in corrosion rate from the nominal hydrogenated condition. Notably, the radiolysis region corrosion rate is still higher than that of the aerated case, and the oxygen activity under radiolysis is between that of the hydrogenated and aerated conditions. The radiolysis region corrosion rates in water are plotted alongside the non-irradiated hydrogenated and aerated values and the calculated parabolic rate constants in Figure 6.15.

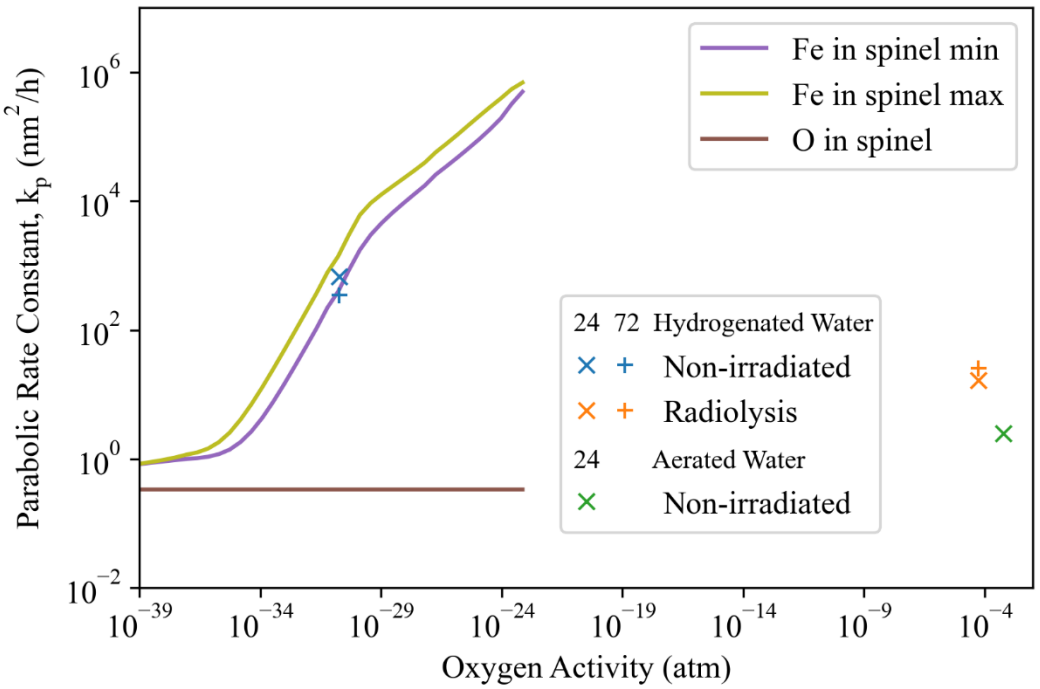

Figure 6.15. Measurements in non-irradiated and radiolysis regions and calculations of parabolic rate constants using Fe and O diffusion in spinel limits for 316L in 320 °C 13.1 MPa water as a function of oxygen activity.

Like the aerated condition, the hydrogenated water with radiolysis increases the oxygen activity which results in a lower corrosion rate. There are two features that differentiate

radiolyzed and aerated water conditions: the difference in corrosion rates and the active dissolution under radiolysis.

Both the aerated and radiolyzed water conditions have no excess volume in the environment-facing sublayer of the inner oxide. See Figure 6.8b for the aerated case. Because the oxygen activity is so similar between these two conditions, the excess volume profile is virtually identical for radiolyzed water as aerated water. The lack of excess volume inhibits porosity as a significant mechanism of oxygen transport to facilitate the corrosion reaction. While the oxygen activity from radiolysis is slightly lower than that of the aerated condition, it is insufficient to account for the large difference in corrosion rates. Therefore, another factor must be responsible for the significant discrepancy in the corrosion rate between the two conditions.

Dissolution under radiolysis is a key feature that is present in neither hydrogenated nor aerated conditions without radiation effects. Without radiation, the stainless steel corrosion vessel saturates the water with the relevant aqueous metal species. However, the locally increased oxygen activity increases the solubility of several cation species (notably $HCrO_4^-$) [22], and thus leads to measurable dissolution of the inner oxide after 72 h of exposure to radiolyzed water. Dissolution is also evident in the 24 h radiolysis regions, but it was not quantifiable within error using the helium bubble marker layer technique. Dissolution of the inner oxide allows both the air-grown layer (responsible for mode 1 corrosion) and the non-porous sublayer (from the excess volume profile in Figure 6.8b) to be breached, causing accelerated corrosion rates relative to the aerated condition. The accelerated loss of the air-grown layer would cause an increase in the fraction of mode 2 corrosion if the modes were distinguishable in either condition. In contrast, the non-irradiated hydrogenated water condition always has available porosity in the inner oxide layer which results in a much higher corrosion rate that serves as an upper boundary

for the corrosion with radiolysis. With radiolysis, the non-porous sublayer both dissolves and reforms, creating a cyclical repassivation process that is rate-limited by oxygen transport via the dissolution of the inner oxide layer. If the non-porous sublayer did not form, then the corrosion rate should match that of the mode 2 non-irradiated hydrogenated water condition. If the non-porous sublayer did not dissolve, then the corrosion rate would approach that of the aerated water condition.

One other feature to consider is the composition of the inner oxide layer under radiolysis. The average Cr content of the inner oxide layer is higher in the radiolysis region than in the non-irradiated region. There are two factors that lead to a more Cr-enriched inner oxide with radiolysis: the stratification of oxygen activity regimes and the ratio between cation diffusion rates and the corrosion rate. Because of the non-porous sublayer, oxygen transport into the inner oxide is limited, creating a more gradual slope of oxygen activity across the inner oxide layer which gives room for the lower activity regimes to manifest their equilibrium oxides. Regime 3 and 4 Cr-rich spinel oxides are more Cr-rich than in regime 5, and so the inner oxide closest to the metal enriches in Cr relative to the rest of the layer. In contrast, with continuous porosity much of the inner oxide layer is exposed to oxygen activity near that of the environment, so the breadth of the inner layer exemplifies the activity regime of the environment (regime 5 in the hydrogenated water condition). While cation diffusion rates are fast and not rate-limiting, they are not instantaneous, so some equilibrium is reached with the oxygen transport. With radiolysis, the cation diffusion rate is higher in some parts of the inner oxide, and the corrosion rate is lower, therefore, there is more time for Fe and Ni to diffuse to the outer layer leaving Cr-rich spinel behind and depleting the amount of Fe-rich spinel in the inner oxide layer. In contrast, the higher corrosion rate and lower cation diffusion rate in the hydrogenated water condition result

in a greater proportion of Fe-rich spinel in the inner oxide layer and thus a lower Cr content than the radiolyzed water condition. This is reflected in the porosity measurements in Table 6.3 where W24 has higher porosity in the non-irradiated region than the radiolysis region; by 72 h in W72, however, the porosity is evened out between the regions.

6.2.2.2. Radiolysis Effect on 480 °C Steam Corrosion

As established earlier, the effective oxygen activity under radiolysis in hydrogenated steam is not significantly different than the non-irradiated condition as plotted in Figure 6.16. The oxidation results bear out this claim in that the corrosion rate in mode 1 and mode 2 is not affected in any statistically significant manner between the non-irradiated and radiolysis regions. One caveat is that both S24 and S72 radiolysis regions have a higher fraction of mode 1 corrosion than the respective non-irradiated regions. The main drivers of this difference are that the two regions are from a bar (radiolysis) and a disc (non-irradiated) and that the surface condition varies from specimen to specimen resulting in more mode 1 corrosion on the bar (radiolysis region). Furthermore, the Cr-content measurements from the inner oxide layer are not notably different between the two regions.

The fact that the measured values in Figure 6.16 lie between the curves elucidates the rate-limiting mechanism. Being above the curve for O diffusion in spinel means that oxygen must have a faster transport mechanism available rather than solid state diffusion. Lying significantly below the curve for Fe in spinel demonstrates that cation transport is not rate-limiting because the corrosion rate would be equal or higher if that were the case.

It was expected for the steam radiolysis region to be indistinct from the non-irradiated region; in fact, the point of the steam condition was to minimize the effects of radiolysis on corrosion. Doing so creates a direct comparison between irradiated and non-irradiated regions to

achieve the objective of this work: isolating the effect of displacement damage, which will be discussed in the next section.

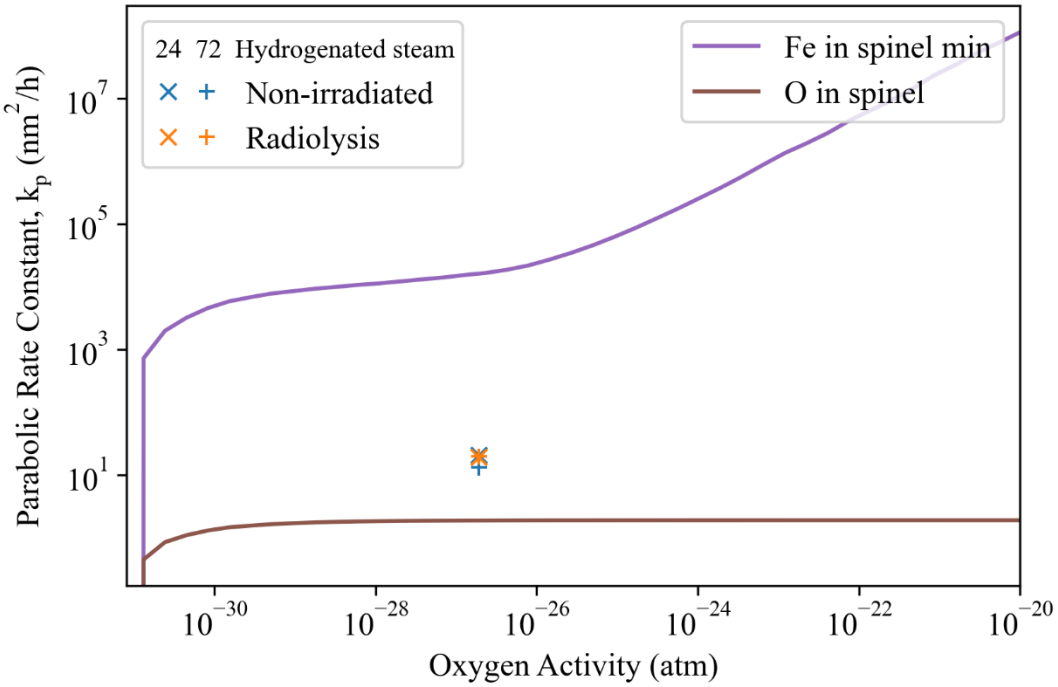

Figure 6.16. Measurements from non-irradiated and radiolysis regions and calculations of parabolic rate constants using Fe and O diffusion in spinel for 316L in 480 °C 1.5 MPa water as a function of oxygen activity.

6.2.3. Conclusion

Radiolysis region oxidation and Cr content were compared to non-irradiated regions in similar corrosion media. In hydrogenated water, radiolysis was found to decrease the corrosion rate, but compared to aerated water, this same radiolysis condition had a much higher corrosion rate. In water, radiolysis causes cycles between the porous oxygen transport mechanism of the non-irradiated hydrogenated water condition and low excess volume of the aerated condition, and this results in intermediate corrosion rates. Cr content was higher in the inner oxide with radiolysis than without due to increased cation diffusion and from oxygen activity stratification via pore blocking. In steam, no effect of radiolysis was observed in mode 1 or mode 2 corrosion rates, and no significant change in inner oxide Cr-content was found. The low dose rate in the

low density of steam prevented a significant quantity of hydrogen peroxide from forming and influencing the corrosion behavior.

6.3. Corrosion with Displacement Damage

All experimental conditions with irradiation in this work had a nominal 7×10^{-7} dpa/s damage rate at the metal surface facing the corrosion medium calculated using SRIM quick K-P. However, the point defect concentration in the metal is largely irrelevant for corrosion kinetics. Therefore, it is useful to calculate both the cation and anion displacement damage rate in spinels on the surface of the metal. The displacement damage rate is identical between the two temperature conditions, but the final point defect concentrations are temperature dependent.

To calculate the damage rate in the oxide, SRIM was run in both quick K-P mode and Full Cascade. Quick K-P was used to calculate the total damage rate in pure magnetite at the surface of the sample material. Full Cascade mode was used to separate the cation and anion point defect generation rates by computing a ratio between Fe and O displacements, and the quick K-P rate was divided between cations and anions according to this ratio. The result is 5.32×10^{-7} dpa/s for cations, 8.33×10^{-7} dpa/s for anions, and a total damage rate of 1.365×10^{-6} dpa/s in the oxide film.

6.3.1. Displacement Damage in 320 °C Water Corrosion

While solid-state diffusion is not always the rate-limiting step for corrosion, the effects of displacement damage on the diffusion coefficients are illustrative of the effects on corrosion and the oxide film. First, a radiation point defect balance is needed to calculate the steady-state point defect concentrations. It is assumed that sinks are irrelevant for the calculation because they are true Frenkel defects in an ionic solid, so sinks may only serve as recombination sites. The

general point defect balance equations in Eq. 2.6 have an analytical solution when sinks are excluded which is given in Eq. 6.11

$$\mathrm{C_{rad}} = -\frac{1}{2}\left(\mathrm{C_{v,th}} + \mathrm{C_{i,th}}\right) + \frac{1}{2}\sqrt{\left(\mathrm{C_{v,th}} - \mathrm{C_{i,th}}\right)^2 + 4\frac{\mathrm{K_0}}{\mathrm{K_{iv}}}}$$

$$C_i = C_{\mathrm{rad}} + C_{i,th}$$

$$C_v = C_{\mathrm{rad}} + C_{v,th} \qquad \text{Eq. 6.11}$$

where C is the concentration of vacancies v or interstitials i induced by radiation rad or thermally th, K_0 is the damage rate in dpa/s, and K_{iv} is the recombination rate constant in s^{-1}.

With the radiation and thermally generated point defects, the radiation enhanced diffusion coefficient can be calculated by using the following equation:

$$D_{A,th} = D_A^i C_{i,th} + D_A^v C_{v,th}$$

$$D_{A,rad} = D_A^i\left(C_{\mathrm{rad}} + C_{i,th}\right) + D_A^v\left(C_{\mathrm{rad}} + C_{v,th}\right) \qquad \text{Eq. 6.12}$$

where D_A^i is the partial diffusion coefficient for species A moving by intersitials i and similarly for D_A^v but with vacancies v.

Using Eq. 6.11, radiation-induced point defect concentrations can be calculated and used to calculate diffusion coefficients with Eq. 6.12 and plot them in comparison to the thermal values in Figure 6.17. However, there is no literature or database information on the anion point defect concentrations in Fe spinels, so the radiation effect on anion diffusion cannot be calculated.

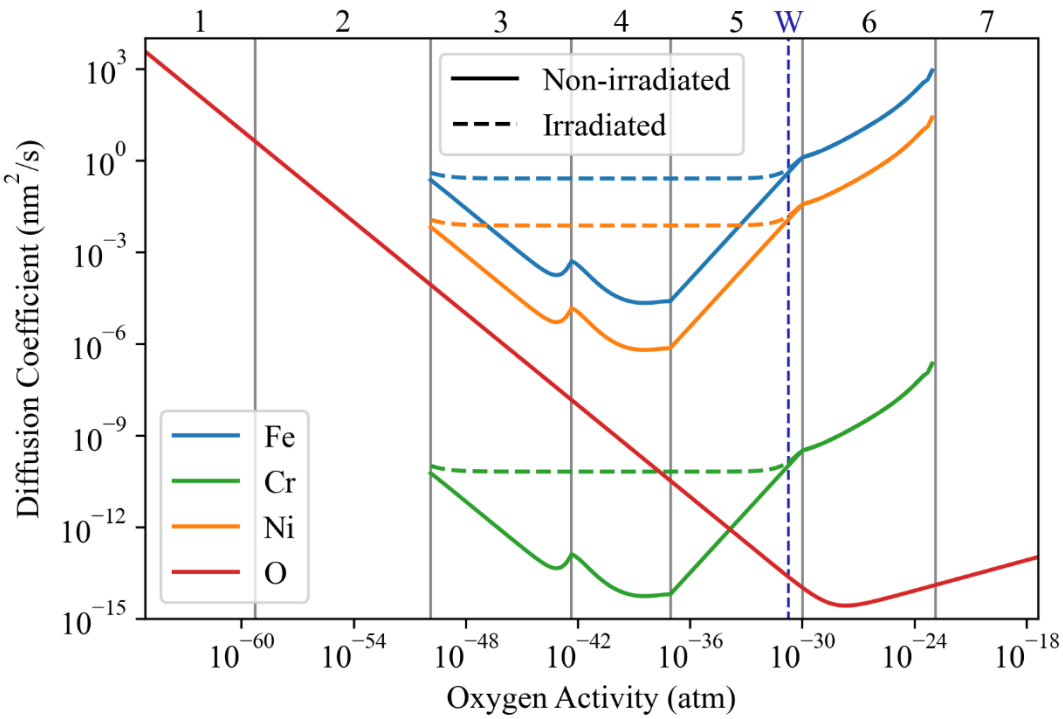

Figure 6.17. Radiation enhancement of diffusion coefficients in spinel oxides grown in the 316L corrosion system at 320 °C and 13.1 MPa.

In the 320 °C water experiments in this work, the non-irradiated and irradiated regions are different in both water chemistry and displacement damage, so they cannot be directly compared to yield the effect of displacement damage at the nominal water chemistry. Radiolysis has a strong effect on the corrosion behavior, thus only by comparing the radiolysis and irradiated regions can any effects of displacement damage be discerned.

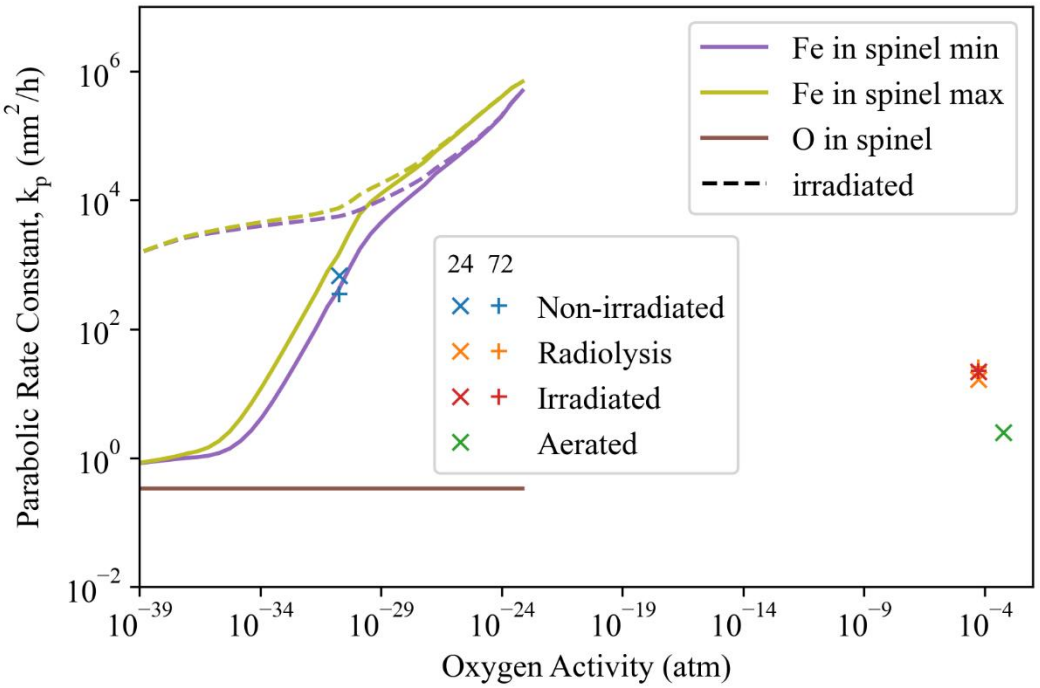

Figure 6.18. Measurements from all regions and calculations of parabolic rate constants using Fe and O diffusion in spinel for 316L in 320 °C 13.1 MPa water as a function of oxygen activity.

The inner oxide thickness, total oxidation, and dissolution for both radiolysis and irradiated regions are within error of one another in both W24 and W72 as plotted in Figure 6.18. Compared to the non-irradiated region data, these regions have much lower oxidation rates and, in W72, are the only regions to show measurable dissolution. The discussion comparing the radiolysis region oxidation rate data to the non-irradiated region is equally relevant to the irradiated region due to their similarity.

Earlier, it was established that mode 1 corrosion is rate-limited by solid-state transport of oxygen, so displacement damage would be relevant in accelerating this corrosion mode. However, mode 1 corrosion was not cleanly separable from the inner oxide thickness distribution in irradiated regions of W24 or W72, so the effect of displacement damage on mode 1 corrosion cannot be determined. The diffusion coefficients calculated for 320 °C water with and without radiation are comparable to non-irradiated steam diffusion coefficients. Mode 1 corrosion did not

increase significantly between 24 h and 72 h in steam, so displacement damage should also result in negligible change in mode 1 corrosion rates up to 72 h in 320 °C water.

Rate-limiting steps for mode 2 corrosion were established earlier to be oxygen transport via porosity. Porosity is limited by increasing oxygen activity because the excess volume to support the pores decreases at higher activity regimes; however, dissolution counteracts this effect and allows the corrosion medium to access the inner oxide pore network intermittently. The two processes here—dissolution and oxygen transport through pores—do not rely on point defects or other solid-state transport mechanisms that may be affected by displacement damage. Therefore, displacement damage has negligible effect on the mode 2 corrosion rate as well as the mode 1 corrosion rate, and the match between corrosion rate data for the radiolysis and irradiated region corroborates this claim.

The one measurable difference between the irradiated and radiolysis regions is the Cr-content of the inner oxide and the Ni content in the metal. The attendant Ni enrichment (Figure 5.46) is correlated with the Cr peak (Figure 5.44) but is found in the metal near the interface. Both radiolysis and irradiated regions have peak Cr-contents in the oxide directly adjacent to the metal/oxide interface and at about the same amount of Cr. However, the inner oxide Cr enrichment is constant in the radiolysis region, and Cr drops off rapidly away from the metal in the irradiated region. Since the only notable difference between the two regions is the displacement damage rate, this must be the cause of the difference. Increased mobility of the species in the oxide—even from ballistic mixing—may be responsible for the sharp drop in Cr content in the irradiated region. Based on the Thermo-Calc results, the Cr should be distributed widely between both inner and outer oxide layers in regime 6–7 compared to virtually no Cr in the outer oxide in regime 5. Therefore, in regimes 6–7, a driving force for Cr to move from the

inner layer to the outer layer emerges. Because of the increased oxygen activity caused by radiolysis, the Cr driving force is appreciable in both radiolysis and irradiated regions. The low mobility of Cr is the key factor in slowing its depletion in the radiolysis case, and displacement damage provides the avenue in the irradiated region. Furthermore, there is virtually no driving force in the non-irradiated region for Cr depletion, and the mobility is even lower, so Cr does not deplete or move significantly in hydrogenated water. Also, the Cr content does not directly impact the corrosion rate because excess volume is the key factor, so the difference in composition between radiolysis and irradiated regions does not affect the corrosion rate. More discussion on this feature is in a later section to compare both water and steam conditions together.

6.3.2. Displacement Damage in 480 °C Steam Corrosion

Again, the effect of radiation on the diffusion coefficients was calculated for cations in spinel in 480 °C steam using Eq. 6.11 and Eq. 6.12 and plotted in Figure 6.19. Cation diffusion coefficients are less affected by radiation-induced displacement damage than at 320 °C because the higher temperature yields higher thermal point defect concentrations.

Both radiolysis and non-irradiated regions in 480 °C steam were indistinguishable in all aspects of corrosion behavior; therefore, both serve as valid controls for the irradiated region for determining the effects of displacement damage. Unlike the 320 °C water condition, displacement damage directly resulted in an increase in corrosion rate, both in the mode 2 corrosion measurements and in the fraction of mode 2.

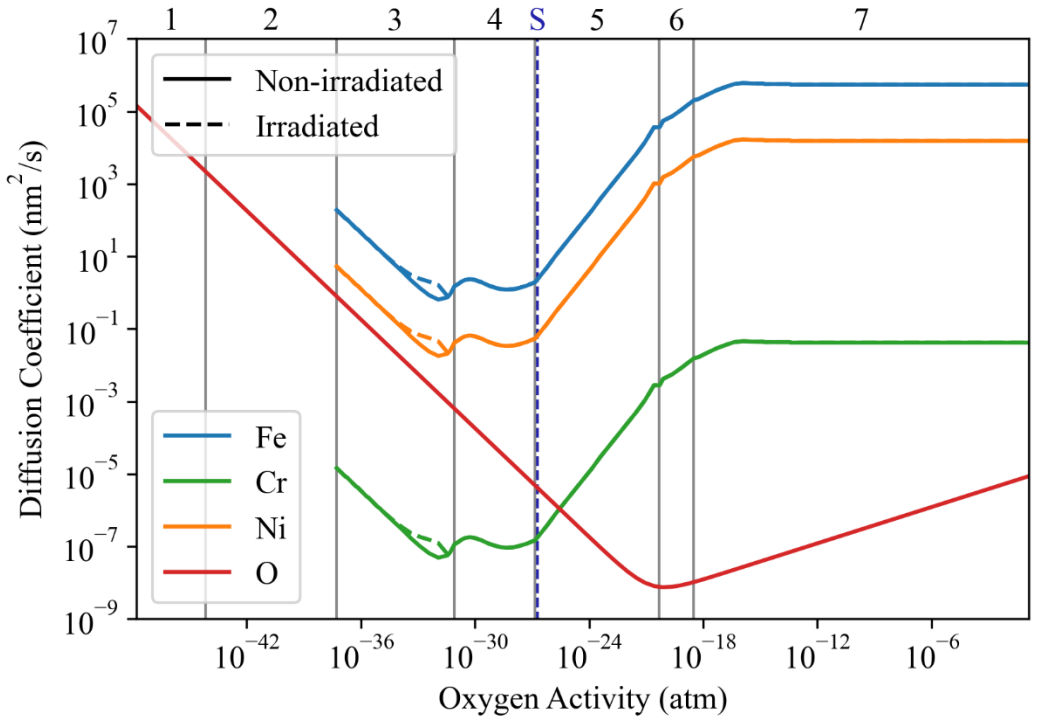

Figure 6.19. Radiation enhancement of diffusion coefficients in spinel oxides grown in the 316L corrosion system at 480 °C and 1.5 MPa.

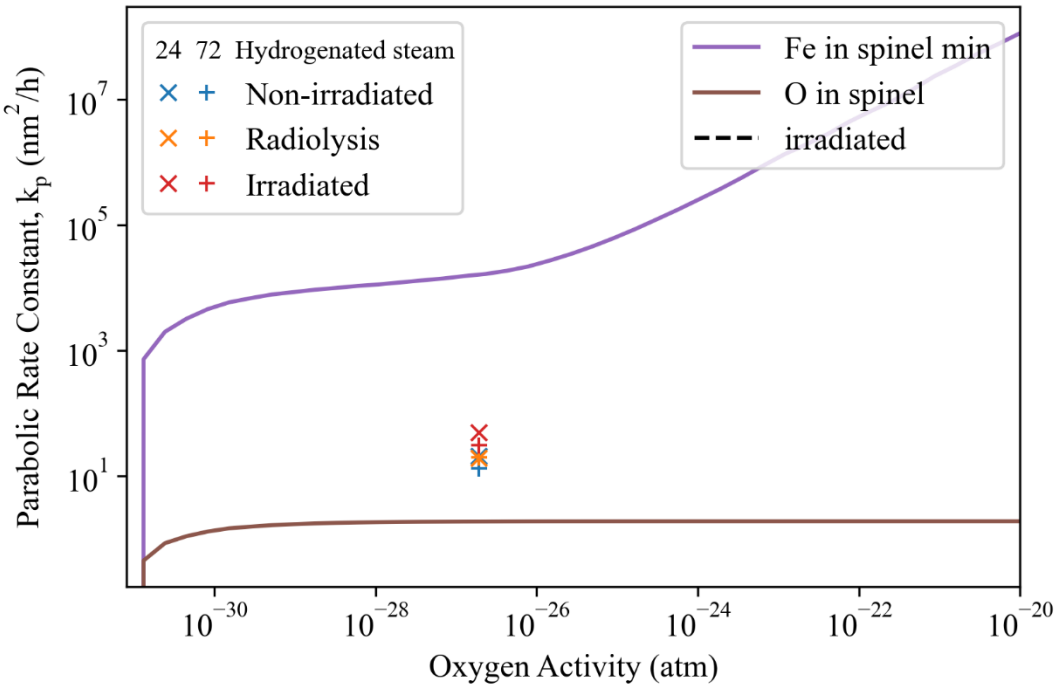

Figure 6.20. Measurements from all regions and calculations of parabolic rate constants using Fe and O diffusion in spinel for 316L in 480 °C 1.5 MPa water as a function of oxygen activity. The line denoting the irradiated condition wholly overlaps with the non-irradiated condition for Fe in spinel, and there is no irradiated line for O in spinel.

Despite the lack of point defect concentration information for anions, the mode 1 corrosion rates in steam show that the effect is small. The only insight into anion point defects is from Dieckmann [120] who states that the anion point defect concentrations are minor compared to cations. If the diffusion coefficient of oxygen were to increase substantially, the minimum corrosion rate of mode 1 would increase, but this was not observed. Therefore, based on the mode 1 corrosion and the calculation of cation diffusion coefficients in Figure 6.19, radiation enhanced diffusion does not impact the corrosion in 480 °C steam within 72 h. However, displacement damage clearly influences the corrosion rate in mode 2, so some other radiation process must be responsible for this effect.

As with all regions in steam, the inner oxide has both porous and non-porous sublayers. However, the irradiated region inner oxide has a much greater number of pores throughout the inner oxide than the other two conditions, as confirmed in Table 6.3. The rate-limiting mechanism of mode 2 corrosion is porous transport of oxygen (and oxygen-bearing compounds) through the inner oxide. Displacement damage accelerates the growth of these pores which increases the mode 2 corrosion rate in turn. Because the concentration of anion point defects is small compared to cation defects, the displacement damage will greatly increase anion point defect concentrations. Forming pores in an ionic solid requires the clustering of Schottkey defects i.e., cation vacancies and anion vacancies. Doing so is the only way to maintain the charge balance and form a cavity, so displacement damage can both nucleate and grow pores in the inner oxide.

Displacement damage also increases the frequency of breakthrough defects in the air-grown layer. The increased fraction of mode 2 corrosion over mode 1 corrosion is evidence of a higher frequency of breakthrough of the air-grown film. Similarly, the portions of the inner oxide

with low excess volume are also susceptible to radiation-induced pores. The formation of pores throughout the inner oxide connects the metal/oxide interface to the environment and increases the both the frequency and magnitude of mode 2 corrosion.

One question with this mechanism is why does pore formation by displacement damage not affect the corrosion rate in 320 °C water? The key difference between the two conditions is dissolution. Thermal point defect concentrations are much lower at 320 °C, so displacement damage would promote pore formation as it does in 480 °C steam. However, the continuous dissolution of the inner oxide layer does not allow enough time for pores to form by displacement damage. There may also be some effect of the decreased mobility of all point defects at lower temperatures that reduces the radiation-induced pore formation. Regardless, the displacement damage at 480 °C results in accelerated corrosion via enhanced pore growth in the inner oxide layer.

The elemental composition of the oxide is not remarkably different between any of the three regions. All three have substantial Ni enrichment in the metal and high Cr-enrichment in the oxide. There is no discernable common profile observed within any region, so there is little information to be learned from this data.

6.3.3. Enrichment of Cr in the Inner Oxide

Previously, the Cr-rich oxide layer was speculated as the reason for decreased corrosion rates in radiolyzed water [113]; however, the causality of this relationship is backwards. There are two arguments to support this theory: one kinetic argument and one thermodynamic.

There are two kinetic factors that lead to the formation of this feature: diffusion in the metal and local corrosion rate. Highly Cr-enriched spinel oxides are a clear feature of regime 3–4 corrosion, and the associated peak in Ni concentration in the metal phase is also consistent with

these regimes. Diffusion in the metal phase delivers Cr and Fe from the metal into the oxide, leaving Ni behind at higher concentrations, so enhanced diffusion in the metal will exaggerate this feature. For example, 480 °C steam corrosion has very high concentrations of Ni in the metal. The localized corrosion rate affects the magnitude of this feature because the metal/oxide interface is a moving boundary, so the enrichment of Ni depends on the relative velocity of the boundary to the diffusion flux in the metal. Because the cation diffusion coefficients are not a strong function of Cr content and because there is no evidence to suggest that oxygen diffusion is either, the peak in Cr concentration is caused by low corrosion rates.

The difference in Cr content in the inner oxide between the irradiated and radiolysis regions can be explained with displacement damage effects. Displacements damage in the metal increases the diffusion coefficients of all species via point defect concentrations, and therefore the Ni enrichment in the metal and Cr enrichment in the oxide on opposite sides of the interface are increased by displacement damage. The corrosion rate between the irradiated and radiolysis regions of W24 and W72 are not significantly different, yet the enrichment levels are higher in the irradiated region, providing further evidence that the corrosion rate is not affected by the level of either Ni or Cr enrichment. Since the corrosion rates are equal between the two regions, increases in the diffusion coefficients will necessarily result in higher enrichment. In steam, there is little observed difference in the interface enrichment levels between all three regions of S24 and S72. Even in the non-irradiated and radiolysis regions of S24 and S72, the Cr peak reaches its maximum value of 0.67 metal molar fraction, so there is no room for displacement damage to result in higher enrichment of Cr in the irradiated region. Furthermore, the irradiated region has a higher corrosion rate which mitigates gains in enrichment from displacement damage, resulting in similar Ni enrichment values.

The thermodynamic argument for the Cr peak in the oxide is based on the oxygen activity profile across the inner oxide layer. In the hydrogenated water condition, the porosity in the inner oxide layer allows for the oxygen activity near the metal/oxide interface to approach that of the environment. This leads to the inner oxide layer closely resembling the oxide compositions of regime 5 throughout the layer. In the cases with less excess volume (hydrogenated steam, aerated water, and radiolyzed water), oxygen activity is more stratified throughout the inner oxide layer. This leads to oxide compositions ranging across regimes 3–7, yielding high Cr enrichment near the metal oxide interface, and where applicable, very low Cr content near the inner/outer oxide interface.

In water, the Cr depletes in the irradiated region inner oxide whereas the Cr in the radiolyzed region inner oxide remains constant. Despite this clear difference in Cr content, the oxidation rate is unaffected by this phenomenon. This is because the enrichment of Cr in the inner oxide is immaterial to the corrosion rate, rather only the presence of a dense oxide results in reduced corrosion rate. Cr serves to increase the thermodynamic regimes where dense oxides may form, thereby reducing corrosion. Even pure iron may form a passive oxide film in alkali conditions, so Cr is not necessary for protective oxide films on steels. With displacement damage from direct irradiation, Cr can redistribute to approach thermodynamic equilibrium in the outer oxide without altering the density of the inner oxide.

6.3.4. Conclusion

The effect of displacement damage on stainless steel corrosion was determined to be primarily through the formation and growth of pores in the inner oxide layer. The presence of mode 1 corrosion and the fact that it is unchanged by displacement damage shows that the effect of radiation enhanced diffusion on the corrosion rate is negligible in the conditions tested in this

work. Instead, the increase of corrosion with displacement damage in steam is due to the increased porosity relative to the radiolysis and non-irradiated regions. Displacement damage causes a redistribution of Cr in the inner oxide layer, but this does not impact the corrosion rate. The dissolution caused by radiolysis in water suppresses the effects of displacement damage at 320 °C.

6.4. Extrapolation to Reactor Conditions

With the key effects of oxygen activity, radiolysis, and displacement damage on corrosion determined and the rate-limiting steps identified, these insights can be applied to practical conditions to predict the effect of radiation on corrosion behavior. Because there is no published characterization of LWR core oxides on stainless steel, this section will be entirely speculative. First, the effects of radiation in typical PWR conditions will be considered because the nominal water conditions in this work partially emulated PWR primary water. Second, BWR HWC and NWC will be briefly discussed. Finally, other coolants will be considered briefly.

One feature that will not significantly impact the corrosion behavior in-core is mode 1 corrosion. Insofar as the air-grown layer responsible for mode 1 corrosion affects the total corrosion rate, the effect is diminished over longer exposure times because all mode 1 corrosion is eventually converted to mode 2. Exposure times of years compared to the 72 h in this work will surely have eliminated mode 1 corrosion.

Overall corrosion rates are important to the operation of reactors due to the release of Co-60 causing increased dose rates for radiation workers and build-up of corrosion products causing fouling. However, overall corrosion rates are not clearly connected to failure mechanisms such as IASCC. Increases in dissolved hydrogen tend to increase corrosion rates but reduce cracking susceptibility, whereas zinc addition to the water decreases both corrosion rate and cracking

susceptibility. Therefore, radiation effects on cracking susceptibility will be considered separately.

PWR primary water chemistry is different from the hydrogenated water condition in this work in a few ways. Most notably, PWRs use boric acid and lithium hydroxide which increase the pH and conductivity of the water compared to the pure water used in this work. Also, depleted zinc oxide is added to the water which has been shown to impact corrosion behavior of stainless steels. The radiation environment is also different: the damage rate (~10^{-8} dpa/s) is approximately 10x lower than the ion irradiation in this work (~10^{-7} dpa/s), but the radiolysis dose rate (< 4 kGy/s) is about 250x lower than this work (600~1500 kGy/s).

The effect of increasing pH is proportional to increasing the oxygen activity because of the Nernst Equation, but the pH has a smaller effect than oxygen. This means that the nominal thermodynamic regime in a PWR core is still regime 5. Radiolysis at the low dose rates in the reactor core are assumed to be too low for significant changes to the oxygen activity. More likely the effect of radiolysis is to increase solubility of cations in the core, but this effect is inseparable from the temperature effects on solubility. Generally, the oxygen activity in the PWR core should not deviate strongly from the nominal condition of 320 °C with 3 mg/kg H_2.

Displacement damage in the PWR core is significantly lower than the irradiation experiments in this work. The effect of radiation enhanced diffusion was found to be irrelevant for corrosion rates of all conditions in this work, so lower displacement damage rates will further decrease the relevance to the corrosion behavior. However, the relationship between displacement damage and porosity is the primary mechanism for changing corrosion rates. Unlike any 320 °C condition in this work, PWR cores have oxygen activity in regime 5 but also have displacement damage. Pores will already be present throughout the thickness of the inner

oxide because of the excess volume profile. Dissolution (of the inner oxide) is not a major factor due to the low (and not localized) radiolysis, so the inner oxide will persist to be affected by accumulated displacement damage. Like the steam condition, the oxide permeability greatly increased with displacement damage up to 0.18 dpa. Therefore, it is expected that radiation in-core will result in accelerated corrosion rate because the inner oxide permeability will increase with accumulated radiation damage. Most other features of the oxide will be unaffected by irradiation because the water chemistry and point defect concentrations will not be affected.

BWR NWC places the thermodynamic regime firmly at 7 because of the added oxygen. Like the PWR condition, water chemistry, solubility, and point defect concentrations will be not be affected by radiation. Therefore, the situation is very similar to the irradiated region in W24 and W72 except without significant dissolution. There will be a large portion of the inner oxide without excess volume, but without dissolution, the inner oxide porosity will resemble the 480 °C steam irradiated region. Pore nucleation and growth by radiation will enhance corrosion rates in the higher oxygen activity water, but the repassivation process will still result in overall lower corrosion rates than a hydrogenated water equivalent (HWC). Therefore, radiation will have a strong effect in increasing the corrosion rate via pore growth in BWR NWC, but the corrosion rate will still be lower than either PWR or BWR HWC without radiation.

BWR HWC is very similar to PWR in terms of the expected response to radiation. One interesting feature is the relatively low hydrogen addition in HWC compared to PWR which will place HWC in early regime 6 rather than 5. Consistent with literature, the corrosion rate should decrease with the lower hydrogen addition because there will be a small sublayer in the inner oxide with no excess volume. Countering this, however, the miscibility gap between Cr-rich and Fe-rich spinels is larger at lower temperatures, so excess volume is greater where it exists within

the inner oxide layer. Displacement damage will cause an increase in corrosion rate by exacerbating the pores in the inner oxide layer like PWR conditions, but also forming pores in the sublayer without excess volume. Furthermore, radiolysis may cause a substantial increase in oxygen activity which will mitigate the corrosion rate. Therefore, it is unclear if corrosion rates would increase or decrease in BWR HWC by radiation effects.

Cracking susceptibility in the various LWR environments is generally expected to be exacerbated by radiation effects on corrosion. Radiolysis increases the effective oxygen activity through H_2O_2 production, and elevated oxygen activity (i.e. ECP) increases cracking susceptibility. Displacement damage may or may not increase the corrosion rate and is very likely to increase the porosity of the inner oxide layer, so an embrittled inner oxide over a grain boundary is more likely to initiate cracking. Regarding crack growth rate, radiolysis in a crevice-like crack tip should be stronger than in the bulk, thereby enhancing the crack growth rate. Displacement damage will have a similar effect for crack growth rate by generally increasing the corrosion rate at the crack tip and generating a more porous oxide along grain boundaries.

Other coolants for advanced reactors often have fundamentally different corrosion mechanisms than light water. Notably, water radiolysis is entirely unrelated to other coolants, although equivalent radiation effects in the given coolant should not be discounted. For example, molten salt does not result in the formation of a protective oxide film, so most of the work here is irrelevant to this coolant. However, liquid metals such as sodium or lead bismuth eutectic with added oxygen may have some similar features of radiation effects on oxidation because of the formation of an oxide film. Porosity in the oxide may be an even more important factor at the higher temperatures for these advanced reactors which may result in significant effects of displacement damage on corrosion.

In summary, radiation effects are complex due to the separate effects of radiolysis and displacement damage. Radiolysis tends to increase oxygen activity which decreases corrosion rates. Displacement damage generally increases corrosion rates by increasing porosity and oxygen permeability to the inner oxide layer. The overall effect of radiation on corrosion rates will depend on the water chemistry. Radiolysis affects the oxygen activity relative to the nominal water chemistry, and displacement damage will change the permeability relative to the distribution of excess volume in the inner oxide layer in the radiolyzed condition.

Chapter 7
Conclusions

Corrosion of stainless steel in both 320 °C water and 480 °C steam, and the radiation effects thereof, were tested in this work. Radiation effects were separated into radiolysis and displacement damage and isolated experimentally to determine their effects on corrosion. The following conclusions were drawn from this work:

In the absence of irradiation and irrespective of environment:

1. Corrosion was broadly split into two modes of corrosion rate. The lower corrosion rate mode was rate-limited by solid-state oxygen transport from the environment to the metal/oxide interface and is caused by a protective air-grown oxide layer. The higher corrosion rate mode was rate-limited by oxygen transport through pores in the inner oxide layer.
2. Excess volume in the inner oxide layer is an essential feature controlling the corrosion rate of stainless steels. The permeability of the inner oxide layer controls the overall corrosion rate which is a function of thermodynamic excess volume in the inner oxide layer. Excess volume decreases with increasing oxygen activity resulting in lower corrosion rates in aerated water as compared to hydrogenated water. Both excess volume and corrosion rate in steam are between the respective values in aerated and hydrogenated water.

With radiolysis:

3. In hydrogenated water, radiolysis decreases the corrosion rate of stainless steel. Radiolysis of water yields hydrogen peroxide which increases the oxygen activity, similar to aerated water. This results in less excess volume in the inner oxide layer which results in less porosity, and this reduces the corrosion rate by limiting oxygen transport to the metal. In steam, radiolysis is minimal and does not alter the corrosion rate.
4. Radiolysis induces dissolution in water. Radiolysis confined to a small local area in the autoclave results in undersaturation of various cation species in the inner oxide layer. This causes localized dissolution of the inner oxide layer. Despite the active dissolution of the inner oxide layer, the corrosion rate is lower than without radiolysis even accounting for the dissolved oxide. In steam, dissolution is not possible and was not observed.

With displacement damage and radiolysis

5. Displacement damage increases the corrosion rate in steam. Radiation causes the growth of pores in the inner oxide by increasing the concentration of both cation and anion vacancies which accelerate both nucleation and growth of pores. This results in increased permeability of the inner oxide layer which allows more oxygen to reach the metal and thereby increase the corrosion rate.
6. Displacement damage has an insignificant effect on corrosion rate in radiolyzed water. The decreased excess volume and dissolution caused by radiolysis on the inner oxide reduce the capacity for displacement damage to grow pores. Without increased porosity, the oxygen permeability is unchanged, thus the corrosion rate is unchanged.

Chapter 8
Future Work

From the conclusions of this work, there are many avenues that would yield valuable information. The relative novelty of this work sets a foundation for many similar experiments with proton irradiation corrosion of stainless steel along different variable axes. Furthermore, there are many non-irradiation experiments that can test the model of excess volume and better define the regime in which porous transport of oxygen is the rate-limiting step for corrosion.

For irradiation-affected corrosion experiments, there are a few unexplored variables that could be examined using the approach laid out in this work.

Porosity

One key feature of stainless steel oxides that warrants further characterization is porosity of the inner oxide. Porosity is sometimes noted in the inner oxide layer, but it is often overlooked since it may be on the nanometer scale when oxide films are commonly measured on the micron scale. If porosity is rate-limiting for corrosion of stainless steels, the volume fraction and continuity of pore networks are very important to quantify. Doing so would enable better models for corrosion rate prediction and better understanding of general corrosion behavior for stainless steels.

For example, porosity could be imaged using tomography to generate a 3D map of pore networks. Tomography would generate quantitative volume fraction information in addition to the continuity of the pores. Another example is the use of a tracer isotope such as O-18 to elucidate the mechanism of oxygen transport to the metal/oxide interface. Introduction of O-18

partway through exposure would highlight the oxides grown in the latter part of the exposure. Used in tandem with atom probe tomography (or other similar techniques), the location of O-18 pores and the oxide/metal interface would provide more empirical evidence for porous transport of oxygen.

Excess Volume

The use of excess volume is a novel approach to understanding the corrosion behavior of multilayered oxide-forming alloys. There are potential applications in the use of stainless steels and other alloys in many different environments. Excess volume is used very narrowly in this work, so there is substantial work needed to determine its validity for each alloy-environment system.

For example, excess volume may be key to understanding the critical chromium content required by a steel to achieve passivation in a given environment. Performing similar thermodynamic modeling across chromium content in addition to oxygen activity would yield a relationship between chromium content and excess volume. Either when the excess volume crosses or otherwise approaches zero, the corresponding chromium content should be the critical amount.

Radiolysis

For radiolysis, the assumption in this work that radiolysis only affects the oxygen activity via hydrogen peroxide could be tested. A systematic study that covers the range of radiolysis dose rates in operating reactors would be a valuable dataset for reactor operators and designers in optimizing water chemistry.

The effect of dose rate could be tested by modulating the proton current density, thereby changing the amount of both hydrogen peroxide and other short-lived radiolysis products. The

LET of the ion can be changed by simply changing the energy of the proton beam to simulate different types of LWR environments. From these experiments, the expected corrosion behavior could be correlated with different levels of radiolysis.

Parallel experiments could be performed using variable amounts of added O_2 and added H_2O_2 to compare results directly with radiolysis experiments. From these sets of experiments, the effective H_2O_2/O_2 concentration can be calibrated to radiolysis dose rate and LET by regression of some characterization metric such as oxide thickness.

Short-lived radiolysis products may have a measurable effect on corrosion. These effects may be equivalent to changes in the oxygen activity and would be integrated into the effective H_2O_2/O_2 concentration value. Otherwise, discrepancies between the behaviors of added H_2O_2/O_2 and radiolysis can be examined in greater details as unique features of radiolysis effects on corrosion. For example, there may be changes in the formation of different oxide phases like hematite compared with equivalent H_2O_2/O_2 additions. Alternatively, there may be morphological or other differences that are not apparent in the corrosion rate.

Damage Rate

To better understand reactor irradiation effects on corrosion, it is important to test different levels of damage rate on corrosion of stainless steel. The damage rate used in this work is significantly higher than LWR damage rates for structural materials, and yet the effect was found to be unmeasurable. However, the fact that the hydrogenated water condition without radiolysis appeared to be partially limited by cation diffusion, it is possible that radiation enhanced diffusion in real LWR conditions would impact the corrosion rate.

To test the effect of damage rate, environments other than liquid water need to be used to avoid the dominating effect of water radiolysis. Low pressure steam as used in this work is one

possibility, but air or CO_2, among other options, may be an adequate surrogate for the radiolysis levels expected in a reactor. Because the oxide morphology and corrosion kinetics are remarkable similar across a wide range of environments and temperatures, similar mechanisms are likely to be rate-limiting among these different environments.

A variety of damage rates could be correlated to measured corrosion rates and compared with both radiation enhanced diffusion and porosity. This would reveal the active mechanisms as a function of damage rate and better determine the conditions in which cation/anion diffusion is or is not rate-limiting. Where porosity is rate-limiting, quantification of porosity within the inner oxide will correlate with the overall corrosion rate. Where atomic diffusion is limiting, radiation enhanced diffusion can be calculated and compared to corrosion rate data. Not only will this type of study determine the displacement damage effects on corrosion, it may also be used to disambiguate solid-state diffusion mechanisms from other mechanism such as porous transport of oxygen.

IASCC

Environment-assisted cracking is the main motivation for this work, so there is direct application to the study of irradiation-assisted stress corrosion cracking. There are several directions for research relevant to IASCC.

Grain boundary corrosion, and the irradiation effects thereof, is topic for future research because IASCC is generally intergranular. Grain boundary corrosion is difficult to study because it has an inherently low sample size compared to bulk corrosion behavior. The conclusions of this work, particularly the porous transport of oxygen as a rate-limiting step for corrosion, may assist in focusing attention on the porosity of intergranular oxides as a function of grain boundary attack. Therefore, a study specifically on grain boundary corrosion under irradiation

may be able to correlate grain boundary character to intergranular attack. Alternatively, the extent of grain boundary corrosion may be correlated to SCC initiation by mechanically testing materials exposed to irradiation corrosion.

Crevice corrosion under irradiation has some potential for improved understanding of radiation effects on crack growth rate. Since crack tips are typically very confined spaces that allow the environment to reach deep into the material, the effects of radiolysis particularly may change significantly compared to bulk corrosion. A crevice with radiolysis is likely to become a much more aggressive environment and may be responsible for increasing crack growth rate in IASCC.

Finally, a laboratory IASCC experiment combining strain, corrosion, and irradiation has great potential for determining the mechanisms of irradiation assistance of SCC. The irradiation would directly affect the metal at the crack tip in addition to the oxide formation along the crack and at the crack tip. Bringing all these elements together may reveal new mechanisms that cannot be observed by sequential testing, much like how SCC cannot be tested by sequential exposure and straining. Furthermore, the ability to change radiation parameters independently from the environment and straining allows for new axes to be studied and correlated with cracking behavior.

Reactor Experiments

One major gap in the literature is the characterization of oxides formed on stainless steels in LWR cores. As the original motivation for this work is improve understanding of radiation effects on corrosion in commercial LWR reactors, the most valuable data would be collected from these reactors. While materials from reactors are often expensive and difficult to handle, they are frequently harvested and used for corrosion and mechanical testing. So, examining the

oxides formed natively on these materials should be eminently achievable. Characterization of reactor-grown oxides would yield a much-needed basis for comparison for further ion irradiation corrosion experiments.

Appendix A

Autoclave and Irradiation Conditions

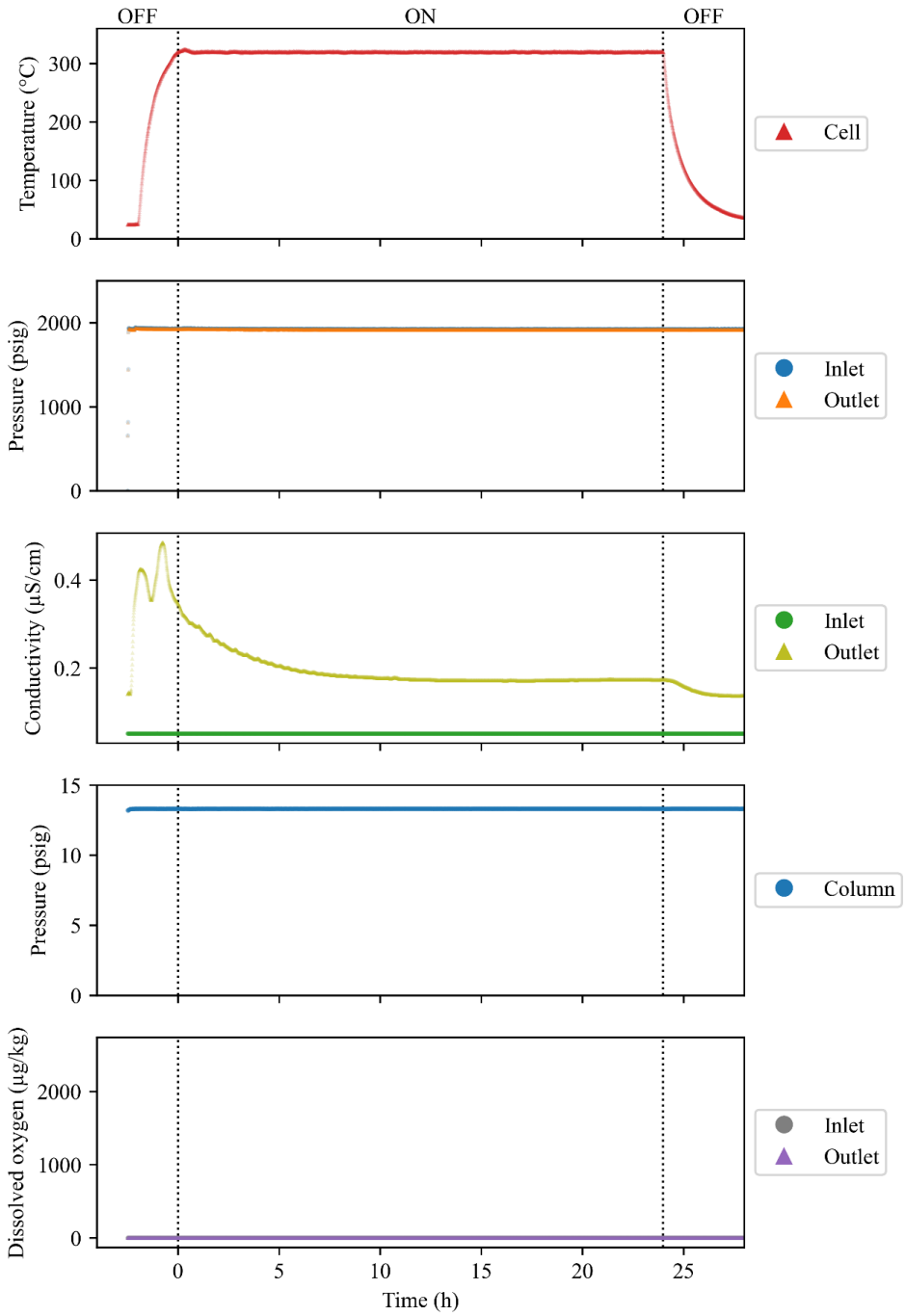

Figure A.1. Recorded cell parameters for control exposure sample X24 in high temperature hydrogenated water.

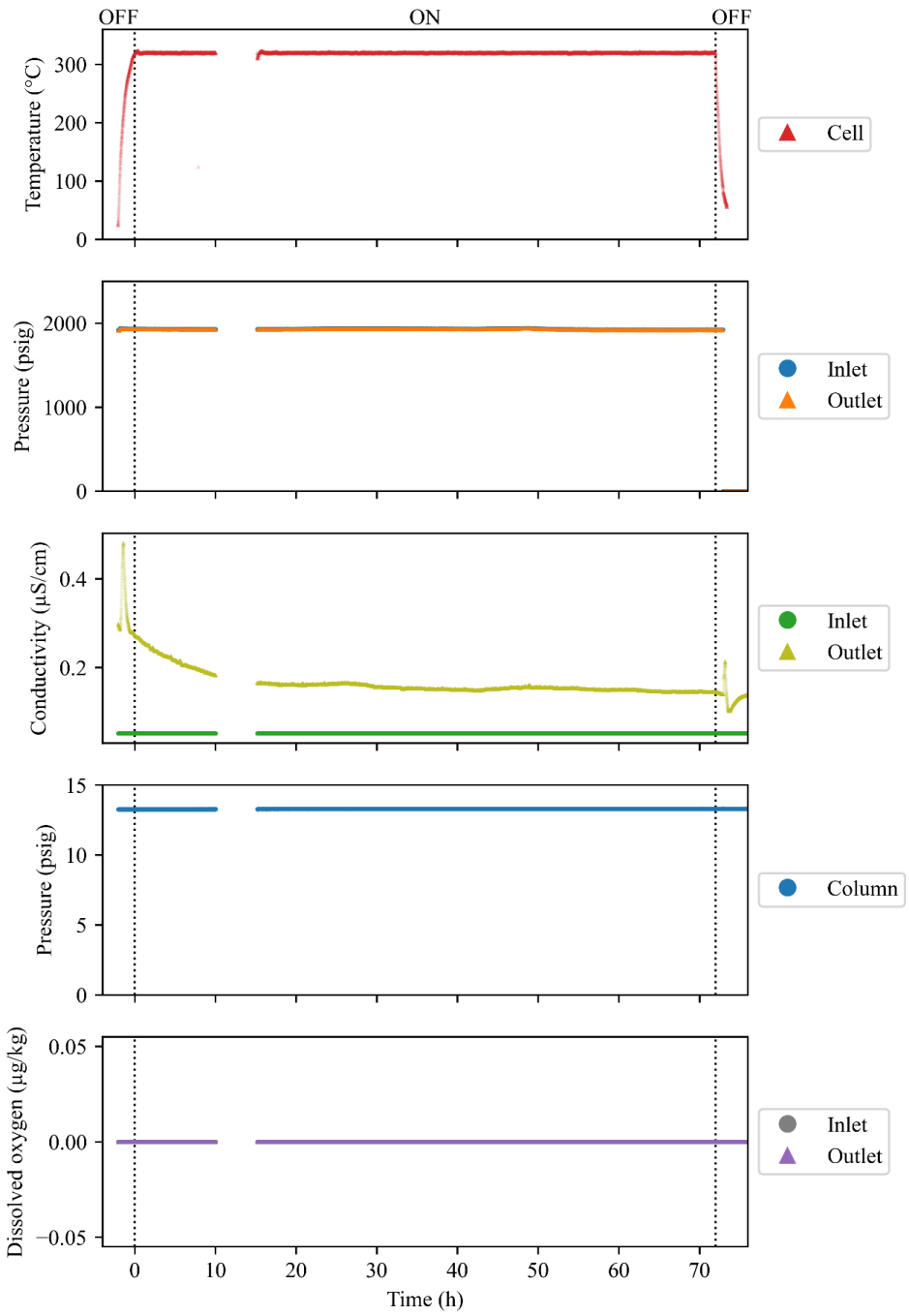

Figure A.2. Recorded cell parameters for control exposure sample X72 in high temperature hydrogenated water.

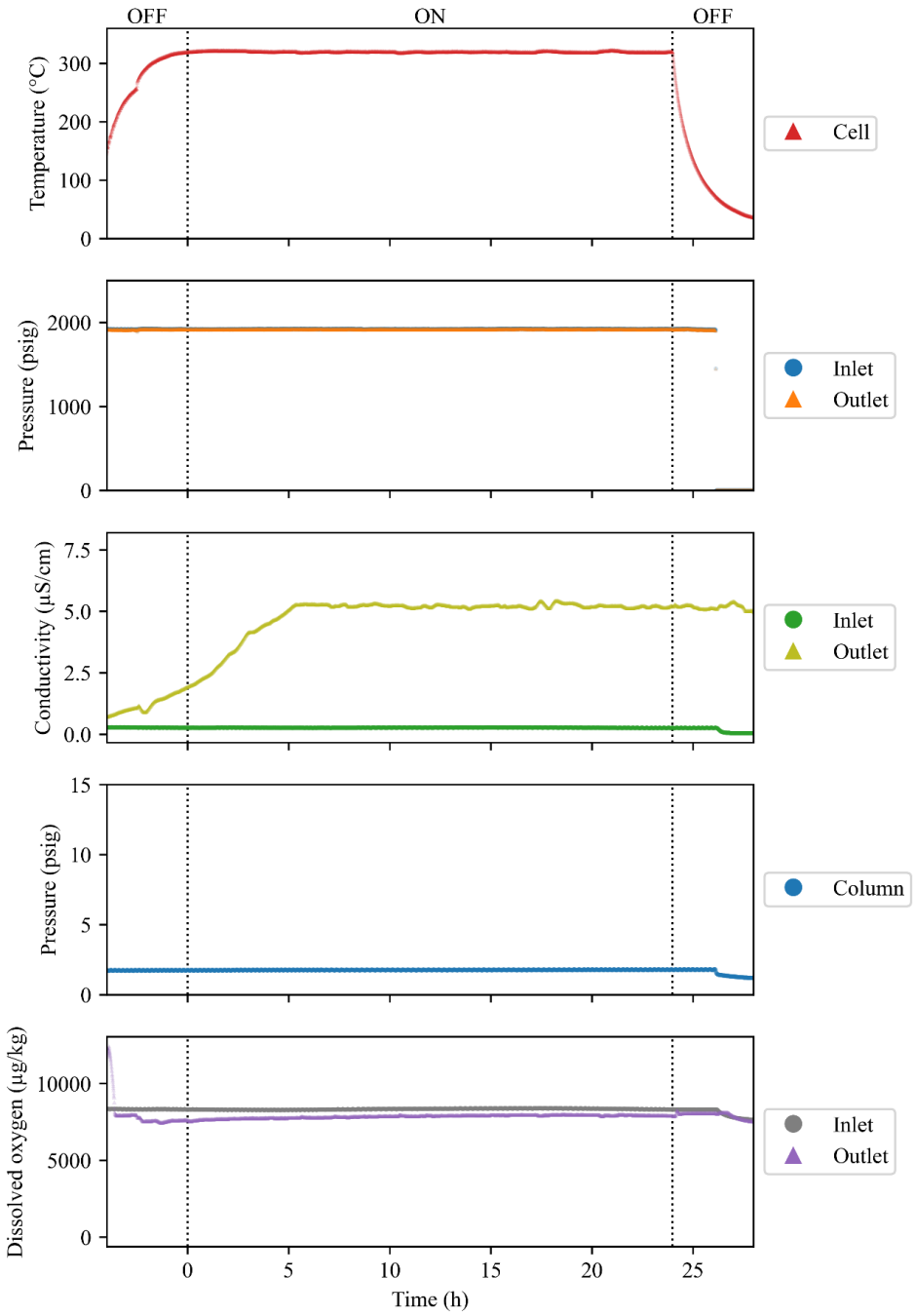

Figure A.3. Recorded cell parameters for control exposure sample A24 in high temperature aerated water.

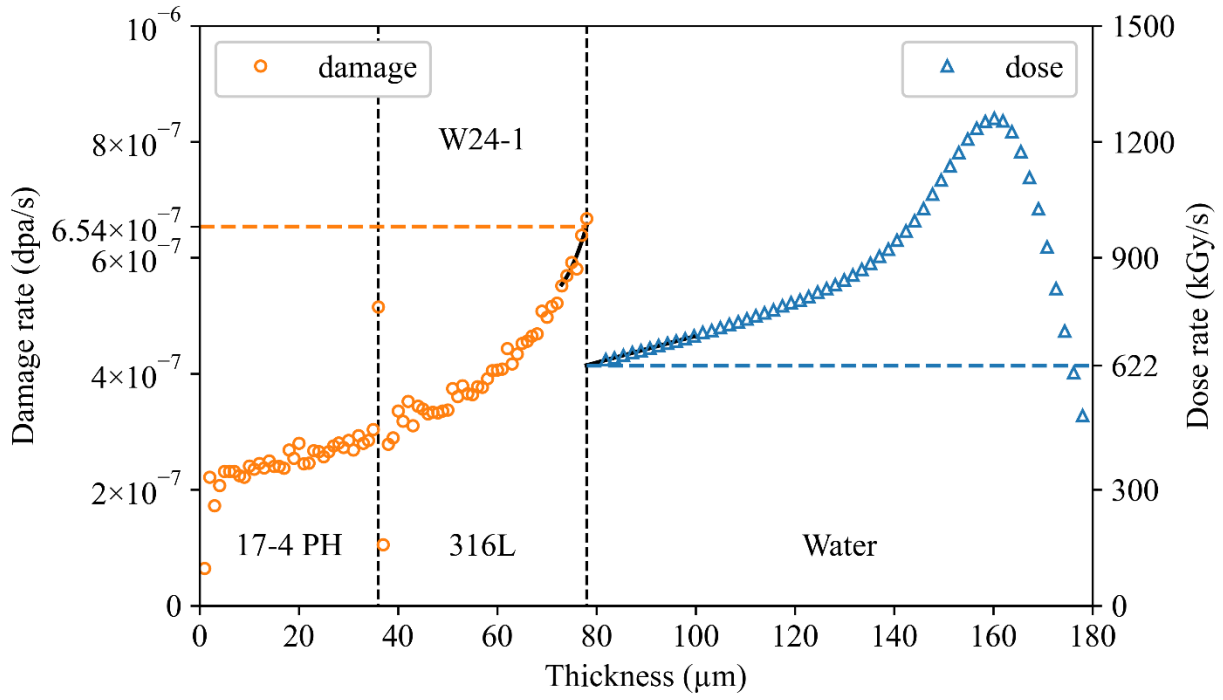

Figure A.4. Calculation of surface damage rate in 316L and dose rate in water using SRIM 2013 for sample W24-1.

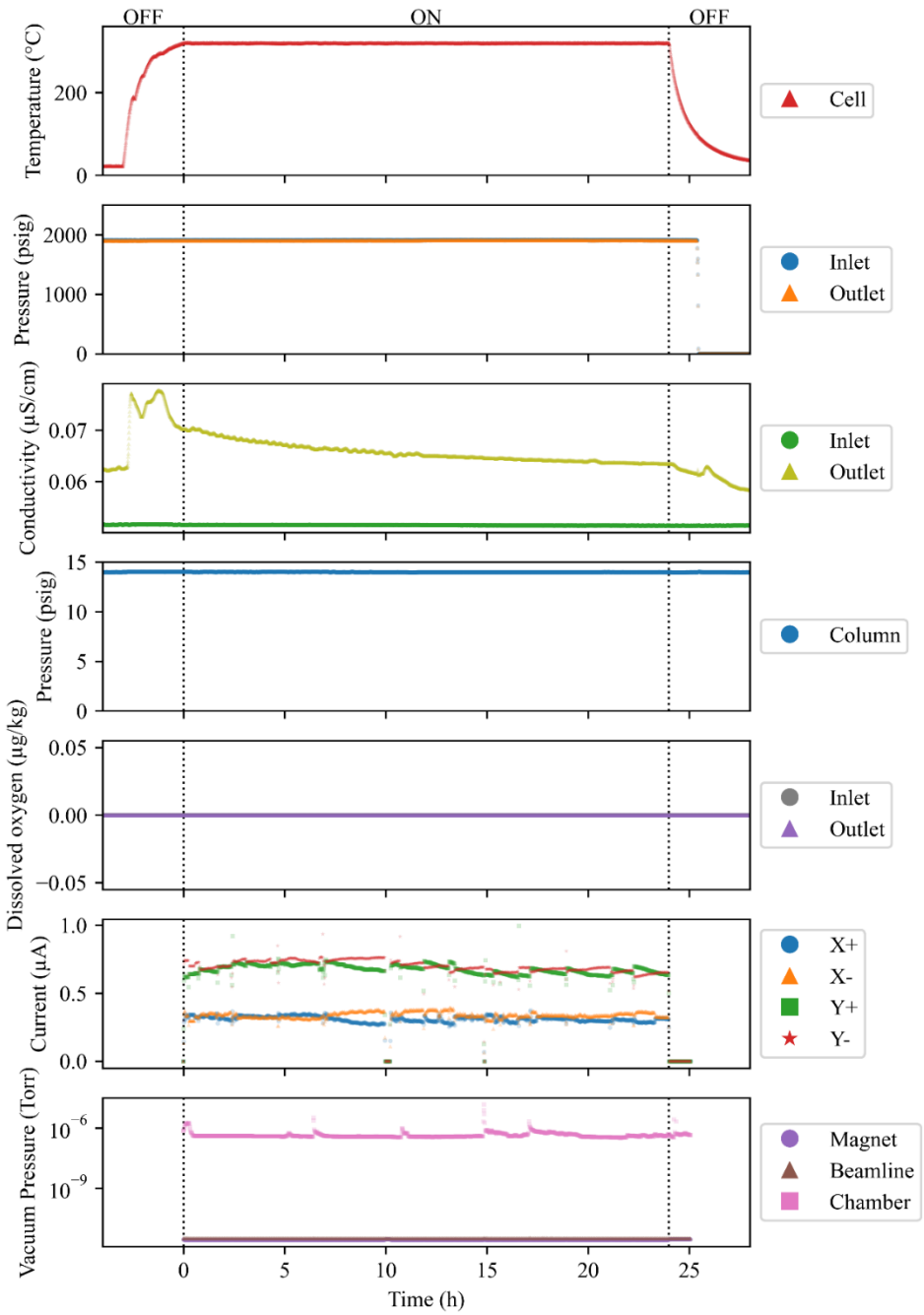

Figure A.5. Recorded cell parameters for proton irradiated exposure W24-1 in high temperature hydrogenated water.

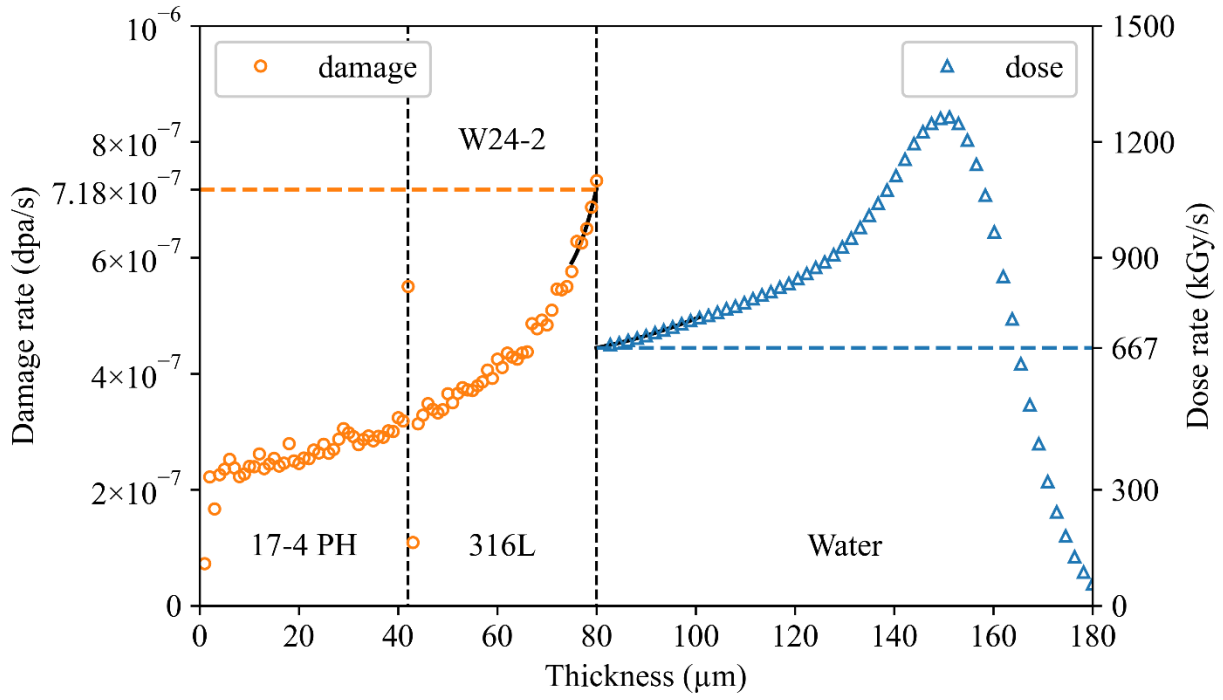

Figure A.6. Calculation of surface damage rate in 316L and dose rate in water using SRIM 2013 for sample W24-2.

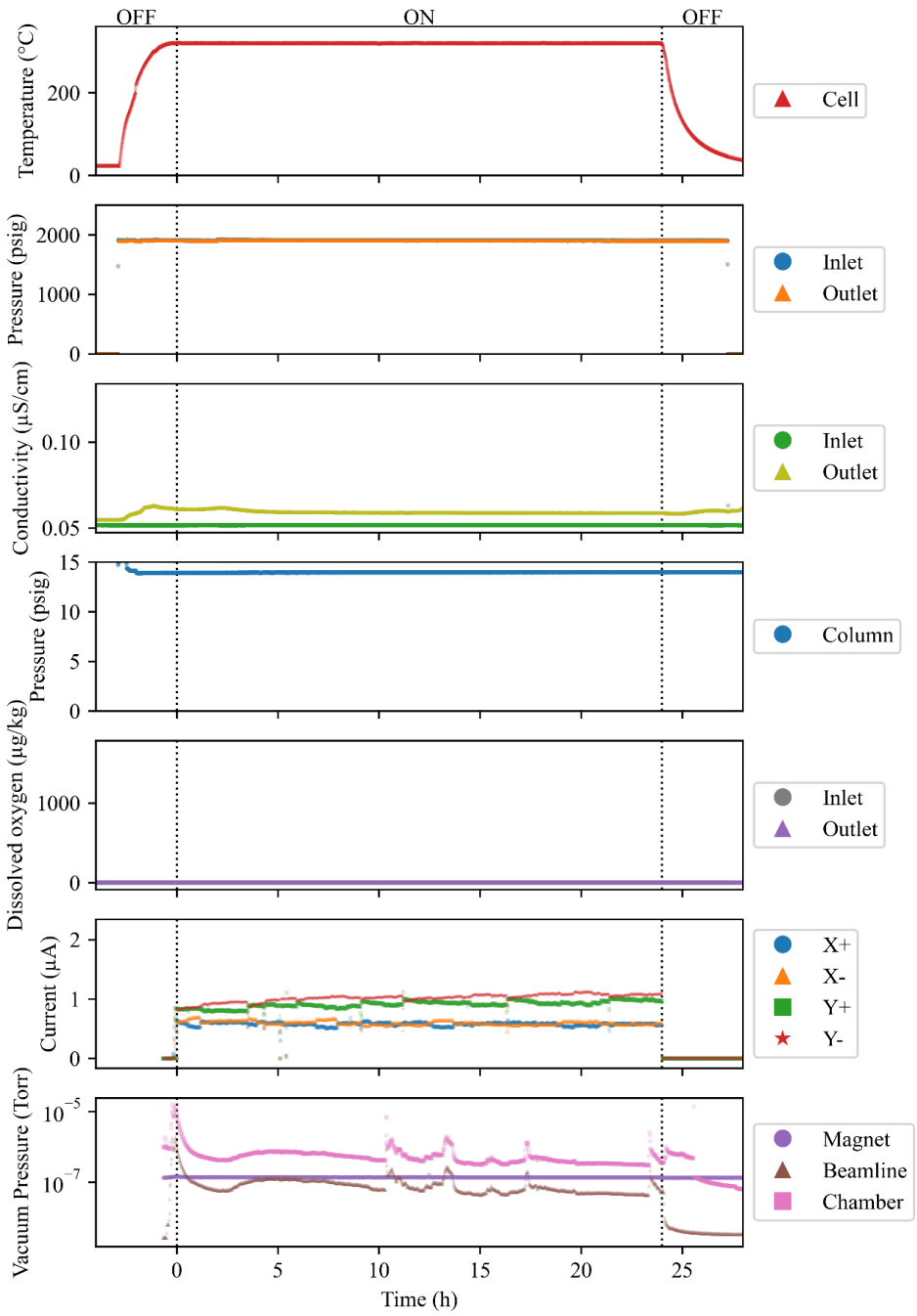

Figure A.7. Recorded cell parameters for proton irradiated exposure W24-2 in high temperature hydrogenated water.

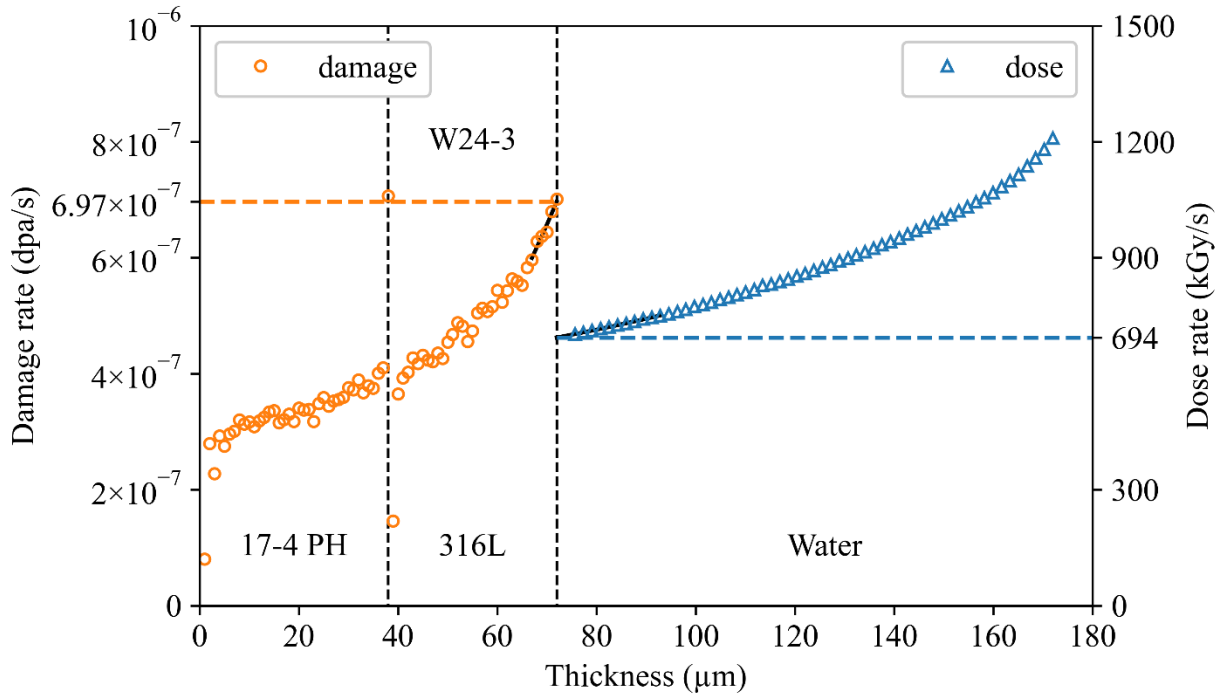

Figure A.8. Calculation of surface damage rate in 316L and dose rate in water using SRIM 2013 for sample W24-3.

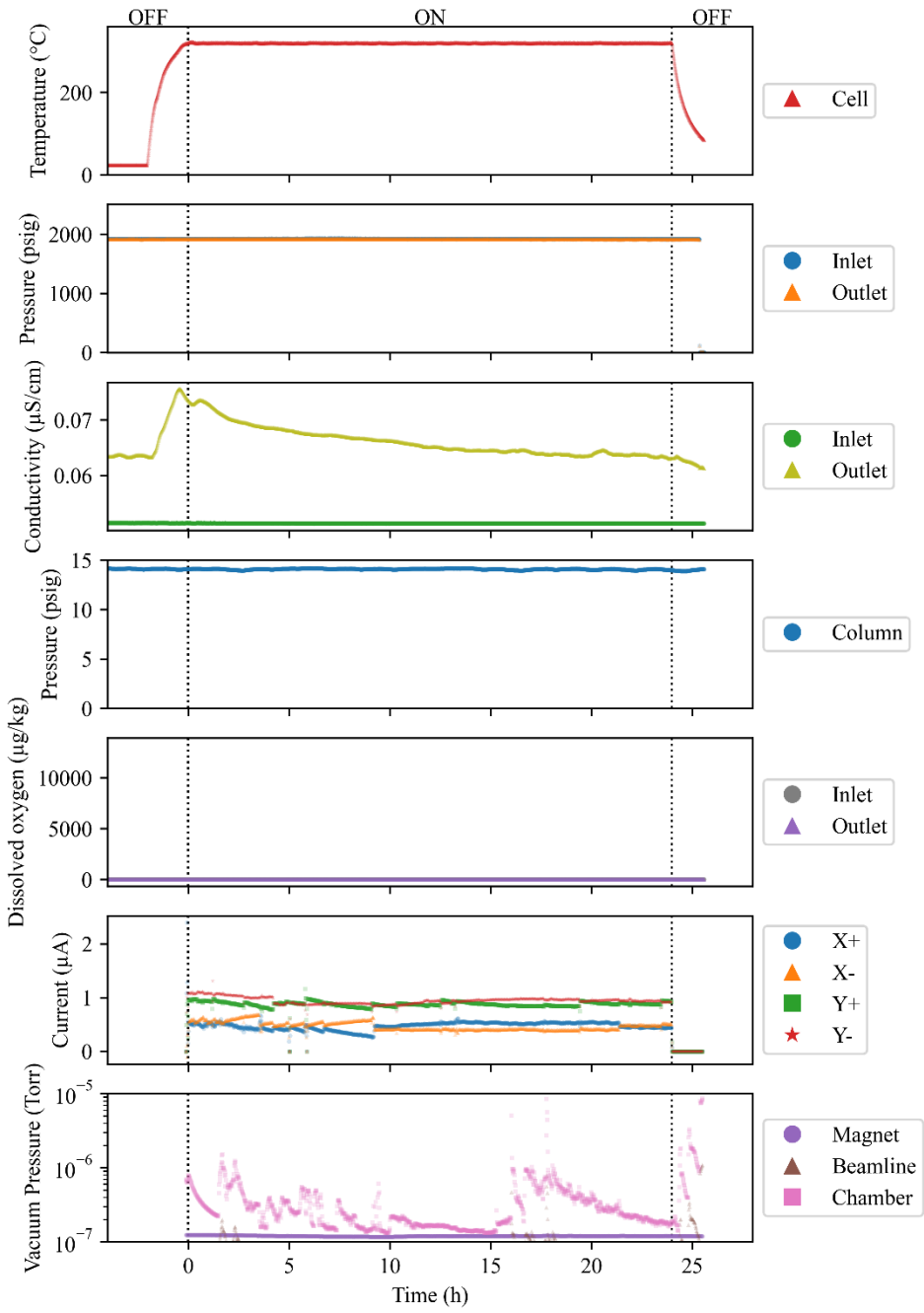

Figure A.9. Recorded cell parameters for proton irradiated exposure W24-3 in high temperature hydrogenated water.

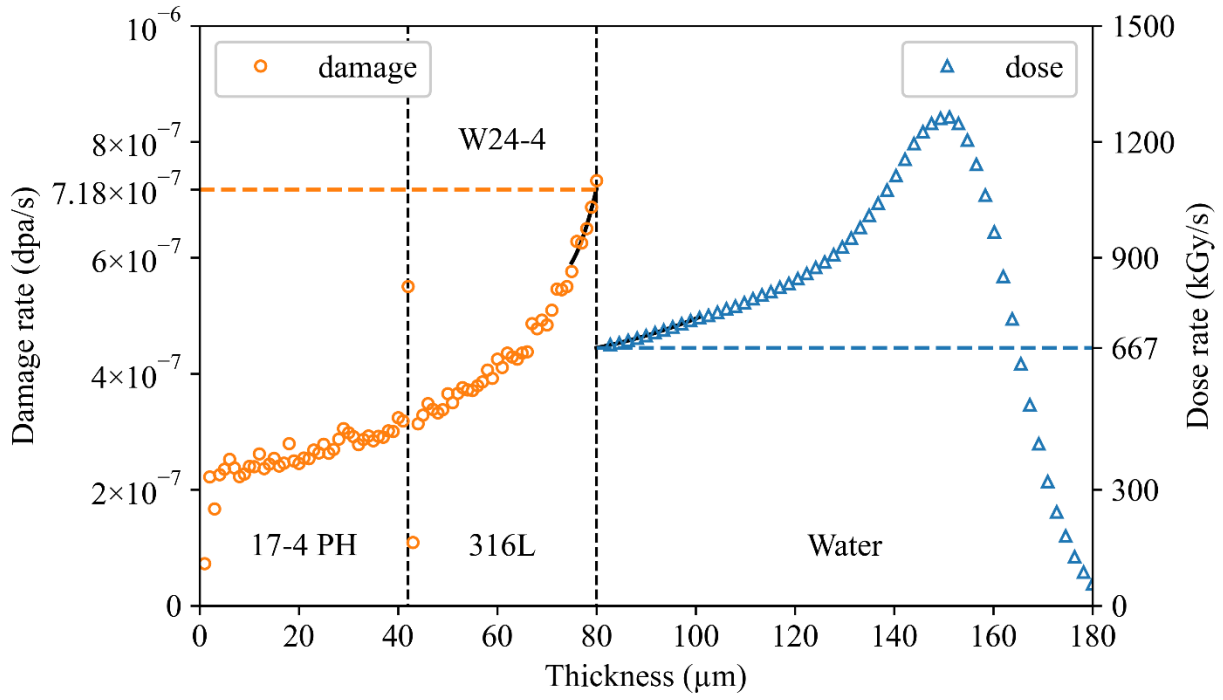

Figure A.10. Calculation of surface damage rate in 316L and dose rate in water using SRIM 2013 for sample W24-4.

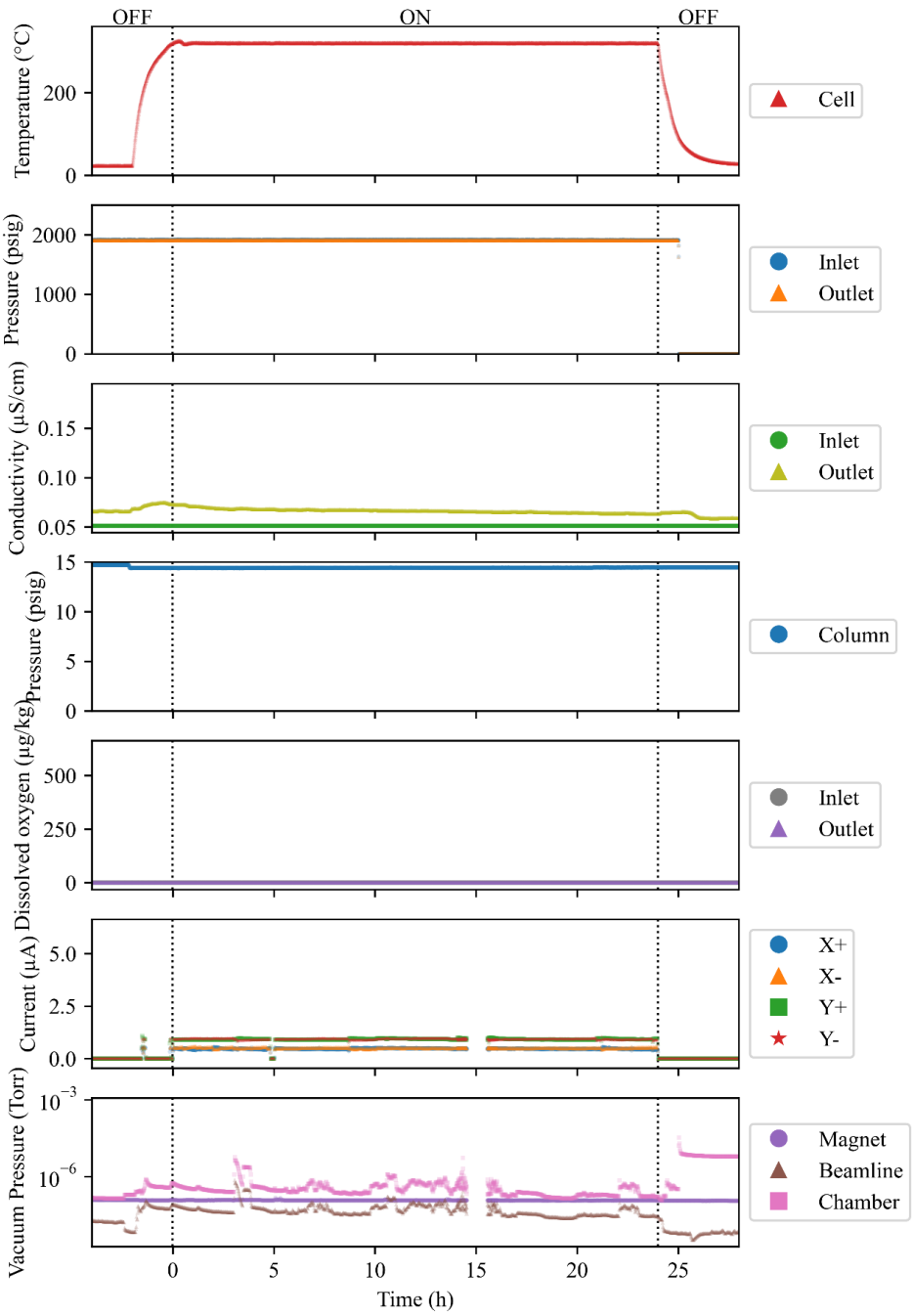

Figure A.11. Recorded cell parameters for proton irradiated exposure W24-4 in high temperature hydrogenated water.

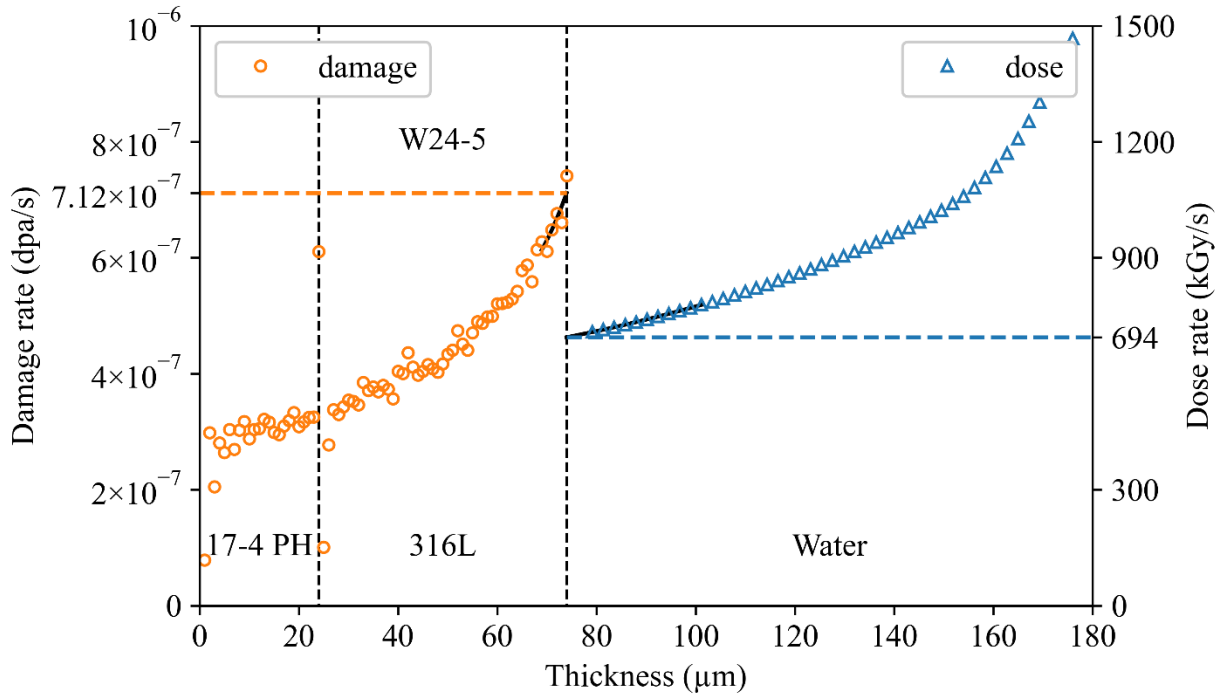

Figure A.12. Calculation of surface damage rate in 316L and dose rate in water using SRIM 2013 for sample W24-5.

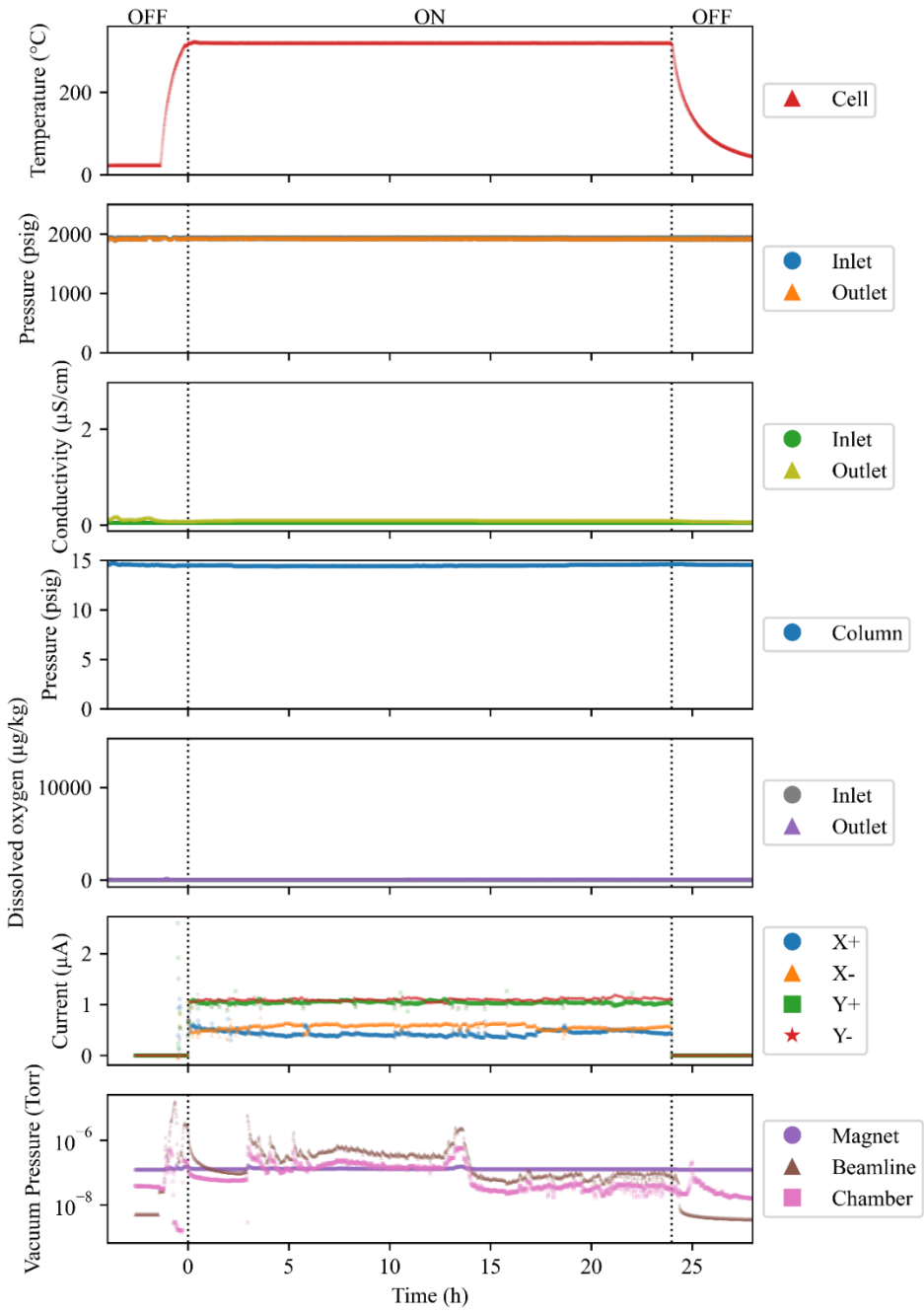

Figure A.13. Recorded cell parameters for proton irradiated exposure W24-5 in high temperature hydrogenated water.

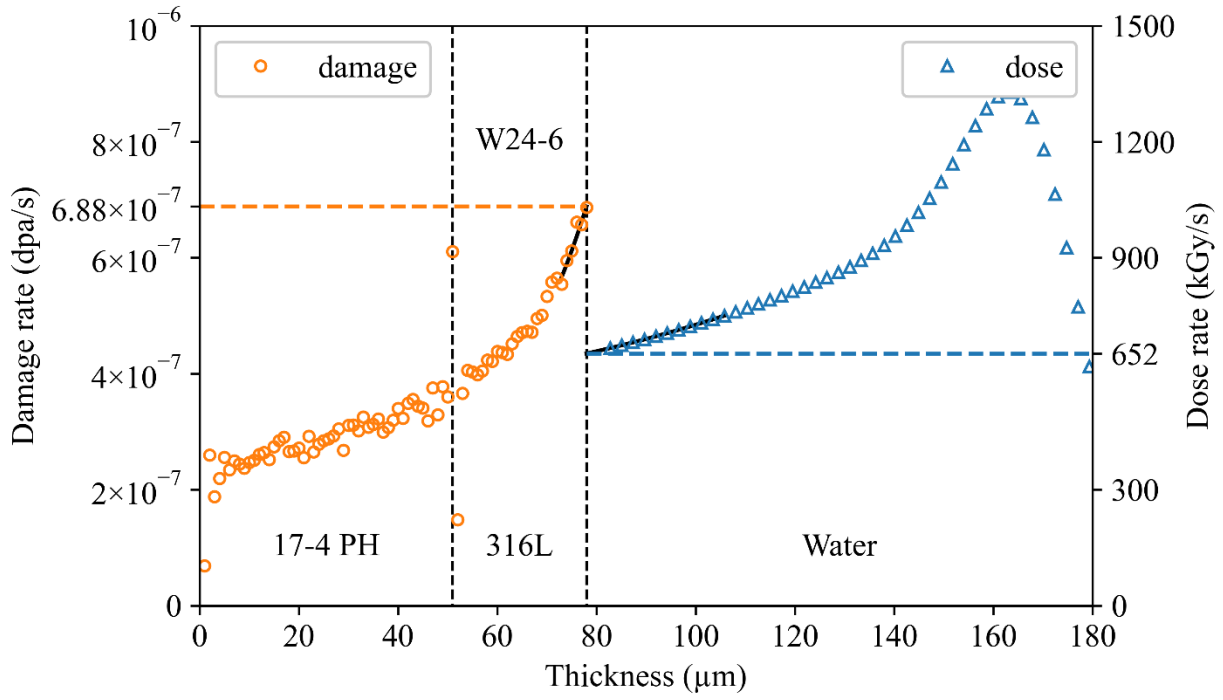

Figure A.14. Calculation of surface damage rate in 316L and dose rate in water using SRIM 2013 for sample W24-6.

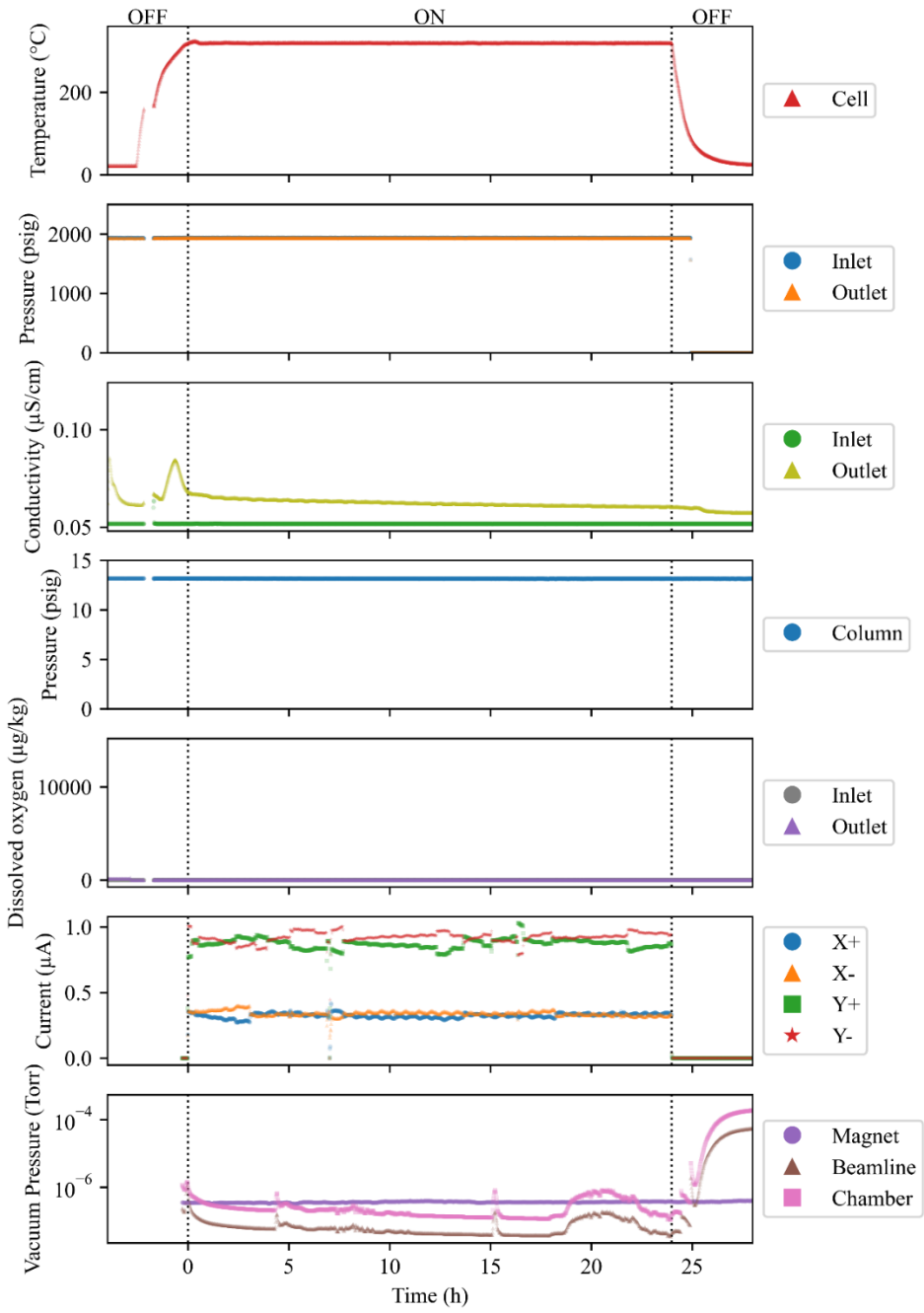

Figure A.15. Recorded cell parameters for proton irradiated exposure W24-6 in high temperature hydrogenated water.

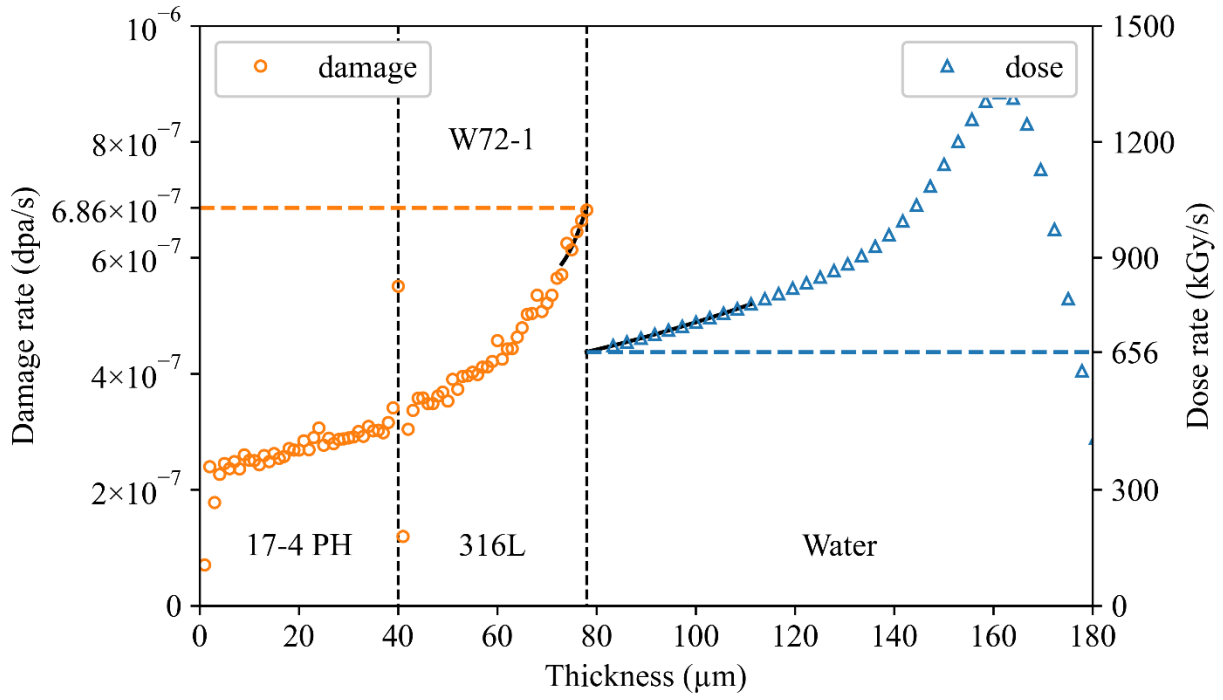

Figure A.16. Calculation of surface damage rate in 316L and dose rate in water using SRIM 2013 for sample W72-1.

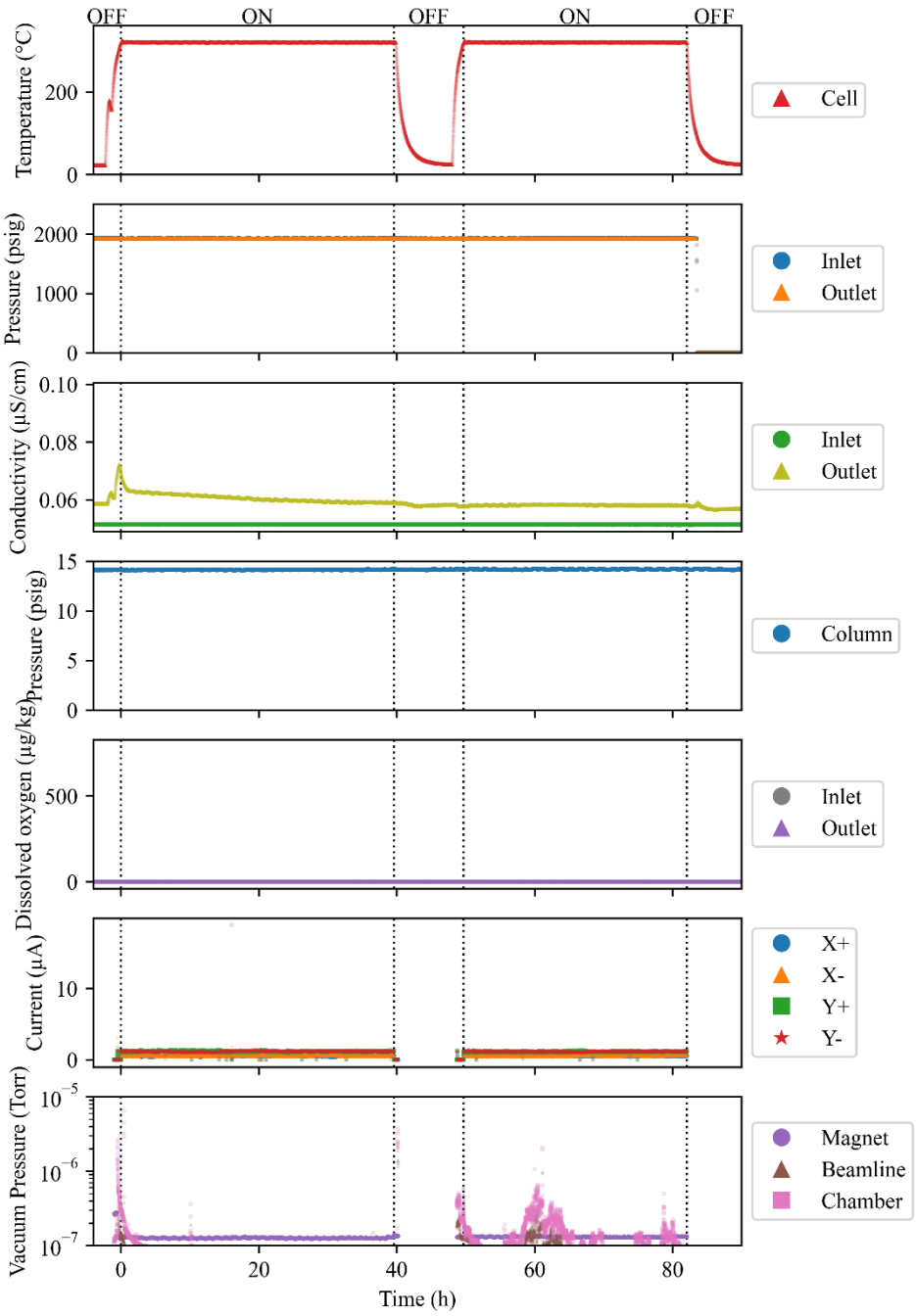

Figure A.17. Recorded cell parameters for proton irradiated exposure W72-1 in high temperature hydrogenated water.

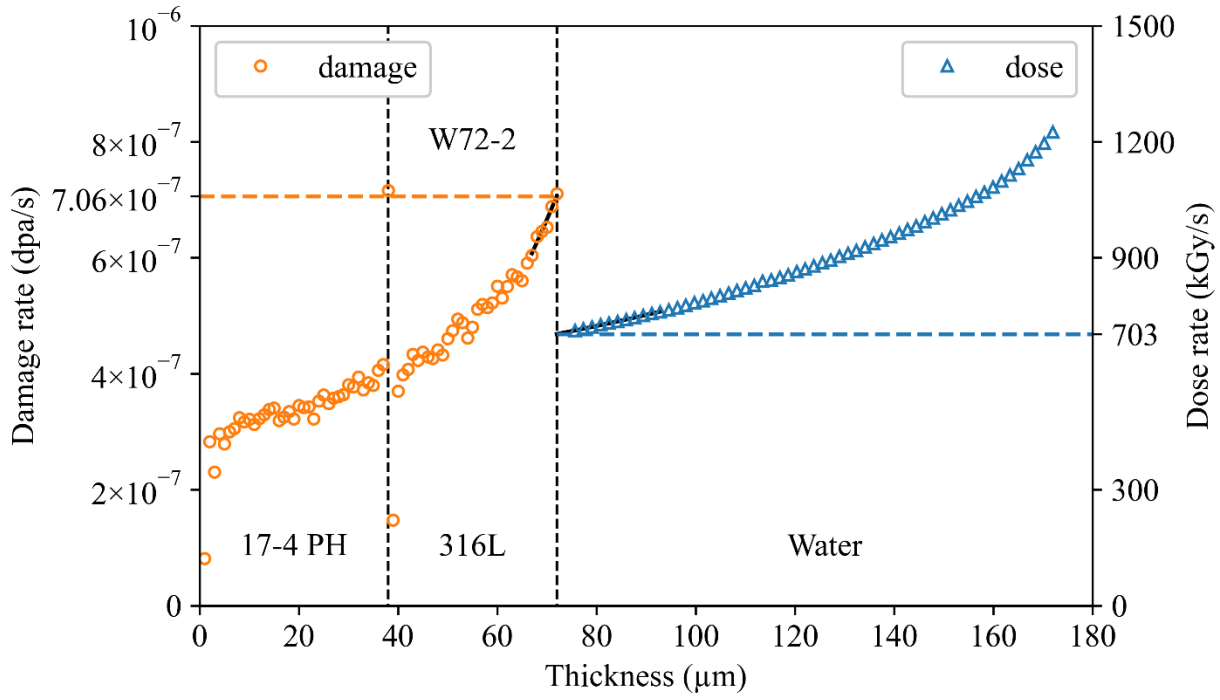

Figure A.18. Calculation of surface damage rate in 316L and dose rate in water using SRIM 2013 for sample W72-2.

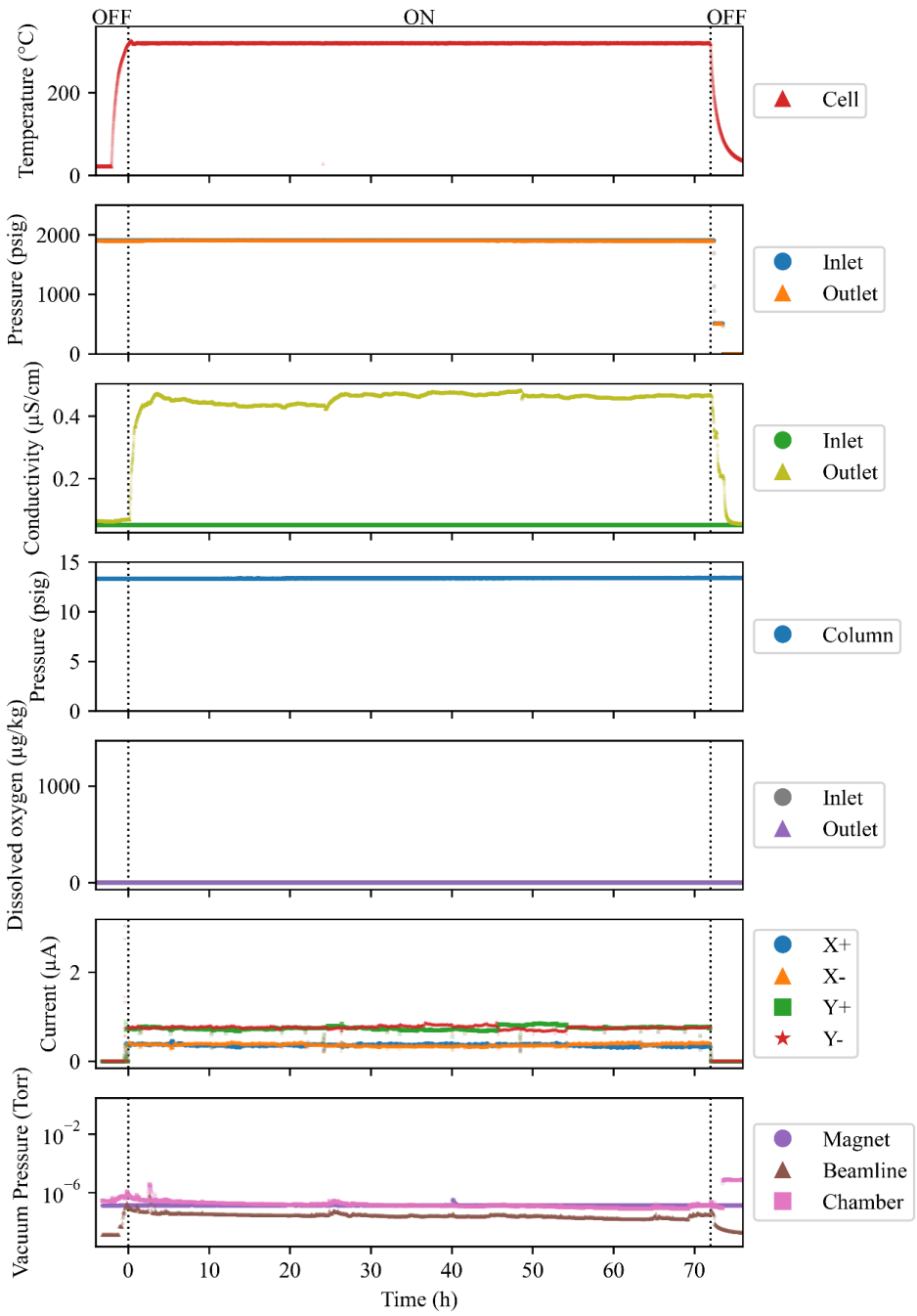

Figure A.19. Recorded cell parameters for proton irradiated exposure W72-2 in high temperature hydrogenated water.

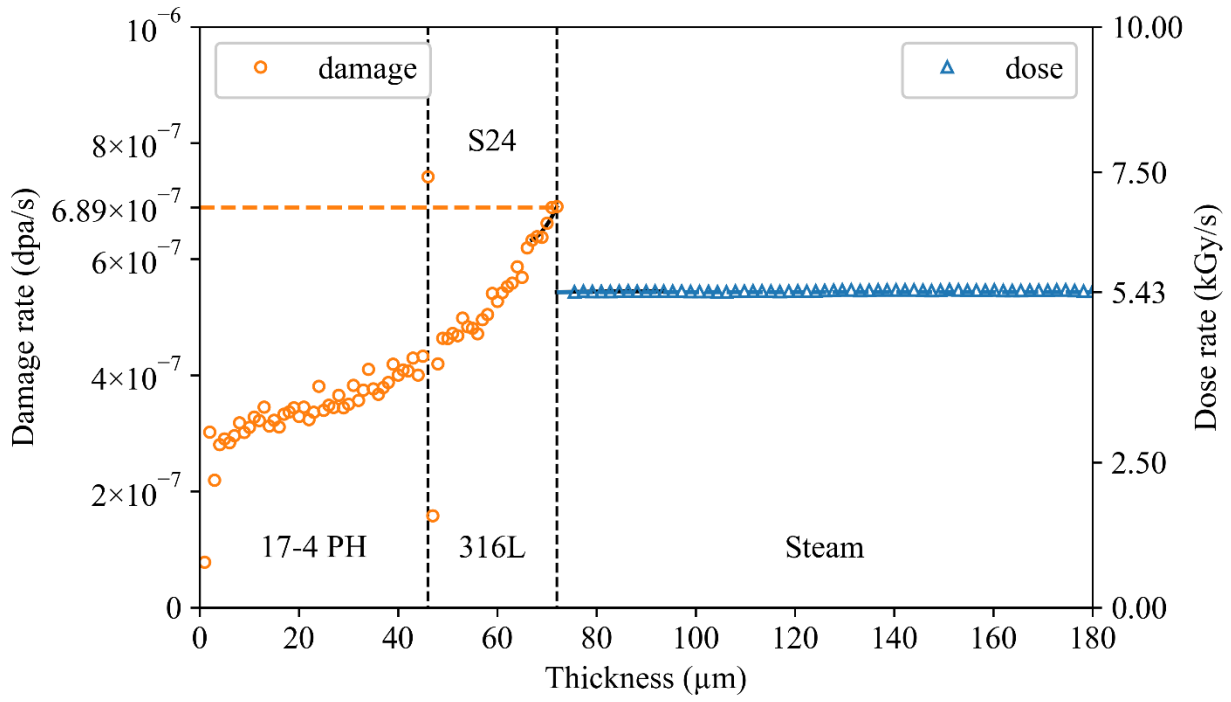

Figure A.20. Calculation of surface damage rate in 316L and dose rate in argon-steam using SRIM 2013 for sample S24.

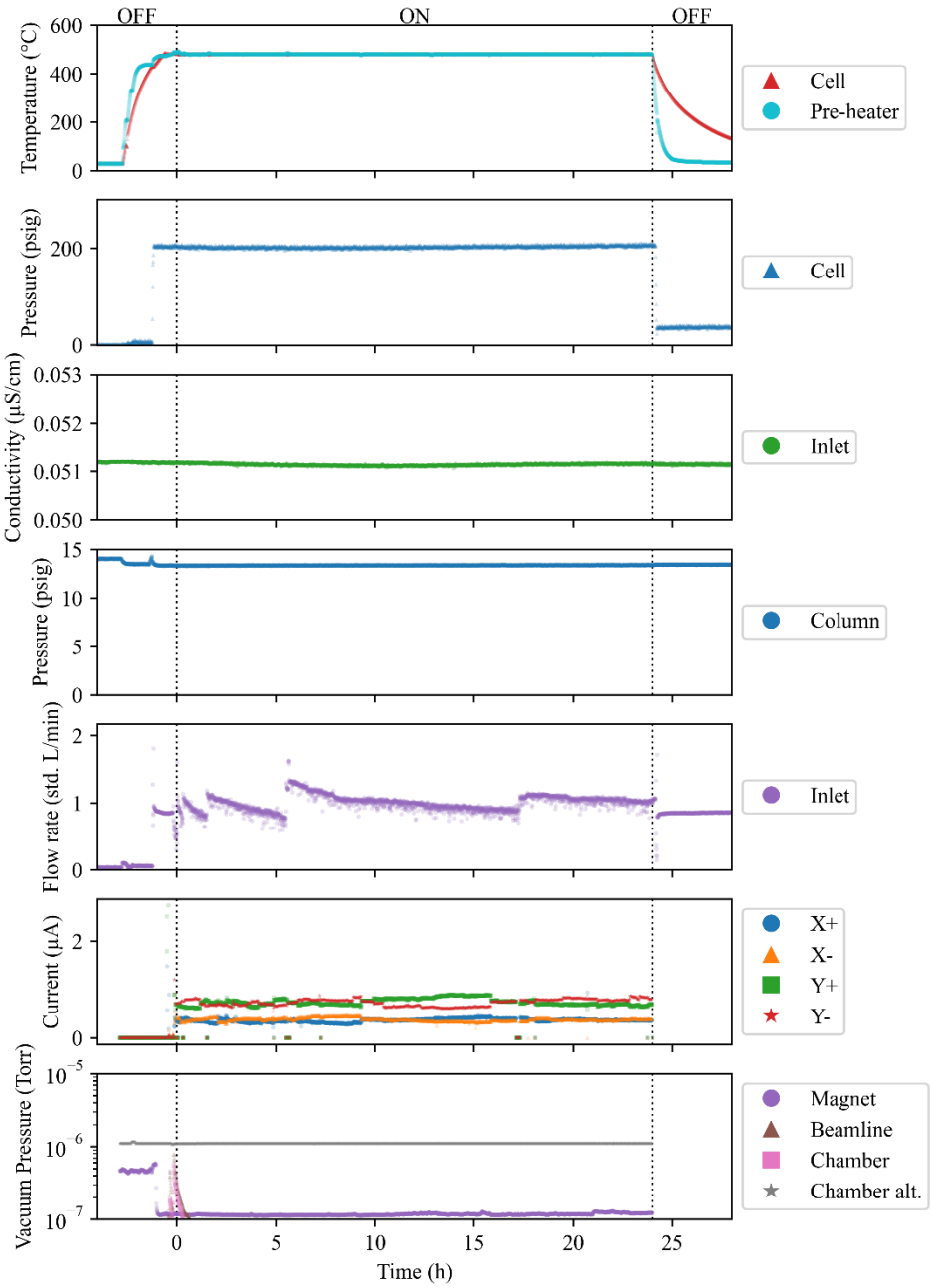

Figure A.21. Recorded cell parameters for proton irradiated exposure S24 in high temperature hydrogenated steam.

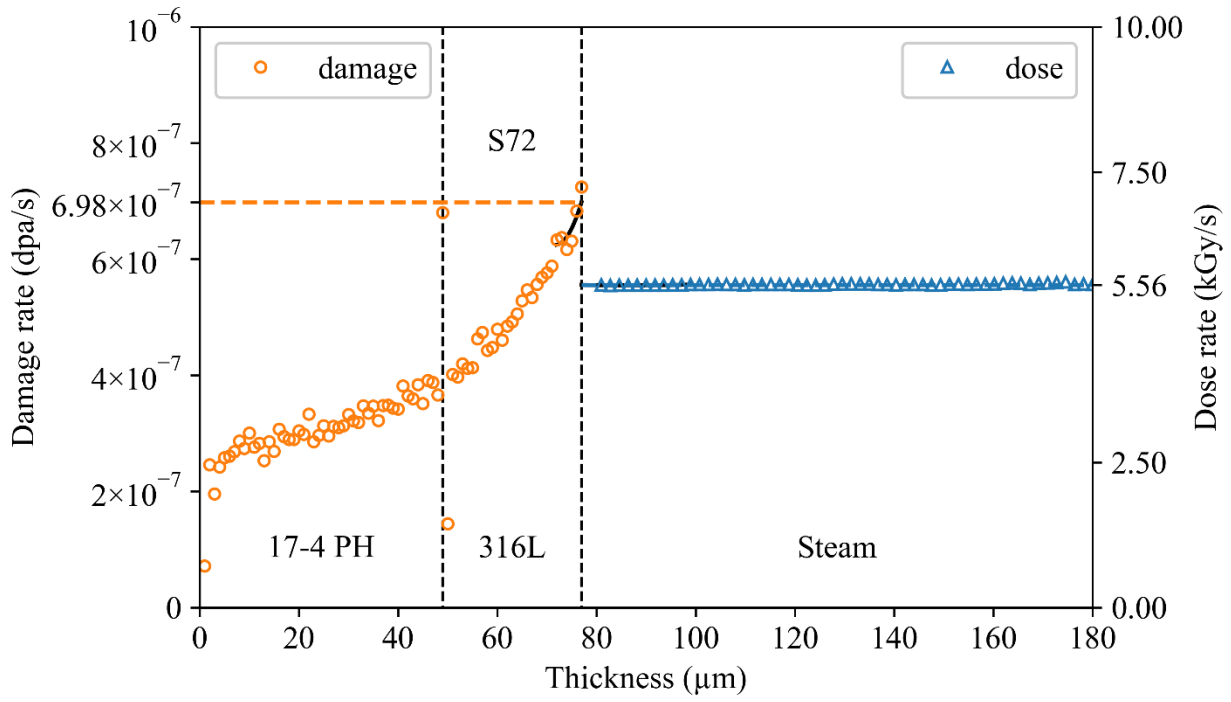

Figure A.22. Calculation of surface damage rate in 316L and dose rate in argon-steam using SRIM 2013 for sample S72.

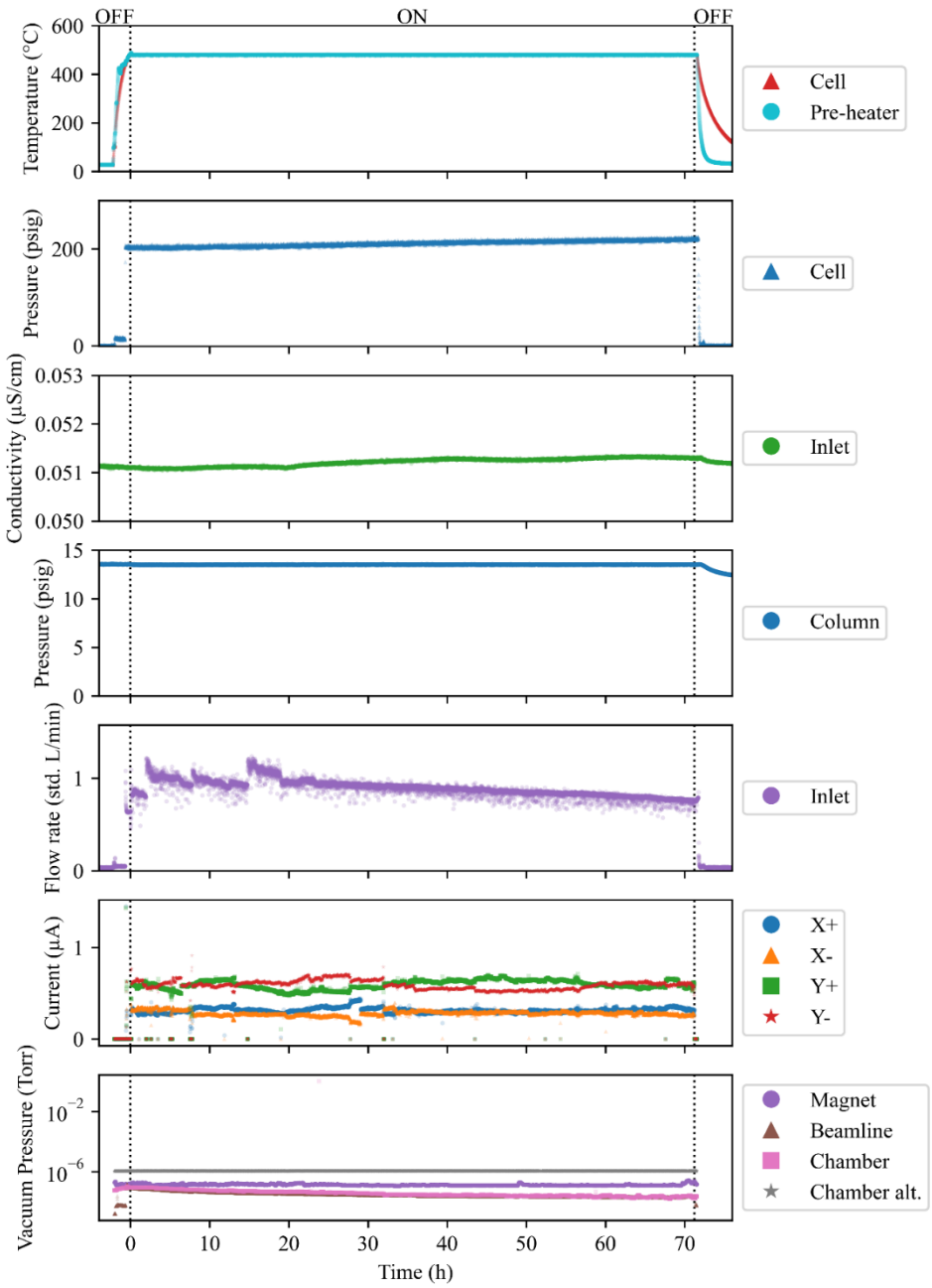

Figure A.23. Recorded cell parameters for proton irradiated exposure S72 in high temperature hydrogenated steam.

Appendix B

Sample Calculations

Inner oxide thickness, total oxidation, and dissolution

For each measurement of oxide thickness, a second measurement was made including all ambiguous areas that may contain a combination of metal and oxide through the thickness of the cross-sectional sample. Therefore, the difference between these values is the measurement error because it contains all ambiguity in the thickness measurement. This error is large enough that other sources of error, such as the magnification calibration of the instruments are negligible. For X72, the overall mean oxide thickness is 178.65 nm and the mean "maximum" oxide thickness is 196.32 nm. So the error in the inner oxide thickness measurement is ± 17.73 nm, and the reported inner oxide thickness is 179 nm ± 18 nm as in Table 5.2.

For total oxidation, the same "maximum" metal/oxide interface is used with the reconstructed original metal surface to generate a "maximum" total oxidation measurement. Additionally, the calibration error of the original metal surface reconstruction (11.3986 nm) is propagated together with the measured error to get the final value. For X72, the mean total oxidation is 183.32 nm, the mean "maximum" total oxidation is 200.99 nm, so the measured error is 17.72 nm. Note that this value is nearly identical to the inner oxide thickness because the upper interface does not contribute to the measurement ambiguity. The overall error is propagated with the reconstruction error to yield $\sqrt{(11.3986)^2 + (17.72)^2} = 21.07$ nm. The reported value for total oxidation is 183 nm ± 21 nm as in Table 5.2.

For dissolution the error is taken to be the reconstruction of the original metal surface error propagated with the relative error of the total oxidation. The measured value of the

dissolution in X72 is 4.67 nm and using the values from the total oxidation error calculation above, the error is calculated as $\sqrt{\{(11.3986)^2 + (21.07 \times 4.67/183.32)^2)} = 11.41$ nm. The reported value for dissolution is 5 nm ± 11 nm as in Table 5.2.

Error for the different modes is handled using the same methodology as the total measurements since they are generated using a subset of the data. The full dataset of X72 is split into mode 1 by taking all datapoints with inner oxide measurements below 75 nm and mode 2 is the remaining data. Mode 1 mean inner oxide thickness is 20.67 nm, the mean "maximum" inner oxide thickness is 25.85 nm, so the measured error is 5.35 nm, and the reported value is 20.7 nm ± 5.4 nm as in Table 5.2. Mode 1 mean total oxidation is 32.13 nm, the mean "maximum" total oxidation is 37.19 nm, so the measured error is 5.24 nm and propagated to $\sqrt{(11.3986)^2 + (5.24)^2} = 12.54$ nm, and the reported value is 32 nm ± 13 nm as in Table 5.2. Mode 2 mean inner oxide thickness is 213.3 nm, the mean "maximum" inner oxide thickness is 230.44 nm, so the measured error is 17.2 nm, and the reported value is 213 nm ± 17 nm as in Table 5.2. Mode 2 mean total oxidation is 215.76 nm, the mean "maximum" total oxidation is 232.52 nm, so the measured error is 16.82 nm and propagated to $\sqrt{(11.3986)^2 + (16.82)^2} = 20.32$ nm, and the reported value is 216 nm ± 20 nm as in Table 5.2.

STEM-EDS composition profile

Calculation of metal content and associated error are calculated point-by-point for each line scan. The first EDS line scan of X72 in Figure 5.7 is used here as an example for the calculation of both the values and error. Error comes from the counts used in the calculation of the K-factor from the ROI, and from the subsequent calculation of the elemental content at each point.

The scan is self-calibrated by identifying the ROI where the metal is relatively consistent in intensity across the metal elements (Fe, Cr, and Ni). The ROI for this case is 388 nm to the end of the scan, and the net counts of each element from the Kα peaks are summed in the ROI. Because iron is the primary element, it is used as the basis for the Cliff-Lorimer method in calculating the K-factors. The relative concentrations of these elements in the alloy are known, so the K-factors are calculated as $K_{AB} = C_A \times I_B/I_A$. Because the intensity values are measurements, they have an associated error $\sqrt{I}$. For convenience, the relative variance is used because error propagation with multiplication and division is simply the sum of relative variances which is $1/I$ for intensities. Therefore, the relative variance of each K-factor is $1/I_A + 1/I_B$. For Fe, the relative variance for the K-factor is $2/I_{\mathrm{Fe}}$.

Calculation of concentrations of each element is given by $C_{AB} = K_{AB} \times I_A/I_B$. Similar to the K-factor relative variance, here it is also $1/I_A + 1/I_B$ but for the particular datapoint intensities rather than the ROI. The final error calculation becomes:

$$\sigma = C_A\sqrt{[1/I_A + 1/I_B]_{\mathrm{ROI}} + [1/I_A + 1/I_B]_{\mathrm{point}}}$$

Table B.1. STEM-EDS concentration and error calculation from the datapoint at 100 nm in the first EDS line scan of X72 in Figure 5.7.

	ROI Intensity (counts)	Point Intensity (counts)	Concentration (%)	Error (%)
Fe	255425	881	26.9	1.3
Cr	71487	2003	62.7	2.5
Ni	49366	380	10.37	0.64

For an example calculation of these error, the intensities and errors from the datapoint at 100 nm in the first EDS line scan of X72 in Figure 5.7 are provided in Table B.1. For Fe, the error is calculated to be $26.9 \times \sqrt{2/255425 + 2/881} = 1.28\%$. For Cr, the error is calculated

to be $62.7 \times \sqrt{1/255425 + 1/71487 + 1/881 + 1/2003} = 2.55\%$. For Ni, the error is calculated to be $26.9 \times \sqrt{1/255425 + 1/49366 + 1/881 + 1/380} = 0.638\%$.

Appendix C

Thermocalc Results and Derived Values

Table C.1. Thermo-Calc results for FCC phase composition and fractions at 320 °C and 13.1 MPa.

O2 Activity (atm)	FCC volume fraction	Number density (mol/cm3)	Fe mole fraction	Cr mole fraction	Ni mole fraction
7.18E-66	1.00E+00	1.44E-01	6.85E-01	1.98E-01	1.19E-01
3.92E-64	1.00E+00	1.44E-01	6.85E-01	1.98E-01	1.19E-01
6.79E-64	1.00E+00	1.44E-01	6.85E-01	1.98E-01	1.19E-01
1.18E-63	1.00E+00	1.44E-01	6.85E-01	1.98E-01	1.19E-01
2.04E-63	1.00E+00	1.44E-01	6.85E-01	1.98E-01	1.19E-01
3.54E-63	1.00E+00	1.44E-01	6.85E-01	1.98E-01	1.19E-01
6.13E-63	1.00E+00	1.44E-01	6.85E-01	1.98E-01	1.19E-01
1.06E-62	1.00E+00	1.44E-01	6.85E-01	1.98E-01	1.19E-01
1.84E-62	1.00E+00	1.44E-01	6.85E-01	1.98E-01	1.19E-01
3.19E-62	1.00E+00	1.44E-01	6.85E-01	1.98E-01	1.19E-01
5.53E-62	1.00E+00	1.44E-01	6.85E-01	1.98E-01	1.19E-01
9.59E-62	1.00E+00	1.44E-01	6.85E-01	1.98E-01	1.19E-01
1.66E-61	1.00E+00	1.44E-01	6.85E-01	1.98E-01	1.19E-01
2.88E-61	1.00E+00	1.44E-01	6.85E-01	1.98E-01	1.19E-01
4.99E-61	1.00E+00	1.44E-01	6.85E-01	1.98E-01	1.19E-01
8.65E-61	1.00E+00	1.44E-01	6.85E-01	1.98E-01	1.19E-01
1.50E-60	1.00E+00	1.44E-01	6.85E-01	1.98E-01	1.19E-01
2.60E-60	1.00E+00	1.44E-01	6.85E-01	1.98E-01	1.19E-01
4.51E-60	1.00E+00	1.44E-01	6.85E-01	1.98E-01	1.19E-01
5.50E-60	8.55E-01	1.43E-01	8.08E-01	5.02E-02	1.41E-01
5.61E-60	8.54E-01	1.43E-01	8.11E-01	4.92E-02	1.41E-01
6.27E-60	8.50E-01	1.42E-01	8.17E-01	4.35E-02	1.42E-01
6.99E-60	8.45E-01	1.43E-01	8.19E-01	3.88E-02	1.43E-01
7.81E-60	8.42E-01	1.43E-01	8.21E-01	3.45E-02	1.43E-01
8.72E-60	8.39E-01	1.42E-01	8.27E-01	3.10E-02	1.44E-01
9.73E-60	8.37E-01	1.42E-01	8.30E-01	2.79E-02	1.45E-01
1.09E-59	8.34E-01	1.43E-01	8.29E-01	2.51E-02	1.45E-01
1.21E-59	8.33E-01	1.42E-01	8.32E-01	2.27E-02	1.45E-01
1.35E-59	8.31E-01	1.42E-01	8.35E-01	2.06E-02	1.46E-01
2.35E-59	8.25E-01	1.42E-01	8.41E-01	1.28E-02	1.46E-01
4.07E-59	8.21E-01	1.43E-01	8.43E-01	8.24E-03	1.47E-01
7.05E-59	8.19E-01	1.42E-01	8.46E-01	5.36E-03	1.47E-01
1.22E-58	8.18E-01	1.42E-01	8.49E-01	3.53E-03	1.48E-01

2.12E-58	8.17E-01	1.42E-01	8.49E-01	2.33E-03	1.48E-01
3.67E-58	8.16E-01	1.42E-01	8.52E-01	1.55E-03	1.49E-01
6.36E-58	8.16E-01	1.42E-01	8.52E-01	1.03E-03	1.49E-01
1.10E-57	8.16E-01	1.42E-01	8.52E-01	6.85E-04	1.48E-01
1.91E-57	8.16E-01	1.42E-01	8.52E-01	4.55E-04	1.48E-01
3.31E-57	8.16E-01	1.42E-01	8.52E-01	3.05E-04	1.48E-01
5.74E-57	8.16E-01	1.42E-01	8.52E-01	2.05E-04	1.48E-01
9.95E-57	8.16E-01	1.42E-01	8.52E-01	1.34E-04	1.48E-01
1.72E-56	8.15E-01	1.42E-01	8.52E-01	9.19E-05	1.48E-01
2.99E-56	8.15E-01	1.42E-01	8.52E-01	5.85E-05	1.48E-01
5.18E-56	8.15E-01	1.42E-01	8.52E-01	4.18E-05	1.48E-01
8.98E-56	8.15E-01	1.42E-01	8.52E-01	2.51E-05	1.48E-01
1.56E-55	8.15E-01	1.42E-01	8.52E-01	1.67E-05	1.48E-01
2.70E-55	8.15E-01	1.42E-01	8.52E-01	1.25E-05	1.48E-01
4.68E-55	8.15E-01	1.42E-01	8.52E-01	8.35E-06	1.48E-01
8.10E-55	8.15E-01	1.42E-01	8.52E-01	4.19E-06	1.48E-01
1.40E-54	8.15E-01	1.42E-01	8.52E-01	3.56E-06	1.48E-01
2.43E-54	8.15E-01	1.42E-01	8.52E-01	2.38E-06	1.48E-01
4.22E-54	8.15E-01	1.42E-01	8.52E-01	1.58E-06	1.48E-01
7.31E-54	8.15E-01	1.42E-01	8.52E-01	1.06E-06	1.48E-01
1.27E-53	8.15E-01	1.42E-01	8.52E-01	7.06E-07	1.48E-01
2.20E-53	8.15E-01	1.42E-01	8.52E-01	4.68E-07	1.48E-01
3.81E-53	8.15E-01	1.42E-01	8.52E-01	3.13E-07	1.48E-01
6.60E-53	8.15E-01	1.42E-01	8.52E-01	2.08E-07	1.48E-01
1.14E-52	8.15E-01	1.42E-01	8.52E-01	1.39E-07	1.48E-01
1.98E-52	8.15E-01	1.42E-01	8.52E-01	9.27E-08	1.48E-01
3.44E-52	8.15E-01	1.42E-01	8.52E-01	6.18E-08	1.48E-01
5.96E-52	8.15E-01	1.42E-01	8.52E-01	4.11E-08	1.48E-01
1.03E-51	8.15E-01	1.42E-01	8.52E-01	2.74E-08	1.48E-01
1.79E-51	8.15E-01	1.42E-01	8.52E-01	1.82E-08	1.48E-01
3.10E-51	8.15E-01	1.42E-01	8.52E-01	1.21E-08	1.48E-01
5.38E-51	8.15E-01	1.42E-01	8.52E-01	8.06E-09	1.48E-01
9.32E-51	8.15E-01	1.42E-01	8.52E-01	5.39E-09	1.48E-01
1.35E-50	5.05E-01	1.43E-01	8.27E-01	3.87E-09	1.69E-01
1.62E-50	5.05E-01	1.43E-01	8.27E-01	3.23E-09	1.69E-01
2.80E-50	5.05E-01	1.43E-01	8.27E-01	1.86E-09	1.69E-01
4.85E-50	5.05E-01	1.43E-01	8.27E-01	1.08E-09	1.69E-01
8.41E-50	5.05E-01	1.43E-01	8.27E-01	6.20E-10	1.69E-01
1.46E-49	5.05E-01	1.43E-01	8.27E-01	3.58E-10	1.69E-01
2.53E-49	5.05E-01	1.43E-01	8.27E-01	2.07E-10	1.69E-01
4.38E-49	5.05E-01	1.43E-01	8.27E-01	1.19E-10	1.69E-01
7.59E-49	5.05E-01	1.43E-01	8.27E-01	6.86E-11	1.69E-01
1.32E-48	5.05E-01	1.43E-01	8.27E-01	3.97E-11	1.69E-01

2.28E-48	5.05E-01	1.43E-01	8.27E-01	2.29E-11	1.69E-01
3.95E-48	5.05E-01	1.43E-01	8.27E-01	1.32E-11	1.69E-01
6.85E-48	5.05E-01	1.43E-01	8.27E-01	7.62E-12	1.69E-01
1.19E-47	5.05E-01	1.43E-01	8.27E-01	4.40E-12	1.69E-01
2.06E-47	5.05E-01	1.43E-01	8.27E-01	2.54E-12	1.69E-01
3.57E-47	5.05E-01	1.43E-01	8.27E-01	1.46E-12	1.69E-01
6.18E-47	5.05E-01	1.43E-01	8.27E-01	8.43E-13	1.69E-01
1.07E-46	5.05E-01	1.43E-01	8.27E-01	4.86E-13	1.69E-01
1.86E-46	5.05E-01	1.43E-01	8.27E-01	2.81E-13	1.69E-01
3.22E-46	5.05E-01	1.43E-01	8.27E-01	1.62E-13	1.69E-01
5.58E-46	5.05E-01	1.43E-01	8.27E-01	9.34E-14	1.69E-01
9.67E-46	5.05E-01	1.43E-01	8.27E-01	5.39E-14	1.69E-01
1.68E-45	5.05E-01	1.43E-01	8.27E-01	3.12E-14	1.69E-01
2.91E-45	5.05E-01	1.43E-01	8.27E-01	1.81E-14	1.69E-01
5.04E-45	5.04E-01	1.43E-01	8.27E-01	1.05E-14	1.69E-01
8.73E-45	5.03E-01	1.42E-01	8.31E-01	6.22E-15	1.70E-01
1.51E-44	5.03E-01	1.42E-01	8.31E-01	3.69E-15	1.70E-01
2.62E-44	5.02E-01	1.42E-01	8.31E-01	2.24E-15	1.70E-01
4.54E-44	4.99E-01	1.42E-01	8.31E-01	1.40E-15	1.70E-01
7.88E-44	4.97E-01	1.43E-01	8.26E-01	1.00E-15	1.70E-01
1.37E-43	4.90E-01	1.42E-01	8.29E-01	1.00E-15	1.72E-01
2.37E-43	4.80E-01	1.42E-01	8.27E-01	1.00E-15	1.74E-01
4.10E-43	4.64E-01	1.42E-01	8.23E-01	1.00E-15	1.77E-01
4.67E-43	4.58E-01	1.42E-01	8.21E-01	1.00E-15	1.79E-01
7.11E-43	1.91E-01	1.39E-01	4.28E-01	1.00E-15	5.72E-01
1.23E-42	1.79E-01	1.39E-01	3.92E-01	1.00E-15	6.08E-01
2.14E-42	1.69E-01	1.39E-01	3.59E-01	1.00E-15	6.39E-01
3.70E-42	1.61E-01	1.39E-01	3.31E-01	1.00E-15	6.69E-01
6.42E-42	1.54E-01	1.38E-01	3.07E-01	1.00E-15	6.95E-01
1.11E-41	1.48E-01	1.38E-01	2.82E-01	1.00E-15	7.18E-01
1.93E-41	1.42E-01	1.38E-01	2.59E-01	1.00E-15	7.41E-01
3.34E-41	1.36E-01	1.38E-01	2.36E-01	1.00E-15	7.64E-01
5.79E-41	1.31E-01	1.38E-01	2.14E-01	1.00E-15	7.85E-01
1.00E-40	1.25E-01	1.38E-01	1.93E-01	1.00E-15	8.05E-01
1.74E-40	1.19E-01	1.37E-01	1.73E-01	1.00E-15	8.30E-01
3.01E-40	1.15E-01	1.37E-01	1.52E-01	1.00E-15	8.48E-01
5.23E-40	1.09E-01	1.37E-01	1.31E-01	1.00E-15	8.69E-01
9.06E-40	1.03E-01	1.37E-01	1.11E-01	1.00E-15	8.91E-01
1.57E-39	9.64E-02	1.37E-01	9.24E-02	1.00E-15	9.09E-01
2.72E-39	8.94E-02	1.37E-01	7.45E-02	1.00E-15	9.25E-01
4.72E-39	8.12E-02	1.37E-01	5.92E-02	1.00E-15	9.40E-01
8.17E-39	7.13E-02	1.36E-01	4.55E-02	1.00E-15	9.57E-01
1.42E-38	5.98E-02	1.36E-01	3.45E-02	1.00E-15	9.70E-01

2.46E-38	4.55E-02	1.37E-01	2.53E-02	1.00E-15	9.74E-01
4.26E-38	2.84E-02	1.36E-01	1.82E-02	1.00E-15	9.82E-01
7.38E-38	7.96E-03	1.37E-01	1.28E-02	1.00E-15	9.85E-01

Table C.2. Thermo-Calc results for Corundum phase composition and fractions at 320 °C and 13.1 MPa.

O2 Activity (atm)	Corundum volume fraction	Number density (mol/cm3)	Fe mole fraction	Cr mole fraction	Ni mole fraction	O mole fraction
5.50E-60	1.45E-01	6.90E-02	6.57E-15	4.08E-01	2.69E-15	5.96E-01
5.61E-60	1.46E-01	6.93E-02	6.62E-15	4.06E-01	2.70E-15	5.93E-01
6.27E-60	1.50E-01	6.95E-02	7.14E-15	4.05E-01	2.83E-15	5.92E-01
6.99E-60	1.55E-01	6.94E-02	7.74E-15	4.06E-01	2.99E-15	5.93E-01
7.81E-60	1.58E-01	6.90E-02	8.39E-15	4.08E-01	3.17E-15	5.96E-01
8.72E-60	1.61E-01	6.94E-02	9.06E-15	4.06E-01	3.32E-15	5.92E-01
9.73E-60	1.63E-01	6.94E-02	9.77E-15	4.05E-01	3.51E-15	5.92E-01
1.09E-59	1.66E-01	6.91E-02	1.06E-14	4.08E-01	3.72E-15	5.95E-01
1.21E-59	1.68E-01	6.93E-02	1.14E-14	4.06E-01	3.92E-15	5.93E-01
1.35E-59	1.69E-01	6.92E-02	1.24E-14	4.07E-01	4.14E-15	5.95E-01
2.35E-59	1.75E-01	6.94E-02	1.83E-14	4.06E-01	5.45E-15	5.94E-01
4.07E-59	1.79E-01	6.94E-02	2.69E-14	4.06E-01	7.16E-15	5.93E-01
7.05E-59	1.81E-01	6.95E-02	3.95E-14	4.05E-01	9.44E-15	5.92E-01
1.22E-58	1.82E-01	6.95E-02	5.83E-14	4.05E-01	1.26E-14	5.93E-01
2.12E-58	1.83E-01	6.91E-02	8.68E-14	4.07E-01	1.67E-14	5.96E-01
3.67E-58	1.84E-01	6.94E-02	1.28E-13	4.06E-01	2.20E-14	5.94E-01
6.36E-58	1.84E-01	6.92E-02	1.89E-13	4.06E-01	2.92E-14	5.95E-01
1.10E-57	1.84E-01	6.96E-02	2.79E-13	4.04E-01	3.85E-14	5.93E-01
1.91E-57	1.85E-01	6.95E-02	4.14E-13	4.05E-01	5.11E-14	5.93E-01
3.31E-57	1.85E-01	6.95E-02	6.15E-13	4.05E-01	6.77E-14	5.94E-01
5.74E-57	1.85E-01	6.94E-02	9.18E-13	4.05E-01	8.97E-14	5.95E-01
9.95E-57	1.85E-01	6.94E-02	1.36E-12	4.05E-01	1.19E-13	5.95E-01
1.72E-56	1.85E-01	6.93E-02	2.03E-12	4.06E-01	1.58E-13	5.95E-01
2.99E-56	1.85E-01	6.93E-02	3.04E-12	4.06E-01	2.09E-13	5.95E-01
5.18E-56	1.85E-01	6.93E-02	4.56E-12	4.06E-01	2.77E-13	5.95E-01
8.98E-56	1.85E-01	6.93E-02	6.83E-12	4.06E-01	3.66E-13	5.96E-01
1.56E-55	1.85E-01	6.93E-02	1.03E-11	4.06E-01	4.85E-13	5.96E-01
2.70E-55	1.85E-01	6.93E-02	1.54E-11	4.06E-01	6.42E-13	5.96E-01
4.68E-55	1.85E-01	6.93E-02	2.32E-11	4.06E-01	8.49E-13	5.97E-01
8.10E-55	1.85E-01	6.93E-02	3.49E-11	4.06E-01	1.12E-12	5.97E-01
1.40E-54	1.85E-01	6.93E-02	5.27E-11	4.06E-01	1.49E-12	5.97E-01
2.43E-54	1.85E-01	6.93E-02	7.95E-11	4.06E-01	1.97E-12	5.97E-01
4.22E-54	1.85E-01	6.93E-02	1.21E-10	4.06E-01	2.60E-12	5.97E-01
7.31E-54	1.85E-01	6.93E-02	1.82E-10	4.06E-01	3.45E-12	5.97E-01
1.27E-53	1.85E-01	6.92E-02	2.76E-10	4.06E-01	4.56E-12	5.98E-01

2.20E-53	1.85E-01	6.92E-02	4.19E-10	4.06E-01	6.02E-12	5.98E-01
3.81E-53	1.85E-01	6.97E-02	6.32E-10	4.03E-01	7.89E-12	5.94E-01
6.60E-53	1.85E-01	6.97E-02	9.59E-10	4.03E-01	1.04E-11	5.94E-01
1.14E-52	1.85E-01	6.97E-02	1.46E-09	4.03E-01	1.38E-11	5.95E-01
1.98E-52	1.85E-01	6.97E-02	2.22E-09	4.03E-01	1.82E-11	5.95E-01
3.44E-52	1.85E-01	6.97E-02	3.40E-09	4.03E-01	2.40E-11	5.95E-01
5.96E-52	1.85E-01	6.97E-02	5.18E-09	4.03E-01	3.18E-11	5.95E-01
1.03E-51	1.85E-01	6.97E-02	7.89E-09	4.03E-01	4.19E-11	5.95E-01
1.79E-51	1.85E-01	6.97E-02	1.21E-08	4.03E-01	5.52E-11	5.95E-01
3.10E-51	1.85E-01	6.96E-02	1.85E-08	4.03E-01	7.28E-11	5.96E-01
5.38E-51	1.85E-01	6.96E-02	2.84E-08	4.03E-01	9.59E-11	5.96E-01
9.32E-51	1.85E-01	6.96E-02	4.34E-08	4.03E-01	1.27E-10	5.96E-01
1.08E-30	2.76E-03	6.67E-02	3.67E-01	3.27E-02	2.01E-16	6.00E-01
1.87E-30	3.92E-02	6.67E-02	3.66E-01	3.34E-02	2.00E-16	6.00E-01
3.25E-30	6.93E-02	6.66E-02	3.66E-01	3.46E-02	2.00E-16	6.01E-01
5.63E-30	9.42E-02	6.66E-02	3.65E-01	3.59E-02	2.01E-16	5.99E-01
9.75E-30	1.17E-01	6.66E-02	3.63E-01	3.72E-02	2.00E-16	6.01E-01
1.69E-29	1.36E-01	6.67E-02	3.61E-01	3.87E-02	2.00E-16	6.01E-01
2.93E-29	1.55E-01	6.67E-02	3.60E-01	4.03E-02	2.00E-16	6.01E-01
5.08E-29	1.73E-01	6.68E-02	3.57E-01	4.21E-02	2.00E-16	6.00E-01
8.80E-29	1.91E-01	6.70E-02	3.55E-01	4.39E-02	2.00E-16	5.98E-01
1.53E-28	2.10E-01	6.65E-02	3.56E-01	4.60E-02	2.00E-16	6.02E-01
2.64E-28	2.27E-01	6.69E-02	3.51E-01	4.81E-02	2.00E-16	5.99E-01
4.58E-28	2.48E-01	6.68E-02	3.50E-01	5.03E-02	2.00E-16	5.99E-01
7.94E-28	2.67E-01	6.68E-02	3.48E-01	5.25E-02	2.00E-16	6.00E-01
1.38E-27	2.87E-01	6.67E-02	3.47E-01	5.49E-02	2.00E-16	6.00E-01
2.39E-27	3.08E-01	6.70E-02	3.42E-01	5.74E-02	2.00E-16	5.98E-01
4.14E-27	3.31E-01	6.69E-02	3.40E-01	5.98E-02	2.00E-16	5.98E-01
7.17E-27	3.54E-01	6.69E-02	3.38E-01	6.26E-02	2.00E-16	6.00E-01
1.24E-26	3.78E-01	6.70E-02	3.34E-01	6.51E-02	2.00E-16	6.00E-01
2.15E-26	4.03E-01	6.70E-02	3.32E-01	6.78E-02	2.00E-16	5.99E-01
3.73E-26	4.28E-01	6.69E-02	3.29E-01	7.07E-02	2.00E-16	6.01E-01
6.47E-26	4.54E-01	6.69E-02	3.27E-01	7.35E-02	2.00E-16	6.00E-01
1.12E-25	4.79E-01	6.71E-02	3.23E-01	7.63E-02	2.00E-16	6.00E-01
1.94E-25	5.04E-01	6.69E-02	3.22E-01	7.92E-02	2.00E-16	6.01E-01
3.37E-25	5.28E-01	6.71E-02	3.18E-01	8.18E-02	2.00E-16	5.99E-01
5.84E-25	5.52E-01	6.70E-02	3.16E-01	8.46E-02	2.00E-16	6.00E-01
1.01E-24	5.74E-01	6.70E-02	3.14E-01	8.72E-02	2.00E-16	5.99E-01
1.75E-24	5.94E-01	6.71E-02	3.10E-01	8.99E-02	2.00E-16	6.01E-01
3.04E-24	6.12E-01	6.73E-02	3.07E-01	9.21E-02	2.00E-16	5.99E-01
5.27E-24	6.29E-01	6.70E-02	3.07E-01	9.43E-02	2.00E-16	6.00E-01
9.13E-24	6.43E-01	6.70E-02	3.05E-01	9.64E-02	2.00E-16	6.01E-01
1.42E-23	6.53E-01	6.73E-02	3.01E-01	9.81E-02	2.00E-16	6.00E-01

1.58E-23	6.53E-01	6.73E-02	3.01E-01	9.81E-02	2.00E-16	6.00E-01
2.74E-23	6.54E-01	6.71E-02	3.03E-01	9.81E-02	2.00E-16	5.99E-01
4.76E-23	6.54E-01	6.71E-02	3.03E-01	9.81E-02	2.00E-16	5.99E-01
8.24E-23	6.55E-01	6.70E-02	3.03E-01	9.83E-02	2.00E-16	6.01E-01
1.43E-22	6.56E-01	6.72E-02	3.02E-01	9.81E-02	2.00E-16	6.00E-01
2.48E-22	6.56E-01	6.72E-02	3.02E-01	9.81E-02	2.00E-16	6.00E-01
4.29E-22	6.56E-01	6.71E-02	3.02E-01	9.83E-02	2.00E-16	6.00E-01
7.52E-22	6.56E-01	6.71E-02	3.02E-01	9.83E-02	2.00E-16	6.00E-01
1.30E-21	6.57E-01	6.73E-02	3.02E-01	9.81E-02	2.00E-16	5.99E-01
2.26E-21	6.57E-01	6.72E-02	3.02E-01	9.81E-02	2.00E-16	6.01E-01
3.91E-21	6.57E-01	6.72E-02	3.02E-01	9.83E-02	2.00E-16	6.01E-01
6.78E-21	6.57E-01	6.72E-02	3.02E-01	9.83E-02	2.00E-16	6.01E-01
1.18E-20	6.57E-01	6.72E-02	3.02E-01	9.83E-02	2.00E-16	6.01E-01
2.04E-20	6.57E-01	6.72E-02	3.02E-01	9.83E-02	2.00E-16	6.01E-01
3.53E-20	6.57E-01	6.72E-02	3.02E-01	9.83E-02	2.00E-16	6.01E-01
6.12E-20	6.57E-01	6.72E-02	3.02E-01	9.83E-02	2.00E-16	6.01E-01
1.06E-19	6.58E-01	6.73E-02	3.01E-01	9.81E-02	2.00E-16	6.00E-01
1.84E-19	6.58E-01	6.73E-02	3.01E-01	9.81E-02	2.00E-16	6.00E-01
3.19E-19	6.58E-01	6.73E-02	3.01E-01	9.81E-02	2.00E-16	6.00E-01
5.52E-19	6.59E-01	6.73E-02	3.01E-01	9.81E-02	2.00E-16	6.00E-01
9.58E-19	6.59E-01	6.73E-02	3.01E-01	9.81E-02	2.00E-16	6.00E-01
1.66E-18	6.59E-01	6.73E-02	3.01E-01	9.81E-02	2.00E-16	6.00E-01
2.88E-18	6.59E-01	6.73E-02	3.01E-01	9.83E-02	2.00E-16	6.00E-01
4.25E-18	6.59E-01	6.73E-02	3.01E-01	9.83E-02	2.00E-16	6.00E-01

Table C.3. Thermo-Calc results for Cr-rich spinel phase composition and fractions at 320 °C and 13.1 MPa.

O2 Activity (atm)	Cr-rich spinel volume fraction	Number density (mol/cm3)	Fe mole fraction	Cr mole fraction	Ni mole fraction	O mole fraction
1.35E-50	4.95E-01	6.97E-02	1.43E-01	2.86E-01	2.23E-07	5.70E-01
1.62E-50	4.95E-01	6.97E-02	1.43E-01	2.86E-01	2.42E-07	5.70E-01
2.80E-50	4.95E-01	6.97E-02	1.43E-01	2.86E-01	3.09E-07	5.70E-01
4.85E-50	4.95E-01	6.97E-02	1.43E-01	2.86E-01	3.97E-07	5.70E-01
8.41E-50	4.95E-01	6.97E-02	1.43E-01	2.86E-01	5.12E-07	5.70E-01
1.46E-49	4.95E-01	6.97E-02	1.43E-01	2.86E-01	6.67E-07	5.70E-01
2.53E-49	4.95E-01	6.97E-02	1.43E-01	2.86E-01	8.65E-07	5.70E-01
4.38E-49	4.95E-01	6.97E-02	1.43E-01	2.86E-01	1.13E-06	5.70E-01
7.59E-49	4.95E-01	6.97E-02	1.43E-01	2.86E-01	1.47E-06	5.70E-01
1.32E-48	4.95E-01	6.97E-02	1.43E-01	2.86E-01	1.93E-06	5.70E-01
2.28E-48	4.95E-01	6.97E-02	1.43E-01	2.86E-01	2.53E-06	5.70E-01
3.95E-48	4.95E-01	6.97E-02	1.43E-01	2.86E-01	3.32E-06	5.70E-01
6.85E-48	4.95E-01	6.97E-02	1.43E-01	2.86E-01	4.37E-06	5.70E-01
1.19E-47	4.95E-01	6.97E-02	1.43E-01	2.86E-01	4.83E-06	5.70E-01

2.06E-47	4.95E-01	6.97E-02	1.43E-01	2.86E-01	9.66E-06	5.70E-01
3.57E-47	4.95E-01	6.97E-02	1.43E-01	2.86E-01	9.66E-06	5.70E-01
6.18E-47	4.95E-01	6.97E-02	1.43E-01	2.86E-01	1.45E-05	5.70E-01
1.07E-46	4.95E-01	6.97E-02	1.43E-01	2.86E-01	1.93E-05	5.70E-01
1.86E-46	4.95E-01	6.97E-02	1.43E-01	2.86E-01	2.42E-05	5.70E-01
3.22E-46	4.95E-01	6.97E-02	1.43E-01	2.86E-01	2.90E-05	5.70E-01
5.58E-46	4.95E-01	6.97E-02	1.43E-01	2.86E-01	3.87E-05	5.70E-01
9.67E-46	4.95E-01	6.97E-02	1.43E-01	2.86E-01	5.31E-05	5.70E-01
1.68E-45	4.95E-01	6.97E-02	1.43E-01	2.86E-01	6.76E-05	5.70E-01
2.91E-45	4.95E-01	6.95E-02	1.44E-01	2.86E-01	8.70E-05	5.75E-01
5.04E-45	4.96E-01	6.98E-02	1.43E-01	2.85E-01	1.15E-04	5.72E-01
8.73E-45	4.97E-01	6.98E-02	1.43E-01	2.85E-01	1.54E-04	5.72E-01
1.51E-44	4.97E-01	6.96E-02	1.44E-01	2.85E-01	1.97E-04	5.72E-01
2.62E-44	4.98E-01	6.98E-02	1.45E-01	2.83E-01	2.58E-04	5.69E-01
4.54E-44	5.01E-01	6.97E-02	1.47E-01	2.82E-01	3.33E-04	5.71E-01
7.88E-44	5.03E-01	6.96E-02	1.50E-01	2.79E-01	4.29E-04	5.71E-01
1.37E-43	5.10E-01	6.98E-02	1.53E-01	2.74E-01	5.32E-04	5.69E-01
2.37E-43	5.20E-01	6.96E-02	1.61E-01	2.67E-01	6.44E-04	5.72E-01
4.10E-43	5.36E-01	6.94E-02	1.73E-01	2.55E-01	7.33E-04	5.73E-01
4.67E-43	5.42E-01	6.92E-02	1.77E-01	2.52E-01	7.40E-04	5.75E-01
7.11E-43	7.20E-01	6.94E-02	1.77E-01	2.51E-01	1.06E-03	5.73E-01
1.23E-42	7.19E-01	6.94E-02	1.76E-01	2.51E-01	1.56E-03	5.73E-01
2.14E-42	7.19E-01	6.96E-02	1.75E-01	2.50E-01	2.15E-03	5.70E-01
3.70E-42	7.21E-01	6.94E-02	1.76E-01	2.50E-01	2.86E-03	5.70E-01
6.42E-42	7.23E-01	6.95E-02	1.75E-01	2.49E-01	3.69E-03	5.72E-01
1.11E-41	7.23E-01	6.92E-02	1.76E-01	2.49E-01	4.66E-03	5.72E-01
1.93E-41	7.25E-01	6.92E-02	1.76E-01	2.48E-01	5.74E-03	5.74E-01
3.34E-41	7.28E-01	6.95E-02	1.75E-01	2.46E-01	6.99E-03	5.69E-01
5.79E-41	7.32E-01	6.93E-02	1.75E-01	2.45E-01	8.38E-03	5.71E-01
1.00E-40	7.37E-01	6.94E-02	1.75E-01	2.43E-01	9.88E-03	5.70E-01
1.74E-40	7.42E-01	6.95E-02	1.75E-01	2.41E-01	1.16E-02	5.70E-01
3.01E-40	7.49E-01	6.94E-02	1.76E-01	2.39E-01	1.34E-02	5.69E-01
5.23E-40	7.55E-01	6.92E-02	1.76E-01	2.37E-01	1.54E-02	5.73E-01
9.06E-40	7.63E-01	6.93E-02	1.76E-01	2.34E-01	1.75E-02	5.70E-01
1.57E-39	7.72E-01	6.93E-02	1.76E-01	2.32E-01	1.98E-02	5.71E-01
2.72E-39	7.82E-01	6.91E-02	1.77E-01	2.29E-01	2.23E-02	5.72E-01
4.72E-39	7.91E-01	6.89E-02	1.78E-01	2.26E-01	2.50E-02	5.73E-01
8.17E-39	8.01E-01	6.89E-02	1.79E-01	2.23E-01	2.78E-02	5.72E-01
1.42E-38	8.13E-01	6.89E-02	1.80E-01	2.19E-01	3.08E-02	5.71E-01
2.46E-38	8.23E-01	6.90E-02	1.80E-01	2.15E-01	3.39E-02	5.71E-01
4.26E-38	8.34E-01	6.90E-02	1.80E-01	2.11E-01	3.72E-02	5.70E-01
7.38E-38	8.41E-01	6.90E-02	1.80E-01	2.08E-01	4.09E-02	5.69E-01
8.92E-38	8.46E-01	6.89E-02	1.80E-01	2.06E-01	4.22E-02	5.71E-01

1.28E-37	8.46E-01	6.89E-02	1.80E-01	2.06E-01	4.22E-02	5.71E-01
2.22E-37	8.46E-01	6.89E-02	1.80E-01	2.06E-01	4.22E-02	5.71E-01
3.84E-37	8.46E-01	6.89E-02	1.80E-01	2.06E-01	4.22E-02	5.71E-01
6.66E-37	8.46E-01	6.89E-02	1.80E-01	2.06E-01	4.22E-02	5.71E-01
1.15E-36	8.46E-01	6.89E-02	1.80E-01	2.06E-01	4.22E-02	5.71E-01
2.00E-36	8.46E-01	6.89E-02	1.80E-01	2.06E-01	4.22E-02	5.71E-01
3.47E-36	8.46E-01	6.89E-02	1.80E-01	2.06E-01	4.22E-02	5.71E-01
6.01E-36	8.46E-01	6.89E-02	1.80E-01	2.06E-01	4.22E-02	5.71E-01
1.04E-35	8.46E-01	6.89E-02	1.80E-01	2.06E-01	4.22E-02	5.71E-01
1.81E-35	8.46E-01	6.89E-02	1.80E-01	2.06E-01	4.22E-02	5.71E-01
3.13E-35	8.46E-01	6.89E-02	1.80E-01	2.06E-01	4.22E-02	5.71E-01
5.42E-35	8.46E-01	6.89E-02	1.80E-01	2.06E-01	4.22E-02	5.71E-01
9.40E-35	8.46E-01	6.89E-02	1.80E-01	2.06E-01	4.22E-02	5.71E-01
1.63E-34	8.46E-01	6.89E-02	1.80E-01	2.06E-01	4.22E-02	5.71E-01
2.82E-34	8.46E-01	6.89E-02	1.80E-01	2.06E-01	4.22E-02	5.71E-01
4.89E-34	8.46E-01	6.89E-02	1.80E-01	2.06E-01	4.22E-02	5.71E-01
8.48E-34	8.46E-01	6.89E-02	1.80E-01	2.06E-01	4.22E-02	5.71E-01
1.47E-33	8.46E-01	6.89E-02	1.80E-01	2.06E-01	4.22E-02	5.71E-01
2.55E-33	8.46E-01	6.89E-02	1.80E-01	2.06E-01	4.22E-02	5.71E-01
4.42E-33	8.46E-01	6.89E-02	1.80E-01	2.06E-01	4.22E-02	5.71E-01
7.66E-33	8.46E-01	6.89E-02	1.80E-01	2.06E-01	4.22E-02	5.71E-01
1.33E-32	8.46E-01	6.89E-02	1.80E-01	2.06E-01	4.22E-02	5.71E-01
2.30E-32	8.46E-01	6.89E-02	1.80E-01	2.06E-01	4.22E-02	5.71E-01
3.99E-32	8.46E-01	6.89E-02	1.80E-01	2.06E-01	4.22E-02	5.71E-01
6.91E-32	8.46E-01	6.89E-02	1.80E-01	2.06E-01	4.22E-02	5.71E-01
1.20E-31	8.46E-01	6.89E-02	1.80E-01	2.06E-01	4.22E-02	5.71E-01
2.08E-31	8.46E-01	6.89E-02	1.80E-01	2.06E-01	4.22E-02	5.71E-01
3.60E-31	8.46E-01	6.89E-02	1.80E-01	2.06E-01	4.22E-02	5.71E-01
6.24E-31	8.46E-01	6.89E-02	1.80E-01	2.06E-01	4.22E-02	5.71E-01
1.08E-30	8.43E-01	6.87E-02	1.80E-01	2.06E-01	4.27E-02	5.73E-01
1.87E-30	8.13E-01	6.88E-02	1.79E-01	2.04E-01	4.54E-02	5.72E-01
3.25E-30	7.89E-01	6.88E-02	1.79E-01	2.02E-01	4.79E-02	5.70E-01
5.63E-30	7.70E-01	6.85E-02	1.78E-01	2.01E-01	5.04E-02	5.74E-01
9.75E-30	7.52E-01	6.86E-02	1.77E-01	1.99E-01	5.28E-02	5.72E-01
1.69E-29	7.35E-01	6.87E-02	1.76E-01	1.98E-01	5.47E-02	5.71E-01
2.93E-29	7.19E-01	6.86E-02	1.75E-01	1.97E-01	5.65E-02	5.73E-01
5.08E-29	7.00E-01	6.87E-02	1.73E-01	1.96E-01	5.84E-02	5.71E-01
8.80E-29	6.81E-01	6.88E-02	1.72E-01	1.96E-01	6.04E-02	5.68E-01
1.53E-28	6.61E-01	6.86E-02	1.71E-01	1.96E-01	6.18E-02	5.73E-01
2.64E-28	6.41E-01	6.86E-02	1.70E-01	1.95E-01	6.39E-02	5.73E-01
4.58E-28	6.16E-01	6.85E-02	1.68E-01	1.95E-01	6.59E-02	5.71E-01
7.94E-28	5.93E-01	6.84E-02	1.67E-01	1.95E-01	6.75E-02	5.74E-01
1.38E-27	5.67E-01	6.87E-02	1.65E-01	1.94E-01	6.88E-02	5.71E-01

2.39E-27	5.41E-01	6.83E-02	1.64E-01	1.95E-01	7.10E-02	5.75E-01
4.14E-27	5.10E-01	6.87E-02	1.61E-01	1.95E-01	7.24E-02	5.70E-01
7.17E-27	4.79E-01	6.84E-02	1.59E-01	1.96E-01	7.48E-02	5.72E-01
1.24E-26	4.46E-01	6.84E-02	1.57E-01	1.96E-01	7.64E-02	5.72E-01
2.15E-26	4.12E-01	6.86E-02	1.54E-01	1.96E-01	7.81E-02	5.70E-01
3.73E-26	3.75E-01	6.87E-02	1.51E-01	1.96E-01	8.00E-02	5.70E-01
6.47E-26	3.38E-01	6.84E-02	1.48E-01	1.98E-01	8.29E-02	5.73E-01
1.12E-25	3.00E-01	6.85E-02	1.45E-01	1.99E-01	8.49E-02	5.71E-01
1.94E-25	2.61E-01	6.84E-02	1.42E-01	2.00E-01	8.75E-02	5.72E-01
3.37E-25	2.23E-01	6.83E-02	1.38E-01	2.02E-01	9.01E-02	5.72E-01
5.84E-25	1.85E-01	6.85E-02	1.33E-01	2.02E-01	9.28E-02	5.72E-01
1.01E-24	1.48E-01	6.85E-02	1.29E-01	2.03E-01	9.57E-02	5.71E-01
1.75E-24	1.13E-01	6.84E-02	1.25E-01	2.05E-01	9.89E-02	5.72E-01
3.04E-24	8.04E-02	6.84E-02	1.21E-01	2.06E-01	1.02E-01	5.71E-01
5.27E-24	4.95E-02	6.83E-02	1.17E-01	2.08E-01	1.06E-01	5.73E-01
9.13E-24	2.11E-02	6.84E-02	1.12E-01	2.09E-01	1.08E-01	5.71E-01

Table C.4. Thermo-Calc results for Fe-rich spinel phase composition and fractions at 320 °C and 13.1 MPa.

O2 Activity (atm)	Fe-rich spinel volume fraction	Number density (mol/cm3)	Fe mole fraction	Cr mole fraction	Ni mole fraction	O mole fraction
7.11E-43	8.89E-02	6.75E-02	4.27E-01	1.13E-03	6.23E-06	5.70E-01
1.23E-42	1.02E-01	6.74E-02	4.27E-01	1.13E-03	9.09E-06	5.73E-01
2.14E-42	1.12E-01	6.74E-02	4.27E-01	1.12E-03	1.78E-05	5.73E-01
3.70E-42	1.19E-01	6.76E-02	4.26E-01	1.11E-03	3.21E-05	5.71E-01
6.42E-42	1.23E-01	6.75E-02	4.27E-01	1.11E-03	5.48E-05	5.71E-01
1.11E-41	1.29E-01	6.74E-02	4.27E-01	1.10E-03	9.12E-05	5.73E-01
1.93E-41	1.34E-01	6.73E-02	4.28E-01	1.09E-03	1.52E-04	5.72E-01
3.34E-41	1.36E-01	6.74E-02	4.27E-01	1.08E-03	2.46E-04	5.70E-01
5.79E-41	1.37E-01	6.73E-02	4.28E-01	1.07E-03	3.94E-04	5.72E-01
1.00E-40	1.38E-01	6.74E-02	4.27E-01	1.05E-03	6.23E-04	5.70E-01
1.74E-40	1.39E-01	6.73E-02	4.27E-01	1.04E-03	9.73E-04	5.70E-01
3.01E-40	1.37E-01	6.75E-02	4.25E-01	1.03E-03	1.50E-03	5.72E-01
5.23E-40	1.36E-01	6.73E-02	4.26E-01	1.02E-03	2.29E-03	5.72E-01
9.06E-40	1.34E-01	6.73E-02	4.24E-01	1.01E-03	3.46E-03	5.73E-01
1.57E-39	1.31E-01	6.74E-02	4.22E-01	1.02E-03	5.13E-03	5.73E-01
2.72E-39	1.29E-01	6.75E-02	4.19E-01	1.03E-03	7.55E-03	5.71E-01
4.72E-39	1.28E-01	6.73E-02	4.16E-01	1.06E-03	1.10E-02	5.73E-01
8.17E-39	1.28E-01	6.72E-02	4.12E-01	1.12E-03	1.56E-02	5.72E-01
1.42E-38	1.28E-01	6.75E-02	4.04E-01	1.22E-03	2.19E-02	5.70E-01
2.46E-38	1.32E-01	6.71E-02	3.98E-01	1.39E-03	3.01E-02	5.71E-01
4.26E-38	1.38E-01	6.72E-02	3.87E-01	1.65E-03	4.02E-02	5.71E-01
7.38E-38	1.51E-01	6.70E-02	3.75E-01	2.06E-03	5.23E-02	5.71E-01

8.92E-38	1.54E-01	6.72E-02	3.68E-01	2.25E-03	5.69E-02	5.72E-01
1.28E-37	1.54E-01	6.72E-02	3.68E-01	2.25E-03	5.69E-02	5.72E-01
2.22E-37	1.54E-01	6.72E-02	3.68E-01	2.25E-03	5.69E-02	5.72E-01
3.84E-37	1.54E-01	6.72E-02	3.68E-01	2.25E-03	5.69E-02	5.72E-01
6.66E-37	1.54E-01	6.72E-02	3.68E-01	2.25E-03	5.69E-02	5.72E-01
1.15E-36	1.54E-01	6.72E-02	3.68E-01	2.25E-03	5.69E-02	5.72E-01
2.00E-36	1.54E-01	6.72E-02	3.68E-01	2.25E-03	5.69E-02	5.72E-01
3.47E-36	1.54E-01	6.72E-02	3.68E-01	2.25E-03	5.69E-02	5.72E-01
6.01E-36	1.54E-01	6.72E-02	3.68E-01	2.25E-03	5.69E-02	5.72E-01
1.04E-35	1.54E-01	6.72E-02	3.68E-01	2.25E-03	5.69E-02	5.72E-01
1.81E-35	1.54E-01	6.72E-02	3.68E-01	2.25E-03	5.69E-02	5.72E-01
3.13E-35	1.54E-01	6.72E-02	3.68E-01	2.25E-03	5.69E-02	5.72E-01
5.42E-35	1.54E-01	6.72E-02	3.68E-01	2.25E-03	5.69E-02	5.72E-01
9.40E-35	1.54E-01	6.72E-02	3.68E-01	2.25E-03	5.69E-02	5.72E-01
1.63E-34	1.54E-01	6.72E-02	3.68E-01	2.25E-03	5.69E-02	5.72E-01
2.82E-34	1.54E-01	6.72E-02	3.68E-01	2.25E-03	5.69E-02	5.72E-01
4.89E-34	1.54E-01	6.72E-02	3.68E-01	2.25E-03	5.69E-02	5.72E-01
8.48E-34	1.54E-01	6.72E-02	3.68E-01	2.25E-03	5.69E-02	5.72E-01
1.47E-33	1.54E-01	6.72E-02	3.68E-01	2.25E-03	5.69E-02	5.72E-01
2.55E-33	1.54E-01	6.72E-02	3.68E-01	2.25E-03	5.69E-02	5.72E-01
4.42E-33	1.54E-01	6.72E-02	3.68E-01	2.25E-03	5.69E-02	5.72E-01
7.66E-33	1.54E-01	6.72E-02	3.68E-01	2.25E-03	5.69E-02	5.72E-01
1.33E-32	1.54E-01	6.72E-02	3.68E-01	2.25E-03	5.69E-02	5.72E-01
2.30E-32	1.54E-01	6.72E-02	3.68E-01	2.25E-03	5.69E-02	5.72E-01
3.99E-32	1.54E-01	6.72E-02	3.68E-01	2.25E-03	5.69E-02	5.72E-01
6.91E-32	1.54E-01	6.72E-02	3.68E-01	2.25E-03	5.69E-02	5.72E-01
1.20E-31	1.54E-01	6.72E-02	3.68E-01	2.25E-03	5.69E-02	5.72E-01
2.08E-31	1.54E-01	6.72E-02	3.68E-01	2.25E-03	5.69E-02	5.72E-01
3.60E-31	1.54E-01	6.72E-02	3.68E-01	2.25E-03	5.69E-02	5.72E-01
6.24E-31	1.54E-01	6.72E-02	3.68E-01	2.25E-03	5.69E-02	5.72E-01
1.08E-30	1.54E-01	6.71E-02	3.69E-01	2.29E-03	5.78E-02	5.70E-01
1.87E-30	1.48E-01	6.70E-02	3.58E-01	2.83E-03	6.80E-02	5.73E-01
3.25E-30	1.41E-01	6.72E-02	3.47E-01	3.47E-03	7.70E-02	5.70E-01
5.63E-30	1.36E-01	6.71E-02	3.39E-01	4.16E-03	8.48E-02	5.69E-01
9.75E-30	1.32E-01	6.70E-02	3.32E-01	4.96E-03	9.19E-02	5.69E-01
1.69E-29	1.28E-01	6.69E-02	3.25E-01	5.85E-03	9.78E-02	5.72E-01
2.93E-29	1.27E-01	6.70E-02	3.18E-01	6.81E-03	1.03E-01	5.69E-01
5.08E-29	1.27E-01	6.68E-02	3.14E-01	7.90E-03	1.08E-01	5.71E-01
8.80E-29	1.28E-01	6.69E-02	3.07E-01	9.04E-03	1.12E-01	5.71E-01
1.53E-28	1.30E-01	6.68E-02	3.03E-01	1.04E-02	1.16E-01	5.71E-01
2.64E-28	1.32E-01	6.68E-02	2.98E-01	1.17E-02	1.19E-01	5.72E-01
4.58E-28	1.36E-01	6.66E-02	2.95E-01	1.32E-02	1.22E-01	5.74E-01
7.94E-28	1.40E-01	6.69E-02	2.90E-01	1.48E-02	1.24E-01	5.69E-01

1.38E-27	1.46E-01	6.68E-02	2.86E-01	1.65E-02	1.26E-01	5.72E-01
2.39E-27	1.51E-01	6.66E-02	2.83E-01	1.84E-02	1.29E-01	5.75E-01
4.14E-27	1.59E-01	6.68E-02	2.78E-01	2.02E-02	1.30E-01	5.72E-01
7.17E-27	1.67E-01	6.66E-02	2.75E-01	2.23E-02	1.32E-01	5.75E-01
1.24E-26	1.75E-01	6.67E-02	2.72E-01	2.44E-02	1.33E-01	5.74E-01
2.15E-26	1.85E-01	6.68E-02	2.68E-01	2.65E-02	1.34E-01	5.70E-01
3.73E-26	1.97E-01	6.70E-02	2.64E-01	2.86E-02	1.35E-01	5.68E-01
6.47E-26	2.09E-01	6.68E-02	2.61E-01	3.08E-02	1.37E-01	5.72E-01
1.12E-25	2.21E-01	6.68E-02	2.58E-01	3.29E-02	1.37E-01	5.73E-01
1.94E-25	2.35E-01	6.67E-02	2.56E-01	3.51E-02	1.38E-01	5.74E-01
3.37E-25	2.49E-01	6.69E-02	2.53E-01	3.71E-02	1.39E-01	5.71E-01
5.84E-25	2.63E-01	6.68E-02	2.51E-01	3.92E-02	1.39E-01	5.74E-01
1.01E-24	2.79E-01	6.71E-02	2.48E-01	4.09E-02	1.39E-01	5.70E-01
1.75E-24	2.93E-01	6.69E-02	2.46E-01	4.28E-02	1.40E-01	5.72E-01
3.04E-24	3.08E-01	6.70E-02	2.44E-01	4.45E-02	1.40E-01	5.72E-01
5.27E-24	3.22E-01	6.70E-02	2.42E-01	4.59E-02	1.41E-01	5.70E-01
9.13E-24	3.36E-01	6.70E-02	2.40E-01	4.74E-02	1.41E-01	5.70E-01
1.42E-23	3.47E-01	6.70E-02	2.39E-01	4.84E-02	1.41E-01	5.71E-01
1.58E-23	3.47E-01	6.70E-02	2.39E-01	4.84E-02	1.41E-01	5.71E-01
2.74E-23	3.46E-01	6.69E-02	2.39E-01	4.82E-02	1.41E-01	5.73E-01
4.76E-23	3.46E-01	6.71E-02	2.39E-01	4.82E-02	1.41E-01	5.69E-01
8.24E-23	3.45E-01	6.69E-02	2.40E-01	4.80E-02	1.42E-01	5.71E-01
1.43E-22	3.44E-01	6.69E-02	2.39E-01	4.80E-02	1.42E-01	5.71E-01
2.48E-22	3.44E-01	6.70E-02	2.39E-01	4.76E-02	1.42E-01	5.71E-01
4.29E-22	3.44E-01	6.70E-02	2.39E-01	4.76E-02	1.42E-01	5.71E-01
7.52E-22	3.44E-01	6.70E-02	2.39E-01	4.76E-02	1.42E-01	5.71E-01
1.30E-21	3.43E-01	6.68E-02	2.39E-01	4.78E-02	1.42E-01	5.74E-01
2.26E-21	3.43E-01	6.69E-02	2.39E-01	4.74E-02	1.42E-01	5.74E-01
3.91E-21	3.43E-01	6.70E-02	2.39E-01	4.74E-02	1.42E-01	5.70E-01
6.78E-21	3.43E-01	6.70E-02	2.39E-01	4.74E-02	1.42E-01	5.70E-01
1.18E-20	3.43E-01	6.70E-02	2.39E-01	4.74E-02	1.42E-01	5.70E-01
2.04E-20	3.43E-01	6.70E-02	2.39E-01	4.74E-02	1.42E-01	5.70E-01
3.53E-20	3.43E-01	6.71E-02	2.38E-01	4.74E-02	1.42E-01	5.70E-01
6.12E-20	3.43E-01	6.71E-02	2.38E-01	4.74E-02	1.42E-01	5.70E-01
1.06E-19	3.42E-01	6.71E-02	2.38E-01	4.74E-02	1.42E-01	5.70E-01
1.84E-19	3.42E-01	6.71E-02	2.38E-01	4.74E-02	1.42E-01	5.70E-01
3.19E-19	3.42E-01	6.71E-02	2.38E-01	4.70E-02	1.42E-01	5.70E-01
5.52E-19	3.42E-01	6.68E-02	2.39E-01	4.72E-02	1.43E-01	5.72E-01
9.58E-19	3.42E-01	6.69E-02	2.39E-01	4.72E-02	1.43E-01	5.72E-01
1.66E-18	3.42E-01	6.69E-02	2.39E-01	4.72E-02	1.43E-01	5.72E-01
2.88E-18	3.42E-01	6.69E-02	2.39E-01	4.72E-02	1.43E-01	5.72E-01
4.25E-18	3.42E-01	6.69E-02	2.39E-01	4.72E-02	1.43E-01	5.72E-01

Table C.5. Thermo-Calc results for Cr-rich spinel diffusion coefficients at 320 °C and 13.1 MPa.

O2 Activity (atm)	Fe diffusion coefficient (nm2/s)	Cr diffusion coefficient (nm2/s)	Ni diffusion coefficient (nm2/s)	O diffusion coefficient (nm2/s)	Fe diffusion coefficient irradiated (nm2/s)	Cr diffusion coefficient irradiated (nm2/s)	Ni diffusion coefficient irradiated (nm2/s)
1.35E-50	2.32E-01	5.91E-11	6.70E-03	8.57E-05	3.98E-01	1.02E-10	1.15E-02
1.62E-50	2.12E-01	5.41E-11	6.14E-03	7.83E-05	3.85E-01	9.81E-11	1.11E-02
2.80E-50	1.63E-01	4.15E-11	4.71E-03	5.95E-05	3.52E-01	8.97E-11	1.02E-02
4.85E-50	1.24E-01	3.17E-11	3.60E-03	4.52E-05	3.27E-01	8.35E-11	9.47E-03
8.41E-50	9.50E-02	2.42E-11	2.75E-03	3.43E-05	3.10E-01	7.90E-11	8.96E-03
1.46E-49	7.23E-02	1.84E-11	2.09E-03	2.61E-05	2.97E-01	7.56E-11	8.58E-03
2.53E-49	5.50E-02	1.40E-11	1.59E-03	1.98E-05	2.87E-01	7.31E-11	8.30E-03
4.38E-49	4.17E-02	1.06E-11	1.21E-03	1.50E-05	2.80E-01	7.13E-11	8.09E-03
7.59E-49	3.17E-02	8.08E-12	9.17E-04	1.14E-05	2.74E-01	6.99E-11	7.93E-03
1.32E-48	2.41E-02	6.14E-12	6.97E-04	8.68E-06	2.70E-01	6.89E-11	7.82E-03
2.28E-48	1.83E-02	4.66E-12	5.29E-04	6.59E-06	2.67E-01	6.81E-11	7.73E-03
3.95E-48	1.39E-02	3.54E-12	4.02E-04	5.01E-06	2.65E-01	6.75E-11	7.66E-03
6.85E-48	1.06E-02	2.69E-12	3.06E-04	3.80E-06	2.63E-01	6.71E-11	7.62E-03
1.19E-47	8.03E-03	2.05E-12	2.32E-04	2.89E-06	2.62E-01	6.68E-11	7.58E-03
2.06E-47	6.08E-03	1.55E-12	1.76E-04	2.19E-06	2.61E-01	6.65E-11	7.55E-03
3.57E-47	4.62E-03	1.18E-12	1.34E-04	1.67E-06	2.60E-01	6.63E-11	7.53E-03
6.18E-47	3.52E-03	8.97E-13	1.02E-04	1.27E-06	2.60E-01	6.62E-11	7.51E-03
1.07E-46	2.68E-03	6.82E-13	7.74E-05	9.62E-07	2.59E-01	6.61E-11	7.50E-03
1.86E-46	2.03E-03	5.18E-13	5.88E-05	7.30E-07	2.59E-01	6.60E-11	7.49E-03
3.22E-46	1.55E-03	3.95E-13	4.48E-05	5.55E-07	2.59E-01	6.59E-11	7.48E-03
5.58E-46	1.18E-03	3.01E-13	3.42E-05	4.21E-07	2.58E-01	6.59E-11	7.48E-03
9.67E-46	9.01E-04	2.30E-13	2.61E-05	3.20E-07	2.58E-01	6.59E-11	7.47E-03
1.68E-45	6.88E-04	1.75E-13	1.99E-05	2.43E-07	2.58E-01	6.58E-11	7.47E-03
2.91E-45	5.28E-04	1.35E-13	1.53E-05	1.85E-07	2.58E-01	6.58E-11	7.47E-03
5.04E-45	4.08E-04	1.04E-13	1.18E-05	1.40E-07	2.58E-01	6.58E-11	7.47E-03
8.73E-45	3.20E-04	8.15E-14	9.25E-06	1.07E-07	2.58E-01	6.58E-11	7.47E-03
1.51E-44	2.55E-04	6.51E-14	7.38E-06	8.09E-08	2.58E-01	6.58E-11	7.46E-03
2.62E-44	2.11E-04	5.37E-14	6.10E-06	6.15E-08	2.58E-01	6.58E-11	7.46E-03
4.54E-44	1.84E-04	4.70E-14	5.33E-06	4.67E-08	2.58E-01	6.58E-11	7.46E-03
7.88E-44	1.76E-04	4.49E-14	5.10E-06	3.55E-08	2.58E-01	6.58E-11	7.46E-03
1.37E-43	1.93E-04	4.92E-14	5.59E-06	2.69E-08	2.58E-01	6.58E-11	7.46E-03
2.37E-43	2.58E-04	6.59E-14	7.47E-06	2.05E-08	2.58E-01	6.58E-11	7.46E-03
4.10E-43	4.38E-04	1.12E-13	1.27E-05	1.55E-08	2.58E-01	6.58E-11	7.47E-03
4.67E-43	5.10E-04	1.30E-13	1.48E-05	1.46E-08	2.58E-01	6.58E-11	7.47E-03
7.11E-43	4.48E-04	1.14E-13	1.30E-05	1.18E-08	2.58E-01	6.58E-11	7.46E-03

1.23E-42	3.45E-04	8.80E-14	9.99E-06	8.97E-09	2.58E-01	6.58E-11	7.46E-03
2.14E-42	2.53E-04	6.45E-14	7.32E-06	6.81E-09	2.58E-01	6.58E-11	7.46E-03
3.70E-42	1.82E-04	4.64E-14	5.26E-06	5.17E-09	2.58E-01	6.57E-11	7.46E-03
6.42E-42	1.32E-04	3.36E-14	3.81E-06	3.93E-09	2.58E-01	6.57E-11	7.46E-03
1.11E-41	9.67E-05	2.47E-14	2.80E-06	2.99E-09	2.58E-01	6.57E-11	7.46E-03
1.93E-41	7.32E-05	1.87E-14	2.12E-06	2.27E-09	2.58E-01	6.57E-11	7.46E-03
3.34E-41	5.68E-05	1.45E-14	1.64E-06	1.72E-09	2.58E-01	6.57E-11	7.46E-03
5.79E-41	4.53E-05	1.15E-14	1.31E-06	1.31E-09	2.58E-01	6.57E-11	7.46E-03
1.00E-40	3.74E-05	9.54E-15	1.08E-06	9.94E-10	2.58E-01	6.57E-11	7.45E-03
1.74E-40	3.19E-05	8.12E-15	9.22E-07	7.55E-10	2.58E-01	6.57E-11	7.45E-03
3.01E-40	2.79E-05	7.12E-15	8.08E-07	5.73E-10	2.58E-01	6.57E-11	7.45E-03
5.23E-40	2.52E-05	6.43E-15	7.29E-07	4.35E-10	2.58E-01	6.57E-11	7.45E-03
9.06E-40	2.34E-05	5.97E-15	6.78E-07	3.31E-10	2.58E-01	6.57E-11	7.45E-03
1.57E-39	2.23E-05	5.69E-15	6.46E-07	2.51E-10	2.57E-01	6.56E-11	7.45E-03
2.72E-39	2.18E-05	5.57E-15	6.32E-07	1.91E-10	2.57E-01	6.56E-11	7.45E-03
4.72E-39	2.18E-05	5.56E-15	6.30E-07	1.45E-10	2.57E-01	6.56E-11	7.45E-03
8.17E-39	2.21E-05	5.65E-15	6.41E-07	1.10E-10	2.57E-01	6.56E-11	7.44E-03
1.42E-38	2.28E-05	5.82E-15	6.60E-07	8.36E-11	2.57E-01	6.56E-11	7.44E-03
2.46E-38	2.36E-05	6.02E-15	6.83E-07	6.35E-11	2.57E-01	6.56E-11	7.44E-03
4.26E-38	2.44E-05	6.21E-15	7.05E-07	4.82E-11	2.57E-01	6.55E-11	7.44E-03
7.38E-38	2.49E-05	6.34E-15	7.19E-07	3.66E-11	2.57E-01	6.55E-11	7.44E-03
8.92E-38	2.49E-05	6.35E-15	7.20E-07	3.33E-11	2.57E-01	6.55E-11	7.44E-03
1.28E-37	3.16E-05	8.05E-15	9.13E-07	2.78E-11	2.57E-01	6.56E-11	7.44E-03
2.22E-37	4.57E-05	1.17E-14	1.32E-06	2.11E-11	2.57E-01	6.56E-11	7.45E-03
3.84E-37	6.57E-05	1.68E-14	1.90E-06	1.61E-11	2.58E-01	6.57E-11	7.45E-03
6.66E-37	9.50E-05	2.42E-14	2.75E-06	1.22E-11	2.58E-01	6.57E-11	7.46E-03
1.15E-36	1.37E-04	3.49E-14	3.96E-06	9.27E-12	2.58E-01	6.57E-11	7.46E-03
2.00E-36	1.98E-04	5.04E-14	5.71E-06	7.04E-12	2.58E-01	6.57E-11	7.46E-03
3.47E-36	2.84E-04	7.25E-14	8.23E-06	5.35E-12	2.58E-01	6.58E-11	7.46E-03
6.01E-36	4.11E-04	1.05E-13	1.19E-05	4.06E-12	2.58E-01	6.58E-11	7.47E-03
1.04E-35	5.95E-04	1.52E-13	1.72E-05	3.08E-12	2.58E-01	6.58E-11	7.47E-03
1.81E-35	8.56E-04	2.18E-13	2.48E-05	2.34E-12	2.58E-01	6.58E-11	7.47E-03
3.13E-35	1.23E-03	3.15E-13	3.57E-05	1.78E-12	2.58E-01	6.59E-11	7.48E-03
5.42E-35	1.78E-03	4.54E-13	5.15E-05	1.35E-12	2.59E-01	6.60E-11	7.49E-03
9.40E-35	2.57E-03	6.55E-13	7.43E-05	1.03E-12	2.59E-01	6.61E-11	7.50E-03
1.63E-34	3.71E-03	9.45E-13	1.07E-04	7.80E-13	2.60E-01	6.62E-11	7.51E-03
2.82E-34	5.37E-03	1.37E-12	1.55E-04	5.93E-13	2.61E-01	6.64E-11	7.54E-03
4.89E-34	7.72E-03	1.97E-12	2.23E-04	4.50E-13	2.62E-01	6.67E-11	7.57E-03
8.48E-34	1.11E-02	2.84E-12	3.22E-04	3.42E-13	2.63E-01	6.72E-11	7.62E-03
1.47E-33	1.61E-02	4.10E-12	4.65E-04	2.60E-13	2.66E-01	6.78E-11	7.70E-03
2.55E-33	2.32E-02	5.91E-12	6.70E-04	1.98E-13	2.70E-01	6.88E-11	7.80E-03
4.42E-33	3.35E-02	8.53E-12	9.68E-04	1.50E-13	2.75E-01	7.01E-11	7.96E-03
7.66E-33	4.84E-02	1.23E-11	1.40E-03	1.14E-13	2.83E-01	7.22E-11	8.19E-03

1.33E-32	6.97E-02	1.78E-11	2.02E-03	8.68E-14	2.95E-01	7.52E-11	8.54E-03
2.30E-32	1.00E-01	2.56E-11	2.90E-03	6.61E-14	3.13E-01	7.98E-11	9.05E-03
3.99E-32	1.45E-01	3.70E-11	4.20E-03	5.03E-14	3.40E-01	8.68E-11	9.85E-03
6.91E-32	2.09E-01	5.34E-11	6.06E-03	3.84E-14	3.83E-01	9.77E-11	1.11E-02
1.20E-31	3.02E-01	7.69E-11	8.73E-03	2.93E-14	4.50E-01	1.15E-10	1.30E-02
2.08E-31	4.36E-01	1.11E-10	1.26E-02	2.25E-14	5.55E-01	1.42E-10	1.61E-02
3.60E-31	6.30E-01	1.61E-10	1.82E-02	1.73E-14	7.22E-01	1.84E-10	2.09E-02
6.24E-31	9.05E-01	2.31E-10	2.62E-02	1.34E-14	9.74E-01	2.48E-10	2.82E-02
1.08E-30	1.28E+00	3.27E-10	3.71E-02	1.04E-14	1.33E+00	3.40E-10	3.86E-02
1.87E-30	1.39E+00	3.54E-10	4.02E-02	8.19E-15	1.44E+00	3.66E-10	4.15E-02
3.25E-30	1.55E+00	3.95E-10	4.48E-02	6.53E-15	1.59E+00	4.06E-10	4.60E-02
5.63E-30	1.76E+00	4.48E-10	5.09E-02	5.30E-15	1.79E+00	4.58E-10	5.19E-02
9.75E-30	2.02E+00	5.14E-10	5.83E-02	4.40E-15	2.05E+00	5.22E-10	5.92E-02
1.69E-29	2.34E+00	5.96E-10	6.77E-02	3.75E-15	2.37E+00	6.03E-10	6.85E-02
2.93E-29	2.73E+00	6.97E-10	7.91E-02	3.29E-15	2.76E+00	7.03E-10	7.98E-02
5.08E-29	3.21E+00	8.19E-10	9.30E-02	2.99E-15	3.23E+00	8.24E-10	9.36E-02
8.80E-29	3.80E+00	9.70E-10	1.10E-01	2.81E-15	3.82E+00	9.74E-10	1.11E-01
1.53E-28	4.53E+00	1.15E-09	1.31E-01	2.72E-15	4.54E+00	1.16E-09	1.31E-01
2.64E-28	5.41E+00	1.38E-09	1.57E-01	2.71E-15	5.43E+00	1.38E-09	1.57E-01
4.58E-28	6.48E+00	1.65E-09	1.88E-01	2.76E-15	6.49E+00	1.66E-09	1.88E-01
7.94E-28	7.85E+00	2.00E-09	2.27E-01	2.87E-15	7.86E+00	2.01E-09	2.28E-01
1.38E-27	9.50E+00	2.42E-09	2.75E-01	3.03E-15	9.50E+00	2.42E-09	2.75E-01
2.39E-27	1.15E+01	2.94E-09	3.34E-01	3.23E-15	1.15E+01	2.94E-09	3.34E-01
4.14E-27	1.41E+01	3.60E-09	4.08E-01	3.47E-15	1.41E+01	3.60E-09	4.08E-01
7.17E-27	1.74E+01	4.42E-09	5.02E-01	3.75E-15	1.74E+01	4.43E-09	5.02E-01
1.24E-26	2.14E+01	5.47E-09	6.20E-01	4.08E-15	2.14E+01	5.47E-09	6.20E-01
2.15E-26	2.67E+01	6.81E-09	7.73E-01	4.44E-15	2.67E+01	6.81E-09	7.73E-01
3.73E-26	3.35E+01	8.54E-09	9.69E-01	4.84E-15	3.35E+01	8.54E-09	9.70E-01
6.47E-26	4.25E+01	1.08E-08	1.23E+00	5.29E-15	4.25E+01	1.08E-08	1.23E+00
1.12E-25	5.46E+01	1.39E-08	1.58E+00	5.78E-15	5.46E+01	1.39E-08	1.58E+00
1.94E-25	7.14E+01	1.82E-08	2.07E+00	6.33E-15	7.14E+01	1.82E-08	2.07E+00
3.37E-25	9.45E+01	2.41E-08	2.74E+00	6.93E-15	9.45E+01	2.41E-08	2.74E+00
5.84E-25	1.28E+02	3.27E-08	3.71E+00	7.58E-15	1.28E+02	3.27E-08	3.71E+00
1.01E-24	1.77E+02	4.50E-08	5.11E+00	8.31E-15	1.77E+02	4.50E-08	5.11E+00
1.75E-24	2.47E+02	6.30E-08	7.15E+00	9.10E-15	2.47E+02	6.30E-08	7.15E+00
3.04E-24	3.50E+02	8.92E-08	1.01E+01	9.97E-15	3.50E+02	8.92E-08	1.01E+01
5.27E-24	4.44E+02	1.13E-07	1.28E+01	1.09E-14	4.44E+02	1.13E-07	1.28E+01
9.13E-24	8.88E+02	2.26E-07	2.57E+01	1.20E-14	8.88E+02	2.26E-07	2.57E+01

Table C.6. Thermo-Calc results for Fe-rich spinel diffusion coefficients at 320 °C and 13.1 MPa.

O2 Activity (atm)	Fe diffusion	Cr diffusion	Ni diffusion	O diffusion coefficient (nm2/s)	Fe diffusion coefficient	Cr diffusion coefficient	Ni diffusion coefficient

	coefficient (nm2/s)	coefficient (nm2/s)	coefficient (nm2/s)		irradiated (nm2/s)	irradiated (nm2/s)	irradiated (nm2/s)
7.11E-43	2.45E-07	6.23E-17	8.66E-08	1.18E-08	1.69E-04	4.31E-14	4.97E-06
1.23E-42	3.52E-07	8.96E-17	6.53E-08	8.97E-09	2.44E-04	6.22E-14	7.12E-06
2.14E-42	5.06E-07	1.29E-16	5.29E-08	6.81E-09	3.52E-04	8.97E-14	1.02E-05
3.70E-42	7.32E-07	1.87E-16	4.77E-08	5.17E-09	5.08E-04	1.30E-13	1.47E-05
6.42E-42	1.05E-06	2.68E-16	4.88E-08	3.93E-09	7.31E-04	1.86E-13	2.12E-05
1.11E-41	1.52E-06	3.87E-16	5.67E-08	2.99E-09	1.06E-03	2.69E-13	3.05E-05
1.93E-41	2.18E-06	5.57E-16	7.20E-08	2.27E-09	1.52E-03	3.87E-13	4.39E-05
3.34E-41	3.14E-06	8.00E-16	9.69E-08	1.72E-09	2.19E-03	5.58E-13	6.33E-05
5.79E-41	4.53E-06	1.15E-15	1.35E-07	1.31E-09	3.15E-03	8.02E-13	9.11E-05
1.00E-40	6.48E-06	1.65E-15	1.90E-07	9.94E-10	4.52E-03	1.15E-12	1.31E-04
1.74E-40	9.23E-06	2.35E-15	2.69E-07	7.55E-10	6.48E-03	1.65E-12	1.88E-04
3.01E-40	1.32E-05	3.36E-15	3.83E-07	5.73E-10	9.29E-03	2.37E-12	2.69E-04
5.23E-40	1.87E-05	4.76E-15	5.42E-07	4.35E-10	1.32E-02	3.37E-12	3.83E-04
9.06E-40	2.63E-05	6.71E-15	7.62E-07	3.31E-10	1.87E-02	4.77E-12	5.42E-04
1.57E-39	3.67E-05	9.37E-15	1.06E-06	2.51E-10	2.63E-02	6.70E-12	7.61E-04
2.72E-39	5.06E-05	1.29E-14	1.46E-06	1.91E-10	3.63E-02	9.27E-12	1.05E-03
4.72E-39	6.79E-05	1.73E-14	1.97E-06	1.45E-10	4.93E-02	1.26E-11	1.43E-03
8.17E-39	8.92E-05	2.27E-14	2.58E-06	1.10E-10	6.50E-02	1.66E-11	1.88E-03
1.42E-38	1.13E-04	2.89E-14	3.27E-06	8.36E-11	8.21E-02	2.09E-11	2.38E-03
2.46E-38	1.37E-04	3.49E-14	3.96E-06	6.35E-11	9.96E-02	2.54E-11	2.88E-03
4.26E-38	1.55E-04	3.96E-14	4.49E-06	4.82E-11	1.15E-01	2.92E-11	3.31E-03
7.38E-38	1.65E-04	4.20E-14	4.76E-06	3.66E-11	1.27E-01	3.23E-11	3.67E-03
8.92E-38	1.65E-04	4.20E-14	4.76E-06	3.33E-11	1.30E-01	3.31E-11	3.76E-03
1.28E-37	2.09E-04	5.33E-14	6.05E-06	2.78E-11	1.48E-01	3.77E-11	4.28E-03
2.22E-37	3.01E-04	7.68E-14	8.72E-06	2.11E-11	1.74E-01	4.43E-11	5.03E-03
3.84E-37	4.35E-04	1.11E-13	1.26E-05	1.61E-11	1.96E-01	4.99E-11	5.66E-03
6.66E-37	6.26E-04	1.60E-13	1.81E-05	1.22E-11	2.13E-01	5.43E-11	6.16E-03
1.15E-36	9.05E-04	2.31E-13	2.62E-05	9.27E-12	2.26E-01	5.76E-11	6.53E-03
2.00E-36	1.31E-03	3.33E-13	3.78E-05	7.04E-12	2.35E-01	6.00E-11	6.81E-03
3.47E-36	1.89E-03	4.81E-13	5.46E-05	5.35E-12	2.43E-01	6.18E-11	7.02E-03
6.01E-36	2.72E-03	6.94E-13	7.87E-05	4.06E-12	2.48E-01	6.32E-11	7.17E-03
1.04E-35	3.92E-03	1.00E-12	1.14E-04	3.08E-12	2.52E-01	6.42E-11	7.29E-03
1.81E-35	5.68E-03	1.45E-12	1.64E-04	2.34E-12	2.55E-01	6.51E-11	7.38E-03
3.13E-35	8.17E-03	2.08E-12	2.36E-04	1.78E-12	2.58E-01	6.58E-11	7.47E-03
5.42E-35	1.18E-02	3.01E-12	3.42E-04	1.35E-12	2.61E-01	6.66E-11	7.56E-03
9.40E-35	1.70E-02	4.33E-12	4.92E-04	1.03E-12	2.65E-01	6.75E-11	7.66E-03
1.63E-34	2.45E-02	6.26E-12	7.10E-04	7.80E-13	2.69E-01	6.86E-11	7.79E-03
2.82E-34	3.54E-02	9.03E-12	1.03E-03	5.93E-13	2.75E-01	7.02E-11	7.96E-03
4.89E-34	5.10E-02	1.30E-11	1.48E-03	4.50E-13	2.84E-01	7.24E-11	8.22E-03
8.48E-34	7.37E-02	1.88E-11	2.13E-03	3.42E-13	2.97E-01	7.57E-11	8.59E-03
1.47E-33	1.07E-01	2.72E-11	3.08E-03	2.60E-13	3.16E-01	8.06E-11	9.15E-03

2.55E-33	1.54E-01	3.92E-11	4.44E-03	1.98E-13	3.46E-01	8.81E-11	1.00E-02
4.42E-33	2.21E-01	5.65E-11	6.41E-03	1.50E-13	3.91E-01	9.97E-11	1.13E-02
7.66E-33	3.20E-01	8.15E-11	9.25E-03	1.14E-13	4.63E-01	1.18E-10	1.34E-02
1.33E-32	4.62E-01	1.18E-10	1.34E-02	8.68E-14	5.77E-01	1.47E-10	1.67E-02
2.30E-32	6.66E-01	1.70E-10	1.93E-02	6.61E-14	7.54E-01	1.92E-10	2.18E-02
3.99E-32	9.59E-01	2.44E-10	2.77E-02	5.03E-14	1.02E+00	2.61E-10	2.96E-02
6.91E-32	1.38E+00	3.53E-10	4.01E-02	3.84E-14	1.43E+00	3.65E-10	4.14E-02
1.20E-31	2.00E+00	5.09E-10	5.78E-02	2.93E-14	2.03E+00	5.18E-10	5.87E-02
2.08E-31	2.88E+00	7.35E-10	8.35E-02	2.25E-14	2.91E+00	7.41E-10	8.41E-02
3.60E-31	4.16E+00	1.06E-09	1.20E-01	1.73E-14	4.18E+00	1.07E-09	1.21E-01
6.24E-31	5.99E+00	1.53E-09	1.73E-01	1.34E-14	6.00E+00	1.53E-09	1.74E-01
1.08E-30	8.48E+00	2.16E-09	2.45E-01	1.04E-14	8.48E+00	2.16E-09	2.46E-01
1.87E-30	8.96E+00	2.29E-09	2.59E-01	8.19E-15	8.97E+00	2.29E-09	2.60E-01
3.25E-30	9.63E+00	2.46E-09	2.79E-01	6.53E-15	9.64E+00	2.46E-09	2.79E-01
5.63E-30	1.04E+01	2.66E-09	3.02E-01	5.30E-15	1.04E+01	2.66E-09	3.02E-01
9.75E-30	1.15E+01	2.92E-09	3.31E-01	4.40E-15	1.15E+01	2.92E-09	3.31E-01
1.69E-29	1.27E+01	3.24E-09	3.67E-01	3.75E-15	1.27E+01	3.24E-09	3.67E-01
2.93E-29	1.42E+01	3.62E-09	4.11E-01	3.29E-15	1.42E+01	3.62E-09	4.11E-01
5.08E-29	1.61E+01	4.10E-09	4.65E-01	2.99E-15	1.61E+01	4.10E-09	4.65E-01
8.80E-29	1.83E+01	4.67E-09	5.30E-01	2.81E-15	1.83E+01	4.67E-09	5.30E-01
1.53E-28	2.11E+01	5.39E-09	6.11E-01	2.72E-15	2.11E+01	5.39E-09	6.11E-01
2.64E-28	2.45E+01	6.26E-09	7.10E-01	2.71E-15	2.45E+01	6.26E-09	7.10E-01
4.58E-28	2.87E+01	7.31E-09	8.30E-01	2.76E-15	2.87E+01	7.31E-09	8.30E-01
7.94E-28	3.36E+01	8.58E-09	9.73E-01	2.87E-15	3.36E+01	8.58E-09	9.73E-01
1.38E-27	3.97E+01	1.01E-08	1.15E+00	3.03E-15	3.97E+01	1.01E-08	1.15E+00
2.39E-27	4.70E+01	1.20E-08	1.36E+00	3.23E-15	4.70E+01	1.20E-08	1.36E+00
4.14E-27	5.55E+01	1.41E-08	1.61E+00	3.47E-15	5.55E+01	1.41E-08	1.61E+00
7.17E-27	6.57E+01	1.68E-08	1.90E+00	3.75E-15	6.57E+01	1.68E-08	1.90E+00
1.24E-26	7.72E+01	1.97E-08	2.23E+00	4.08E-15	7.72E+01	1.97E-08	2.23E+00
2.15E-26	9.01E+01	2.30E-08	2.61E+00	4.44E-15	9.01E+01	2.30E-08	2.61E+00
3.73E-26	1.05E+02	2.68E-08	3.04E+00	4.84E-15	1.05E+02	2.68E-08	3.04E+00
6.47E-26	1.21E+02	3.09E-08	3.51E+00	5.29E-15	1.21E+02	3.09E-08	3.51E+00
1.12E-25	1.38E+02	3.53E-08	4.01E+00	5.78E-15	1.38E+02	3.53E-08	4.01E+00
1.94E-25	1.57E+02	3.99E-08	4.53E+00	6.33E-15	1.57E+02	3.99E-08	4.53E+00
3.37E-25	1.75E+02	4.47E-08	5.07E+00	6.93E-15	1.75E+02	4.47E-08	5.07E+00
5.84E-25	1.94E+02	4.96E-08	5.62E+00	7.58E-15	1.94E+02	4.96E-08	5.62E+00
1.01E-24	2.13E+02	5.44E-08	6.18E+00	8.31E-15	2.13E+02	5.44E-08	6.18E+00
1.75E-24	2.33E+02	5.93E-08	6.73E+00	9.10E-15	2.33E+02	5.93E-08	6.73E+00
3.04E-24	2.51E+02	6.39E-08	7.26E+00	9.97E-15	2.51E+02	6.39E-08	7.26E+00
5.27E-24	2.68E+02	6.83E-08	7.76E+00	1.09E-14	2.68E+02	6.83E-08	7.76E+00
9.13E-24	2.84E+02	7.25E-08	8.23E+00	1.20E-14	2.84E+02	7.25E-08	8.23E+00
1.42E-23	2.97E+02	7.58E-08	8.60E+00	1.29E-14	2.97E+02	7.58E-08	8.60E+00
1.58E-23	2.98E+02	7.60E-08	8.63E+00	1.31E-14	2.98E+02	7.60E-08	8.63E+00

2.74E-23	3.04E+02	7.74E-08	8.78E+00	1.44E-14	3.04E+02	7.74E-08	8.78E+00
4.76E-23	3.08E+02	7.86E-08	8.92E+00	1.58E-14	3.08E+02	7.86E-08	8.92E+00
8.24E-23	3.13E+02	7.98E-08	9.05E+00	1.73E-14	3.13E+02	7.98E-08	9.05E+00
1.43E-22	3.17E+02	8.08E-08	9.17E+00	1.89E-14	3.17E+02	8.08E-08	9.17E+00
2.48E-22	3.20E+02	8.17E-08	9.27E+00	2.08E-14	3.20E+02	8.17E-08	9.27E+00
4.29E-22	3.24E+02	8.26E-08	9.37E+00	2.28E-14	3.24E+02	8.26E-08	9.37E+00
7.52E-22	3.27E+02	8.34E-08	9.46E+00	2.50E-14	3.27E+02	8.34E-08	9.46E+00
1.30E-21	3.30E+02	8.41E-08	9.54E+00	2.74E-14	3.30E+02	8.41E-08	9.54E+00
2.26E-21	3.32E+02	8.48E-08	9.62E+00	3.00E-14	3.32E+02	8.48E-08	9.62E+00
3.91E-21	3.35E+02	8.53E-08	9.68E+00	3.29E-14	3.35E+02	8.53E-08	9.68E+00
6.78E-21	3.37E+02	8.59E-08	9.75E+00	3.60E-14	3.37E+02	8.59E-08	9.75E+00
1.18E-20	3.39E+02	8.63E-08	9.80E+00	3.95E-14	3.39E+02	8.63E-08	9.80E+00
2.04E-20	3.40E+02	8.67E-08	9.84E+00	4.33E-14	3.40E+02	8.67E-08	9.84E+00
3.53E-20	3.41E+02	8.70E-08	9.87E+00	4.74E-14	3.41E+02	8.70E-08	9.87E+00
6.12E-20	3.43E+02	8.74E-08	9.91E+00	5.20E-14	3.43E+02	8.74E-08	9.91E+00
1.06E-19	3.44E+02	8.77E-08	9.95E+00	5.70E-14	3.44E+02	8.77E-08	9.95E+00
1.84E-19	3.45E+02	8.79E-08	9.98E+00	6.25E-14	3.45E+02	8.79E-08	9.98E+00
3.19E-19	3.46E+02	8.81E-08	1.00E+01	6.84E-14	3.46E+02	8.81E-08	1.00E+01
5.52E-19	3.46E+02	8.83E-08	1.00E+01	7.50E-14	3.46E+02	8.83E-08	1.00E+01
9.58E-19	3.47E+02	8.85E-08	1.00E+01	8.22E-14	3.47E+02	8.85E-08	1.00E+01
1.66E-18	3.47E+02	8.86E-08	1.01E+01	9.01E-14	3.47E+02	8.86E-08	1.01E+01
2.88E-18	3.48E+02	8.87E-08	1.01E+01	9.88E-14	3.48E+02	8.87E-08	1.01E+01
4.25E-18	3.48E+02	8.88E-08	1.01E+01	1.05E-13	3.48E+02	8.88E-08	1.01E+01

Table C.7. Thermo-Calc results for element chemical potentials and the Pilling-Bedworth ratio at 320 °C and 13.1 MPa.

O2 Activity (atm)	Fe chemical potential (J/mol)	Cr chemical potential (J/mol)	Ni chemical potential (J/mol)	O chemical potential (J/mol)	Pilling-Bedworth ratio
7.18E-66	-1.95E+04	-1.68E+04	-3.09E+04	-4.20E+05	1.00E+00
3.92E-64	-1.95E+04	-1.68E+04	-3.09E+04	-4.10E+05	1.00E+00
6.79E-64	-1.95E+04	-1.68E+04	-3.09E+04	-4.09E+05	1.00E+00
1.18E-63	-1.95E+04	-1.68E+04	-3.09E+04	-4.08E+05	1.00E+00
2.04E-63	-1.95E+04	-1.68E+04	-3.09E+04	-4.06E+05	1.00E+00
3.54E-63	-1.95E+04	-1.68E+04	-3.09E+04	-4.05E+05	1.00E+00
6.13E-63	-1.95E+04	-1.68E+04	-3.09E+04	-4.04E+05	1.00E+00
1.06E-62	-1.95E+04	-1.68E+04	-3.09E+04	-4.02E+05	1.00E+00
1.84E-62	-1.95E+04	-1.68E+04	-3.09E+04	-4.01E+05	1.00E+00
3.19E-62	-1.95E+04	-1.68E+04	-3.09E+04	-4.00E+05	1.00E+00
5.53E-62	-1.95E+04	-1.68E+04	-3.09E+04	-3.98E+05	1.00E+00
9.59E-62	-1.95E+04	-1.68E+04	-3.09E+04	-3.97E+05	1.00E+00
1.66E-61	-1.95E+04	-1.68E+04	-3.09E+04	-3.95E+05	1.00E+00
2.88E-61	-1.95E+04	-1.68E+04	-3.09E+04	-3.94E+05	1.00E+00
4.99E-61	-1.95E+04	-1.68E+04	-3.09E+04	-3.93E+05	1.00E+00

8.65E-61	-1.95E+04	-1.68E+04	-3.09E+04	-3.91E+05	1.00E+00
1.50E-60	-1.95E+04	-1.68E+04	-3.09E+04	-3.90E+05	1.00E+00
2.60E-60	-1.95E+04	-1.68E+04	-3.09E+04	-3.89E+05	1.00E+00
4.51E-60	-1.95E+04	-1.68E+04	-3.09E+04	-3.87E+05	1.00E+00
5.50E-60	-1.95E+04	-1.68E+04	-3.09E+04	-3.87E+05	1.17E+00
5.61E-60	-1.95E+04	-1.68E+04	-3.09E+04	-3.87E+05	1.17E+00
6.27E-60	-1.95E+04	-1.72E+04	-3.10E+04	-3.87E+05	1.18E+00
6.99E-60	-1.95E+04	-1.76E+04	-3.10E+04	-3.86E+05	1.18E+00
7.81E-60	-1.95E+04	-1.80E+04	-3.10E+04	-3.86E+05	1.19E+00
8.72E-60	-1.94E+04	-1.84E+04	-3.10E+04	-3.86E+05	1.19E+00
9.73E-60	-1.94E+04	-1.88E+04	-3.10E+04	-3.85E+05	1.19E+00
1.09E-59	-1.94E+04	-1.92E+04	-3.10E+04	-3.85E+05	1.20E+00
1.21E-59	-1.94E+04	-1.96E+04	-3.11E+04	-3.85E+05	1.20E+00
1.35E-59	-1.94E+04	-2.00E+04	-3.11E+04	-3.85E+05	1.20E+00
2.35E-59	-1.93E+04	-2.20E+04	-3.11E+04	-3.83E+05	1.21E+00
4.07E-59	-1.93E+04	-2.40E+04	-3.11E+04	-3.82E+05	1.21E+00
7.05E-59	-1.93E+04	-2.60E+04	-3.11E+04	-3.81E+05	1.22E+00
1.22E-58	-1.93E+04	-2.79E+04	-3.11E+04	-3.79E+05	1.22E+00
2.12E-58	-1.93E+04	-2.99E+04	-3.12E+04	-3.78E+05	1.22E+00
3.67E-58	-1.93E+04	-3.19E+04	-3.12E+04	-3.77E+05	1.22E+00
6.36E-58	-1.93E+04	-3.39E+04	-3.12E+04	-3.75E+05	1.22E+00
1.10E-57	-1.93E+04	-3.59E+04	-3.12E+04	-3.74E+05	1.22E+00
1.91E-57	-1.93E+04	-3.79E+04	-3.12E+04	-3.72E+05	1.22E+00
3.31E-57	-1.93E+04	-3.99E+04	-3.12E+04	-3.71E+05	1.22E+00
5.74E-57	-1.92E+04	-4.19E+04	-3.12E+04	-3.70E+05	1.22E+00
9.95E-57	-1.92E+04	-4.38E+04	-3.12E+04	-3.68E+05	1.22E+00
1.72E-56	-1.92E+04	-4.58E+04	-3.12E+04	-3.67E+05	1.22E+00
2.99E-56	-1.92E+04	-4.78E+04	-3.12E+04	-3.66E+05	1.22E+00
5.18E-56	-1.92E+04	-4.98E+04	-3.12E+04	-3.64E+05	1.22E+00
8.98E-56	-1.92E+04	-5.18E+04	-3.12E+04	-3.63E+05	1.22E+00
1.56E-55	-1.92E+04	-5.38E+04	-3.12E+04	-3.62E+05	1.22E+00
2.70E-55	-1.92E+04	-5.58E+04	-3.12E+04	-3.60E+05	1.22E+00
4.68E-55	-1.92E+04	-5.78E+04	-3.12E+04	-3.59E+05	1.22E+00
8.10E-55	-1.92E+04	-5.98E+04	-3.12E+04	-3.58E+05	1.22E+00
1.40E-54	-1.92E+04	-6.18E+04	-3.12E+04	-3.56E+05	1.22E+00
2.43E-54	-1.92E+04	-6.38E+04	-3.12E+04	-3.55E+05	1.22E+00
4.22E-54	-1.92E+04	-6.58E+04	-3.12E+04	-3.53E+05	1.22E+00
7.31E-54	-1.92E+04	-6.78E+04	-3.12E+04	-3.52E+05	1.22E+00
1.27E-53	-1.92E+04	-6.98E+04	-3.12E+04	-3.51E+05	1.22E+00
2.20E-53	-1.92E+04	-7.18E+04	-3.12E+04	-3.49E+05	1.22E+00
3.81E-53	-1.92E+04	-7.38E+04	-3.12E+04	-3.48E+05	1.22E+00
6.60E-53	-1.92E+04	-7.58E+04	-3.12E+04	-3.47E+05	1.22E+00
1.14E-52	-1.92E+04	-7.78E+04	-3.12E+04	-3.45E+05	1.22E+00

1.98E-52	-1.92E+04	-7.98E+04	-3.12E+04	-3.44E+05	1.22E+00
3.44E-52	-1.92E+04	-8.18E+04	-3.12E+04	-3.43E+05	1.22E+00
5.96E-52	-1.92E+04	-8.38E+04	-3.12E+04	-3.41E+05	1.22E+00
1.03E-51	-1.92E+04	-8.58E+04	-3.12E+04	-3.40E+05	1.22E+00
1.79E-51	-1.92E+04	-8.78E+04	-3.12E+04	-3.39E+05	1.22E+00
3.10E-51	-1.92E+04	-8.98E+04	-3.12E+04	-3.37E+05	1.22E+00
5.38E-51	-1.92E+04	-9.18E+04	-3.12E+04	-3.36E+05	1.22E+00
9.32E-51	-1.92E+04	-9.38E+04	-3.12E+04	-3.34E+05	1.22E+00
1.35E-50	-1.92E+04	-9.52E+04	-3.12E+04	-3.34E+05	1.33E+00
1.62E-50	-1.92E+04	-9.61E+04	-3.12E+04	-3.33E+05	1.33E+00
2.80E-50	-1.92E+04	-9.88E+04	-3.12E+04	-3.32E+05	1.33E+00
4.85E-50	-1.92E+04	-1.01E+05	-3.12E+04	-3.30E+05	1.33E+00
8.41E-50	-1.92E+04	-1.04E+05	-3.12E+04	-3.29E+05	1.33E+00
1.46E-49	-1.92E+04	-1.07E+05	-3.12E+04	-3.28E+05	1.33E+00
2.53E-49	-1.92E+04	-1.10E+05	-3.12E+04	-3.26E+05	1.33E+00
4.38E-49	-1.92E+04	-1.12E+05	-3.12E+04	-3.25E+05	1.33E+00
7.59E-49	-1.92E+04	-1.15E+05	-3.12E+04	-3.24E+05	1.33E+00
1.32E-48	-1.92E+04	-1.18E+05	-3.12E+04	-3.22E+05	1.33E+00
2.28E-48	-1.92E+04	-1.20E+05	-3.12E+04	-3.21E+05	1.33E+00
3.95E-48	-1.92E+04	-1.23E+05	-3.12E+04	-3.20E+05	1.33E+00
6.85E-48	-1.92E+04	-1.26E+05	-3.12E+04	-3.18E+05	1.33E+00
1.19E-47	-1.92E+04	-1.29E+05	-3.12E+04	-3.17E+05	1.33E+00
2.06E-47	-1.92E+04	-1.31E+05	-3.12E+04	-3.15E+05	1.33E+00
3.57E-47	-1.92E+04	-1.34E+05	-3.12E+04	-3.14E+05	1.33E+00
6.18E-47	-1.92E+04	-1.37E+05	-3.12E+04	-3.13E+05	1.33E+00
1.07E-46	-1.92E+04	-1.39E+05	-3.12E+04	-3.11E+05	1.33E+00
1.86E-46	-1.92E+04	-1.42E+05	-3.12E+04	-3.10E+05	1.33E+00
3.22E-46	-1.92E+04	-1.45E+05	-3.12E+04	-3.09E+05	1.33E+00
5.58E-46	-1.92E+04	-1.48E+05	-3.12E+04	-3.07E+05	1.33E+00
9.67E-46	-1.92E+04	-1.50E+05	-3.12E+04	-3.06E+05	1.33E+00
1.68E-45	-1.92E+04	-1.53E+05	-3.12E+04	-3.05E+05	1.33E+00
2.91E-45	-1.92E+04	-1.56E+05	-3.12E+04	-3.03E+05	1.33E+00
5.04E-45	-1.92E+04	-1.58E+05	-3.12E+04	-3.02E+05	1.33E+00
8.73E-45	-1.92E+04	-1.61E+05	-3.12E+04	-3.01E+05	1.33E+00
1.51E-44	-1.92E+04	-1.64E+05	-3.12E+04	-2.99E+05	1.33E+00
2.62E-44	-1.92E+04	-1.67E+05	-3.12E+04	-2.98E+05	1.33E+00
4.54E-44	-1.92E+04	-1.69E+05	-3.12E+04	-2.97E+05	1.33E+00
7.88E-44	-1.92E+04	-1.72E+05	-3.12E+04	-2.95E+05	1.34E+00
1.37E-43	-1.92E+04	-1.75E+05	-3.12E+04	-2.94E+05	1.34E+00
2.37E-43	-1.92E+04	-1.78E+05	-3.12E+04	-2.92E+05	1.35E+00
4.10E-43	-1.92E+04	-1.81E+05	-3.12E+04	-2.91E+05	1.37E+00
4.67E-43	-1.92E+04	-1.81E+05	-3.12E+04	-2.91E+05	1.38E+00
7.11E-43	-2.06E+04	-1.83E+05	-3.01E+04	-2.90E+05	1.89E+00

1.23E-42	-2.24E+04	-1.85E+05	-2.88E+04	-2.88E+05	1.91E+00
2.14E-42	-2.43E+04	-1.87E+05	-2.77E+04	-2.87E+05	1.92E+00
3.70E-42	-2.61E+04	-1.88E+05	-2.68E+04	-2.86E+05	1.93E+00
6.42E-42	-2.79E+04	-1.90E+05	-2.59E+04	-2.84E+05	1.94E+00
1.11E-41	-2.97E+04	-1.92E+05	-2.52E+04	-2.83E+05	1.95E+00
1.93E-41	-3.15E+04	-1.94E+05	-2.45E+04	-2.82E+05	1.95E+00
3.34E-41	-3.33E+04	-1.96E+05	-2.39E+04	-2.80E+05	1.96E+00
5.79E-41	-3.51E+04	-1.98E+05	-2.34E+04	-2.79E+05	1.97E+00
1.00E-40	-3.69E+04	-2.00E+05	-2.29E+04	-2.78E+05	1.97E+00
1.74E-40	-3.87E+04	-2.01E+05	-2.25E+04	-2.76E+05	1.98E+00
3.01E-40	-4.05E+04	-2.03E+05	-2.21E+04	-2.75E+05	1.99E+00
5.23E-40	-4.24E+04	-2.05E+05	-2.18E+04	-2.73E+05	1.99E+00
9.06E-40	-4.42E+04	-2.07E+05	-2.16E+04	-2.72E+05	2.00E+00
1.57E-39	-4.60E+04	-2.09E+05	-2.14E+04	-2.71E+05	2.01E+00
2.72E-39	-4.78E+04	-2.11E+05	-2.12E+04	-2.69E+05	2.02E+00
4.72E-39	-4.97E+04	-2.13E+05	-2.11E+04	-2.68E+05	2.03E+00
8.17E-39	-5.16E+04	-2.15E+05	-2.10E+04	-2.67E+05	2.04E+00
1.42E-38	-5.35E+04	-2.17E+05	-2.09E+04	-2.65E+05	2.05E+00
2.46E-38	-5.54E+04	-2.19E+05	-2.09E+04	-2.64E+05	2.07E+00
4.26E-38	-5.74E+04	-2.21E+05	-2.08E+04	-2.63E+05	2.09E+00
7.38E-38	-5.94E+04	-2.23E+05	-2.08E+04	-2.61E+05	2.12E+00
8.92E-38	-6.01E+04	-2.24E+05	-2.08E+04	-2.61E+05	2.13E+00
1.28E-37	-6.13E+04	-2.25E+05	-2.19E+04	-2.60E+05	2.13E+00
2.22E-37	-6.31E+04	-2.27E+05	-2.37E+04	-2.59E+05	2.13E+00
3.84E-37	-6.49E+04	-2.28E+05	-2.56E+04	-2.57E+05	2.13E+00
6.66E-37	-6.67E+04	-2.30E+05	-2.74E+04	-2.56E+05	2.13E+00
1.15E-36	-6.85E+04	-2.32E+05	-2.92E+04	-2.54E+05	2.13E+00
2.00E-36	-7.03E+04	-2.34E+05	-3.10E+04	-2.53E+05	2.13E+00
3.47E-36	-7.21E+04	-2.36E+05	-3.28E+04	-2.52E+05	2.13E+00
6.01E-36	-7.39E+04	-2.38E+05	-3.46E+04	-2.50E+05	2.13E+00
1.04E-35	-7.57E+04	-2.39E+05	-3.64E+04	-2.49E+05	2.13E+00
1.81E-35	-7.76E+04	-2.41E+05	-3.82E+04	-2.48E+05	2.13E+00
3.13E-35	-7.94E+04	-2.43E+05	-4.00E+04	-2.46E+05	2.13E+00
5.42E-35	-8.12E+04	-2.45E+05	-4.18E+04	-2.45E+05	2.13E+00
9.40E-35	-8.30E+04	-2.47E+05	-4.36E+04	-2.44E+05	2.13E+00
1.63E-34	-8.48E+04	-2.48E+05	-4.54E+04	-2.42E+05	2.13E+00
2.82E-34	-8.66E+04	-2.50E+05	-4.72E+04	-2.41E+05	2.13E+00
4.89E-34	-8.84E+04	-2.52E+05	-4.91E+04	-2.40E+05	2.13E+00
8.48E-34	-9.02E+04	-2.54E+05	-5.09E+04	-2.38E+05	2.13E+00
1.47E-33	-9.20E+04	-2.56E+05	-5.27E+04	-2.37E+05	2.13E+00
2.55E-33	-9.38E+04	-2.57E+05	-5.45E+04	-2.35E+05	2.13E+00
4.42E-33	-9.56E+04	-2.59E+05	-5.63E+04	-2.34E+05	2.13E+00
7.66E-33	-9.74E+04	-2.61E+05	-5.81E+04	-2.33E+05	2.13E+00

1.33E-32	-9.92E+04	-2.63E+05	-5.99E+04	-2.31E+05	2.13E+00
2.30E-32	-1.01E+05	-2.65E+05	-6.17E+04	-2.30E+05	2.13E+00
3.99E-32	-1.03E+05	-2.66E+05	-6.35E+04	-2.29E+05	2.13E+00
6.91E-32	-1.05E+05	-2.68E+05	-6.53E+04	-2.27E+05	2.13E+00
1.20E-31	-1.06E+05	-2.70E+05	-6.71E+04	-2.26E+05	2.13E+00
2.08E-31	-1.08E+05	-2.72E+05	-6.89E+04	-2.25E+05	2.13E+00
3.60E-31	-1.10E+05	-2.74E+05	-7.07E+04	-2.23E+05	2.13E+00
6.24E-31	-1.12E+05	-2.75E+05	-7.26E+04	-2.22E+05	2.13E+00
1.08E-30	-1.14E+05	-2.77E+05	-7.43E+04	-2.21E+05	2.13E+00
1.87E-30	-1.16E+05	-2.79E+05	-7.47E+04	-2.19E+05	2.14E+00
3.25E-30	-1.18E+05	-2.81E+05	-7.53E+04	-2.18E+05	2.14E+00
5.63E-30	-1.20E+05	-2.83E+05	-7.61E+04	-2.17E+05	2.14E+00
9.75E-30	-1.22E+05	-2.85E+05	-7.70E+04	-2.15E+05	2.14E+00
1.69E-29	-1.24E+05	-2.87E+05	-7.79E+04	-2.14E+05	2.14E+00
2.93E-29	-1.26E+05	-2.88E+05	-7.89E+04	-2.12E+05	2.14E+00
5.08E-29	-1.28E+05	-2.90E+05	-8.00E+04	-2.11E+05	2.14E+00
8.80E-29	-1.30E+05	-2.92E+05	-8.11E+04	-2.10E+05	2.14E+00
1.53E-28	-1.32E+05	-2.94E+05	-8.22E+04	-2.08E+05	2.14E+00
2.64E-28	-1.34E+05	-2.96E+05	-8.33E+04	-2.07E+05	2.15E+00
4.58E-28	-1.36E+05	-2.97E+05	-8.45E+04	-2.06E+05	2.14E+00
7.94E-28	-1.38E+05	-2.99E+05	-8.57E+04	-2.04E+05	2.15E+00
1.38E-27	-1.41E+05	-3.01E+05	-8.69E+04	-2.03E+05	2.15E+00
2.39E-27	-1.43E+05	-3.03E+05	-8.81E+04	-2.02E+05	2.15E+00
4.14E-27	-1.45E+05	-3.05E+05	-8.93E+04	-2.00E+05	2.15E+00
7.17E-27	-1.47E+05	-3.06E+05	-9.06E+04	-1.99E+05	2.15E+00
1.24E-26	-1.49E+05	-3.08E+05	-9.18E+04	-1.98E+05	2.15E+00
2.15E-26	-1.51E+05	-3.10E+05	-9.31E+04	-1.96E+05	2.15E+00
3.73E-26	-1.53E+05	-3.12E+05	-9.44E+04	-1.95E+05	2.15E+00
6.47E-26	-1.55E+05	-3.14E+05	-9.56E+04	-1.93E+05	2.15E+00
1.12E-25	-1.57E+05	-3.15E+05	-9.69E+04	-1.92E+05	2.15E+00
1.94E-25	-1.59E+05	-3.17E+05	-9.82E+04	-1.91E+05	2.15E+00
3.37E-25	-1.61E+05	-3.19E+05	-9.95E+04	-1.89E+05	2.15E+00
5.84E-25	-1.63E+05	-3.21E+05	-1.01E+05	-1.88E+05	2.15E+00
1.01E-24	-1.65E+05	-3.23E+05	-1.02E+05	-1.87E+05	2.15E+00
1.75E-24	-1.68E+05	-3.25E+05	-1.03E+05	-1.85E+05	2.15E+00
3.04E-24	-1.70E+05	-3.27E+05	-1.05E+05	-1.84E+05	2.15E+00
5.27E-24	-1.72E+05	-3.28E+05	-1.06E+05	-1.83E+05	2.15E+00
9.13E-24	-1.74E+05	-3.30E+05	-1.07E+05	-1.81E+05	2.15E+00
1.42E-23	-1.75E+05	-3.32E+05	-1.08E+05	-1.80E+05	2.15E+00
1.58E-23	-1.76E+05	-3.32E+05	-1.09E+05	-1.80E+05	2.15E+00
2.74E-23	-1.78E+05	-3.34E+05	-1.10E+05	-1.79E+05	2.15E+00
4.76E-23	-1.80E+05	-3.36E+05	-1.11E+05	-1.77E+05	2.15E+00
8.24E-23	-1.82E+05	-3.38E+05	-1.13E+05	-1.76E+05	2.15E+00

1.43E-22	-1.84E+05	-3.40E+05	-1.14E+05	-1.74E+05	2.15E+00
2.48E-22	-1.86E+05	-3.43E+05	-1.15E+05	-1.73E+05	2.15E+00
4.29E-22	-1.88E+05	-3.45E+05	-1.17E+05	-1.72E+05	2.15E+00
7.52E-22	-1.90E+05	-3.47E+05	-1.18E+05	-1.70E+05	2.15E+00
1.30E-21	-1.92E+05	-3.49E+05	-1.20E+05	-1.69E+05	2.15E+00
2.26E-21	-1.94E+05	-3.51E+05	-1.21E+05	-1.68E+05	2.15E+00
3.91E-21	-1.96E+05	-3.53E+05	-1.22E+05	-1.66E+05	2.15E+00
6.78E-21	-1.98E+05	-3.55E+05	-1.24E+05	-1.65E+05	2.15E+00
1.18E-20	-2.00E+05	-3.57E+05	-1.25E+05	-1.64E+05	2.15E+00
2.04E-20	-2.02E+05	-3.59E+05	-1.26E+05	-1.62E+05	2.15E+00
3.53E-20	-2.04E+05	-3.61E+05	-1.28E+05	-1.61E+05	2.15E+00
6.12E-20	-2.06E+05	-3.63E+05	-1.29E+05	-1.60E+05	2.15E+00
1.06E-19	-2.08E+05	-3.65E+05	-1.30E+05	-1.58E+05	2.15E+00
1.84E-19	-2.10E+05	-3.67E+05	-1.32E+05	-1.57E+05	2.15E+00
3.19E-19	-2.12E+05	-3.69E+05	-1.33E+05	-1.55E+05	2.15E+00
5.52E-19	-2.15E+05	-3.71E+05	-1.34E+05	-1.54E+05	2.15E+00
9.58E-19	-2.17E+05	-3.73E+05	-1.36E+05	-1.53E+05	2.15E+00
1.66E-18	-2.19E+05	-3.75E+05	-1.37E+05	-1.51E+05	2.15E+00
2.88E-18	-2.21E+05	-3.77E+05	-1.38E+05	-1.50E+05	2.15E+00
4.25E-18	-2.22E+05	-3.79E+05	-1.39E+05	-1.49E+05	2.15E+00

Table C.8. Thermo-Calc derived calculation of parabolic rate constant at 320 °C and 13.1 MPa.

O2 Activity (atm)	Parabolic rate constant in Cr-rich spinel with Fe (nm2/s)	Parabolic rate constant in Cr-rich spinel with O (nm2/s)	Parabolic rate constant in irradiated Cr-rich spinel with Fe (nm2/s)	Parabolic rate constant in Fe-rich spinel with Fe (nm2/s)	Parabolic rate constant in Fe-rich spinel with O (nm2/s)	Parabolic rate constant in irradiated Fe-rich spinel with Fe (nm2/s)
7.11E-43	3.79E-01	9.60E-06	1.99E+02	3.87E-04	9.79E-06	2.97E-01
1.23E-42	6.10E-01	2.48E-05	3.49E+02	8.19E-04	2.53E-05	5.96E-01
2.14E-42	7.90E-01	3.05E-05	5.04E+02	1.47E-03	3.13E-05	1.05E+00
3.70E-42	9.16E-01	3.48E-05	6.52E+02	2.35E-03	3.58E-05	1.66E+00
6.42E-42	1.00E+00	4.15E-05	7.96E+02	3.59E-03	4.26E-05	2.52E+00
1.11E-41	1.06E+00	4.40E-05	9.37E+02	5.37E-03	4.52E-05	3.75E+00
1.93E-41	1.11E+00	4.59E-05	1.08E+03	7.92E-03	4.71E-05	5.53E+00
3.34E-41	1.15E+00	4.88E-05	1.22E+03	1.16E-02	5.01E-05	8.08E+00
5.79E-41	1.17E+00	4.99E-05	1.36E+03	1.68E-02	5.13E-05	1.17E+01
1.00E-40	1.20E+00	5.08E-05	1.50E+03	2.43E-02	5.21E-05	1.69E+01
1.74E-40	1.22E+00	5.20E-05	1.64E+03	3.48E-02	5.34E-05	2.43E+01
3.01E-40	1.23E+00	5.25E-05	1.78E+03	4.98E-02	5.39E-05	3.48E+01
5.23E-40	1.25E+00	5.32E-05	1.92E+03	7.18E-02	5.47E-05	5.04E+01
9.06E-40	1.26E+00	5.35E-05	2.05E+03	1.01E-01	5.50E-05	7.12E+01
1.57E-39	1.27E+00	5.37E-05	2.19E+03	1.42E-01	5.52E-05	1.00E+02
2.72E-39	1.29E+00	5.40E-05	2.33E+03	1.98E-01	5.55E-05	1.40E+02

4.72E-39	1.29E+00	5.42E-05	2.46E+03	2.75E-01	5.56E-05	1.96E+02
8.17E-39	1.30E+00	5.43E-05	2.60E+03	3.77E-01	5.57E-05	2.70E+02
1.42E-38	1.32E+00	5.44E-05	2.75E+03	5.05E-01	5.59E-05	3.64E+02
2.46E-38	1.33E+00	5.45E-05	2.87E+03	6.55E-01	5.59E-05	4.72E+02
4.26E-38	1.34E+00	5.45E-05	3.01E+03	8.36E-01	5.60E-05	6.05E+02
7.38E-38	1.35E+00	5.46E-05	3.14E+03	1.02E+00	5.60E-05	7.44E+02
8.92E-38	1.36E+00	5.46E-05	3.20E+03	1.09E+00	5.60E-05	7.97E+02
1.28E-37	1.37E+00	5.46E-05	3.28E+03	1.21E+00	5.61E-05	8.89E+02
2.22E-37	1.39E+00	5.46E-05	3.40E+03	1.47E+00	5.61E-05	1.05E+03
3.84E-37	1.41E+00	5.46E-05	3.52E+03	1.83E+00	5.61E-05	1.23E+03
6.66E-37	1.45E+00	5.46E-05	3.65E+03	2.36E+00	5.61E-05	1.44E+03
1.15E-36	1.51E+00	5.47E-05	3.77E+03	3.13E+00	5.61E-05	1.66E+03
2.00E-36	1.58E+00	5.47E-05	3.89E+03	4.23E+00	5.62E-05	1.89E+03
3.47E-36	1.70E+00	5.47E-05	4.01E+03	5.82E+00	5.62E-05	2.13E+03
6.01E-36	1.86E+00	5.47E-05	4.14E+03	8.12E+00	5.62E-05	2.37E+03
1.04E-35	2.10E+00	5.47E-05	4.26E+03	1.14E+01	5.62E-05	2.62E+03
1.81E-35	2.47E+00	5.47E-05	4.39E+03	1.65E+01	5.62E-05	2.89E+03
3.13E-35	2.96E+00	5.47E-05	4.51E+03	2.34E+01	5.62E-05	3.14E+03
5.42E-35	3.68E+00	5.47E-05	4.63E+03	3.34E+01	5.62E-05	3.40E+03
9.40E-35	4.71E+00	5.47E-05	4.76E+03	4.77E+01	5.62E-05	3.66E+03
1.63E-34	6.20E+00	5.47E-05	4.88E+03	6.85E+01	5.62E-05	3.93E+03
2.82E-34	8.36E+00	5.47E-05	5.00E+03	9.84E+01	5.62E-05	4.20E+03
4.89E-34	1.15E+01	5.47E-05	5.13E+03	1.42E+02	5.62E-05	4.48E+03
8.48E-34	1.60E+01	5.47E-05	5.25E+03	2.04E+02	5.62E-05	4.77E+03
1.47E-33	2.24E+01	5.47E-05	5.38E+03	2.94E+02	5.62E-05	5.08E+03
2.55E-33	3.17E+01	5.47E-05	5.51E+03	4.24E+02	5.62E-05	5.41E+03
4.42E-33	4.52E+01	5.47E-05	5.64E+03	6.11E+02	5.62E-05	5.77E+03
7.66E-33	6.46E+01	5.47E-05	5.77E+03	8.81E+02	5.62E-05	6.20E+03
1.33E-32	9.27E+01	5.47E-05	5.91E+03	1.27E+03	5.62E-05	6.72E+03
2.30E-32	1.33E+02	5.47E-05	6.05E+03	1.83E+03	5.62E-05	7.38E+03
3.99E-32	1.98E+02	5.47E-05	6.22E+03	2.73E+03	5.62E-05	8.37E+03
6.91E-32	2.91E+02	5.47E-05	6.41E+03	4.03E+03	5.62E-05	9.73E+03
1.20E-31	3.59E+02	5.47E-05	6.52E+03	4.97E+03	5.62E-05	1.07E+04
2.08E-31	5.54E+02	5.47E-05	6.79E+03	7.68E+03	5.62E-05	1.34E+04
3.60E-31	8.35E+02	5.47E-05	7.13E+03	1.16E+04	5.62E-05	1.74E+04
6.24E-31	1.24E+03	5.47E-05	7.57E+03	1.72E+04	5.62E-05	2.30E+04
1.08E-30	1.82E+03	5.47E-05	8.17E+03	2.52E+04	5.62E-05	3.10E+04
1.87E-30	2.52E+03	5.47E-05	8.89E+03	3.47E+04	5.62E-05	4.05E+04
3.25E-30	3.29E+03	5.47E-05	9.71E+03	4.46E+04	5.62E-05	5.04E+04
5.63E-30	4.15E+03	5.47E-05	1.06E+04	5.48E+04	5.62E-05	6.07E+04
9.75E-30	5.12E+03	5.47E-05	1.16E+04	6.57E+04	5.62E-05	7.15E+04
1.69E-29	6.24E+03	5.47E-05	1.27E+04	7.75E+04	5.62E-05	8.33E+04
2.93E-29	7.54E+03	5.47E-05	1.40E+04	9.05E+04	5.62E-05	9.63E+04

5.08E-29	9.01E+03	5.47E-05	1.55E+04	1.04E+05	5.62E-05	1.10E+05
8.80E-29	1.08E+04	5.47E-05	1.73E+04	1.21E+05	5.62E-05	1.26E+05
1.53E-28	1.28E+04	5.47E-05	1.93E+04	1.38E+05	5.62E-05	1.44E+05
2.64E-28	1.53E+04	5.47E-05	2.18E+04	1.59E+05	5.62E-05	1.64E+05
4.58E-28	1.82E+04	5.47E-05	2.46E+04	1.82E+05	5.62E-05	1.87E+05
7.94E-28	2.17E+04	5.47E-05	2.82E+04	2.09E+05	5.62E-05	2.15E+05
1.38E-27	2.79E+04	5.47E-05	3.44E+04	2.56E+05	5.62E-05	2.62E+05
2.39E-27	3.28E+04	5.47E-05	3.93E+04	2.92E+05	5.62E-05	2.98E+05
4.14E-27	3.90E+04	5.47E-05	4.55E+04	3.36E+05	5.62E-05	3.41E+05
7.17E-27	4.61E+04	5.47E-05	5.26E+04	3.84E+05	5.62E-05	3.90E+05
1.24E-26	5.50E+04	5.47E-05	6.15E+04	4.42E+05	5.62E-05	4.48E+05
2.15E-26	6.59E+04	5.47E-05	7.24E+04	5.10E+05	5.62E-05	5.16E+05
3.73E-26	7.94E+04	5.47E-05	8.59E+04	5.89E+05	5.62E-05	5.95E+05
6.47E-26	9.56E+04	5.47E-05	1.02E+05	6.75E+05	5.62E-05	6.81E+05
1.12E-25	1.16E+05	5.47E-05	1.23E+05	7.76E+05	5.62E-05	7.81E+05
1.94E-25	1.42E+05	5.47E-05	1.49E+05	8.87E+05	5.62E-05	8.92E+05
3.37E-25	1.76E+05	5.47E-05	1.82E+05	1.01E+06	5.62E-05	1.02E+06
5.84E-25	2.19E+05	5.47E-05	2.26E+05	1.15E+06	5.62E-05	1.16E+06
1.01E-24	2.78E+05	5.47E-05	2.85E+05	1.31E+06	5.62E-05	1.31E+06
1.75E-24	3.94E+05	5.47E-05	4.00E+05	1.55E+06	5.62E-05	1.55E+06
3.04E-24	5.00E+05	5.47E-05	5.06E+05	1.72E+06	5.62E-05	1.73E+06
5.27E-24	6.36E+05	5.47E-05	6.43E+05	1.91E+06	5.62E-05	1.92E+06
9.13E-24	8.56E+05	5.47E-05	8.63E+05	2.11E+06	5.62E-05	2.11E+06
1.42E-23	-	-	-	2.21E+06	5.62E-05	2.22E+06
1.58E-23	-	-	-	2.32E+06	5.62E-05	2.32E+06
2.74E-23	-	-	-	2.52E+06	5.62E-05	2.53E+06
4.76E-23	-	-	-	2.75E+06	5.62E-05	2.75E+06
8.24E-23	-	-	-	2.96E+06	5.62E-05	2.96E+06
1.43E-22	-	-	-	3.18E+06	5.62E-05	3.19E+06
2.48E-22	-	-	-	3.41E+06	5.62E-05	3.42E+06
4.29E-22	-	-	-	3.64E+06	5.62E-05	3.65E+06
7.52E-22	-	-	-	3.87E+06	5.62E-05	3.88E+06
1.30E-21	-	-	-	4.09E+06	5.62E-05	4.10E+06
2.26E-21	-	-	-	4.33E+06	5.62E-05	4.33E+06
3.91E-21	-	-	-	4.58E+06	5.62E-05	4.58E+06
6.78E-21	-	-	-	4.81E+06	5.62E-05	4.82E+06
1.18E-20	-	-	-	5.05E+06	5.62E-05	5.06E+06
2.04E-20	-	-	-	5.29E+06	5.62E-05	5.30E+06
3.53E-20	-	-	-	5.53E+06	5.62E-05	5.54E+06
6.12E-20	-	-	-	5.77E+06	5.62E-05	5.78E+06
1.06E-19	-	-	-	6.02E+06	5.62E-05	6.02E+06
1.84E-19	-	-	-	6.26E+06	5.62E-05	6.26E+06
3.19E-19	-	-	-	6.51E+06	5.62E-05	6.51E+06

5.52E-19	-	-	-	6.85E+06	5.62E-05	6.85E+06
9.58E-19	-	-	-	7.09E+06	5.62E-05	7.10E+06
1.66E-18	-	-	-	7.34E+06	5.62E-05	7.35E+06
2.88E-18	-	-	-	7.59E+06	5.62E-05	7.59E+06
4.25E-18	-	-	-	7.71E+06	5.62E-05	7.71E+06

Table C.9. Thermo-Calc results for FCC phase composition and fractions at 480 °C and 1.5 MPa.

O2 Activity (atm)	FCC volume fraction	Number density (mol/cm3)	Fe mole fraction	Cr mole fraction	Ni mole fraction
1.69E-48	1.00E+00	1.45E-01	6.82E-01	1.97E-01	1.19E-01
1.69E-48	1.00E+00	1.45E-01	6.82E-01	1.97E-01	1.19E-01
4.59E-48	1.00E+00	1.45E-01	6.82E-01	1.97E-01	1.19E-01
3.39E-47	1.00E+00	1.45E-01	6.82E-01	1.97E-01	1.19E-01
9.22E-47	1.00E+00	1.45E-01	6.82E-01	1.97E-01	1.19E-01
2.51E-46	1.00E+00	1.45E-01	6.82E-01	1.97E-01	1.19E-01
6.81E-46	1.00E+00	1.45E-01	6.82E-01	1.97E-01	1.19E-01
1.85E-45	1.00E+00	1.45E-01	6.82E-01	1.97E-01	1.19E-01
5.04E-45	1.00E+00	1.45E-01	6.82E-01	1.97E-01	1.19E-01
5.04E-45	1.00E+00	1.45E-01	6.82E-01	1.97E-01	1.19E-01
5.04E-45	1.00E+00	1.45E-01	6.82E-01	1.97E-01	1.19E-01
5.04E-45	1.00E+00	1.45E-01	6.82E-01	1.97E-01	1.19E-01
1.37E-44	8.61E-01	1.43E-01	8.03E-01	5.73E-02	1.40E-01
1.37E-44	8.61E-01	1.43E-01	8.03E-01	5.73E-02	1.40E-01
1.37E-44	8.61E-01	1.43E-01	8.03E-01	5.73E-02	1.40E-01
1.37E-44	8.61E-01	1.43E-01	8.03E-01	5.73E-02	1.40E-01
1.37E-44	8.61E-01	1.43E-01	8.03E-01	5.73E-02	1.40E-01
1.37E-44	8.61E-01	1.43E-01	8.03E-01	5.73E-02	1.40E-01
3.72E-44	8.53E-01	1.43E-01	8.12E-01	4.82E-02	1.41E-01
3.72E-44	8.53E-01	1.43E-01	8.12E-01	4.82E-02	1.41E-01
1.01E-43	8.28E-01	1.42E-01	8.38E-01	1.76E-02	1.46E-01
3.04E-43	8.21E-01	1.42E-01	8.45E-01	7.74E-03	1.47E-01
9.13E-43	8.18E-01	1.42E-01	8.50E-01	3.44E-03	1.48E-01
2.48E-42	8.16E-01	1.42E-01	8.51E-01	1.54E-03	1.48E-01
7.45E-42	8.15E-01	1.42E-01	8.50E-01	6.90E-04	1.49E-01
2.24E-41	8.16E-01	1.42E-01	8.55E-01	3.12E-04	1.49E-01
6.73E-41	8.16E-01	1.42E-01	8.55E-01	1.37E-04	1.49E-01
2.02E-40	8.15E-01	1.42E-01	8.55E-01	6.24E-05	1.49E-01
5.49E-40	8.15E-01	1.42E-01	8.55E-01	2.91E-05	1.49E-01
1.65E-39	8.15E-01	1.42E-01	8.55E-01	1.25E-05	1.49E-01
4.96E-39	8.15E-01	1.42E-01	8.55E-01	5.72E-06	1.49E-01
1.49E-38	8.15E-01	1.42E-01	8.55E-01	2.57E-06	1.49E-01
4.47E-38	8.15E-01	1.42E-01	8.55E-01	1.15E-06	1.49E-01
5.46E-38	5.05E-01	1.42E-01	8.33E-01	1.01E-06	1.69E-01

5.46E-38	5.05E-01	1.42E-01	8.33E-01	1.01E-06	1.69E-01
6.67E-38	5.05E-01	1.42E-01	8.33E-01	8.10E-07	1.69E-01
8.15E-38	5.05E-01	1.42E-01	8.33E-01	6.52E-07	1.69E-01
9.96E-38	5.05E-01	1.42E-01	8.33E-01	5.26E-07	1.69E-01
1.22E-37	5.05E-01	1.42E-01	8.33E-01	4.24E-07	1.69E-01
1.49E-37	5.05E-01	1.42E-01	8.33E-01	3.41E-07	1.69E-01
2.01E-37	5.05E-01	1.42E-01	8.33E-01	2.75E-07	1.69E-01
2.45E-37	5.05E-01	1.42E-01	8.33E-01	2.22E-07	1.69E-01
2.99E-37	5.05E-01	1.42E-01	8.33E-01	1.78E-07	1.69E-01
3.65E-37	5.05E-01	1.42E-01	8.33E-01	1.44E-07	1.69E-01
4.46E-37	5.05E-01	1.42E-01	8.33E-01	1.16E-07	1.69E-01
5.45E-37	5.05E-01	1.42E-01	8.33E-01	9.35E-08	1.69E-01
7.36E-37	5.05E-01	1.42E-01	8.33E-01	7.52E-08	1.69E-01
8.99E-37	5.05E-01	1.42E-01	8.33E-01	6.06E-08	1.69E-01
1.10E-36	5.05E-01	1.42E-01	8.33E-01	4.88E-08	1.69E-01
1.34E-36	5.05E-01	1.42E-01	8.33E-01	3.93E-08	1.69E-01
1.64E-36	5.05E-01	1.42E-01	8.33E-01	3.17E-08	1.69E-01
2.00E-36	5.05E-01	1.42E-01	8.33E-01	2.56E-08	1.69E-01
2.70E-36	5.05E-01	1.42E-01	8.33E-01	2.06E-08	1.69E-01
3.30E-36	5.05E-01	1.42E-01	8.33E-01	1.66E-08	1.69E-01
4.03E-36	5.05E-01	1.42E-01	8.33E-01	1.34E-08	1.69E-01
4.92E-36	5.05E-01	1.42E-01	8.33E-01	1.08E-08	1.69E-01
6.01E-36	5.05E-01	1.42E-01	8.33E-01	8.67E-09	1.69E-01
7.34E-36	5.05E-01	1.42E-01	8.33E-01	6.99E-09	1.69E-01
9.91E-36	5.05E-01	1.42E-01	8.33E-01	5.63E-09	1.69E-01
1.21E-35	5.05E-01	1.42E-01	8.32E-01	4.53E-09	1.69E-01
1.48E-35	5.05E-01	1.42E-01	8.32E-01	3.66E-09	1.69E-01
1.81E-35	5.05E-01	1.42E-01	8.32E-01	2.94E-09	1.69E-01
1.81E-35	5.05E-01	1.42E-01	8.32E-01	2.94E-09	1.69E-01
5.42E-35	5.05E-01	1.42E-01	8.32E-01	9.99E-10	1.69E-01
1.63E-34	5.05E-01	1.42E-01	8.32E-01	3.39E-10	1.69E-01
4.43E-34	5.04E-01	1.42E-01	8.32E-01	1.15E-10	1.69E-01
1.33E-33	5.04E-01	1.43E-01	8.28E-01	3.89E-11	1.69E-01
4.00E-33	5.00E-01	1.42E-01	8.31E-01	1.31E-11	1.70E-01
1.20E-32	4.94E-01	1.42E-01	8.30E-01	4.37E-12	1.71E-01
3.61E-32	4.71E-01	1.41E-01	8.28E-01	1.40E-12	1.76E-01
4.41E-32	4.63E-01	1.42E-01	8.21E-01	1.11E-12	1.78E-01
4.41E-32	4.63E-01	1.42E-01	8.21E-01	1.11E-12	1.78E-01
5.38E-32	4.51E-01	1.42E-01	8.19E-01	8.68E-13	1.80E-01
6.57E-32	4.34E-01	1.42E-01	8.15E-01	6.76E-13	1.85E-01
8.03E-32	4.10E-01	1.42E-01	8.09E-01	5.21E-13	1.92E-01
8.03E-32	4.10E-01	1.42E-01	8.09E-01	5.21E-13	1.92E-01
8.03E-32	4.10E-01	1.42E-01	8.09E-01	5.21E-13	1.92E-01

8.03E-32	4.10E-01	1.42E-01	8.09E-01	5.21E-13	1.92E-01
8.03E-32	4.10E-01	1.42E-01	8.09E-01	5.21E-13	1.92E-01
9.80E-32	2.48E-01	1.40E-01	5.81E-01	3.91E-13	4.19E-01
1.32E-31	2.21E-01	1.40E-01	5.14E-01	2.24E-13	4.86E-01
1.62E-31	2.00E-01	1.40E-01	4.56E-01	7.73E-14	5.43E-01
1.97E-31	1.89E-01	1.39E-01	4.27E-01	4.81E-14	5.75E-01
2.41E-31	1.82E-01	1.39E-01	4.03E-01	3.56E-14	5.98E-01
2.95E-31	1.75E-01	1.39E-01	3.83E-01	2.86E-14	6.18E-01
3.60E-31	1.69E-01	1.39E-01	3.64E-01	2.41E-14	6.34E-01
4.86E-31	1.64E-01	1.39E-01	3.48E-01	2.11E-14	6.52E-01
5.93E-31	1.60E-01	1.39E-01	3.32E-01	1.89E-14	6.68E-01
7.24E-31	1.56E-01	1.38E-01	3.18E-01	1.73E-14	6.82E-01
8.85E-31	1.51E-01	1.39E-01	3.03E-01	1.62E-14	6.95E-01
1.08E-30	1.48E-01	1.38E-01	2.91E-01	1.54E-14	7.10E-01
1.32E-30	1.44E-01	1.38E-01	2.78E-01	1.48E-14	7.22E-01
1.61E-30	1.40E-01	1.38E-01	2.65E-01	1.44E-14	7.35E-01
2.18E-30	1.37E-01	1.38E-01	2.54E-01	1.43E-14	7.46E-01
2.66E-30	1.34E-01	1.38E-01	2.42E-01	1.42E-14	7.59E-01
3.25E-30	1.31E-01	1.38E-01	2.30E-01	1.44E-14	7.69E-01
3.97E-30	1.28E-01	1.38E-01	2.18E-01	1.47E-14	7.80E-01
4.84E-30	1.25E-01	1.38E-01	2.07E-01	1.51E-14	7.92E-01
5.92E-30	1.22E-01	1.38E-01	1.96E-01	1.58E-14	8.05E-01
7.99E-30	1.19E-01	1.38E-01	1.85E-01	1.66E-14	8.15E-01
9.75E-30	1.16E-01	1.37E-01	1.74E-01	1.76E-14	8.26E-01
1.19E-29	1.13E-01	1.38E-01	1.64E-01	1.88E-14	8.35E-01
1.46E-29	1.10E-01	1.37E-01	1.53E-01	2.03E-14	8.47E-01
1.78E-29	1.07E-01	1.37E-01	1.43E-01	2.20E-14	8.57E-01
2.17E-29	1.03E-01	1.37E-01	1.33E-01	2.41E-14	8.67E-01
2.93E-29	1.00E-01	1.37E-01	1.23E-01	2.64E-14	8.78E-01
3.58E-29	9.68E-02	1.37E-01	1.13E-01	2.92E-14	8.87E-01
4.37E-29	9.38E-02	1.37E-01	1.04E-01	3.24E-14	8.96E-01
5.34E-29	9.01E-02	1.37E-01	9.43E-02	3.58E-14	9.05E-01
6.52E-29	8.63E-02	1.37E-01	8.56E-02	4.01E-14	9.16E-01
7.96E-29	8.25E-02	1.36E-01	7.71E-02	4.50E-14	9.26E-01
1.08E-28	7.85E-02	1.36E-01	6.90E-02	4.88E-14	9.34E-01
1.31E-28	7.45E-02	1.37E-01	6.25E-02	4.82E-14	9.39E-01
1.60E-28	7.01E-02	1.37E-01	5.63E-02	4.63E-14	9.44E-01
1.96E-28	6.52E-02	1.37E-01	5.07E-02	4.45E-14	9.49E-01
2.39E-28	6.05E-02	1.37E-01	4.54E-02	4.20E-14	9.55E-01
2.92E-28	5.49E-02	1.36E-01	4.06E-02	3.92E-14	9.61E-01
3.57E-28	4.91E-02	1.37E-01	3.62E-02	3.62E-14	9.63E-01
4.82E-28	4.28E-02	1.37E-01	3.21E-02	3.33E-14	9.65E-01
5.89E-28	3.57E-02	1.36E-01	2.86E-02	3.03E-14	9.75E-01

7.19E-28	2.81E-02	1.37E-01	2.51E-02	2.73E-14	9.74E-01
8.78E-28	2.00E-02	1.37E-01	2.20E-02	2.46E-14	9.78E-01
1.07E-27	1.13E-02	1.37E-01	1.92E-02	2.18E-14	9.79E-01
1.31E-27	2.15E-03	1.36E-01	1.63E-02	1.94E-14	9.84E-01

Table C.10. Thermo-Calc results for Corundum phase composition and fractions at 480 °C and 1.5 MPa.

O2 Activity (atm)	Corundum volume fraction	Number density (mol/cm3)	Fe mole fraction	Cr mole fraction	Ni mole fraction	O mole fraction
1.37E-44	1.39E-01	6.95E-02	1.32E-11	4.05E-01	1.36E-11	5.95E-01
1.37E-44	1.39E-01	6.95E-02	1.32E-11	4.05E-01	1.36E-11	5.95E-01
1.37E-44	1.39E-01	6.95E-02	1.32E-11	4.05E-01	1.36E-11	5.95E-01
1.37E-44	1.39E-01	6.95E-02	1.32E-11	4.05E-01	1.36E-11	5.95E-01
1.37E-44	1.39E-01	6.95E-02	1.32E-11	4.05E-01	1.36E-11	5.95E-01
1.37E-44	1.39E-01	6.95E-02	1.32E-11	4.05E-01	1.36E-11	5.95E-01
3.72E-44	1.47E-01	6.93E-02	1.56E-11	4.05E-01	1.54E-11	5.96E-01
3.72E-44	1.47E-01	6.93E-02	1.56E-11	4.05E-01	1.54E-11	5.96E-01
1.01E-43	1.72E-01	6.96E-02	4.20E-11	4.04E-01	3.16E-11	5.93E-01
3.04E-43	1.79E-01	6.96E-02	9.51E-11	4.04E-01	5.60E-11	5.94E-01
9.13E-43	1.82E-01	6.92E-02	2.17E-10	4.06E-01	9.86E-11	5.97E-01
2.48E-42	1.84E-01	6.97E-02	4.88E-10	4.03E-01	1.70E-10	5.94E-01
7.45E-42	1.85E-01	6.94E-02	1.12E-09	4.04E-01	2.95E-10	5.97E-01
2.24E-41	1.84E-01	6.93E-02	2.56E-09	4.05E-01	5.11E-10	5.98E-01
6.73E-41	1.84E-01	6.98E-02	5.81E-09	4.02E-01	8.78E-10	5.95E-01
2.02E-40	1.85E-01	6.97E-02	1.33E-08	4.03E-01	1.50E-09	5.95E-01
5.49E-40	1.85E-01	6.96E-02	3.07E-08	4.03E-01	2.59E-09	5.96E-01
1.65E-39	1.85E-01	6.96E-02	7.08E-08	4.03E-01	4.43E-09	5.97E-01
4.96E-39	1.85E-01	6.96E-02	1.63E-07	4.03E-01	7.55E-09	5.97E-01
1.49E-38	1.85E-01	6.96E-02	3.78E-07	4.03E-01	1.29E-08	5.97E-01
4.47E-38	1.85E-01	6.96E-02	8.71E-07	4.03E-01	2.20E-08	5.98E-01
1.56E-17	3.07E-02	6.72E-02	3.29E-01	7.01E-02	2.00E-16	5.99E-01
4.24E-17	8.58E-02	6.70E-02	3.23E-01	7.67E-02	2.00E-16	6.00E-01
1.27E-16	1.31E-01	6.70E-02	3.18E-01	8.18E-02	2.00E-16	6.01E-01
3.82E-16	1.60E-01	6.69E-02	3.16E-01	8.53E-02	2.09E-16	6.01E-01
1.40E-15	1.82E-01	6.72E-02	3.12E-01	8.75E-02	2.52E-16	6.00E-01
1.71E-15	1.84E-01	6.73E-02	3.11E-01	8.80E-02	2.55E-16	5.99E-01
2.09E-15	1.87E-01	6.73E-02	3.11E-01	8.82E-02	2.57E-16	6.00E-01
2.56E-15	1.91E-01	6.70E-02	3.13E-01	8.87E-02	2.61E-16	6.00E-01
3.45E-15	1.93E-01	6.70E-02	3.12E-01	8.87E-02	2.63E-16	6.00E-01
4.22E-15	1.94E-01	6.71E-02	3.11E-01	8.89E-02	2.62E-16	5.99E-01
5.15E-15	1.96E-01	6.71E-02	3.11E-01	8.92E-02	2.62E-16	6.00E-01
6.29E-15	1.98E-01	6.71E-02	3.11E-01	8.94E-02	2.64E-16	6.00E-01
7.68E-15	1.99E-01	6.72E-02	3.10E-01	8.94E-02	2.61E-16	6.01E-01

9.38E-15	2.00E-01	6.73E-02	3.09E-01	8.96E-02	2.61E-16	6.00E-01
1.27E-14	2.05E-01	6.70E-02	3.11E-01	8.98E-02	2.59E-16	6.00E-01
1.55E-14	2.05E-01	6.70E-02	3.11E-01	8.99E-02	2.58E-16	6.00E-01
1.89E-14	2.06E-01	6.70E-02	3.11E-01	9.01E-02	2.56E-16	6.00E-01
2.31E-14	2.08E-01	6.71E-02	3.10E-01	9.01E-02	2.51E-16	5.99E-01
2.82E-14	2.09E-01	6.71E-02	3.10E-01	9.03E-02	2.49E-16	5.99E-01
3.44E-14	2.10E-01	6.72E-02	3.10E-01	9.01E-02	2.46E-16	6.00E-01
4.21E-14	2.10E-01	6.72E-02	3.10E-01	9.03E-02	2.42E-16	6.00E-01
5.68E-14	2.11E-01	6.71E-02	3.10E-01	9.05E-02	2.40E-16	6.00E-01
6.93E-14	2.13E-01	6.72E-02	3.09E-01	9.06E-02	2.35E-16	5.99E-01
8.47E-14	2.13E-01	6.72E-02	3.09E-01	9.06E-02	2.33E-16	6.01E-01
1.03E-13	2.14E-01	6.72E-02	3.09E-01	9.08E-02	2.29E-16	6.01E-01
1.26E-13	2.14E-01	6.73E-02	3.08E-01	9.08E-02	2.24E-16	6.00E-01
1.54E-13	2.14E-01	6.73E-02	3.08E-01	9.08E-02	2.20E-16	6.00E-01
2.08E-13	2.15E-01	6.72E-02	3.08E-01	9.10E-02	2.16E-16	6.00E-01
2.54E-13	2.19E-01	6.70E-02	3.10E-01	9.10E-02	2.14E-16	6.00E-01
3.11E-13	2.20E-01	6.71E-02	3.10E-01	9.08E-02	2.08E-16	6.00E-01
3.80E-13	2.20E-01	6.70E-02	3.10E-01	9.10E-02	2.04E-16	6.00E-01
4.64E-13	2.20E-01	6.70E-02	3.10E-01	9.10E-02	2.00E-16	6.00E-01
5.66E-13	2.21E-01	6.70E-02	3.10E-01	9.12E-02	2.00E-16	6.00E-01
7.64E-13	2.21E-01	6.70E-02	3.10E-01	9.12E-02	2.00E-16	6.00E-01
9.33E-13	2.21E-01	6.70E-02	3.10E-01	9.12E-02	2.00E-16	6.00E-01
1.14E-12	2.21E-01	6.71E-02	3.09E-01	9.12E-02	2.00E-16	5.99E-01
1.39E-12	2.21E-01	6.71E-02	3.09E-01	9.12E-02	2.00E-16	5.99E-01
1.70E-12	2.22E-01	6.71E-02	3.09E-01	9.12E-02	2.00E-16	5.99E-01
2.08E-12	2.22E-01	6.71E-02	3.09E-01	9.14E-02	2.00E-16	5.99E-01
2.80E-12	2.24E-01	6.70E-02	3.09E-01	9.14E-02	2.00E-16	6.01E-01
3.43E-12	2.24E-01	6.70E-02	3.09E-01	9.14E-02	2.00E-16	6.01E-01
4.18E-12	2.24E-01	6.70E-02	3.09E-01	9.14E-02	2.00E-16	6.01E-01
5.11E-12	2.24E-01	6.72E-02	3.08E-01	9.13E-02	2.00E-16	6.00E-01
6.24E-12	2.24E-01	6.72E-02	3.08E-01	9.15E-02	2.00E-16	6.00E-01
7.62E-12	2.24E-01	6.72E-02	3.08E-01	9.15E-02	2.00E-16	6.00E-01
9.31E-12	2.25E-01	6.72E-02	3.08E-01	9.15E-02	2.00E-16	6.00E-01
1.26E-11	2.25E-01	6.72E-02	3.08E-01	9.15E-02	2.00E-16	6.00E-01
1.54E-11	2.25E-01	6.72E-02	3.08E-01	9.15E-02	2.00E-16	6.00E-01
1.88E-11	2.25E-01	6.71E-02	3.08E-01	9.17E-02	2.00E-16	6.00E-01
2.29E-11	2.25E-01	6.71E-02	3.08E-01	9.17E-02	2.00E-16	6.00E-01
2.80E-11	2.25E-01	6.71E-02	3.08E-01	9.17E-02	2.00E-16	6.00E-01
3.42E-11	2.25E-01	6.71E-02	3.08E-01	9.17E-02	2.00E-16	6.00E-01
4.61E-11	2.25E-01	6.71E-02	3.08E-01	9.17E-02	2.00E-16	6.00E-01
5.63E-11	2.25E-01	6.71E-02	3.08E-01	9.17E-02	2.00E-16	6.00E-01
6.88E-11	2.25E-01	6.73E-02	3.08E-01	9.15E-02	2.00E-16	5.99E-01
8.40E-11	2.26E-01	6.73E-02	3.08E-01	9.15E-02	2.00E-16	5.99E-01

1.03E-10	2.26E-01	6.73E-02	3.08E-01	9.15E-02	2.00E-16	5.99E-01
1.25E-10	2.26E-01	6.73E-02	3.08E-01	9.17E-02	2.00E-16	5.99E-01
1.69E-10	2.26E-01	6.73E-02	3.08E-01	9.17E-02	2.00E-16	5.99E-01
2.07E-10	2.26E-01	6.73E-02	3.08E-01	9.17E-02	2.00E-16	5.99E-01
2.52E-10	2.26E-01	6.73E-02	3.08E-01	9.17E-02	2.00E-16	5.99E-01
3.08E-10	2.26E-01	6.73E-02	3.08E-01	9.17E-02	2.00E-16	5.99E-01
3.77E-10	2.26E-01	6.72E-02	3.08E-01	9.17E-02	2.00E-16	6.01E-01
6.21E-10	2.26E-01	6.72E-02	3.08E-01	9.17E-02	2.00E-16	6.01E-01
7.58E-10	2.26E-01	6.72E-02	3.08E-01	9.17E-02	2.00E-16	6.01E-01
9.26E-10	2.26E-01	6.72E-02	3.08E-01	9.17E-02	2.00E-16	6.01E-01
1.13E-09	2.28E-01	6.72E-02	3.08E-01	9.17E-02	2.00E-16	6.01E-01
1.38E-09	2.28E-01	6.72E-02	3.08E-01	9.17E-02	2.00E-16	6.01E-01
1.69E-09	2.28E-01	6.72E-02	3.08E-01	9.17E-02	2.00E-16	6.01E-01
2.06E-09	2.28E-01	6.72E-02	3.08E-01	9.17E-02	2.00E-16	6.01E-01
2.78E-09	2.28E-01	6.72E-02	3.08E-01	9.17E-02	2.00E-16	6.01E-01
3.40E-09	2.28E-01	6.72E-02	3.08E-01	9.17E-02	2.00E-16	6.01E-01
4.15E-09	2.28E-01	6.72E-02	3.08E-01	9.17E-02	2.00E-16	6.01E-01
5.07E-09	2.28E-01	6.72E-02	3.08E-01	9.19E-02	2.00E-16	6.01E-01
6.19E-09	2.28E-01	6.72E-02	3.08E-01	9.19E-02	2.00E-16	6.01E-01
7.56E-09	2.28E-01	6.72E-02	3.08E-01	9.19E-02	2.00E-16	6.01E-01
1.02E-08	2.28E-01	6.72E-02	3.08E-01	9.19E-02	2.00E-16	6.01E-01
1.25E-08	2.28E-01	6.72E-02	3.08E-01	9.19E-02	2.00E-16	6.01E-01
1.52E-08	2.28E-01	6.72E-02	3.08E-01	9.19E-02	2.00E-16	6.01E-01
1.86E-08	2.28E-01	6.72E-02	3.08E-01	9.19E-02	2.00E-16	6.01E-01
2.27E-08	2.28E-01	6.72E-02	3.08E-01	9.19E-02	2.00E-16	6.01E-01
2.78E-08	2.28E-01	6.72E-02	3.08E-01	9.19E-02	2.00E-16	6.01E-01
3.75E-08	2.28E-01	6.72E-02	3.08E-01	9.19E-02	2.00E-16	6.01E-01
4.58E-08	2.28E-01	6.72E-02	3.08E-01	9.19E-02	2.00E-16	6.01E-01
5.59E-08	2.28E-01	6.72E-02	3.08E-01	9.19E-02	2.00E-16	6.01E-01
6.83E-08	2.28E-01	6.72E-02	3.08E-01	9.19E-02	2.00E-16	6.01E-01
8.34E-08	2.28E-01	6.72E-02	3.08E-01	9.19E-02	2.00E-16	6.01E-01
1.02E-07	2.28E-01	6.72E-02	3.08E-01	9.19E-02	2.00E-16	6.01E-01
1.38E-07	2.28E-01	6.72E-02	3.08E-01	9.19E-02	2.00E-16	6.01E-01
1.68E-07	2.28E-01	6.72E-02	3.08E-01	9.19E-02	2.00E-16	6.01E-01
2.05E-07	2.28E-01	6.72E-02	3.08E-01	9.19E-02	2.00E-16	6.01E-01
2.51E-07	2.28E-01	6.72E-02	3.08E-01	9.19E-02	2.00E-16	6.01E-01
3.06E-07	2.28E-01	6.72E-02	3.08E-01	9.19E-02	2.00E-16	6.01E-01
3.74E-07	2.28E-01	6.72E-02	3.08E-01	9.19E-02	2.00E-16	6.01E-01
4.56E-07	2.28E-01	6.72E-02	3.08E-01	9.19E-02	2.00E-16	6.01E-01
6.16E-07	2.28E-01	6.72E-02	3.08E-01	9.19E-02	2.00E-16	6.01E-01
7.52E-07	2.28E-01	6.72E-02	3.08E-01	9.19E-02	2.00E-16	6.01E-01
9.19E-07	2.28E-01	6.72E-02	3.08E-01	9.19E-02	2.00E-16	6.01E-01
1.12E-06	2.28E-01	6.72E-02	3.08E-01	9.19E-02	2.00E-16	6.01E-01

1.37E-06	2.28E-01	6.72E-02	3.08E-01	9.19E-02	2.00E-16	6.01E-01
1.67E-06	2.28E-01	6.72E-02	3.08E-01	9.19E-02	2.00E-16	6.01E-01
2.26E-06	2.28E-01	6.72E-02	3.08E-01	9.19E-02	2.00E-16	6.01E-01
2.76E-06	2.28E-01	6.72E-02	3.08E-01	9.19E-02	2.00E-16	6.01E-01
3.37E-06	2.28E-01	6.72E-02	3.08E-01	9.19E-02	2.00E-16	6.01E-01
4.12E-06	2.28E-01	6.72E-02	3.08E-01	9.19E-02	2.00E-16	6.01E-01
5.03E-06	2.28E-01	6.72E-02	3.08E-01	9.19E-02	2.00E-16	6.01E-01
6.14E-06	2.28E-01	6.72E-02	3.08E-01	9.19E-02	2.00E-16	6.01E-01
8.29E-06	2.28E-01	6.72E-02	3.08E-01	9.19E-02	2.00E-16	6.01E-01
1.01E-05	2.28E-01	6.72E-02	3.08E-01	9.19E-02	2.00E-16	6.01E-01
1.24E-05	2.28E-01	6.72E-02	3.08E-01	9.19E-02	2.00E-16	6.01E-01
1.51E-05	2.28E-01	6.72E-02	3.08E-01	9.19E-02	2.00E-16	6.01E-01
1.85E-05	2.28E-01	6.72E-02	3.08E-01	9.19E-02	2.00E-16	6.01E-01
2.25E-05	2.28E-01	6.72E-02	3.08E-01	9.19E-02	2.00E-16	6.01E-01
3.04E-05	2.28E-01	6.72E-02	3.08E-01	9.19E-02	2.00E-16	6.01E-01
3.72E-05	2.28E-01	6.72E-02	3.08E-01	9.19E-02	2.00E-16	6.01E-01
4.54E-05	2.28E-01	6.72E-02	3.08E-01	9.19E-02	2.00E-16	6.01E-01
5.55E-05	2.28E-01	6.72E-02	3.08E-01	9.19E-02	2.00E-16	6.01E-01
6.91E-05	2.28E-01	6.72E-02	3.08E-01	9.19E-02	2.00E-16	6.01E-01
8.52E-05	2.28E-01	6.72E-02	3.08E-01	9.19E-02	2.00E-16	6.01E-01
1.06E-04	2.28E-01	6.72E-02	3.08E-01	9.19E-02	2.00E-16	6.01E-01
1.31E-04	2.28E-01	6.72E-02	3.08E-01	9.19E-02	2.00E-16	6.01E-01
1.63E-04	2.28E-01	6.72E-02	3.08E-01	9.19E-02	2.00E-16	6.01E-01
2.04E-04	2.28E-01	6.72E-02	3.08E-01	9.19E-02	2.00E-16	6.01E-01
2.51E-04	2.28E-01	6.73E-02	3.07E-01	9.17E-02	2.00E-16	6.00E-01
3.13E-04	2.28E-01	6.73E-02	3.07E-01	9.17E-02	2.00E-16	6.00E-01
3.86E-04	2.28E-01	6.73E-02	3.07E-01	9.17E-02	2.00E-16	6.00E-01
4.81E-04	2.28E-01	6.73E-02	3.07E-01	9.17E-02	2.00E-16	6.00E-01
5.99E-04	2.28E-01	6.73E-02	3.07E-01	9.17E-02	2.00E-16	6.00E-01
7.39E-04	2.28E-01	6.73E-02	3.07E-01	9.17E-02	2.00E-16	6.00E-01
9.21E-04	2.28E-01	6.73E-02	3.07E-01	9.17E-02	2.00E-16	6.00E-01
1.14E-03	2.28E-01	6.73E-02	3.07E-01	9.17E-02	2.00E-16	6.00E-01
1.42E-03	2.28E-01	6.73E-02	3.07E-01	9.17E-02	2.00E-16	6.00E-01
1.76E-03	2.28E-01	6.73E-02	3.07E-01	9.17E-02	2.00E-16	6.00E-01
2.18E-03	2.28E-01	6.73E-02	3.07E-01	9.17E-02	2.00E-16	6.00E-01
2.71E-03	2.28E-01	6.73E-02	3.07E-01	9.17E-02	2.00E-16	6.00E-01
3.35E-03	2.28E-01	6.73E-02	3.07E-01	9.17E-02	2.00E-16	6.00E-01
4.17E-03	2.28E-01	6.73E-02	3.07E-01	9.17E-02	2.00E-16	6.00E-01
5.20E-03	2.28E-01	6.73E-02	3.07E-01	9.17E-02	2.00E-16	6.00E-01
6.41E-03	2.28E-01	6.73E-02	3.07E-01	9.17E-02	2.00E-16	6.00E-01
7.99E-03	2.28E-01	6.73E-02	3.07E-01	9.17E-02	2.00E-16	6.00E-01
9.85E-03	2.28E-01	6.73E-02	3.07E-01	9.17E-02	2.00E-16	6.00E-01
1.23E-02	2.28E-01	6.73E-02	3.07E-01	9.17E-02	2.00E-16	6.00E-01

1.53E-02	2.28E-01	6.73E-02	3.07E-01	9.17E-02	2.00E-16	6.00E-01
1.89E-02	2.28E-01	6.73E-02	3.07E-01	9.17E-02	2.00E-16	6.00E-01
2.35E-02	2.28E-01	6.73E-02	3.07E-01	9.17E-02	2.00E-16	6.00E-01
2.90E-02	2.28E-01	6.73E-02	3.07E-01	9.17E-02	2.00E-16	6.00E-01
3.62E-02	2.28E-01	6.73E-02	3.07E-01	9.17E-02	2.00E-16	6.00E-01
4.51E-02	2.28E-01	6.73E-02	3.07E-01	9.17E-02	2.00E-16	6.00E-01
5.56E-02	2.28E-01	6.73E-02	3.07E-01	9.17E-02	2.00E-16	6.00E-01
6.93E-02	2.28E-01	6.73E-02	3.07E-01	9.17E-02	2.00E-16	6.00E-01
8.54E-02	2.28E-01	6.73E-02	3.07E-01	9.17E-02	2.00E-16	6.00E-01
1.07E-01	2.28E-01	6.73E-02	3.07E-01	9.17E-02	2.00E-16	6.00E-01
1.33E-01	2.28E-01	6.73E-02	3.07E-01	9.17E-02	2.00E-16	6.00E-01
1.35E-01	2.28E-01	6.73E-02	3.07E-01	9.17E-02	2.00E-16	6.00E-01

Table C.11. Thermo-Calc results for Cr-rich spinel phase composition and fractions at 480 °C and 1.5 MPa.

O2 Activity (atm)	Cr-rich spinel volume fraction	Number density (mol/cm3)	Fe mole fraction	Cr mole fraction	Ni mole fraction	O mole fraction
5.46E-38	4.95E-01	6.97E-02	1.43E-01	2.86E-01	1.44E-06	5.70E-01
5.46E-38	4.95E-01	6.97E-02	1.43E-01	2.86E-01	1.44E-06	5.70E-01
6.67E-38	4.95E-01	6.97E-02	1.43E-01	2.86E-01	1.55E-06	5.70E-01
8.15E-38	4.95E-01	6.97E-02	1.43E-01	2.86E-01	1.68E-06	5.70E-01
9.96E-38	4.95E-01	6.97E-02	1.43E-01	2.86E-01	1.82E-06	5.70E-01
1.22E-37	4.95E-01	6.97E-02	1.43E-01	2.86E-01	1.98E-06	5.70E-01
1.49E-37	4.95E-01	6.97E-02	1.43E-01	2.86E-01	2.16E-06	5.70E-01
2.01E-37	4.95E-01	6.97E-02	1.43E-01	2.86E-01	2.35E-06	5.70E-01
2.45E-37	4.95E-01	6.97E-02	1.43E-01	2.86E-01	2.57E-06	5.70E-01
2.99E-37	4.95E-01	6.97E-02	1.43E-01	2.86E-01	2.81E-06	5.70E-01
3.65E-37	4.95E-01	6.97E-02	1.43E-01	2.86E-01	3.08E-06	5.70E-01
4.46E-37	4.95E-01	6.97E-02	1.43E-01	2.86E-01	3.37E-06	5.70E-01
5.45E-37	4.95E-01	6.97E-02	1.43E-01	2.86E-01	3.71E-06	5.70E-01
7.36E-37	4.95E-01	6.97E-02	1.43E-01	2.86E-01	4.08E-06	5.70E-01
8.99E-37	4.95E-01	6.97E-02	1.43E-01	2.86E-01	4.49E-06	5.70E-01
1.10E-36	4.95E-01	6.97E-02	1.43E-01	2.86E-01	4.83E-06	5.70E-01
1.34E-36	4.95E-01	6.97E-02	1.43E-01	2.86E-01	4.83E-06	5.70E-01
1.64E-36	4.95E-01	6.97E-02	1.43E-01	2.86E-01	4.83E-06	5.70E-01
2.00E-36	4.95E-01	6.97E-02	1.43E-01	2.86E-01	4.83E-06	5.70E-01
2.70E-36	4.95E-01	6.97E-02	1.43E-01	2.86E-01	9.66E-06	5.70E-01
3.30E-36	4.95E-01	6.97E-02	1.43E-01	2.86E-01	9.66E-06	5.70E-01
4.03E-36	4.95E-01	6.97E-02	1.43E-01	2.86E-01	9.66E-06	5.70E-01
4.92E-36	4.95E-01	6.97E-02	1.43E-01	2.86E-01	9.66E-06	5.70E-01
6.01E-36	4.95E-01	6.97E-02	1.43E-01	2.86E-01	9.66E-06	5.70E-01
7.34E-36	4.95E-01	6.97E-02	1.43E-01	2.86E-01	1.45E-05	5.70E-01
9.91E-36	4.95E-01	6.97E-02	1.43E-01	2.86E-01	1.45E-05	5.70E-01

1.21E-35	4.95E-01	6.97E-02	1.43E-01	2.86E-01	1.45E-05	5.70E-01
1.48E-35	4.95E-01	6.97E-02	1.43E-01	2.86E-01	1.45E-05	5.70E-01
1.81E-35	4.95E-01	6.97E-02	1.43E-01	2.86E-01	1.93E-05	5.70E-01
1.81E-35	4.95E-01	6.97E-02	1.43E-01	2.86E-01	1.93E-05	5.70E-01
5.42E-35	4.95E-01	6.97E-02	1.43E-01	2.86E-01	3.38E-05	5.70E-01
1.63E-34	4.95E-01	6.97E-02	1.44E-01	2.86E-01	5.31E-05	5.70E-01
4.43E-34	4.96E-01	6.98E-02	1.43E-01	2.85E-01	9.14E-05	5.72E-01
1.33E-33	4.96E-01	6.97E-02	1.44E-01	2.85E-01	1.54E-04	5.72E-01
4.00E-33	5.00E-01	6.98E-02	1.46E-01	2.82E-01	2.57E-04	5.71E-01
1.20E-32	5.07E-01	6.97E-02	1.51E-01	2.77E-01	4.07E-04	5.70E-01
3.61E-32	5.29E-01	6.95E-02	1.67E-01	2.61E-01	5.51E-04	5.73E-01
4.41E-32	5.37E-01	6.96E-02	1.73E-01	2.54E-01	5.58E-04	5.71E-01
4.41E-32	5.37E-01	6.96E-02	1.73E-01	2.54E-01	5.58E-04	5.71E-01
5.38E-32	5.49E-01	6.94E-02	1.81E-01	2.47E-01	5.54E-04	5.71E-01
6.57E-32	5.66E-01	6.94E-02	1.92E-01	2.36E-01	5.22E-04	5.70E-01
8.03E-32	5.90E-01	6.93E-02	2.06E-01	2.22E-01	4.61E-04	5.69E-01
8.03E-32	5.90E-01	6.93E-02	2.06E-01	2.22E-01	4.61E-04	5.69E-01
8.03E-32	5.90E-01	6.93E-02	2.06E-01	2.22E-01	4.61E-04	5.69E-01
8.03E-32	5.90E-01	6.93E-02	2.06E-01	2.22E-01	4.61E-04	5.69E-01
8.03E-32	5.90E-01	6.93E-02	2.06E-01	2.22E-01	4.61E-04	5.69E-01
9.80E-32	7.52E-01	6.93E-02	2.06E-01	2.22E-01	6.67E-04	5.70E-01
1.32E-31	7.79E-01	6.92E-02	2.05E-01	2.22E-01	8.99E-04	5.72E-01
1.62E-31	7.87E-01	6.92E-02	2.06E-01	2.22E-01	1.16E-03	5.70E-01
1.97E-31	7.87E-01	6.93E-02	2.05E-01	2.22E-01	1.45E-03	5.70E-01
2.41E-31	7.84E-01	6.91E-02	2.05E-01	2.22E-01	1.80E-03	5.73E-01
2.95E-31	7.84E-01	6.91E-02	2.04E-01	2.22E-01	2.20E-03	5.73E-01
3.60E-31	7.83E-01	6.92E-02	2.04E-01	2.22E-01	2.64E-03	5.73E-01
4.86E-31	7.81E-01	6.92E-02	2.03E-01	2.22E-01	3.14E-03	5.73E-01
5.93E-31	7.82E-01	6.92E-02	2.02E-01	2.22E-01	3.69E-03	5.73E-01
7.24E-31	7.82E-01	6.92E-02	2.02E-01	2.22E-01	4.28E-03	5.73E-01
8.85E-31	7.80E-01	6.92E-02	2.01E-01	2.22E-01	4.94E-03	5.73E-01
1.08E-30	7.81E-01	6.91E-02	2.01E-01	2.22E-01	5.61E-03	5.73E-01
1.32E-30	7.81E-01	6.91E-02	2.01E-01	2.22E-01	6.35E-03	5.73E-01
1.61E-30	7.82E-01	6.92E-02	2.00E-01	2.21E-01	7.11E-03	5.70E-01
2.18E-30	7.82E-01	6.91E-02	2.00E-01	2.21E-01	7.93E-03	5.70E-01
2.66E-30	7.86E-01	6.92E-02	1.99E-01	2.20E-01	8.76E-03	5.72E-01
3.25E-30	7.87E-01	6.93E-02	1.99E-01	2.19E-01	9.61E-03	5.70E-01
3.97E-30	7.88E-01	6.90E-02	1.99E-01	2.19E-01	1.05E-02	5.74E-01
4.84E-30	7.92E-01	6.90E-02	1.99E-01	2.19E-01	1.15E-02	5.71E-01
5.92E-30	7.97E-01	6.92E-02	1.99E-01	2.17E-01	1.24E-02	5.71E-01
7.99E-30	7.99E-01	6.91E-02	1.99E-01	2.16E-01	1.34E-02	5.73E-01
9.75E-30	8.03E-01	6.91E-02	1.99E-01	2.15E-01	1.45E-02	5.70E-01
1.19E-29	8.08E-01	6.91E-02	1.99E-01	2.14E-01	1.55E-02	5.70E-01

1.46E-29	8.11E-01	6.90E-02	1.99E-01	2.13E-01	1.66E-02	5.71E-01
1.78E-29	8.16E-01	6.90E-02	1.99E-01	2.12E-01	1.77E-02	5.71E-01
2.17E-29	8.22E-01	6.90E-02	2.00E-01	2.10E-01	1.89E-02	5.70E-01
2.93E-29	8.27E-01	6.91E-02	2.00E-01	2.09E-01	2.01E-02	5.70E-01
3.58E-29	8.34E-01	6.89E-02	2.00E-01	2.07E-01	2.14E-02	5.73E-01
4.37E-29	8.43E-01	6.88E-02	2.01E-01	2.05E-01	2.27E-02	5.73E-01
5.34E-29	8.49E-01	6.90E-02	2.01E-01	2.03E-01	2.40E-02	5.70E-01
6.52E-29	8.57E-01	6.89E-02	2.01E-01	2.01E-01	2.54E-02	5.71E-01
7.96E-29	8.64E-01	6.87E-02	2.03E-01	2.00E-01	2.69E-02	5.74E-01
1.08E-28	8.73E-01	6.88E-02	2.03E-01	1.98E-01	2.84E-02	5.71E-01
1.31E-28	8.84E-01	6.89E-02	2.03E-01	1.95E-01	2.99E-02	5.70E-01
1.60E-28	8.92E-01	6.88E-02	2.04E-01	1.93E-01	3.15E-02	5.71E-01
1.96E-28	9.04E-01	6.88E-02	2.05E-01	1.90E-01	3.32E-02	5.71E-01
2.39E-28	9.15E-01	6.86E-02	2.06E-01	1.88E-01	3.49E-02	5.71E-01
2.92E-28	9.28E-01	6.87E-02	2.06E-01	1.85E-01	3.66E-02	5.72E-01
3.57E-28	9.40E-01	6.87E-02	2.07E-01	1.82E-01	3.87E-02	5.71E-01
4.82E-28	9.53E-01	6.85E-02	2.09E-01	1.80E-01	4.08E-02	5.73E-01
5.89E-28	9.64E-01	6.86E-02	2.09E-01	1.77E-01	4.30E-02	5.71E-01
7.19E-28	9.72E-01	6.85E-02	2.11E-01	1.74E-01	4.51E-02	5.71E-01
8.78E-28	9.80E-01	6.84E-02	2.11E-01	1.70E-01	4.73E-02	5.73E-01
1.07E-27	9.89E-01	6.85E-02	2.12E-01	1.66E-01	4.97E-02	5.71E-01
1.31E-27	9.98E-01	6.85E-02	2.13E-01	1.63E-01	5.21E-02	5.70E-01
1.45E-27	1.00E+00	6.84E-02	2.14E-01	1.62E-01	5.28E-02	5.71E-01
1.45E-27	1.00E+00	6.84E-02	2.14E-01	1.62E-01	5.28E-02	5.71E-01
2.16E-27	1.00E+00	6.84E-02	2.14E-01	1.62E-01	5.28E-02	5.71E-01
6.49E-27	1.00E+00	6.84E-02	2.14E-01	1.62E-01	5.28E-02	5.71E-01
1.76E-26	1.00E+00	6.84E-02	2.14E-01	1.62E-01	5.28E-02	5.71E-01
5.30E-26	1.00E+00	6.84E-02	2.14E-01	1.62E-01	5.28E-02	5.71E-01
1.59E-25	1.00E+00	6.84E-02	2.14E-01	1.62E-01	5.28E-02	5.71E-01
4.78E-25	1.00E+00	6.84E-02	2.14E-01	1.62E-01	5.28E-02	5.71E-01
1.44E-24	1.00E+00	6.84E-02	2.14E-01	1.62E-01	5.28E-02	5.71E-01
3.90E-24	1.00E+00	6.84E-02	2.14E-01	1.62E-01	5.28E-02	5.71E-01
1.17E-23	1.00E+00	6.84E-02	2.14E-01	1.62E-01	5.28E-02	5.71E-01
3.52E-23	1.00E+00	6.84E-02	2.14E-01	1.62E-01	5.28E-02	5.71E-01
1.06E-22	1.00E+00	6.84E-02	2.14E-01	1.62E-01	5.28E-02	5.71E-01
3.18E-22	1.00E+00	6.84E-02	2.14E-01	1.62E-01	5.28E-02	5.71E-01
8.64E-22	1.00E+00	6.84E-02	2.14E-01	1.62E-01	5.28E-02	5.71E-01
2.60E-21	1.00E+00	6.84E-02	2.14E-01	1.62E-01	5.28E-02	5.71E-01
5.23E-21	1.00E+00	6.84E-02	2.14E-01	1.62E-01	5.28E-02	5.71E-01
5.23E-21	1.00E+00	6.84E-02	2.14E-01	1.62E-01	5.28E-02	5.71E-01
7.80E-21	1.00E+00	6.83E-02	2.16E-01	1.55E-01	5.77E-02	5.71E-01
2.34E-20	1.00E+00	6.82E-02	2.19E-01	1.41E-01	6.81E-02	5.71E-01
7.04E-20	1.00E+00	6.81E-02	2.22E-01	1.29E-01	7.78E-02	5.70E-01

1.91E-19	1.00E+00	6.78E-02	2.26E-01	1.16E-01	8.74E-02	5.71E-01
3.16E-19	1.00E+00	6.78E-02	2.27E-01	1.11E-01	9.11E-02	5.71E-01
3.16E-19	1.00E+00	6.78E-02	2.27E-01	1.11E-01	9.11E-02	5.71E-01
5.75E-19	1.00E+00	6.78E-02	2.24E-01	1.10E-01	9.42E-02	5.70E-01
1.73E-18	1.00E+00	6.78E-02	2.21E-01	1.07E-01	9.97E-02	5.70E-01
5.19E-18	1.00E+00	6.76E-02	2.20E-01	1.03E-01	1.06E-01	5.73E-01
1.56E-17	9.69E-01	6.76E-02	2.20E-01	9.59E-02	1.13E-01	5.71E-01
4.24E-17	9.14E-01	6.73E-02	2.21E-01	8.79E-02	1.20E-01	5.74E-01
1.27E-16	8.69E-01	6.73E-02	2.23E-01	7.99E-02	1.26E-01	5.70E-01
3.82E-16	8.40E-01	6.72E-02	2.24E-01	7.41E-02	1.30E-01	5.73E-01
1.40E-15	8.18E-01	6.71E-02	2.26E-01	6.92E-02	1.34E-01	5.71E-01
1.71E-15	8.16E-01	6.73E-02	2.25E-01	6.84E-02	1.34E-01	5.71E-01
2.09E-15	8.13E-01	6.73E-02	2.25E-01	6.79E-02	1.35E-01	5.70E-01
2.56E-15	8.10E-01	6.72E-02	2.25E-01	6.74E-02	1.35E-01	5.72E-01
3.45E-15	8.07E-01	6.72E-02	2.26E-01	6.69E-02	1.36E-01	5.70E-01
4.22E-15	8.06E-01	6.70E-02	2.26E-01	6.68E-02	1.36E-01	5.73E-01
5.15E-15	8.04E-01	6.72E-02	2.25E-01	6.60E-02	1.36E-01	5.73E-01
6.29E-15	8.02E-01	6.72E-02	2.26E-01	6.59E-02	1.37E-01	5.71E-01
7.68E-15	8.01E-01	6.70E-02	2.26E-01	6.58E-02	1.37E-01	5.73E-01
9.38E-15	8.00E-01	6.71E-02	2.26E-01	6.50E-02	1.37E-01	5.73E-01
1.27E-14	7.95E-01	6.71E-02	2.26E-01	6.49E-02	1.38E-01	5.71E-01
1.55E-14	7.95E-01	6.71E-02	2.26E-01	6.45E-02	1.38E-01	5.71E-01
1.89E-14	7.94E-01	6.70E-02	2.26E-01	6.43E-02	1.38E-01	5.74E-01
2.31E-14	7.92E-01	6.72E-02	2.26E-01	6.40E-02	1.38E-01	5.70E-01
2.82E-14	7.91E-01	6.73E-02	2.26E-01	6.36E-02	1.38E-01	5.70E-01
3.44E-14	7.90E-01	6.71E-02	2.26E-01	6.34E-02	1.39E-01	5.72E-01
4.21E-14	7.90E-01	6.71E-02	2.26E-01	6.34E-02	1.39E-01	5.72E-01
5.68E-14	7.89E-01	6.69E-02	2.27E-01	6.33E-02	1.40E-01	5.74E-01
6.93E-14	7.87E-01	6.71E-02	2.26E-01	6.29E-02	1.40E-01	5.70E-01
8.47E-14	7.87E-01	6.72E-02	2.26E-01	6.25E-02	1.40E-01	5.70E-01
1.03E-13	7.87E-01	6.72E-02	2.26E-01	6.25E-02	1.40E-01	5.70E-01
1.26E-13	7.86E-01	6.70E-02	2.26E-01	6.24E-02	1.40E-01	5.73E-01
1.54E-13	7.86E-01	6.70E-02	2.26E-01	6.24E-02	1.40E-01	5.73E-01
2.08E-13	7.85E-01	6.71E-02	2.26E-01	6.20E-02	1.40E-01	5.73E-01
2.54E-13	7.81E-01	6.72E-02	2.26E-01	6.20E-02	1.40E-01	5.69E-01
3.11E-13	7.81E-01	6.71E-02	2.26E-01	6.18E-02	1.41E-01	5.71E-01
3.80E-13	7.80E-01	6.71E-02	2.26E-01	6.18E-02	1.41E-01	5.71E-01
4.64E-13	7.80E-01	6.71E-02	2.26E-01	6.18E-02	1.41E-01	5.71E-01
5.66E-13	7.80E-01	6.71E-02	2.26E-01	6.14E-02	1.41E-01	5.71E-01
7.64E-13	7.80E-01	6.71E-02	2.26E-01	6.14E-02	1.41E-01	5.71E-01
9.33E-13	7.79E-01	6.70E-02	2.27E-01	6.13E-02	1.41E-01	5.73E-01
1.14E-12	7.79E-01	6.70E-02	2.27E-01	6.13E-02	1.41E-01	5.73E-01
1.39E-12	7.79E-01	6.70E-02	2.27E-01	6.13E-02	1.41E-01	5.73E-01

1.70E-12	7.79E-01	6.70E-02	2.26E-01	6.13E-02	1.41E-01	5.73E-01
2.08E-12	7.78E-01	6.71E-02	2.26E-01	6.09E-02	1.41E-01	5.73E-01
2.80E-12	7.77E-01	6.72E-02	2.26E-01	6.09E-02	1.41E-01	5.69E-01
3.43E-12	7.76E-01	6.72E-02	2.26E-01	6.09E-02	1.41E-01	5.69E-01
4.18E-12	7.76E-01	6.72E-02	2.26E-01	6.09E-02	1.41E-01	5.69E-01
5.11E-12	7.76E-01	6.70E-02	2.27E-01	6.07E-02	1.42E-01	5.71E-01
6.24E-12	7.76E-01	6.70E-02	2.27E-01	6.07E-02	1.42E-01	5.71E-01
7.62E-12	7.76E-01	6.70E-02	2.27E-01	6.07E-02	1.42E-01	5.71E-01
9.31E-12	7.76E-01	6.70E-02	2.26E-01	6.07E-02	1.42E-01	5.71E-01
1.26E-11	7.76E-01	6.70E-02	2.26E-01	6.07E-02	1.42E-01	5.71E-01
1.54E-11	7.75E-01	6.71E-02	2.26E-01	6.03E-02	1.42E-01	5.71E-01
1.88E-11	7.75E-01	6.71E-02	2.26E-01	6.03E-02	1.42E-01	5.71E-01
2.29E-11	7.75E-01	6.71E-02	2.26E-01	6.03E-02	1.42E-01	5.71E-01
2.80E-11	7.75E-01	6.71E-02	2.26E-01	6.03E-02	1.42E-01	5.71E-01
3.42E-11	7.75E-01	6.71E-02	2.26E-01	6.03E-02	1.42E-01	5.71E-01
4.61E-11	7.75E-01	6.71E-02	2.26E-01	6.03E-02	1.42E-01	5.71E-01
5.63E-11	7.75E-01	6.71E-02	2.26E-01	6.03E-02	1.42E-01	5.71E-01
6.88E-11	7.75E-01	6.71E-02	2.26E-01	6.03E-02	1.42E-01	5.71E-01
8.40E-11	7.75E-01	6.72E-02	2.26E-01	5.99E-02	1.42E-01	5.71E-01
1.03E-10	7.75E-01	6.69E-02	2.27E-01	6.02E-02	1.42E-01	5.74E-01
1.25E-10	7.74E-01	6.69E-02	2.27E-01	6.02E-02	1.42E-01	5.74E-01
1.69E-10	7.74E-01	6.69E-02	2.27E-01	6.02E-02	1.42E-01	5.74E-01
2.07E-10	7.74E-01	6.69E-02	2.27E-01	6.02E-02	1.42E-01	5.74E-01
2.52E-10	7.74E-01	6.70E-02	2.26E-01	6.02E-02	1.42E-01	5.74E-01
3.08E-10	7.74E-01	6.70E-02	2.26E-01	6.02E-02	1.42E-01	5.74E-01
3.77E-10	7.74E-01	6.70E-02	2.26E-01	6.02E-02	1.42E-01	5.74E-01
6.21E-10	7.74E-01	6.70E-02	2.26E-01	6.02E-02	1.42E-01	5.74E-01
7.58E-10	7.74E-01	6.70E-02	2.26E-01	6.02E-02	1.42E-01	5.74E-01
9.26E-10	7.74E-01	6.70E-02	2.26E-01	6.02E-02	1.42E-01	5.74E-01
1.13E-09	7.73E-01	6.71E-02	2.26E-01	6.02E-02	1.42E-01	5.70E-01
1.38E-09	7.73E-01	6.71E-02	2.26E-01	6.02E-02	1.42E-01	5.70E-01
1.69E-09	7.72E-01	6.71E-02	2.26E-01	5.98E-02	1.42E-01	5.70E-01
2.06E-09	7.72E-01	6.71E-02	2.26E-01	5.98E-02	1.42E-01	5.70E-01
2.78E-09	7.72E-01	6.71E-02	2.26E-01	5.98E-02	1.42E-01	5.70E-01
3.40E-09	7.72E-01	6.71E-02	2.26E-01	5.98E-02	1.42E-01	5.70E-01
4.15E-09	7.72E-01	6.71E-02	2.26E-01	5.98E-02	1.42E-01	5.70E-01
5.07E-09	7.72E-01	6.71E-02	2.26E-01	5.98E-02	1.42E-01	5.70E-01
6.19E-09	7.72E-01	6.71E-02	2.26E-01	5.98E-02	1.42E-01	5.70E-01
7.56E-09	7.72E-01	6.71E-02	2.26E-01	5.98E-02	1.42E-01	5.70E-01
1.02E-08	7.72E-01	6.71E-02	2.26E-01	5.98E-02	1.42E-01	5.70E-01
1.25E-08	7.72E-01	6.71E-02	2.26E-01	5.98E-02	1.42E-01	5.70E-01
1.52E-08	7.72E-01	6.72E-02	2.26E-01	5.98E-02	1.42E-01	5.70E-01
1.86E-08	7.72E-01	6.72E-02	2.26E-01	5.98E-02	1.42E-01	5.70E-01

2.27E-08	7.72E-01	6.72E-02	2.26E-01	5.98E-02	1.42E-01	5.70E-01
2.78E-08	7.72E-01	6.72E-02	2.26E-01	5.98E-02	1.42E-01	5.70E-01
3.75E-08	7.72E-01	6.72E-02	2.26E-01	5.98E-02	1.42E-01	5.70E-01
4.58E-08	7.72E-01	6.72E-02	2.26E-01	5.98E-02	1.42E-01	5.70E-01
5.59E-08	7.72E-01	6.72E-02	2.26E-01	5.98E-02	1.42E-01	5.70E-01
6.83E-08	7.72E-01	6.72E-02	2.26E-01	5.98E-02	1.42E-01	5.70E-01
8.34E-08	7.72E-01	6.72E-02	2.26E-01	5.98E-02	1.42E-01	5.70E-01
1.02E-07	7.72E-01	6.72E-02	2.26E-01	5.98E-02	1.42E-01	5.70E-01
1.38E-07	7.72E-01	6.72E-02	2.26E-01	5.98E-02	1.42E-01	5.70E-01
1.68E-07	7.72E-01	6.72E-02	2.26E-01	5.98E-02	1.42E-01	5.70E-01
2.05E-07	7.72E-01	6.72E-02	2.26E-01	5.98E-02	1.42E-01	5.70E-01
2.51E-07	7.72E-01	6.72E-02	2.26E-01	5.98E-02	1.42E-01	5.70E-01
3.06E-07	7.72E-01	6.72E-02	2.26E-01	5.98E-02	1.42E-01	5.70E-01
3.74E-07	7.72E-01	6.72E-02	2.26E-01	5.98E-02	1.42E-01	5.70E-01
4.56E-07	7.72E-01	6.72E-02	2.26E-01	5.98E-02	1.42E-01	5.70E-01
6.16E-07	7.72E-01	6.72E-02	2.26E-01	5.98E-02	1.42E-01	5.70E-01
7.52E-07	7.72E-01	6.72E-02	2.26E-01	5.98E-02	1.42E-01	5.70E-01
9.19E-07	7.72E-01	6.72E-02	2.26E-01	5.98E-02	1.42E-01	5.70E-01
1.12E-06	7.72E-01	6.72E-02	2.26E-01	5.98E-02	1.42E-01	5.70E-01
1.37E-06	7.72E-01	6.72E-02	2.26E-01	5.98E-02	1.42E-01	5.70E-01
1.67E-06	7.72E-01	6.72E-02	2.26E-01	5.98E-02	1.42E-01	5.70E-01
2.26E-06	7.72E-01	6.72E-02	2.26E-01	5.98E-02	1.42E-01	5.70E-01
2.76E-06	7.72E-01	6.72E-02	2.26E-01	5.98E-02	1.42E-01	5.70E-01
3.37E-06	7.72E-01	6.72E-02	2.26E-01	5.98E-02	1.42E-01	5.70E-01
4.12E-06	7.72E-01	6.72E-02	2.26E-01	5.98E-02	1.42E-01	5.70E-01
5.03E-06	7.72E-01	6.72E-02	2.26E-01	5.98E-02	1.42E-01	5.70E-01
6.14E-06	7.72E-01	6.72E-02	2.26E-01	5.98E-02	1.42E-01	5.70E-01
8.29E-06	7.72E-01	6.72E-02	2.26E-01	5.98E-02	1.42E-01	5.70E-01
1.01E-05	7.72E-01	6.72E-02	2.26E-01	5.98E-02	1.42E-01	5.70E-01
1.24E-05	7.72E-01	6.72E-02	2.26E-01	5.98E-02	1.42E-01	5.70E-01
1.51E-05	7.72E-01	6.72E-02	2.26E-01	5.98E-02	1.42E-01	5.70E-01
1.85E-05	7.72E-01	6.72E-02	2.26E-01	5.98E-02	1.42E-01	5.70E-01
2.25E-05	7.72E-01	6.72E-02	2.26E-01	5.98E-02	1.42E-01	5.70E-01
3.04E-05	7.72E-01	6.72E-02	2.26E-01	5.98E-02	1.42E-01	5.70E-01
3.72E-05	7.72E-01	6.72E-02	2.26E-01	5.98E-02	1.42E-01	5.70E-01
4.54E-05	7.72E-01	6.72E-02	2.26E-01	5.98E-02	1.42E-01	5.70E-01
5.55E-05	7.72E-01	6.72E-02	2.26E-01	5.98E-02	1.42E-01	5.70E-01
6.91E-05	7.72E-01	6.72E-02	2.26E-01	5.98E-02	1.42E-01	5.70E-01
8.52E-05	7.72E-01	6.72E-02	2.26E-01	5.98E-02	1.42E-01	5.70E-01
1.06E-04	7.72E-01	6.72E-02	2.26E-01	5.98E-02	1.42E-01	5.70E-01
1.31E-04	7.72E-01	6.72E-02	2.26E-01	5.98E-02	1.42E-01	5.70E-01
1.63E-04	7.72E-01	6.72E-02	2.26E-01	5.98E-02	1.42E-01	5.70E-01
2.04E-04	7.72E-01	6.72E-02	2.26E-01	5.98E-02	1.42E-01	5.70E-01

2.51E-04	7.72E-01	6.72E-02	2.26E-01	5.98E-02	1.42E-01	5.70E-01
3.13E-04	7.72E-01	6.72E-02	2.26E-01	5.98E-02	1.42E-01	5.70E-01
3.86E-04	7.72E-01	6.72E-02	2.26E-01	5.98E-02	1.42E-01	5.70E-01
4.81E-04	7.72E-01	6.72E-02	2.26E-01	5.98E-02	1.42E-01	5.70E-01
5.99E-04	7.72E-01	6.72E-02	2.26E-01	5.98E-02	1.42E-01	5.70E-01
7.39E-04	7.72E-01	6.72E-02	2.26E-01	5.98E-02	1.42E-01	5.70E-01
9.21E-04	7.72E-01	6.72E-02	2.26E-01	5.98E-02	1.42E-01	5.70E-01
1.14E-03	7.72E-01	6.72E-02	2.26E-01	5.98E-02	1.42E-01	5.70E-01
1.42E-03	7.72E-01	6.72E-02	2.26E-01	5.98E-02	1.42E-01	5.70E-01
1.76E-03	7.72E-01	6.72E-02	2.26E-01	5.98E-02	1.42E-01	5.70E-01
2.18E-03	7.72E-01	6.72E-02	2.26E-01	5.98E-02	1.42E-01	5.70E-01
2.71E-03	7.72E-01	6.72E-02	2.26E-01	5.98E-02	1.42E-01	5.70E-01
3.35E-03	7.72E-01	6.72E-02	2.26E-01	5.98E-02	1.42E-01	5.70E-01
4.17E-03	7.72E-01	6.72E-02	2.26E-01	5.98E-02	1.42E-01	5.70E-01
5.20E-03	7.72E-01	6.72E-02	2.26E-01	5.98E-02	1.42E-01	5.70E-01
6.41E-03	7.72E-01	6.72E-02	2.26E-01	5.98E-02	1.42E-01	5.70E-01
7.99E-03	7.72E-01	6.72E-02	2.26E-01	5.98E-02	1.42E-01	5.70E-01
9.85E-03	7.72E-01	6.72E-02	2.26E-01	5.98E-02	1.42E-01	5.70E-01
1.23E-02	7.72E-01	6.72E-02	2.26E-01	5.98E-02	1.42E-01	5.70E-01
1.53E-02	7.72E-01	6.72E-02	2.26E-01	5.98E-02	1.42E-01	5.70E-01
1.89E-02	7.72E-01	6.72E-02	2.26E-01	5.98E-02	1.42E-01	5.70E-01
2.35E-02	7.72E-01	6.72E-02	2.26E-01	5.98E-02	1.42E-01	5.70E-01
2.90E-02	7.72E-01	6.72E-02	2.26E-01	5.98E-02	1.42E-01	5.70E-01
3.62E-02	7.72E-01	6.72E-02	2.26E-01	5.98E-02	1.42E-01	5.70E-01
4.51E-02	7.72E-01	6.72E-02	2.26E-01	5.98E-02	1.42E-01	5.70E-01
5.56E-02	7.72E-01	6.72E-02	2.26E-01	5.98E-02	1.42E-01	5.70E-01
6.93E-02	7.72E-01	6.72E-02	2.26E-01	5.98E-02	1.42E-01	5.70E-01
8.54E-02	7.72E-01	6.72E-02	2.26E-01	5.98E-02	1.42E-01	5.70E-01
1.07E-01	7.72E-01	6.72E-02	2.26E-01	5.98E-02	1.42E-01	5.70E-01
1.33E-01	7.72E-01	6.72E-02	2.26E-01	5.98E-02	1.42E-01	5.70E-01
1.35E-01	7.72E-01	6.72E-02	2.26E-01	5.98E-02	1.42E-01	5.70E-01

Table C.12. Thermo-Calc results for Fe-rich spinel phase composition and fractions at 480 °C and 1.5 MPa.

O2 Activity (atm)	Fe-rich spinel volume fraction	Number density (mol/cm3)	Fe mole fraction	Cr mole fraction	Ni mole fraction	O mole fraction
1.62E-31	1.31E-02	6.73E-02	4.21E-01	8.05E-03	3.43E-05	5.72E-01
1.97E-31	2.37E-02	6.77E-02	4.19E-01	8.01E-03	4.65E-05	5.71E-01
2.41E-31	3.42E-02	6.75E-02	4.20E-01	8.01E-03	5.86E-05	5.70E-01
2.95E-31	4.11E-02	6.75E-02	4.20E-01	7.98E-03	7.37E-05	5.71E-01
3.60E-31	4.81E-02	6.74E-02	4.21E-01	7.98E-03	9.49E-05	5.73E-01
4.86E-31	5.51E-02	6.73E-02	4.22E-01	7.97E-03	1.19E-04	5.72E-01
5.93E-31	5.85E-02	6.75E-02	4.20E-01	7.90E-03	1.45E-04	5.71E-01

7.24E-31	6.20E-02	6.76E-02	4.19E-01	7.89E-03	1.80E-04	5.72E-01
8.85E-31	6.87E-02	6.74E-02	4.21E-01	7.85E-03	2.21E-04	5.70E-01
1.08E-30	7.18E-02	6.73E-02	4.22E-01	7.83E-03	2.71E-04	5.72E-01
1.32E-30	7.50E-02	6.74E-02	4.21E-01	7.76E-03	3.31E-04	5.70E-01
1.61E-30	7.81E-02	6.73E-02	4.21E-01	7.72E-03	4.04E-04	5.73E-01
2.18E-30	8.11E-02	6.73E-02	4.22E-01	7.67E-03	4.90E-04	5.72E-01
2.66E-30	7.95E-02	6.75E-02	4.19E-01	7.63E-03	5.92E-04	5.72E-01
3.25E-30	8.23E-02	6.73E-02	4.21E-01	7.57E-03	7.16E-04	5.73E-01
3.97E-30	8.36E-02	6.72E-02	4.22E-01	7.50E-03	8.61E-04	5.73E-01
4.84E-30	8.31E-02	6.74E-02	4.20E-01	7.45E-03	1.03E-03	5.71E-01
5.92E-30	8.11E-02	6.75E-02	4.19E-01	7.40E-03	1.23E-03	5.72E-01
7.99E-30	8.19E-02	6.73E-02	4.21E-01	7.35E-03	1.47E-03	5.74E-01
9.75E-30	8.14E-02	6.74E-02	4.20E-01	7.27E-03	1.75E-03	5.72E-01
1.19E-29	7.89E-02	6.76E-02	4.18E-01	7.22E-03	2.07E-03	5.70E-01
1.46E-29	7.98E-02	6.73E-02	4.20E-01	7.14E-03	2.45E-03	5.71E-01
1.78E-29	7.75E-02	6.73E-02	4.20E-01	7.11E-03	2.89E-03	5.71E-01
2.17E-29	7.51E-02	6.73E-02	4.19E-01	7.04E-03	3.42E-03	5.73E-01
2.93E-29	7.29E-02	6.72E-02	4.19E-01	7.01E-03	4.02E-03	5.73E-01
3.58E-29	6.89E-02	6.73E-02	4.18E-01	6.96E-03	4.69E-03	5.71E-01
4.37E-29	6.34E-02	6.76E-02	4.15E-01	6.93E-03	5.48E-03	5.71E-01
5.34E-29	6.10E-02	6.75E-02	4.15E-01	6.90E-03	6.42E-03	5.71E-01
6.52E-29	5.70E-02	6.73E-02	4.15E-01	6.90E-03	7.47E-03	5.71E-01
7.96E-29	5.33E-02	6.72E-02	4.15E-01	6.90E-03	8.67E-03	5.71E-01
1.08E-28	4.80E-02	6.74E-02	4.12E-01	6.93E-03	1.01E-02	5.71E-01
1.31E-28	4.13E-02	6.75E-02	4.09E-01	6.96E-03	1.16E-02	5.71E-01
1.60E-28	3.78E-02	6.73E-02	4.09E-01	7.02E-03	1.34E-02	5.71E-01
1.96E-28	3.11E-02	6.73E-02	4.06E-01	7.07E-03	1.54E-02	5.71E-01
2.39E-28	2.48E-02	6.74E-02	4.03E-01	7.19E-03	1.77E-02	5.71E-01
2.92E-28	1.72E-02	6.74E-02	4.01E-01	7.33E-03	2.03E-02	5.71E-01
3.57E-28	1.12E-02	6.73E-02	3.98E-01	7.53E-03	2.32E-02	5.71E-01
4.82E-28	4.02E-03	6.73E-02	3.94E-01	7.73E-03	2.64E-02	5.72E-01

Table C.13. Thermo-Calc results for Cr-rich spinel diffusion coefficients at 480 °C and 1.5 MPa.

O2 Activity (atm)	Fe diffusion coefficient (nm2/s)	Cr diffusion coefficient (nm2/s)	Ni diffusion coefficient (nm2/s)	O diffusion coefficient (nm2/s)	Fe diffusion coefficient irradiated (nm2/s)	Cr diffusion coefficient irradiated (nm2/s)	Ni diffusion coefficient irradiated (nm2/s)
5.46E-38	1.89E+02	1.45E-05	5.29E+00	7.84E-01	1.89E+02	1.45E-05	5.29E+00
5.46E-38	1.89E+02	1.45E-05	5.29E+00	7.84E-01	1.89E+02	1.45E-05	5.29E+00
6.67E-38	1.72E+02	1.31E-05	4.79E+00	7.09E-01	1.72E+02	1.31E-05	4.79E+00
8.15E-38	1.55E+02	1.18E-05	4.33E+00	6.42E-01	1.55E+02	1.18E-05	4.33E+00
9.96E-38	1.40E+02	1.07E-05	3.91E+00	5.81E-01	1.40E+02	1.07E-05	3.91E+00

1.22E-37	1.26E+02	9.65E-06	3.53E+00	5.25E-01	1.26E+02	9.65E-06	3.53E+00
1.49E-37	1.14E+02	8.69E-06	3.18E+00	4.75E-01	1.14E+02	8.69E-06	3.18E+00
2.01E-37	1.03E+02	7.82E-06	2.86E+00	4.09E-01	1.03E+02	7.83E-06	2.86E+00
2.45E-37	9.23E+01	7.05E-06	2.58E+00	3.70E-01	9.23E+01	7.05E-06	2.58E+00
2.99E-37	8.30E+01	6.34E-06	2.32E+00	3.35E-01	8.30E+01	6.34E-06	2.32E+00
3.65E-37	7.46E+01	5.70E-06	2.08E+00	3.03E-01	7.47E+01	5.70E-06	2.09E+00
4.46E-37	6.70E+01	5.11E-06	1.87E+00	2.74E-01	6.70E+01	5.12E-06	1.87E+00
5.45E-37	6.03E+01	4.60E-06	1.68E+00	2.48E-01	6.03E+01	4.60E-06	1.68E+00
7.36E-37	5.41E+01	4.13E-06	1.51E+00	2.14E-01	5.41E+01	4.13E-06	1.51E+00
8.99E-37	4.86E+01	3.71E-06	1.36E+00	1.93E-01	4.87E+01	3.72E-06	1.36E+00
1.10E-36	4.37E+01	3.34E-06	1.22E+00	1.75E-01	4.38E+01	3.34E-06	1.22E+00
1.34E-36	3.91E+01	2.99E-06	1.09E+00	1.58E-01	3.92E+01	2.99E-06	1.10E+00
1.64E-36	3.51E+01	2.68E-06	9.81E-01	1.43E-01	3.52E+01	2.69E-06	9.83E-01
2.00E-36	3.17E+01	2.42E-06	8.84E-01	1.30E-01	3.18E+01	2.43E-06	8.87E-01
2.70E-36	2.84E+01	2.17E-06	7.93E-01	1.12E-01	2.85E+01	2.18E-06	7.95E-01
3.30E-36	2.55E+01	1.95E-06	7.12E-01	1.01E-01	2.56E+01	1.95E-06	7.14E-01
4.03E-36	2.29E+01	1.75E-06	6.40E-01	9.13E-02	2.31E+01	1.76E-06	6.44E-01
4.92E-36	2.06E+01	1.57E-06	5.74E-01	8.26E-02	2.07E+01	1.58E-06	5.78E-01
6.01E-36	1.84E+01	1.40E-06	5.13E-01	7.47E-02	1.85E+01	1.42E-06	5.17E-01
7.34E-36	1.66E+01	1.27E-06	4.62E-01	6.76E-02	1.67E+01	1.28E-06	4.67E-01
9.91E-36	1.49E+01	1.14E-06	4.15E-01	5.82E-02	1.51E+01	1.15E-06	4.20E-01
1.21E-35	1.34E+01	1.02E-06	3.73E-01	5.27E-02	1.36E+01	1.04E-06	3.79E-01
1.48E-35	1.20E+01	9.16E-07	3.35E-01	4.77E-02	1.22E+01	9.33E-07	3.41E-01
1.81E-35	1.08E+01	8.23E-07	3.01E-01	4.31E-02	1.10E+01	8.42E-07	3.08E-01
1.81E-35	1.08E+01	8.23E-07	3.01E-01	4.31E-02	1.10E+01	8.42E-07	3.08E-01
5.42E-35	6.30E+00	4.81E-07	1.76E-01	2.49E-02	6.70E+00	5.12E-07	1.87E-01
1.63E-34	3.70E+00	2.82E-07	1.03E-01	1.44E-02	4.32E+00	3.30E-07	1.21E-01
4.43E-34	2.18E+00	1.67E-07	6.10E-02	8.71E-03	3.06E+00	2.33E-07	8.53E-02
1.33E-33	1.32E+00	1.01E-07	3.67E-02	5.02E-03	2.39E+00	1.83E-07	6.67E-02
4.00E-33	8.45E-01	6.45E-08	2.36E-02	2.90E-03	2.00E+00	1.53E-07	5.59E-02
1.20E-32	6.41E-01	4.89E-08	1.79E-02	1.67E-03	1.62E+00	1.24E-07	4.52E-02
3.61E-32	7.37E-01	5.63E-08	2.06E-02	9.65E-04	8.06E-01	6.16E-08	2.25E-02
4.41E-32	8.25E-01	6.30E-08	2.30E-02	8.73E-04	8.25E-01	6.30E-08	2.30E-02
4.41E-32	8.25E-01	6.30E-08	2.30E-02	8.73E-04	8.25E-01	6.30E-08	2.30E-02
5.38E-32	9.56E-01	7.30E-08	2.67E-02	7.90E-04	9.56E-01	7.30E-08	2.67E-02
6.57E-32	1.15E+00	8.78E-08	3.21E-02	7.15E-04	1.15E+00	8.78E-08	3.21E-02
8.03E-32	1.43E+00	1.10E-07	4.01E-02	6.47E-04	1.43E+00	1.10E-07	4.01E-02
8.03E-32	1.43E+00	1.10E-07	4.01E-02	6.47E-04	1.43E+00	1.10E-07	4.01E-02
8.03E-32	1.43E+00	1.10E-07	4.01E-02	6.47E-04	1.43E+00	1.10E-07	4.01E-02
8.03E-32	1.43E+00	1.10E-07	4.01E-02	6.47E-04	1.43E+00	1.10E-07	4.01E-02
8.03E-32	1.43E+00	1.10E-07	4.01E-02	6.47E-04	1.43E+00	1.10E-07	4.01E-02
9.80E-32	1.58E+00	1.20E-07	4.40E-02	5.85E-04	1.58E+00	1.20E-07	4.40E-02
1.32E-31	1.72E+00	1.31E-07	4.80E-02	5.04E-04	1.72E+00	1.31E-07	4.80E-02

1.62E-31	1.86E+00	1.42E-07	5.18E-02	4.56E-04	1.86E+00	1.42E-07	5.18E-02
1.97E-31	2.00E+00	1.53E-07	5.59E-02	4.12E-04	2.00E+00	1.53E-07	5.59E-02
2.41E-31	2.11E+00	1.61E-07	5.90E-02	3.73E-04	2.11E+00	1.61E-07	5.90E-02
2.95E-31	2.22E+00	1.70E-07	6.20E-02	3.38E-04	2.22E+00	1.70E-07	6.20E-02
3.60E-31	2.28E+00	1.74E-07	6.35E-02	3.05E-04	2.28E+00	1.74E-07	6.35E-02
4.86E-31	2.33E+00	1.78E-07	6.51E-02	2.63E-04	2.33E+00	1.78E-07	6.51E-02
5.93E-31	2.33E+00	1.78E-07	6.51E-02	2.38E-04	2.33E+00	1.78E-07	6.51E-02
7.24E-31	2.31E+00	1.77E-07	6.45E-02	2.15E-04	2.31E+00	1.77E-07	6.45E-02
8.85E-31	2.28E+00	1.74E-07	6.35E-02	1.95E-04	2.28E+00	1.74E-07	6.35E-02
1.08E-30	2.20E+00	1.68E-07	6.15E-02	1.76E-04	2.20E+00	1.68E-07	6.15E-02
1.32E-30	2.13E+00	1.63E-07	5.95E-02	1.59E-04	2.13E+00	1.63E-07	5.95E-02
1.61E-30	2.04E+00	1.56E-07	5.69E-02	1.44E-04	2.04E+00	1.56E-07	5.69E-02
2.18E-30	1.95E+00	1.49E-07	5.44E-02	1.24E-04	1.95E+00	1.49E-07	5.44E-02
2.66E-30	1.86E+00	1.42E-07	5.18E-02	1.12E-04	1.86E+00	1.42E-07	5.18E-02
3.25E-30	1.76E+00	1.35E-07	4.92E-02	1.02E-04	1.76E+00	1.35E-07	4.92E-02
3.97E-30	1.68E+00	1.28E-07	4.69E-02	9.20E-05	1.68E+00	1.28E-07	4.69E-02
4.84E-30	1.60E+00	1.22E-07	4.47E-02	8.32E-05	1.60E+00	1.22E-07	4.47E-02
5.92E-30	1.53E+00	1.17E-07	4.26E-02	7.53E-05	1.53E+00	1.17E-07	4.26E-02
7.99E-30	1.46E+00	1.12E-07	4.09E-02	6.48E-05	1.46E+00	1.12E-07	4.09E-02
9.75E-30	1.41E+00	1.08E-07	3.93E-02	5.87E-05	1.41E+00	1.08E-07	3.93E-02
1.19E-29	1.36E+00	1.04E-07	3.80E-02	5.31E-05	1.36E+00	1.04E-07	3.80E-02
1.46E-29	1.32E+00	1.01E-07	3.68E-02	4.80E-05	1.32E+00	1.01E-07	3.68E-02
1.78E-29	1.29E+00	9.81E-08	3.59E-02	4.35E-05	1.29E+00	9.81E-08	3.59E-02
2.17E-29	1.26E+00	9.60E-08	3.51E-02	3.93E-05	1.26E+00	9.60E-08	3.51E-02
2.93E-29	1.24E+00	9.44E-08	3.45E-02	3.38E-05	1.24E+00	9.44E-08	3.45E-02
3.58E-29	1.22E+00	9.34E-08	3.42E-02	3.06E-05	1.22E+00	9.34E-08	3.42E-02
4.37E-29	1.21E+00	9.27E-08	3.39E-02	2.77E-05	1.21E+00	9.27E-08	3.39E-02
5.34E-29	1.21E+00	9.26E-08	3.39E-02	2.51E-05	1.21E+00	9.26E-08	3.39E-02
6.52E-29	1.22E+00	9.30E-08	3.40E-02	2.27E-05	1.22E+00	9.30E-08	3.40E-02
7.96E-29	1.23E+00	9.38E-08	3.43E-02	2.05E-05	1.23E+00	9.38E-08	3.43E-02
1.08E-28	1.24E+00	9.49E-08	3.47E-02	1.77E-05	1.24E+00	9.49E-08	3.47E-02
1.31E-28	1.27E+00	9.67E-08	3.54E-02	1.60E-05	1.27E+00	9.67E-08	3.54E-02
1.60E-28	1.29E+00	9.88E-08	3.61E-02	1.45E-05	1.29E+00	9.88E-08	3.61E-02
1.96E-28	1.33E+00	1.02E-07	3.71E-02	1.31E-05	1.33E+00	1.02E-07	3.71E-02
2.39E-28	1.37E+00	1.05E-07	3.82E-02	1.18E-05	1.37E+00	1.05E-07	3.82E-02
2.92E-28	1.41E+00	1.08E-07	3.95E-02	1.07E-05	1.41E+00	1.08E-07	3.95E-02
3.57E-28	1.47E+00	1.12E-07	4.10E-02	9.70E-06	1.47E+00	1.12E-07	4.10E-02
4.82E-28	1.53E+00	1.17E-07	4.26E-02	8.35E-06	1.53E+00	1.17E-07	4.26E-02
5.89E-28	1.59E+00	1.22E-07	4.44E-02	7.55E-06	1.59E+00	1.22E-07	4.44E-02
7.19E-28	1.66E+00	1.27E-07	4.64E-02	6.83E-06	1.66E+00	1.27E-07	4.64E-02
8.78E-28	1.74E+00	1.33E-07	4.85E-02	6.18E-06	1.74E+00	1.33E-07	4.85E-02
1.07E-27	1.82E+00	1.39E-07	5.07E-02	5.59E-06	1.82E+00	1.39E-07	5.07E-02
1.31E-27	1.89E+00	1.45E-07	5.29E-02	5.06E-06	1.89E+00	1.45E-07	5.29E-02

1.45E-27	1.91E+00	1.46E-07	5.34E-02	4.82E-06	1.91E+00	1.46E-07	5.34E-02
1.45E-27	1.91E+00	1.46E-07	5.34E-02	4.82E-06	1.91E+00	1.46E-07	5.34E-02
2.16E-27	2.48E+00	1.89E-07	6.91E-02	3.94E-06	2.48E+00	1.89E-07	6.91E-02
6.49E-27	5.10E+00	3.89E-07	1.42E-01	2.28E-06	5.10E+00	3.89E-07	1.42E-01
1.76E-26	1.05E+01	7.99E-07	2.92E-01	1.38E-06	1.05E+01	7.99E-07	2.92E-01
5.30E-26	2.15E+01	1.64E-06	6.00E-01	7.97E-07	2.15E+01	1.64E-06	6.00E-01
1.59E-25	4.42E+01	3.38E-06	1.24E+00	4.60E-07	4.42E+01	3.38E-06	1.24E+00
4.78E-25	9.07E+01	6.92E-06	2.53E+00	2.66E-07	9.07E+01	6.92E-06	2.53E+00
1.44E-24	1.86E+02	1.42E-05	5.18E+00	1.54E-07	1.86E+02	1.42E-05	5.18E+00
3.90E-24	3.82E+02	2.92E-05	1.07E+01	9.42E-08	3.82E+02	2.92E-05	1.07E+01
1.17E-23	7.86E+02	6.00E-05	2.20E+01	5.53E-08	7.86E+02	6.00E-05	2.20E+01
3.52E-23	1.62E+03	1.23E-04	4.51E+01	3.31E-08	1.62E+03	1.23E-04	4.51E+01
1.06E-22	3.31E+03	2.53E-04	9.25E+01	2.05E-08	3.31E+03	2.53E-04	9.25E+01
3.18E-22	6.83E+03	5.21E-04	1.91E+02	1.35E-08	6.83E+03	5.21E-04	1.91E+02
8.64E-22	1.40E+04	1.07E-03	3.91E+02	9.98E-09	1.40E+04	1.07E-03	3.91E+02
2.60E-21	3.64E+04	2.78E-03	1.02E+03	8.10E-09	3.64E+04	2.78E-03	1.02E+03
5.23E-21	3.64E+04	2.78E-03	1.02E+03	7.59E-09	3.64E+04	2.78E-03	1.02E+03
5.23E-21	3.64E+04	2.78E-03	1.02E+03	7.59E-09	3.64E+04	2.78E-03	1.02E+03
7.80E-21	5.46E+04	4.17E-03	1.53E+03	7.48E-09	5.46E+04	4.17E-03	1.53E+03
2.34E-20	7.28E+04	5.56E-03	2.03E+03	7.70E-09	7.28E+04	5.56E-03	2.03E+03
7.04E-20	1.09E+05	8.34E-03	3.05E+03	8.50E-09	1.09E+05	8.34E-03	3.05E+03
1.91E-19	1.64E+05	1.25E-02	4.57E+03	9.64E-09	1.64E+05	1.25E-02	4.57E+03
3.16E-19	2.00E+05	1.53E-02	5.59E+03	1.04E-08	2.00E+05	1.53E-02	5.59E+03
3.16E-19	2.00E+05	1.53E-02	5.59E+03	1.04E-08	2.00E+05	1.53E-02	5.59E+03
5.75E-19	2.18E+05	1.67E-02	6.10E+03	1.13E-08	2.18E+05	1.67E-02	6.10E+03
1.73E-18	2.91E+05	2.22E-02	8.13E+03	1.35E-08	2.91E+05	2.22E-02	8.13E+03
5.19E-18	3.82E+05	2.92E-02	1.07E+04	1.61E-08	3.82E+05	2.92E-02	1.07E+04
1.56E-17	4.73E+05	3.61E-02	1.32E+04	1.93E-08	4.73E+05	3.61E-02	1.32E+04
4.24E-17	5.64E+05	4.31E-02	1.58E+04	2.27E-08	5.64E+05	4.31E-02	1.58E+04
1.27E-16	6.01E+05	4.59E-02	1.68E+04	2.73E-08	6.01E+05	4.59E-02	1.68E+04
3.82E-16	5.83E+05	4.45E-02	1.63E+04	3.27E-08	5.83E+05	4.45E-02	1.63E+04
1.40E-15	5.83E+05	4.45E-02	1.63E+04	4.07E-08	5.83E+05	4.45E-02	1.63E+04
1.71E-15	5.64E+05	4.31E-02	1.58E+04	4.20E-08	5.64E+05	4.31E-02	1.58E+04
2.09E-15	5.64E+05	4.31E-02	1.58E+04	4.35E-08	5.64E+05	4.31E-02	1.58E+04
2.56E-15	5.64E+05	4.31E-02	1.58E+04	4.49E-08	5.64E+05	4.31E-02	1.58E+04
3.45E-15	5.64E+05	4.31E-02	1.58E+04	4.72E-08	5.64E+05	4.31E-02	1.58E+04
4.22E-15	5.64E+05	4.31E-02	1.58E+04	4.88E-08	5.64E+05	4.31E-02	1.58E+04
5.15E-15	5.64E+05	4.31E-02	1.58E+04	5.05E-08	5.64E+05	4.31E-02	1.58E+04
6.29E-15	5.64E+05	4.31E-02	1.58E+04	5.22E-08	5.64E+05	4.31E-02	1.58E+04
7.68E-15	5.64E+05	4.31E-02	1.58E+04	5.40E-08	5.64E+05	4.31E-02	1.58E+04
9.38E-15	5.64E+05	4.31E-02	1.58E+04	5.58E-08	5.64E+05	4.31E-02	1.58E+04
1.27E-14	5.64E+05	4.31E-02	1.58E+04	5.87E-08	5.64E+05	4.31E-02	1.58E+04
1.55E-14	5.64E+05	4.31E-02	1.58E+04	6.06E-08	5.64E+05	4.31E-02	1.58E+04

1.89E-14	5.64E+05	4.31E-02	1.58E+04	6.27E-08	5.64E+05	4.31E-02	1.58E+04
2.31E-14	5.64E+05	4.31E-02	1.58E+04	6.48E-08	5.64E+05	4.31E-02	1.58E+04
2.82E-14	5.64E+05	4.31E-02	1.58E+04	6.70E-08	5.64E+05	4.31E-02	1.58E+04
3.44E-14	5.64E+05	4.31E-02	1.58E+04	6.93E-08	5.64E+05	4.31E-02	1.58E+04
4.21E-14	5.46E+05	4.17E-02	1.53E+04	7.16E-08	5.46E+05	4.17E-02	1.53E+04
5.68E-14	5.46E+05	4.17E-02	1.53E+04	7.53E-08	5.46E+05	4.17E-02	1.53E+04
6.93E-14	5.46E+05	4.17E-02	1.53E+04	7.79E-08	5.46E+05	4.17E-02	1.53E+04
8.47E-14	5.46E+05	4.17E-02	1.53E+04	8.05E-08	5.46E+05	4.17E-02	1.53E+04
1.03E-13	5.46E+05	4.17E-02	1.53E+04	8.32E-08	5.46E+05	4.17E-02	1.53E+04
1.26E-13	5.46E+05	4.17E-02	1.53E+04	8.61E-08	5.46E+05	4.17E-02	1.53E+04
1.54E-13	5.46E+05	4.17E-02	1.53E+04	8.90E-08	5.46E+05	4.17E-02	1.53E+04
2.08E-13	5.46E+05	4.17E-02	1.53E+04	9.35E-08	5.46E+05	4.17E-02	1.53E+04
2.54E-13	5.46E+05	4.17E-02	1.53E+04	9.67E-08	5.46E+05	4.17E-02	1.53E+04
3.11E-13	5.46E+05	4.17E-02	1.53E+04	1.00E-07	5.46E+05	4.17E-02	1.53E+04
3.80E-13	5.46E+05	4.17E-02	1.53E+04	1.03E-07	5.46E+05	4.17E-02	1.53E+04
4.64E-13	5.46E+05	4.17E-02	1.53E+04	1.07E-07	5.46E+05	4.17E-02	1.53E+04
5.66E-13	5.46E+05	4.17E-02	1.53E+04	1.11E-07	5.46E+05	4.17E-02	1.53E+04
7.64E-13	5.46E+05	4.17E-02	1.53E+04	1.16E-07	5.46E+05	4.17E-02	1.53E+04
9.33E-13	5.46E+05	4.17E-02	1.53E+04	1.20E-07	5.46E+05	4.17E-02	1.53E+04
1.14E-12	5.46E+05	4.17E-02	1.53E+04	1.24E-07	5.46E+05	4.17E-02	1.53E+04
1.39E-12	5.46E+05	4.17E-02	1.53E+04	1.28E-07	5.46E+05	4.17E-02	1.53E+04
1.70E-12	5.46E+05	4.17E-02	1.53E+04	1.33E-07	5.46E+05	4.17E-02	1.53E+04
2.08E-12	5.46E+05	4.17E-02	1.53E+04	1.37E-07	5.46E+05	4.17E-02	1.53E+04
2.80E-12	5.46E+05	4.17E-02	1.53E+04	1.44E-07	5.46E+05	4.17E-02	1.53E+04
3.43E-12	5.46E+05	4.17E-02	1.53E+04	1.49E-07	5.46E+05	4.17E-02	1.53E+04
4.18E-12	5.46E+05	4.17E-02	1.53E+04	1.54E-07	5.46E+05	4.17E-02	1.53E+04
5.11E-12	5.46E+05	4.17E-02	1.53E+04	1.59E-07	5.46E+05	4.17E-02	1.53E+04
6.24E-12	5.46E+05	4.17E-02	1.53E+04	1.65E-07	5.46E+05	4.17E-02	1.53E+04
7.62E-12	5.46E+05	4.17E-02	1.53E+04	1.70E-07	5.46E+05	4.17E-02	1.53E+04
9.31E-12	5.46E+05	4.17E-02	1.53E+04	1.76E-07	5.46E+05	4.17E-02	1.53E+04
1.26E-11	5.46E+05	4.17E-02	1.53E+04	1.85E-07	5.46E+05	4.17E-02	1.53E+04
1.54E-11	5.46E+05	4.17E-02	1.53E+04	1.92E-07	5.46E+05	4.17E-02	1.53E+04
1.88E-11	5.46E+05	4.17E-02	1.53E+04	1.98E-07	5.46E+05	4.17E-02	1.53E+04
2.29E-11	5.46E+05	4.17E-02	1.53E+04	2.05E-07	5.46E+05	4.17E-02	1.53E+04
2.80E-11	5.46E+05	4.17E-02	1.53E+04	2.12E-07	5.46E+05	4.17E-02	1.53E+04
3.42E-11	5.46E+05	4.17E-02	1.53E+04	2.19E-07	5.46E+05	4.17E-02	1.53E+04
4.61E-11	5.46E+05	4.17E-02	1.53E+04	2.30E-07	5.46E+05	4.17E-02	1.53E+04
5.63E-11	5.46E+05	4.17E-02	1.53E+04	2.38E-07	5.46E+05	4.17E-02	1.53E+04
6.88E-11	5.46E+05	4.17E-02	1.53E+04	2.46E-07	5.46E+05	4.17E-02	1.53E+04
8.40E-11	5.46E+05	4.17E-02	1.53E+04	2.54E-07	5.46E+05	4.17E-02	1.53E+04
1.03E-10	5.46E+05	4.17E-02	1.53E+04	2.63E-07	5.46E+05	4.17E-02	1.53E+04
1.25E-10	5.46E+05	4.17E-02	1.53E+04	2.72E-07	5.46E+05	4.17E-02	1.53E+04
1.69E-10	5.46E+05	4.17E-02	1.53E+04	2.86E-07	5.46E+05	4.17E-02	1.53E+04

2.07E-10	5.46E+05	4.17E-02	1.53E+04	2.95E-07	5.46E+05	4.17E-02	1.53E+04
2.52E-10	5.46E+05	4.17E-02	1.53E+04	3.05E-07	5.46E+05	4.17E-02	1.53E+04
3.08E-10	5.46E+05	4.17E-02	1.53E+04	3.16E-07	5.46E+05	4.17E-02	1.53E+04
3.77E-10	5.46E+05	4.17E-02	1.53E+04	3.27E-07	5.46E+05	4.17E-02	1.53E+04
6.21E-10	5.46E+05	4.17E-02	1.53E+04	3.55E-07	5.46E+05	4.17E-02	1.53E+04
7.58E-10	5.46E+05	4.17E-02	1.53E+04	3.67E-07	5.46E+05	4.17E-02	1.53E+04
9.26E-10	5.46E+05	4.17E-02	1.53E+04	3.79E-07	5.46E+05	4.17E-02	1.53E+04
1.13E-09	5.46E+05	4.17E-02	1.53E+04	3.92E-07	5.46E+05	4.17E-02	1.53E+04
1.38E-09	5.46E+05	4.17E-02	1.53E+04	4.05E-07	5.46E+05	4.17E-02	1.53E+04
1.69E-09	5.46E+05	4.17E-02	1.53E+04	4.19E-07	5.46E+05	4.17E-02	1.53E+04
2.06E-09	5.46E+05	4.17E-02	1.53E+04	4.33E-07	5.46E+05	4.17E-02	1.53E+04
2.78E-09	5.46E+05	4.17E-02	1.53E+04	4.56E-07	5.46E+05	4.17E-02	1.53E+04
3.40E-09	5.46E+05	4.17E-02	1.53E+04	4.71E-07	5.46E+05	4.17E-02	1.53E+04
4.15E-09	5.46E+05	4.17E-02	1.53E+04	4.87E-07	5.46E+05	4.17E-02	1.53E+04
5.07E-09	5.46E+05	4.17E-02	1.53E+04	5.04E-07	5.46E+05	4.17E-02	1.53E+04
6.19E-09	5.46E+05	4.17E-02	1.53E+04	5.21E-07	5.46E+05	4.17E-02	1.53E+04
7.56E-09	5.46E+05	4.17E-02	1.53E+04	5.38E-07	5.46E+05	4.17E-02	1.53E+04
1.02E-08	5.46E+05	4.17E-02	1.53E+04	5.66E-07	5.46E+05	4.17E-02	1.53E+04
1.25E-08	5.46E+05	4.17E-02	1.53E+04	5.85E-07	5.46E+05	4.17E-02	1.53E+04
1.52E-08	5.46E+05	4.17E-02	1.53E+04	6.05E-07	5.46E+05	4.17E-02	1.53E+04
1.86E-08	5.46E+05	4.17E-02	1.53E+04	6.25E-07	5.46E+05	4.17E-02	1.53E+04
2.27E-08	5.46E+05	4.17E-02	1.53E+04	6.47E-07	5.46E+05	4.17E-02	1.53E+04
2.78E-08	5.46E+05	4.17E-02	1.53E+04	6.68E-07	5.46E+05	4.17E-02	1.53E+04
3.75E-08	5.46E+05	4.17E-02	1.53E+04	7.03E-07	5.46E+05	4.17E-02	1.53E+04
4.58E-08	5.46E+05	4.17E-02	1.53E+04	7.27E-07	5.46E+05	4.17E-02	1.53E+04
5.59E-08	5.46E+05	4.17E-02	1.53E+04	7.51E-07	5.46E+05	4.17E-02	1.53E+04
6.83E-08	5.46E+05	4.17E-02	1.53E+04	7.77E-07	5.46E+05	4.17E-02	1.53E+04
8.34E-08	5.46E+05	4.17E-02	1.53E+04	8.03E-07	5.46E+05	4.17E-02	1.53E+04
1.02E-07	5.46E+05	4.17E-02	1.53E+04	8.30E-07	5.46E+05	4.17E-02	1.53E+04
1.38E-07	5.46E+05	4.17E-02	1.53E+04	8.73E-07	5.46E+05	4.17E-02	1.53E+04
1.68E-07	5.46E+05	4.17E-02	1.53E+04	9.02E-07	5.46E+05	4.17E-02	1.53E+04
2.05E-07	5.46E+05	4.17E-02	1.53E+04	9.33E-07	5.46E+05	4.17E-02	1.53E+04
2.51E-07	5.46E+05	4.17E-02	1.53E+04	9.65E-07	5.46E+05	4.17E-02	1.53E+04
3.06E-07	5.46E+05	4.17E-02	1.53E+04	9.97E-07	5.46E+05	4.17E-02	1.53E+04
3.74E-07	5.46E+05	4.17E-02	1.53E+04	1.03E-06	5.46E+05	4.17E-02	1.53E+04
4.56E-07	5.46E+05	4.17E-02	1.53E+04	1.07E-06	5.46E+05	4.17E-02	1.53E+04
6.16E-07	5.46E+05	4.17E-02	1.53E+04	1.12E-06	5.46E+05	4.17E-02	1.53E+04
7.52E-07	5.46E+05	4.17E-02	1.53E+04	1.16E-06	5.46E+05	4.17E-02	1.53E+04
9.19E-07	5.46E+05	4.17E-02	1.53E+04	1.20E-06	5.46E+05	4.17E-02	1.53E+04
1.12E-06	5.46E+05	4.17E-02	1.53E+04	1.24E-06	5.46E+05	4.17E-02	1.53E+04
1.37E-06	5.46E+05	4.17E-02	1.53E+04	1.28E-06	5.46E+05	4.17E-02	1.53E+04
1.67E-06	5.46E+05	4.17E-02	1.53E+04	1.32E-06	5.46E+05	4.17E-02	1.53E+04
2.26E-06	5.46E+05	4.17E-02	1.53E+04	1.39E-06	5.46E+05	4.17E-02	1.53E+04

2.76E-06	5.46E+05	4.17E-02	1.53E+04	1.44E-06	5.46E+05	4.17E-02	1.53E+04
3.37E-06	5.46E+05	4.17E-02	1.53E+04	1.49E-06	5.46E+05	4.17E-02	1.53E+04
4.12E-06	5.46E+05	4.17E-02	1.53E+04	1.54E-06	5.46E+05	4.17E-02	1.53E+04
5.03E-06	5.46E+05	4.17E-02	1.53E+04	1.59E-06	5.46E+05	4.17E-02	1.53E+04
6.14E-06	5.46E+05	4.17E-02	1.53E+04	1.64E-06	5.46E+05	4.17E-02	1.53E+04
8.29E-06	5.46E+05	4.17E-02	1.53E+04	1.73E-06	5.46E+05	4.17E-02	1.53E+04
1.01E-05	5.46E+05	4.17E-02	1.53E+04	1.79E-06	5.46E+05	4.17E-02	1.53E+04
1.24E-05	5.46E+05	4.17E-02	1.53E+04	1.85E-06	5.46E+05	4.17E-02	1.53E+04
1.51E-05	5.46E+05	4.17E-02	1.53E+04	1.91E-06	5.46E+05	4.17E-02	1.53E+04
1.85E-05	5.46E+05	4.17E-02	1.53E+04	1.98E-06	5.46E+05	4.17E-02	1.53E+04
2.25E-05	5.46E+05	4.17E-02	1.53E+04	2.04E-06	5.46E+05	4.17E-02	1.53E+04
3.04E-05	5.46E+05	4.17E-02	1.53E+04	2.15E-06	5.46E+05	4.17E-02	1.53E+04
3.72E-05	5.46E+05	4.17E-02	1.53E+04	2.22E-06	5.46E+05	4.17E-02	1.53E+04
4.54E-05	5.46E+05	4.17E-02	1.53E+04	2.30E-06	5.46E+05	4.17E-02	1.53E+04
5.55E-05	5.46E+05	4.17E-02	1.53E+04	2.37E-06	5.46E+05	4.17E-02	1.53E+04
6.91E-05	5.46E+05	4.17E-02	1.53E+04	2.46E-06	5.46E+05	4.17E-02	1.53E+04
8.52E-05	5.46E+05	4.17E-02	1.53E+04	2.55E-06	5.46E+05	4.17E-02	1.53E+04
1.06E-04	5.46E+05	4.17E-02	1.53E+04	2.64E-06	5.46E+05	4.17E-02	1.53E+04
1.31E-04	5.46E+05	4.17E-02	1.53E+04	2.74E-06	5.46E+05	4.17E-02	1.53E+04
1.63E-04	5.46E+05	4.17E-02	1.53E+04	2.84E-06	5.46E+05	4.17E-02	1.53E+04
2.04E-04	5.46E+05	4.17E-02	1.53E+04	2.95E-06	5.46E+05	4.17E-02	1.53E+04
2.51E-04	5.46E+05	4.17E-02	1.53E+04	3.05E-06	5.46E+05	4.17E-02	1.53E+04
3.13E-04	5.46E+05	4.17E-02	1.53E+04	3.17E-06	5.46E+05	4.17E-02	1.53E+04
3.86E-04	5.46E+05	4.17E-02	1.53E+04	3.28E-06	5.46E+05	4.17E-02	1.53E+04
4.81E-04	5.46E+05	4.17E-02	1.53E+04	3.40E-06	5.46E+05	4.17E-02	1.53E+04
5.99E-04	5.46E+05	4.17E-02	1.53E+04	3.53E-06	5.46E+05	4.17E-02	1.53E+04
7.39E-04	5.46E+05	4.17E-02	1.53E+04	3.65E-06	5.46E+05	4.17E-02	1.53E+04
9.21E-04	5.46E+05	4.17E-02	1.53E+04	3.79E-06	5.46E+05	4.17E-02	1.53E+04
1.14E-03	5.46E+05	4.17E-02	1.53E+04	3.92E-06	5.46E+05	4.17E-02	1.53E+04
1.42E-03	5.46E+05	4.17E-02	1.53E+04	4.07E-06	5.46E+05	4.17E-02	1.53E+04
1.76E-03	5.46E+05	4.17E-02	1.53E+04	4.22E-06	5.46E+05	4.17E-02	1.53E+04
2.18E-03	5.46E+05	4.17E-02	1.53E+04	4.37E-06	5.46E+05	4.17E-02	1.53E+04
2.71E-03	5.46E+05	4.17E-02	1.53E+04	4.54E-06	5.46E+05	4.17E-02	1.53E+04
3.35E-03	5.46E+05	4.17E-02	1.53E+04	4.70E-06	5.46E+05	4.17E-02	1.53E+04
4.17E-03	5.46E+05	4.17E-02	1.53E+04	4.87E-06	5.46E+05	4.17E-02	1.53E+04
5.20E-03	5.46E+05	4.17E-02	1.53E+04	5.06E-06	5.46E+05	4.17E-02	1.53E+04
6.41E-03	5.46E+05	4.17E-02	1.53E+04	5.24E-06	5.46E+05	4.17E-02	1.53E+04
7.99E-03	5.46E+05	4.17E-02	1.53E+04	5.43E-06	5.46E+05	4.17E-02	1.53E+04
9.85E-03	5.46E+05	4.17E-02	1.53E+04	5.63E-06	5.46E+05	4.17E-02	1.53E+04
1.23E-02	5.46E+05	4.17E-02	1.53E+04	5.84E-06	5.46E+05	4.17E-02	1.53E+04
1.53E-02	5.46E+05	4.17E-02	1.53E+04	6.05E-06	5.46E+05	4.17E-02	1.53E+04
1.89E-02	5.46E+05	4.17E-02	1.53E+04	6.27E-06	5.46E+05	4.17E-02	1.53E+04
2.35E-02	5.46E+05	4.17E-02	1.53E+04	6.50E-06	5.46E+05	4.17E-02	1.53E+04

2.90E-02	5.46E+05	4.17E-02	1.53E+04	6.73E-06	5.46E+05	4.17E-02	1.53E+04
3.62E-02	5.46E+05	4.17E-02	1.53E+04	6.99E-06	5.46E+05	4.17E-02	1.53E+04
4.51E-02	5.46E+05	4.17E-02	1.53E+04	7.25E-06	5.46E+05	4.17E-02	1.53E+04
5.56E-02	5.46E+05	4.17E-02	1.53E+04	7.51E-06	5.46E+05	4.17E-02	1.53E+04
6.93E-02	5.46E+05	4.17E-02	1.53E+04	7.79E-06	5.46E+05	4.17E-02	1.53E+04
8.54E-02	5.46E+05	4.17E-02	1.53E+04	8.06E-06	5.46E+05	4.17E-02	1.53E+04
1.07E-01	5.46E+05	4.17E-02	1.53E+04	8.36E-06	5.46E+05	4.17E-02	1.53E+04
1.33E-01	5.46E+05	4.17E-02	1.53E+04	8.68E-06	5.46E+05	4.17E-02	1.53E+04
1.35E-01	5.46E+05	4.17E-02	1.53E+04	8.71E-06	5.46E+05	4.17E-02	1.53E+04

Table C.14. Thermo-Calc results for Fe-rich spinel diffusion coefficients at 480 °C and 1.5 MPa.

O2 Activity (atm)	Fe diffusion coefficient (nm2/s)	Cr diffusion coefficient (nm2/s)	Ni diffusion coefficient (nm2/s)	O diffusion coefficient (nm2/s)	Fe diffusion coefficient irradiated (nm2/s)	Cr diffusion coefficient irradiated (nm2/s)	Ni diffusion coefficient irradiated (nm2/s)
1.62E-31	8.52E-03	6.18E-10	2.93E-02	4.56E-04	8.52E-03	6.18E-10	2.93E-02
1.97E-31	9.67E-03	7.10E-10	2.52E-02	4.12E-04	9.67E-03	7.10E-10	2.52E-02
2.41E-31	1.10E-02	8.18E-10	2.11E-02	3.73E-04	1.10E-02	8.18E-10	2.11E-02
2.95E-31	1.26E-02	9.41E-10	1.90E-02	3.38E-04	1.26E-02	9.41E-10	1.90E-02
3.60E-31	1.44E-02	1.08E-09	1.70E-02	3.05E-04	1.44E-02	1.08E-09	1.70E-02
4.86E-31	1.66E-02	1.25E-09	1.50E-02	2.63E-04	1.66E-02	1.25E-09	1.50E-02
5.93E-31	1.90E-02	1.43E-09	1.30E-02	2.38E-04	1.90E-02	1.43E-09	1.30E-02
7.24E-31	2.18E-02	1.66E-09	1.10E-02	2.15E-04	2.18E-02	1.66E-09	1.10E-02
8.85E-31	2.49E-02	1.89E-09	9.00E-03	1.95E-04	2.49E-02	1.89E-09	9.00E-03
1.08E-30	2.87E-02	2.18E-09	9.11E-03	1.76E-04	2.87E-02	2.18E-09	9.11E-03
1.32E-30	3.29E-02	2.50E-09	7.15E-03	1.59E-04	3.29E-02	2.50E-09	7.15E-03
1.61E-30	3.78E-02	2.88E-09	7.28E-03	1.44E-04	3.78E-02	2.88E-09	7.28E-03
2.18E-30	4.34E-02	3.31E-09	7.44E-03	1.24E-04	4.34E-02	3.31E-09	7.44E-03
2.66E-30	4.98E-02	3.80E-09	5.54E-03	1.12E-04	4.98E-02	3.80E-09	5.54E-03
3.25E-30	5.71E-02	4.35E-09	5.75E-03	1.02E-04	5.71E-02	4.35E-09	5.75E-03
3.97E-30	6.52E-02	4.98E-09	5.97E-03	9.20E-05	6.52E-02	4.98E-09	5.97E-03
4.84E-30	7.49E-02	5.71E-09	4.17E-03	8.32E-05	7.49E-02	5.71E-09	4.17E-03
5.92E-30	8.56E-02	6.53E-09	4.47E-03	7.53E-05	8.56E-02	6.53E-09	4.47E-03
7.99E-30	9.78E-02	7.46E-09	4.81E-03	6.48E-05	9.78E-02	7.46E-09	4.81E-03
9.75E-30	1.12E-01	8.53E-09	5.10E-03	5.87E-05	1.12E-01	8.53E-09	5.10E-03
1.19E-29	1.28E-01	9.74E-09	5.29E-03	5.31E-05	1.28E-01	9.74E-09	5.29E-03
1.46E-29	1.46E-01	1.11E-08	5.57E-03	4.80E-05	1.46E-01	1.11E-08	5.57E-03
1.78E-29	1.66E-01	1.27E-08	5.95E-03	4.35E-05	1.66E-01	1.27E-08	5.95E-03
2.17E-29	1.89E-01	1.45E-08	6.43E-03	3.93E-05	1.89E-01	1.45E-08	6.43E-03
2.93E-29	2.15E-01	1.64E-08	7.00E-03	3.38E-05	2.15E-01	1.64E-08	7.00E-03
3.58E-29	2.44E-01	1.86E-08	7.69E-03	3.06E-05	2.44E-01	1.86E-08	7.69E-03
4.37E-29	2.77E-01	2.11E-08	8.49E-03	2.77E-05	2.77E-01	2.11E-08	8.49E-03

5.34E-29	3.13E-01	2.39E-08	9.41E-03	2.51E-05	3.13E-01	2.39E-08	9.41E-03
6.52E-29	3.53E-01	2.70E-08	1.05E-02	2.27E-05	3.53E-01	2.70E-08	1.05E-02
7.96E-29	3.99E-01	3.04E-08	1.17E-02	2.05E-05	3.99E-01	3.04E-08	1.17E-02
1.08E-28	4.48E-01	3.42E-08	1.30E-02	1.77E-05	4.48E-01	3.42E-08	1.30E-02
1.31E-28	5.02E-01	3.84E-08	1.44E-02	1.60E-05	5.02E-01	3.84E-08	1.44E-02
1.60E-28	5.63E-01	4.29E-08	1.61E-02	1.45E-05	5.63E-01	4.29E-08	1.61E-02
1.96E-28	6.26E-01	4.78E-08	1.78E-02	1.31E-05	6.26E-01	4.78E-08	1.78E-02
2.39E-28	6.95E-01	5.31E-08	1.97E-02	1.18E-05	6.95E-01	5.31E-08	1.97E-02
2.92E-28	7.68E-01	5.87E-08	2.17E-02	1.07E-05	7.68E-01	5.87E-08	2.17E-02
3.57E-28	8.45E-01	6.45E-08	2.38E-02	9.70E-06	8.45E-01	6.45E-08	2.38E-02
4.82E-28	9.23E-01	7.05E-08	2.60E-02	8.35E-06	9.23E-01	7.05E-08	2.60E-02

Table C.15. Thermo-Calc results for element chemical potentials and the Pilling-Bedworth ratio at 480 °C and 1.5 MPa.

O2 Activity (atm)	Fe chemical potential (J/mol)	Cr chemical potential (J/mol)	Ni chemical potential (J/mol)	O chemical potential (J/mol)	Pilling-Bedworth ratio
1.69E-48	-2.85E+04	-2.44E+04	-4.34E+04	-4.17E+05	1.00E+00
1.69E-48	-2.85E+04	-2.44E+04	-4.34E+04	-4.16E+05	1.00E+00
4.59E-48	-2.85E+04	-2.44E+04	-4.34E+04	-4.12E+05	1.00E+00
3.39E-47	-2.85E+04	-2.44E+04	-4.34E+04	-4.09E+05	1.00E+00
9.22E-47	-2.85E+04	-2.44E+04	-4.34E+04	-4.05E+05	1.00E+00
2.51E-46	-2.85E+04	-2.44E+04	-4.34E+04	-4.02E+05	1.00E+00
6.81E-46	-2.85E+04	-2.44E+04	-4.34E+04	-3.99E+05	1.00E+00
1.85E-45	-2.85E+04	-2.44E+04	-4.34E+04	-3.95E+05	1.00E+00
5.04E-45	-2.85E+04	-2.44E+04	-4.34E+04	-3.92E+05	1.00E+00
5.04E-45	-2.85E+04	-2.44E+04	-4.34E+04	-3.91E+05	1.00E+00
5.04E-45	-2.85E+04	-2.44E+04	-4.34E+04	-3.91E+05	1.00E+00
5.04E-45	-2.84E+04	-2.49E+04	-4.34E+04	-3.91E+05	1.00E+00
1.37E-44	-2.82E+04	-2.59E+04	-4.33E+04	-3.90E+05	1.17E+00
1.37E-44	-2.81E+04	-2.69E+04	-4.32E+04	-3.89E+05	1.17E+00
1.37E-44	-2.80E+04	-2.79E+04	-4.31E+04	-3.88E+05	1.17E+00
1.37E-44	-2.80E+04	-2.79E+04	-4.31E+04	-3.88E+05	1.17E+00
1.37E-44	-2.79E+04	-2.89E+04	-4.30E+04	-3.88E+05	1.17E+00
1.37E-44	-2.79E+04	-2.99E+04	-4.29E+04	-3.87E+05	1.17E+00
3.72E-44	-2.78E+04	-3.09E+04	-4.28E+04	-3.86E+05	1.18E+00
3.72E-44	-2.78E+04	-3.18E+04	-4.27E+04	-3.86E+05	1.18E+00
1.01E-43	-2.77E+04	-3.68E+04	-4.25E+04	-3.82E+05	1.21E+00
3.04E-43	-2.76E+04	-4.18E+04	-4.23E+04	-3.79E+05	1.21E+00
9.13E-43	-2.76E+04	-4.68E+04	-4.23E+04	-3.76E+05	1.22E+00
2.48E-42	-2.76E+04	-5.18E+04	-4.22E+04	-3.72E+05	1.22E+00
7.45E-42	-2.76E+04	-5.67E+04	-4.22E+04	-3.69E+05	1.22E+00
2.24E-41	-2.76E+04	-6.17E+04	-4.22E+04	-3.65E+05	1.22E+00
6.73E-41	-2.76E+04	-6.67E+04	-4.22E+04	-3.62E+05	1.22E+00

2.02E-40	-2.76E+04	-7.17E+04	-4.22E+04	-3.59E+05	1.22E+00
5.49E-40	-2.76E+04	-7.67E+04	-4.22E+04	-3.55E+05	1.22E+00
1.65E-39	-2.76E+04	-8.17E+04	-4.22E+04	-3.52E+05	1.22E+00
4.96E-39	-2.76E+04	-8.67E+04	-4.22E+04	-3.49E+05	1.22E+00
1.49E-38	-2.76E+04	-9.18E+04	-4.22E+04	-3.45E+05	1.22E+00
4.47E-38	-2.76E+04	-9.68E+04	-4.22E+04	-3.42E+05	1.22E+00
5.46E-38	-2.76E+04	-9.78E+04	-4.22E+04	-3.41E+05	1.33E+00
5.46E-38	-2.76E+04	-9.78E+04	-4.22E+04	-3.41E+05	1.33E+00
6.67E-38	-2.76E+04	-9.91E+04	-4.22E+04	-3.40E+05	1.33E+00
8.15E-38	-2.76E+04	-1.00E+05	-4.22E+04	-3.40E+05	1.33E+00
9.96E-38	-2.76E+04	-1.02E+05	-4.22E+04	-3.39E+05	1.33E+00
1.22E-37	-2.76E+04	-1.03E+05	-4.22E+04	-3.38E+05	1.33E+00
1.49E-37	-2.76E+04	-1.05E+05	-4.22E+04	-3.38E+05	1.33E+00
2.01E-37	-2.76E+04	-1.06E+05	-4.22E+04	-3.37E+05	1.33E+00
2.45E-37	-2.76E+04	-1.07E+05	-4.22E+04	-3.36E+05	1.33E+00
2.99E-37	-2.76E+04	-1.09E+05	-4.22E+04	-3.36E+05	1.33E+00
3.65E-37	-2.76E+04	-1.10E+05	-4.22E+04	-3.35E+05	1.33E+00
4.46E-37	-2.76E+04	-1.11E+05	-4.22E+04	-3.34E+05	1.33E+00
5.45E-37	-2.76E+04	-1.13E+05	-4.22E+04	-3.34E+05	1.33E+00
7.36E-37	-2.76E+04	-1.14E+05	-4.22E+04	-3.33E+05	1.33E+00
8.99E-37	-2.76E+04	-1.15E+05	-4.22E+04	-3.32E+05	1.33E+00
1.10E-36	-2.76E+04	-1.17E+05	-4.22E+04	-3.32E+05	1.33E+00
1.34E-36	-2.76E+04	-1.18E+05	-4.22E+04	-3.31E+05	1.33E+00
1.64E-36	-2.76E+04	-1.19E+05	-4.22E+04	-3.30E+05	1.33E+00
2.00E-36	-2.76E+04	-1.21E+05	-4.22E+04	-3.30E+05	1.33E+00
2.70E-36	-2.76E+04	-1.22E+05	-4.22E+04	-3.29E+05	1.33E+00
3.30E-36	-2.76E+04	-1.23E+05	-4.22E+04	-3.28E+05	1.33E+00
4.03E-36	-2.76E+04	-1.25E+05	-4.22E+04	-3.28E+05	1.33E+00
4.92E-36	-2.76E+04	-1.26E+05	-4.22E+04	-3.27E+05	1.33E+00
6.01E-36	-2.76E+04	-1.28E+05	-4.22E+04	-3.26E+05	1.33E+00
7.34E-36	-2.76E+04	-1.29E+05	-4.22E+04	-3.26E+05	1.33E+00
9.91E-36	-2.76E+04	-1.30E+05	-4.22E+04	-3.25E+05	1.33E+00
1.21E-35	-2.76E+04	-1.32E+05	-4.22E+04	-3.24E+05	1.33E+00
1.48E-35	-2.76E+04	-1.33E+05	-4.22E+04	-3.24E+05	1.33E+00
1.81E-35	-2.76E+04	-1.34E+05	-4.22E+04	-3.23E+05	1.33E+00
1.81E-35	-2.76E+04	-1.34E+05	-4.22E+04	-3.23E+05	1.33E+00
5.42E-35	-2.76E+04	-1.41E+05	-4.22E+04	-3.20E+05	1.33E+00
1.63E-34	-2.76E+04	-1.48E+05	-4.22E+04	-3.16E+05	1.33E+00
4.43E-34	-2.76E+04	-1.55E+05	-4.22E+04	-3.13E+05	1.33E+00
1.33E-33	-2.76E+04	-1.61E+05	-4.22E+04	-3.09E+05	1.33E+00
4.00E-33	-2.76E+04	-1.68E+05	-4.22E+04	-3.06E+05	1.33E+00
1.20E-32	-2.76E+04	-1.75E+05	-4.22E+04	-3.03E+05	1.34E+00
3.61E-32	-2.76E+04	-1.82E+05	-4.22E+04	-2.99E+05	1.36E+00

4.41E-32	-2.76E+04	-1.84E+05	-4.22E+04	-2.99E+05	1.37E+00
4.41E-32	-2.76E+04	-1.84E+05	-4.22E+04	-2.99E+05	1.37E+00
5.38E-32	-2.76E+04	-1.85E+05	-4.22E+04	-2.98E+05	1.38E+00
6.57E-32	-2.76E+04	-1.87E+05	-4.22E+04	-2.97E+05	1.40E+00
8.03E-32	-2.76E+04	-1.89E+05	-4.22E+04	-2.97E+05	1.42E+00
8.03E-32	-2.76E+04	-1.89E+05	-4.22E+04	-2.97E+05	1.42E+00
8.03E-32	-2.76E+04	-1.89E+05	-4.22E+04	-2.97E+05	1.42E+00
8.03E-32	-2.76E+04	-1.89E+05	-4.22E+04	-2.97E+05	1.42E+00
8.03E-32	-2.76E+04	-1.89E+05	-4.22E+04	-2.97E+05	1.42E+00
9.80E-32	-2.85E+04	-1.89E+05	-4.07E+04	-2.96E+05	1.81E+00
1.32E-31	-2.94E+04	-1.90E+05	-3.96E+04	-2.95E+05	1.85E+00
1.62E-31	-3.03E+04	-1.91E+05	-3.88E+04	-2.94E+05	1.88E+00
1.97E-31	-3.12E+04	-1.92E+05	-3.80E+04	-2.94E+05	1.90E+00
2.41E-31	-3.21E+04	-1.93E+05	-3.74E+04	-2.93E+05	1.90E+00
2.95E-31	-3.30E+04	-1.94E+05	-3.68E+04	-2.92E+05	1.91E+00
3.60E-31	-3.39E+04	-1.95E+05	-3.63E+04	-2.92E+05	1.92E+00
4.86E-31	-3.48E+04	-1.96E+05	-3.58E+04	-2.91E+05	1.93E+00
5.93E-31	-3.57E+04	-1.97E+05	-3.53E+04	-2.90E+05	1.93E+00
7.24E-31	-3.66E+04	-1.98E+05	-3.49E+04	-2.90E+05	1.94E+00
8.85E-31	-3.75E+04	-1.99E+05	-3.45E+04	-2.89E+05	1.94E+00
1.08E-30	-3.84E+04	-2.00E+05	-3.41E+04	-2.88E+05	1.95E+00
1.32E-30	-3.93E+04	-2.01E+05	-3.37E+04	-2.88E+05	1.95E+00
1.61E-30	-4.02E+04	-2.01E+05	-3.34E+04	-2.87E+05	1.95E+00
2.18E-30	-4.11E+04	-2.02E+05	-3.31E+04	-2.86E+05	1.96E+00
2.66E-30	-4.20E+04	-2.03E+05	-3.28E+04	-2.86E+05	1.96E+00
3.25E-30	-4.29E+04	-2.04E+05	-3.25E+04	-2.85E+05	1.97E+00
3.97E-30	-4.38E+04	-2.05E+05	-3.23E+04	-2.84E+05	1.97E+00
4.84E-30	-4.47E+04	-2.06E+05	-3.20E+04	-2.84E+05	1.97E+00
5.92E-30	-4.56E+04	-2.07E+05	-3.18E+04	-2.83E+05	1.98E+00
7.99E-30	-4.65E+04	-2.08E+05	-3.16E+04	-2.82E+05	1.98E+00
9.75E-30	-4.74E+04	-2.09E+05	-3.14E+04	-2.82E+05	1.98E+00
1.19E-29	-4.83E+04	-2.10E+05	-3.12E+04	-2.81E+05	1.99E+00
1.46E-29	-4.92E+04	-2.11E+05	-3.10E+04	-2.80E+05	1.99E+00
1.78E-29	-5.01E+04	-2.12E+05	-3.09E+04	-2.80E+05	2.00E+00
2.17E-29	-5.10E+04	-2.13E+05	-3.07E+04	-2.79E+05	2.00E+00
2.93E-29	-5.20E+04	-2.14E+05	-3.06E+04	-2.78E+05	2.00E+00
3.58E-29	-5.29E+04	-2.15E+05	-3.05E+04	-2.78E+05	2.01E+00
4.37E-29	-5.38E+04	-2.16E+05	-3.03E+04	-2.77E+05	2.01E+00
5.34E-29	-5.47E+04	-2.17E+05	-3.02E+04	-2.76E+05	2.02E+00
6.52E-29	-5.56E+04	-2.18E+05	-3.02E+04	-2.76E+05	2.02E+00
7.96E-29	-5.65E+04	-2.19E+05	-3.01E+04	-2.75E+05	2.03E+00
1.08E-28	-5.74E+04	-2.20E+05	-3.00E+04	-2.74E+05	2.03E+00
1.31E-28	-5.84E+04	-2.21E+05	-2.99E+04	-2.74E+05	2.04E+00

1.60E-28	-5.93E+04	-2.22E+05	-2.99E+04	-2.73E+05	2.04E+00
1.96E-28	-6.02E+04	-2.23E+05	-2.98E+04	-2.72E+05	2.05E+00
2.39E-28	-6.12E+04	-2.24E+05	-2.98E+04	-2.72E+05	2.05E+00
2.92E-28	-6.21E+04	-2.25E+05	-2.97E+04	-2.71E+05	2.06E+00
3.57E-28	-6.31E+04	-2.26E+05	-2.97E+04	-2.70E+05	2.07E+00
4.82E-28	-6.40E+04	-2.27E+05	-2.97E+04	-2.69E+05	2.08E+00
5.89E-28	-6.50E+04	-2.28E+05	-2.96E+04	-2.69E+05	2.08E+00
7.19E-28	-6.60E+04	-2.29E+05	-2.96E+04	-2.68E+05	2.09E+00
8.78E-28	-6.69E+04	-2.30E+05	-2.96E+04	-2.67E+05	2.11E+00
1.07E-27	-6.79E+04	-2.31E+05	-2.96E+04	-2.67E+05	2.12E+00
1.31E-27	-6.90E+04	-2.33E+05	-2.95E+04	-2.66E+05	2.13E+00
1.45E-27	-6.92E+04	-2.33E+05	-2.95E+04	-2.66E+05	2.13E+00
1.45E-27	-6.92E+04	-2.33E+05	-2.95E+04	-2.66E+05	2.13E+00
2.16E-27	-7.08E+04	-2.34E+05	-3.11E+04	-2.65E+05	2.13E+00
6.49E-27	-7.53E+04	-2.39E+05	-3.56E+04	-2.61E+05	2.13E+00
1.76E-26	-7.98E+04	-2.43E+05	-4.02E+04	-2.58E+05	2.13E+00
5.30E-26	-8.43E+04	-2.48E+05	-4.47E+04	-2.55E+05	2.13E+00
1.59E-25	-8.88E+04	-2.52E+05	-4.92E+04	-2.51E+05	2.13E+00
4.78E-25	-9.33E+04	-2.57E+05	-5.37E+04	-2.48E+05	2.13E+00
1.44E-24	-9.78E+04	-2.61E+05	-5.82E+04	-2.44E+05	2.13E+00
3.90E-24	-1.02E+05	-2.66E+05	-6.27E+04	-2.41E+05	2.13E+00
1.17E-23	-1.07E+05	-2.70E+05	-6.72E+04	-2.38E+05	2.13E+00
3.52E-23	-1.11E+05	-2.75E+05	-7.17E+04	-2.34E+05	2.13E+00
1.06E-22	-1.16E+05	-2.79E+05	-7.62E+04	-2.31E+05	2.13E+00
3.18E-22	-1.20E+05	-2.84E+05	-8.07E+04	-2.28E+05	2.13E+00
8.64E-22	-1.25E+05	-2.88E+05	-8.52E+04	-2.24E+05	2.13E+00
2.60E-21	-1.29E+05	-2.93E+05	-8.97E+04	-2.21E+05	2.13E+00
5.23E-21	-1.32E+05	-2.96E+05	-9.24E+04	-2.19E+05	2.13E+00
5.23E-21	-1.32E+05	-2.96E+05	-9.24E+04	-2.19E+05	2.13E+00
7.80E-21	-1.34E+05	-2.98E+05	-9.27E+04	-2.17E+05	2.14E+00
2.34E-20	-1.39E+05	-3.03E+05	-9.42E+04	-2.14E+05	2.14E+00
7.04E-20	-1.44E+05	-3.07E+05	-9.64E+04	-2.11E+05	2.14E+00
1.91E-19	-1.49E+05	-3.12E+05	-9.91E+04	-2.07E+05	2.14E+00
3.16E-19	-1.52E+05	-3.14E+05	-1.00E+05	-2.06E+05	2.15E+00
3.16E-19	-1.52E+05	-3.14E+05	-1.00E+05	-2.06E+05	2.15E+00
5.75E-19	-1.55E+05	-3.16E+05	-1.02E+05	-2.04E+05	2.15E+00
1.73E-18	-1.60E+05	-3.21E+05	-1.05E+05	-2.01E+05	2.15E+00
5.19E-18	-1.65E+05	-3.25E+05	-1.08E+05	-1.97E+05	2.15E+00
1.56E-17	-1.70E+05	-3.30E+05	-1.11E+05	-1.94E+05	2.15E+00
4.24E-17	-1.75E+05	-3.34E+05	-1.15E+05	-1.90E+05	2.15E+00
1.27E-16	-1.81E+05	-3.39E+05	-1.18E+05	-1.87E+05	2.15E+00
3.82E-16	-1.86E+05	-3.44E+05	-1.21E+05	-1.84E+05	2.15E+00
1.40E-15	-1.92E+05	-3.50E+05	-1.25E+05	-1.80E+05	2.15E+00

1.71E-15	-1.93E+05	-3.51E+05	-1.26E+05	-1.79E+05	2.15E+00
2.09E-15	-1.94E+05	-3.52E+05	-1.26E+05	-1.78E+05	2.15E+00
2.56E-15	-1.95E+05	-3.53E+05	-1.27E+05	-1.78E+05	2.15E+00
3.45E-15	-1.96E+05	-3.54E+05	-1.28E+05	-1.77E+05	2.15E+00
4.22E-15	-1.97E+05	-3.55E+05	-1.28E+05	-1.76E+05	2.15E+00
5.15E-15	-1.98E+05	-3.56E+05	-1.29E+05	-1.75E+05	2.15E+00
6.29E-15	-1.99E+05	-3.57E+05	-1.30E+05	-1.75E+05	2.15E+00
7.68E-15	-2.00E+05	-3.58E+05	-1.30E+05	-1.74E+05	2.15E+00
9.38E-15	-2.01E+05	-3.59E+05	-1.31E+05	-1.73E+05	2.15E+00
1.27E-14	-2.02E+05	-3.60E+05	-1.32E+05	-1.73E+05	2.15E+00
1.55E-14	-2.03E+05	-3.61E+05	-1.32E+05	-1.72E+05	2.15E+00
1.89E-14	-2.04E+05	-3.62E+05	-1.33E+05	-1.71E+05	2.15E+00
2.31E-14	-2.05E+05	-3.63E+05	-1.34E+05	-1.71E+05	2.15E+00
2.82E-14	-2.06E+05	-3.64E+05	-1.34E+05	-1.70E+05	2.15E+00
3.44E-14	-2.07E+05	-3.65E+05	-1.35E+05	-1.69E+05	2.15E+00
4.21E-14	-2.08E+05	-3.66E+05	-1.36E+05	-1.69E+05	2.15E+00
5.68E-14	-2.09E+05	-3.67E+05	-1.36E+05	-1.68E+05	2.15E+00
6.93E-14	-2.10E+05	-3.68E+05	-1.37E+05	-1.67E+05	2.15E+00
8.47E-14	-2.11E+05	-3.69E+05	-1.38E+05	-1.67E+05	2.15E+00
1.03E-13	-2.12E+05	-3.70E+05	-1.38E+05	-1.66E+05	2.15E+00
1.26E-13	-2.13E+05	-3.71E+05	-1.39E+05	-1.65E+05	2.15E+00
1.54E-13	-2.14E+05	-3.72E+05	-1.40E+05	-1.65E+05	2.15E+00
2.08E-13	-2.15E+05	-3.73E+05	-1.40E+05	-1.64E+05	2.15E+00
2.54E-13	-2.16E+05	-3.74E+05	-1.41E+05	-1.63E+05	2.15E+00
3.11E-13	-2.17E+05	-3.75E+05	-1.42E+05	-1.63E+05	2.15E+00
3.80E-13	-2.18E+05	-3.76E+05	-1.42E+05	-1.62E+05	2.15E+00
4.64E-13	-2.19E+05	-3.77E+05	-1.43E+05	-1.61E+05	2.15E+00
5.66E-13	-2.20E+05	-3.78E+05	-1.44E+05	-1.61E+05	2.15E+00
7.64E-13	-2.21E+05	-3.79E+05	-1.44E+05	-1.60E+05	2.15E+00
9.33E-13	-2.22E+05	-3.80E+05	-1.45E+05	-1.59E+05	2.15E+00
1.14E-12	-2.23E+05	-3.81E+05	-1.46E+05	-1.59E+05	2.15E+00
1.39E-12	-2.24E+05	-3.82E+05	-1.46E+05	-1.58E+05	2.15E+00
1.70E-12	-2.25E+05	-3.83E+05	-1.47E+05	-1.57E+05	2.15E+00
2.08E-12	-2.26E+05	-3.84E+05	-1.48E+05	-1.57E+05	2.15E+00
2.80E-12	-2.27E+05	-3.85E+05	-1.48E+05	-1.56E+05	2.15E+00
3.43E-12	-2.28E+05	-3.86E+05	-1.49E+05	-1.55E+05	2.15E+00
4.18E-12	-2.29E+05	-3.87E+05	-1.50E+05	-1.55E+05	2.15E+00
5.11E-12	-2.30E+05	-3.88E+05	-1.50E+05	-1.54E+05	2.15E+00
6.24E-12	-2.31E+05	-3.89E+05	-1.51E+05	-1.53E+05	2.15E+00
7.62E-12	-2.32E+05	-3.90E+05	-1.52E+05	-1.52E+05	2.15E+00
9.31E-12	-2.33E+05	-3.91E+05	-1.52E+05	-1.52E+05	2.15E+00
1.26E-11	-2.34E+05	-3.92E+05	-1.53E+05	-1.51E+05	2.15E+00
1.54E-11	-2.35E+05	-3.93E+05	-1.54E+05	-1.50E+05	2.15E+00

1.88E-11	-2.36E+05	-3.94E+05	-1.54E+05	-1.50E+05	2.15E+00
2.29E-11	-2.37E+05	-3.95E+05	-1.55E+05	-1.49E+05	2.15E+00
2.80E-11	-2.39E+05	-3.96E+05	-1.56E+05	-1.48E+05	2.15E+00
3.42E-11	-2.40E+05	-3.97E+05	-1.56E+05	-1.48E+05	2.15E+00
4.61E-11	-2.41E+05	-3.98E+05	-1.57E+05	-1.47E+05	2.15E+00
5.63E-11	-2.42E+05	-3.99E+05	-1.58E+05	-1.46E+05	2.15E+00
6.88E-11	-2.43E+05	-4.00E+05	-1.58E+05	-1.46E+05	2.15E+00
8.40E-11	-2.44E+05	-4.01E+05	-1.59E+05	-1.45E+05	2.15E+00
1.03E-10	-2.45E+05	-4.02E+05	-1.60E+05	-1.44E+05	2.15E+00
1.25E-10	-2.46E+05	-4.03E+05	-1.60E+05	-1.44E+05	2.15E+00
1.69E-10	-2.47E+05	-4.04E+05	-1.61E+05	-1.43E+05	2.15E+00
2.07E-10	-2.48E+05	-4.05E+05	-1.62E+05	-1.42E+05	2.15E+00
2.52E-10	-2.49E+05	-4.06E+05	-1.63E+05	-1.42E+05	2.15E+00
3.08E-10	-2.50E+05	-4.07E+05	-1.63E+05	-1.41E+05	2.15E+00
3.77E-10	-2.51E+05	-4.08E+05	-1.64E+05	-1.40E+05	2.15E+00
6.21E-10	-2.53E+05	-4.10E+05	-1.65E+05	-1.39E+05	2.15E+00
7.58E-10	-2.54E+05	-4.11E+05	-1.66E+05	-1.38E+05	2.15E+00
9.26E-10	-2.55E+05	-4.12E+05	-1.67E+05	-1.38E+05	2.15E+00
1.13E-09	-2.56E+05	-4.13E+05	-1.67E+05	-1.37E+05	2.15E+00
1.38E-09	-2.57E+05	-4.14E+05	-1.68E+05	-1.36E+05	2.15E+00
1.69E-09	-2.58E+05	-4.15E+05	-1.69E+05	-1.36E+05	2.15E+00
2.06E-09	-2.59E+05	-4.16E+05	-1.69E+05	-1.35E+05	2.15E+00
2.78E-09	-2.60E+05	-4.17E+05	-1.70E+05	-1.34E+05	2.15E+00
3.40E-09	-2.61E+05	-4.18E+05	-1.71E+05	-1.34E+05	2.15E+00
4.15E-09	-2.62E+05	-4.19E+05	-1.71E+05	-1.33E+05	2.15E+00
5.07E-09	-2.63E+05	-4.20E+05	-1.72E+05	-1.32E+05	2.15E+00
6.19E-09	-2.64E+05	-4.22E+05	-1.73E+05	-1.32E+05	2.15E+00
7.56E-09	-2.65E+05	-4.23E+05	-1.73E+05	-1.31E+05	2.15E+00
1.02E-08	-2.66E+05	-4.24E+05	-1.74E+05	-1.30E+05	2.15E+00
1.25E-08	-2.67E+05	-4.25E+05	-1.75E+05	-1.30E+05	2.15E+00
1.52E-08	-2.68E+05	-4.26E+05	-1.75E+05	-1.29E+05	2.15E+00
1.86E-08	-2.69E+05	-4.27E+05	-1.76E+05	-1.28E+05	2.15E+00
2.27E-08	-2.70E+05	-4.28E+05	-1.77E+05	-1.27E+05	2.15E+00
2.78E-08	-2.71E+05	-4.29E+05	-1.77E+05	-1.27E+05	2.15E+00
3.75E-08	-2.72E+05	-4.30E+05	-1.78E+05	-1.26E+05	2.15E+00
4.58E-08	-2.73E+05	-4.31E+05	-1.79E+05	-1.25E+05	2.15E+00
5.59E-08	-2.74E+05	-4.32E+05	-1.79E+05	-1.25E+05	2.15E+00
6.83E-08	-2.75E+05	-4.33E+05	-1.80E+05	-1.24E+05	2.15E+00
8.34E-08	-2.76E+05	-4.34E+05	-1.81E+05	-1.23E+05	2.15E+00
1.02E-07	-2.77E+05	-4.35E+05	-1.81E+05	-1.23E+05	2.15E+00
1.38E-07	-2.78E+05	-4.36E+05	-1.82E+05	-1.22E+05	2.15E+00
1.68E-07	-2.79E+05	-4.37E+05	-1.83E+05	-1.21E+05	2.15E+00
2.05E-07	-2.80E+05	-4.38E+05	-1.83E+05	-1.21E+05	2.15E+00

2.51E-07	-2.81E+05	-4.39E+05	-1.84E+05	-1.20E+05	2.15E+00
3.06E-07	-2.82E+05	-4.40E+05	-1.85E+05	-1.19E+05	2.15E+00
3.74E-07	-2.83E+05	-4.41E+05	-1.85E+05	-1.19E+05	2.15E+00
4.56E-07	-2.84E+05	-4.42E+05	-1.86E+05	-1.18E+05	2.15E+00
6.16E-07	-2.85E+05	-4.43E+05	-1.87E+05	-1.17E+05	2.15E+00
7.52E-07	-2.86E+05	-4.44E+05	-1.88E+05	-1.17E+05	2.15E+00
9.19E-07	-2.87E+05	-4.45E+05	-1.88E+05	-1.16E+05	2.15E+00
1.12E-06	-2.88E+05	-4.46E+05	-1.89E+05	-1.15E+05	2.15E+00
1.37E-06	-2.89E+05	-4.47E+05	-1.90E+05	-1.15E+05	2.15E+00
1.67E-06	-2.90E+05	-4.48E+05	-1.90E+05	-1.14E+05	2.15E+00
2.26E-06	-2.91E+05	-4.49E+05	-1.91E+05	-1.13E+05	2.15E+00
2.76E-06	-2.92E+05	-4.50E+05	-1.92E+05	-1.13E+05	2.15E+00
3.37E-06	-2.93E+05	-4.51E+05	-1.92E+05	-1.12E+05	2.15E+00
4.12E-06	-2.94E+05	-4.52E+05	-1.93E+05	-1.11E+05	2.15E+00
5.03E-06	-2.95E+05	-4.53E+05	-1.94E+05	-1.11E+05	2.15E+00
6.14E-06	-2.96E+05	-4.54E+05	-1.94E+05	-1.10E+05	2.15E+00
8.29E-06	-2.97E+05	-4.55E+05	-1.95E+05	-1.09E+05	2.15E+00
1.01E-05	-2.98E+05	-4.56E+05	-1.96E+05	-1.09E+05	2.15E+00
1.24E-05	-2.99E+05	-4.57E+05	-1.96E+05	-1.08E+05	2.15E+00
1.51E-05	-3.00E+05	-4.58E+05	-1.97E+05	-1.07E+05	2.15E+00
1.85E-05	-3.01E+05	-4.59E+05	-1.98E+05	-1.07E+05	2.15E+00
2.25E-05	-3.02E+05	-4.60E+05	-1.98E+05	-1.06E+05	2.15E+00
3.04E-05	-3.03E+05	-4.61E+05	-1.99E+05	-1.05E+05	2.15E+00
3.72E-05	-3.04E+05	-4.62E+05	-2.00E+05	-1.04E+05	2.15E+00
4.54E-05	-3.05E+05	-4.63E+05	-2.00E+05	-1.04E+05	2.15E+00
5.55E-05	-3.06E+05	-4.64E+05	-2.01E+05	-1.03E+05	2.15E+00
6.91E-05	-3.07E+05	-4.65E+05	-2.02E+05	-1.02E+05	2.15E+00
8.52E-05	-3.08E+05	-4.66E+05	-2.02E+05	-1.02E+05	2.15E+00
1.06E-04	-3.10E+05	-4.67E+05	-2.03E+05	-1.01E+05	2.15E+00
1.31E-04	-3.11E+05	-4.68E+05	-2.04E+05	-1.00E+05	2.15E+00
1.63E-04	-3.12E+05	-4.69E+05	-2.04E+05	-9.97E+04	2.15E+00
2.04E-04	-3.13E+05	-4.70E+05	-2.05E+05	-9.91E+04	2.15E+00
2.51E-04	-3.14E+05	-4.71E+05	-2.06E+05	-9.84E+04	2.15E+00
3.13E-04	-3.15E+05	-4.72E+05	-2.06E+05	-9.77E+04	2.15E+00
3.86E-04	-3.16E+05	-4.73E+05	-2.07E+05	-9.70E+04	2.15E+00
4.81E-04	-3.17E+05	-4.74E+05	-2.08E+05	-9.64E+04	2.15E+00
5.99E-04	-3.18E+05	-4.75E+05	-2.08E+05	-9.57E+04	2.15E+00
7.39E-04	-3.19E+05	-4.76E+05	-2.09E+05	-9.50E+04	2.15E+00
9.21E-04	-3.20E+05	-4.77E+05	-2.10E+05	-9.43E+04	2.15E+00
1.14E-03	-3.21E+05	-4.78E+05	-2.10E+05	-9.37E+04	2.15E+00
1.42E-03	-3.22E+05	-4.79E+05	-2.11E+05	-9.30E+04	2.15E+00
1.76E-03	-3.23E+05	-4.80E+05	-2.12E+05	-9.23E+04	2.15E+00
2.18E-03	-3.24E+05	-4.81E+05	-2.13E+05	-9.16E+04	2.15E+00

2.71E-03	-3.25E+05	-4.82E+05	-2.13E+05	-9.10E+04	2.15E+00
3.35E-03	-3.26E+05	-4.83E+05	-2.14E+05	-9.03E+04	2.15E+00
4.17E-03	-3.27E+05	-4.84E+05	-2.15E+05	-8.96E+04	2.15E+00
5.20E-03	-3.28E+05	-4.85E+05	-2.15E+05	-8.89E+04	2.15E+00
6.41E-03	-3.29E+05	-4.86E+05	-2.16E+05	-8.83E+04	2.15E+00
7.99E-03	-3.30E+05	-4.87E+05	-2.17E+05	-8.76E+04	2.15E+00
9.85E-03	-3.31E+05	-4.88E+05	-2.17E+05	-8.69E+04	2.15E+00
1.23E-02	-3.32E+05	-4.89E+05	-2.18E+05	-8.62E+04	2.15E+00
1.53E-02	-3.33E+05	-4.90E+05	-2.19E+05	-8.56E+04	2.15E+00
1.89E-02	-3.34E+05	-4.91E+05	-2.19E+05	-8.49E+04	2.15E+00
2.35E-02	-3.35E+05	-4.92E+05	-2.20E+05	-8.42E+04	2.15E+00
2.90E-02	-3.36E+05	-4.94E+05	-2.21E+05	-8.35E+04	2.15E+00
3.62E-02	-3.37E+05	-4.95E+05	-2.21E+05	-8.28E+04	2.15E+00
4.51E-02	-3.38E+05	-4.96E+05	-2.22E+05	-8.22E+04	2.15E+00
5.56E-02	-3.39E+05	-4.97E+05	-2.23E+05	-8.15E+04	2.15E+00
6.93E-02	-3.40E+05	-4.98E+05	-2.23E+05	-8.08E+04	2.15E+00
8.54E-02	-3.41E+05	-4.99E+05	-2.24E+05	-8.01E+04	2.15E+00
1.07E-01	-3.42E+05	-5.00E+05	-2.25E+05	-7.95E+04	2.15E+00
1.33E-01	-3.43E+05	-5.01E+05	-2.25E+05	-7.88E+04	2.15E+00
1.35E-01	-3.43E+05	-5.01E+05	-2.25E+05	-7.87E+04	2.15E+00

Table C.16. Thermo-Calc derived calculation of parabolic rate constant at 480 °C and 1.5 MPa.

O2 Activity (atm)	Parabolic rate constant in Cr-rich spinel with Fe (nm2/s)	Parabolic rate constant in Cr-rich spinel with O (nm2/s)	Parabolic rate constant in irradiated Cr-rich spinel with Fe (nm2/s)	Parabolic rate constant in Fe-rich spinel with Fe (nm2/s)	Parabolic rate constant in Fe-rich spinel with O (nm2/s)	Parabolic rate constant in irradiated Fe-rich spinel with Fe (nm2/s)
9.80E-32	3.56E+02	2.09E-01	3.56E+02	0.00E+00	0.00E+00	0.00E+00
1.32E-31	7.24E+02	4.48E-01	7.24E+02	0.00E+00	0.00E+00	0.00E+00
1.62E-31	1.11E+03	6.64E-01	1.11E+03	3.23E-02	1.77E-03	3.23E-02
1.97E-31	1.53E+03	6.64E-01	1.53E+03	1.30E-01	1.77E-03	1.30E-01
2.41E-31	1.96E+03	8.42E-01	1.96E+03	3.00E-01	8.40E-03	3.00E-01
2.95E-31	2.42E+03	1.00E+00	2.42E+03	5.49E-01	1.62E-02	5.49E-01
3.60E-31	2.87E+03	1.00E+00	2.87E+03	8.83E-01	1.62E-02	8.83E-01
4.86E-31	3.33E+03	1.13E+00	3.33E+03	1.32E+00	2.49E-02	1.32E+00
5.93E-31	3.81E+03	1.24E+00	3.81E+03	1.88E+00	3.33E-02	1.88E+00
7.24E-31	4.28E+03	1.24E+00	4.28E+03	2.55E+00	3.33E-02	2.55E+00
8.85E-31	4.72E+03	1.34E+00	4.72E+03	3.37E+00	4.12E-02	3.37E+00
1.08E-30	5.15E+03	1.42E+00	5.15E+03	4.38E+00	4.89E-02	4.38E+00
1.32E-30	5.58E+03	1.42E+00	5.58E+03	5.61E+00	4.89E-02	5.61E+00
1.61E-30	5.97E+03	1.49E+00	5.97E+03	7.04E+00	5.57E-02	7.04E+00
2.18E-30	6.35E+03	1.55E+00	6.35E+03	8.76E+00	6.21E-02	8.76E+00
2.66E-30	6.75E+03	1.55E+00	6.75E+03	1.08E+01	6.21E-02	1.08E+01

3.25E-30	7.07E+03	1.60E+00	7.07E+03	1.30E+01	6.72E-02	1.30E+01
3.97E-30	7.39E+03	1.64E+00	7.39E+03	1.57E+01	7.19E-02	1.57E+01
4.84E-30	7.72E+03	1.64E+00	7.72E+03	1.88E+01	7.19E-02	1.88E+01
5.92E-30	8.03E+03	1.68E+00	8.03E+03	2.22E+01	7.58E-02	2.22E+01
7.99E-30	8.28E+03	1.71E+00	8.28E+03	2.60E+01	7.92E-02	2.60E+01
9.75E-30	8.58E+03	1.71E+00	8.58E+03	3.05E+01	7.92E-02	3.05E+01
1.19E-29	8.86E+03	1.74E+00	8.86E+03	3.55E+01	8.18E-02	3.55E+01
1.46E-29	9.09E+03	1.76E+00	9.09E+03	4.09E+01	8.42E-02	4.09E+01
1.78E-29	9.33E+03	1.76E+00	9.33E+03	4.71E+01	8.42E-02	4.71E+01
2.17E-29	9.58E+03	1.78E+00	9.58E+03	5.40E+01	8.61E-02	5.40E+01
2.93E-29	9.84E+03	1.80E+00	9.84E+03	6.23E+01	8.77E-02	6.23E+01
3.58E-29	1.01E+04	1.80E+00	1.01E+04	7.06E+01	8.77E-02	7.06E+01
4.37E-29	1.04E+04	1.81E+00	1.04E+04	7.94E+01	8.88E-02	7.94E+01
5.34E-29	1.06E+04	1.82E+00	1.06E+04	8.83E+01	8.98E-02	8.83E+01
6.52E-29	1.08E+04	1.82E+00	1.08E+04	9.78E+01	8.98E-02	9.78E+01
7.96E-29	1.10E+04	1.83E+00	1.10E+04	1.08E+02	9.05E-02	1.08E+02
1.08E-28	1.13E+04	1.84E+00	1.13E+04	1.18E+02	9.11E-02	1.18E+02
1.31E-28	1.16E+04	1.84E+00	1.16E+04	1.30E+02	9.11E-02	1.30E+02
1.60E-28	1.19E+04	1.85E+00	1.19E+04	1.39E+02	9.14E-02	1.39E+02
1.96E-28	1.21E+04	1.86E+00	1.21E+04	1.49E+02	9.17E-02	1.49E+02
2.39E-28	1.25E+04	1.86E+00	1.25E+04	1.59E+02	9.17E-02	1.59E+02
2.92E-28	1.28E+04	1.86E+00	1.28E+04	1.66E+02	9.18E-02	1.66E+02
3.57E-28	1.31E+04	1.87E+00	1.31E+04	1.71E+02	9.19E-02	1.71E+02
4.82E-28	1.34E+04	1.87E+00	1.34E+04	1.74E+02	9.20E-02	1.74E+02
5.89E-28	1.38E+04	1.87E+00	1.38E+04	1.75E+02	9.20E-02	1.75E+02
7.19E-28	1.42E+04	1.88E+00	1.42E+04	1.75E+02	9.20E-02	1.75E+02
8.78E-28	1.45E+04	1.88E+00	1.45E+04	1.75E+02	9.20E-02	1.75E+02
1.07E-27	1.49E+04	1.88E+00	1.49E+04	1.74E+02	9.20E-02	1.74E+02
1.31E-27	1.55E+04	1.89E+00	1.55E+04	1.75E+02	9.20E-02	1.75E+02
1.45E-27	1.56E+04	1.89E+00	1.56E+04	1.75E+02	9.20E-02	1.75E+02
1.45E-27	1.56E+04	1.89E+00	1.56E+04	1.75E+02	9.20E-02	1.75E+02
2.16E-27	1.64E+04	1.89E+00	1.64E+04	1.75E+02	9.20E-02	1.75E+02
6.49E-27	2.07E+04	1.90E+00	2.07E+04	1.75E+02	9.20E-02	1.75E+02
1.76E-26	2.94E+04	1.90E+00	2.94E+04	1.75E+02	9.20E-02	1.75E+02
5.30E-26	4.73E+04	1.90E+00	4.73E+04	1.75E+02	9.20E-02	1.75E+02
1.59E-25	8.41E+04	1.90E+00	8.41E+04	1.75E+02	9.20E-02	1.75E+02
4.78E-25	1.60E+05	1.90E+00	1.60E+05	1.75E+02	9.20E-02	1.75E+02
1.44E-24	3.14E+05	1.90E+00	3.14E+05	1.75E+02	9.20E-02	1.75E+02
3.90E-24	6.11E+05	1.90E+00	6.11E+05	1.75E+02	9.20E-02	1.75E+02
1.17E-23	1.34E+06	1.90E+00	1.34E+06	1.75E+02	9.20E-02	1.75E+02
3.52E-23	2.53E+06	1.90E+00	2.53E+06	1.75E+02	9.20E-02	1.75E+02
1.06E-22	5.60E+06	1.90E+00	5.60E+06	1.75E+02	9.20E-02	1.75E+02
3.18E-22	1.07E+07	1.90E+00	1.07E+07	1.75E+02	9.20E-02	1.75E+02

8.64E-22	2.36E+07	1.90E+00	2.36E+07	1.75E+02	9.20E-02	1.75E+02
2.60E-21	4.87E+07	1.90E+00	4.87E+07	1.75E+02	9.20E-02	1.75E+02
5.23E-21	7.59E+07	1.90E+00	7.59E+07	1.75E+02	9.20E-02	1.75E+02
5.23E-21	7.59E+07	1.90E+00	7.59E+07	1.75E+02	9.20E-02	1.75E+02
7.80E-21	9.86E+07	1.90E+00	9.86E+07	1.74E+02	9.20E-02	1.74E+02
2.34E-20	1.79E+08	1.90E+00	1.79E+08	1.74E+02	9.20E-02	1.74E+02
7.04E-20	2.95E+08	1.90E+00	2.95E+08	1.75E+02	9.20E-02	1.75E+02
1.91E-19	4.72E+08	1.90E+00	4.72E+08	1.74E+02	9.20E-02	1.74E+02
3.16E-19	0.00E+00	1.90E+00	0.00E+00	-	-	-
3.16E-19	0.00E+00	1.90E+00	0.00E+00	-	-	-
5.75E-19	0.00E+00	1.90E+00	0.00E+00	-	-	-
1.73E-18	0.00E+00	1.90E+00	0.00E+00	-	-	-
5.19E-18	0.00E+00	1.90E+00	0.00E+00	-	-	-
1.56E-17	0.00E+00	1.90E+00	0.00E+00	-	-	-
4.24E-17	0.00E+00	1.90E+00	0.00E+00	-	-	-
1.27E-16	0.00E+00	1.90E+00	0.00E+00	-	-	-
3.82E-16	0.00E+00	1.90E+00	0.00E+00	-	-	-
1.40E-15	0.00E+00	1.90E+00	0.00E+00	-	-	-
1.71E-15	0.00E+00	1.90E+00	0.00E+00	-	-	-
2.09E-15	0.00E+00	1.90E+00	0.00E+00	-	-	-
2.56E-15	0.00E+00	1.90E+00	0.00E+00	-	-	-
3.45E-15	0.00E+00	1.90E+00	0.00E+00	-	-	-
4.22E-15	0.00E+00	1.90E+00	0.00E+00	-	-	-
5.15E-15	0.00E+00	1.90E+00	0.00E+00	-	-	-
6.29E-15	0.00E+00	1.90E+00	0.00E+00	-	-	-
7.68E-15	0.00E+00	1.90E+00	0.00E+00	-	-	-
9.38E-15	0.00E+00	1.90E+00	0.00E+00	-	-	-
1.27E-14	0.00E+00	1.90E+00	0.00E+00	-	-	-
1.55E-14	0.00E+00	1.90E+00	0.00E+00	-	-	-
1.89E-14	0.00E+00	1.90E+00	0.00E+00	-	-	-
2.31E-14	0.00E+00	1.90E+00	0.00E+00	-	-	-
2.82E-14	0.00E+00	1.90E+00	0.00E+00	-	-	-
3.44E-14	0.00E+00	1.90E+00	0.00E+00	-	-	-
4.21E-14	0.00E+00	1.90E+00	0.00E+00	-	-	-
5.68E-14	0.00E+00	1.90E+00	0.00E+00	-	-	-
6.93E-14	0.00E+00	1.90E+00	0.00E+00	-	-	-
8.47E-14	0.00E+00	1.90E+00	0.00E+00	-	-	-
1.03E-13	0.00E+00	1.90E+00	0.00E+00	-	-	-
1.26E-13	0.00E+00	1.90E+00	0.00E+00	-	-	-
1.54E-13	0.00E+00	1.90E+00	0.00E+00	-	-	-
2.08E-13	0.00E+00	1.90E+00	0.00E+00	-	-	-
2.54E-13	0.00E+00	1.90E+00	0.00E+00	-	-	-
3.11E-13	0.00E+00	1.90E+00	0.00E+00	-	-	-

3.80E-13	0.00E+00	1.90E+00	0.00E+00	-	-	-
4.64E-13	0.00E+00	1.90E+00	0.00E+00	-	-	-
5.66E-13	0.00E+00	1.90E+00	0.00E+00	-	-	-
7.64E-13	0.00E+00	1.90E+00	0.00E+00	-	-	-
9.33E-13	0.00E+00	1.90E+00	0.00E+00	-	-	-
1.14E-12	0.00E+00	1.90E+00	0.00E+00	-	-	-
1.39E-12	0.00E+00	1.90E+00	0.00E+00	-	-	-
1.70E-12	0.00E+00	1.90E+00	0.00E+00	-	-	-
2.08E-12	0.00E+00	1.90E+00	0.00E+00	-	-	-
2.80E-12	0.00E+00	1.91E+00	0.00E+00	-	-	-
3.43E-12	0.00E+00	1.91E+00	0.00E+00	-	-	-
4.18E-12	0.00E+00	1.91E+00	0.00E+00	-	-	-
5.11E-12	0.00E+00	1.91E+00	0.00E+00	-	-	-
6.24E-12	0.00E+00	1.91E+00	0.00E+00	-	-	-
7.62E-12	0.00E+00	1.91E+00	0.00E+00	-	-	-
9.31E-12	0.00E+00	1.91E+00	0.00E+00	-	-	-
1.26E-11	0.00E+00	1.91E+00	0.00E+00	-	-	-
1.54E-11	0.00E+00	1.91E+00	0.00E+00	-	-	-
1.88E-11	0.00E+00	1.91E+00	0.00E+00	-	-	-
2.29E-11	0.00E+00	1.91E+00	0.00E+00	-	-	-
2.80E-11	0.00E+00	1.91E+00	0.00E+00	-	-	-
3.42E-11	0.00E+00	1.91E+00	0.00E+00	-	-	-
4.61E-11	0.00E+00	1.91E+00	0.00E+00	-	-	-
5.63E-11	0.00E+00	1.91E+00	0.00E+00	-	-	-
6.88E-11	0.00E+00	1.91E+00	0.00E+00	-	-	-
8.40E-11	0.00E+00	1.91E+00	0.00E+00	-	-	-
1.03E-10	0.00E+00	1.91E+00	0.00E+00	-	-	-
1.25E-10	0.00E+00	1.91E+00	0.00E+00	-	-	-
1.69E-10	0.00E+00	1.91E+00	0.00E+00	-	-	-
2.07E-10	0.00E+00	1.91E+00	0.00E+00	-	-	-
2.52E-10	0.00E+00	1.91E+00	0.00E+00	-	-	-
3.08E-10	0.00E+00	1.91E+00	0.00E+00	-	-	-
3.77E-10	0.00E+00	1.91E+00	0.00E+00	-	-	-
6.21E-10	0.00E+00	1.91E+00	0.00E+00	-	-	-
7.58E-10	0.00E+00	1.91E+00	0.00E+00	-	-	-
9.26E-10	0.00E+00	1.91E+00	0.00E+00	-	-	-
1.13E-09	0.00E+00	1.91E+00	0.00E+00	-	-	-
1.38E-09	0.00E+00	1.91E+00	0.00E+00	-	-	-
1.69E-09	0.00E+00	1.91E+00	0.00E+00	-	-	-
2.06E-09	0.00E+00	1.91E+00	0.00E+00	-	-	-
2.78E-09	0.00E+00	1.91E+00	0.00E+00	-	-	-
3.40E-09	0.00E+00	1.91E+00	0.00E+00	-	-	-
4.15E-09	0.00E+00	1.91E+00	0.00E+00	-	-	-

5.07E-09	0.00E+00	1.91E+00	0.00E+00	-	-	-
6.19E-09	0.00E+00	1.91E+00	0.00E+00	-	-	-
7.56E-09	0.00E+00	1.91E+00	0.00E+00	-	-	-
1.02E-08	0.00E+00	1.91E+00	0.00E+00	-	-	-
1.25E-08	0.00E+00	1.91E+00	0.00E+00	-	-	-
1.52E-08	0.00E+00	1.91E+00	0.00E+00	-	-	-
1.86E-08	0.00E+00	1.91E+00	0.00E+00	-	-	-
2.27E-08	0.00E+00	1.91E+00	0.00E+00	-	-	-
2.78E-08	0.00E+00	1.91E+00	0.00E+00	-	-	-
3.75E-08	0.00E+00	1.91E+00	0.00E+00	-	-	-
4.58E-08	0.00E+00	1.91E+00	0.00E+00	-	-	-
5.59E-08	0.00E+00	1.91E+00	0.00E+00	-	-	-
6.83E-08	0.00E+00	1.91E+00	0.00E+00	-	-	-
8.34E-08	0.00E+00	1.91E+00	0.00E+00	-	-	-
1.02E-07	0.00E+00	1.91E+00	0.00E+00	-	-	-
1.38E-07	0.00E+00	1.91E+00	0.00E+00	-	-	-
1.68E-07	0.00E+00	1.91E+00	0.00E+00	-	-	-
2.05E-07	0.00E+00	1.91E+00	0.00E+00	-	-	-
2.51E-07	0.00E+00	1.91E+00	0.00E+00	-	-	-
3.06E-07	0.00E+00	1.91E+00	0.00E+00	-	-	-
3.74E-07	0.00E+00	1.91E+00	0.00E+00	-	-	-
4.56E-07	0.00E+00	1.91E+00	0.00E+00	-	-	-
6.16E-07	0.00E+00	1.91E+00	0.00E+00	-	-	-
7.52E-07	0.00E+00	1.91E+00	0.00E+00	-	-	-
9.19E-07	0.00E+00	1.91E+00	0.00E+00	-	-	-
1.12E-06	0.00E+00	1.91E+00	0.00E+00	-	-	-
1.37E-06	0.00E+00	1.91E+00	0.00E+00	-	-	-
1.67E-06	0.00E+00	1.92E+00	0.00E+00	-	-	-
2.26E-06	0.00E+00	1.92E+00	0.00E+00	-	-	-
2.76E-06	0.00E+00	1.92E+00	0.00E+00	-	-	-
3.37E-06	0.00E+00	1.92E+00	0.00E+00	-	-	-
4.12E-06	0.00E+00	1.92E+00	0.00E+00	-	-	-
5.03E-06	0.00E+00	1.92E+00	0.00E+00	-	-	-
6.14E-06	0.00E+00	1.92E+00	0.00E+00	-	-	-
8.29E-06	0.00E+00	1.92E+00	0.00E+00	-	-	-
1.01E-05	0.00E+00	1.92E+00	0.00E+00	-	-	-
1.24E-05	0.00E+00	1.92E+00	0.00E+00	-	-	-
1.51E-05	0.00E+00	1.92E+00	0.00E+00	-	-	-
1.85E-05	0.00E+00	1.92E+00	0.00E+00	-	-	-
2.25E-05	0.00E+00	1.92E+00	0.00E+00	-	-	-
3.04E-05	0.00E+00	1.92E+00	0.00E+00	-	-	-
3.72E-05	0.00E+00	1.92E+00	0.00E+00	-	-	-
4.54E-05	0.00E+00	1.92E+00	0.00E+00	-	-	-

5.55E-05	0.00E+00	1.92E+00	0.00E+00	-	-	-
6.91E-05	0.00E+00	1.93E+00	0.00E+00	-	-	-
8.52E-05	0.00E+00	1.93E+00	0.00E+00	-	-	-
1.06E-04	0.00E+00	1.93E+00	0.00E+00	-	-	-
1.31E-04	0.00E+00	1.93E+00	0.00E+00	-	-	-
1.63E-04	0.00E+00	1.93E+00	0.00E+00	-	-	-
2.04E-04	0.00E+00	1.93E+00	0.00E+00	-	-	-
2.51E-04	0.00E+00	1.93E+00	0.00E+00	-	-	-
3.13E-04	0.00E+00	1.93E+00	0.00E+00	-	-	-
3.86E-04	0.00E+00	1.93E+00	0.00E+00	-	-	-
4.81E-04	0.00E+00	1.93E+00	0.00E+00	-	-	-
5.99E-04	0.00E+00	1.93E+00	0.00E+00	-	-	-
7.39E-04	0.00E+00	1.94E+00	0.00E+00	-	-	-
9.21E-04	0.00E+00	1.94E+00	0.00E+00	-	-	-
1.14E-03	0.00E+00	1.94E+00	0.00E+00	-	-	-
1.42E-03	0.00E+00	1.94E+00	0.00E+00	-	-	-
1.76E-03	0.00E+00	1.94E+00	0.00E+00	-	-	-
2.18E-03	0.00E+00	1.94E+00	0.00E+00	-	-	-
2.71E-03	0.00E+00	1.94E+00	0.00E+00	-	-	-
3.35E-03	0.00E+00	1.94E+00	0.00E+00	-	-	-
4.17E-03	0.00E+00	1.95E+00	0.00E+00	-	-	-
5.20E-03	0.00E+00	1.95E+00	0.00E+00	-	-	-
6.41E-03	0.00E+00	1.95E+00	0.00E+00	-	-	-
7.99E-03	0.00E+00	1.95E+00	0.00E+00	-	-	-
9.85E-03	0.00E+00	1.95E+00	0.00E+00	-	-	-
1.23E-02	0.00E+00	1.95E+00	0.00E+00	-	-	-
1.53E-02	0.00E+00	1.96E+00	0.00E+00	-	-	-
1.89E-02	0.00E+00	1.96E+00	0.00E+00	-	-	-
2.35E-02	0.00E+00	1.96E+00	0.00E+00	-	-	-
2.90E-02	0.00E+00	1.96E+00	0.00E+00	-	-	-
3.62E-02	0.00E+00	1.96E+00	0.00E+00	-	-	-
4.51E-02	0.00E+00	1.97E+00	0.00E+00	-	-	-
5.56E-02	0.00E+00	1.97E+00	0.00E+00	-	-	-
6.93E-02	0.00E+00	1.97E+00	0.00E+00	-	-	-
8.54E-02	0.00E+00	1.97E+00	0.00E+00	-	-	-
1.07E-01	0.00E+00	1.98E+00	0.00E+00	-	-	-
1.33E-01	0.00E+00	1.98E+00	0.00E+00	-	-	-
1.35E-01	0.00E+00	1.98E+00	0.00E+00	-	-	-

Appendix D

Derivation of the Parabolic Rate Law

One basic premise of the parabolic rate law is that the corrosion reaction is limited by the transport of reactants across a barrier oxide film. Therefore, the flux of some specie A is proportional to the oxide film growth rate:

$$\mathrm{J_A} = \mathrm{f_g} N_A^g \frac{\mathrm{d}x}{\mathrm{d}t} \qquad \text{Eq. D.1}$$

where x is the thickness of the corrosion product film, t is time, J_A is the flux of specie A through the barrier layer, f_g is the fraction of the total oxide volume which depends on the flux to grow, and N_A^g is the number density of A in the growing oxide layer, g. The number density depends on the identity of A and the stoichiometry of the oxide:

$$\mathrm{M}_a\mathrm{O}_b \qquad \text{Eq. D.2}$$

$$N_{\mathrm{M}}^g = \frac{a\rho_g}{M_g} \qquad \text{Eq. D.3}$$

$$N_{\mathrm{O}}^g = \frac{b\rho_g}{M_g} \qquad \text{Eq. D.4}$$

where ρ is the mass density of the oxide and M is the molecular weight of the oxide with subscripts denoting the oxide layer.

The flux within the barrier oxide layer is described by Fick's first law:

$$J_A = -D_A^b \nabla C_A^b \qquad \text{Eq. D.5}$$

where D_A is the diffusion coefficient of element A in the barrier oxide, b, and C_A is the concentration of A. For corrosion reactions, it is more useful to describe the driving force in terms of chemical potential rather than concentration gradient:

$$\mu_A = \mu_A^0 + \mathrm{RT}\ln\left(C_A^b\right) \quad \text{Eq. D.6}$$

where μ_A is the chemical potential of species A, μ_A^0 is the standard chemical potential, R is the universal gas constant, and T is the absolute temperature. The left side of the equation can be differentiated with respect to chemical potential, and the right to concentration:

$$\mathrm{d}\mu_A = \frac{RT}{C_A^b}\mathrm{d}C_A^b \quad \text{Eq. D.7}$$

This result can be used to transform Fick's first law into a more general form as below.

$$J_A = -D_A^b \frac{C_A^b}{RT}\nabla\mu_A \quad \text{Eq. D.8}$$

Then, evaluating the gradient operator on chemical potential as one-dimensional with depth yields:

$$J_A = -\frac{\mathrm{D_A^b}C_A^b}{\mathrm{f_b RT}}\frac{\mathrm{d}\mu_A}{\mathrm{d}x} \quad \text{Eq. D.9}$$

where f_b is the fraction of the total oxide volume that serves as a barrier to the flux. One assumption made at this point is that the transport is pseudo steady-state; the flux is constant across the barrier layer and is therefore independent of x. A simple separation of variables yields a definite integral across the oxide film from a reference state μ_A^1 at the metal/oxide interface to the state μ_A^2 at the environment.

$$J_A = -\frac{1}{x}\int_{\mu_A^1}^{\mu_A^2}\frac{\mathrm{D_A^b}C_A^b}{\mathrm{f_b RT}}\mathrm{d}\mu_A \quad \text{Eq. D.10}$$

Both expressions of the flux in Eq. D.1 and Eq. D.10 can be equated to yield an ordinary differential equation. By collecting the integral and all variables other than x, as the parabolic rate constant, k_p, the familiar form of the parabolic law is obtained as the analytical solution to the differential equation, and an expression for the parabolic rate constant is obtained:

$$\frac{\mathrm{d}x}{\mathrm{d}t} = \frac{k_p}{x} \qquad \text{Eq. D.11}$$

$$x^2 = k_p t \qquad \text{Eq. D.12}$$

$$k_p = -\frac{1}{f_b f_g N_A^g} \int_{\mu_A^1}^{\mu_A^2} \frac{\mathrm{D_A^b} C_A^b}{\mathrm{RT}} \mathrm{d}\mu_A \qquad \text{Eq. D.13}$$

References

[1] A.J. Jarvis, J.F. Giannelli, B. Gordon, D. Segletes, Impact of corrosion of nickel based coatings for flow accelerated corrosion control on BWR radiation fields, 19th Int. Conf. Environ. Degrad. Mater. Nucl. Power Syst. - Water React. EnvDeg 2019. (2019) 199–206.

[2] American Society for Testing and Materials, ASTM A240: Standard Specification for Chromium and Chromium-Nickel Stainless Steel Plate, Sheet, and Strip for Pressure Vessels and for General Applications, ASTM Int. I (2004) 12. https://doi.org/10.1520/A0240.

[3] A.J. Sedriks, Corrosion of Stainless Steel, 2nd ed., 1996.

[4] P.J. Maziasz, J.T. Busby, Properties of Austenitic Steels for Nuclear Reactor Applications, in: R.J.M. Konings (Ed.), Compr. Nucl. Mater., Elsevier, Oxford, 2012: pp. 267–283. https://doi.org/10.1016/B978-0-08-056033-5.00019-7.

[5] U. Ehrnstén, Corrosion and stress corrosion cracking of austenitic stainless steels, Compr. Nucl. Mater. 5 (2012) 93–104. https://doi.org/10.1016/B978-0-08-056033-5.00080-X.

[6] R.P. Matthews, R.D. Knusten, J.E. Westraadt, T. Couvant, Intergranular oxidation of 316L stainless steel in the PWR primary water environment, Corros. Sci. 125 (2017) 175–183. https://doi.org/10.1016/j.corsci.2017.06.023.

[7] S. Cissé, L. Laffont, B. Tanguy, M.C. Lafont, E. Andrieu, Effect of surface preparation on the corrosion of austenitic stainless steel 304L in high temperature steam and simulated PWR primary water, Corros. Sci. 56 (2012) 209–216. https://doi.org/10.1016/j.corsci.2011.12.007.

[8] T. Maekawa, M. Kagawa, N. Nakajima, Corrosion Behaviors of Stainless Steel in High-Temperature Water and Superheated Steam, Trans. Japan Inst. Met. 9 (1968) 130–136. https://doi.org/10.2320/matertrans1960.9.130.

[9] J. Robertson, The mechanism of high temperature aqueous corrosion of stainless steels, Corros. Sci. 32 (1991) 443–465. https://doi.org/10.1016/0010-938X(91)90125-9.

[10] M. Warzee, J. Hennaut, M. Maurice, C. Sonnen, J. Waty, P. Berge, Effect of Surface Treatment on the Corrosion of Stainless Steels in High-Temperature Water and Steam, J. Electrochem. Soc. 112 (1965) 670. https://doi.org/10.1149/1.2423661.

[11] S. Wang, Y. Hu, K. Fang, W. Zhang, X. Wang, Effect of surface machining on the

corrosion behaviour of 316 austenitic stainless steel in simulated PWR water, Corros. Sci. 126 (2017) 104–120. https://doi.org/10.1016/j.corsci.2017.06.019.

[12] S.E. Ziemniak, M. Hanson, P.C. Sander, Electropolishing effects on corrosion behavior of 304 stainless steel in high temperature, hydrogenated water, Corros. Sci. 50 (2008) 2465–2477. https://doi.org/10.1016/j.corsci.2008.06.032.

[13] F. Scenini, J. Lindsay, L. Chang, Y.L. Wang, M.G. Burke, S. Lozano-Perez, G. Pimentel, D. Tice, K. Mottershead, V. Addepalli, Oxidation and SCC Initiation Studies of Type 304L SS in PWR Primary Water, in: J.H. Jackson, D. Paraventi, M. Wright (Eds.), Proc. 18th Int. Conf. Environ. Degrad. Mater. Nucl. Power Syst. - Water React., TMS, Portland, Oregon, USA, 2017: pp. 793–810. https://doi.org/10.1007/978-3-030-04639-2_51.

[14] R. Riess, N.P.C. Neunkirchen, F.P. Ford, LCC-2 Annual Report, (n.d.).

[15] C.J. Wood, Water Chemistry Control in LWRs, in: Compr. Nucl. Mater., Elsevier, 2012: pp. 17–47. https://doi.org/10.1016/B978-0-08-056033-5.00082-3.

[16] R. Cochran, N. Tsoulfanidis, The Nuclear Fuel Cycle: Analysis and Management, American Nuclear Society, 1999.

[17] P.L. Andresen, G.S. Was, Irradiation assisted stress corrosion cracking, Elsevier Inc., 2012. https://doi.org/10.1016/B978-0-08-056033-5.00084-7.

[18] P. Andresen, J. Hickling, K. Ahluwalia, J. Wilson, Effects of PWR Primary Water Chemistry on PWSCC of Ni Alloys, in: Proc. 13th Int. Conf. Environ. Degrad. Mater. Nucl. Power Syst. — Water React., Candian Nuclear Society, 2007.

[19] T.A. Lang, Significant Corrosion of the Davis-Besse Nuclear Reactor Pressure Vessel Head, in: Proceesings 2003 ASME Press. Vessel. Pip. Conf., 2003: pp. 1–8.

[20] H.B. Lee, J. Chen, S. Meng, C. Jang, S.H. Park, Q. Xiao, H.J. Lee, K.H. Na, Characterization of oxide layers formed on type 316 stainless steel exposed to the simulated PWR primary water environment with varying dissolved hydrogen and zinc concentrations, J. Nucl. Mater. 556 (2021) 153193. https://doi.org/10.1016/j.jnucmat.2021.153193.

[21] D.H.H. Lister, R.D.D. Davidson, E. McAlpine, The mechanism and kinetics of corrosion product release from stainless steel in lithiated high temperature water, Corros. Sci. 27 (1987) 113–140. https://doi.org/10.1016/0010-938X(87)90068-0.

[22] S.S. Raiman, D.M. Bartels, G.S. Was, Radiolysis driven changes to oxide stability during irradiation-corrosion of 316L stainless steel in high temperature water, J. Nucl. Mater. 493 (2017) 40–52. https://doi.org/10.1016/j.jnucmat.2017.05.042.

[23] J. Robertson, The mechanism of high temperature aqueous corrosion of steel, Corros. Sci. 29 (1989) 1275–1291. https://doi.org/10.1016/0010-938X(89)90120-0.

[24] B. Stellwag, The mechanism of oxide film formation on austenitic stainless steels in high temperature water, Corros. Sci. 40 (1998) 337–370. https://doi.org/10.1016/S0010-938X(97)00140-6.

[25] Y.-J. Kim, Characterization of the Oxide Film Formed on Type 316 Stainless Steel in 288°C Water in Cyclic Normal and Hydrogen Water Chemistries, Corrosion. 51 (1995) 849–860. https://doi.org/10.5006/1.3293562.

[26] Y.-J. Kim, Analysis of Oxide Film Formed on Type 304 Stainless Steel in 288°C Water Containing Oxygen, Hydrogen, and Hydrogen Peroxide, Corrosion. 55 (1999) 81–88. https://doi.org/10.5006/1.3283969.

[27] M. da Cunha Belo, M. Walls, N.E. Hakiki, J. Corset, E. Picquenard, G. Sagon, D. Noël, Composition, structure and properties of the oxide films formed on the stainless steel 316L in a primary type PWR environment, Corros. Sci. 40 (1998) 447–463. https://doi.org/10.1016/S0010-938X(97)00158-3.

[28] T. Cui, J. Ma, F. Ning, Z. Lu, K. Zhang, Y. Jia, T. Shoji, Coupling Effect of Charged-Hydrogen and Cold Work on Oxidation Behavior of 316L Stainless Steel in Deaerated High Temperature Water, in: 19th Int. Conf. Environ. Degrad. Mater. Nucl. Power Syst. - Water React., American Nuclear Society, Boston, 2019: pp. 810–823.

[29] L. Dong, Q. Peng, Z. Zhang, T. Shoji, E.-H. Han, W. Ke, L. Wang, Effect of dissolved hydrogen on corrosion of 316NG stainless steel in high temperature water, Nucl. Eng. Des. 295 (2015) 403–414. https://doi.org/10.1016/j.nucengdes.2015.08.030.

[30] J. Gupta, Intergranular Stress Corrosion Cracking of Ion Irradiated 304L Stainless Steel in PWR Environment, University of Toulouse, 2016.

[31] K. Ishida, D. Lister, In situ measurement of corrosion of type 316L stainless steel in 553 K pure water via the electrical resistance of a thin wire, J. Nucl. Sci. Technol. 49 (2012) 1078–1091. https://doi.org/10.1080/00223131.2012.730899.

[32] T. Terachi, K. Fujii, K. Arioka, Microstructural characterization of SCC crack tip and oxide film for SUS 316 stainless steel in simulated PWR primary water at 320°C, J. Nucl. Sci. Technol. 42 (2005) 225–232. https://doi.org/10.1080/18811248.2005.9726383.

[33] T. Terachi, T. Yamada, T. Miyamoto, K. Arioka, K. Fukuya, Corrosion Behavior of Stainless Steels in Simulated PWR Primary Water—Effect of Chromium Content in Alloys and Dissolved Hydrogen—, J. Nucl. Sci. Technol. 45 (2008) 975–984. https://doi.org/10.1080/18811248.2008.9711883.

[34] X. Lin, Q. Peng, J. Mei, E.H. Han, W. Ke, L. Qiao, Z. Jiao, Corrosion of phase and phase boundary in proton-irradiated 308L stainless steel weld metal in simulated PWR primary water, Corros. Sci. 165 (2020) 108401. https://doi.org/10.1016/j.corsci.2019.108401.

[35] R. Soulas, M. Cheynet, E. Rauch, T. Neisius, L. Legras, C. Domain, Y. Brechet, TEM investigations of the oxide layers formed on a 316L alloy in simulated PWR environment,

J. Mater. Sci. 48 (2013) 2861–2871.

[36] M. Boisson, L. Legras, E. Andrieu, L. Laffont, Role of irradiation and irradiation defects on the oxidation first stages of a 316L austenitic stainless steel, Corros. Sci. 161 (2019) 108194. https://doi.org/10.1016/j.corsci.2019.108194.

[37] W. Kuang, X. Wu, E.-H. Han, L. Ruan, Effect of nickel ion from autoclave material on oxidation behaviour of 304 stainless steel in oxygenated high temperature water, Corros. Sci. 53 (2011) 1107–1114. https://doi.org/10.1016/j.corsci.2010.12.008.

[38] Z. Shen, D. Tweddle, H. Yu, G. He, A. Varambhia, P. Karamched, F. Hofmann, A.J. Wilkinson, M.P. Moody, L. Zhang, S. Lozano-Perez, Microstructural understanding of the oxidation of an austenitic stainless steel in high-temperature steam through advanced characterization, Acta Mater. 194 (2020) 321–336. https://doi.org/10.1016/j.actamat.2020.05.010.

[39] F. Rouillard, G. Moine, L. Martinelli, J.C. Ruiz, Corrosion of 9Cr steel in CO 2 at intermediate temperature I: Mechanism of void-induced duplex oxide formation, Oxid. Met. 77 (2012) 27–55. https://doi.org/10.1007/s11085-011-9271-5.

[40] K. Kruska, S. Lozano-Perez, D.W. Saxey, T. Terachi, T. Yamada, G.D.W. Smith, Nanoscale characterisation of grain boundary oxidation in cold-worked stainless steels, Corros. Sci. 63 (2012) 225–233. https://doi.org/10.1016/j.corsci.2012.06.030.

[41] N. Otsuka, Y. Shida, H. Fujikawa, Internal-external transition for the oxidation of Fe-Cr-Ni austenitic stainless steels in steam, Oxid. Met. 32 (1989) 13–45. https://doi.org/10.1007/BF00665267.

[42] J. Sumner, N. Simms, A. Shin, J. Pearson, Kinetics of Duplex Oxide Growth on 9Cr Steels Exposed in CO2: Application of Dimensional Metrology, Oxid. Met. 87 (2017) 617–629. https://doi.org/10.1007/s11085-017-9766-9.

[43] S. Perrin, L. Marchetti, C. Duhamel, M. Sennour, F. Jomard, Influence of irradiation on the oxide film formed on 316 L stainless steel in PWR primary water, Oxid. Met. 80 (2013) 623–633. https://doi.org/10.1007/s11085-013-9401-3.

[44] S.E. Ziemniak, M. Hanson, Corrosion behavior of 304 stainless steel in high temperature, hydrogenated water, Corros. Sci. 44 (2002) 2209–2230. https://doi.org/10.1016/S0010-938X(02)00004-5.

[45] P. Atkins, J. de Paula, Atkins' Physical Chemistry, 9th ed., OUP Oxford, 2010.

[46] W.G. Cook, R.P. Olive, Pourbaix diagrams for the iron–water system extended to high-subcritical and low-supercritical conditions, Corros. Sci. 55 (2012) 326–331. https://doi.org/10.1016/j.corsci.2011.10.034.

[47] V.A. Kurepin, D.A. Kulik, A. Hiltpold, M. Nicolet, Thermodynamic modelling of Fe-Cr-Ni spinel formation at the light-water reactor conditions, Bericht/Paul Scherrer Inst. 2

(2002) 4.

[48] B. Beverskog, Revised Diagrams for Iron At 25-300 ° C, Science (80-.). 38 (1996) 2121–2135. http://www.sciencedirect.com/science/article/pii/S0010938X96000674.

[49] B. Beverskog, I. Puigdomenech, Revised pourbaix diagrams for chromium at 25-300°C, Corros. Sci. 39 (1997) 43–57. https://doi.org/10.1016/S0010-938X(97)89244-X.

[50] B. Beverskog, I. Puigdomenech, Revised Pourbaix diagrams for nickel at 25-300°c, Corros. Sci. 39 (1997) 969–980. https://doi.org/10.1016/S0010-938X(97)00002-4.

[51] B. Beverskog, I. Puigdomenech, Pourbaix diagrams for the ternary system of iron-chromium-nickel, Corrosion. 55 (1999) 1077–1087. https://doi.org/10.5006/1.3283945.

[52] K.E. Sickafus, J.M. Wills, N.W. Grimes, Structure of spinel, J. Am. Ceram. Soc. 82 (1999) 3279–3292. https://doi.org/10.1111/j.1151-2916.1999.tb02241.x.

[53] G.C. Allen, J.M. Dyke, S.J. Harris, A. Morris, A surface study of the oxidation of type 304L stainless steel at 600 K in air, Oxid. Met. 29 (1988) 391–408. https://doi.org/10.1007/BF00666841.

[54] R. Dieckmann, H. Schmalzried, Defects and Cation Diffusion in Magnetite (I), Berichte Der Bunsengesellschaft Für Phys. Chemie. 81 (1977) 344–347. https://doi.org/10.1002/bbpc.19770810320.

[55] R. Dieckmann, M.R. Hilton, T.O. Mason, Defects and Cation Diffusion in Magnetite (Viii): Migration Enthalpies for Iron and Impurity Cations., Berichte Der Bunsengesellschaft/Physical Chem. Chem. Phys. 91 (1987) 59–66. https://doi.org/10.1002/bbpc.19870910113.

[56] J. Töpfer, S. Aggarwal, R. Dieckmann, Point defects and cation tracer diffusion in (CrxFe1 - x)3 - δO4 spinels, Solid State Ionics. 81 (1995) 251–266. https://doi.org/10.1016/0167-2738(95)00190-H.

[57] L.K. Moleko, A.R. Allnatt, E.L. Allnatt, A self-consistent theory of matter transport in a random lattice gas and some simulation results, Philos. Mag. A Phys. Condens. Matter, Struct. Defects Mech. Prop. 59 (1989) 141–160. https://doi.org/10.1080/01418618908220335.

[58] I. V. Belova, G.E. Murch, Tracer correlation factors in the random alloy, Philos. Mag. A Phys. Condens. Matter, Struct. Defects Mech. Prop. 80 (2000) 1469–1479. https://doi.org/10.1080/01418610008212131.

[59] J.E. Castle, P.L. Surman, The self-diffusion of oxygen in magnetite. The effect of anion vacancy concentration and cation distribution, J. Phys. Chem. 73 (1969) 632–634. https://doi.org/10.1021/j100723a025.

[60] F. Millot, J. Lorin, B. Klossa, Y. Niu, J. Tarento, Oxygen Self-Diffusion in Fe, O.: An

Experimental Example of Interactions Between Defects, Ber Bunsenges Phys Chem. 101 (1997) 1351–1354.

[61] B.J. Giletti, K.C. Hess, Oxygen diffusion in magnetite, Earth Planet. Sci. Lett. 89 (1988) 115–122. https://doi.org/10.1016/0012-821X(88)90037-4.

[62] C. Xu, W. Gao, Pilling-Bedworth ratio for oxidation of alloys, Mater. Res. Innov. 3 (2000) 231–235. https://doi.org/10.1007/s100190050008.

[63] J.E. Castle, P.L. Surman, Gas phase transport in the oxidation of Fe and steel, Corros. Sci. 9 (1969). http://www.sciencedirect.com/science/article/pii/S0010938X69800831.

[64] M.R. Taylor, J.M. Calvert, D.G. Lees, D.B. Meadowcroft, The mechanism of corrosion of Fe-9%Cr alloys in carbon dioxide, Oxid. Met. 14 (1980) 499–516. https://doi.org/10.1007/BF00603476.

[65] A. Atkinson, Transport processes during the growth of oxide films at elevated temperature, Rev. Mod. Phys. 57 (1985) 437–470. https://doi.org/10.1103/RevModPhys.57.437.

[66] F. Rouillard, L. Martinelli, Corrosion of 9Cr steel in CO 2 at intermediate temperature III: Modelling and simulation of void-induced duplex oxide growth, Oxid. Met. 77 (2012) 71–83. https://doi.org/10.1007/s11085-011-9273-3.

[67] E.J. Verwey, P.W. Haayman, F.C. Romeijn, Physical properties and cation arrangement of oxides with spinel structures II. Electronic conductivity, J. Chem. Phys. 15 (1947) 181–187. https://doi.org/10.1063/1.1746466.

[68] D. Laverde, T. Gómez-Acebo, F. Castro, Continuous and cyclic oxidation of T91 ferritic steel under steam, Corros. Sci. 46 (2004) 613–631. https://doi.org/10.1016/S0010-938X(03)00173-2.

[69] C. Wagner, Formation of Composite Scales Consisting of Oxides of Different Metals, J. Electrochem. Soc. 103 (1956) 627. https://doi.org/10.1149/1.2430176.

[70] I.G. Wright, R.B. Dooley, A review of the oxidation behaviour of structural alloys in steam, Int. Mater. Rev. 55 (2010) 129–167. https://doi.org/10.1179/095066010X12646898728165.

[71] Z. Jiao, G.S. Was, Oxidation of a Proton-Irradiated 316 Stainless Steel in Simulated BWR NWC Environment, in: Proc. 15th Int. Conf. Environ. Degrad. Mater. Nucl. Power Syst. — Water React., Springer International Publishing, Cham, 2011: pp. 1329–1338. https://doi.org/10.1007/978-3-319-48760-1_81.

[72] M. Wang, Electrochemical Behaviour of Stainless Steel under Radiation and Exposed to Representative Chemistry in Pressurised Water Reactor Conditions., (2013).

[73] Y. Chimi, Y. Kitsunai, S. Kasahara, K. Chatani, M. Koshiishi, Y. Nishiyama, Correlation

between locally deformed structure and oxide film properties in austenitic stainless steel irradiated with neutrons, J. Nucl. Mater. 475 (2016) 71–80. https://doi.org/10.1016/j.jnucmat.2016.03.024.

[74] Y. Murayama, T. Satoh, S. Uchida, Y. Satoh, S. Nagata, T. Satoh, Y. Wada, M. Tachibana, Effects of hydrogen peroxide on intergranular stress corrosion cracking of stainless steel in high temperature water, (V): Characterization of oxide film on stainless steel by multilateral surface analyses, J. Nucl. Sci. Technol. 39 (2002) 1199–1206. https://doi.org/10.1080/18811248.2002.9715311.

[75] C.F. Perry, P. Zhang, F.B. Nunes, I. Jordan, A. Von Conta, H.J. Wörner, Ionization Energy of Liquid Water Revisited, J. Phys. Chem. Lett. 11 (2020) 1789–1794. https://doi.org/10.1021/acs.jpclett.9b03391.

[76] 1996 (2009) ASTM Standard E521, Standard Practice for Neutron Radiation Damage Simulation by Charged-Particle, ASTM International, West Conshohocken, PA, 2009. https://doi.org/10.1520/E0521-96R09E02.Copyright.

[77] F.A. Garner, Radiation damage in austenitic steels, Elsevier Inc., 2012. https://doi.org/10.1016/B978-0-08-056033-5.00065-3.

[78] G.S. WAS, Fundamentals of Radiation Materials Science, Springer New York, New York, NY, 2017. https://doi.org/10.1007/978-1-4939-3438-6.

[79] S.I. Golubov, A. V. Barashev, R.E. Stoller, Radiation damage theory, 1st ed., Elsevier Inc., 2012. https://doi.org/10.1016/B978-0-08-056033-5.00029-X.

[80] G.F. Knoll, Radiation Detection and Measurement, Wiley, 2010.

[81] M. Nastar, F. Soisson, Radiation-induced segregation, Elsevier Inc., 2012. https://doi.org/10.1016/B978-0-08-056033-5.00035-5.

[82] G.S. Was, S.M. Bruemmer, Effects of irradiation on intergranular stress corrosion cracking, J. Nucl. Mater. 216 (1994) 326–347. https://doi.org/10.1016/0022-3115(94)90019-1.

[83] S.J. Zinkle, Radiation-induced effects on microstructure, Elsevier Inc., 2012. https://doi.org/10.1016/B978-0-08-056033-5.00003-3.

[84] B. Pastina, J.A. LaVerne, Effect of Molecular Hydrogen on Hydrogen Peroxide in Water Radiolysis, J. Phys. Chem. A. 105 (2001) 9316–9322. https://doi.org/10.1021/jp012245j.

[85] B. Pastina, J.A. LaVerne, Hydrogen peroxide production in the radiolysis of water with heavy ions, J. Phys. Chem. A. 103 (1999) 1592–1597. https://doi.org/10.1021/jp984433o.

[86] B. Pastina, J. Isabey, B. Hickel, The influence of water chemistry on the radiolysis of the primary coolant water in pressurized water reactors, J. Nucl. Mater. 264 (1999) 309–318. https://doi.org/10.1016/S0022-3115(98)00494-2.

[87] B. Muzeau, S. Perrin, C. Corbel, D. Simon, D. Feron, Electrochemical behaviour of stainless steel in PWR primary coolant conditions: Effects of radiolysis, J. Nucl. Mater. 419 (2011) 241–247. https://doi.org/10.1016/j.jnucmat.2011.08.051.

[88] P. Deng, Q. Peng, E.-H. Han, W. Ke, C. Sun, Z. Jiao, Effect of irradiation on corrosion of 304 nuclear grade stainless steel in simulated PWR primary water, Corros. Sci. 127 (2017) 91–100. https://doi.org/10.1016/j.corsci.2017.08.010.

[89] T. Fukumura, K. Fukuya, K. Fujii, T. Miura, Y. Kitsunai, Grain boundary oxidation of neutron irradiated stainless steels in simulated pwr water, in: J.H. Jackson, D. Paraventi, M. Wright (Eds.), Miner. Met. Mater. Ser., Springer, Portland, Oregon, USA, 2019: pp. 2153–2163. https://doi.org/10.1007/978-3-030-04639-2_144.

[90] R.C. Asher, D. Davies, T.B.A. Kirstein, P.A.J. McCullen, J.F. White, The effects of radiation on the corrosion of some Zr alloys, Corros. Sci. 10 (1970) 695–707. https://doi.org/10.1016/S0010-938X(70)80041-5.

[91] R.C. Asher, D. Davies, T.B.A. Kirstein, The corrosion of some zirconium alloys under radiation in moist carbon dioxide-air mixtures, J. Nucl. Mater. 49 (1973) 189–196. https://doi.org/10.1016/0022-3115(73)90007-X.

[92] M. Vankeerberghen, R.W. Bosch, R. Van Nieuwenhoven, In-pile electrochemical measurements on AISI 316 L(N) IG and EUROFER 97 - I: Experimental results, J. Nucl. Mater. 312 (2003) 191–198. https://doi.org/10.1016/S0022-3115(02)01594-5.

[93] R.W. Bosch, M. Wéber, M. Vankeerberghen, In-pile electrochemical measurements on AISI 304 and AISI 306 in PWR conditions - Experimental results, J. Nucl. Mater. 360 (2007) 304–314. https://doi.org/10.1016/j.jnucmat.2006.11.002.

[94] K. Daub, X. Zhang, J.J. Noël, J.C. Wren, Effects of γ-radiation versus H2O2 on carbon steel corrosion, Electrochim. Acta. 55 (2010) 2767–2776. https://doi.org/10.1016/j.electacta.2009.12.028.

[95] K. Daub, X. Zhang, J.J. Noël, J.C. Wren, Gamma-radiation-induced corrosion of carbon steel in neutral and mildly basic water at 150°C, Corros. Sci. 53 (2011) 11–16. https://doi.org/10.1016/j.corsci.2010.09.048.

[96] M. Kawaguchi, K. Ishigure, N. Fujita, K. Oshima, Effect of Radiation on Release of Corrosion Products in High Temperature Aqueous System, Radiat. Phys. Chem. 18 (1981) 733–740.

[97] K. Ishigure, H. Ikuse, K. Oshima, N. Fujita, S. Ono, The effect of radiation on the release of corrosion products from 304 stainless steel in high temperature water—II, Radiat. Phys. Chem. 21 (1983) 281–287. https://doi.org/10.1016/0146-5724(83)90156-5.

[98] M.. B. Lewis, J.. D. Hunn, Investigations of ion radiation effects at metal/liquid interfaces, J. Nucl. Mater. 265 (1999) 325–330. https://doi.org/10.1016/S0022-3115(98)00885-X.

[99] S. Lapuerta, N. Moncoffre, N. Millard-Pinard, E. Mendes, C. Corbel, D. Crusset, Use of ion beam analysis techniques to characterise iron corrosion under water radiolysis, Nucl. Instruments Methods Phys. Res. Sect. B Beam Interact. with Mater. Atoms. 240 (2005) 288–292. https://doi.org/10.1016/j.nimb.2005.06.131.

[100] S. Lapuerta, N. Millard-Pinard, N. Moncoffre, N. Bérerd, H. Jaffrezic, G. Brunel, D. Crusset, T. Mennecart, Origin of the hydrogen involved in iron corrosion under irradiation, Surf. Coatings Technol. 201 (2007) 8197–8201. https://doi.org/10.1016/j.surfcoat.2006.01.094.

[101] M. Wang, S. Perrin, C. Corbel, D. Féron, Electrochemical behaviour of 316L stainless steel exposed to representative chemistry in pressurised water reactors under proton radiation, J. Electroanal. Chem. 737 (2015) 141–149. https://doi.org/10.1016/j.jelechem.2014.10.015.

[102] S.S. Raiman, P. Wang, Z. Jiao, G.S. Was, TEM Studies of the Oxidation of 316 Stainless Steel with In-Situ Proton Irradiation, Microsc. Microanal. 19 (2013) 1734–1735. https://doi.org/10.1017/s1431927613010660.

[103] S.S. Raiman, Irradiation Accelerated Corrosion of 316L Stainless Steel in Simulated Primary Water, University of Michigan, 2016.

[104] S.S. Raiman, G.S. Was, Accelerated corrosion and oxide dissolution in 316L stainless steel irradiated in situ in high temperature water, J. Nucl. Mater. 493 (2017) 207–218. https://doi.org/10.1016/j.jnucmat.2017.05.043.

[105] S.S. Raiman, A. Flick, O. Toader, P. Wang, N.A. Samad, Z. Jiao, G.S. Was, A facility for studying irradiation accelerated corrosion in high temperature water, J. Nucl. Mater. 451 (2014) 40–47. https://doi.org/10.1016/j.jnucmat.2014.03.022.

[106] R. Sander, Henry's Law Constants, in: P.J. Linstrom, W.G. Mallard (Eds.), NIST Chem. WebBook, NIST Stand. Ref. Database Number 69, National Institute of Standards and Technology, Gaithersburg MD, n.d. https://doi.org/10.18434/T4D303.

[107] A.J. Koning, D. Rochman, J.-C. Sublet, N. Dzysiuk, M. Fleming, S. van der Marck, TENDL: Complete Nuclear Data Library for Innovative Nuclear Science and Technology, Nucl. Data Sheets. 155 (2019) 1–55. https://doi.org/10.1016/j.nds.2019.01.002.

[108] J.F. Ziegler, M.D. Ziegler, J.P. Biersack, SRIM – The stopping and range of ions in matter (2010), Nucl. Instruments Methods Phys. Res. Sect. B Beam Interact. with Mater. Atoms. 268 (2010) 1818–1823. https://doi.org/10.1016/j.nimb.2010.02.091.

[109] 316/316L Stainless Steel, AK Steel. (n.d.). https://www.aksteel.com/sites/default/files/2018-01/316316L201706_2.pdf.

[110] 17-4 PH Stainless Steel, AK Steel. (n.d.). https://www.aksteel.com/sites/default/files/2018-01/174ph201706.pdf (accessed April 5, 2021).

[111] T. Wierzbicki, Deflections of Circular Plates, Massachusettes Inst. Technol. (2021). https://chem.libretexts.org/@go/page/21505 (accessed March 17, 2021).

[112] W.J. Choyke, J.N. Mcgruer, J.R. Townsend, J.A. Spitznagel, N.J. Doyle, F.J. Venskytis, Helium effects in ion-bombarded 304 stainless steel, J. Nucl. Mater. 85–86 (1979) 647–651. https://doi.org/10.1016/0022-3115(79)90333-7.

[113] R.D. Hanbury, G.S. Was, Oxide growth and dissolution on 316L stainless steel during irradiation in high temperature water, Corros. Sci. 157 (2019) 305–311. https://doi.org/10.1016/j.corsci.2019.06.006.

[114] F. Scenini, R.C. Newman, R.A. Cottis, R.J. Jacko, Alloy oxidation studies related to PWSCC, Proc. Twelfth Int. Conf. Environ. Degrad. Mater. Nucl. Power Syst. React. (2005) 891–902.

[115] F. Scenini, R.C. Newman, R.A. Cottis, R.J. Jacko, Effect of surface preparation on intergranular stress corrosion cracking of Alloy 600 in hydrogenated steam, Corrosion. 64 (2008) 824–835. https://doi.org/10.5006/1.3279916.

[116] J.-O. Andersson, T. Helander, L. Höglund, P. Shi, B. Sundman, Thermo-Calc & DICTRA, computational tools for materials science, Calphad. 26 (2002) 273–312. https://doi.org/10.1016/S0364-5916(02)00037-8.

[117] T. Ohta, ed., DIRECT THERMAL DECOMPOSITION OF WATER, in: Solar-Hydrogen Energy Syst., Elsevier, 1979: pp. 59–79. https://doi.org/10.1016/B978-0-08-022713-9.50010-0.

[118] G. Cliff, G.W. Lorimer, The quantitative analysis of thin specimens, J. Microsc. 103 (1975) 203–207. https://doi.org/10.1111/j.1365-2818.1975.tb03895.x.

[119] L. Tomlinson, N.J. Cory, Hydrogen emission during the steam oxidation of ferritic steels: Kinetics and mechanism, Corros. Sci. 29 (1989) 939–965. https://doi.org/10.1016/0010-938X(89)90086-3.

[120] R. Dieckmann, Solution and transport of water in oxides, Mater. High Temp. 22 (2005) 93–103. https://doi.org/10.1179/mht.2005.011.

[121] M. Nakai, K. Nagai, Y. Murata, M. Morinaga, S. Matsuda, M. Kanno, Correlation of high-temperature steam oxidation with hydrogen dissolution in pure iron and ternary high-chromium ferritic steel, ISIJ Int. 45 (2005) 1066–1072. https://doi.org/10.2355/isijinternational.45.1066.